Magnetic Materials Based on Coordination Chemistry:

From Switching Molecules to Multifunctional Magnets

VNIVERSITAT DE VALÈNCIA

Instituto de Ciencia Molecular

****

Mario Palacios Corella

Thesis submitted for the degree of Doctor in

Nanoscience and Nanotechnology

****

Supervised by:

Dr. Miguel Clemente León Prof. Eugenio Coronado Miralles

January 2021

Los profesores Eugenio Coronado Miralles y Miguel Clemente-León, investigadores del Instituto de Ciencia Molecular (ICMol) de la Universidad de Valencia.

CERTIFICAN

Que Mario Palacios Corella ha realizado la presente Tesis Doctoral, titulada: *"Magnetic Materials Based on Coordination Chemistry: From Switching Molecules to Multifunctional Magnets"* bajo su dirección en el Instituto de Ciencia Molecular (ICMol), autorizando mediante este escrito la presentación de la misma para optar al grado de Doctor en Nanociencia y Nanotecnología por la Universidad de Valencia.

En Paterna, el 18 de enero de 2021

Miguel Clemente León Eugenio Coronado Miralles

A Nuka.
Per mostrar-nos amor incondicional.
Allà on estigues espere que sigues tant feliç com tu ens vas fer a nosaltres.
Et trobem a faltar cada dia de la nostra vida.

"Sit down there kid and don't disturb
Búscate una chica que te cuide y que te deje pensar"
Ramos y Soukin "*never know*" 2013

"Por lo que buscas, por lo que encuentras
Por el calor de su cama, por estas letras
Por mi familia que me cubre las espaldas
Por la humildad de compartir todo lo que tengas"
Suite Soprano "*por los siglos*" 2012

"Mantente atento a quien te fía
Casi todos sobreactúan
Ojo a quien te ríe la gracia
y diente al que te hace la púa"
Charlie "*Un mundo de ocio*" 2010

"Vivimos en un mundo enfermo el cual muere por dentro
Aquí cualquiera se cree Dios, pero ni Dios es para tanto, y punto"
Chaman y Charlie "De ayer a Hoy" 2012

Acknowledgments

I aquí aplega la fi d'un altre dels capitols de la meva vida, possiblement un dels més interesants i bonics que he pogut disfrutar. Vagi per davant que espere no oblidar-me de ningú, però si succeeix, ho senc.

First of all, I would like to thank my directors Eugenio and Miguel, both of them made this work possible by giving me the financial support and teaching me, without them none of this would have been possible. My whole evolution during this last years is a consequence of what they have taught me. Again, thanks.

I would also like to acknowledge the senior researchers of the ICMol, for their comments during my presentations in the group meetings, and all the research staff: Jose, Gloria, Chema and specially Ángel, with whom I have shared amazing times in synchrotron facilities and who I consider a very good friend of mine. Also, to my office mates Laura and Lidón and the coffee guest, Dani, who showed me where Saturn or Jupiter are in the sky (I don't remember which one, nor where). To my not so far away lab colleagues Miguel G., Samuel, Katia, Ivan, Roger, Isaac, Vero, Garin, Marc and Manel, who obtained a much-deserved position in Portugal.

Secondly, my friends in the lab: Victor, my tireless hood mate, with whom I had the pleasure to share the working space, and who I am certain will be a great scientist when his shining time comes; Belén, Ana, Carmen, Alejandro, Nestor, Eugenia, Luis, thanks for all the parties, coffees and favors that we shared. I could not forget to mention my best friends of "el club del pepino": Ramón, Miguel, Jesús, Jorge, Javi C. and Javi L.; these last two are among the best people I have ever met in my life, they offered me their beds and couches several times to sleep overnight during our countless parties

and drinking sessions without thinking it twice, even when they didn't know me. Thanks for being there. One of them owes me a visit to Alton Towers, I won't say which one. To all these people I wish the best in their future, whether it is in research or outside of it.

This paragraph is dedicated to my online friends: PoWaLoLa, and Culoman (A.K.A chuspi, A.K.A Froruto, A.K.A Bigchochete, A.K.A BigCho). Thanks for all the afternoons we shared in the countless servers we visited. Here I should also include the latest acquisitions: Jorge and Javi. L, but they were just too bad at any game we played that I could not put them here.

My next acknowledgments are dedicated to the people that helped me to see a different future in research, people who showed me a different way of making science and treated me like a friend. I am talking about Salvador Pané and Josep Puigmartí, probably the best researchers I had the chance to collaborate with. The opportunity they gave me in 2019 cannot be overlooked simply because I feel that it changed my life forever. I have no words to describe how much I feel I am in debt with you guys. Thanks.
I can't forget in these lines Carlos Franco and Anastasia, my closest people in Zürich, with whom I shared many moments in the labs and helped me with characterization and synthetic problems. Carlos, you are going to be an amazing father and one day science will repay you what it owes you. Good luck guys.

These last paragraphs are about my people, my family.
María, my love, partner and caretaker. I cannot express with words how boring my life was before our paths collided. You have showed me new ways to enjoy life, people and moments, thanks for being there, anytime, anywhere. We still have many places (and theme parks) to visit, together.

My brother Adrian, who already got the future he deserves after working as hard as it can get, my mirror my entire life. It's been a long time since I looked in the mirror and it's not going so bad. Brother, thanks.
Sagrario, my brother's wife, who takes care of what I appreciate the most and makes him happy. Nothing more valuable than that. Thanks again.

Ricardo and Verónica, my parents. I cannot describe how I feel while I write these lines. They did the possible and the impossible to make sure that me and my brother had the best possible future. Humble and hard-working taught me that I am the only one putting a rooftop to my dreams. I will certainly not put one. I Love you mom and dad. Saying thanks means nothing here, that word is too little compared to what you deserve.

Abreviations

0D	Zero-dimensional
1D	One-dimensional
1-bpp	2,6-bispyrazol-1-yl pyridine
2D	Two-dimensional
3-bpp	2,6-bispyrazol-3-yl pyridine
3-D	3-dimensional
bppCOOH	2,6-bis(pyrazol-1-yl)pyridine-4-carboxylic acid
bppCOOEt	2,6-bis(1*H*-pyrazol-1-yl)isonicotinate
Br_2An^{2-}	Bromanilate
Cl_2An^{2-}	Chloranilate
CP	Coordination polymer
dbhq	Dihidroxybenzoquinone
DMF	Dimethylformamide
DFT	Density functional theory
EDX	Energy dispersive X-ray spectroscopy
EtOH	Ethanol
EPR	Electron paramagnetic resonance
F_2An	Fluoranilate
HS	High-spin
ICP-MS	Inductively Couple Plasma - Mass Spectrometry
K_B	Boltzmann constant
LIESST	Light-Induced Excited Spin-State Trapping
LS	Low-spin
MeOH	Methanol
MeCN	Acetonitrile
Me_2CO	Acetone
MLCT	Metal-ligand charge transfer

MOF	Metal-organic framework
NMR	Nuclear magnetic resonance
ox	Oxalate
POM	Polyoxometalate
PXRD	Powder X-ray diffraction
RH	Relative humidity
SAM	Self-assembled monolayer
SCO	Spin-crossover
SEM	Scanning electron microscopy
SMM	Single-molecule magnet
SIM	Single-ion magnet
T_c	Curie tempertature
TBA	Tetrabuthylammonium
TEM	Transmission electron microscopy
TGA	Thermogravimetric analysis
UV-VIS	Ultraviolet-visible
χ_M	Molar magnetic susceptibility

Table of Contents

Chapter 1.

Introduction

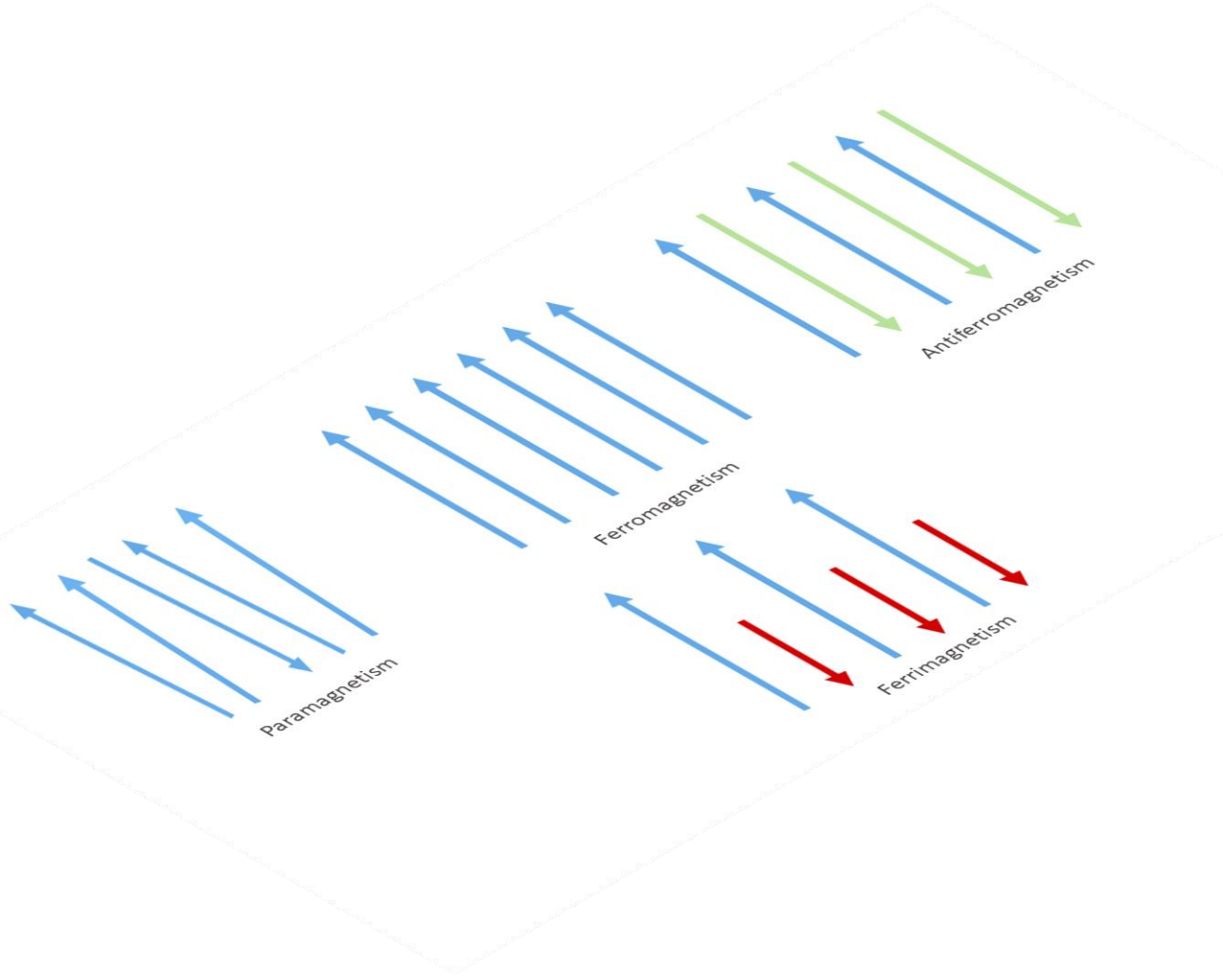

1. Introduction

The design of multifunctional molecular materials can be considered as one of the best ways to define men finality: create materials that make life easier. Among these, coordination polymers (CPs) are one of the most recurrent examples in all fields: magnetism[1], electronics[2], gas uptake[3], drug release[4], etc. The main topic of this thesis englobes multifunctional magnetic molecular materials, in other words, materials whose main property is the magnetism, in this particular case accompanied by a secondary subunit that provides another property to the material.

Every-day (conventional) magnets are inorganic solids whose compositions are usually mixtures of rare earth and metal oxides[5] and show spontaneous magnetization above room temperature. Typically, in these materials, the existence of metal-metal bonds or short mono/di atomic ligands facilitate the long-range magnetic ordering of the material through the efficient communication of the spins of the metal centers[6]. These materials, although they perform an excellent job at room and high temperatures, lack predictability through the design.

In this sense, molecular based magnets are a challenging and an emerging class of materials since the last decades of the past century. The possibility to design them chemically and tune their properties through the building units that integrate their structure makes them promising candidates to compete with conventional magnets and find new applications[7,8]. For instance, their processability and low density may enable their application as lightweight permanent magnets for electrical devices and energy technologies. Although this kind of materials have potential applications in many fields, they endure low magnetic ordering temperatures[9], which prevents them from being used in real life applications. One of the main interests in this research field involves the design and synthesis of materials showing stronger magnetic

interactions, thus affording higher ordering temperature materials. An additional advantage of molecular-based magnets is that their chemical versatility may give rise to fascinating multifunctional properties, including coexistence of long-range magnetic order with other properties, which are difficult or impossible to attaint with conventional magnets. This approach has been a source of new properties and physical phenomena, which are interesting from a fundamental point of view and could afford new applications. Finally, another advantage of such materials is that their preparation and processing can be done at low temperatures[10], allowing building devices at a very low cost.

In this thesis we took advantage of a bottom-up approach, where molecular building blocks are assembled to form functional networks. When this approach is used, the final product can be a "two-network material", in which each network exhibits its own property. If these two networks are strongly coupled the result may be a stimuli responsive material[8]. To design these multifunctional materials we have used two approaches:

The first strategy consists in an ionic approach, where an anionic network, which affords magnetic order to the material, was mixed with one functional cation, which affords a second property to the material (proton conductivity and single ion magnet behavior, chapters 2 and 3). Thus, a neutral two-network material with coexistence of the properties of the two networks is obtained.

The second strategy is a covalent approach, in which the two subnetworks are linked covalently. In this case, polynuclear Fe(II) complexes of the well-known spin crossover ligand 2,6-bispyrazol-1-yl pyridine (1-bpp) were prepared and functionalized covalently with a second component, which provides a second property to the system. Using this approach, we took advantage of the luminescent properties of a 1-bpp functionalized fullerene in a charged polynuclear complex to characterize it in solution and solid state

(chapter 4) and we studied the switching properties of the spin crossover unit with the redox properties of a polyoxometalate (chapter 5) in a 1D neutral polymeric network.

2. Multifunctional Extended Networks Based on Oxalate and Anilate Ligands

Most of the reported magnets based on CPs are comprised of paramagnetic metal centers bridged by diamagnetic ligands. In these materials, magnetic interactions between metal centers occur via a superexchange coupling mechanism[9]. Interestingly, some of these CPs exhibit also porosity, giving rise to the so-called magnetic metal-organic frameworks (MOFs). In this thesis, we have used two types of anionic magnetic extended networks with bis(bidentate) diamagnetic ligands: the oxalate and the anilate-based networks (see scheme 1). The preparation of these magnetic materials, combined with functional cations in order to provide a second property to the final material, has been the focus of this research.

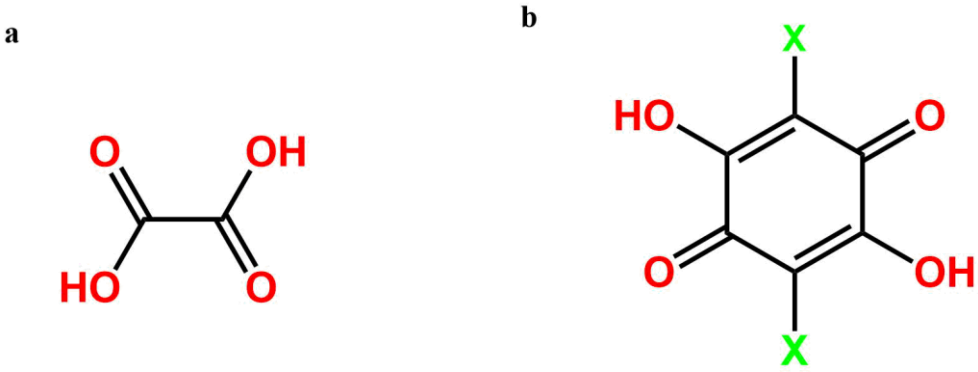

Scheme 1. Oxalic acid (a) and dihidroxybenzoquinone (b) derivatives (X= H, Cl, Br, I, CN)

2.1 Oxalate Based Hybrid Magnetic Networks

Bimetallic oxalate magnetic networks are one of the oldest and most used examples in the building of molecular hybrid magnetic materials. Most of the oxalate-based molecular magnets described till this date have been obtained by following the classical "*bimetallic approach*". This synthetic strategy involves a molecular building block, the homoleptic $[M^{III}(ox)_3]^{3-}$ (M^{III} = Cr, Fe, Ru, Rh, Mn and V) tris-oxalate metalate octahedral complex, used as a ligand towards divalent metal cations (M^{II}). This combination results in the formation of low-dimensional negatively charged complexes, which remain in solution due to their anionic nature. In a second step, the addition of a bulky organic cation, i.e. $[XR_4]^+$, forces the self-assembly of the charged moieties resulting in the precipitation of non-soluble CPs. The first example was reported by Okawa in the beginning of the 90s, with the synthesis of a family of 2D layered honeycomb-like magnets with general formula: $[XR_4][M^{II}Cr^{III}(ox)_3]$ ($XR_4^+ = NBu_4^+$; M^{II} = Mn, Fe, Co, Ni, Cu, Zn) (see figure 1), which presented ferromagnetic ordering with T_c ranging from 6 to 12 K[11] (Curie Temperature "T_C" = critical temperature in a ferromagnet). Soon after this discovery, the use of the Fe (III), Ru (IIII), V(III) and Mn(III) derivatives yielded analogous layered molecular magnets showing ferro-, ferri- and weak ferromagnetic ordering with critical temperatures of up to 45 K.[12–17] It is very important to remark that the cation and solvents used during the synthetic procedure have a very high impact in the dimensionality of the final structure of the magnetic network. 2D is not the only dimensionality that one can reach. 0D to 3D oxalate networks can be obtained through the proper design and choice of the cation used to template the crystalline structure. This point is well exemplified in a family of materials in which the substitution of templating cations of the type $[XR_4]^+$ with chiral metal complexes, such as $[Z^{II}(bpy)_3]^{2+}$ (Z^{II} = Fe^{II}, Co^{II}, Ni^{II}, or Ru^{II}; bpy = 2,2'-bipyridine), induce the spontaneous resolution of 3D chiral lattices of general formulas $[Z(bpy)_3]_X[MM'(ox)_3]$[18,19,20,21], $[Ru(ppy)(bpy)_2][MM'(ox)_3]$[22],

and $[Ir(ppy)_2(bpy)][MM'(ox)_3]$[23] (Z = Ru^{II}, Fe^{II}, Co^{II} and Ni^{II}; X = ClO_4^-, BF_4^-, PF_6^-; M, M' = Li^I, Na^I, Mn^{II}, Ni^{II}, Co^{II}, Fe^{II}, Cu^{II}, Zn^{II}, Rh^{III}, Co^{III}, Cr^{III} and Fe^{III}; ppy = 2-phenylpyridine) (see figure 1).

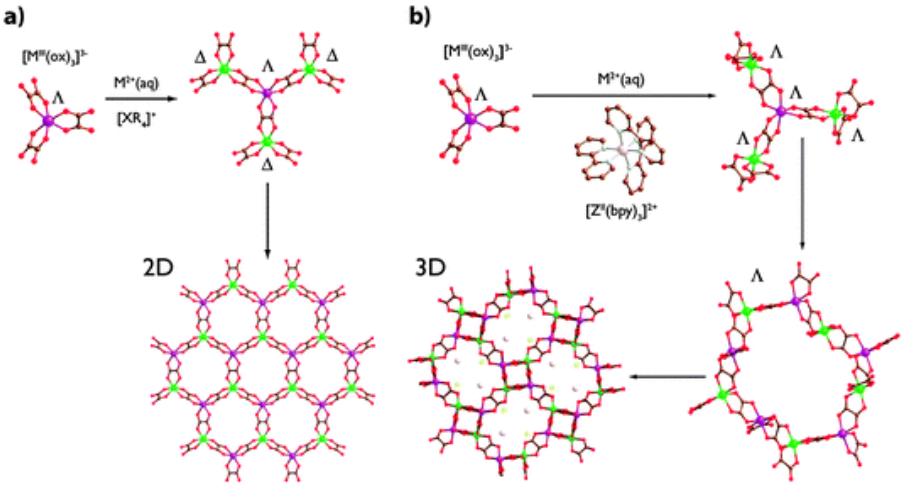

Figure 1. Different templating cations used to obtain 2D oxalate based layered materials (a) and 3D achiral extended networks (b).[17]

This increase in dimensionality can be understood by the chirality of the bimetallic network. Metallic centers exhibit an alternated chirality in 2D systems while, in contrast, 3D CPs are usually composed of homochiral units as a result of the intrinsic D_3 symmetry of the templating complexes, which force the $[M^{III}(ox)_3]^{3-}$ building blocks to adopt an homochiral configuration ($\Delta\Delta$ or $\Lambda\Lambda$). Geometrically, the existence of only one diasteroisomer building-block avoids the possibility of growing along the plane, forcing the system to grow in the three dimensions. From a magnetic point of view, these compounds behave as ferro- and ferrimagnets with lower critical temperatures than their 2D analogues. Taking into account that the magnetic connectivity is mainly the same despite the higher dimensionality, this change can be explained on the basis of the weaker magnetic exchange mediated by the longer metal-to-metal distances and the different relative orientation of the magnetic orbitals[24]. Finally, a different type of 3D oxalate-based

network containing metals of both chiralities is obtained when less symmetric templating cations are used. This type of achiral 3D network has been obtained in compounds of formula $[Fe^{II}(bpp)_2][MnCr(ox)_3]_2 \cdot bpp \cdot CH_3OH$ (bpp = 2,6(bis(pyrazol-3-yl)pyridine)[25], $[Z^{III}(sal_2\text{-trien})][Mn^{II}Cr^{III}(ox)_3] \cdot solv$ (Z = Fe, In)[26], $[Fe^{III}(5\text{-}CH_3Osal_2\text{-trien})][Mn^{II}Cr^{III}(ox)_3]$[27] or $[Mn^{III}(salen)(H_2O)]_2[Mn^{II}Cr^{III}(ox)_3]_2 \cdot (CH_3OH) \cdot (CH_3CN)_2$[28] (see figure 2).

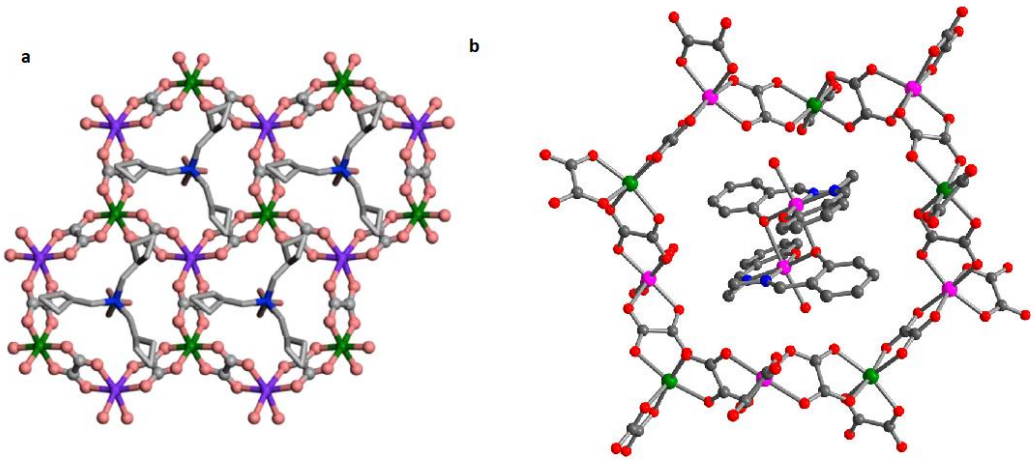

Figure 2. 2D layered oxalate network with $\{NBu_3(CH_2COOH)\}^+$ cation inserted (a)[47] and 3D heterometallic oxalate network with single molecule magnet $[Mn^{III}(salen)(H_2O)]^+$ cation inserted (b)[9]

Furthermore, these negatively charged frameworks have been combined with functional molecular cations in order to afford hybrid salts that show two different physical properties. An important example of chemically designed multifunctionality was provided by hybrid materials combining ferromagnetism with metal-like conductivity by intercalation of the organic π donor bis(ethylenedithio)tetrafulvalene (BEDT-TTF) into the bi- metallic anionic oxalate network $[Mn^{II}Cr^{III}(ox)_3]^-$. This compound with a ferromagnetic behavior (T_c = 5.5 K) showed metallic conductivity down to at least 0.3 K.[1] Other properties that have been introduced alongside magnetism are paramagnetism[29–32], spin crossover

properties[25–27,33–37], electrical properties[38–40], photochromism[41,42], proton conductivity[43–49], ferroelectricity[50,51] and fluorescence[52] amongst many others. Most of these examples are based on 2D honeycomb networks, which have led to unusual combination of properties. However, compounds demonstrating synergy between the properties of the two subnetworks are scarce and have mostly been obtained with 3D networks. Indeed, chiral 3D oxalate frameworks were the first examples of 3D molecule-based magnets displaying optical activity.[53] In addition to this, 2D oxalate-based ferromagnets with methyl-(1-methylpropyl)di(*n*-propyl)ammonium cations $[N(CH_3)(n\text{-}C_3H_7)_2(s\text{-}C_4H_9)]^+$ were the first enantiopure single crystals of a molecule-based ferromagnet showing magneto-chiral dichroism[54]. Another interesting example of synergy between the properties of the two subnetworks is a 3D achiral oxalate-based magnet with an inserted single molecule magnet[28], which will be described in section 2.3.

2.2 Anilate Based Hybrid Magnetic Networks

After oxalate linkers proved to be a reliable source to furnish magnets with predictable structures and relatively high ordering temperatures, researchers explored the use of similar bis(bidentate) bridging ligands[9]. Of particular interest are 2,5-Dihydroxy-1,4-benzoquinone and its derivatives with formula $C_6O_4X_2$ (X= H, Cl, Br, I or CN) (see schemes 1b and 2), which show similar coordination modes to those of the oxalate (see scheme 1a) but, at the same time, offer important improvements such as: (i) they are easier to modify or functionalize than the oxalates by changing the X group; (ii) despite the long distance between metal centers, the conjugated system can provide an effective pathway for magnetic exchange interactions with higher magnetic ordering temperatures than the oxalate-based compounds; (iii) their bigger size may give rise to porous compounds; (iv) they can be readily accessed in three redox states (−2, −3•, and −4) (see scheme 2). All of this demonstrates a high degree of chemical tunability that endows this family of ligands

as a promising source of magnetic materials with predictable structures and properties.

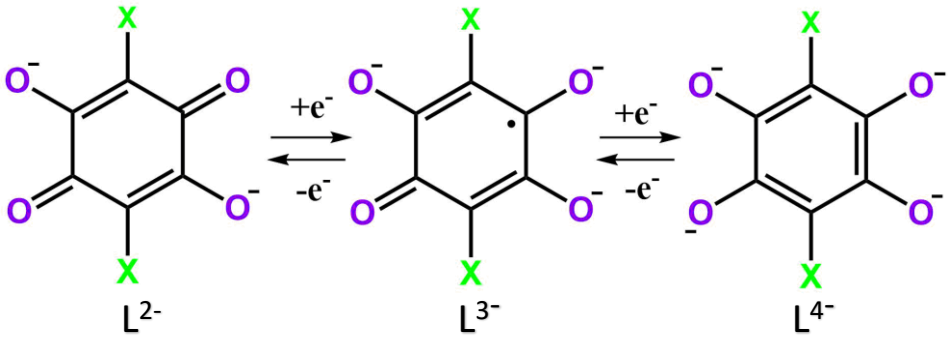

Scheme 2. Accessible redox states of deprotonated benzoquinoid ligands with different substituents.

Anilate-based ligands give rise to homo- and heterometallic 1D, 2D, and 3D CPs of diverse structure types[55,56]. Similarly to the oxalate networks, the anilate based CPs are comprised of octahedral metal centers that are tris-chelated by bis-(bidentate) benzoquinoid ligands and their absolute configurations is what dictates the topology of the network. Thus, a 2D honeycomb lattice is formed when neighboring metal centers show opposing chirality (Δ or Λ). On the other hand, a 3D network of (10,3)-*a* topology can be obtained when all of the metal centers adopt the same absolute configuration. Due to the larger nature of benzoquinoid ligands with respect to oxalate linkers, this type of 3D structure features two interpenetrated (10,3)-*a* nets of opposing chirality, which results in achiral compounds[57,58]. The bridging ability and the coordination modes of benzoquinoid ligands was first reported by Kitagawa and Kawata[59].

The first examples of 2D homometallic networks of 2,5-chloro-1,4-benzoquinone (Cl_2An) contained divalent[60] centers $[M^{II}_2(Cl_2An)^3]^{2-}$ (M^{II}=Co, Cu, Cd and Zn) or trivalent[55,61,62] centers $[[M^{III}_2(Cl_2An)_3]$ (M^{III}=Sc, Y, La, Pr, Nd, Gd, Tb, Yb, Lu). The anionic nature of the homometallic divalent network required of the cationic species $[(H_3O)_2(phz)_3]^{2+}$(phz= phenazine) to give rise to the final 2D CP of

formulae $[(H_3O)_2(phz)_3][M^{II}_2(Cl_2An)_3]\cdot G$ (M^{II}=Co, Cu, Cd and Zn; G=solvent molecules.) Homometallic interpenetrated 3D compounds with (10,3)-*a* topology of formula $[NBu_4]_2[M^{II}_2(dhbq)_3]$ (M^{II} = Mn, Fe, Ni, Co, Zn and Cd; $dhbq^{2-}$ = 2,5-Dihydroxy-1,4-benzoquinone) were reported afterwards[57] (see figure 3). Magnetic properties reported for the 2D homometallic compounds $[(H_3O)_2(phz)_3][M^{II}_2(Cl_2An)_3]$ (M^{II}=Cu, Mn and Fe) are dominated by weak antiferromagnetic interactions in the case of the Cu[60] and Mn derivative and ferromagnetic behavior in the case of the Fe derivative due to mixed valence Fe^{2+}/Fe^{3+} state.[63]

Our group in collaboration with the group of Prof. M. L. Mercuri was responsible for the discovery of the first 2D heterometallic magnetic lattices with honeycomb crystalline structure and formulae $A[M^{II}M^{III}(X_2An)_3]\cdot solv$ (A = $[(H_3O)(phz)_3]^+$ or (NBu_4^+); M^{II} = Mn, Fe; M^{III} = Cr, Fe; X = H, Cl, Br, I; solv = H_2O or $(CH_3)_2CO$))[64]. They showed ferrimagnetic long-range order, but the most interesting feature of this family is the tunability of the critical temperature depending on the nature of the X substituents. Thus, as an example, an increase in T_c from ca. 5.5 to 6.3, 8.2, and 11.0 K (for X = Cl, Br, I, and H, respectively) is observed in the MnCr derivatives.

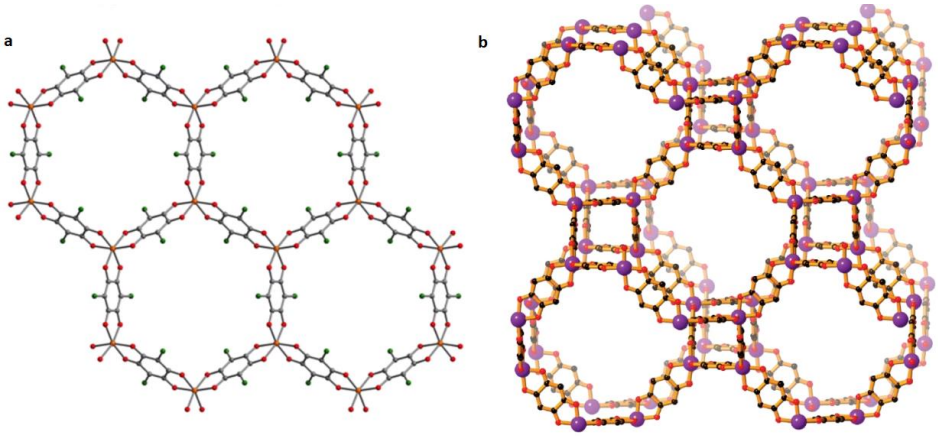

Figure 3. 2D layered homometallic anilate based network (a)[69] and 3D homometallic $[Fe^{II}_2(dhbq)_3]^{2-}$ network with (10,3)-a topology (b).[57]

In line with earlier studies with bimetallic oxalates, spin-crossover cations such as $[Fe^{III}(sal_2\text{-trien})]^+$ and $[Fe^{III}(acac_2\text{-trien})]^+$ were used by our group to prepare bimetallic 2D anilate-based compounds but, in contrast to the oxalate-based compounds, the inserted complexes remained in the low- or high-spin states in all range of temperatures and coexistence of properties was not achieved[65]. The reduction of size of $[Fe^{III}(acac_2\text{-trien})]^+$ with respect to $[Fe^{III}(sal_2\text{-trien})]^+$ afforded a new type of structure in which the charge-compensating cations were placed inside the hexagonal channels of the 2D network, instead of being inserted in the interlamellar spacing as in the previous oxalate and anilate 2D networks. Showing a similar behavior to that of the graphene, these layered materials could be mechanically exfoliated down to atomically-thin layers with heights down to 2 nm by using the well-known Scotch tape method.[10]

In addition to the heterobimetallic $Mn^{II}Cr^{III}$ and $Mn^{II}Fe^{III}$ 2D benzoquinoid frameworks, homometallic mixed-valence $Fe^{II}Fe^{III}$ frameworks have also been recently reported in the compounds $[(H_3O)(H_2O)(phz)_3][Fe^{II}Fe^{III}(X_2An)_3]\cdot 12H_2O$ and $(tag)\text{-}[Fe^{II}Fe^{III}(ClCNAn)_3]\cdot 29H_2O$ (X = Cl, Br; tag^+ = triaminoguanidinium)[66,67]. Compared to those of the $Mn^{II}Cr^{III}$ anilate-based frameworks with similar cations, the ordering temperatures for the $Fe^{II}Fe^{III}$ derivatives

(T_cs = 2.1–4 K) are much lower[64]. Interestingly, they exhibit electrical conductivities that are much higher than those of analogous oxalato-bridged compounds[68], owing to their greater effectiveness in promoting electron delocalization through a small-polaron hopping mechanism.[67]

The most interesting results of this family of ligands have been obtained by reducing the anilate ligands affording extraordinarily high magnetic ordering temperatures and electrical conductivities. The compound $(Me_2NH_2)_2[Fe^{III}_2L_3]\cdot 2H_2O\cdot 6DMF$ was the first example of a structurally characterized extended solid with tetraoxolene radical linkers[69]. The structure of this compound is formed by eclipsed 2D honeycomb layers, with each Fe center ligated by three bis(bidentate) chloranilate ligands. The charge of the dianionic network is compensated by $(Me_2NH_2)^+$ ions located in the hexagonal channels formed by the eclipsed layers. Electron transfer occurred spontaneously from the Fe^{II} starting material to Cl_2An^{2-} during the synthesis to provide a framework formulated as $[Fe^{III}_2(Cl_2An^{8/3-})_3]^{2-}$. Magnetic studies revealed a T_c = 80 K. The desolvated compound also displays ferrimagnetic behavior, albeit with a lower ordering temperature of T_c = 26 K, attributed to structural distortions of the framework. Accordingly, this magnet is one of the few metal–organic compounds that display reversible solvent-induced switching of magnetic ordering temperature. Interestingly, the material exhibits room temperature electrical conductivity values of $\sigma = 1.4(7) \times 10^{-2}$ for the solvated and $\sigma = 1.0(3) \times 10^{-3}$ S·cm^{-1} for the desolvated forms[70]. Two years later the same group reported the one electron reduction of this compound using cobaltocene ($[Co^{II}Cp_2]$) in a postsynthetic single-crystal-to-single-crystal process to afford the compound $[Co^{III}Cp_2]_{1.43}(Me_2NH_2)_{1.57}[Fe^{III}_2(Cl_2An^{3-\bullet})_3]\cdot 4.9DMF$, which features exclusively $Cl_2An^{3-\bullet}$ radical bridging ligands[70](see figure 4). The 2D honeycomb structure is preserved, and T_c increased to 105 K. However, the room-temperature electrical conductivity for the reduced compound was significantly less than that for the parent framework $\sigma = 5.1(3) \times 10^{-4}$ S. The origin in the decrease in

conductivity was hypothesized to arise from loss of ligand mixed valency. Other 2D compounds with similar structure were reported by Long et al. with Ti, V and Cr showing high electronic conductivities at room temperature (σ = 0.5 S·cm^{-1})[71]. In addition to this, Harris et al. have demonstrated the chemical versatility and tunability of this family of complexes by performing postsynthetic single-crystal-to-single-crystal exchanges of metal and ligands[72,73] and reduction of the 2D compound $(Me_4N)_2[Mn^{II}(Cl_2An)_3]$.[74]

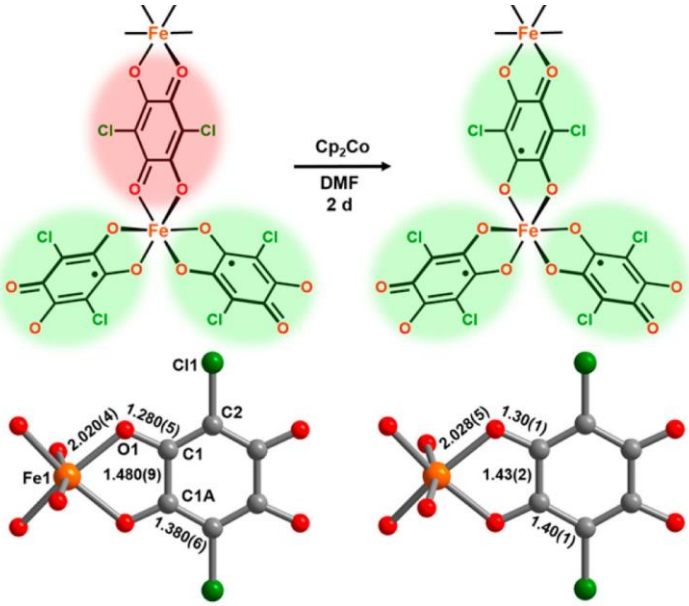

Figure 4. Portion of the $[Co^{III}Cp_2]_{1.43}(Me_2NH_2)_{1.57}[Fe^{III}_2(Cl_2An^{3-\bullet})_3]\cdot 4.9DM$ before (left) and after (right) reduction of the chloranilate ligand highlighting the change in the bond distances.[70]

Besides these 2D metal–semiquinoid magnets, 3D interpenetrated frameworks with similar compositions have been obtained by Long et al. in compound $(Bu_4N)_2[Fe^{III}_2(dhbq^{3-\bullet})_2(dhbq^{2-})]$. In contrast to the low magnetic ordering temperature (8 K), this compound exhibits the highest room-temperature electrical conductivity value of $\sigma = 1.6(1) \times 10^{-1}$ S·cm^{-1} reported for a 3D MOF[75]. The high conductivity was attributed to strong electronic correlation within

this material owing to the mixed-valence state of the quinoid linkers. Postsynthetic chemical reduction of this compound afforded the compound $Na_{0.9}(Bu_4N)_{1.8}[Fe^{III}_2(dhbq^{3-\bullet})_{2.7}(dhbq^{2-})_{0.3}]$, which exhibits a 3D structure nearly identical to that of the parent material and a slightly higher T_c of 12 K but a significantly lower room-temperature conductivity of $\sigma = 6.2(1) \times 10^{-3}$ S·cm^{-1} compared to those of the parent framework. These correlated changes in magnetic ordering temperature and electrical conductivity are similar with those observed for the 2D compounds prepared by Harris et al. Preparation of the fluoroderivatives of this semibenzoquinoids has been explored by D'Alessandro et al. who prepared $(NEt_4)_2[Fe_2(F_2An)_3]$, a 2D layered material with eclipsed configuration in the layers showing conductivity values of $\sigma = 1.8(1) \times 10^{-2}$ S·cm^{-1} at 300K[76]. Very recently, Long et al. have proposed the use of the $(H_2NMe_2)_2Fe_2(Cl_2An)_3$ and $(H_2NMe_2)_4Fe_3(Cl_2An)_3(SO_4)_2$ compounds as cathodes for batteries due to the high capacities showed from the materials, which go up to 195mAhg^{-1}.[77] Also, the preparation of $(NPr_4)_2[Fe_2(Cl_2An)_3]$, which possesses three charge ordered states: a low-temperature (LT) phase $[(Fe^{3+})_2(Cl_2An^{2-})(Cl_2An^{3-\bullet})_2]^{2-}$; an intermediate (IM) phase $[(Fe^{2.5+})_2(Cl_2An^{2-})(Cl_2An^{2.5-})_2]^{2-}$; and a high-temperature (HT) phase $[(Fe^{2+})_2(Cl_2An^{2-})_3]^{2-}$, has demonstrated that multiple switching system whose states can be reached varying the temperature can be obtained using the benzoquinoid ligand.[78]

The preparation of multifunctional compounds based on anilate ligands is an unexplored field, which has been the focus of the chapter 2 of this thesis inspired by work of Kitagawa et al. with the oxalate-based magnets showing proton conductivity (see section 2.4).

2.3 SMMs and SIMs and its Insertion into MOFs and Oxalate-Based CPs

A milestone in the field of molecular magnetism around the 90s was the discovery of Mn_{12},[79] (see figure 5) a zero-dimensional oxo-cluster that changed the perspective of how molecular magnetism had to be looked onto. Magnetically, at high temperatures it is a paramagnet with a very high ground spin value S=10. Magnetic measurements performed at very low temperatures showed an unusual magnetic behavior[80,81]. The system behaved like a small magnet showing slow relaxation of the magnetization below 4.5 K giving rise to the presence of a hysteretic behavior. Molecules that showed this behavior started to get called single-molecule magnets (SMMs). The origin of this magnetic behavior was attributed to the uniaxial magnetic anisotropy |D| and a very high ground spin state. Thus, for reversing the magnetization of these nanomagnets one needs to overcome an energy barrier, $U = |D| S^2$.

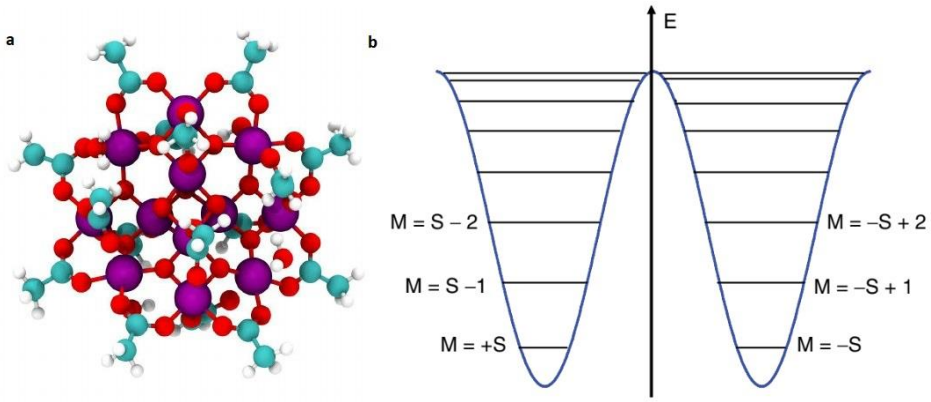

Figure 5. Ball and stick representation of the Mn_{12} compound (a)[82] and Magnetization values for the different spin levels (b), being $\pm S$ the ground state or lowest lying level and 0 the highest energy.

Interest in SMMs grew after the findings of Mn_{12} for their potential applications in high density data storage[83], quantum computing[84], and spintronics[85]. To approach these fascinating applications, long

relaxation times and high blocking temperatures (T_B) were required[86] and the scientific community tried to follow the same approach that had been used with the Mn_{12}: build polynuclear complexes with metals in high oxidation state. Much focus in molecular magnetism research was invested towards increasing the spin reversal barrier, U, the energy barrier for relaxation (where $U = |D|\,S^2$ for an integer spin, or $U = |D|(S^2 - \frac{1}{4})$ for half-integer spin). The quadratic dependence of U_{eff} on S motivated initial investigation into exchange-coupled transition metal clusters with large total spin. However, theoretical studies later showed that the anisotropy term D is inversely proportional to S^2, rendering U virtually invariant to S [87–89]. Some examples of this strategy were a family of Mn_6 cages[90] reported by E. K. Brechin et al. with an energy barrier of 60 cm^{-1}, [91] which is still a great achievement nowadays, and Fe_8 $[Fe_8O_2(OH)_{12}(tacn)_6]Br_8$ and Fe_4 $[Fe_4(OR)_6L_3]$ (R = Me, Et; L =β-diketonate) Fe^{III} SMMs[92].

These factors combined with the first report by Ishikawa and co-workers in 2003 of mononuclear lanthanide systems, $[Bu_4N][Pc_2Ln]$, (Pc = pthalocyanine; Ln = Tb, Dy) exhibiting slow relaxation of their magnetization[93], helped to shift focus away from polymetallic clusters to single-ion systems[94]. SMMs with a single paramagnetic ion started to be also known as single-ion magnets (SIM). The rapid development of SIMs verified the importance of the anisotropy controlling strategy. Some important results were the first polyoxometalates behaving as a SIM ($[LnW_{10}O_{36}]^{9-}$) reported by our group.[95] These systems were proposed to be excellent spin qubit candidates[96]. Very recently, the most remarkable results in lanthanide SIMs have been achieved with derivatives of dysprosium metallocenes. Independently Layfield et. al.[97] and Chilton et al.[98] described a sandwiched lanthanide with formula $[Dy(Cpttt)_2][B(C_6F_5)_4]$, with Cpttt = $\{C_5H_2tBu_3\text{-}1,2,4\}$ tBu = $C(CH_3)_3$ that showed thermal hysteresis up to 60 K. One year later, Layfield et. al, with a similar approach, described a compound with formula

[(Cp^{iPr5})Dy(Cp*)]$^{+}$ (Cp^{iPr5}, penta-iso-propylcyclopentadienyl; Cp*****, pentamethylcyclopentadienyl) increasing the temperature at which the compound showed hysteretic behavior up to 80 K[99](see figure 6). This significant advance has been possible thanks to the knowledge developed to understand the role of the vibration in the spin relaxation processes.[100]

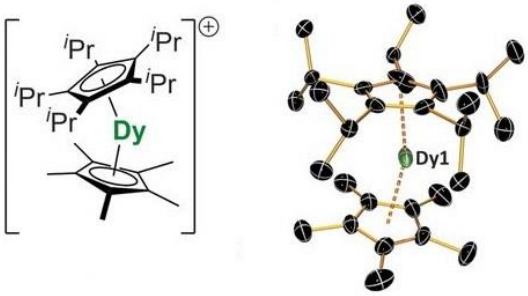

Figure 6. Chemical structure of [(Cp^{iPr5})Dy(Cp*)]$^{+}$.[97]

Transition metals are another major source for SIMs construction. In 2010 the first SIM containing a single metallic center from the first row of transition metals was reported by Long et. al. It was an Fe^{II} complex of formula [(tpa^{Mes})Fe]$^{-}$ (tpa^{Mes} = H_3tpa^{Mes} = tris[(5-mesityl-1H-pyrrol-2-yl)methyl]amine}) that displayed trigonal-pyramidal structure. The system showed slow relaxation of the magnetization when an external dc field was applied[101]. In this sense Co^{II} has proven to be a very reliable source for the building of SIMs thanks to its high ground spin level value (3/2) and the magnetic anisotropy. Long et al. reported the first Co^{2+} SIM in a tetrahedral environment with formula $[Co(SPh)_4]^{2-}$.[102] Freedman et al. reported a pseudotetahedral complex with formula $[Co(C_3S_5)_2]^{2-}$, this system was built of a nuclear spin free ligand and was reported to be one of the first Co^{II} spin qubits candidates[103]. Following these four coordinated Co complexes reports, J. Van Slageren et al. reported the complex $(HNEt_3)_2[Co^{II}(L^{2-})_2]$ (H_2L=1,2-bis(methanesulfonamido)benzene) which showed an energy barrier of 200 cm^{-1}.[104] This result is still considered a milestone in this field nowadays. A higher energy

barrier was observed in the complex [(sIPr)Co^{II}NDmp] (sIPr = 1,3-bis(2,6-diisopropylphenyl)-4,5- dihydro-imidazole-2-ylidene, Dmp = 2,6-dimesitylphenyl) which is one of the representatives with the highest energy barrier (413 cm^{-1}) among the TM-SIMs[105]. The first octahedral SIM Co^{II} complex was reported by M. Julve et al. [$Co^{II}(dmphen)_2(NCS)_2$]·0.25EtOH (dmphen = 2,9-dimethyl-1,10-phenanthroline). This system showed slow relaxation of the magnetization after applying a magnetic field and large axial and rhombic single-ion zero-field-splitting parameters[106]. Octahedral Co(II) SIMs are introduced in chapter 3.

The study of the spin relaxation in these SIMs is a complex problem that involves several relaxation mechanisms. It has been extensively discussed in this kind of SMMs as scientists have provided ideal models to understand these mechanisms.[107] The determination of the relaxation energy barrier in SMMs is normally measured by temperature dependent alternating current (ac) susceptibility measurements[94,108]. Whenever the magnetization of a given system cannot follow a progressively larger oscillating magnetic field is indicative (but not conclusive proof) of some energy barrier to relaxation of the magnetization[94]. This manifests itself as frequency dependent signals in the in-phase (χ'_m) and out-of-phase components (χ''_m) of the AC susceptibility. Because the peak maximum χ'' is the temperature at which the angular frequency (ω) of the oscillating magnetic field is equal to the rate of spin reversal (τ_{eff}), the experiment follows an Arrhenius rate law according to the following relationship:

$$\frac{1}{\tau_{eff}} = \frac{1}{\tau_0 e^{-\frac{U_{eff}}{k_B T}}}$$

The use of this equation implies that the relaxation observed arises solely from a thermal process. This is rarely the case as relaxation may occur through several possible processes[94,108]. This has been, in particular, observed in the case of SIMs. Quantum tunneling of the

magnetization (QTM)[109] allows the spin flipping from an M_S state on one side of the barrier to a resonant M_S state on the other side by tunneling. When QTM is particularly efficient, the barrier may be bypassed completely, and no signal in χ''_m will be observed. In order to suppress this QTM a magnetic dc field can be applied cancelling this resonance. QTM can arise from lower than ideal symmetry in a molecule, which induces a transverse component (E and/or allowed higher order terms) to the anisotropy. Alternatively, the relaxation mechanism can be phonon-assisted in either a two phonon process (Orbach[110], Raman[111]) or a one phonon process (direct)[108]. Orbach processes involve absorption of a phonon causing excitation to a real state, before emission of a phonon and relaxation. This relaxation process follows a thermal Arrhenius law. A Raman process involves the absorption of a phonon causing the excitation of a spin to an intermediate level, before relaxation and emission of a phonon. A direct process involves the spin flipping of the molecule with emission of a phonon[108]. Generally, at high temperatures the Orbach process is the dominant relaxation mechanism, whereas other relaxation processes such as the Raman-type relaxation and QTM ones are dominant at lower temperatures[112]. The Raman process shows a power law dependence on the temperature CT^n, while the QTM is temperature independent and appears usually at the lowest temperatures. (see figure 7)

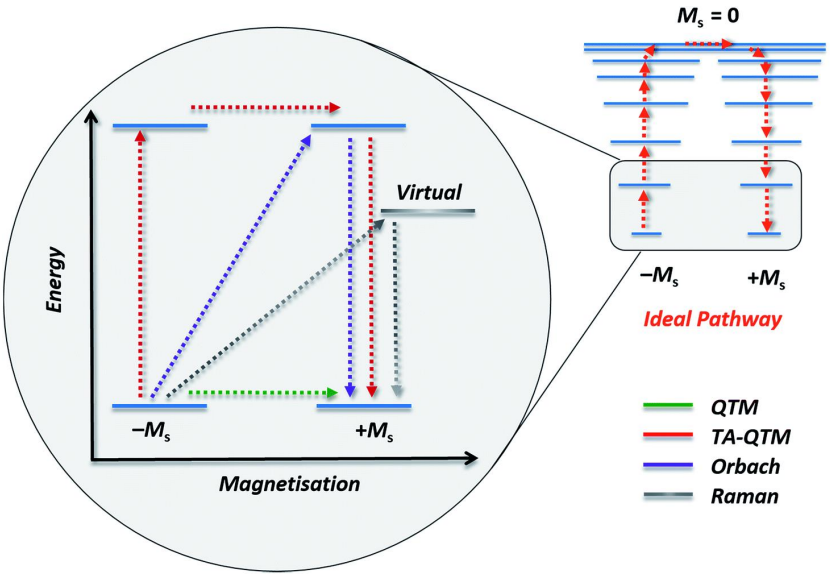

Figure 7. Graphical description of the most common relaxation mechanisms[94].

A further step is to assemble SIM building blocks into 2D and 3D networks such as CPs or MOFs. This constitutes a possible strategy to create addressable arrays for device fabrication and to tune the distance of magnetic interactions between SIM units using linker ligands of varying length[94]. In addition to this, the synthesis of MOFs in which SIM or SMM units are used as nodes also affords the introduction of new functionalities such as the design of porous magnetic materials[8]. Additionally, controlled organization of SIMs is an important issue due to their feasible application in quantum computing since each SIM can behave as a quantum bit.[113] Indeed, the ability to tune the spatial arrangement of more than one non-identical SIM qubit is precisely what is currently needed to advance in the global control paradigm of quantum computing[114]. A very remarkable result in this context, reported by Freedman et al., was the demonstration of atomic clock-like transitions in $[(TCPP)Co_{0.07}Zn_{0.93}]_3[Zr_6O_4(OH)_4(H_2O)_6]_2$ (TCCP = 5,10,15,20-tetrakis(carboxyphenyl)-porphyrin) (see figure 8), where the

cobalt(II) porphyrin units, diluted within a diamagnetic network, possess lifetimes of 13.7 ms at 5 K (1.8 ms at 15 K), observed with pulsed EPR spectroscopy[115]. More recently, the same group have taken advantage again of this framework chemistry to deliver an array of systems that perform as qubits. In the study the group introduced copper atoms in different ratios in the porphyrinic PCN-224 framework stablishing spin coherence time of 25 ns[116] up to 80K . The role of low-energy vibrations on the spin dynamics in this SIM-MOF materials has been studied by Yamashita et al. using the framework [VO(TCPP-Zn_2-bpy)] (TCPP = tetracarboxylphenylporphyrinate; bpy = 4,4'-bipyridyl) and the molecular building block [VO(TPP)] (TPP = tetraphenylporphyrinate)[117].

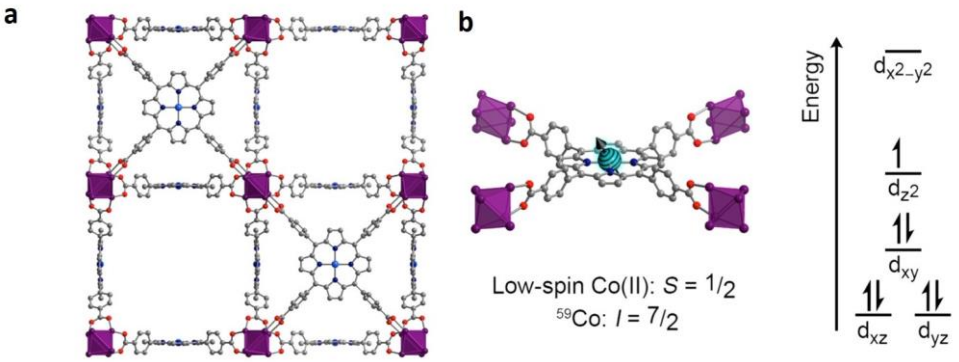

Figure 8. Crystal structure of $[(TCPP)Co]_3[Zr_6O_4(OH)_4(H_2O)_6]_2$ network (a) and view of the Co^{II} porphyrin complex with splitting of the d orbitals in the square planar configuration.[115]

Another approach is the incorporation of SMMs or SIMs into the pores of MOFs[118], as a means of both magnetically isolating them from their surroundings and studying the effects of host–guest interactions and confinement effects on relaxation dynamics.[94] In a previous report of our group it was reported that a Mn(III) dimer SMM behaved differently when it was inserted within a paramagnetic network or into a ferromagnetic 3D achiral oxalate-based lattice[28]. The coupling to the ferromagnetic network of the inserted SMM generated an exchange-bias, which blocks the

quantum tunneling of the SMMs and therefore slows down their magnetic relaxation. A remarkable manifestation of this phenomenon was the onset, below 1 K, of a large magnetization hysteresis, which contrasts sharply with the near-reversible behavior observed in the SMM inserted into a paramagnetic network or in the pure ferromagnetic compound at the same temperature. A very recent result is the direct imaging of Mn_{12} SMMs encapsulated in a mesoporous MOF matrix using high-resolution transmission electron microscopy. These images deliver, for the first time, direct and unambiguous evidence to support the adsorption of molecular guests within the porous host. Bulk magnetic measurements further support the successful nanostructuring of SMMs. The preparation of the first magnetic composite thin films of this kind paves the way for the development of molecular spintronics[119].

The insertion of Co(II) SIMs inside magnetic CPs and the synergy between the properties of both magnetic units is an unexplored and very attractive field, which is one the main topics of the chapter 3 of this thesis.

2.4 Proton Conductivity in Oxalate-Based CPs

Proton conductivity can be understood as a conduction pathway for an efficient proton transport between sites or molecules with similar proton affinity, which are separated by small energy barriers[120]. Thus, the lower the energy barrier, the more efficient the conduction through the material. Proton conduction can usually take place through two common mechanisms, Grotthuss[121] and vehicle mechanism[122]. In the former a proton travels through an infinite network of hydrogen bonds in two steps, first the translation of a proton from an oxonium ion to a water molecule in a hydrogen bond takes place by tunneling and then a reorientation (rotation) of the water molecule thus formed in order to be able to take up the next proton happens[123]. In the vehicle mechanism the charge does not travel as a H^+ but as a H_3O^+, NH_4^+ i.e. using a molecule as a “vehicle”

(H_2O, NH_3..). The vehicle shows a diffusion coefficient corresponding to the proton conduction[123].

Replacing old proton conductors with newer molecular materials exhibiting high proton conductivity is of paramount importance for both fundamental science, to better understand the mechanisms of proton transport, and technology, to design fuel cell materials with enhanced efficiency[48]. Inorganic oxides such as $SrZrO_3$ and $CsHSO_4$ have been widely explored in proton conduction, and organic membranes such as the organic polymer Nafion have been fabricated as synthetic proton-conductive materials. Nonetheless, problems with this materials arise from the impossibility to achieve precise control over the proton-conductive pathway[124]. This control can be achieved with CPs or MOFs because of their tunability and design possibilities. In particular, the molecularity and the crystallinity of CPs enable to understand proton conduction mechanisms on fundamental grounds[125]. Additionally, the well-designed pores in these CPs can provide efficient proton-conducting pathways and host various conducting media, such as water molecules[46]. Finally, proton conductivity of these materials could be combined with other physical properties leading to multifunctional materials.

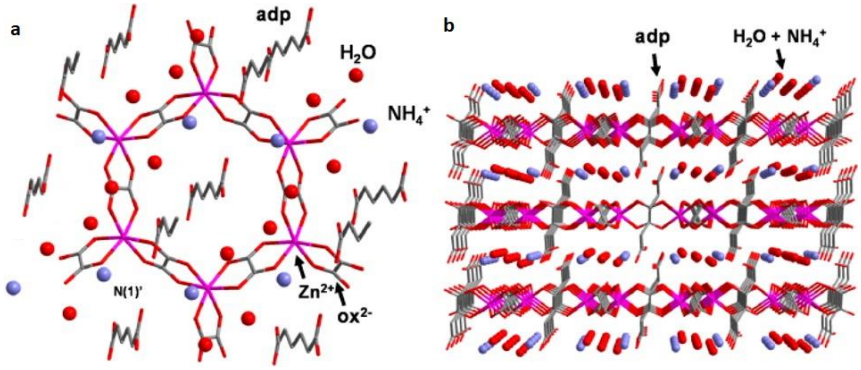

Figure 9. Top view of the crystal structure of $(NH_4)_2(adp)[Zn_2(ox)_3]\cdot nH_2O$ network (a) and lateral view of the layers.[127]

Reports of magnetic materials that simultaneously show such proton conductive properties are not abundant. Most of them have been reported by Kitagawa et. al. First in 2009 they reported a series of oxalate bridged complexes of formula $\{NH(prol)_3\}[M^{II}Cr^{III}(ox)_3]$ (M^{II} =Mn^{II}, Fe^{II}, Co^{II}) with hydrophilic tri(3-hydroxypropyl)ammonium ($NH(prol)_3^+$).[44] The system presented a classical 2D honeycomb layered structure layer with ferromagnetic ordering with T_c of 5.5 K for the MnCr complex, 9.0 K for the FeCr complex, and 10.0 K for the CoCr complex and proton conduction of 1.2×10^{-10} to 4.4×10^{-10} $S \cdot cm^{-1}$ under 40% relative humidity (RH) and $\sim 1 \times 10^{-4}$ $S \cdot cm^{-1}$ under 75% RH. This was the first example of a CP showing coexistence of magnetic and proton conduction properties. Following this report, Verdaguer et al. reported the 3D chiral network $(NH_4)_4[MnCr_2(ox)_6] \cdot 4H_2O$. This system ordered as a ferromagnet with a T_c of 3 K and showed very high proton conduction values of $\sigma = 1.1 \times 10^{-3}$ $S \cdot cm^{-1}$ at room temperature[45]. In 2012, Kitagawa's group developed a new family of proton conduction CPs[47]. In this case the group took advantage of a carboxyl residue to increase the proton conduction of the oxalate layered material. Most of the compounds, with general formula $\{NR_3(CH_2COOH)\}[M^{II}M^{III}(ox)_3]$ (R = ethyl (Et), *n*-butyl (Bu); $M^{II}M^{III}$ = MnCr, FeCr, FeFe) showed ferromagnetic ordering with T_c of 5.5-11.5 K. At the same time, the compounds with an ethyl substituent in the carboxylate residue showed higher proton conductions at low RH with values of 10^{-11} $S \cdot cm^{-1}$ at 45% RH and 10^{-6} $S \cdot cm^{-1}$ at 65% RH. Only the Et-MnCr derivative showed a conductivity of 10^{-3} $S \cdot cm^{-1}$ at 70% RH. Atypical stoichiometry in the Mn:Cr ratios in the 3D magnet reported by Verdaguer et al. led to a curious 3D material of formula $(NH_4)_5[Mn^{II}_2Cr^{III}_3(ox)_9] \cdot 10H_2O$ which showed proton conductivity values of 7.1×10^{-4} $S \cdot cm^{-1}$ at 75% RH. Interestingly when this compound was brought down to 10% RH the proton conductivity decreased in 5 orders of magnitude[126]. Insertion of adipic acid into the diamagnetic Zn oxalate network gave rise to a layered material with formula $(NH_4)_2(adp)[Zn_2(ox)_3] \cdot nH_2O$ (adp: adipic acid, n = 0, 2, 3) (see figure 9). This system showed important

crystallographic changes with the increase of water in the structure, which produced a rearrangement of the hydrogen bonding network between the ammonium cations, the adipic acid and the water molecules. Huge changes of the proton conduction were observed with increasing humidity from the anhydrate $\sigma\sim10^{-12}$ S·cm^{-1} to the trihydrate $\sigma\sim10^{-2}$ S·cm^{-1}.[127] In 2015 Kitagawa et al. reported a family of compounds as a result of the combination of La and transition metals with formulae $LaM(ox)_3\cdot10H_2O$ (M = Cr, Co, Ru, La). The difference in rigidity of the smaller transition metals with respect to the bigger ones gave rise to CPs with different dimensionalities and proton conductivities[125]. A different approach was taken by Lin et al. with the solvent-free synthesis of open frameworks by using templating agents such as 1,4-dimethylpiperazine, diisopropylamine, 1,2-diaminopropane or 1-ethylpiperazine combined with oxalate and metals (Zn, Co, Mn, Bi, In). The $[(H_2dmp)(SO_4)_2][Zn_3(ox)_2(H_2O)_7]$ (dmp = 1,4-dimethylpiperazine) derivative was reported to show proton conductivity of 2.6×10^{-3} S·cm^{-1} at 60 °C under 98% RH[128]. More recently, reports of other MnCr proton conductive networks with high values of proton conductivity $\sigma = 10^{-3}$-10^{-4} S·cm^{-1} have been found in 2D and 3D oxalate networks with the implementation of cations such as $C_3N_2H_5$ (imidazolium)[48] or $\{P(CH_2OH)_4\}^+$.[49]

There are very few reports of anilate based magnets that showed proton conduction. Kitagawa et al. reported isostructural 1D CPs with formula $M(dhbq)\cdot nH_2O$ (M = Mg, Mn, Co, Ni, and Zn, n = 2, 2.5, or 3) with proton conductivity values of $\sigma = 10^{-4}$ S·cm^{-1} when noncoordinating crystalline water was absorbed into the voids of the 1D array with humidity[129].

All these reports showed a promising pathway to design and synthesize new materials that combined magnetism alongside proton conduction. In this thesis, we have used an approach similar to the one formerly used by Kitagawa et al. but instead of using the oxalate-based frameworks we took advantage of the anilate-based ones. This is an unexplored field since 2D or 3D anilate based

compounds that combine magnetism with proton conduction have not been reported so far.

3. Spin Crossover (SCO)

Spin crossover is a well-known and very deeply studied property in the molecular magnetism field due to its intrinsic switching nature. The phenomenon usually occurs in octahedral complexes of the first-row transition metals with an electronic configuration d^4-d^7. It involves the rearrangement of electrons in the metal center between two different states. These states correspond to the different distribution of electrons within the metal orbital energy levels, which in this case, yields the maximum and minimum number of unpaired electrons respectively[130]. The most studied and typical example of spin crossover occurs in Fe^{II} complexes (d^6) with two possible electronic configurations by the different filling of the atomic orbitals: $t_{2g}^6\ e_g^0$ (A_{1g}, singlet state), also known as low spin (LS) configuration; and $t_{2g}^4 e_g^2$ (T_{2g}, triplet state), known as high spin (HS) configuration (see scheme 3). The LS state is diamagnetic and the HS state is paramagnetic[131]. The stabilization of one of the states with respect to the other depends on the strength of the ligand field. For intermediate fields, the energy difference between the two states may be sufficiently small in such a way that the application of an external perturbation induces a spin-crossover between the higher enthalpy of the LS state and the greater electronic and vibrational entropy of the HS state (see scheme 3). Most commonly, this spin transition can be induced by a change in temperature. The HS state is stabilized relative to the LS as the transition temperature is raised, so that above the transition temperature the HS state becomes the thermodynamic ground state of the compound. Equations that treat the spin transition as a thermodynamic equilibrium between starting materials (LS) and products (HS) are required to reproduce the behavior[130,132]. The transition involves changes in the metal-ligand bond lengths and leads to differences in the physical properties such

as different optical properties[133], structural changes[134], modification of the electrical conductivity[135] etc. Fe^{II} spin crossover materials are usually found in a typical coordination environment M-N_6[131,132,136–138] although other coordination environments are also possible such as N_5O[139], N_4O[140–144]$_2$, N_4S_2[139,145], or N_4C_2[146].

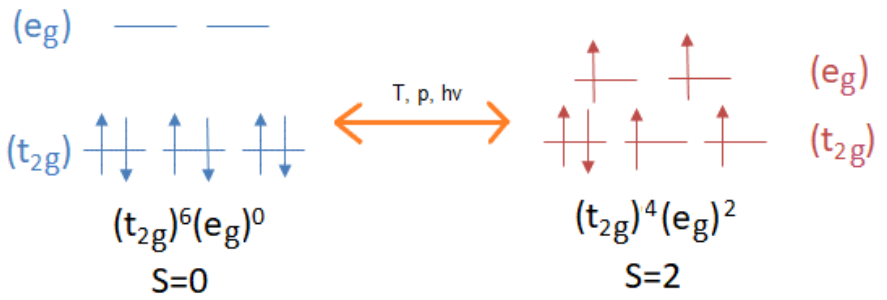

Scheme 3. Schematic representation of the SCO phenomenon in a d^6 metallic center in O_h environment.

From the physical point of view, spin crossover properties are determined by the cooperativity in the solid state, due to elastic forces in the lattice. This means that cooperativity is a fundamental factor in the transmission of the changes from one metal ion to the next one through the material and controls the shape of the transition[147] (see figure 10). Fe^{II} systems usually show high degrees of cooperativity and abrupt spin transitions[148], these are rarer in Fe^{III} SCO compounds[149] and almost nonexistent in other spin crossover compounds. From the electronic point of view, spin transition in d^6 and d^5 metals involves greater structural changes due to the bigger depopulation of the antibonding (e_g) orbital compared to that of the d^7 and d^4 respectively. From the point of view of the ligand, atoms from the group 15 of the periodic table (N and P) have the biggest capacity of contraction (10-13%)[130]. Within a crystalline complex there are other key points that will change the cooperativity shown by the system. The intermolecular interactions play a very important role. Thus, hydrogen bonding, π-π interactions or simple contacts between molecules will have a huge impact in the shape of the

transition[150,151]. In addition to this, whether the final material is formed by discrete molecular complexes or by CPs, where SCO molecules are covalently bonded, will also have an important effect in the magnetic properties[152]. Cooperativity, in the end, arises from a mixture of all the factors that can influence in some way the M-L bond distances and cannot be understood as the effect of a single perturbation. SCO materials formed by molecules that contain aromatic rings, for example, show very well this effect. π-π interactions between the aromatic rings are partially responsible for the cooperativity in the transition, but additionally, the presence of aromatic rings implies bigger contact surfaces areas between neighboring molecules, which also has a strong influence in the cooperativity. Hydrogen bonding is another great example, although this kind of contacts are short, they propagate very well interactions through molecules and this allows better molecular reshaping to be facilitated during the spin transition[153].

The use of these molecular compounds to build devices such as sensors[154], optoelectronic devices[155] or a switch[156] itself is one of the most promising applications for this type of compounds. Another important feature of this kind of materials is that they can present hysteretic behaviors at temperatures around room temperature, which can be useful for nonvolatile memory devices[157–159].

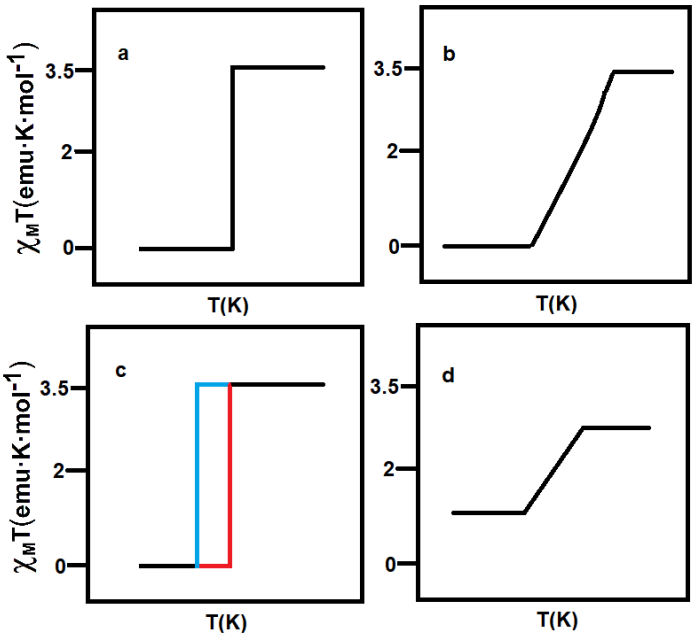

Figure 10. Different cooperative behaviors that can be observed in spin transition: a) abrupt and complete spin transition b) gradual and complete spin transition c) hysteretic abrupt spin transition d) gradual and incomplete spin transition.

3.1 Light-Induced Excited Spin-State Trapping effect (LIESST)

Light is one of the external stimuli that can be used to induce a spin transition. The first to realize about this were Mcgarvey et al.[160] and Decurtins et al.[161] with experiments performed in solution and in solid state respectively. In this last case, the phenomenon was originally observed by Hauser et al. at very low temperatures (<50K) irradiating with a green laser tetrazole Fe^{II} complexes. They demonstrated that this effect could be reversed with red light (reverse LIESST)[162].

Irradiation of the sample at low temperatures (LS state) induces a spin-allowed $^1A_1 \cdot ^1T_n$ transition (Figure 11). The photoexcited state

presents a very short lifetime (a few nanoseconds), inducing fast relaxation of the system back to the $^1A_1$ ground state. A second decay path is possible thanks to the spin orbit coupling, which enables an "intersystem crossing" (ISC) step with $\Delta S = 1$ to the intermediate states $^3T_1$ or $^3T_2$. These spin states can in turn decay via two possible ISC, one implies the relaxation to the $^1A_1$ ground state, the other to the metastable $^5T_2$ state. In this last case, the system remains trapped in the HS state with a very long lifetime if the thermal energy (K_BT) is lower than the energy barrier between HS and LS potential surfaces (ΔE^0_{HL})(see Jablonski diagram).

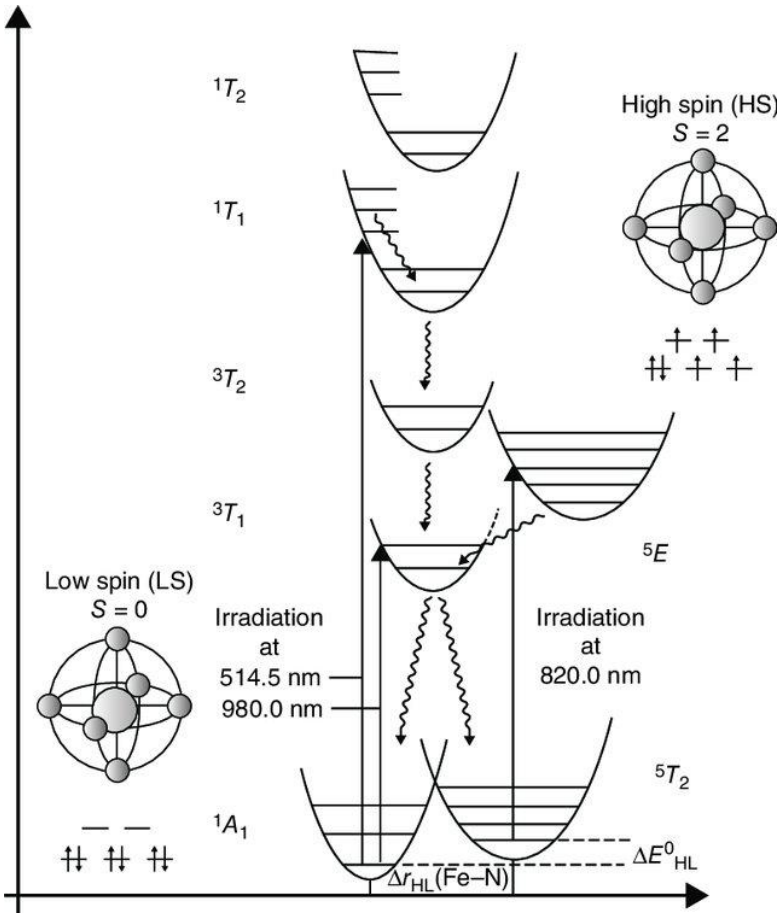

Figure 11. Jablonski diagram for an Fe^{II}-N spin crossover system[131].

LIESST effect in a sample is usually observed monitoring the change in the magnetic moment of the irradiated sample in a SQUID magnetometer where a Laser is coupled. Light irradiation is applied to the material at 10 K, and results in the population of the paramagnetic HS state through the LIESST phenomenon. This can be observed by a sharp increase of the magnetic signal. The irradiation is only stopped when saturation of the signal is reached, that is when an equilibrium is operating between the population and relaxation of the excited state. The temperature is then slowly increased at a rate of 0.3 $K \cdot min^{-1}$ and the magnetic behavior recorded. The magnetic response of the light-induced HS state remains almost constant until the energy barrier between HS and LS can be overcome thermally, typically up to 40-50 K. Then, $\chi_M T$ drastically decreases and rapidly recovers its initial value. The minimum of the $\delta\chi_M T/\delta T$ *vs. T* curve determines the T_{LIESST} temperature (see figure 12).

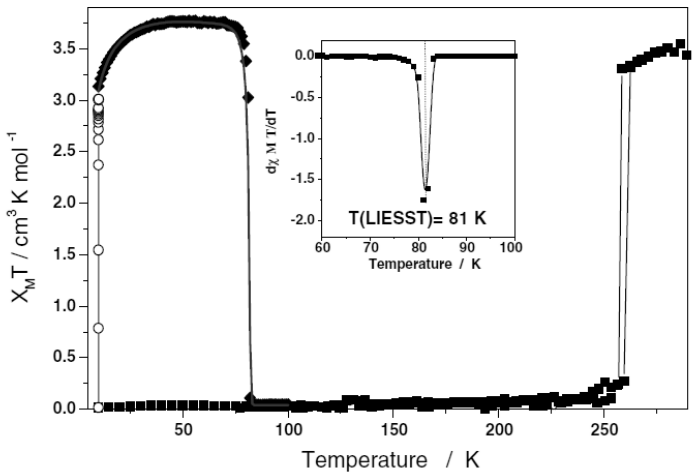

Figure 12. The LIESST behavior of $[Fe(1\text{-}bpp)_2](BF_4)_2$. ■ = Data recorded in the cooling and warming mode without irradiation; ○ = data recorded with irradiation at 10 K; ◆ = T_{LIESST} measurement, data recorded in the warming mode with the laser turned off after irradiation for one hour. The inset graph shows the derivative $\delta\chi_M T/\delta T$ plot as function of the temperature.[163]

The group of Letard et al. have registered the thermal spin-transition $T_{1/2}$, temperature of 50 % HS to LS conversion, and T_{LIESST} temperatures of many SCO materials. They observed that these two temperatures are related by the empirical equation, $T_{LIESST} = T_0 - 0.3\ T_{1/2}$.[164] Experimentally, T_0 is a function of the denticity of the ligand donor sphere. Thus, complexes of monodentate ligands follow the equation with T_0 = 100 K, while complexes of bidentate ligands show T_0 = 120 K, and tridentate tris-heterocyclic ligands such as the 2,6-bis(pyrazol-1-yl)pyridine (1-bpp) one described in next section give T_0 = 150 K. Until now, the T_{LIESST} database compiles the properties of more than 80 SCO materials (Figure 13). A general tendency, noticeable for all the five T_0 lines, is a decrease of T_{LIESST} with the increase of $T_{1/2}$, reflecting the fact that the higher the thermal spin-transition occurs, the less photomagnetic information remains. Thus, mean-field theory predicts an inverse relationship between the thermodynamic thermal SCO temperature, $T_{1/2}$, and the lifetime of the photoinduced metastable state. This is the "inverse energy gap law" described by Hauser[165,166]. More recently, the limitations of this empirical expression have been pointed out by a growing number of complexes with photomagnetic properties deviating from this equation. These exceptions are related to photo-induced crystallographic transitions[167] and other factors such as the rigidity of the ligand. Indeed, the introduction of flexibility into the inner coordination sphere drastically reduces the T_0 value[168].

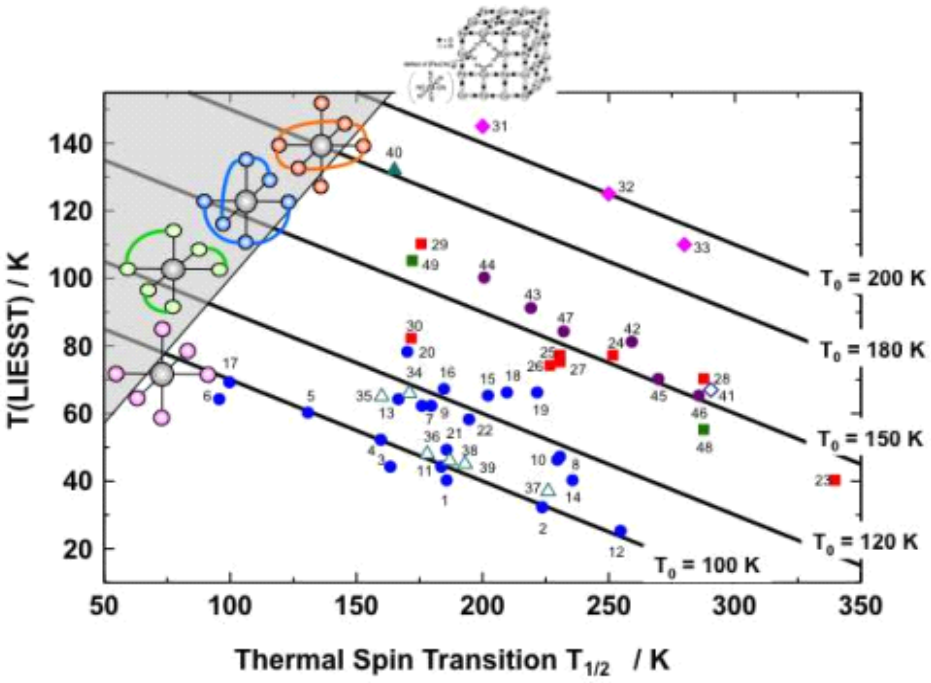

Figure 13. Variation of T(LIESST) versus $T_{1/2}$ for spin crossover compounds[169].

3.2 Spin Crossover Compounds Based on 2,6-bispyrazol-1-yl pyridine (1-bpp)

Derivatives of 1-bpp and 2,6-bis(pyrazol-3-yl)pyridine (3-bpp) have been thoroughly used for the preparation of SCO Fe^{II} complexes, which can show unusual and useful switching properties. Furthermore, derivatives of these ligands have been used for the preparation of strongly emissive lanthanide complexes[170]. In particular, Fe^{II} complexes of 1-bpp and its derivatives have been reported as interesting SCO compounds since they often exhibit spin transitions near room temperature[171]. Additionally this family of complexes often exhibit the LIESST effect described in the previous paragraph[171]. Photoconversions of 80-100% during irradiation are common for samples that exhibit thermal spin-crossover around

room temperature. Depending on the $T_{1/2}$ values, the T_{LIESST} are usually between 65 and 100 K[172–174].

Functionalization of almost every site of the 1-bpp ligand can be achieved through different synthetic routes. Substitution at the pyrazole 3-position can modify the steric environment of the coordinated Fe^{II} ion, giving some control over its spin state[175] (Figure 14, A). Alternatively, substitution at the pyrazole 4-position or pyridine 4-position allows modification of the periphery of the complex, without perturbing the Fe^{II} center (Figure 14, B and C)[176–181]. As the Fe^{II} complexes of all these derivatives often undergo thermal spin-crossover at accessible temperatures, we can conclude that no other ligand system used in spin-crossover research is so synthetically flexible.

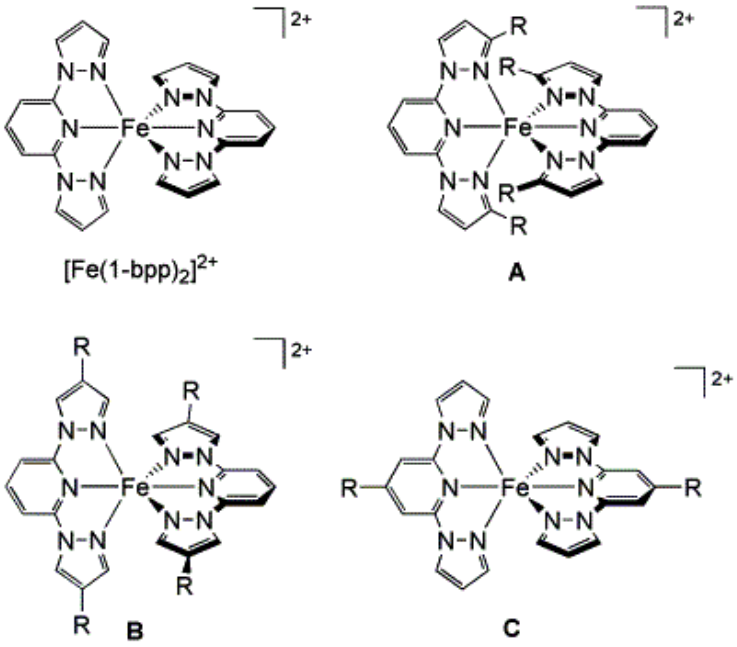

Figure 14. Structure of $[Fe^{II}(1\text{-bpp})_2]^{2+}$, and the orientation of ligand substituents at the pyrazole 3-position (A), the pyrazole 4-position (B) and the pyridine 4-position (C)[171].

Most syntheses of 4-substituted-1-bpp ligands begin from commercially available 2,6-dihydroxyisonicotinic acid. After a halogenation step, this is readily converted to 2,6-bis(pyrazol-1-yl)pyridine-4-carboxylic acid (bppCOOH, see Scheme 4)[182,183]. From there, a variety of functional group transformations are available. This is the most common route for attaching additional functionality to the 1-bpp pyridine ring, which we have followed in this thesis.

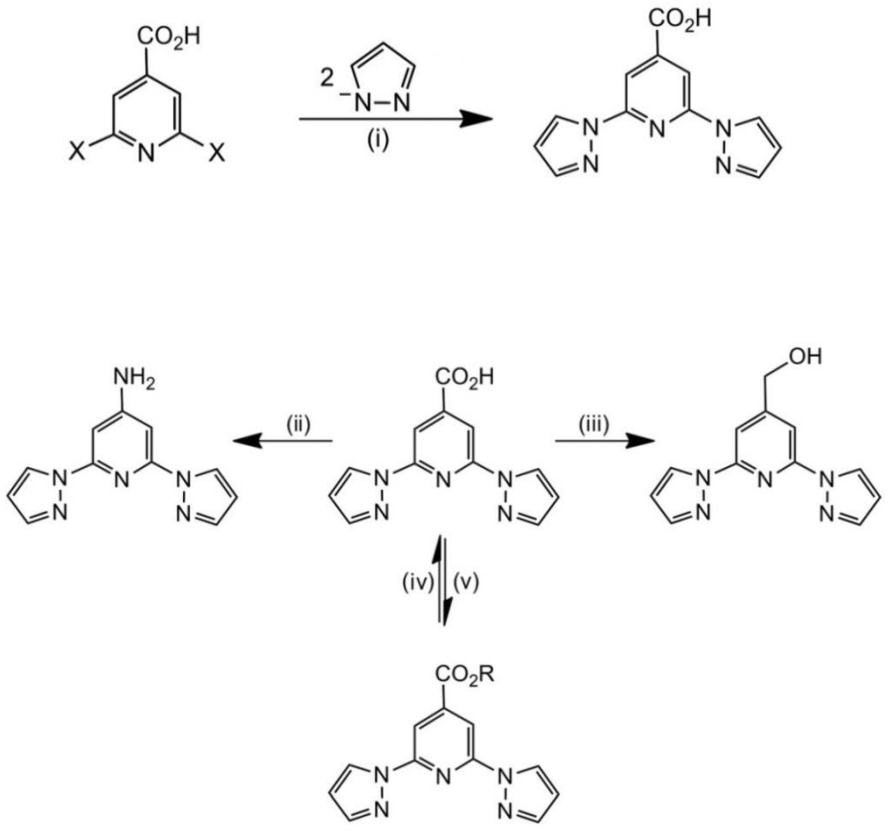

Scheme 4. Synthetic routes to 4-substituted-1-bpp derivatives. Typical reaction conditions: (i) diglyme, 110-130 ºC, 3-5 days. (ii) $COCl_2$, THF; NaN_3, acetone-water; CF_3CO_2H, benzene; K_2CO_3, MeOH. (iii) $NaBH_4$, EtOH. (iv) ROH, H_2SO_4 (cat). (v) LiOH, THF then dil. HCl[184].

In 2014 we reported the functionalization of the pyridine with a carboxylic group and its combination with $Fe(ClO_4)_2$, which gave rise to the complex $[Fe(bppCOOH)_2](ClO_4)_2$ with $T_{1/2}$ of *ca.* 380 K and a T_{LIESST} of 60 K, which showed an abrupt SCO due to the presence of a hydrogen-bonded linear network of complexes[185]. More recently, we completed the previous study with the series of $Fe(bppCOOH)_2^{2+}$ complexes with ClO_4^- , BF_4^-, $CF_3SO_3^-$, SbF_6^- counterions and different solvents in order to have a rational understanding on how different solvates behave on different ways[186]. We also explored the possibility to tune the transition by modifying the position of the carboxylic group in the pyridine[187]. Further derivatization of the carboxylic group into a ethyl ester and its combination with $Fe(ClO_4)_2$ lead to a complex of formula $[Fe(bppCOOEt)_2](ClO_4)_2$·solv (bppCOOEt = ethyl 2,6-bis(1*H*-pyrazol-1-yl)isonicotinate) with a different magnetic behavior to that of the $[Fe(bppCOOH)_2](ClO_4)_2$ showing a similar effect to that of the use of the bulkier counterions in the acid derivative[186]. We also explored the possibility to build heteroleptic complexes based on a mixture of ligands to give rise to the compounds $[Fe(bppCOOH)(bppCOOEt)](ClO_4)_2$·solv and $[Fe(bppCOOH)(3bpp\text{-}bph)](ClO_4)_2$·solv (3bpp-bph = 2,6-bis(5-([1,1'-biphenyl]-4-yl)-1*H*-pyrazol-3-yl)pyridine). Both compounds showed photomagnetic effects, and a gradual incomplete transition was observed in the case of $[Fe(bppCOOH)(bppCOOEt)](ClO_4)_2$, which was the first example of an heteroleptic complex built of 1-bpp ligands.[188] The effect of the length of the alkyl chain in the ester group of the compounds $[Fe(bppCOOR)_2](ClO_4)_2$, where R = C_nH_{2n+1} (n = 6, 12, 14, 16, 18) was studied by Halcrow et al[189]. Further derivatization of the ester group can be achieved by reacting the bppCOOEt, with tris(hydroxymethyl)aminomethane (tris) to obtain the bppTris. Reaction of these ligand with $Fe(ClO_4)_2$ affords the complex $[Fe(bppTris)_2](ClO_4)_2$, which exhibits a LS configuration at room temperature and a thermally-induced SCO behavior at T > 400 K, along with LIESST effect at low temperature, with T_{LIESST} = 38 K[190]. Other examples of derivatization of the pyridine can be found. These

lead to interesting derivatives that can be used to build radical containing complexes[191], interesting metallacycles[192] or 1D linear CPs[193]. Functionalization of the 4-pyrazolyl groups is more challenging due to their more complicated chemistry and because they must be synthesized in a previous step. Halcrow et al. reported the functionalization of the pyrazol with an ethyl ester to yield 2,6-di[4-(ethylcarboxy)pyrazol-1-yl]pyridine, a step later, after reduction of the ethyl ester group they obtained the alcohol derivative 2,6-di[4-(hydroxymethyl)pyrazol-1-yl]pyridine. Complexes $Fe(bppCOOEt_2p)_2(BF_4)_2$ and $Fe(bpCH2OH_2p)_2(BF_4)_2$ were LS at room temperature[194]. This report motivated us to synthesized the 2,6-di[4-(carboxylic acid)pyrazol-1-yl]pyridine by saponification of $bppCOOEt_2p$ to afford $bppCOOH_2p$. The iron(II) complex $[Fe^{II}(bpCOOH_2p)_2](ClO_4)_2 \cdot 3.5Me_2CO$ showed an abrupt thermal SCO around room temperature and a photoinduced SCO with an unusually high *T*(LIESST) of 120 K[195].

Alternatively to the building of discrete molecular complexes, one can take advantage of the multiple ways in which the 1-bpp ligand can be functionalized in order to build more complex functional ligands through the creation of covalent bonds between the bpp subunit and another pre accommodated subunit. These ligands can be further used to build CPs or polynuclear SCO systems that show interesting or novel properties. This has been the main topic of the second part of this thesis with the functionalization of fullerenes with bppCOOH and alkoxymethyl derivative $bppCH_2OH$ in chapter 4 and the functionalization of a Lindqvist polyoxometalate in chapter 5 (see scheme 5).

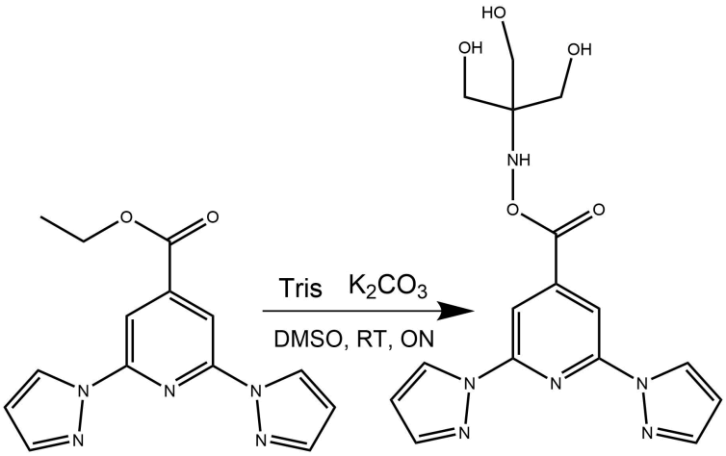

Scheme 5. Synthetic route from bppCOOEt to bpp-Tris.

4. Luminescent Spin Crossover Complexes

This topic has been a focus of interest during the last five years due to the possible luminescent signal modulation through the SCO switching property. Building systems that combine luminescent and spin crossover properties represents a huge challenge. This difficulty arises from the fact that $Fe^{II/III}$, Co^{II} and Ni^{II} metal ions are usually luminescence quenchers[130].

Luminescent materials are those that upon energy absorption transform this energy into light emission. Photoluminescent materials are one specific type of luminescent materials, which, upon the absorption of electromagnetic radiation, perform the emission of electromagnetic radiation with a different wavelength. In section 3 we introduced how drastic changes in the packing and electronic structure of the atoms occur upon SCO. When the luminophore—the light emitting entity of the molecule— is affected by these changes, a modulation of the emission wavelength of the radiation can be achieved, affording a synergistic effect between the SCO and the luminescence of the material.

Two main strategies have been employed in the preparation of luminescent SCO systems: The first strategy involves the introduction of doping luminescent entities into the SCO material. Using this strategy, Real et al. have reported Hofmann type CPs of formula $Fe^{II}(bpben)[Au(CN)_2]$ (bpben = 1,4-bis(4-pyridyl)benzene). Insertion of pyrene guests into the pores of this compound allows tuning the guest emission wavelength by the compression or expansion of the network accompanying the SCO[196] (see figure 15). Similar results have been reported, more recently, in a new family of CPs with formula $\{Fe^{II}(bpb)[M^{I}(CN)_2]_2\}\cdot$pyrene (bpb = bis(4-pyridyl)butadiyne), M^{I} = Ag or Au.[197] The use of lanthanoid as emitting doping entities has been explored by Piguet et al. In this work, segmental ligands are employed to prepare SCO systems doped with rare earths to obtain triple-stranded helicates of formula $[LnFe(L)_3]^{5+}$. The introduction of the photophysically active Eu(III) probe results in europium-centered luminescence modulated by variable intramolecular Eu(III) → Fe(II) energy-transfer processes[198].

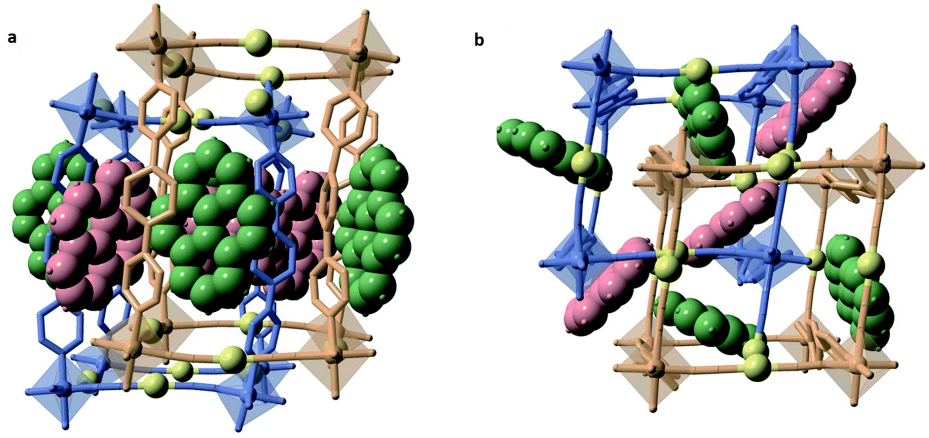

Figure 15. Lateral (a) and top (b) view of the interpenetrated $Fe^{II}(bpben)[Au(CN)_2]$ Hofmann type network[196].

The second strategy to obtain this type of switching hybrid materials consists in the use of luminescent ligands that can complex Fe^{2+} in order to obtain a single entity that combines the SCO with

luminescence. This strategy can be exploited in two ways: building Fe(II) discrete molecular complexes or building extended networks. Following the former approach, several examples have been reported. In an interesting example, Kou et al. have prepared Rhodamine 6G-labeled pyridyl arylhydrazone Fe(II) complexes with a synergistic effect between the SCO and the fluorescence of the rhodamine[199]. In another example reported by S. Triki et al., the Fe(II) mononuclear complexes with six monodentate naphthalene functionalized triazole ligands of formula $[Fe(naph\text{-}trz)_6]^{2+}$ showed an interplay between the SCO and light emission properties in the thermal region where the SCO was taking place[200]. Following the second approach, Weber et al. reported in 2018 a CP of formula $[Fe(L)(bipy)]_n$ (L^{2-} is a N_2O_2 Schiff base-like ligand bearing a phenazine fluorophore and bipy is 4,4'-bipyridine). In this system, the thermal SCO could be monitored by the emission spectra since the emission undergoes a change from green to yellow upon the low spin-to-high spin transition with the temperature[201]. A 2D CP of formula $\{[Fe(L)(TPPE)_{0.5}]\cdot 3\,CH_3OH\}_n$, (L= diethyl(E,E)-2,2'-[1,2-phenyl-bis(iminomethylidyne)]bis(3-oxobutanoate)-(2-)-N,N',O^3,$O^{3'}$ and TPPE = 1,1,2,2-tetrakis(4-(pyridin-4-yl)phenyl)-ethene) was reported by Lin et al. The system was formed by SCO molecular complexes Fe(L) connected through the luminescent TPPE ligands[202]. Very recently, Real et al. demonstrated the implementation of luminescent ligands as pillars in the Hofmann extended clathrate networks besides the extrinsic integration of luminescent pyrene guests mentioned above [197].

The few examples of luminescent SCO complexes based on 1-bpp have been reported by Ruben et al. They are 4-substituted-1-bpp ligands with pyrene and alkynyl coordinated Pt(II) terpyridine complexes. In both cases, the emission is dominated by the substituent[203,204] (see scheme 6). Temperature-dependent studies of the photophysical properties of these compounds do not reveal any

obvious correlation between the fluorescence of the luminophore group and the spin state of the spin transition core.

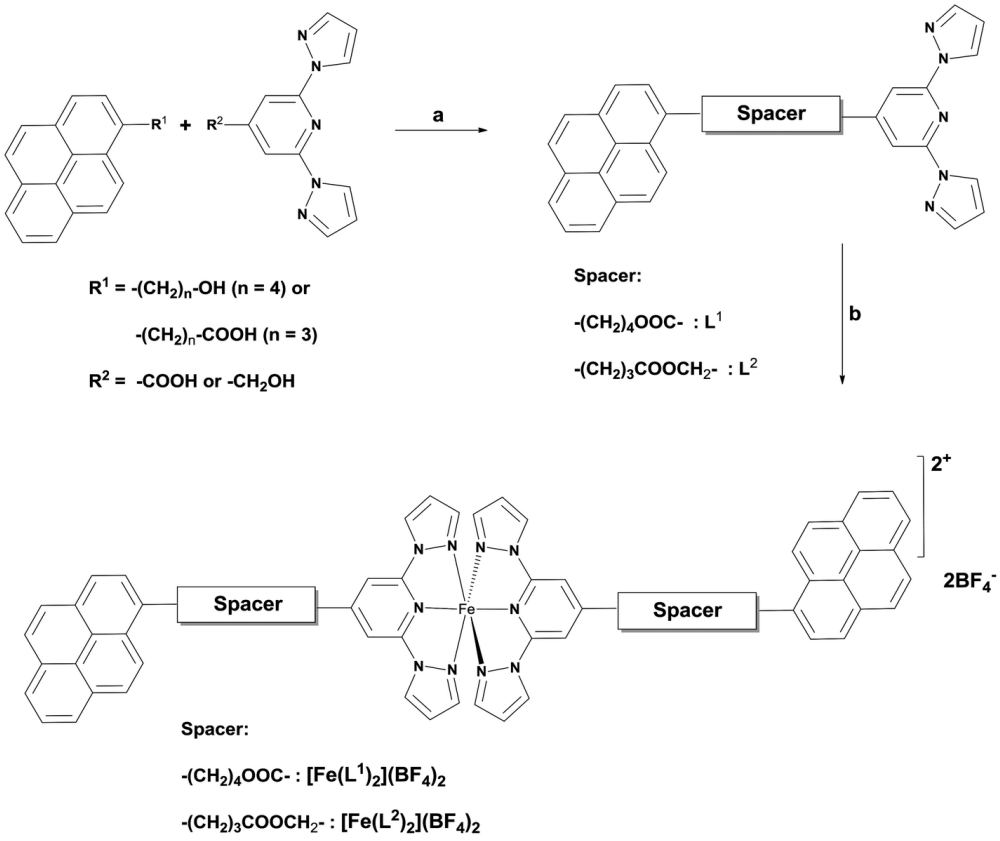

Scheme 6. Synthetic scheme for the preparation of pyrene-decorated bpp SCO molecules[203].

In chapter 4 we have anchored twelve 1-bpp units to a fullerene through spacers of different length. The role of the fullerene was that of a scaffold to concentrate a high density of 1-bpp units around. This allowed the preparation of polynuclear spin crossover systems. In this chapter, we used the luminescent properties of 1-

bpp, which have not been studied in detail in the literature, to monitor the formation of the polynuclear complexes.

5. Functionalized Polyoxometalates

Polyoxometalates (or POMs) are a family of inorganic clusters, usually built by oxides of metals in their highest oxidation state (mainly W^{VI}, Mo^{VI} or V^{V}) (see figure 16). They have been widely used in fields such as catalysis[205], materials science[206] and medicine[207] amongst others[208,209]. They are very diverse due to the almost infinite compositions that can be found and are a source of new materials.

Chemical functionalization of polyoxometalates is a promising strategy in order to enable them to build more complex materials and achieve synergy between the properties of the different parts composing the final material. There are several examples of hybrid materials formed by POMs with organic[210–212] and inorganic subunits[213,214].

The main strategy used to functionalize POMs is through the use of a trisalkoxy organic ligand that can create μ-oxo bridges with the metal[215]. This rational functionalization usually gives rise to stable products with functional groups that can be utilized in further reactions with other functional molecules to achieve a hybrid material. A different strategy consists in the mixing of a preformed molecular complex with the POM in one pot syntheses. Unpredictable products usually arise from this approach.

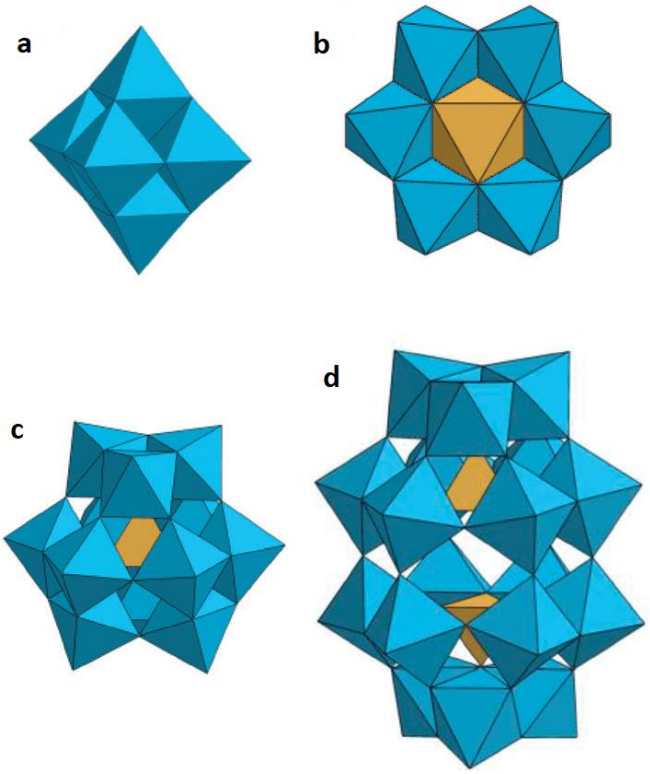

Figure 16. Polyhedral representation of polyoxometalates: Lindqvist (a), Anderson-Evans (b), Keggin (c) and Wells-Dawson (d)[216].

By following the rational approach, discrete or polymeric materials can be obtained as a final product depending on the organic entity that has been chosen to functionalize the POM. Early reports of Anderson type heteropolymolybdates functionalized with trisalkoxy ligands were done by Hasenknopf et al. in 2002. TBA salts (TBA = $N(C_4H_9)_4^+$) of the molecular clusters $[MMo_6O_{18}\{(OCH_2)_3CR\}_2]^{3-}$ (M = Mn^{III}, Fe^{III}) and $[H_2MMo_6O_{18}\{(OCH_2)_3CR\}_2]^{2-}$ (M = Ni^{II}, Zn^{II}), (R = CH_3, NO_2, CH_2OH) were prepared by treatment of $[N(C_4H_9)_4]_4[\alpha\text{-}Mo_8O_{26}]$ with tris(hydroxymethyl)methane derivatives and the metal salt[217]. A year later, the same group reported the amino derivative $TBA_3[MMo_6O_{18}\{(OCH_2)_3\text{-}CNH_2\}_2]$ (M = Mn^{III}, Fe^{III}).[218] Reports of functionalized Anderson type heteropolymolybdates with pyridine[219]

and terpyridine[220] showed that these functionalized clusters could be used as building blocks to synthesize CPs. In 2013 Cronin et al. synthesized the first asymmetrically functionalized Anderson type POMs with formula $TBA_3[MnMo_6O_{18}((OCH_2)_3CNHR_1)((OCH_2)_3CNHR_2)]$ (R1 = $COC_{14}H_9$,R2 = H) by direct reaction of two different TRIS-based ligands with the Anderson precursors. In a different approach, and starting from a symmetric precursor, reaction of the amino functionalized $TBA_3[MnMo_6O_{18}\{(OCH_2)_3\text{-}CNH_2\}_2]$ with acetic anhydride led to an asymmetric POM by a "post functionalization" method[221]. Taking advantage of the terpyridine functionalization of the Mn-Anderson derivative, our group reported a 1-bpp functionalized Anderson POM $TBA_3[MnMo_6O_{24}(C_{16}H_{15}N_6O)_2]$. Reaction of this bpp-functionalized cluster with Fe^{2+} gave rise to a polymeric compound whose formula was determined to be $TBA[Fe(MnMo_6O_{24}(C_{16}H_{15}N_6O)_2)]\cdot(H_2O)_4$. This non-crystalline jelly material showed field induced slow relaxation of the magnetization due to the presence of isolated Mn^{III} anisotropic magnetic ions[222]. Fe^{II} remains in the low-spin state, while irradiation at 10 K with green light induces LIESST effect with a small but significant photoconversion (~8%) (see figure 17).

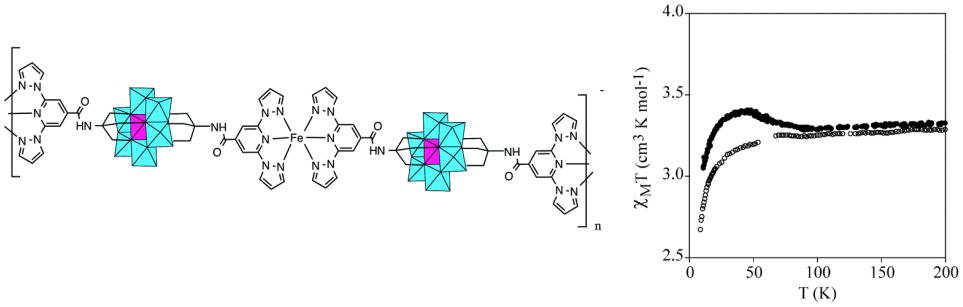

Figure 17. Chemical representation of the Anderson based linear CP and magnetic behavior with (black dots) and without (empty dots) irradiation[222].

A different family of POMs containing a redox active hexavanadate moiety are the Lindqvist type polyoxovanadates. Pyridine[219] $(C_{16}H_{36}N)_2[V_6O_{13}\{(OCH_2)_3CNHCO(4\text{-}C_5H_4N)\}_2]$ and terpyridine[220]

$(C_{16}H_{36}N)_2[V_6O_{19}(C_{20}H_{17}N_4O)_2]$ functionalization of this vanadium cluster was reported at the same time than the Anderson structure. Reaction of this family of POMs with metals was studied by Hill et al. First, in 2006 they reported a linear CP formed by bis(pyridyl)-capped hexavanadate units bound to each other by divalent metallic centers in $M[V_6O_{13}\{(OCH_2)_3C(4\text{-}CONHC_5H_4N)\}_2]$ (M = Mn^{II}, Co^{II}, Ni^{II}, or Zn^{II}). These compounds could be reversibly reduced by chemical reductants[223].(see figure 18)

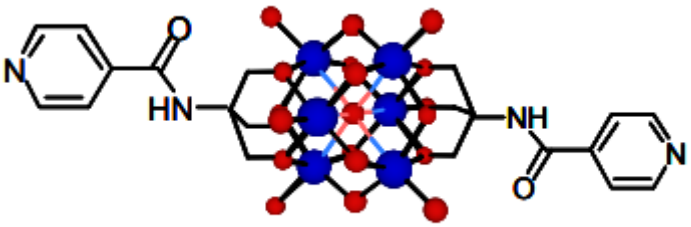

Figure 18. Bis(pyridyl)-capped hexavanadate anionic building block $[V_6O_{13}\{(OCH_2)_3C(4\text{-}CONHC_5H_4N)\}_2]^{2-}$.[223]

A year later, an open framework pillared type CP was obtained as a result of the combination of a bis(benzoic acid) terminated hexavanadate, Tb^{III}, and bpdo (4,4'-bis(pyridine-N-dioxide)) (see figure 19). The resulting polymer, with formula $Tb[V_6O_{13}\{(OCH_2)_3C(NH_2CH_2C_6H_4\text{-}4\text{-}CO_2)\}\{(OCH_2)_3C(NHCH_2C_6H_4\text{-}4\text{-}CO_2)\}_2]$, showed large pores and O_2-based reaction catalytic features[224]. More recently, Yang et al. have reported two examples of cluster frameworks $(TBA)_3Cu[V_6O_{13}(L)_2]_2\cdot solv$ and $(TBA)Ag[V_6O_{13}(L)_2]$ (H_3L = tris(hydroxymethyl)-4-picoline) that exhibit efficient electrocatalytic activity and strong durability in oxygen reduction reactions[225].

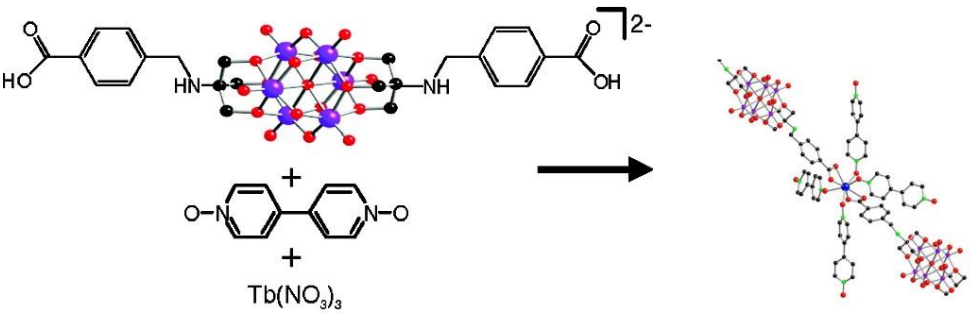

Figure 19. Building blocks and basic subunit of the Lindqvist based CP $Tb[V_6O_{13}\{(OCH_2)_3C(NH_2CH_2C_6H_4\text{-}4\text{-}CO_2)\}\{(OCH_2)_3C(NHCH_2C_6H_4\text{-}4\text{-}CO_2)\}_2]$.[224]

Following our reports in 2015 with the Mn-Anderson derivative, we prepared a 1-bpp-functionalized hexavanadate and combined it with Fe^{2+} to build a functional CP that could show synergistic effects between the redox properties of the POM unit and the switching properties of the Fe^{II} SCO complex. Structural, magnetic and redox properties of these complexes are the main topic of the discussion in chapter 5.

6. Summary and Aims of the Work

The main objective of this thesis is the preparation of multifunctional molecular magnetic materials. In order to address this, we have used two different approaches: an ionic approach where we prepared salts of functional cations and combined them with anionic extended networks (chapters 2 and 3); and a covalent approach where, through the use of covalent bonds between a functional ligand and a fullerene (chapter 4) or a POM (chapter 5) we have obtained SCO systems with synergistic effects.

In chapter 2 we report the synthesis and characterization of several 2D layered CPs based on the anilate ligand with inserted ammonium cations of different sizes that modulate the proton conductivity of the material. The compounds, with formulas $(Me_2NH_2)[Mn^{II}Cr^{III}(Br_2An)_3]\cdot 2H_2O$, $(Et_2NH_2)[Mn^{II}Cr^{III}(Br_2An)_3]$,

$(Et_3NH)[Mn^{II}Cr^{III}(Cl_2An)_3]$, and $[(Et)(i\text{-}Pr)_2NH[Mn^{II}Cr^{III}(Br_2An)_3]\cdot(CHCl_3)_{0.5}\cdot(H_2O)$ (Me =methyl, Et = ethyl and i-Pr = isopropyl) present the typical hexagonal honeycomb structure. The cations, in the case of the methyl and ethylammonium derivatives, are inserted within the hexagonal channels, while in the isopropyl ammonium derivative, the cation is inserted within and between the layers. All the systems behave as ferrimagnets with T_C 8-9K. In the isopropyl ammonium derivative, the presence of different interlayer distances leads to a metamagnetic behavior when the sample is measured in contact with the mother liquor. The behavior changes in the dry sample, which shows a ferrimagnetic ordering due to collapse of the structure. Interestingly, the metamagnetic behavior is recovered after reimmersing the crystals in the mother liquor, thus proving the reversibility of the process. All compounds follow a Grotthuss-type proton conduction with low conductivity values ranging between 2.3×10^{-6} $S\cdot cm^{-1}$ and 2.4×10^{-5} $S\cdot cm^{-1}$.

In chapter 3 we report the preparation and characterization of Co(II) complexes, that behave as SMMs, and their insertion in a 3D oxalate-based network. Structural characterization of all the compounds shows two different cobalt complexes with octahedral symmetry, $[Co^{II}(L)_2](ClO_4)_2\cdot 0.5MeCN\cdot Et_2O\cdot 0.25H_2O$ and $[Co^{II}(L)(CH_3CN)_2(H_2O)](ClO_4)_2\cdot MeCN$ (L = 6-(3,5-Diamino-2,4,6-triazinyl)2,2'-bipyridine). Insertion of the Co:L 1:2 complex into an oxalate network yields a 3D achiral CP of formula $[Co^{II}(L)_2][Mn^{II}Cr^{III}(ox)_3]_2\cdot$(solvate), which shows a ferromagnetic ordering. X-band EPR measurements suggest exchange interactions between the two magnetic sublattices.

In chapter 4, the design and preparation of hexakis-substituted [60]fullerene adducts of 1-bpp are reported. Combination with Fe(II) affords different SCO molecules with up to 6 SCO complexes per fullerene. UV-VIS and fluorescence spectroscopies are employed to monitor the formation of the Fe(II) complexes in solution through

the sequential apparition of MLCT bands and the decrease of the luminescence of the ligand. Some of these polynuclear complexes show SCO properties in the solid state induced by temperature and light as external stimuli, with spin transitions that, although gradual, are much sharper than those reported in mononuclear complexes based on fullerene. These results demonstrate that [60]fullerene hexa-adducts are excellent and versatile platforms to develop new SCO materials and provide an interesting alternative to prepare SAMs of this tridentate ligand, a possibility that has remained unsuccessful due to the lability of these Fe^{II} complexes.

Finally, in chapter 5 we report the functionalization and characterization of a Lindqvist-type polyoxovanadate functionalized with 1-bpp. The 1-bpp bifunctionalized $[V_6O_{19}(C_{16}H_{15}N_6O)_2]^{2-}$ moiety is combined with Fe(II) and Zn(II) to afford 1D polymeric chains. Structural characterization of the zinc derivative $Zn[V_6O_{19}(C_{16}H_{15}N_6O)_2]_2$·solv by single crystal X-ray diffraction shows a neutral 1D polymeric system where the polyoxometalates are linked to each other through the divalent metallic centre. The isostructural Fe(II) derivative shows a versatile magnetic behavior upon reduction and reoxidation and solvent exchange leading to a tunable thermal and light-induced SCO. This is related to the structural flexibility of the polymeric POM chains that enable uptake and release of reductants, oxidants or solvent guest molecules.

7. References

1 E. Coronado, J. R. Galán-Mascarós, C. J. Gómez-García and V. Laukhin, *Nature*, 2000, **408**, 447–449.

2 E. Coronado and P. Day, *Chem. Rev.*, 2004, **104**, 5419–5448.

3 E. Coronado, M. Giménez-Marqués, G. M. Espallargas and L. Brammer, *Nat. Commun.*, 2012, **3**, 828.

4 T. K. Jain, J. Richey, M. Strand, D. L. Leslie-Pelecky, C. A. Flask and V. Labhasetwar, *Biomaterials*, 2008, **29**, 4012–4021.

5 O. Gutfleisch, M. A. Willard, E. Brück, C. H. Chen, S. G. Sankar and J. P. Liu, *Adv. Mater.*, 2011, **23**, 821–842.

6 J. S. Miller, *J. Chem. Soc. Dalton Trans.*, 2006, **23**, 2742–2749.

7 J. S. Miller, *Chem. Soc. Rev.*, 2011, **40**, 3266–3296.

8 G. Mínguez Espallargas and E. Coronado, *Chem. Soc. Rev.*, 2018, **47**, 533–557.

9 A. E. Thorarinsdottir and T. D. Harris, *Chem. Rev.*, 2020, **12**, 8716–8789.

10 A. Abhervé, S. Mañas-Valero, M. Clemente-León and E. Coronado, *Chem. Sci.*, 2015, **6**, 4665–4673.

11 H. Tamaki, N. Matsumoto, M. Koikawa, N. Achiwa, H. Okawa, Z. J. Zhong, S. Kida and Y. Hashimoto, *J. Am. Chem. Soc.*, 1992, **114**, 6974–6979.

12 K. S. Min and J. S. Miller, *J. Chem. Soc. Dalton Trans.*, 2006, **20**, 2463–2467.

13 C. Mathonière, C. J. Nuttall, S. G. Carting and P. Day, *Inorg. Chem.*, 1996, **35**, 1201–1206.

14 S. G. Carling, C. Mathonière, P. Day, K. M. A. Malik, S. J. Coles and M. B. Hursthouse, *J. Chem. Soc. - Dalt. Trans.*, 1996, **9**, 1839–1843.

15 E. Coronado, J. R. Galán-Mascarós and C. Martí-Gastaldo, *J. Mater. Chem.*, 2006, **16**, 2685–2689.

16 C. Mathonière, S. G. Carling, D. Yusheng and P. Day, *J. Chem. Soc. Chem. Commun.*, 1994, **13**, 1551–1552.

17 M. Clemente-León, E. Coronado, C. Martí-Gastaldo and F. M. Romero, *Chem. Soc. Rev.*, 2011, **40**, 473–497.

18 L. M. Zheng, X. Fang, K. H. Lii, H. H. Song, X. Q. Xin, H. K. Fun, K. Chinnakali and I. A. Razak, *J. Chem. Soc. - Dalt. Trans.*, 1999, **3**, 2311–2316.

19 S. Decurtins, H. W. Schmalle, P. Schneuwly, J. Ensling and P. Gütlich, *J. Am. Chem. Soc.*, 1994, **116**, 9521–9528.

20 M. Hernández-Molina, F. Lloret, C. Ruiz-Pérez and M. Julve, *Inorg. Chem.*, 1998, **37**, 4131–4135.

21 E. Coronado, J. R. Galán-Mascarós, C. J. Gómez-García and J. M. Martínez-Agudo, *Inorg. Chem.*, 2001, **40**, 113–120.

22 F. Pointillart, C. Train, M. Gruselle, F. Villain, H. W. Schmalle, D. Talbot, P. Gredin, S. Decurtins and M. Verdaguer, *Chem. Mater.*, 2004, **16**, 832–841.

23 M. Clemente-Léon, E. Coronado, C. J. Gómez-García and A. Soriano-Portillo, *Inorg. Chem.*, 2006, **45**, 5653–5660.

24 R. S. Fishman, C. L. Miguel and E. Coronado, *Inorg. Chem.*, 2009, **48**, 3039–3046.

25 E. Coronado, J. R. Galán Mascarós, M. C. Giménez-López, M. Almeida and J. C. Waerenborgh, *Polyhedron*, 2007, **26**, 1838–1844.

26 M. Clemente-León, E. Coronado, M. López-Jordà, G. M. Espallargas, A. Soriano-Portillo and J. C. Waerenborgh, *Chem. - A Eur. J.*, 2010, **16**, 2207–2219.

27 M. Clemente-León, E. Coronado and M. López-Jordà, *Dalton Trans.*, 2010, **39**, 4903–4910.

28 M. Clemente-León, E. Coronado, C. J. Gómez-García, M. López-Jordà, A. Camón, A. Repollés and F. Luis, *Chem. - A Eur. J.*, 2014, **20**, 1669–1676.

29 M. Clemente-León, E. Coronado, J. R. Galán-Mascarós and C. J. Gómez-García, *Chem. Commun.*, 1997, **0**, 1727–1728.

30 E. Coronado, J. R. Galán-Mascarós, C. J. Gómez-García and J. M. Martínez-Agudo, *Adv. Mater.*, 1999, **11**, 558–561.

31 E. Coronado, J. R. Galán-Mascarós, C. J. Gómez-García, J. Ensling and P. Gütlich, *Chem. - A Eur. J.*, 2000, **6**, 552–563.

32 M. Clemente-León, E. Coronado and M. López-Jordà, *Dalton Trans.*, 2013, **42**, 5100–5110.

33 M. Clemente-León, E. Coronado, M. López-Jordà and J. C. Waerenborgh, *Inorg. Chem.*, 2011, **50**, 9122–9130.

34 M. Clemente-León, E. Coronado, M. C. Giménez-López, A. Soriano-Portillo, J. C. Waerenborgh, F. S. Delgado and C. Ruiz-Pérez, *Inorg. Chem.*, 2008, **47**, 9111–9120.

35 M. Clemente-León, E. Coronado, M. López-Jordá, C. Desplanches, S. Asthana, H. Wang and J. F. Létard, *Chem. Sci.*, 2011, **2**, 1121–1127.

36 M. Clemente-León, E. Coronado, M. López-Jordà, J. C. Waerenborgh, C. Desplanches, H. Wang, J. F. Létard, A. Hauser and A. Tissot, *J. Am. Chem. Soc.*, 2013, **135**, 8655–8667.

37 M. López-Jordà, M. Giménez-Marqués, C. Desplanches, G. Mínguez Espallargas, M. Clemente-León and E. Coronado, *Eur. J. Inorg. Chem.*, 2016, **2016**, 2187–2192.

38 A. Alberola, E. Coronado, J. R. Galán-Mascarós, C. Giménez-Saiz and C. J. Gómez-García, *J. Am. Chem. Soc.*, 2003, **125**, 10774–10775.

39 E. Coronado, J. R. Galán-Mascarós, C. J. Gómez-García, E. Martínez-Ferrero and S. Van Smaalen, *Inorg. Chem.*, 2004, **43**, 4808–4810.

40 B. Zhang, Y. Zhang and D. Zhu, *Chem. Commun.*, 2012, **48**, 197–199.

41 S. Bénard, P. Yu, J. P. Audière, E. Rivière, R. Clément, J. Guilhem, L. Tchertanov and K. Nakatani, *J. Am. Chem. Soc.*, 2000, **122**, 9444–9454.

42 S. M. Aldoshin, N. A. Sanina, V. I. Minkin, N. A. Voloshin, V. N. Ikorskii, V. I. Ovcharenko, V. A. Smirnov and N. K. Nagaeva, *J. Mol. Struct.*, 2007, **826**, 69–74.

43 M. Sadakiyo, T. Yamada and H. Kitagawa, *J. Am. Chem. Soc.*, 2009, **131**, 9906–9907.

44 H. Okawa, A. Shigematsu, M. Sadakiyo, T. Miyagawa, K. Yoneda, M. Ohba and H. Kitagawa, *J. Am. Chem. Soc.*, 2009, **131**, 13516–13522.

45 E. Pardo, C. Train, G. Gontard, K. Boubekeur, O. Fabelo, H. Liu, B. Dkhil, F. Lloret, K. Nakagawa, H. Tokoro, S. I. Ohkoshi and M. Verdaguer, *J. Am. Chem. Soc.*, 2011, **133**, 15328–15331.

46 M. Sadakiyo, H. Okawa, A. Shigematsu, M. Ohba, T. Yamada and H. Kitagawa, *J. Am. Chem. Soc.*, 2012, **134**, 5472–5475.

47 H. Okawa, M. Sadakiyo, T. Yamada, M. Maesato, M. Ohba and H. Kitagawa, *J. Am. Chem. Soc.*, 2013, **135**, 2256–2262.

48 M. Mon, J. Vallejo, J. Pasán, O. Fabelo, C. Train, M. Verdaguer, S. I. Ohkoshi, H. Tokoro, K. Nakagawa and E. Pardo, *Dalton Trans.*, 2017, **46**, 15130–15137.

49 H. Ō Kawa, Y. Yoshida, K. Otsubo and H. Kitagawa, *Inorg. Chem.*, 2020, **59**, 623–628.

50 T. Endo, T. Akutagawa, S. I. Noro and T. Nakamura, *Dalton Trans.*, 2011, **40**, 1491–1496.

51 E. Pardo, C. Train, H. Liu, L. M. Chamoreau, B. Dkhil, K. Boubekeur, F. Lloret, K. Nakatani, H. Tokoro, S. I. Ohkoshi and M. Verdaguer, *Angew. Chem. Int. Ed.*, 2012, **51**, 8356–8360.

52 S. Benmansour, C. Cerezo-Navarrete, J. Canet-Ferrer, G. Muñoz-Matutano, J. Martínez-Pastor and C. J. Gómez-García, *Dalton Trans.*, 2018, **47**, 11909–11916.

53 R. Andrés, M. Brissard, M. Gruselle, C. Train, J. Vaissermann, B. Malézieux, J. P. Jamet and M. Verdaguer, *Inorg. Chem.*, 2001, **40**, 4633–4640.

54 C. Train, R. Gheorghe, V. Krstic, L. M. Chamoreau, N. S. Ovanesyan, G. L. J. A. Rikken, M. Gruselle and M. Verdaguer,

Nat. Mater., 2008, **7**, 729–734.

55 B. F. Abrahams, J. Coleiro, K. Ha, B. F. Hoskins, S. D. Orchard and R. Robson, *J. Chem. Soc. Dalton Trans.*, 2002, **8**, 1586–1594.

56 M. L. Mercuri, F. Congiu, G. Concas and S. A. Sahadevan, *Magnetochemistry*, 2017, **3**, 17.

57 B. F. Abrahams, T. A. Hudson, L. J. McCormick and R. Robson, *Cryst. Growth Des.*, 2011, **11**, 2717–2720.

58 S. Benmansour, C. Vallés-García, P. Gómez-Claramunt, G. Mínguez Espallargas and C. J. Gómez-García, *Inorg. Chem.*, 2015, **54**, 5410–5418.

59 S. Kitagawa and S. Kawata, *Coord. Chem. Rev.*, 2002, **224**, 11–34.

60 T. T. Luo, Y. H. Liu, H. L. Tsai, C. C. Su, C. H. Ueng and K. L. Lu, *Eur. J. Inorg. Chem.*, 2004, **21**, 4253–4258.

61 B. F. Abrahams, J. Coleiro, B. F. Hoskins and R. Robson, *Chem. Commun.*, 1996, **5**, 603–604.

62 C. Robl, *Mater. Res. Bull.*, 1987, **22**, 1483–1491.

63 G. V. Shilov, Z. K. Nikitina, N. S. Ovanesyan, S. M. Aldoshin and V. D. Makhaev, *Russ. Chem. Bull.*, 2011, **60**, 1209–1219.

64 M. Atzori, S. Benmansour, G. Mínguez Espallargas, M. Clemente-León, A. Abhervé, P. Gómez-Claramunt, E. Coronado, F. Artizzu, E. Sessini, P. Deplano, A. Serpe, M. L. Mercuri and C. J. Gómez García, *Inorg. Chem.*, 2013, **52**, 10031–10040.

65 A. Abhervé, M. Clemente-León, E. Coronado, C. J. Gómez-García and M. Verneret, *Inorg. Chem.*, 2014, **53**, 12014–12026.

66 S. Benmansour, A. Abhervé, P. Gómez-Claramunt, C. Vallés-García and C. J. Gómez-García, *ACS Appl. Mater. Interfaces*, 2017, **9**, 26210–26218.

67 S. A. Sahadevan, A. Abhervé, N. Monni, C. Sáenz De Pipaón, J. R. Galán-Mascarós, J. C. Waerenborgh, B. J. C. Vieira, P. Auban-Senzier, S. Pillet, E. E. Bendeif, P. Alemany, E. Canadell, M. L. Mercuri and N. Avarvari, *J. Am. Chem. Soc.*, 2018, **140**, 12611–12621.

68 A. Bhattacharjee, D. Bhakat, M. Roy and J. Kusz, *Phys. B Condens. Matter*, 2010, **405**, 1546–1550.

69 I. R. Jeon, B. Negru, R. P. Van Duyne and T. D. Harris, *J. Am. Chem. Soc.*, 2015, **137**, 15699–15702.

70 J. A. DeGayner, I. R. Jeon, L. Sun, M. Dincă and T. D. Harris, *J. Am. Chem. Soc.*, 2017, **139**, 4175–4184.

71 M. E. Ziebel, L. E. Darago and J. R. Long, *J. Am. Chem. Soc.*, 2018, **140**, 3040–3051.

72 C. Hua, J. A. Degayner and T. D. Harris, *Inorg. Chem.*, 2019, **58**, 7044–7053.

73 L. Liu, L. Li, M. E. Ziebel and T. D. Harris, *J. Am. Chem. Soc.*, 2020, **142**, 4705–4713.

74 L. Liu, J. A. Degayner, L. Sun, D. Z. Zee and T. D. Harris, *Chem. Sci.*, 2019, **10**, 4652–4661.

75 L. E. Darago, M. L. Aubrey, C. J. Yu, M. I. Gonzalez and J. R. Long, *J. Am. Chem. Soc.*, 2015, **137**, 15703–15711.

76 R. Murase, C. J. Commons, T. A. Hudson, G. N. L. Jameson, C. D. Ling, K. S. Murray, W. Phonsri, R. Robson, Q. Xia, B. F. Abrahams and D. M. D'Alessandro, *Inorg. Chem.*, 2020, **59**, 3619–3630.

77 M. E. Ziebel, C. A. Gaggioli, A. B. Turkiewicz, W. Ryu, L. Gagliardi and J. R. Long, *J. Am. Chem. Soc.*, 2020, **142**, 2653–2664.

78 J. Chen, Y. Sekine, A. Okazawa, H. Sato, W. Kosaka and H. Miyasaka, *Chem. Sci.*, 2020, **11**, 3610–3618.

79 T. Lis, *Acta Crystallogr. Sect. B Struct. Crystallogr. Cryst. Chem.*, 1980, **36**, 2042–2046.

80 A. Caneschi, D. Gatteschi, R. Sessoli, A. L. Barra, L. C. Brunei and M. Guillot, *J. Am. Chem. Soc.*, 1991, **113**, 5873–5874.

81 R. Sessoli, D. Gatteschi, A. Caneschi and M. A. Novak, *Nature*, 1993, **365**, 141–143.

82 D. M. Packwood, K. T. Reaves, F. L. Federici, H. G. Katzgraber and W. Teizer, *Proc. R. Soc. A Math. Phys. Eng. Sci.*, 2013, **469**, 20130373.

83 M. Mannini, F. Pineider, P. Sainctavit, C. Danieli, E. Otero, C. Sciancalepore, A. M. Talarico, M. A. Arrio, A. Cornia, D. Gatteschi and R. Sessoli, *Nat. Mater.*, 2009, **8**, 194–197.

84 K. S. Pedersen, A. M. Ariciu, S. McAdams, H. Weihe, J. Bendix, F. Tuna and S. Piligkos, *J. Am. Chem. Soc.*, 2016, **138**, 5801–5804.

85 A. R. Rocha, V. M. García-Suarez, S. W. Bailey, C. J. Lambert, J. Ferrer and S. Sanvito, *Nat. Mater.*, 2005, **4**, 335–339.

86 M. Feng and M. L. Tong, *Chem. - A Eur. J.*, 2018, **24**, 7574-7594.

87 E. Ruiz, J. Cirera, J. Cano, S. Alvarez, C. Loose and J. Kortus, *Chem. Commun.*, 2008, **1**, 52–54.

88 F. Neese and D. A. Pantazis, *Faraday Discuss.*, 2011, **148**, 229–238.

89 K. Chakarawet, P. C. Bunting and J. R. Long, *J. Am. Chem. Soc.*, 2018, **140**, 2058–2061.

90 C. J. Milios, R. Inglis, A. Vinslava, R. Bagai, W. Wernsdorfer, S. Parsons, S. P. Perlepes, G. Christou and E. K. Brechin, *J. Am. Chem. Soc.*, 2007, **129**, 12505–12511.

91 C. J. Milios, A. Vinslava, W. Wernsdorfer, S. Moggach, S. Parsons, S. P. Perlepes, G. Christou and E. K. Brechin, *J. Am.*

Chem. Soc., 2007, **129**, 2754–2755.

92 C. Sangregorio, T. Ohm, C. Paulsen, R. Sessoli and D. Gatteschi, *Phys. Rev. Lett.*, 1997, **78**, 4645–4648.

93 N. Ishikawa, M. Sugita, T. Ishikawa, S. Y. Koshihara and Y. Kaizu, *J. Am. Chem. Soc.*, 2003, **125**, 8694–8695.

94 J. M. Frost, K. L. M. Harriman and M. Murugesu, *Chem. Sci.*, 2016, **7**, 2470–2491.

95 M. A. AlDamen, J. M. Clemente-Juan, E. Coronado, C. Martí-Gastaldo and A. Gaita-Ariño, *J. Am. Chem. Soc.*, 2008, **130**, 8874–8875.

96 M. Shiddiq, D. Komijani, Y. Duan, A. Gaita-Ariño, E. Coronado and S. Hill, *Nature*, 2016, **531**, 348–351.

97 F. S. Guo, B. M. Day, Y. C. Chen, M. L. Tong, A. Mansikkamäki and R. A. Layfield, *Angew. Chem. Int. Ed.*, 2017, **56**, 11445–11449.

98 C. A. P. Goodwin, F. Ortu, D. Reta, N. F. Chilton and D. P. Mills, *Nature*, 2017, **548**, 439–442.

99 F. S. Guo, B. M. Day, Y. C. Chen, M. L. Tong, A. Mansikkamäki and R. A. Layfield, *Science*, 2018, **362**, 1400–1403.

100 L. Escalera-Moreno, J. J. Baldoví, A. Gaita-Ariño and E. Coronado, *Chem. Sci.*, 2018, **9**, 3265–3275.

101 D. E. Freedman, W. H. Harman, T. D. Harris, G. J. Long, C. J. Chang and J. R. Long, *J. Am. Chem. Soc.*, 2010, **132**, 1224–1225.

102 J. M. Zadrozny, J. Telser and J. R. Long, *Polyhedron*, 2013, **64**, 209–217.

103 M. S. Fataftah, J. M. Zadrozny, D. M. Rogers and D. E. Freedman, *Inorg. Chem.*, 2014, **53**, 10716–10721.

104 Y. Rechkemmer, F. D. Breitgoff, M. Van Der Meer, M.

Atanasov, M. Hakl, M. Orlita, P. Neugebauer, F. Neese, B. Sarkar and J. Van Slageren, *Nat. Commun.*, 2016, **7**, 10467.

105 X. N. Yao, J. Z. Du, Y. Q. Zhang, X. B. Leng, M. W. Yang, S. Da Jiang, Z. X. Wang, Z. W. Ouyang, L. Deng, B. W. Wang and S. Gao, *J. Am. Chem. Soc.*, 2017, **139**, 373–380.

106 J. Vallejo, I. Castro, R. Ruiz-García, J. Cano, M. Julve, F. Lloret, G. De Munno, W. Wernsdorfer and E. Pardo, *J. Am. Chem. Soc.*, 2012, **134**, 15704–15707.

107 G. Christou, D. Gatteschi, D. N. Hendrickson and R. Sessoli, *MRS Bull.*, 2000, **25**, 66–71.

108 G. A. Craig and M. Murrie, *Chem. Soc. Rev.*, 2015, **44**, 2135–2147.

109 D. Gatteschi and R. Sessoli, *Angew. Chem. Int. Ed.*, 2003, **42**, 268–297.

110 R. Orbach, *Proc. Phys. Soc.*, 1961, **77**, 821–826.

111 K. N. Shrivastava, *Phys. Status Solidi*, 1983, **117**, 437–458.

112 M. J. Giansiracusa, A. K. Kostopoulos, D. Collison, R. E. P. Winpenny and N. F. Chilton, *Chem. Commun.*, 2019, **55**, 7025–7028.

113 J. J. Baldoví, E. Coronado, A. Gaita-Ariño, C. Gamer, M. Giménez-Marqués and G. Mínguez Espallargas, *Chem. - A Eur. J.*, 2014, **20**, 10695–10702.

114 R. Layfield and M. Murugesu, *Lanthanides and Actinides in Molecular Magnetism.*, Wiley, 2015.

115 J. M. Zadrozny, A. T. Gallagher, T. D. Harris and D. E. Freedman, *J. Am. Chem. Soc.*, 2017, **139**, 7089–7094.

116 C. J. Yu, M. D. Krzyaniak, M. S. Fataftah, M. R. Wasielewski and D. E. Freedman, *Chem. Sci.*, 2019, **10**, 1702–1708.

117 T. Yamabayashi, M. Atzori, L. Tesi, G. Cosquer, F. Santanni, M.

E. Boulon, E. Morra, S. Benci, R. Torre, M. Chiesa, L. Sorace, R. Sessoli and M. Yamashita, *J. Am. Chem. Soc.*, 2018, **140**, 12090–12101.

118 D. Aulakh, J. B. Pyser, X. Zhang, A. A. Yakovenko, K. R. Dunbar and M. Wriedt, *J. Am. Chem. Soc.*, 2015, **137**, 9254–9257.

119 D. Aulakh, L. Liu, J. R. Varghese, H. Xie, T. Islamoglu, K. Duell, C. W. Kung, C. E. Hsiung, Y. Zhang, R. J. Drout, O. K. Farha, K. R. Dunbar, Y. Han and M. Wriedt, *J. Am. Chem. Soc.*, 2019, **141**, 2997–3005.

120 G. K. H. Shimizu, J. M. Taylor and S. R. Kim, *Science*, 2013, **341**, 354–355.

121 T. Grancha, J. Ferrando-Soria, J. Cano, P. Amorós, B. Seoane, J. Gascon, M. Bazaga-García, E. R. Losilla, A. Cabeza, D. Armentano and E. Pardo, *Chem. Mater.*, 2016, **28**, 4608–4615.

122 J. Felsche, *Angew. Chem. Int. Ed*, 1993, **105**, 1158–1159.

123 G. -V Röschenthaler and W. Storzer, *Angew. Chem. Int. Ed.* , 1982, **21**, 208–208.

124 T. Yamada, M. Sadakiyo, A. Shigematsu and H. Kitagawa, *Bull. Chem. Soc. Jpn.*, 2016, **89**, 1–10.

125 H. Okawa, M. Sadakiyo, K. Otsubo, K. Yoneda, T. Yamada, M. Ohba and H. Kitagawa, *Inorg. Chem.*, 2015, **54**, 8529–8535.

126 C. Maxim, S. Ferlay, H. Tokoro, S. I. Ohkoshi and C. Train, *Chem. Commun.*, 2014, **50**, 5629–5632.

127 M. Sadakiyo, T. Yamada, K. Honda, H. Matsui and H. Kitagawa, *J. Am. Chem. Soc.*, 2014, **136**, 7701–7707.

128 F. Guo, C. Chen, K. Wang, Q. Zhang and Z. Lin, *Inorg. Chem.*, 2016, **55**, 7817–7819.

129 T. Yamada, S. Morikawa and H. Kitagawa, *Bull. Chem. Soc. Jpn.*, 2010, **83**, 42–48.

130 M. A. Halcrow, *Spin-Crossover Materials: Properties and Applications*, Wiley, 2013.

131 P. Gütlich, Y. Garcia and H. A. Goodwin, *Chem. Soc. Rev.*, 2000, **29**, 419–427.

132 P. Gütlich and H. A. Goodwin, in *Spin Crossover in Transition Metal Compounds*, 2012, pp. 1–47.

133 L. G. Lavrenova and O. G. Shakirova, *Eur. J. Inorg. Chem.*, 2013, **2013**, 670–682.

134 E. König, in *Progress in Inorganic Chemistry*, wiley, 2007, **35**, 527–622.

135 R. Ishikawa, S. Ueno, S. Nifuku, Y. Horii, H. Iguchi, Y. Miyazaki, M. Nakano, S. Hayami, S. Kumagai, K. Katoh, Z. Li, M. Yamashita and S. Kawata, *Chem. – A Eur. J.*, 2020, **26**, 1278–1285.

136 C. Atmani, F. El Hajj, S. Benmansour, M. Marchivie, S. Triki, F. Conan, V. Patinec, H. Handel, G. Dupouy and C. J. Gómez-García, *Coord. Chem. Rev.*, 2010, **254**, 1559–1569.

137 P. Gütlich, *Eur. J. Inorg. Chem.*, 2013, **2013**, 581–591.

138 S. Heider, H. Petzold, G. Chastanet, S. Schlamp, T. Rüffer, B. Weber and J. F. Létard, *Dalton Trans.*, 2013, **42**, 8575–8584.

139 H. J. Krüger, *Coord. Chem. Rev.*, 2009, **253**, 2450–2459.

140 V. Petrouleas and J. P. Tuchagues, *Chem. Phys. Lett.*, 1987, **137**, 21–25.

141 D. Boinnard, A. Bousseksou, A. Dworkin, J. M. Savariault, F. Varret and J. P. Tuchagues, *Inorg. Chem.*, 1994, **33**, 271–281.

142 G. Psomas, N. Bréfuel, F. Dahan and J. P. Tuchagues, *Inorg. Chem.*, 2004, **43**, 4590–4594.

143 L. Salmon, A. Bousseksou, B. Donnadieu and J. P. Tuchagues, *Inorg. Chem.*, 2005, **44**, 1763–1773.

144 L. Zhang, G. C. Xu, H. Bin Xu, T. Zhang, Z. M. Wang, M. Yuan and S. Gao, *Chem. Commun.*, 2010, **46**, 2554–2556.

145 V. A. Grillo, L. R. Gahan, G. R. Hanson, R. Stranger, T. W. Hambley, K. S. Murray, B. Moubaraki and J. D. Cashion, *J. Chem. Soc. - Dalt. Trans.*, 1998, **0**, 2341–2348.

146 J. S. Costa, C. Balde, C. Carbonera, D. Denux, A. Wattiaux, C. Desplanches, J. P. Ader, P. Gütlich and J. F. Létard, *Inorg. Chem.*, 2007, **46**, 4114–4119.

147 J. A. Real, A. B. Gaspar and M. Carmen Muñoz, *Dalton Trans.*, 2005, **0**, 2062–2079.

148 M. A. Halcrow, *Polyhedron*, 2007, **26**, 3523–3576.

149 M. Nihei, T. Shiga, Y. Maeda and H. Oshio, *Coord. Chem. Rev.*, 2007, **251**, 2606–2621.

150 J. A. Real, A. B. Gaspar, V. Niel and M. C. Muñoz, *Coord. Chem. Rev.*, 2003, **236**, 121–141.

151 M. A. Halcrow, *Chem. Soc. Rev.*, 2011, **40**, 4119–4142.

152 M. C. Muñoz and J. A. Real, *Coord. Chem. Rev.*, 2011, **255**, 2068–2093.

153 I. Nemec, R. Herchel and Z. Trávníček, *Dalton Trans.*, 2015, **44**, 4474–4484.

154 E. Coronado, M. Giménez-Marqués, G. Mínguez Espallargas, F. Rey and I. J. Vitórica-Yrezábal, *J. Am. Chem. Soc.*, 2013, **135**, 15986–15989.

155 F. Guillaume, Y. A. Tobon, S. Bonhommeau, J. F. Létard, L. Moulet and E. Freysz, *Chem. Phys. Lett.*, 2014, **604**, 105–109.

156 F. Prins, M. Monrabal-Capilla, E. A. Osorio, E. Coronado and H. S. J. van der Zant, *Adv. Mater.*, 2011, **23**, 1545–1549.

157 O. Kahn and C. J. Martinez, *Science*, 1998, **279**, 44–48.

158 C. Lefter, S. Rat, J. S. Costa, M. D. Manrique-Juárez, C. M.

Quintero, L. Salmon, I. Séguy, T. Leichle, L. Nicu, P. Demont, A. Rotaru, G. Molnár and A. Bousseksou, *Adv. Mater.*, 2016, **28**, 7508–7514.

159 V. Shalabaeva, K. Ridier, S. Rat, M. D. Manrique-Juarez, L. Salmon, I. Séguy, A. Rotaru, G. Molnár and A. Bousseksou, *Appl. Phys. Lett.*, 2018, **112**, 013301.

160 J. J. McGarvey and I. Lawthers, *J. Chem. Soc. Chem. Commun.*, 1982, **16**, 906–907.

161 S. Decurtins, P. Gütlich, C. P. Köhler, H. Spiering and A. Hauser, *Chem. Phys. Lett.*, 1984, **105**, 1–4.

162 A. Hauser, *Chem. Phys. Lett.*, 1986, **124**, 543–548.

163 V. A. Money, J. S. Costa, S. Marcén, G. Chastanet, J. Elhaïk, M. A. Halcrow, J. A. K. Howard and J. F. Létard, *Chem. Phys. Lett.*, 2004, **391**, 273–277.

164 J. F. Létard, L. Capes, G. Chastanet, N. Moliner, S. Létard, J. A. Real and O. Kahn, *Chem. Phys. Lett.*, 1999, **313**, 115–120.

165 A. Hauser, *Coord. Chem. Rev.*, 1991, **111**, 275–290.

166 A. Hauser, C. Enachescu, M. L. Daku, A. Vargas and N. Amstutz, *Coord. Chem. Rev.*, 2006, **250**, 1642–1652.

167 R. Kulmaczewski, E. Trzop, L. J. Kershaw Cook, E. Collet, G. Chastanet and M. A. Halcrow, *Chem. Commun.*, 2017, **53**, 13268–13271.

168 G. Chastanet, C. Desplanches, C. Baldé, P. Rosa, M. Marchivie and P. Guionneau, *Chem. Squared*, 2018, **2**, 2.

169 J.-F. Létard, P. Guionneau, O. Nguyen, J. S. Costa, S. Marcén, G. Chastanet, M. Marchivie and L. Goux-Capes, *Chem. - A Eur. J.*, 2005, **11**, 4582–4589.

170 M. A. Halcrow, *Coord. Chem. Rev.*, 2005, **249**, 2880–2908.

171 M. A. Halcrow, *Coord. Chem. Rev.*, 2009, **253**, 2493–2514.

172 C. Carbonera, J. Sánchez Costa, V. A. Money, J. Elhaïk, J. A. K. Howard, M. A. Halcrow and J. F. Létard, *J. Chem. Soc. Dalton Trans.*, 2006, **0**, 3058–3066.

173 V. A. Money, C. Carbonera, J. Elhaïk, M. A. Halcrow, J. A. K. Howard and J. F. Létard, *Chem. - A Eur. J.*, 2007, **13**, 5503–5514.

174 R. Pritchard, H. Lazar, S. A. Barrett, C. A. Kilner, S. Asthana, C. Carbonera, J. F. Létard and M. A. Halcrow, *J. Chem. Soc. Dalton Trans.*, 2009, **0**, 6656–6666.

175 J. M. Holland, S. A. Barrett, C. A. Kilner and M. A. Halcrow, *Inorg. Chem. Commun.*, 2002, **5**, 328–332.

176 M. Nihei, L. Han and H. Oshio, *J. Am. Chem. Soc.*, 2007, **129**, 5312–5313.

177 C. Rajadurai, O. Fuhr, R. Kruk, M. Ghafari, H. Hahn and M. Ruben, *Chem. Commun.*, 2007, **0**, 2636–2638.

178 C. A. Tovee, C. A. Kilner, S. A. Barrett, J. A. Thomas and M. A. Halcrow, *Eur. J. Inorg. Chem.*, 2010, **2010**, 1007–1012.

179 R. González-Prieto, B. Fleury, F. Schramm, G. Zoppellaro, R. Chandrasekar, O. Fuhr, S. Lebedkin, M. Kappes and M. Ruben, *Dalton Trans.*, 2011, **40**, 7564–7570.

180 K. Takahashi, Y. Hasegawa, R. Sakamoto, M. Nishikawa, S. Kume, E. Nishibori and H. Nishihara, *Inorg. Chem.*, 2012, **51**, 5188–5198.

181 M. S. Alam, M. Stocker, K. Gieb, P. Müller, M. Haryono, K. Student and A. Grohmann, *Angew. Chem. Int. Ed.*, 2010, **49**, 1159–1163.

182 T. Vermonden, D. Branowska, A. T. M. Marcelis and E. J. R. Sudhölter, *Tetrahedron*, 2003, **59**, 5039–5045.

183 C. Klein, E. Baranoff, M. Grätzel and M. K. Nazeeruddin, *Tetrahedron Lett.*, 2011, **52**, 584–587.

184 M. A. Halcrow, *New J. Chem.*, 2014, **38**, 1868–1882.

185 A. Abhervé, M. Clemente-León, E. Coronado, C. J. Gómez-García and M. López-Jordà, *Dalton Trans.*, 2014, **43**, 9406–9409.

186 V. Garciá-López, M. Palacios-Corella, A. Abhervé, I. Pellicer-Carrenõ, C. Desplanches, M. Clemente-León and E. Coronado, *Dalton Trans.*, 2018, **47**, 16958–16968.

187 V. García-López, M. Palacios-Corella, M. Clemente-León and E. Coronado, *Polyhedron*, 2019, **170**, 95–100.

188 V. García-López, M. Palacios-Corella, V. Gironés-Pérez, C. Bartual-Murgui, J. A. Real, E. Pellegrin, J. Herrero-Martín, G. Aromí, M. Clemente-León and E. Coronado, *Inorg. Chem.*, 2019, **58**, 12199–12208.

189 I. Galadzhun, R. Kulmaczewski, O. Cespedes, M. Yamada, N. Yoshinari, T. Konno and M. A. Halcrow, *Inorg. Chem.*, 2018, **57**, 13761–13771.

190 N. Bridonneau, L. Rigamonti, G. Poneti, D. Pinkowicz, A. Forni and A. Cornia, *Dalton Trans.*, 2017, **46**, 4075–4085.

191 M. Nihei, T. Maeshima, Y. Kose and H. Oshio, *Polyhedron*, 2007, **26**, 1993–1996.

192 L. J. Kershaw Cook, J. Fisher, L. P. Harding and M. A. Halcrow, *Dalton Trans.*, 2015, **44**, 9417–9425.

193 C. Rajadurai, F. Schramm, S. Brink, O. Fuhr, M. Ghafari, R. Kruk and M. Ruben, *Inorg. Chem.*, 2006, **45**, 10019–10021.

194 R. Pritchard, C. A. Kilner, S. A. Barrett and M. A. Halcrow, *Inorganica Chim. Acta*, 2009, **362**, 4365–4371.

195 V. García-López, M. Palacios-Corella, S. Cardona-Serra, M. Clemente-León and E. Coronado, *Chem. Commun.*, 2019, **55**, 12227–12230.

196 T. Delgado, M. Meneses-Sánchez, L. Piñeiro-López, C. Bartual-

Murgui, M. C. Muñoz and J. A. Real, *Chem. Sci.*, 2018, **9**, 8446–8452.

197 M. Meneses-Sánchez, L. Piñeiro-López, T. Delgado, C. Bartual-Murgui, M. C. Muñoz, P. Chakraborty and J. A. Real, *J. Mater. Chem. C*, 2020, **8**, 1623–1633.

198 T. Lathion, A. Fürstenberg, C. Besnard, A. Hauser, A. Bousseksou and C. Piguet, *Inorg. Chem.*, 2020, **59**, 1091–1103.

199 J. Yuan, S. Q. Wu, M. J. Liu, O. Sato and H. Z. Kou, *J. Am. Chem. Soc.*, 2018, **140**, 9426–9433.

200 B. Benaicha, K. Van Do, A. Yangui, N. Pittala, A. Lusson, M. Sy, G. Bouchez, H. Fourati, C. J. Gómez-Garciá, S. Triki and K. Boukheddaden, *Chem. Sci.*, 2019, **10**, 6791–6798.

201 C. Lochenie, K. Schötz, F. Panzer, H. Kurz, B. Maier, F. Puchtler, S. Agarwal, A. Köhler and B. Weber, *J. Am. Chem. Soc.*, 2018, **140**, 700–709.

202 J. Y. Ge, Z. Chen, L. Zhang, X. Liang, J. Su, M. Kurmoo and J. L. Zuo, *Angew. Chem. Int. Ed.*, 2019, **58**, 8789–8793.

203 B. Schäfer, T. Bauer, I. Faus, J. A. Wolny, F. Dahms, O. Fuhr, S. Lebedkin, H. C. Wille, K. Schlage, K. Chevalier, F. Rupp, R. Diller, V. Schünemann, M. M. Kappes and M. Ruben, *Dalton Trans.*, 2017, **46**, 2289–2302.

204 R. González-Prieto, B. Fleury, F. Schramm, G. Zoppellaro, R. Chandrasekar, O. Fuhr, S. Lebedkin, M. Kappes and M. Ruben, *Dalton Trans.*, 2011, **40**, 7564–7570.

205 N. I. Gumerova and A. Rompel, *Nat. Rev. Chem.*, 2018, **2**, 1–20.

206 L. Vilà-Nadal and L. Cronin, *Nat. Rev. Mater.*, 2017, **2**, 1–15.

207 J. T. Rhule, C. L. Hill, D. A. Judd and R. F. Schinazi, *Polyoxometalates in medicine*, 1998, vol. 98.

208 J. A. McCleverty and T. J. Meyer, *Comprehensive Coordination Chemistry II*, Elsevier Science, 2004, vol. 1–9.

209 C. L. Hill, *Chem. Rev.*, 1998, **98**, 1–2.

210 M. Sadakane and E. Steckhan, *Chem. Rev.*, 1998, **98**, 219–237.

211 T. Yamase and M. T. Pope, in *Igarss 2014*, Kluwer Academic/Plenum Publishers, 2014, pp. 1–5.

212 M. S. Wang, G. Xu, Z. J. Zhang and G. C. Guo, *Chem. Commun.*, 2010, **46**, 361–376.

213 E. Coronado and C. J. Gómez-García, *Chem. Rev.*, 1998, **98**, 273–296.

214 E. Coronado, C. Giménez-Saiz and C. J. Gómez-García, *Coord. Chem. Rev.*, 2005, **249**, 1776–1796.

215 J. Zhang, Y. Huang, G. Li and Y. Wei, *Coord. Chem. Rev.*, 2019, **378**, 395–414.

216 X. López, J. J. Carbó, C. Bo and J. M. Poblet, *Chem. Soc. Rev.*, 2012, **41**, 7537–7571.

217 B. Hasenknopf, R. Delmont, P. Herson and P. Gouzerh, *Eur. J. Inorg. Chem.*, 2002, **5**, 1081–1087.

218 P. R. Marcoux, B. Hasenknopf, J. Vaissermann and P. Gouzerh, *Eur. J. Inorg. Chem.*, 2003, **13**, 2406–2412.

219 C. Allain, S. Favette, L. M. Chamoreau, J. Vaissermann, L. Ruhlmann and B. Hasenknopf, *Eur. J. Inorg. Chem.*, 2008, **22**, 3433–3441.

220 M. P. Santoni, A. K. Pal, G. S. Hanan, A. Proust and B. Hasenknopf, *Inorg. Chem.*, 2011, **50**, 6737–6745.

221 C. Yvon, A. Macdonell, S. Buchwald, A. J. Surman, N. Follet, J. Alex, D. L. Long and L. Cronin, *Chem. Sci.*, 2013, **4**, 3810–3817.

222 A. Abhervé, M. Palacios-Corella, J. M. Clemente-Juan, R. Marx, P. Neugebauer, J. Van Slageren, M. Clemente-León and E. Coronado, *J. Mater. Chem. C*, 2015, **3**, 7936–7945.

223 W. H. Jong, K. I. Hardcastle and C. L. Hill, *Eur. J. Inorg. Chem.*,

2006, **13**, 2598–2603.

224 W. H. Jong and C. L. Hill, *J. Am. Chem. Soc.*, 2007, **129**, 15094–15095.

225 X. X. Li, L. J. Zhang, C. Y. Cui, R. H. Wang and G. Y. Yang, *Inorg. Chem.*, 2018, **57**, 10323–10330.

Resumen y objetivos de la tesis doctoral.

Esta tesis tiene como objetivo principal la preparación de materiales moleculares multifuncionales magnéticos. Para ello se han usado dos estrategias diferentes: una aproximación iónica, en la que se han preparado sales de cationes funcionales y se han combinado con redes aniónicas extendidas (capítulos 2 y 3); y la segunda estrategia, donde, a través de enlaces covalentes entre ligandos funcionales y fulerenos (capitulo 4), o polioxometalatos (capítulo 5) se han obtenido sistemas que presentan la propiedad de transición de espín con efectos sinérgicos.

En el capítulo 2 se presenta la síntesis y caracterización de varios polímeros de coordinación basados en el ligando anilato con cationes insertados de tipo amonio de diferentes tamaños que modulan la conductividad protónica del material. Las redes, con formula $(Me_2NH_2)[Mn^{II}Cr^{III}(Br_2An)_3]\cdot 2H_2O$, $(Et_2NH_2)[Mn^{II}Cr^{III}(Br_2An)_3]$, $(Et_3NH)[Mn^{II}Cr^{III}(Cl_2An)_3]$ y $[(Et)(i\text{-}Pr)_2NH[Mn^{II}Cr^{III}(Br_2An)_3]\cdot(CHCl_3)_{0.5}\cdot(H_2O)$ (Me = metilo, Et = etilo y i-Pr = isopropilo) estructuralmente presentan la típica estructura de tipo panal de abeja con canales hexagonales. Los cationes más pequeños ($Me_2NH_2^+$, $Et_2NH_2^+$ y Et_3NH^+), se insertan dentro de los canales hexagonales, mientras que en el caso del derivado isopropilo de amonio, los cationes se encuentran insertados en los canales y entre las capas. Todos los sistemas se ordenan ferrimagnéticamente con T_c de 8-9 K. En el caso del compuesto con $[(Et)(i\text{-}Pr)_2NH]^+$, la diferencia de distancias entre capas provoca un comportamiento metamagnético cuando la muestra se mide en contacto con las aguas madre. Este comportamiento se ve alterado en la muestra desolvatada que muestra el mismo ordenamiento ferrimagnético del resto de compuestos debido al colapso de la estructura. El comportamiento metamagnético se puede recuperar simplemente volviendo a sumergir la muestra en aguas madre, lo que muestra la reversibilidad de las propiedades magnéticas del compuesto. Todos

los compuestos presentan valores bajos de conductividad protónica de tipo Grotthuss con valores entre 2.3×10^{-6} $S \cdot cm^{-1}$ y 2.4×10^{-5} $S \cdot cm^{-1}$.

En el capítulo 3 se presenta la preparación y caracterización de complejos de Co(II), que se comportan como imanes unimoleculares, y su inserción en redes 3D de tipo oxalato. La caracterización estructural de los complejos muestra dos complejos de simetría octaédrica de cobalto, $[Co^{II}(L)_2](ClO_4)_2 \cdot 0.5MeCN \cdot Et_2O \cdot 0.25H_2O$ y $[Co^{II}(L)(CH_3CN)_2(H_2O)](ClO_4)_2 \cdot MeCN$ (L = 3,5-Diamino-2,4,6-triazinil)2,2'-bipiridina). La inserción del complejo Co:L 1:2 en la red de tipo oxalato da lugar a un polímero de coordinación 3D aquiral. Esta red se ordena ferromagnéticamente. Las medidas de resonancia paramagnética electrónica sugieren interacciones débiles de tipo canje entre las dos subredes.

En el capítulo 4, se muestra el diseño y la preparación de aductos hexakis-substituidos de [60]fulereno con bpp. La combinación de Fe(II) con estos aductos da lugar a diferentes moléculas con transición de espín, con hasta seis complejos de transición de espín por fulereno. Espectroscopías de ultravioleta visible y fluorescencia se utilizan como herramientas para monitorizar la formación de complejos de Fe(II) en disolución a través de la aparición secuencial de bandas de transferencia de carga metal-ligando y la disminución de la luminiscencia del ligando. Algunos de estos complejos polinucleares muestran transición de espín térmica y fotoinducida en estado sólido. Estos resultados demuestran que los derivados de fulereno presentados son plataformas muy versátiles para el desarrollo de nuevos materiales que presentan transición de espín y además son una alternativa interesante para la preparación de monocapas autoensambladas de este ligando tridentado, cosa que ha sido imposible hasta el momento.

Finalmente, en el capítulo 5 se presenta la funcionalización y caracterización de un polioxovanadato de tipo Lindqvist. La

subunidad $[V_6O_{19}(C_{16}H_{15}N_6O)_2]^{2-}$, bifuncionalizada con 1-bpp, se combina con Fe(II) y Zn(II) para dar lugar a un polímero de coordinación 1D. La estructura del compuesto $Zn[V_6O_{19}(C_{16}H_{15}N_6O)_2]_2 \cdot solv$, resuelta por difracción de rayos X de monocristal, muestra POMs unidos unos a otros a través de los centros metálicos divalentes. El derivado de Fe(II), isoestructural al de Zn(II), muestra una transición de espín térmica y fotoinducida que se puede controlar mediante la reducción y reoxidación química o intercambios de disolvente. Esto es debido a la flexibilidad estructural de las cadenas de POM que admiten la entrada de moléculas huésped (reductores, oxidantes y disolventes) que modulan el estado de espín de los complejos de Fe(II) y la cooperatividad de sus transiciones de espín.

Resum i objectius de la tesi doctoral.

Aquesta tesi té com a objectiu principal la preparació de materials moleculars multifuncionals magnètics. Per a això s'han fet servir dues estratègies diferents: una aproximació iònica, en la qual s'han preparat sals de cations funcionals i s'han combinat amb xarxes aniòniques esteses (capítols 2 i 3); i la segona estratègia, on, a través d'enllaços covalents entre lligands funcionals i ful·lerens (capítol 4), o polioxometalats (capítol 5) s'han obtingut sistemes que presenten la propietat de transició d'espí amb efectes sinergics.

Al capítol 2 es presenta la síntesi i caracterització de diversos polímers de coordinació basats en el lligand anilat amb cations inserits de tipus amoni de diferents tamanys que modulen la conductivitat protònica del material. Les xarxes, amb formula $(Me_2NH_2)[Mn^{II}Cr^{III}(Br_2An)_3]\cdot 2H_2O$, $(Et_2NH_2)[Mn^{II}Cr^{III}(Br_2An)_3]$, $(Et_3NH)[Mn^{II}Cr^{III}(Cl_2An)_3]$ i $[(Et)(i\text{-}Pr)_2NH[Mn^{II}Cr^{III}(Br_2An)_3]\cdot(CHCl_3)_{0.5}\cdot(H_2O)$ (Me = metil, Et = etil y i-Pr = isopropil) presenten la típica estructura de tipus bresca d'abella amb canals hexagonals. Els cation mes petits ($Me_2NH_2^+$, $Et_2NH_2^+$ y Et_3NH^+), es troben inserits dins dels canals hexagonals, mentre que en el cas del catió més voluminós $[(Et)(i\text{-}Pr)_2NH]^+$, el catió es troba inserit als canals i entre les capes. Tots els sistemes s'ordenen ferrimagnèticament amb T_c de 8-9K. En el cas del derivat d'isopropil d'amoni, la diferència de distàncies entre capes provoca un comportament metamagnètic quan la mostra es mesura en contacte amb aigües mare. Aquest comportament es veu alterat quan es desolvata la mostra, mostrant el mateix ordenament ferrimagnètic de la resta de compostos degut al col·lapse de l'estructura. El comportament metamagnètic pot ser recuperat simplement tornant a submergir la mostra en aigües mare, cosa que mostra la reversibilitat de les propietats magnètiques del compost. Tots els compostos presenten valors baixos de conductivitat protònica de

tipus Grotthuss amb valors entre 2.3×10^{-6} $S \cdot cm^{-1}$ and 2.4×10^{-5} $S \cdot cm^{-1}$.

Al capítol 3 es presenta la preparació i caracterització de complexos de Co (II), que es comporten com imants unimoleculars, i la seva inserció en xarxes 3D de tipus oxalat. La caracterització estructural dels complexos revela dos complexos de simetria octaèdrica de cobalt, $[Co^{II}(L)_2](ClO_4)_2 \cdot 0.5MeCN \cdot Et_2O \cdot 0.25H_2O$ i $[Co^{II}(L)(CH_3CN)_2(H_2O)](ClO_4)_2 \cdot MeCN$ (L = 3,5-Diamino-2,4,6-triazinil)2,2'-bipiridina). L'inserció del complex Co:L 1:2 a la xarxa de tipus oxalat dóna lloc a un polímer de coordinació 3D aquiral. Aquesta xarxa s'ordena ferromagnèticament. Les mesures de ressonància paramagnètica electrònica suggereixen interaccions dèbils de tipus bescanvi entre les dues xarxes.

Al capítol 4, el disseny i la preparació d'adductes hexakis-substituïts de [60]ful·lerè amb bpp són reportats. La combinació de Fe(II) amb aquests adductes dóna lloc a diferents molècules amb transició d'espí, amb un máxim de sis complexos de transició d'espí per ful·lerè. Espectroscopies d'ultra violeta visible i fluorescència s'utilitzen com a eines per monitoritzar la formació de complexos de Fe(II) en dissolució a través de l'aparició seqüencial de bandes de transferència de carrega metall-lligand. A més a més, la disminució de la luminiscència del lligand és una mostra de la formació d'aquests complexos. Alguns d'aquests complexos polinuclears mostren transició d'espí tèrmica i fotoindüida en estat sòlid. Aquests resultats demostren que els derivats de ful·lerè presentats són plataformes molt versàtils per al desenvolupament de nous materials que presenten transició d'espí i, a més, són una alternativa interessant per a la preparació de monocapes autoacoblades d'aquest lligant tridentat, cosa que ha estat impossible fins al moment.

Finalment, al capítol 5 es presenta la funcionalització i caracterització d'un polioxovanadat de tipus Lindqvist. La sub-unitat

$[V_6O_{19}(C_{16}H_{15}N_6O)_2]^{2-}$, bifuncionalizada amb 1-bpp, es combina amb Fe(II) i Zn(II) per donar lloc a un polímer de coordinació 1D. L'estructura del compost $Zn[V_6O_{19}(C_{16}H_{15}N_6O)_2]_2$·solv, resolta per difracció de rajos X de monocristall, mostra polioxometalats units uns als altres a través dels centres metálics divalents. El derivat de Fe(II), isostructural al de Zn(II), mostra una transició d'espí tèrmica y fotoinducida que es pot controlar mitjançant la reducció y reoxidació química o intercanvis de disolvent. Açò es deu a la flexibilitat estructural de les cadenes de POM que admeten l'entrada de mol·lècules hoste (reductors, oxidants i disolvents) que modulen l'estat d'espí dels complexos de Fe(II) i la cooperativitat de les seves transicions d'espí.

Chapter 2.

Influence of Proton Conducting Cations on the Structure and Properties of 2D Anilate-Based Magnets

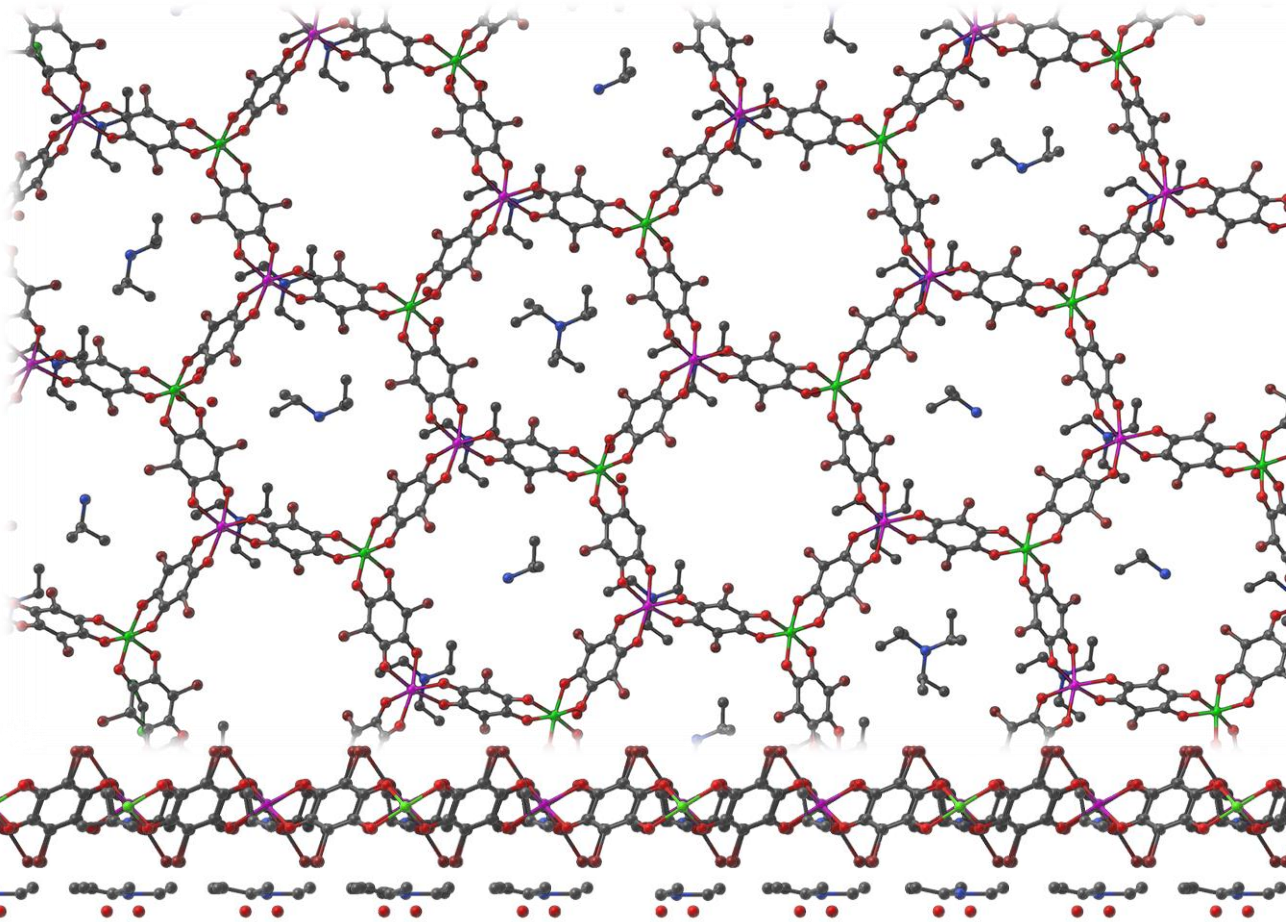

Mario Palacios-Corella, Alejandro Fernández-Espejo, Montse Bazaga-García, Enrique R. Losilla, Aurelio Cabeza, Miguel Clemente-León, and Eugenio Coronado, *Inorg. Chem.* 2017, **56**, 22, 13865–13877.

Introduction

The formation of extended solids that combine magnetic ordering with a second property is one of the most appealing topics in chemical science. A rational approach to design this type of multifunctional compounds is the use of extended anionic magnetic lattices, in which the choice of the appropriate countercation provides the second property of interest.[1]

This strategy has been exhaustively investigated in oxalate-based networks.[2] Thus, compounds combining the cooperative magnetism from the oxalate network with paramagnetism,[3] photochromism,[4] electrical conductivity,[5] ferroelectricity,[6] chirality,[7] single-molecule magnetic behavior[8] or spin crossover properties[9] have been reported. Several groups have explored the use of hydrophilic cations to grow bimetallic 2D or 3D oxalate-based networks as proton mediators or proton carriers. This has allowed the preparation of oxalate-based magnets at very low-temperatures (< 12 K) with high proton conductivities at room temperature such as 0.8×10^{-4} $S\cdot cm^{-1}$ at 65% RH in $\{NMe_3(CH_2COOH)\}[FeCr(ox)_3]\cdot3H_2O$ or 1.1×10^{-3} $S\cdot cm^{-1}$ at 95% RH in $(NH_4)_2[MnCr_2(ox)_6]\cdot34H_2O$.[10]

An alternative source for this type of coordination polymers is based on 2,5-dihydroxy-1,4-benzoquinone dianion and derivatives of formula $C_6O_4X^{2-}{}_2$ (anilates, X_2An^{2-}; X = F, Cl, Br or I, see Scheme 1). Both 2D and 3D homometallic anilate-based compounds have been reported in the literature.[11] These ligands present similar coordination and bridging modes as the oxalate ones with several advantages: (i) they are easier to modify or functionalize than the oxalates by changing the X group; (ii) they present higher magnetic ordering temperatures; (iii) their bigger size may give rise to porous compounds. The first heterometallic lattices based on the anilate ligand were the compounds of formula $A[M^{II}M^{III}(X_2An)_3]\cdot G$ (A = $[(H_3O)(phz)_3]^+$ (phz = phenazine) or NBu_4^+; M^{II} = Mn, Fe, Co; M^{III} = Cr,

Fe; X = H, Cl, Br, I; G = water or acetone).[12] These compounds show a 2D honeycomb structure. More recently, spin-crossover cations such as $[Fe^{III}(sal_2\text{-trien})]^+$ and $[Fe^{III}(acac_2\text{-trien})]^+$ were used to prepare bimetallic 2D anilate-based compounds.[13,14] The reduction of size of $[Fe^{III}(acac_2\text{-trien})]^+$ with respect to $[Fe^{III}(sal_2\text{-trien})]^+$ afforded a new type of structure in which the charge-compensating cations were placed inside the hexagonal channels of the 2D network, instead of being inserted in the interlamellar spacing as in the previous oxalate and anilate 2D networks.[14] As for graphene, these layered materials could be mechanically exfoliated in atomically thin layers with heights down to 2 nm by using the well-known Scotch tape method. In the last two years, the groups of Harris and Long have proven that the partial reduction of 2,5-dihydroxy-1,4-benzoquinone ligands and derivatives can lead to homometallic compounds showing coexistence of high magnetic ordering temperatures and electronic conductivity. Thus, a 3D compound with coexistence of a magnetic ordering with a T_c = 26 K and high electronic conductivity (0.16 ± 0.01 $S{\cdot}cm^{-1}$ at 298 K) was prepared by Long et al.[15] On the other hand, Harris et al. prepared a 2D porous compound with high conductivity ($1.4\ (7) \times 10^{-2}$ $S{\cdot}cm^{-1}$ at 300 K) and a solvent-induced switching of the magnetic ordering from T_c = 26 to 80 K of formula $(Me_2NH_2)_2[Fe_2(L_1)_3]{\cdot}2H_2O{\cdot}6DMF$ where L_1 is a mixture of Cl_2An^{2-} and its reduced semiquinone ligand ($(L_1)_3^{2-}$) and DMF is dimethylformamide.[16] More recently, the same group has demonstrated that this compound undergoes a single-crystal-to-single-crystal one-electron reduction to give $(CoCp_2)_{1.43}(Me_2NH_2)_{1.57}[Fe_2L_3]{\cdot}4.9DMF$ after soaking in a DMF solution of cobaltocene. This compound shows very high magnetic ordering temperature (T_c = 105 K) and electrical conductivity.[17] Very recently, S. Benmansour et al. have shown that reduction of the ligand is not necessary to give high electrical conductivities as the 2D compounds, $[(H_3O)(H_2O)(phz)_3][Fe^{II}Fe^{III}(X_2An)_3]{\cdot}12H_2O$ (X = Cl and Br), present 0.06 and 0.004 $S{\cdot}cm^{-1}$ conductivity values at room temperature attributed to the Fe(II)/Fe(III) mixed valence.[18]

In this work, we have explored the use of alkylammonium cations of increasing size, $Me_2NH_2^+$, $Et_2NH_2^+$, Et_3NH^+ and $[(Et)(i\text{-}Pr)_2NH]^+$, as templating cations for the growth of bimetallic anilate networks. The relatively small size of these cations could afford the formation of new networks in which the cations are placed into the hexagonal channels of the anilate-based network as reported before for $[Fe^{III}(acac_2\text{-trien})]^+$ cations. This could help to understand if there is a critical cation size for the formation of this type of structure and lead to new properties related to the different organizations of the anilate-based layers. On the other hand, the use of these cations could provide proton conduction to the systems thanks to the presence of acidic NH groups. As mentioned above, the formation of oxalate-based proton conducting materials has been explored previously leading to very interesting results but, to our knowledge, there are no reports of bimetallic anilate-based networks using the same type of cations. Possible advantages of the anilate-based networks to reach this goal are the larger size of the hexagonal channels, which could provide additional paths for proton conduction between cations placed in different layers, and the higher T_cs of the magnetic ordering, especially when anilate ligands are reduced. This could help to reduce the large gap between the temperatures at which proton conductivity and magnetic ordering occur in the oxalate-based compounds.

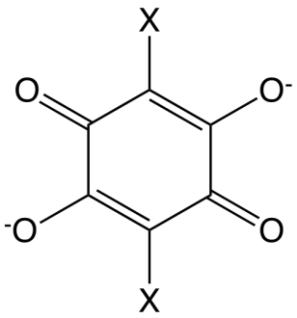

X = F, Cl, Br, I (X_2An^{2-}), or X = H ($dhbq^{2-}$).

Scheme 1. 2,5-Dihydroxy-1,4-benzoquinone dianion derivatives.

Experimental Section

General Information. Reagents and Materials. The starting reagents were from commercial sources and used as received.

Thermogravimetric analysis (TGA) data were recorded on a SDT-Q600 analyzer TA Instruments. Measurements were carried out on samples in open platinum crucibles under air flow from room temperature up to 600 °C at a heating rate of 10 °C·min^{-1}. Elemental analyses (C, H, and N) were performed with a Pekin-Elmer 240 analyzer.

Syntheses. The synthesis of the anilate precursor, $(Et_3NH)_3[Cr(Cl_2An)_3]\cdot H_2O$, was performed as reported in the literature.[19]

Synthesis of $(Me_2NH_2)_3[Cr(Br_2An)_3]\cdot 2H_2O$. Bromanilic acid (500 mg, 1.68 mmol) was dissolved in 50 mL of acetonitrile, and 0.65 mL (3.87 mmol) of a solution of dimethylamine (40 % in water) was added. A white-pink precipitate appeared. A solution of 330 mg (0.66 mmol) of $KCr(SO_4)_2\cdot 12H_2O$ in 15mL of water was added and the mixture turned into a purple solution. The solution was refluxed overnight and filtered. After 5 days, a dark purple crystalline powder was obtained and collected by filtration. FT-IR (ν/cm^{-1}, KBr pellets): 3439(m), 3062(w), 3019(w), 2952(w), 2781(w), 1623(m), 1519(vs), 1346(vs), 1306(s), 1018(w), 989(m), 811(m), 602(m), 558(m), 505(w), 409(w).

Anal. Calcd (%) for **(**$Me_2NH_2)_3[Cr(Br_2An)_3]\cdot 2H_2O$: C, 25.88; H, 2.53; N, 3.77 %. Found: C, 24.43; H, 2.36; N, 3.41 %.

Synthesis of $(Et_2NH_2)_3[Cr(Br_2An)_3]$. Bromanilic acid (500 mg, 1.68 mmol) was dissolved in 50 mL of acetonitrile, and 0.435 mL (4.15 mmol) of a solution of diethylamine (99.5% in water) was added. A white-pink precipitate appears. A solution of 280 mg (0.56 mmoL) of $KCr(SO_4)_2\cdot 12H_2O$ in 15mL of water was added and the mixture turned

into a purple solution. The solution was refluxed overnight and filtered. After 5 days, a dark purple crystalline powder was obtained and collected by filtration. FT-IR (ν/cm^{-1}, KBr pellets): 3442(m), 3043(w), 2986(w), 2926(w), 2841(w), 2777(w), 1636(m), 1518(vs), 1344(vs), 1303(s), 1056(w), 986(m), 811(m), 604(m), 561(m), 505(w), 415(w).

Anal. Calcd (%) for **(**$Et_2NH_2)_3[Cr(Br_2An)_3]$: C, 31.01; H, 3.12; N, 3.62 %. Found: C, 30.53; H, 3.04; N, 3.74 %.

Synthesis of [(Et)(i-Pr)$_2$NH]$_3$[Cr(Br$_2$An)$_3$]. Bromanilic acid (1 g, 3.3 mmol) is dissolved was 40 mL of acetonitrile, and 1.94 mL (11.1 mmol) of N,N-diisopropylethylamine and 800 mg (1.6 mmol) of $KCr(SO_4)_2{\cdot}12H_2O$ dissolved in 20 mL of water were added to the solution. The solution was refluxed overnight and filtered. After 4 days a dark red crystalline precipitate was obtained and collected by filtration. FT-IR (ν/cm^{-1}, KBr pellets): 3448(m), 3052(m), 2986(m), 2939(w), 2873(w), 2822(w), 2775(w), 2711(w), 1643(m), 1519(vs), 1344(vs), 1298(s), 1179(w), 1129(w), 1066(w), 984(m), 809(m), 598(m), 559(m), 503(w), 404(w).

Anal. Calcd (%) for $[(Et)(i\text{-}Pr)_2NH]_3[Cr^{III}(Br_2An)_3]$: C, 37.92; H, 4.55; N, 3.16 %. Found: C, 37.63; H, 4.51; N, 3.22 %.

Synthesis of (Me$_2$NH$_2$)[Mn^{II}Cr^{III}(Br$_2$An)$_3$]·2H$_2$O (1), (Et$_2$NH$_2$)[Mn^{II}Cr^{III}(Br$_2$An)$_3$] (2), (Et$_3$NH)[Mn^{II}Cr^{III}(Cl$_2$An)$_3$] (3) and [(Et)(i-Pr)$_2$NH][CrMn(Br$_2$An)$_3$]·(CHCl$_3$)$_{0.5}$·(H$_2$O) (4). Single crystals were obtained by a slow diffusion of a 5 x 10^{-3} M solution of $MnCl_2{\cdot}4H_2O$ in MeOH/CH_2Cl_2 1:9 (**2** and **3**) or MeOH/$CHCl_3$ 1:9 (**1** and **4**) and a 5 x 10^{-3} M solution of $(Me_2NH_2)_3[Cr^{III}(Br_2An)_3]{\cdot}2H_2O$, $(Et_2NH_2)_3[Cr^{III}(Br_2An)_3]$, $(Et_3NH)_3[Cr(Cl_2An)_3]{\cdot}H_2O$ or $[(Et)(i\text{-}Pr)_2NH]_3[Cr(Br_2An)_3]$ in MeOH. After several weeks black crystals were obtained. Powder samples were obtained by mixing quickly the two solutions with $MnCl_2{\cdot}4H_2O$ dissolved in MeOH.

Anal. Calcd (%) for **1**, $C_{20}H_{12}Br_6CrMnNO_{14}$: C 22.31, H 1.12, N 1.30. Found: C 21.89, H 1.32, N 1.29. Anal. Calcd (%) for **2**, $C_{22}H_{12}Br_6CrMnNO_{12}$: C 24.73, H 1.13, N 1.31. Found: C 23.05, H 1.13, N 1.19. Anal. Calcd (%) for **3**, $C_{24}H_{16}Cl_6CrMnNO_{12}$: C 34.73, H 1.94, N 1.69. Found: C 34.25, H 2.07, N 1.79. Anal. Calcd (%) for **4**, $C_{53}H_{45}Br_{12}Cl_3Cr_2Mn_2N_2O_{26}$: C 26.47, H 1.89, N 1.16. Found: C 26.58, H 2.07, N 1.08.

Structural Characterization. Single crystals of the four compounds were mounted on glass fibers using a viscous hydrocarbon oil to coat the crystal and then transferred directly to the cold nitrogen stream for data collection. All reflection data were collected at 120 K for **1**, **2** and **4** and 180 K for **3**, on a Supernova diffractometer equipped with a graphite-monochromated Enhance (Mo) X-ray Source (λ = 0.7107 Å) (**1**, **2** and **4**) and on a Supernova Atlas Dual Source diffractometer with a Cu X-ray source (λ = 1.54184 Å) (**3**). The CrysAlisPro program, Oxford Diffraction Ltd., was used for unit cell determinations and data reduction. Empirical absorption correction was performed using spherical harmonics, implemented in the SCALE3 ABSPACK scaling algorithm. Crystal structures were solved by direct methods with the SIR97 program[20] and refined against all F^2 values with the SHELXL-2013 program[21] using the WinGX graphical user interface.[22] All non-hydrogen atoms were refined anisotropically except disordered solvent molecules and countercations. Due to this disorder, the overall quality of the data of **1**, **2** and **4** is poor and this results in high R factors (0.121, 0.166 and 0.199, respectively). Hydrogen atoms for disordered alkylammonium cations and disordered chloroform or water molecules in **4** and water molecules in **1** were not introduced but are taken into account in the chemical formulas. Data collection and refinement statistics are collected in Table 1. CCDC-1564529, 1564530, 1491090 and 1491091 contain the supplementary crystallographic data for this paper. These data can be obtained free of charge from The Cambridge Crystallographic Data Centre via www.ccdc.cam.ac.uk/data_request/cif. Glass capillaries (0.5 mm)

were filled with polycrystalline samples of the compounds and mounted and aligned on a Empyrean PANalytical powder diffractometer, using Cu Kα radiation (λ = 1.54177 Å). A total of three scans were collected at room temperature in the 2ϑ range 2-40º. To check the stability of samples after proton conductivity measurements, powder X-ray diffraction (PXRD) patterns were collected using a Bragg-Brentano configuration in the 2ϑ range of 4-50°. Additionally, in order to prove the recrystallization of compound **4** in presence of solvent molecules, a transmission geometry was selected. For this study, a small amount of 4 was placed in a holder between two Kapton films and some drops of a MeOH/$CHCl_3$ mixture were added. The powder diffraction pattern of the resolvated sample was recorded on an Empyrean PANalytical powder diffractometer equipped with a θ/θ goniometer and Cu K_α radiation in the 2ϑ range of 5-50°.

Physical Measurements. Magnetic measurements were performed with a Quantum Design MPMS-XL-5 SQUID magnetometer and a Quantum Design PPMS on crystalline samples of **1** (2.2 mg), **2** (9.5 mg), **3** (5.5 mg), and **4** (7.2 mg). Crystals of **4** were measured first in contact with the mother liquor (solvated sample). Afterward, the solvent was removed and the magnetic measurements were performed in the dry sample. Finally, to check the reversibility, the crystals were reimmersed in a MeOH/$CHCl_3$ mixture overnight and the measurements were repeated in contact with the solvent mixture (resolvated sample). The Mn/Cr/X (X = Cl or Br) ratios were measured with a Philips ESEM XL30 scanning electron microscope equipped with an EDAX DX-4 microsonde.

Conductivity Characterization. Impedance data were collected on cylindrical pellet (5 mm of diameter and ~ 1 mm of thickness) obtained by pressing 30-40 mg of powder samples of **1** - **4** at 250 MPa, for 2 min. The pellets were pressed between porous C electrodes (Sigracet, GDL 10 BB, no Pt). The sample cells were places inside a temperature and humidity controlled chamber (Espec SH-

222) and connected to a HP4284A impedance analyzer. AC impedance data were collected over the frequency range from 20 Hz to 1 MHz with an applied voltage of 1 V. All measurements were electronically controlled by the winDETA package of programs.[23] Pellets were first equilibrated at 95% relative humidity (RH) and preheated (0.2 °C/min) from 25 to 70 °C. Impedance spectra were recorded on cooling using a stabilization time of 3 h from 70 to 25 °C (0.2 °C/min) at 10 °C intervals. Water condensation on sample was avoided by reducing first the relative humidity before decreasing temperature.

Table 1. Crystallographic data for compounds **1**, **2**, **3** and **4**.

Compound	**1**	**2**	**3**	**4**
Empirical formula	$C_{20}H_{12}Br_6CrMnNO_{14}$	$C_{22}H_{12}Br_6CrMnNO_{12}$	$C_{24}H_{16}Cl_6CrMnNO_{12}$	$C_{53}H_{45}Br_{12}Cl_3Cr_2Mn_2N_2O_{26}$
Formula weight	1040.62	1068.63	829.89	2397.70
Crystal colour	Black	Black	Black	Black
Crystal size	0.09x0.03x0.02	0.12x0.07x0.03	0.06x0.02x0.01	0.13x0.10x0.06
Temperature (K)	120(2)	120(2)	180(2)	120(2)
Wavelength (Å)	0.71073	0.71073	1.54184	0.71073
Crystal system	Trigonal	Trigonal	Trigonal	Trigonal
Space group	*P*-31c	*P*-31c	*P*-31c	*P*-3c1
a (Å)	13.7524(8)	13.7058(7)	13.6939(15)	13.7008(6)
c (Å)	9.3395(7)	9.4887(6)	9.1823(8)	26.366(2)
γ (°)	120	120	120	120
V (Å^3)	1529.7(2)	1543.6(2)	1491.2(4)	4286.1(6)

ρ_{calc} (Mg/m^3)	2.242	2.273	1.813	1.828
$\mu(Mo_{K\alpha})$ (mm^{-1})	8.660	8.585	11.979	6.287
θ range (°)	3.421- 27.511	3.433-27.544	3.727-70.320	3.351-26.446
Reflns collected	33285	28079	4509	84273
Independent reflns (R_{int})	1181(0.1682)	1194 (0.0845)	719 (0.0510)	2122 (0.1493)
L. S. parameters, *p*/ restraints, *r*	65/2	69/0	75/0	150/10
$R1(F)$,[a] $I > 2\sigma(I)$	0.1210	0.1662	0.0689	0.1988
$wR2(F^2)$,[b] all data	0.3456	0.2672	0.1985	0.4377
$S(F^2)$,[c] all data	1.073	1.204	1.090	1.142

[a]$R1(F) = \sum||Fo|-|Fc||/\sum|Fo|$; [b]$wR2(F^2) = [\sum w(Fo^2-Fc^2)^2/\sum wFo^4]^{1/2}$; [c]$S(F^2) = [\sum w(Fo^2-Fc^2)^2/\sum n + r - p)]^{1/2}$

Results and Discussion

Syntheses. The preparation of $(Me_2NH_2)[Mn^{II}Cr^{III}(Br_2An)_3]\cdot 2H_2O$ (**1**), $(Et_2NH_2)[Mn^{II}Cr^{III}(Br_2An)_3]$ (**2**), $(Et_3NH)[Mn^{II}Cr^{III}(Cl_2An)_3]$ (**3**) and $[(Et)(i\text{-}Pr)_2NH][Mn^{II}Cr^{III}(Br_2An)_3]\cdot(CHCl_3)_{0.5}\cdot(H_2O)$ (**4**) is based on the slow diffusion of solutions of the anilate precursor salts $(Me_2NH_2)_3[Cr^{III}(Br_2An)_3]\cdot 2H_2O$ (**1**), $(Et_2NH_2)_3[Cr(Br_2An)_3]$ (**2**), $(Et_3NH)_3[Cr^{III}(Cl_2An)_3]$ (**3**) and $[(Et)(i\text{-}Pr)_2NH]_3[Cr^{III}(Br_2An)_3]$ (**4**) into a Mn^{2+} solution in other solvent. This method is simpler than that used to prepare other 2D bimetallic anilate-based networks containing cationic Fe(III) Schiff-base complexes for which $[Cr^{III}(Cl_2An)_3]^{3-}$ or $[Cr^{III}(Br_2An)_3]^{3-}$ salts were not known.[13,14] The best results were obtained with methanol/dichloromethane (**1** and **3**) or

methanol/chloroform (**2** and **4**) mixtures to dissolve the Mn^{2+} salt, and methanol to dissolve the anilate precursor. The chemical composition of these compounds, checked by microanalysis, shows Mn/Cr/Cl (**3**) or Mn/Cr/Br (**1**, **2** and **4**) ratios close to the expected 1/1/6. Composition obtained by elemental analysis of **1** is consistent with the presence of two water molecules. The weight loss corresponding to these water molecules is in agreement with the 3.5 % weight loss below 140 ºC observed in TGA of this compound (see below), which is not shown by the other three compounds. Composition of **2** obtained by elemental analysis deviates slightly from the theoretical composition. This could suggest the presence of an amorphous impurity or a solvated phase in the polycrystalline sample, which are not detected by PXRD. Synthesis of **1, 2** and **3** could be performed by mixing methanolic solutions of $(Me_2NH_2)_3[Cr^{III}(Br_2An)_3]\cdot 2H_2O$ (**1**), $(Et_2NH_2)_3[Cr(Br_2An)_3]$ (**2**) or $(Et_3NH)_3[Cr^{III}(Cl_2An)_3]$ (**3**) and $MnCl_2$. PXRD pattern confirms that these powders are isostructural with the single crystals (see below). In the case of **4**, the same direct precipitation method led to a product with a PXRD pattern completely different to that of the single crystals.

Structures of 1, 2 and 3. The three compounds crystallize in the trigonal space group *P*-31c. The structure is formed by anionic 2D anilate-based layers in the *ab* plane of formula $[Mn^{II}Cr^{III}(Br_2An)_3]^-$ (**1** and **2**) or $[Mn^{II}Cr^{III}(Cl_2An)_3]^-$ (**3**) with the well-known honeycomb structure, which is similar to that reported in other bimetallic anilate-based compounds.[12-14] It consists in a hexagonal layer where the Cr(III) and Mn(II) ions occupy alternating vertices of the hexagons and are linked through X_2An bridges in such a way that each Mn(II) is surrounded by three neighboring Cr(III) and vice versa (see Figure 1). It contains crystallographically independent Mn and Cr ions with occupancies of 0.16667 and characteristic Mn-O and Cr-O distances (2.208(10) and 1.972(8) Å in **1**, 2.171(14) and 1.963(9) Å in **2** and 2.174(4) and 1.964(4) Å in **3**). Within the honeycomb layer, the

bridged Mn(II) and Cr(III) present the opposite chirality, as expected. Mn(II) and Cr(III) centers are situated on a site of crystallographic three-fold symmetry, with three Br_2An or Cl_2An related in a propeller-like arrangement. Due to the centrosymmetric character of the structure, Mn(II) and Cr(III) present the opposite configuration in neighboring layers. These layers are alternated due to the presence of an inversion center between Mn ions from different layers that gives rise to two possible dispositions of the neighboring layers (see Figure S1).

a)

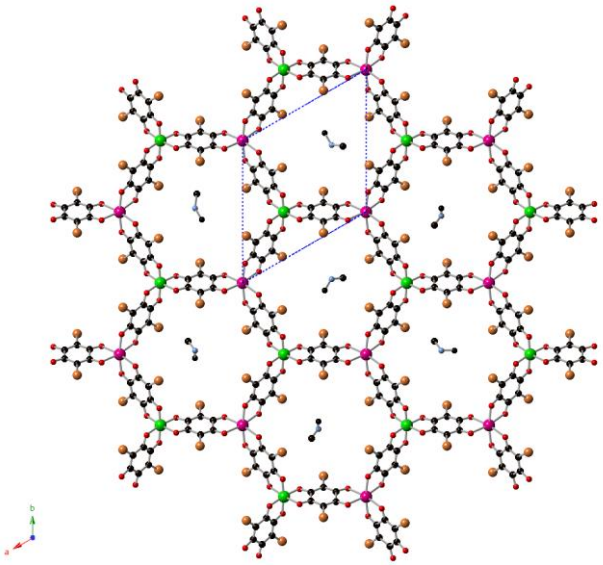

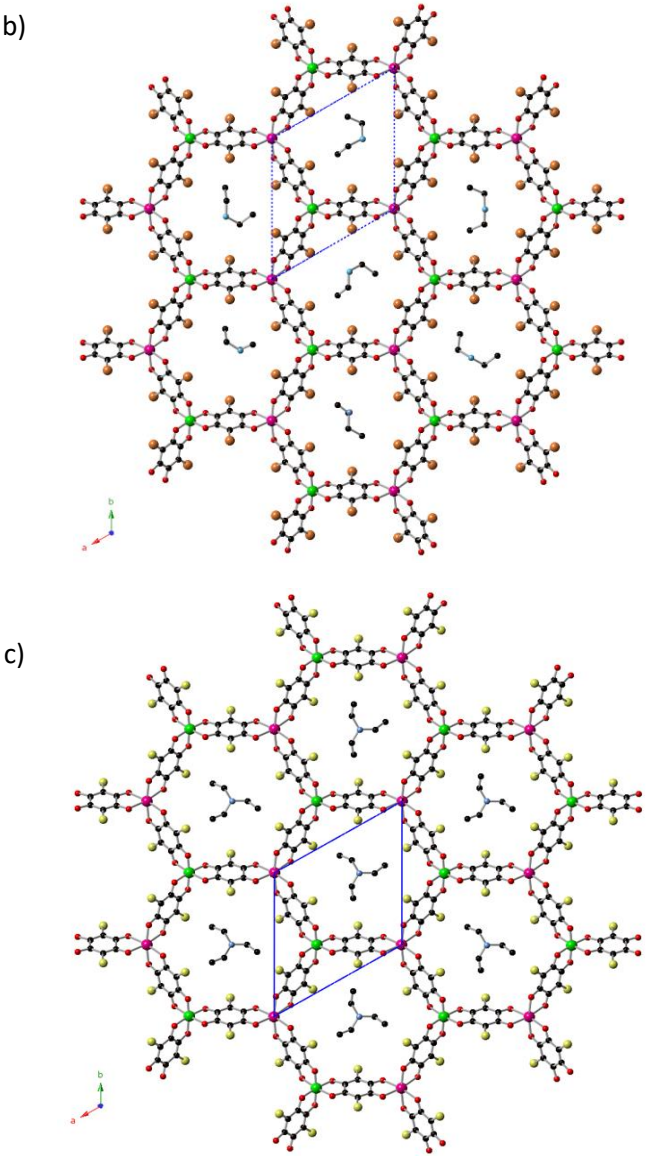

Figure 1. Projection in the ab plane of the compounds $(Me_2NH_2)[Mn^{II}Cr^{III}(Br_2An)_3]\cdot 2H_2O$ (**1**) (a), $(Et_2NH_2)[Mn^{II}Cr^{III}(Br_2An)_3]$ (**2**) (b), and (Et_3NH)**[**$Mn^{II}Cr^{III}(Cl_2An)_3]$ (**3**) (c). (Cr (green), Mn (pink) C (black), N (blue), O (red), Br (brown), Cl (yellow). Part of the disordered methylene or methyl groups of $Me_2NH_2^+$, $Et_2NH_2^+$, or Et_3NH^+ have been omitted for clarity.

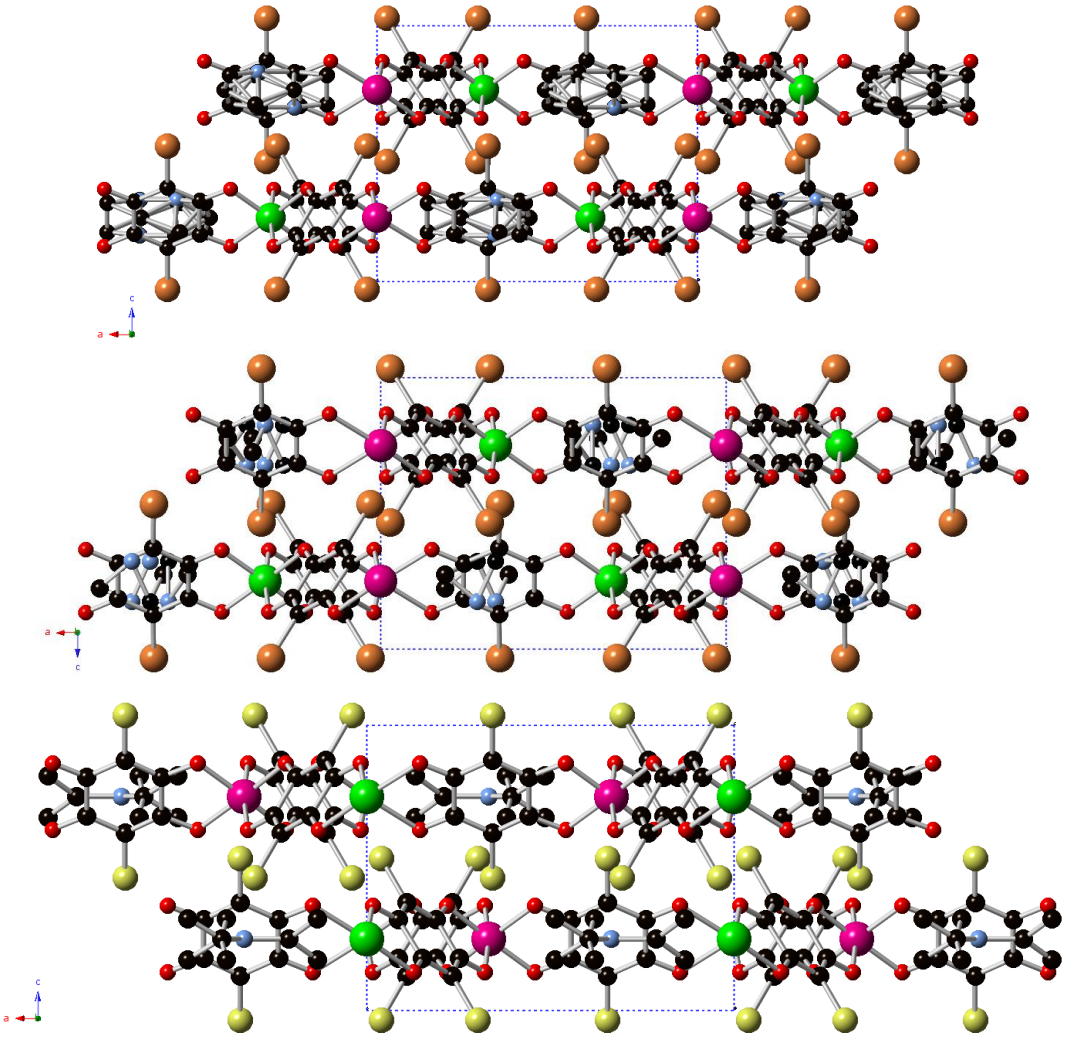

Figure 2. Projection in the ac plane of the compounds $(Me_2NH_2)[Mn^{II}Cr^{III}(Br_2An)_3]\cdot 2H_2O$ (**1**) (top), $(Et_2NH_2)[Mn^{II}Cr^{III}(Br_2An)_3]$ (**2**) (middle), and (Et_3NH)**[**$Mn^{II}Cr^{III}(Cl_2An)_3]$ (**3**) (bottom). (Cr (green), Mn (pink) C (black), N (blue), O (red), Cl (yellow), and Br(brown)). Part of the disordered methyl groups of $(Me_2NH_2)^+$ have been omitted for clarity.

As recently found by us in the structures of 2D anilate-based compounds obtained with small templating cations such as $[Fe^{III}(acac_2\text{-trien})]^+$,[14] $Me_2NH_2^+$ cations of **1**, $Et_2NH_2^+$ cations of **2**, and

Et_3NH^+ cations of **3** are inserted into the hexagons of the 2D anilate-based network and not between the layers as in most of the previous oxalate or anilate-based 2D compounds (see Figure 2). Thus, in **3** the center of the hexagons is occupied by the N of a crystallographically independent Et_3NH^+ cation (N1) with an occupancy of 0.16667 as it is placed in a 3-fold axis (see Figure 1). On the other hand, N1 and the methylene C atom (C4) of $(Et_3NH)^+$ cation are placed in the same 2-fold axis perpendicular to the 3-fold axis mentioned before. Consequently, the methyl C atom (C5) of $(Et_3NH)^+$ cation presents a disorder between two different configurations with occupancies of 0.5. The N atoms from Et_3NH^+ cations are placed below and above the Cr atoms from the two neighboring layers. The smaller size of $Me_2NH_2^+$ and $Et_2NH_2^+$ cations of **1** and **2** with respect to Et_3NH^+ ones of **3**, gives rise to a higher degree of disorder. To solve it, $Me_2NH_2^+$ cations of **1** have been modeled with three atoms with occupancies of 0.16667 (N, C4 and C5) with two of them, N and C4, occupying the same position. On the other hand, $Et_2NH_2^+$ cations of **2** have been modeled with four atoms with occupancies of 0.16667 (N, C100 and C101) and 0.33333 (C102) with two of them, N and C100, occupying the same position. The disordered $Me_2NH_2^+$ of **1** and $Me_2NH_2^+$ of **2** are generated from these atoms by a 3-fold axis in the middle of the hexagons perpendicular to the anilate-based layers and three 2-fold axis perpendicular to it.

The minimum distances between metals of neighboring layers are 4.67 Å for **1**, 4.74 Å for **2** and 4.59 Å for **3**, much shorter than those of compounds with $[Fe^{III}(acac_2\text{-trien})]^+$ (7.39 Å). This is a consequence of the smaller size of $Me_2NH_2^+$, $Et_2NH_2^+$ and Et_3NH^+ cations, which permits a larger degree of interpenetration between neighboring layers, and the alternated disposition of these layers. The higher interlayer distances of **1** and **2** compared with that of **3** are due to the presence of Br instead of Cl. As expected, these distances are much shorter than those reported in the bimetallic 2D anilate-based compounds with the templating cations NBu_4^+ (9.69 Å),

$[(H_3O)(phz)_3]^+$ (9.03-9.21 Å) or $[Fe^{III}(sal_2\text{-trien})]^+$ and derivatives (11.06-11.92 Å) between the layers.[12-14]

The structure of **1** resembles those of $(Me_2NH_2)_2[Fe^{III}_2(L_1)_3]\cdot 2H_2O\cdot 6DMF$,[16] $(Me_2NH_2)_3[Al_4(L_2)_3(L_1\bullet)_3]\cdot 3DMF$ and $(Me_2NH_2)_3[Al_4(L_1)_3(L_1\bullet)_3]\cdot 9DMF$[24] ($L_1$ and $L_1\bullet$, oxidized and reduced forms of Cl_2An and L_2 and $L_2\bullet$, oxidized and reduced forms of 2,5-dihydroxy-1,4-benzoquinone). Indeed, *a* and *b* parameters of these compounds are very close to those of **1, 2** and **3** indicating that the 2D layers have a very similar structure. However, neighboring anilate layers in these compounds are eclipsed defining channels as in other homometallic and heterometallic 2D anilate-based compounds.[12,25] Furthermore, the higher number of $Me_2NH_2^+$ cations, needed to compensate the higher charge of the anilate-based layers in these compounds, occupy the interlamellar space and not the center of the hexagons as those of **1**, **2** and **3**. This leads to longer interlayer distances 8.7449(5) Å for $(Me_2NH_2)_2[Fe^{III}_2(L_1)_3]\cdot 2H_2O\cdot 6DMF$,[16] 8.7701(2) Å for $(Me_2NH_2)_3[Al_4(L_2)_3(L_1\bullet)_3]\cdot 3DMF$ and 8.7473(5) Å for $(Me_2NH_2)_3[Al_4(L_1)_3(L_1\bullet)_3]\cdot 9DMF$.[24] Similar structures have been obtained very recently with the homometallic compounds $(Et_4N)_2[M_2(Cl_2An)_3]$ (M = Mg, Mn, Fe, Co, Ni, Cu, and Zn) and $(Et_4N)_2[Zn_2(F_2An)_3]$ with Et_4N^+ cations occupying the space between the $[Zn_2(F_2An)_3]^{2-}$ layers.[26]

The presence of the alkylammonium cations in the center of the hexagons together with the eclipsed disposition of the layers gives rise to the isolation of the cations in the structures. Thus, N···N, N···O, and N···X (X=Cl, Br) distances in the three compounds are longer than 3.4 Å leading to the absence of clear hydrogen bonding.

PXRD patterns of crystals of **1** and **2** at 300 K are shown in Figure S2. They confirm the structures obtained from single crystal X-ray diffraction experiments although that of **1** presents some differences with the simulated one from the single crystal X-ray diffraction

structure obtained at 120 K, which could be related to the solvate water molecules. PXRD pattern of a sample of **1** obtained by mixing quickly the two precursor solutions fits very well to the simulated one (Figure S2). In the case of **3**, it was not possible to obtain enough crystalline sample for magnetic and proton conduction measurements (see below). As a result, these measurements were performed in a powder sample obtained in the same way as described for **1**. PXRD pattern of this sample confirms the structure obtained from single crystal X-ray diffraction (see Figure S2).

Structure of $[(Et)(i\text{-}Pr)_2NH][Mn^{II}Cr^{III}(Br_2An)_3]\cdot(CHCl_3)_{0.5}\cdot(H_2O)$ (4). This compound crystallizes in the trigonal space group *P*-3c1. The structure of **4** is formed by anionic 2D anilate-based layers in the *ab* plane of formula $[Mn^{II}Cr^{III}(Br_2An)_3]^-$, which are very similar to those of **1** and **2** (Figure 3). However, the increase of size of the templating cation ($[(Et)(i\text{-}Pr)_2NH]^+$) with respect to those used in the previous compounds gives rise to important structural changes. Thus, a lateral view of the structure shows the presence of bilayers formed by two $[Mn^{II}Cr^{III}(Br_2An)_3]^-$ layers with a high degree of interpenetration, which is similar to that of **1**, **2** and **3** (Figure 4). These bilayers are separated by a layer of disordered $[(Et)(i\text{-}Pr)_2NH]^+$ cations and solvent molecules (disordered $CHCl_3$ and H_2O molecules). Consequently, there are two types of interlayer distances; intrabilayer ones (~4.42 Å), which are similar to those of **1**, **2,** and **3**, and interbilayer ones (~8.76 Å), which are similar to those of $(Me_2NH_2)_2[Fe^{III}_2L_3]\cdot 2H_2O\cdot 6DMF$.[16] Another important difference is that only half of the hexagons of the $[Mn^{II}Cr^{III}(Br_2An)_3]^-$ layers are occupied by $[(Et)(i\text{-}Pr)_2NH]^+$ cations. The remaining cations, needed to compensate the charge, are placed between the bilayers. The presence of $CHCl_3$ molecules is confirmed by microanalysis, which shows a Mn:Cr:Cl ratio close to 1:1:0.3. The Cl content calculated by microanalysis is lower than that predicted from the structure (Mn:Cr:Cl ratio of 1:1:1.5) due to desolvation after extracting the crystals from the mother liquor.

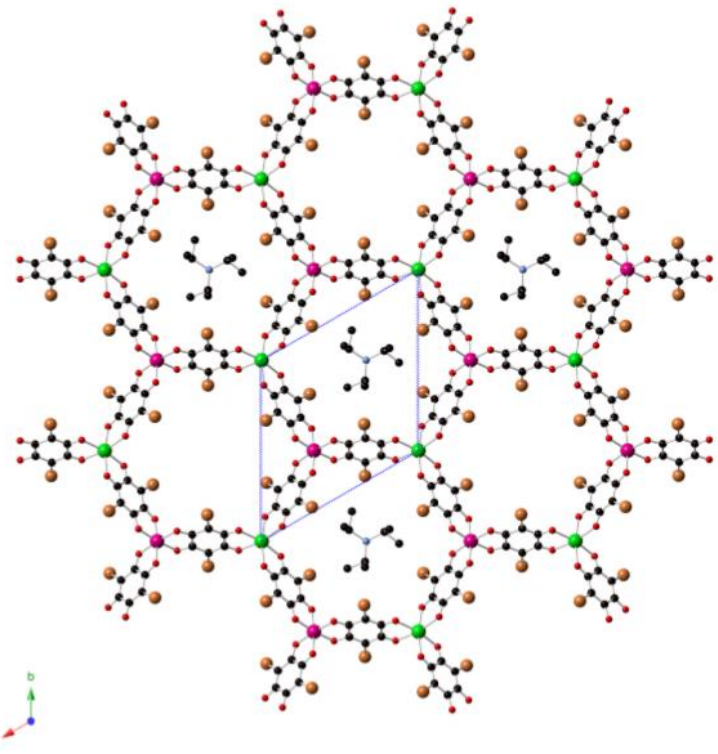

Figure 3. Projection in the ab plane of the compound [(Et)(i-Pr)$_2$NH][Mn^{II}Cr^{III}(Br$_2$An)$_3$]·(CHCl$_3$)$_{0.5}$·(H$_2$O) (**4**). (Cr (green), Mn (pink) C (black), N (blue), O (red), Br (brown)).

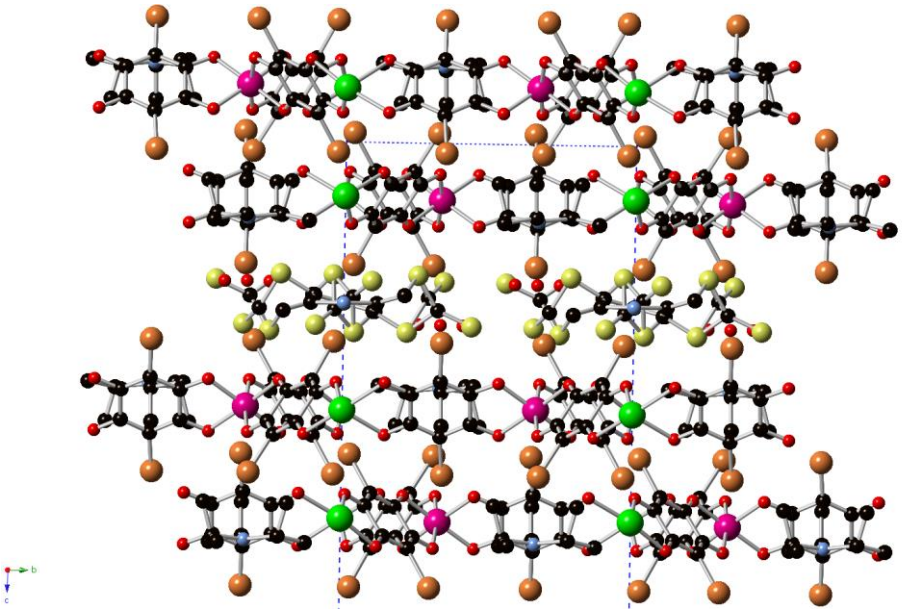

Figure 4. Projection in the bc plane of the compound [(Et)(i-Pr)$_2$NH][Mn^{II}Cr^{III}(Br$_2$An)$_3$]·(CHCl$_3$)$_{0.5}$·(H$_2$O) (**4**). (Cr (green), Mn (pink) C (black), N (blue), O (red), Cl (yellow), Br (brown)).

The [Mn^{II}Cr^{III}(Br$_2$An)$_3$]$^-$ layers contain crystallographically independent Mn and Cr ions with occupancies of 0.33333 and characteristic Mn-O and Cr-O distances (2.156(17)-2.182(16) and 1.983(14)-1.986(13) Å, respectively). As in **1**, **2** and **3**, Mn(II) and Cr(III) centers are situated on a site of crystallographic 3-fold symmetry, with three Br$_2$An related in a propeller-like arrangement. Within the honeycomb layer, the bridged Mn(II) and Cr(III) present the opposite chirality, as expected (Figure 3). Due to the centrosymmetric character of the structure, Mn(II) and Cr(III) present the opposite configuration in neighboring layers belonging to the same bilayer. These two layers are alternated due to the presence of an inversion center between two Mn ions (see Figure S3). The neighboring [Mn^{II}Cr^{III}(Br$_2$An)$_3$]$^-$ layers from different bilayers present halogen-halogen interactions[27] involving half of Br atoms from Br$_2$An ligands (Br2) with minimum Br···Br interlayer distances of ca 3.25 Å

(see Figure S4). These interactions are not present between neighboring layers belonging to the same bilayer and in **1**, **2** and **3**.

As mentioned above, there are two crystallographically independent $[(Et)(i\text{-}Pr)_2NH]^+$ cations. $[(Et)(i\text{-}Pr)_2NH]^+$ cations with N2 are inserted into the hexagons of the 2D anilate-based network as in **1** (see Figure 3), while those with N1 are placed in the interlayer space (see Figure S5). N1 and N2 present occupancies of 0.16667. N2 is placed in the same 3-fold axis as Cr ions. Disordered solvent molecules ($CHCl_3$ and H_2O) are placed in these interlayer space and give rise to problems in the structural resolution (see Experimental Section).

PXRD patterns of freshly filtered crystals of **4** at 300 K shows some differences with respect to the one calculated from the single crystal X-ray diffraction data, which indicate a very fast loss of solvent molecules (Figure S6). However, the main peaks from the simulated pattern are still observed coexisting with those of a second phase. This pattern changes drastically if it is measured after several days with a clear loss of crystallinity (Figure S6). Interestingly, the change is not irreversible and the original PXRD pattern is partially recovered after soaking the crystals several days in a $CHCl_3/CH_3OH$ mixture and measuring them with a kapton tape to avoid the loss of solvent molecules. This indicates that the disordered solvent molecules of the interlayer space can be lost and recovered in a reversible way. A similar "breathing" behavior has been observed in the 2D homometallic anilate-based compound $(Me_2NH_2)_2[Fe_2L_3]\cdot 2H_2O\cdot 6DMF$ mentioned above and other MOFs.[16] Finally, the crystallinity of the dry crystals of **4** could be improved by heating at 80° C probably thanks to complete desolvation (see Figure S6). On the other hand, PXRD patterns of the precipitate obtained by mixing quickly $MnCl_2$ and $[(Et)(i\text{-}Pr)_2NH]_3[Cr^{III}(Br_2An)_3]$ precursors in methanol is very close to that of the desolvated crystals (see Figure S6). This indicates that the slow diffusion in $CHCl_3$/MeOH mixtures of these precursors used in the synthesis of **4** favors the formation of a structure formed by bilayers, which collapses after losing the solvent molecules in a

different one, and is similar to that obtained by mixing quickly the precursors. Interestingly, the two structures can be interconverted in a reversible way.

Magnetic Properties. The product of the molar magnetic susceptibility times the temperature ($\chi_M T$) of **1**, **2** and **3** is shown in Figure 5. It presents at 300 K values of 7.0 $cm^3 \cdot K \cdot mol^{-1}$ for **1**, 6.7 $cm^3 \cdot K \cdot mol^{-1}$ for **2,** and 6.9 $cm^3 \cdot K \cdot mol^{-1}$ for **3**, which are close to the expected value for noninteracting Mn(II) and Cr(III) (spin only value of 6.3 cm^3 K mol^{-1}). When the temperature is lowered, $\chi_M T$ of the three compounds shows a continuous decrease reaching minima of 2.6 $cm^3 \cdot K \cdot mol^{-1}$ at 19 K for **1**, 3.6 $cm^3 \cdot K \cdot mol^{-1}$ at 16 K for **2** and 3.1 $cm^3 \cdot K \cdot mol^{-1}$ at 16 K for **3** followed by a sharp increase at lower temperatures with maxima at ca. 5.6 K for **1**, 6.4 K for **2** and 6.3 K for **3**. The decrease of $\chi_M T$ with the temperature may be attributed to antiferromagnetic Mn-Cr interactions mediated through the X_2An^{2-} bridges, as observed in other compounds containing similar $[Mn^{II}Cr^{III}(X_2An)_3]^-$ layers.[12-14] Since the ground spin states of Cr(III) and Mn(II) are different (3/2 and 5/2, respectively), this interaction leads to an antiferromagnetic coupling that results in a $\chi_m T$ minimum, followed by an increase of $\chi_m T$ below ca. 20 K, and finally by a ferrimagnetic long range ordering at low temperatures for the three compounds.

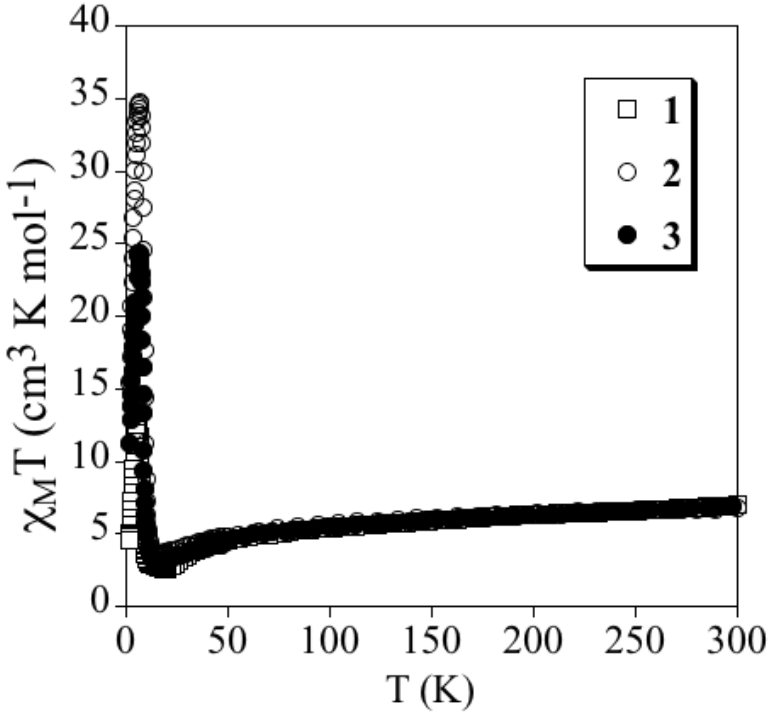

Figure 5. Temperature dependence of the product of the molar magnetic susceptibility times the temperature ($\chi_M T$) of **1** (empty squares), **2** (empty circles), and **3** (full circles).

The confirmation of the long-range order and a more accurate determination of the ordering temperatures are obtained from the susceptibility measurements performed with an alternating magnetic field (AC susceptibility). These measurements show a frequency-independent peak in the in phase molar susceptibility (χ'_M) and out of phase molar susceptibility (χ''_M) for **1** and **3** (Figure 6). In **2** a secondary peak appears at higher temperatures, which could be related to the presence of some impurity of a solvated phase as suggested by elemental analysis (see above). The T_c, determined as the temperature at which χ''_M becomes nonzero, is 7.9 K for **1**, 8.9 K for **2** and 8.0 K for **3**. These T_c values are close to those found for

$[Mn^{II}Cr^{III}(Cl_2An)_3]^-$ or $[Mn^{II}Cr^{III}(Br_2An)_3]^-$ salts of $[Fe^{III}(acac_2\text{-trien})]^+$ and $[Fe^{III}(sal_2\text{-trien})]^+$.[13,14]

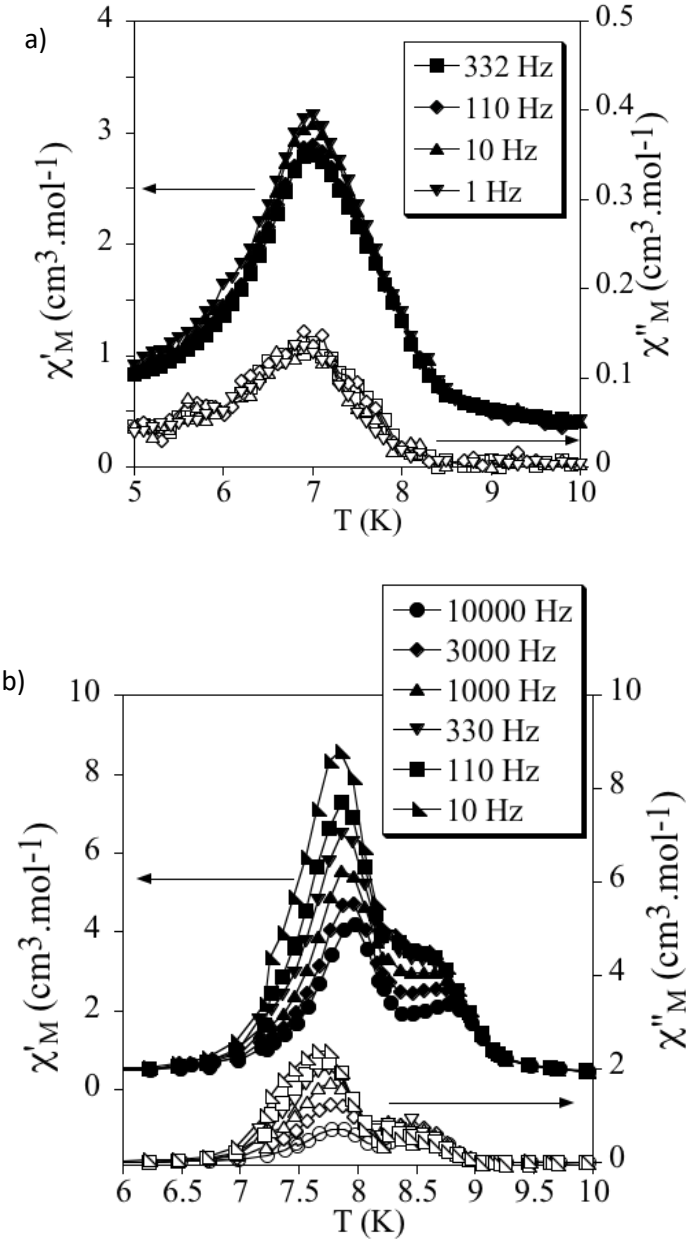

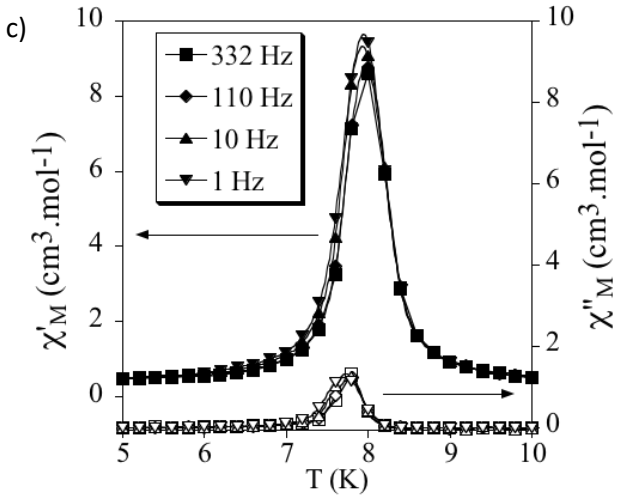

Figure 6. Temperature dependence of the in-phase AC susceptibility (χ') (filled symbols) and the out-of-phase AC susceptibility (χ") of **1** (a), **2** (b), and **3** (c).

The ferrimagnetic nature of the long-range ordering is confirmed by the isothermal magnetization measurements at 2 K that show a sharp increase of the magnetization at low fields that becomes more gradual at higher fields (Figure 7). At low fields (H < 0.3 T), the magnetization of the three compounds increases with a high slope reaching values of 0.9 μB (**1**), 1.1 μB (**2**) and 1.1 μB (**3**) at H = 0.3 T (insets in Figure 7). At higher fields, the magnetization of **1**, **2** and **3** tends to saturation (2.5 μB (**1**), 2.1 μB (**2**) and 2.2 μB (**3**) at 5 T). These values are close to that expected for a ferrimagnetic $Mn^{II}Cr^{III}$ network (Ms = 5 μB - 3 μB = 2 μB). These isothermal magnetization measurements also indicate that these compounds are soft ferrimagnets since they present hysteresis below the ordering temperatures with coercive fields of ca. 90 mT for **1**, 100 mT for **2** and 150 mT for **3** (insets in Figure 7).

a)

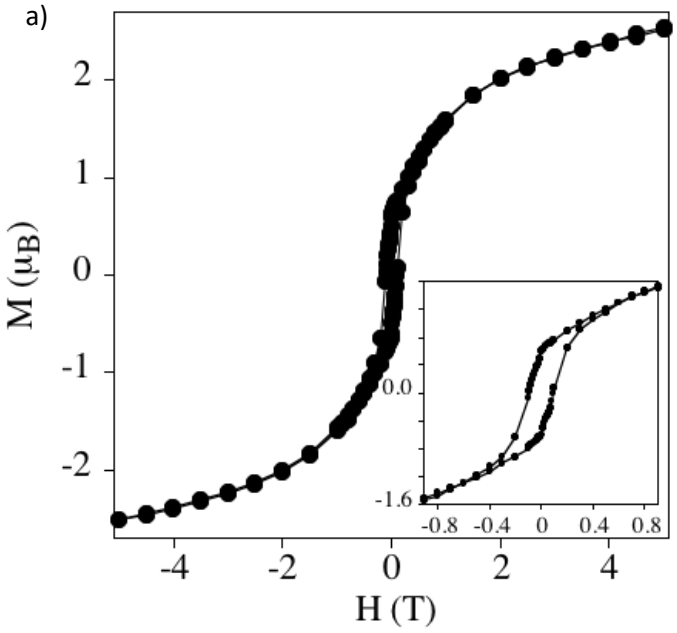
M (μB)
H (T)
2
1
0
-1
-2
-4
-2
0
2
4
0.0
-1.6
-0.8
-0.4
0
0.4
0.8

b)

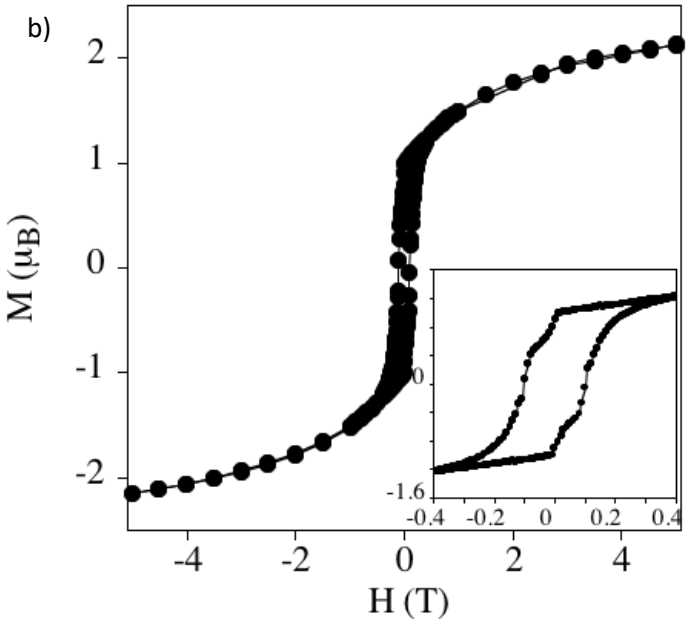
M (μB)
H (T)
2
1
0
-1
-2
-4
-2
0
2
4
-1.6
-0.4
-0.2
0
0.2
0.4

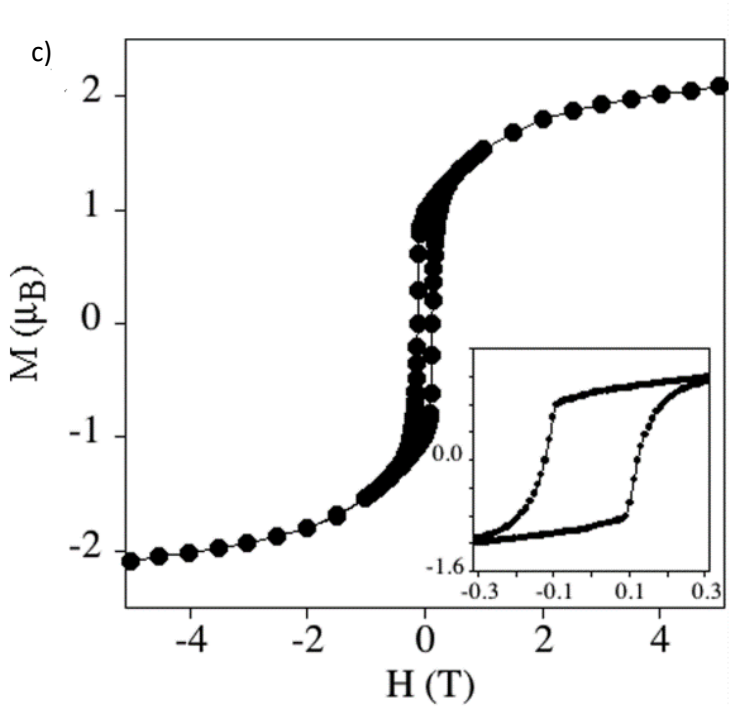

Figure 7. Hysteresis measurements of **1** (a), **2** (b), and **3** (c) at 2 K.

Due to the loss of crystallinity of **4** after extracting the crystals from the mother liquor (see above), the magnetic properties of this compound were measured in contact with the solvent ($CHCl_3$/MeOH mixture). The thermal dependence of $\chi_M T$ of solvated crystals of **4** is shown in Figure 8. It presents at 300 K a value of 6.5 $cm^3 \cdot K \cdot mol^{-1}$, as expected for noninteracting Mn(II) and Cr(III). When the temperature is lowered, $\chi_M T$ shows a continuous decrease to a minimum of 2.7 $cm^3 \cdot K \cdot mol^{-1}$ at 15.8 K close to that of **1**, **2** and, **3**. The major differences of $\chi_M T$ of **4** with respect to the other compounds were observed at lower temperatures. Thus, $\chi_M T$ value increases to a maximum of 5.6 $cm^3 \cdot K \cdot mol^{-1}$ at 8.9 K, and then decreases to 1.0 $cm^3 \cdot K \cdot mol^{-1}$ at 2 K. This result indicates that, in contrast to **1**, **2**, and **3**, compound **4** does not present a ferrimagnetic long range ordering. The inset of Figure 8 shows the thermal dependence of χ_M measured

under different external dc fields in the temperature range of 2-20 K. A sharp peak is observed at ca. 9 K at 100 and 1000 Oe, which disappears when the external field is 10000 Oe. This could indicate the presence of weak antiferrimagnetic interactions between the ferrimagnetic layers that can be overcome by a high field. These features are characteristic of a metamagnetic behavior, which is confirmed by the sigmoidal shape of the isothermal magnetization at 2 K (Figure 9). The magnetization curve shows a gradual and linear increase at low fields reaching 0.3 μB at H = 0.4 T. This increase becomes very sharp from 0.4 to 1 T (M = 1.6 μB at H = 1 T) and increases more gradually at higher magnetic fields without reaching saturation (M = 2.8 μB at H = 5 T, see Figure 7). The critical field is approximately H_c = 4900 Oe for this metamagnetic transition determined by the maximum in the dM/dH vs H curve. Small hystereses are observed below and above the H_c with a coercive field of 80 mT (see inset of Figure 9). The ac susceptibility measurements (Figure S7) show a frequency-independent peak in χ' at 9.6 K, whereas no out-of-phase signal is observed. All the above magnetic properties are consistent with a field-induced transition from an antiferromagnet to a canted spin structure showing spontaneous magnetization.

The origin of this behavior may be related to the presence of two very different interlayer distances. This novel feature is not observed in compounds containing analogous anilate-based networks, which shows interlayer distances close to the intrabilayer ones of **4** (~4.42 Å as in **1**, **2,** and **3**), or close to the interbilayer ones (~8.76 Å) ($[Fe^{III}(acac_2\text{-trien})][Mn^{II}Cr^{III}(Br_2An)_3]\cdot(CH_3CN)_2$ (7.53 Å), $[Ga^{III}(acac_2\text{-trien})][Mn^{II}Cr^{III}(Br_2An)_3]\cdot(CH_3CN)_2$ (7.57 Å)).[14] The Br···Br interactions interbilayer interactions mentioned above, which are not observed between the anilate-based layers of **1**, **2,** or **3**, could be responsible of the weak antiferromagnetic interaction among the ferrimagnetic layers. On the other hand, intrabilayer interactions seems to be

ferromagnetic as in **1**, **2,** or **3**. The synthesis of analogous compounds with I_2An ligands is in progress to confirm this.

When crystals of **4** were extracted from the mother liquor, the magnetic properties change completely and become close to those of **1**, **2,** and **3**. Thus, $\chi_M T$ of filtered crystals of **4** shows a continuous decrease from 6.9 $cm^3 \cdot K \cdot mol^{-1}$ at 300 K to a minimum of 3.0 $cm^3 \cdot K \cdot mol^{-1}$ at 18 K followed by a sharp increase at lower temperatures with maxima at ca. 6.9 K and a very high $\chi_M T$ value suggesting a ferrimagnetic long range ordering as that observed in **1**, **2** and **3** (see Figure S8). Thermal dependence of χ_M of the dry crystals of **4** under an applied magnetic field of 0.1 T confirms this behavior as it shows a sharp increase of χ_M at decreasing temperatures with much higher values than those of the solvated sample and (Figure 10). This is further confirmed by AC susceptibility measurements, which show a frequency-independent peak in χ'_M and χ''_M with a T_c of 9.0 K (see Figure S9), and the isothermal magnetization at 2 K. Thus, M of dried crystals of **4** shows a sharp increase at low fields that becomes more gradual at higher fields reaching 2.0 μB at 5 T (see Figure S10). It presents a hysteresis loop with a coercive field of ca. 4 mT (inset in Figure S10). The shape of the hysteresis loop of the dried crystals of **4** is different to that of **1**, **2** and **3** and other compounds with similar anilate-based networks. Thus, it presents a much more abrupt increase of M at low magnetic fields and the presence of steps. A possible explanation of the absence of metamagnetism in the desolvated crystals is the collapse of the structure after extracting the crystals from the mother liquor suggested by powder X-ray diffraction data (see above and Figure S6), which could lead to different interlayer magnetic interactions in the absence of Br···Br interlayer interactions. Interestingly, this behavior is reversible in agreement with X-ray powder diffraction data that suggest that the original structure is recovered after reimmersing the crystals in a $CHCl_3$/MeOH mixture. AC susceptibility measurements of the same crystals reimmersed in a $CHCl_3$/MeOH

mixture overnight and measured in contact with this solvent mixture (resolvated sample) do not show the peak in χ''_M observed in the dry sample (Figure S11). On the other hand, the maximum in χ'_M at 9 K, of the solvated sample is observed in the resolvated sample with similar values. Therefore, the metamagnetic behavior of a solvated sample of **4** is recovered. We thus observe a reversible switching of the magnetic properties, which resembles that observed in the 2D homometallic anilate-based compound $(Me_2NH_2)_2[Fe_2(L_1)_3]\cdot 2H_2O\cdot 6DMF$ mentioned above[16] that shows a reversible decrease of the magnetic ordering temperature after desolvation from 80 to 26 K. Still, this solvent-induced magnetic switching has a different origin to that of **4**. This is attributed to the distortion of the framework and/or the creation of defects upon desolvation, as the absence of an inflection point in M vs H curves suggests that the interlayer interaction is negligible or ferromagnetic.[16] In fact, halogen-halogen interactions are not observed in this homometallic compound.

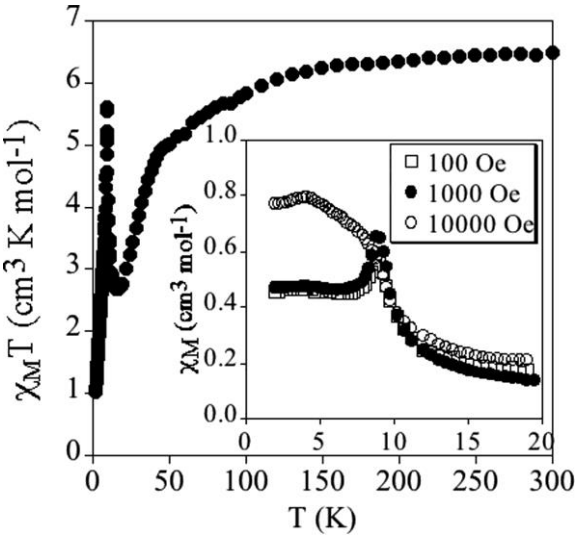

Figure 8. Temperature dependence of the product of the molar magnetic susceptibility times the temperature ($\chi_M T$) of crystals of **4** in contact with the mother liquor under an applied dc field of 1000 Oe. The inset shows

the temperature dependence of χ_M under an applied dc field of 100 Oe (empty squares), 1000 Oe (full circles), and 10000 Oe (empty circles).

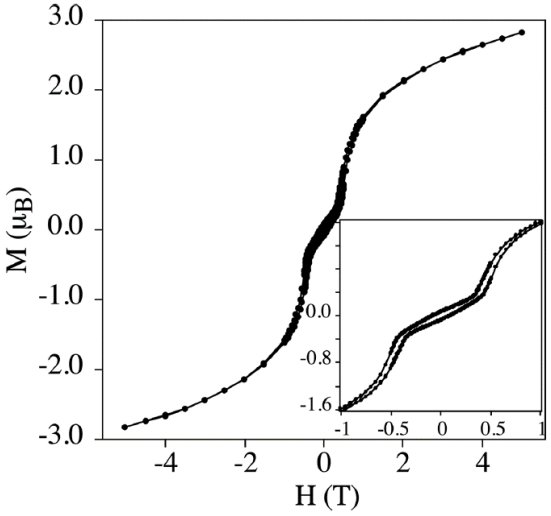

Figure 9. Hysteresis measurements of crystals of **4** at 2 K measured in contact with the mother liquor.

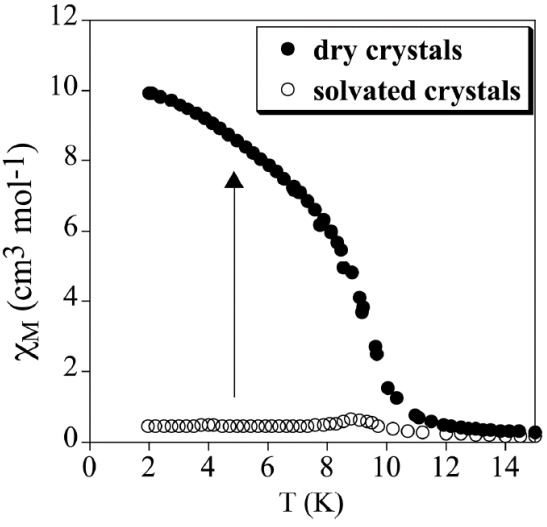

Figure 10. Temperature dependence of the molar magnetic susceptibility times the temperature (χ_M) of crystals of **4** in contact with the mother

liquor (empty circles) or after filtering (full circles) under an applied dc field of 1000 Oe.

Thermal Analysis and Proton Conductivity. 2, **3**, and **4** show similar thermal behavior with a small weight loss between room temperature and 50 °C which is due, likely, to the removal of an amount of physisorbed water/solvent by the solids. After this temperature, compounds remain thermally stable up to ~240 - 260 °C, temperature at which decomposition of the solids take place (data not shown). In **1**, a higher weight loss was observed below 140 °C (3.5 %), which is consistent with the presence of two water molecules in the polycrystalline sample (Figure S12). After proton conductivity measurements, pelletized samples were analyzed by TGA and PXRD, in order to notice possible structural and/or water content changes. None of the solids displayed significant weight gain or changes in their PXRD patterns (Figure S13), underlining the stability of the samples in the full range of temperature (25 to 70 °C) and relative humidity (95% RH) analyzed. Impedance spectra registered under these conditions are shown in Figure S14. The total pellet resistance, R_T, was obtained from the intercept of the spike and/or the arc (low- frequency end) on the Z' axis. The highest proton conductivity values, at 70 °C and 95 % RH, are obtained for compounds **1** (2.4×10^{-5} S·cm^{-1}) and **4** (1×10^{-5} S·cm^{-1}) and the lowest for **2** and **3**, with proton conductivities close to 2×10^{-6} S·cm^{-1}. The weak H-bond network formed between the protonated nitrogen atoms of the intercalated alkylammonium cations with the oxygen and halogen atoms of the anilate groups, with interaction distances N···O and N···X (X=Cl, Br) longer than 3.4 Å, makes difficult the proton transfers and leads to low proton conductivity values. The low activation energy values, range between 0.26 eV (for **1, 2** and **4**) and 0.15 eV (**3**) obtained from the Arrhenius plot, Figure 11, are consistent with a Grotthuss H^+ transfer mechanism,[28] although a vehicle mechanism contribution cannot be discarded.[29] These results confirm the existence of proton conductivity without reaching the

best results for oxalate-based systems (σ ~ 10^{-3} S·cm^{-1}).[10] On the other hand, these values are similar to those found on coordination polymers based on similar ligands with a 1D structure in compounds $M^{II}(dhbq)\cdot nH_2O$ (M = Mg, Mn, Co, Ni, and Zn), which have shown σ values of 10^{-4} S·cm^{-1} when noncoordinating crystalline water is absorbed into the voids of the 1D array with humidity.[30]

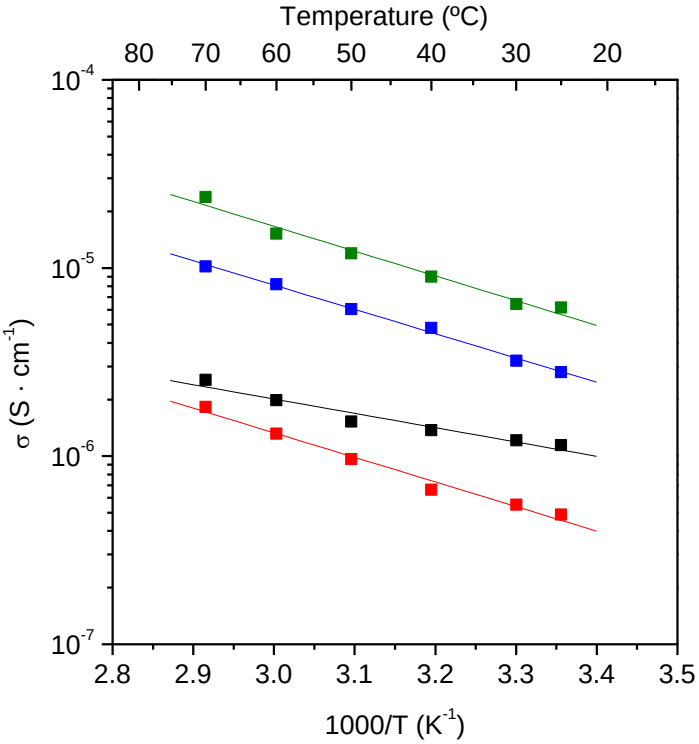

Figure 11. Arrhenius plot at 95% RH for compounds **1** (green), **2** (red), **3** (black), and **4** (blue)).

Conclusions

Four novel magnetic compounds formed by $Me_2NH_2^+$, $Et_2NH_2^+$, Et_3NH^+ and $[(Et)(i\text{-}Pr)_2NH]^+$ and anionic bimetallic coordination polymers based on the anilate ligand have been prepared and characterized. They contain 2D anilate-based networks with a

honeycomb structure. The compounds containing the smaller templating cations $Me_2NH_2^+$, $Et_2NH_2^+$ and Et_3NH^+ (**1**, **2** and **3**) present structures, in which the cations are placed into the hexagonal channels of the 2D network as observed previously with $[Fe^{III}(acac_2\text{-}trien)]^+$. Interestingly, a relatively small increase in the size of the templating cation ($[(Et)(i\text{-}Pr)_2NH]^+$), gives rise in **4** to a different structure with half of the cations placed within the layers and the other half between them leading to bilayers separated by a layer of disordered solvent molecules and countercations. These structural differences lead to abrupt changes in the magnetism of these lattices. Compounds **1**, **2**, and **3** present a ferrimagnetic ordering with a T_c similar to that of other 2D anilate-based compounds with the same metals, while in **4**, the presence of weak magnetic interactions between the ferrimagnetic layers, which could be mediated by halogen-halogen interactions, gives rise to a metamagnetic behavior when the sample is measured in contact with the mother liquor. The behavior changes in the desolvated sample, which shows a ferrimagnetic ordering as that of **1**, **2** and **3** due to collapse of the structure. Interestingly, the metamagnetic behavior is recovered after reimmersing the crystals in the mother liquor proving the reversibility of the process, which is confirmed by powder X-ray diffraction.

Proton conductivity measurements for the four compounds show values comparable to those of bimetallic oxalate-based compounds containing acidic cations without reaching the best values of these systems. One reason for the lower conductivity could be the alternated configuration of the anilate layers, which prevents close contacts between the alkylammonium cations. These results indicate that anilate-based compounds are promising candidates for the preparation of multifunctional compounds with coexistence of magnetic ordering and proton conduction. The interplay between both properties could be reached in compounds with higher magnetic ordering temperature and proton conduction. Possible

strategies to improve the proton conduction are the enhancement of the interlayer and intralayer transport trough the proton carriers. This could be achieved with an eclipsed disposition of the layers to favor the interlayer transport and increasing the number of proton carriers to favor the intralayer transport. Homometallic anilate-based compounds reported in the literature such as $(Me_2NH_2)_2[Fe_2(L_1)_3]\cdot 2H_2O\cdot 6DMF$ containing partially reduced anilate ligands fulfill these two requisites together with porosity and electric conductivity.[16] However, the proton conduction of these compounds could be limited due to stability problems as they are prepared and studied in an inert atmosphere.

Possible advantages of the heterometallic compounds prepared in this work are the neutral character of the anilate-based layers due to the presence of the countercations into the hexagonal channels of the 2D network of the structure. This opens interesting perspectives for the exfoliation of single magnetic layers of these compounds as it has been done with $[Fe^{III}(acac_2\text{-trien})]^+$ anilate-based compounds. On the other hand, the reversible solvent-induced change of the structure and magnetic properties of **4** could be extended to other solvents or neutral molecules for sensing or for the preparation of multifunctional compounds. To reach this goal, we are currently exploring the intercalation chemistry of this compound and related ones.

ACKNOWLEDGMENTS

Financial support from the EU (ERC Advanced Grant SPINMOL), the Spanish MINECO (CTQ2014-52758-P Project MAT-2014-56143-R and Unidad de Excelencia María de Maeztu MDM-2015-0538), the Generalitat Valenciana (Prometeo) is gratefully acknowledged. The work at UMA was funded by Spanish MINECO through MAT2016-77648-R, which is cofunded by FEDER and by Junta de Andalucía through P12-FQM-1656 research projects. We thank J. M. Martínez-Agudo and G. Agustí from the Universidad de Valencia for the

magnetic measurements. Gabriel Peris-Pérez from Universitat Jaume I is gratefully acknowledged for single crystal X-ray diffraction measurements of **3**.

REFERENCES

[1] (a) E. Coronado, P. Day, *Chem. Rev.* 2004, **104**, 5419-5448. (b) E. Coronado, C. Martí-Gastaldo, E. Navarro-Moratalla, A. Ribera, S. J. Blundell, P. J. Baker, *Nat. Chem.* 2010, **2**, 1031-1036. (c) E. Coronado, C. Martí-Gastaldo, E. Navarro-Moratalla, E. Burzuri, E. Camon, F. Luis, *Adv. Mater.* 2011, **23**, 5021-5026. (d) G. Abellán, C. Martí-Gastaldo, A. Ribera, E. Coronado, *Acc. Chem. Res.* 2015, **48**, 1601-1611.

[2] M. Clemente-León, E. Coronado, C. Martí-Gastaldo, F. M. Romero, *Chem. Soc. Rev.* 2011, **40**, 473-497.

[3] (a) M. Clemente-León, E. Coronado, J. R. Galán-Mascarós, C. J.Gómez-García, *Chem. Commun.* 1997, 1727-1728. (b) E. Coronado, J. R. Galán-Mascarós, C. J.Gómez-García, J. M. Martínez-Agudo, *Adv. Mater.* 1999, **11**, 558-561. (c) E. Coronado, J. R. Galán-Mascarós, C. J.Gómez-García, J. Ensling, P. Gutlich, *Chem. Eur. J.* 2000, **6**, 552-563.

[4] (a) S. Bénard, P. Yu, J. P. Audière, E. Rivière, R. Clèment, J. Ghilhem, L. Tchertanov, K. Nakatami, *J. Am. Chem. Soc.* 2000, **122**, 9444-9454. (b) S. M. Aldoshin, N. A. Sanina, V. I. Minkin, N. A. Voloshin, V. N. Ikorskii, V. I. Ovcharenko, V. A. Smirnov, N. K. Nagaeva, *J. Mol. Struct,* 2007, **826**, 69-74.

[5] (a) E. Coronado, J. R. Galán-Mascarós, C. J.Gómez-García, V. Laukhin, *Nature,* 2000, **408**, 447-449. (b) A. Alberola, E. Coronado, J. R. Galán-Mascarós, C. Giménez-Saiz, C. J. Gómez-García, *J. Am. Chem. Soc.* 2003, **125**, 10774-10775. (c) E. Coronado, J. R. Galán-Mascarós, P. A. Goddard, J. Singleton, A. I. Coldea, J. D. Wallis, S. J. Coles, A. Alberola, *J. Am. Chem. Soc.* 2010, **132**, 9271-9273. (d) E. Coronado, J. R. Galán-Mascarós, C. J.Gómez-García, E. Martínez-

Ferrero, *Inorg. Chem.* 2004, **43**, 4808-4810. (d) B. Zhang, Y. Zhang, D. Zhu, *Chem. Commun.* 2012, **48**, 197-199.

[6] (a) T. Endo, T. Akutagawa, S. I. Noro, T. Nakamura, *Dalton Trans.* 2011, **40**, 1491-1496. (b) E. Pardo, C. Train, H. Liu, L.-M. Chamoreau, B. Dkhil, K. Boubekeur, F. Lloret, K. Nakatani, H. Tokoro, S.-i. Ohkoshi, M. Verdaguer, *Angew. Chem. Int. Ed*. 2012, **51**, 8356-8360.

[7] (a) R. Andrés, M. Gruselle, B. Malézieux, M. Verdaguer, J. Vaissermann, *Inorg. Chem.* 1999, **38**, 4637-4646. (b) R. Andrés, M. Brissard, M. Gruselle, C. Train, J. Vaissermann, B. Malézieux, J. P. Jamet, M. Verdaguer, *Inorg. Chem.* 2001, **40**, 4633-4640. (c) M. Clemente-León, E. Coronado, J. C. Dias, A. Soriano-Portillo, R. D. Willett, *Inorg. Chem.* 2008, **47**, 6458-6463. (d) C. Train, R. Gheorghe, V. Krstic, L. M. Chamoreau, N. S. Ovanesyan, G. L. J. A. Rikken, M. Gruselle, M. Verdaguer, *Nat. Mater.* 2008, **7**, 729-734. (e) C. Train, T. Nuida, R. Gheorghe, M. Gruselle, S. Ohkoshi, *J. Am. Chem. Soc.* 2009, **131**, 16838-16843. (f) M. Gruselle, Y. Li, N. Ovanesyan, V. Markhaev, G. Shilov, F. Mushenok, C. Train, S. Aldoshin, *Chirality* 2013, **25**, 444-448.

[8] Clemente-León, M.; Coronado, E.; Gómez-García, C. J.; López-Jordà, M.; Camón, A.; Repollés, A.; Luis, F., *Chem. Eur. J*. 2014, **20**, 1669-1676.

[9] a) M. Clemente-León, E. Coronado, M. C. Giménez-López, A. Soriano-Portillo, J. C. Waerenborgh, F. S. Delgado, C. Ruiz-Pérez, *Inorg. Chem.* 2008, **47**, 9111-9120. (b) M. Clemente-León, E. Coronado, M. López-Jordà, G. Mínguez Espallargas, A. Soriano-Portillo, J. C. Waerenborgh, *Chem. Eur. J*. 2010, **16**, 2207-2219. (c) M. Clemente-León, E. Coronado, M. López-Jordà, *Dalton Trans.* 2010, **39**, 4903-4910. (d) M. Clemente-León, E. Coronado, M. López-Jordà, J. C. Waerenborgh, *Inorg. Chem.* 2011, **50**, 9122-9130. (e) M. Clemente-León, E. Coronado, M. López-Jordà, C. Desplanches, S. Asthana, H. Wang, J.-F. Létard, *Chem. Sci.* 2011, **2**, 1121-1127. (f) M. Clemente-León, E. Coronado, M. López-Jordà, *Eur. J. Inorg. Chem.*

2013, **2013**, 753-762. (g) A. Ben Djamâa, M. Clemente-León, E. Coronado, M. López-Jordà, *Polyhedron* 2013, **64**, 142-150. (h) M. Clemente-León, E. Coronado, M. López-Jordà, J. C. Waerenborgh, C. Desplanches, H. Wang, J.-F. Létard, A. Hauser, A. Tissot, *J. Am. Chem.* Soc. 2013, **135**, 8655-8677. (i) M. López-Jordà, M. Giménez-Marqués, C. Desplanches, G. Mínguez Espallargas, Clemente-León, E. Coronado, *Eur. J. Inorg. Chem.* 2016, **2016**, 2187-2192.

[10] (a) H. Okawa, A. Shigematsu, M. Sadakiyo, T. Miyagawa, K. Yoneda, M. Ohba, H. Kitagawa, *J. Am. Chem. Soc.* 2009, **131**, 13516-13522. (b) E. Pardo, C. Train, G. Contard, K. Boubekeur, O. Fabelo, H. Liu, B. Dkhil, F. Lloret, K. Nakagawa, H. Tokoro, S. –I. Ohkoshi, M. Verdaguer, *J. Am. Chem. Soc.* 2011, **133**, 15328-15331. (c) M. Sadayiko, H. Okawa, A. Shigematsu, M. Ohba, T. Yamada, H. Kitagawa, *J. Am. Chem. Soc.* 2012, **134**, 5472-5475. (d) H. Okawa, M. Sadakiyo, T. Yamada, M. Maesato, M. Ohba, H. Kitagawa, *J. Am. Chem. Soc.* 2013, **135**, 2256-2262. (e) C. Maxim, S. Ferlay, H. Tokoro, S. I. Ohkoshi, C. Train, *Chem. Commun.* 2014, **50**, 5629-5632. (f) M. Sadayiko, T. Yamada, K. Honda, H. Matsui, H. Kitagawa, *J. Am. Chem. Soc.* 2014, **136**, 7701-7707. (g) H. Okawa, M. Sadayiko, K. Otsubo, K. Yoneda, T. Yamada, M. Ohba, H. Kitagawa, *Inorg. Chem.* 2015, **54**, 8529-8535. (h) F. Guo, C. Chen, K. Wang, Q. Zhang, Z. Lin, *Inorg. Chem.* 2016, **55**, 7817-7819.

[11] (a) S. Kitagawa, S. Kanata. *Coord. Chem. Rev.* 2002, **224**, 11-34. (b) B. F. Abrahams, T. A. Hudson, L. J. McCormick, R. C. Robson, *Cryst. Growth Des.* 2011, **11**, 2717-2720. (c) M. L. Mercuri, F. Congiu, G. Concas, S. A. Sahadevan, *Magnetochemistry* 2017, **3***(2)*, 17; doi:10.3390/magnetochemistry3020017.

[12] M. Atzori, S. Benmansour, Mínguez G. Espallargas, M. Clemente-León, A. Abhervé, P. Gómez-Claramunt, E. Coronado, F. Artizzu, E. Sessini, P. Deplano, A. Serpe, M: L. Mercuri, C. J. Gómez-García, *Inorg. Chem.* 2013, **52**, 10031-10040.

[13] A. Abhervé, M. Clemente-León, E. Coronado, C. J. Gómez-García, M. Verneret, *Inorg. Chem.* 2014, **53**, 12014-12026.

[14] A. Abhervé, S. Mañas-Valero, M. Clemente-León, E. Coronado, *Chem. Sci.* 2015, **6**, 4665-4673.

[15] L. E. Darago, M. L. Aubrey, C. J. Yu, M. I. Gonzalez, J. R. Long, *J. Am. Chem. Soc.* 2015, **137**, 15703-15711.

[16] I. R. Jeon, B. Negru, R. P. Van Duyne, T. D. Harris, *J. Am. Chem. Soc.* 2015, **137**, 15699-15702.

[17] J. A. DeGayner, I. R. Jeon, L. Sun, M. Dinca, T. D. Harris, *J. Am. Chem. Soc.* 2017, **139**, 4175-4184.

[18] S. Benmansour, A. Abhervé, P. Gómez- Claramunt, C. Vallés - García, C. J. Gómez García, *ACS Appl. Mater. Interfaces* 2017, **9**, 26210-26218.

[19] M. Atzori, F. Artizzu, E. Sessini, L. Marchiò, D. Loche, A. Serpe, P. Deplano, G. Concas, F. Pop, N. Avarvari, M. L. Mercuri, *Dalton Trans.* 2014, **43**, 7006-7019.

[20] A. Altomare, M. C. Burla, M. Camalli, G. L. Cascarano, C. Giacovazzo, A. Guagliardi, A. G. G. Moliterni, G. Polidori, R. Spagna, *J. Appl. Cryst*. 1999, **32**, 115-119.

[21] G. M. Sheldrick, *Acta Cryst.* 2008, **A64**, 112-122.

[22] L. J. Farrugia, *J. Appl. Cryst.* 2012, **45**, 849-854.

[23] *winDETA;* Novocontrol GmbH: Hundsangen, Germany, 1995.

[24] S. Halis, A. K. Inge, N. Dehning, T. Weyrich, H. Reinsch, N. Stock, *Inorg. Chem.* 2016, **55**, 7425-7431.

[25] T. Luo, Y. Liu, H. Tsai, C. Su, C. Ueng, K. Lu, *Eur. J. Inorg. Chem.* 2004, 4253-4258.

[26] C. J. Kingsbury, B. F. Abrahams, D. M.; D'Alessandro, T. A. Hudson, R. Murase, R. Robson, K. F. White, *Cryst. Growth Des.* 2017, **17**, 1465-1470.

[27] G. Mínguez Espallargas, L. Brammer, D. R. Allan, C. R. Pulha, N. Robertson, J. E. Warren, *J. Am. Chem. Soc*. 2008, **130***,* 9058-9071.

[28] P. Colomban, Cambridge University Press: Cambridge, U.K., 1992; Vol. **2**.

[29]T. Grancha, J. Ferrando-Soria, J. Cano, P. Amorós, B. Seoane, J. Gascon, M. Bazaga-García, E. R Losilla, A. Cabeza, D. Armentano, E. Pardo, *Chem. Mater.* 2016, **28**, 4608-4615.

[30] T. Yamada, S. Morikawa, H. Kitagawa, *Bull. Chem. Soc. Jpn. 2*010, **83**, 42-48.

Supporting Information: Influence of Proton Conducting Cations on the Structure and Properties of 2D Anilate-Based Magnets

Contents

Figure S7. Temperature dependence of the in-phase AC susceptibility (χ') (filled symbols) and the out-of-phase AC susceptibility (χ'') of crystals of **4** measured in contact with the mother liquor.

Figure S8. Temperature dependence of the product of the molar magnetic susceptibility times the temperature ($\chi_M T$) of filtered crystals of **4**.

Figure S9. Temperature dependence of the in-phase AC susceptibility (χ') (filled symbols) and the out-of-phase AC susceptibility (χ'') of filtered crystals of **4**.

Figure S10. Hysteresis measurements of filtered crystals **4** at 2 K.

Figure S11. Temperature dependence of the in-phase AC susceptibility (χ') (filled symbols) and the out-of-phase AC susceptibility (χ'') at 110 Hz of crystals of **4** in contact with the mother liquor (circles), filtered (squares) and reimmersed in a MeOH/$CHCl_3$ solvent mixture (triangles).

Figure S12. TGA of **1**.

Figure S13. As synthesized (blue) and after impedance measurement (red) PXRD patterns for: **1** (a), **2** (b), **3** (c) and **4** (d).

Figure S14. Complex impedance plane plot for **1** (a), **2** (b), **3** (c) and **4** (d) at 95% RH and six temperatures: 343 K (black), 333 K (red), 323 K (green), 313 K (blue), 303 K (cyan) and 298 K (magenta).

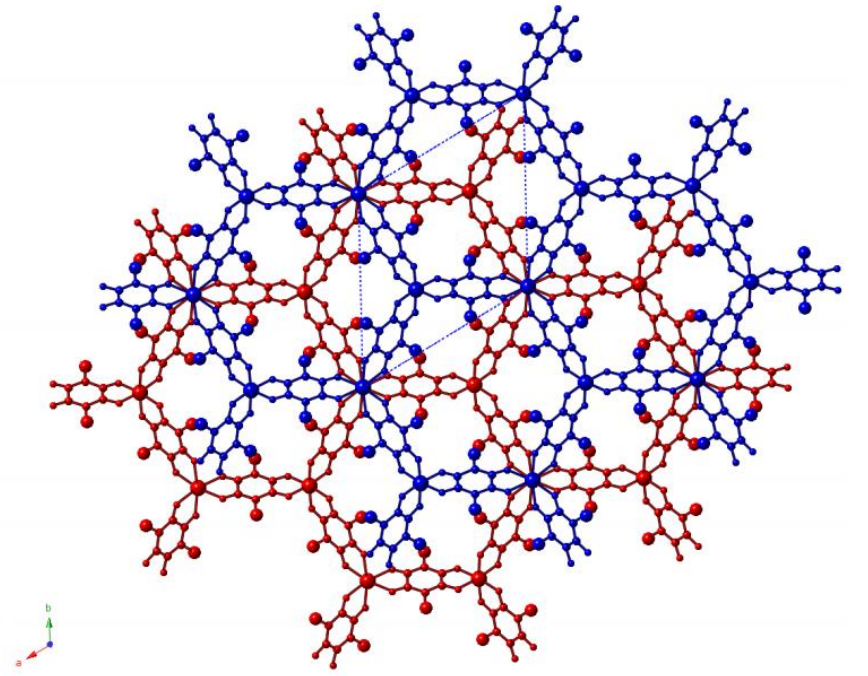
b
a

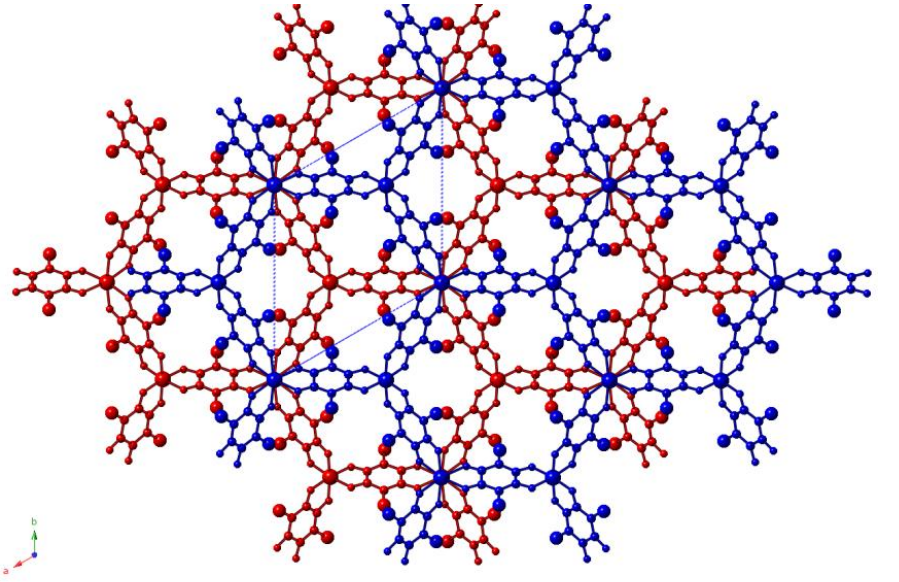
b
a

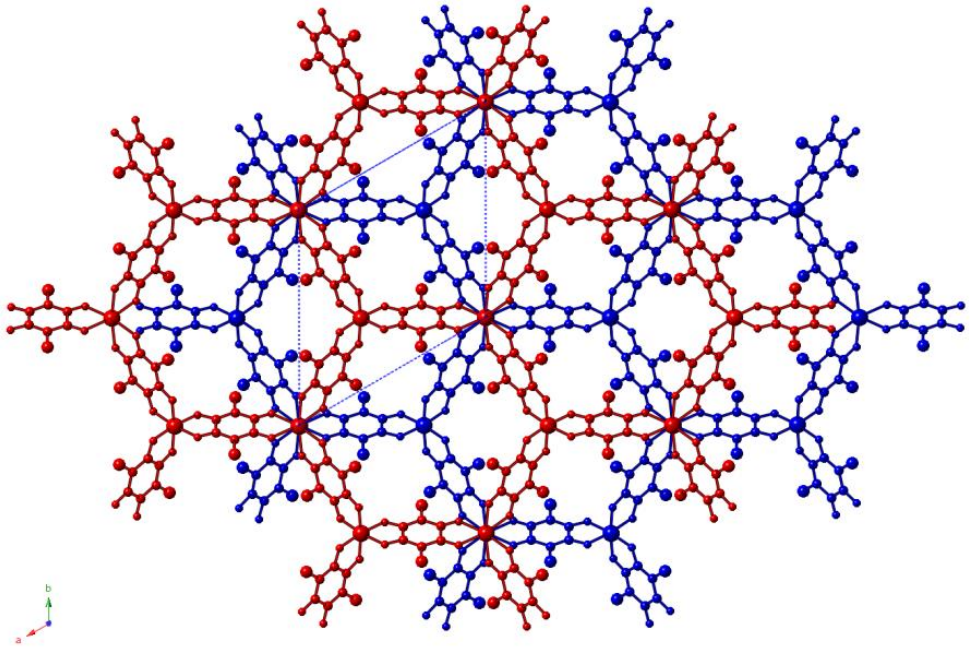

Figure S1. Projection in the *ab* plane of two neighboring layers of **1** (top), **2** (middle) and **3** (bottom).

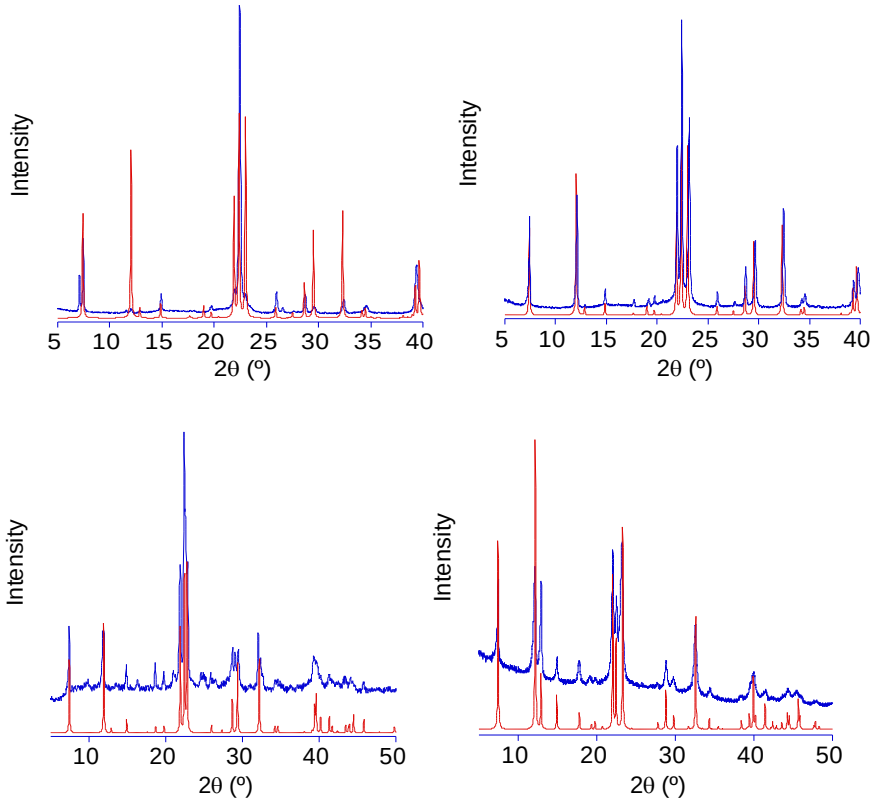

Figure S2. (top left) Powder X ray diffraction pattern (blue) and simulated one (red) for crystals of **1**; (top right) Comparison between simulated powder diffraction data (red) from single crystal and powder pattern (blue) obtained by quick precipitation for **1**; (bottom left) Simulated (red) and observed (blue) powder diffraction pattern for **2**; and (bottom right) Simulated (red) and observed (blue) powder diffraction pattern for **3**.

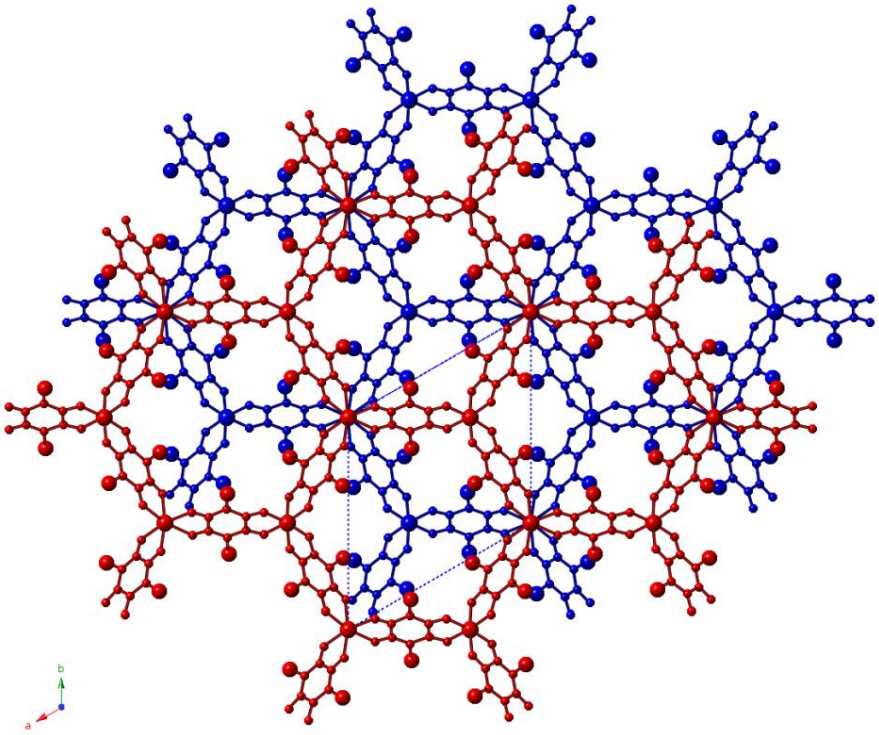

Figure S3. Projection in the *ab* plane of two neighboring layers of **4** belonging to the same bilayer.

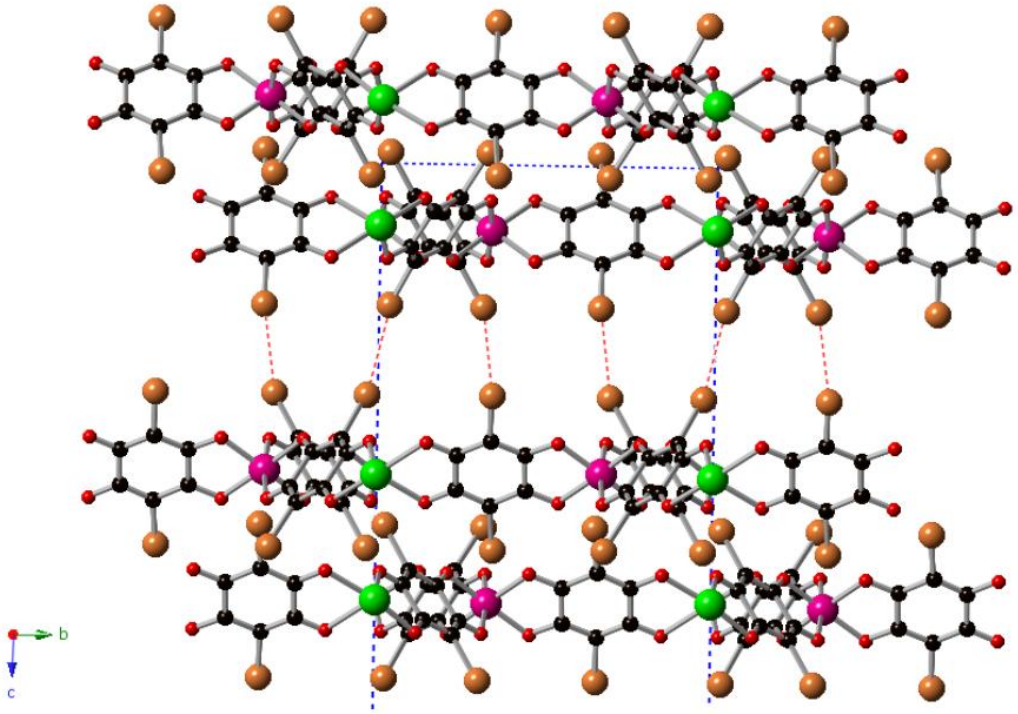

Figure S4. Projection in the *bc* plane of the compound [(Et)(i-Pr)$_2$NH]**[**Mn^{II}Cr^{III}(Br$_2$An)$_3$]·(CHCl$_3$)$_{0.5}$·(H$_2$O) (**4**) showing Br···Br intermolecular interactions (red dashed lines). (Cr (green), Mn (pink) C (black), N (blue), O (red), Cl (yellow) Br (brown)). Solvent molecules and [(Et)(i-Pr)$_2$NH]$^+$ cations have been omitted for clarity.

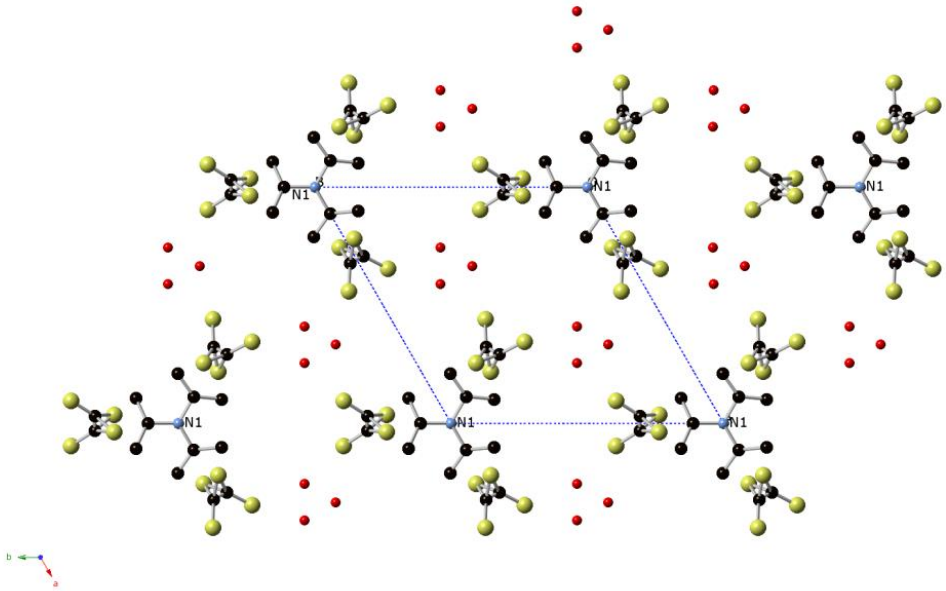

Figure S5. Projection in the *ab* plane with $[(Et)(i\text{-}Pr)_2NH]^+$ cations and disordered solvent molecules ($CHCl_3$ and H_2O) in the interlayer space of **4**.

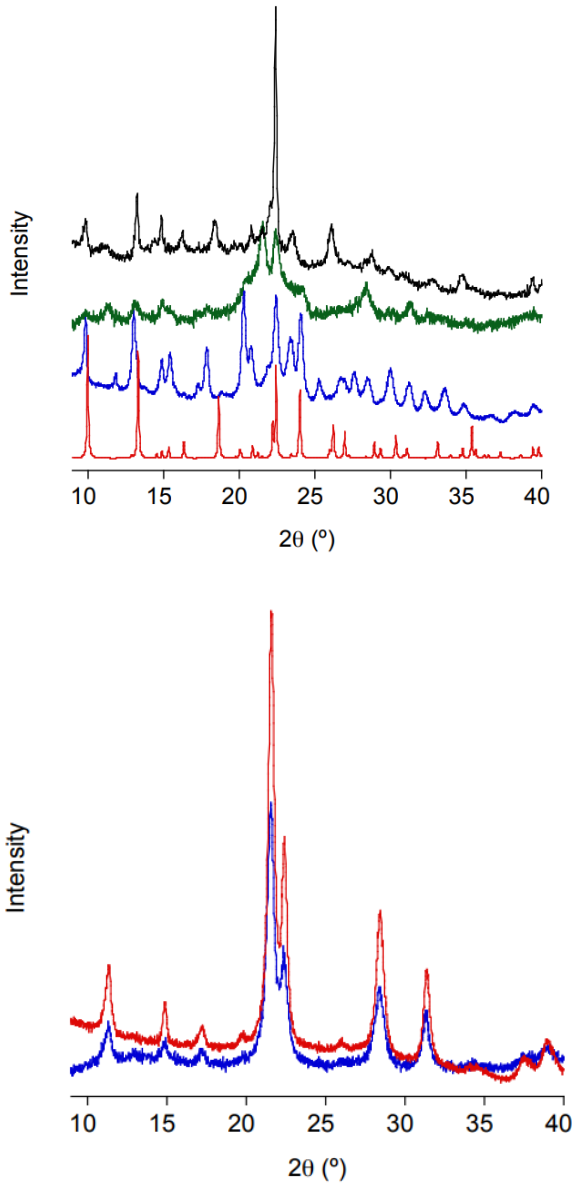

Figure S6. (top) Powder X ray diffraction pattern of a powdered sample of crystals of **4** immediately after filtering (blue), several days after filtering (green) and after several days in contact with a $CHCl_3$/MeOH mixture (black) and simulated pattern obtained from the single crystal X-ray

diffraction structure solved at 120 K (red). (b) Powder X ray diffraction pattern of a powder of **4** obtained by mixing quickly the precursors in methanol (red) and of dry crystals of **4** after proton conduction measurements at 80° C with 95 % RH (blue).

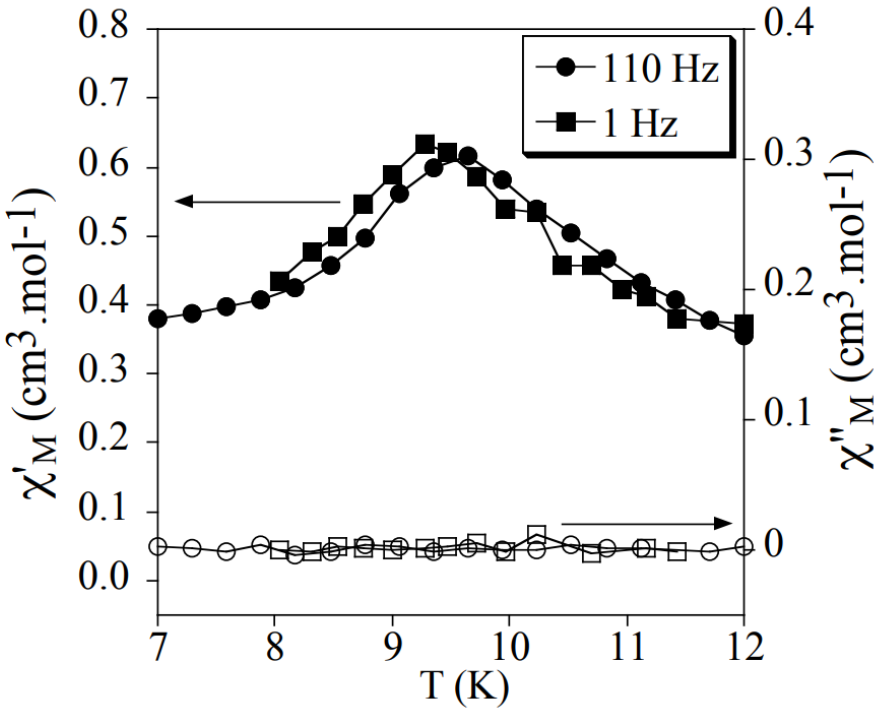

Figure S7. Temperature dependence of the in-phase AC susceptibility (χ') (filled symbols) and the out-of-phase AC susceptibility (χ'') of crystals of **4** measured in contact with the mother liquor.

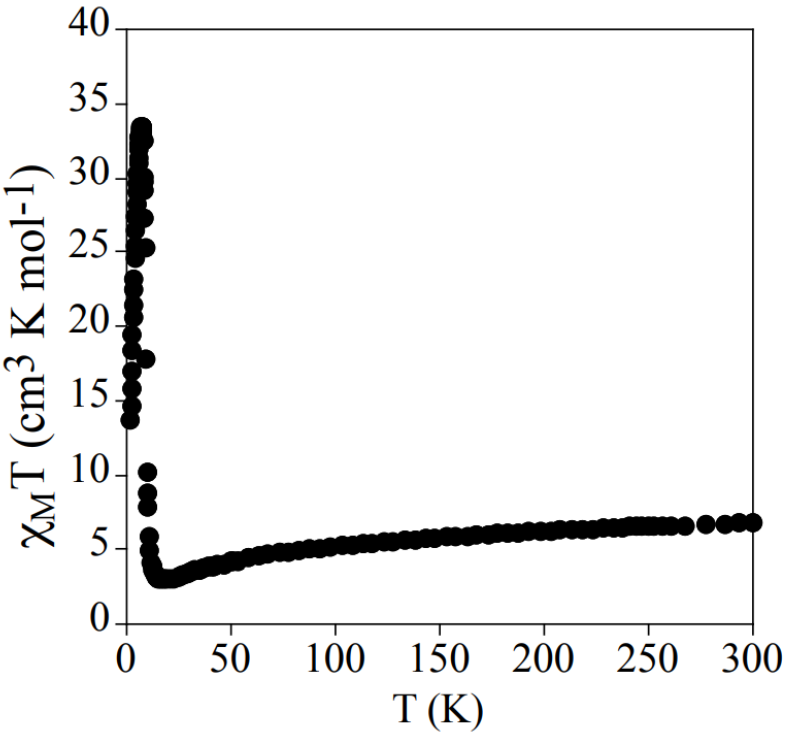

Figure S8. Temperature dependence of the product of the molar magnetic susceptibility times the temperature ($\chi_M T$) of filtered crystals of **4**.

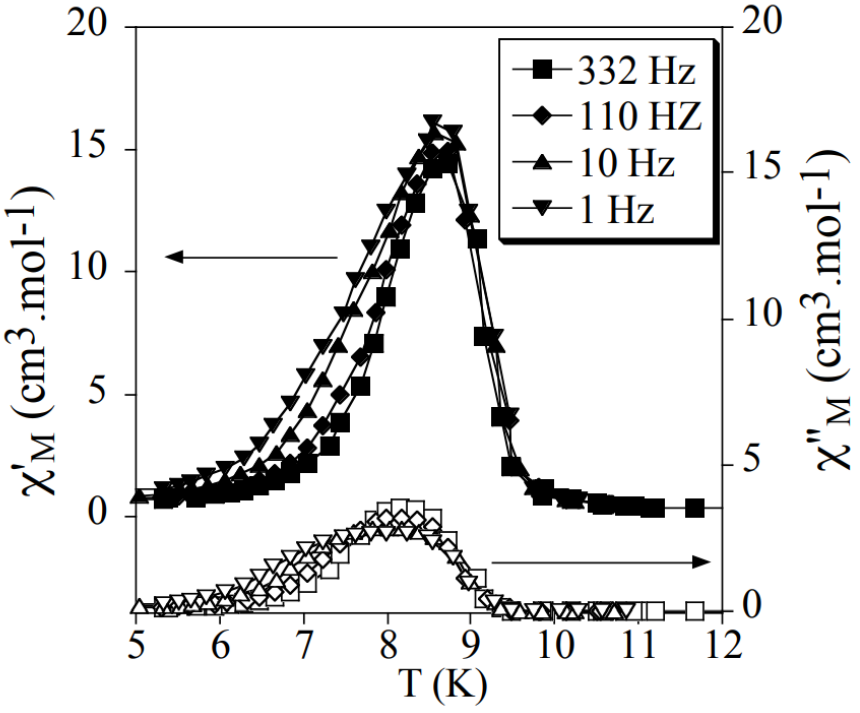

Figure S9. Temperature dependence of the in-phase AC susceptibility (χ') (filled symbols) and the out-of-phase AC susceptibility (χ'') of filtered crystals of **4**.

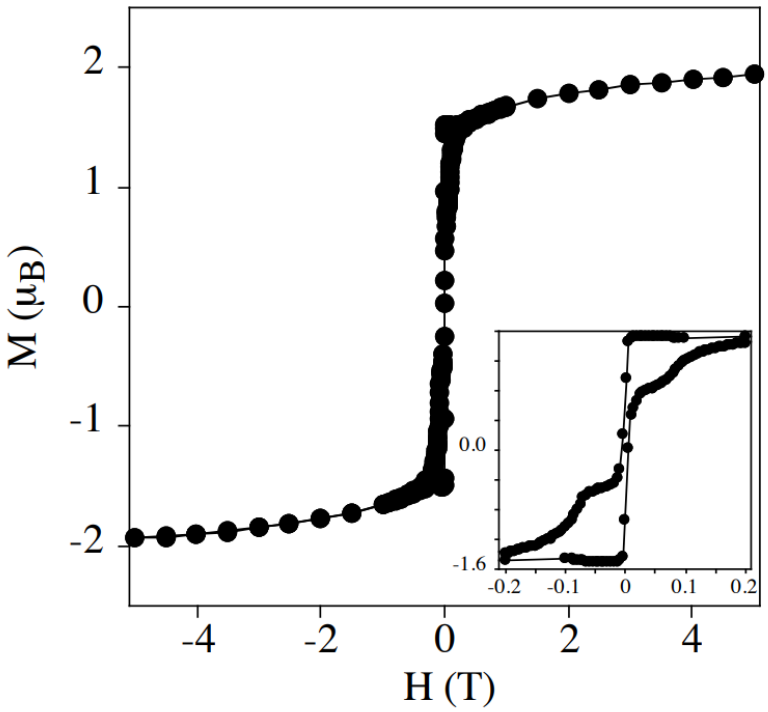

Figure S10. Hysteresis measurements of filtered crystals **4** at 2 K.

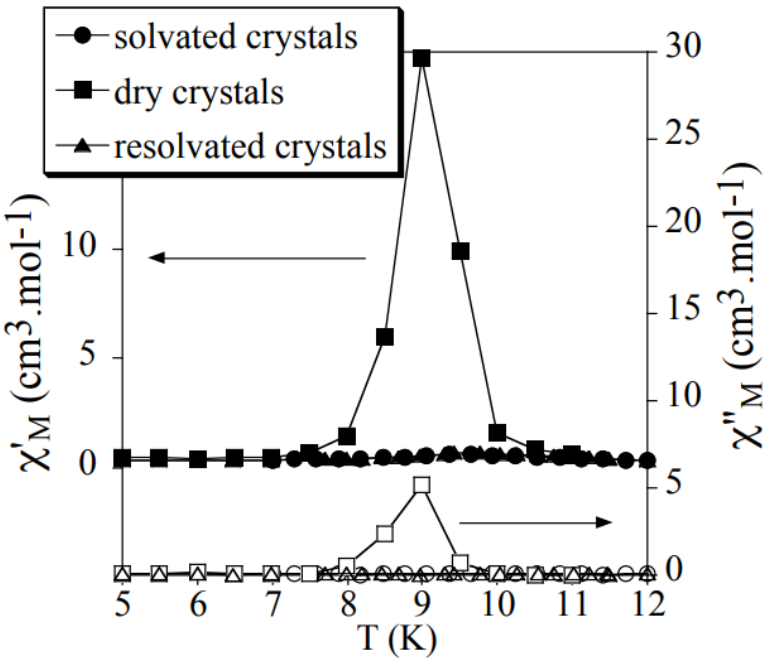

Figure S11. Temperature dependence of the in-phase AC susceptibility (χ') (filled symbols) and the out-of-phase AC susceptibility (χ'') at 110 Hz of crystals of **4** in contact with the mother liquor (circles), filtered (squares) and reimmersed in a MeOH/$CHCl_3$ solvent mixture (triangles).

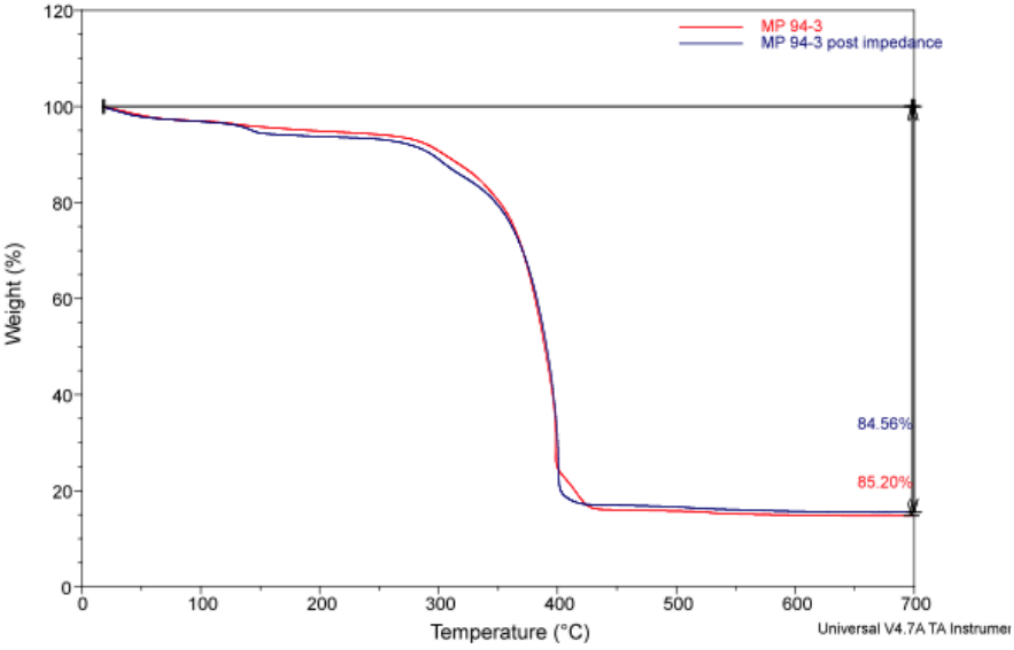

Figure S12. TGA of **1**.

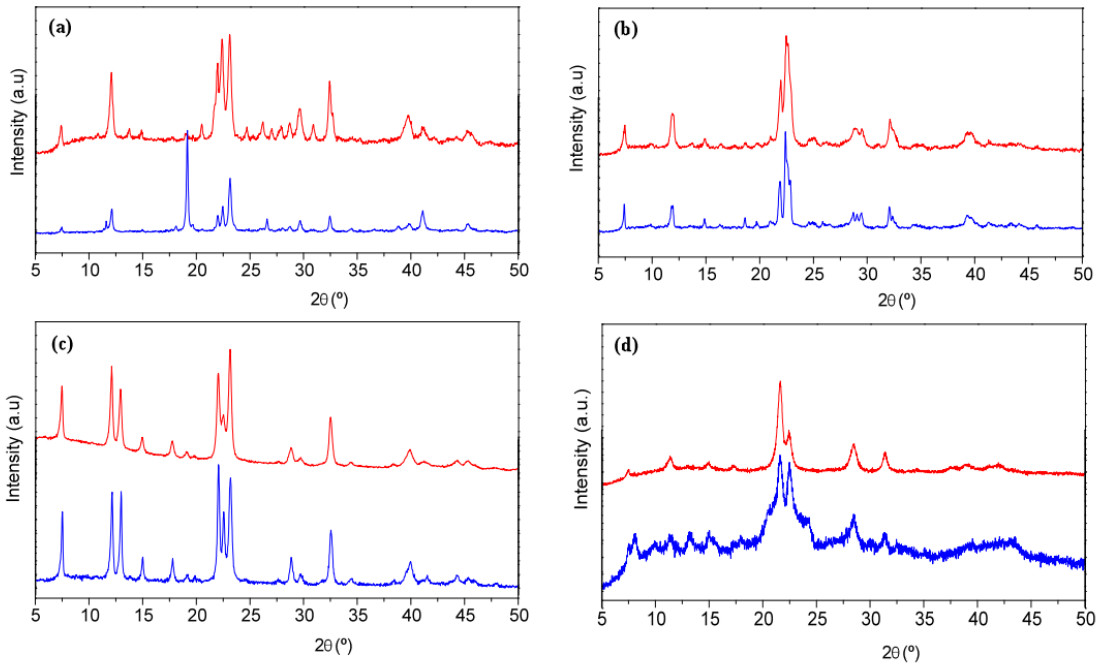

Figure S13. As synthesized (blue) and after impedance measurement (red) PXRD patterns for: **1** (a), **2** (b), **3** (c), and **4** (d).

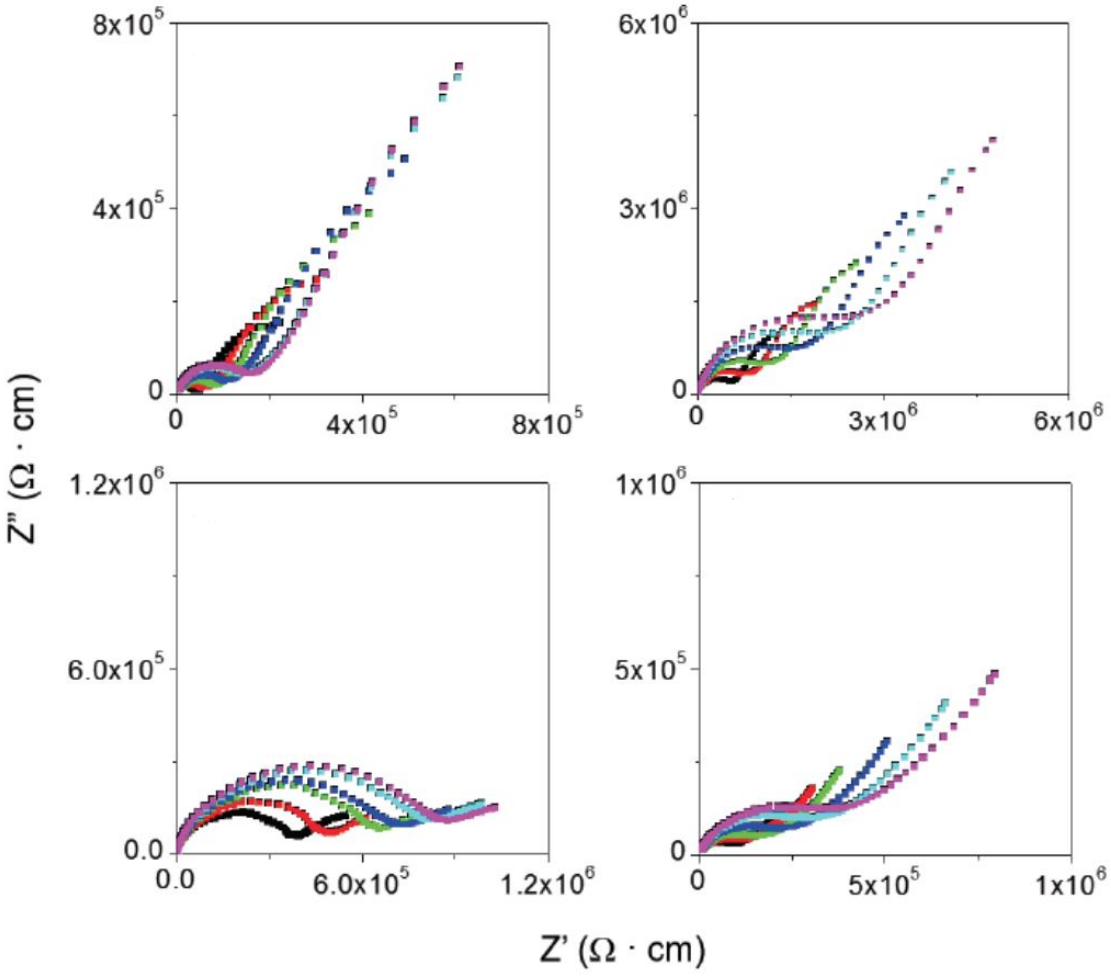

Figure S14. Complex impedance plane plot for **1** (top left), **2** (top right), **3** (bottom left) and **4** (bottom right) at 95% RH and six temperatures: 343 K (black), 333 K (red), 323 K (green), 313 K (blue), 303 K (cyan) and 298 K (magenta).

Chapter 3.

Insertion of Single-ion Magnets Based on Mononuclear Co(II) Complexes into Ferromagnetic Oxalate-Based Networks

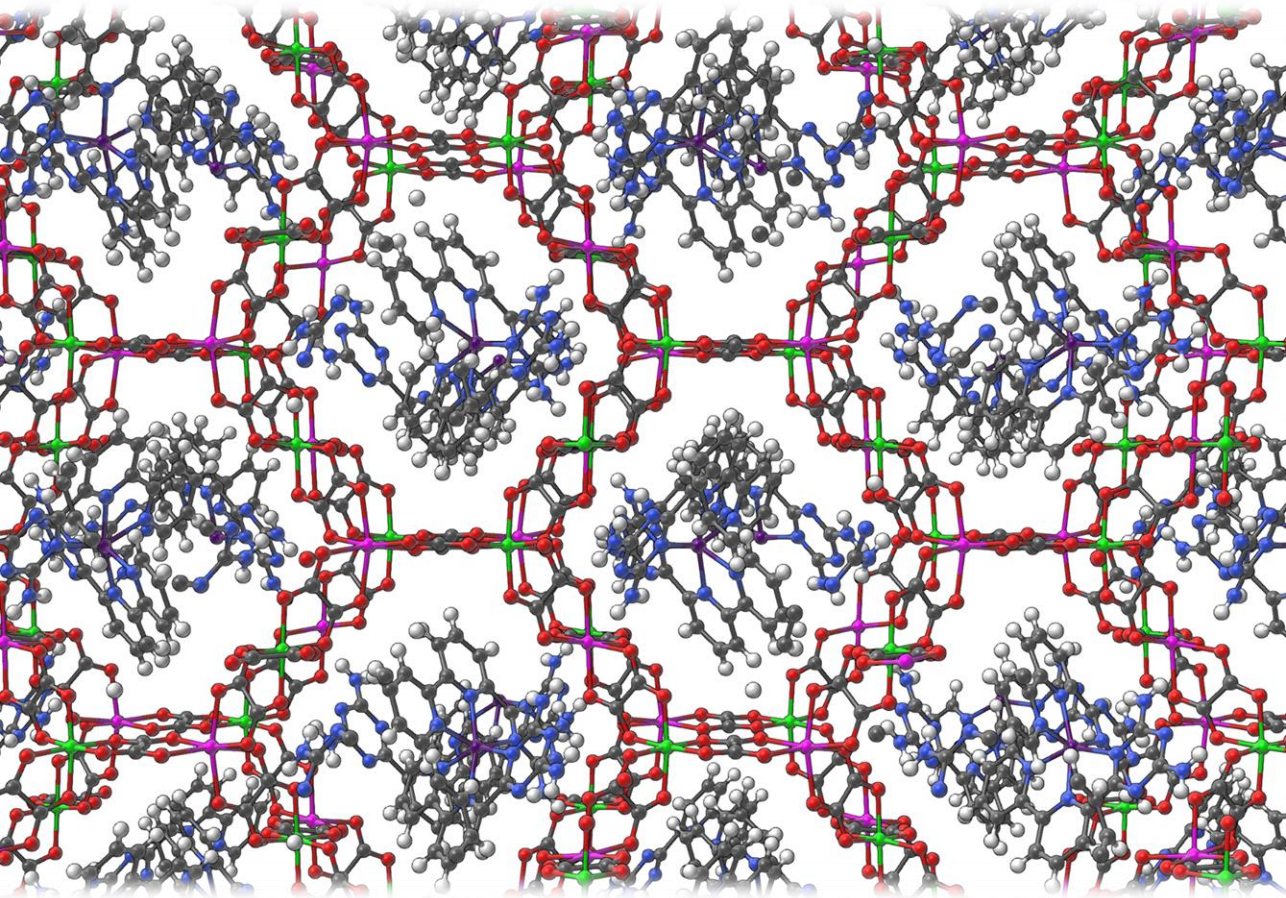

M. Palacios-Corella, V. García-López, C. Sánchez-Sánchez, J. M. Clemente-Juan, M. Clemente-León and E. Coronado, *To be submitted.*

Introduction

In the area of coordination chemistry, a strategy that has gained increasing interest in the last few years is the control of magnetic properties of molecular magnetic units by their insertion inside coordination polymers (CPs). For instance, lanthanoid and transition metal single-ion magnets (SIMs) and single-molecule magnets (SMMs) have been incorporated in the nodes or encapsulated into porous CPs[1]. Another example is that of assembling single-chain magnets (SCMs) inside the pores of a CP[2]. This hybrid approach has resulted in the creation of multifunctional materials with multiple physical properties. In this context, oxalate-based networks have been widely used to prepare multifunctional compounds. They are formed by 2D[3] or 3D[4] anionic magnetic networks, which can host different functional cations.[5,6] These compounds combine the cooperative magnetism from the oxalate network with paramagnetism,[7] photochromism,[8] electrical conductivity,[9] proton conductivity,[10] ferroelectricity,[11] chirality,[12] spin-crossover (SCO)[13] or fluorescence[14] from the counter-cation. In these structures the dimensionality of the coordination network is controlled by the relative configuration of the adjacent metal ions linked by an oxalate bridge. Thus, a 2D honeycomb structure is obtained when the relative configurations are opposite, e.g. (Δ, Λ), leading to non-chiral networks. On the contrary, if they are identical, (Λ, Λ) or (Δ, Δ), a chiral 3D network is formed.[15] The counter-ions associated with the formation of these 3D chiral networks have been essentially chiral dicationic complexes such as $[Z^{II}(bpy)_3]^{2+}$ (Z = Ru, Fe, Co and Ni; bpy = bipyridine)[4] or $[Fe^{II}(pyimH)_3]^{2+}$ (pyimH = 2-(1H-Imidazol-2-yl)pyridine),[13j] while non-chiral 2D networks can be formed with a larger variety of templating monocations with different shapes and sizes. Apart from these two types of structures, other atypical 3D networks have also been obtained.

Worth to mention are the non-chiral networks formed by metals in the two configurations, which have been obtained with a variety of Mn^{III},[7d,16] Fe^{II}[13a] and Fe^{III} complexes[13c,d,i] and triethylammonium cations[17] or organic radicals,[18] together with chiral 3D networks of lower symmetry (see Table 1).[7d,13e] In addition, other topologies have been obtained in oxalate networks with hepta-[13i] or octacoordinated metal ions.[10b,e,h,i] One of these hybrids exhibits coexistence and even coupling of ferromagnetism and SMM behavior. Thus, the insertion of the SMM $[Mn^{III}(salen)(H_2O)]_2^{2+}$ ($salen^{2-}$ = N,N'-ethylenebis-(salicylideneiminate)) in an oxalate-based 3D network gives rise to the compound $[Mn^{III}(salen)(H_2O)]_2[Mn^{II}Cr^{III}(ox)_3]_2\cdot(CH_3OH)\cdot(CH_3CN)_2$ in which the coupling between the spin anisotropy of the SMM with the soft ferromagnetic network results in an enhancement in the magnetic hysteresis of the compound.[16]

Table 1. Examples of cations leading to chiral or achiral 3D oxalate-based networks and Curie temperatures (T_C) of the 3D compounds formed with these cations containing oxalate-based $Mn^{II}Cr^{III}$ networks.

	T_C (K)
Achiral	
$(C_2H_5)_3NH^{+}$[17]	
$[M^{III}(sal_2\text{-trien})]^{+}$ (M = Fe or In) [13b]	5.2
$[Mn((R/S)\text{-salmen})(CH_3OH)_2]^{+}$ [7d]	5.2
$(H_2PPD)^{2+}$(benzo[18]crown-6)$_2$ [4i]	5.5
$[Mn^{III}(salen)(H_2O)]_2^{2+}$ [16]	5.5
$[Fe^{III}(5\text{-X-}sal_2\text{-trien})]^{+}$ (X=MeO) [13d]	5.2
$[Fe(bpp)_2]^{2+}$ [13a]	3
Chiral	
$[Z(bpy)_3]^{2/3+}$ (Z = Cr^{III}, Co^{III}, Ru^{II}, Fe^{II}, Co^{II} and Ni^{II})[4a-e]	2.2-4.2
$[Ru^{II}(ppy)(bpy)_2]^{+}$ [b,12b]	5.8
$[Ir^{III}(ppy)_2(bpy)]^{+}$ [4g]	5.1
$[M^{III}(5\text{-X-}sal_2\text{-trien})]^{+}$ (M = Fe or In, X=Cl, Br)[13e]	4.8-5
$[Fe^{II}(L)_2]^{2+}$ [20]	4.2
$[Fe^{II}(pyimH)_3]^{2+}$ [13j]	4.5
$[Mn^{III}(salpn)(solvent)_2]^{+}$ [7d]	5.4

[a] H_2PPD^{2+} = p-phenylenediammonium. [b] ppy = 2-phenylpyridine.

In a previous work, we showed that the $[Fe^{II}(L)_2]^{2+}$ complex with L = 6-(3,5-Diamino-2,4,6-triazinyl)2,2'-bipyridine (see Scheme 1)[19] stabilized both a 2D oxalate network and a chiral 3D structure.[20] Interestingly, the $[Fe^{II}(L)_2](ClO_4)_2 \cdot CH_3CN$ precursor exhibited a photo-induced spin transition.[20]

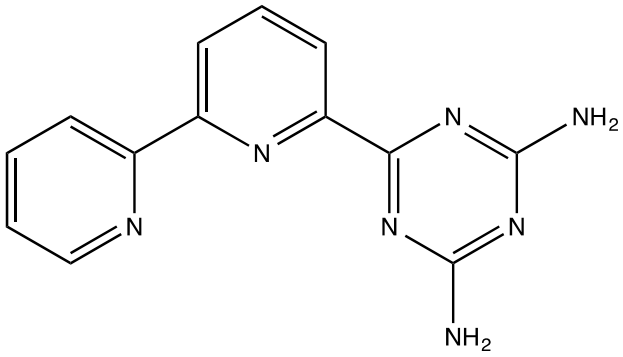

Scheme 1. Structural view of L ligand

In this paper, we have explored the preparation of analogous precursors with Co(II) instead of Fe(II) and its insertion in an oxalate-based network. These Co(II) analogues present interesting magnetic properties such as SMM behavior[21,22] or SCO,[23] which could interact or coexist with that of the oxalate-based network. In this work, the syntheses, structures and magnetic properties of the 1:1 and 1:2 Co(II):L complexes are reported together with those the bimetallic oxalate-based compounds obtained with the 1:2 complex.

Results

Synthesis. L was synthesized as described in the literature.[19] It was reacted with Co(II) in acetonitrile with 1:2 and 1:1 metal:ligand ratios to give the mononuclear Co(II) complexes $[Co^{II}(L)_2](ClO_4)_2 \cdot 0.5MeCN \cdot Et_2O \cdot 0.25H_2O$ (**1**) and $[Co^{II}(L)(CH_3CN)_2(H_2O)](ClO_4)_2 \cdot MeCN$ (**2**), respectively, which were crystallized by layering with diethyl ether. This method is

similar to that used to obtain the analogous Fe(II) complexes.[20] In a further step the hybrid compound $[Co^{II}(L)_2][Mn^{II}Cr^{III}(ox)_3]_2\cdot$(solvate) (**3**) formed by an achiral 3D network was prepared using a protocol similar to that reported in other bimetallic oxalate-based compounds.[13c-j,20] The preparation method is based on a slow diffusion of a solution containing the Co(II) complex **1** dissolved in nitromethane into another solution with the precursors of the oxalate network dissolved in methanol. Long diffusion times led to crystals of a different compound with the same formula $[Co^{II}(L)_2][Mn^{II}Cr^{III}(ox)_3]_2\cdot$(solvate) (**4**) but with a 2D oxalate network. This last compound appears as a minority product always mixed with **3**. The crystal structures of **1**, **2**, **3** and **4** were solved by single-crystal X-ray diffraction at 120 K. The composition of crystals of these compounds, checked by energy dispersive X-ray spectroscopy (EDAX), shows a Co:Cl ratio of 1:2 for **1** and **2** and a Co:Mn:Cr: ratio of 1:2:2 for **3** and **4**. Elemental analysis indicates possible replacement of MeCN and Et_2O molecules of **1** by water molecules after filtering the crystals (see experimental section). In the case of **3**, elemental analysis is more consistent with the presence of H_2O after filtering the crystals (see experimental section). The structure of **4** is reported in the ESI† (Figs. S10 and S11, Table S1 and associated text).

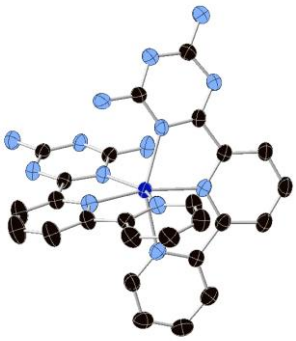

Fig. 1 Structural view of the $[Co^{II}(L)_2]^{2+}$ complex in **1**.

Structure of $[Co^{II}(L)_2](ClO_4)_2 \cdot 0.5MeCN \cdot Et_2O \cdot 0.25H_2O$ (1). **1** crystallizes in the monoclinic $P2_1/c$ space group. The unit cell of this compound is different from that of the Fe(II):L 1:2 complex $[Fe^{II}(L)_2](ClO_4)_2 \cdot CH_3CN$.[19a] The asymmetric unit at 120 K is composed by two $[Co^{II}(L)_2]^{2+}$ cations, four perchlorate anions, some of them disordered, one acetonitrile molecule, two diethyl ether molecules and half water molecule (see Fig. S1 in the ESI†). The central cobalt(II) ions (Co1 and Co2) of the two crystallographically independent Co(II) complexes are coordinated by six nitrogen atoms from two tridentate L ligands with a distorted octahedral coordination geometry with two shorter Co-N axial bond distances to the inner pyridine rings (2.063(3) Å (Co1) and 2.044(3) Å (Co2)) and four longer equatorial Co-N bond distances (2.165(4) and 2.167(3) Å (Co1) and 2.182(4) and 2.186(4) Å (Co2) for the external pyridine and triazine rings, respectively) (Fig. 1). A similar distortion is observed in another octahedral Co(II) SIMs such as $[Co^{II}(dmphen)(NCS)_2]$.[21a] These distances are typical of Co(II) in the high-spin state although Co-N distances in this type of compound are not very sensitive to the metal ion spin state. The trans N(pyridyl)-Co-N(Pyridyl) angles between the two ligands (167.58(14)° for Co1 and 167.66(14)° for Co2) deviate from the ideal octahedron. This deviation is more important for the trans N(triazine)-Co-N(pyridyl) intraligand angles (150.72(13) and 151.81(13)° for Co1 and 153.04(13) and 151.38(14)° for Co2). Two neighbouring $[Co^{II}(L)_2]^{2+}$ complexes form hydrogen bonds between the NH_2 groups of complexes with Co2 and a N from triazine ligand of a complex with Co1 (dN2···N20 = 3.02 Å). Beside these interactions, the two neighbouring complexes are linked through several short contacts involving their two triazine rings. These dimers of complexes are linked through short contacts between a CH group from the central pyridine ring and a triazine ring (see Fig. S2 in the ESI†). This gives rise to chains of complexes running

along the *c* axis, which are surrounded by perchlorate anions and solvent molecules. Perchlorates form hydrogen bonds with triazine rings of $[Co^{II}(L)_2]^{2+}$ complexes. Three of the four crystallographically independent perchlorate anions with Cl2, Cl3 and Cl4 are disordered. Powder X-ray diffraction (PXRD) pattern measured in contact with the mother liquor agrees with the simulated pattern from the structure at 120 K (Fig. S3 in the ESI†).

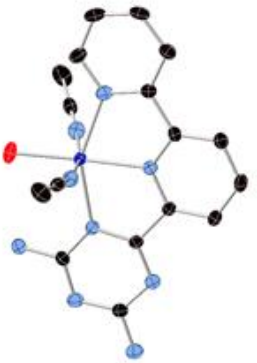

Fig. 2 Structural view of the $[Co^{II}(L)(CH_3CN)_2(H_2O)]^{2+}$ complex in **2**.

$[Co^{II}(L)(CH_3CN)_2(H_2O)](ClO_4)_2\cdot$MeCN (2). The structure of **2** is similar to that of the Fe(II):L 1:1 compound of formula $[Fe^{II}(L)(CH_3CN)_2(H_2O)](ClO_4)_2\cdot CH_3CN$.[20] Both compounds crystallize in the triclinic *P*-1 space group with similar unit cells. The asymmetric unit is composed by one $[Co^{II}(L)(CH_3CN)_2(H_2O)]^{2+}$ cation, two perchlorate anions and one acetonitrile solvent molecule (Fig. S4 in the ESI†). The cobalt(II) ion of the complex present a distorted N_5O octahedral coordination. It is coordinated by three nitrogen atoms from a tridentate L ligand, one water molecule in trans to the N from the inner pyridine ring of L and two nitrogen atoms from two acetonitrile molecules in trans (Fig. 2). The Co-N bond distances are 2.065(2), 2.135(2) and 2.156(2) Å for the inner pyridine ring, the external pyridine ring and the triazine ring of L, respectively. Co-N

distances to the two acetonitrile coordinating molecules are similar (2.112(2) and 2.137(2) Å), while Co-O distance to water molecule is the shortest one (2.043(2) Å). As in **1**, there are two axial ligands (N from the inner pyridine ring and water molecule) at shorter distances than the four equatorial ones. These distances are typical high-spin Co(II) bond lengths. The trans N(acetonitrile)-Co-N(acetonitrile) and O(water)-Co-N(pyridyl) angles (167.75(8) and 174.33(9)°, respectively) are closer to the ideal one for a perfect octahedron (180°) than the trans N(triazine)-Co-N(pyridyl) intraligand angle (151.23(8)°), which present a stronger distortion similar to that of **1**. The $[Co^{II}(L)(CH_3CN)_2(H_2O)]^{2+}$ complexes present short contacts with four neighbouring complexes (Fig. S5 in the ESI†). These contacts involve the triazine rings of two of them, the coordinated acetonitrile molecules and the triazine or pyridine rings. Finally, the L rings of all complexes are almost parallel but they do not present intermolecular contacts shorter than the sum of Van-der-Waals radii (shortest contacts $d_{C4\text{-}C8}$ = 3.63 Å and $d_{C5\text{-}C7}$ = 3.57 Å). Due to this, significant π-π stacking interactions could be excluded. The coordinated water molecule forms hydrogen bonds with the two perchlorate anions. On the other hand, one of the two amino groups from triazine forms hydrogen bonds with an acetonitrile solvent molecule and perchlorate anions. PXRD pattern agrees with the simulated pattern from the structure at 120 K (see Fig. S6 in the ESI†).

Structure of $[Co^{II}(L)_2][Mn^{II}Cr^{III}(ox)_3]_2\cdot$(solvate) (3). **3** crystallises in the centrosymmetric orthorhombic space group *Pnna*. In contrast to $[Fe^{II}(L)_2]^{2+}$, which gives rise to a chiral 3D bimetallic oxalate-based network in the same synthetic conditions,[20] the structure of **3** contains a 3D network involving metals of both chiralities. This network contains two crystallographically independent Mn(II) and Cr(III) ions with occupancies of 0.5. Mn–O distances lye between 2.137(5) and 2.199(4) Å, while Cr–O ones lye between 1.970(4) and

1.988(4) Å. These are typical Cr^{III}–O and Mn^{II}–O distances similar to those found in other oxalate networks. $[Co^{II}(L)_2]^{2+}$ and disordered solvent molecules occupy the cavities of this network (Fig. 3). Similar achiral 3D oxalate networks have been found in the compounds of formula $[Fe^{II}(bpp)_2][MnCr(ox)_3]_2 \cdot bpp \cdot CH_3OH$ that crystallizes in the centrosymmetric $P2_1/n$ space group,[13a] $[Fe^{III}(sal_2\text{-}trien)][Mn^{II}Cr^{III}(ox)_3] \cdot (CH_3OH)$ and $[In^{III}(sal_2\text{-}trien)][Mn^{II}Cr^{III}(ox)_3] \cdot 0.25(H_2O) \cdot 0.25(CH_3OH) \cdot 0.25(CH_3CN)$ that crystallize in the acentric *Cc* space group,[13c] $[In^{III}(sal_2\text{-}trien)][Mn^{II}Cr^{III}(ox)_3] \cdot (CH_3NO_2) \cdot 0.5(H_2O)$[13c] and $[Fe^{III}(5\text{-}CH_3Osal_2\text{-}trien)][Mn^{II}Cr^{III}(ox)_3]$[13d] that crystallize in the acentric orthorhombic space group $Pna2_1$ or $[Mn^{III}(salen)(H_2O)]_2[Mn^{II}Cr^{III}(ox)_3]_2 \cdot (CH_3OH) \cdot (CH_3CN)_2$, that crystallizes in the centrosymmetric *C*2/c space group (see Table 1).[16] This network is formed by bis-chelating oxalate ligands connecting Mn^{II} and Cr^{III} ions in such a way that each Mn^{II} is surrounded by three Cr^{III} and vice versa, building ten-membered rings in a (10, 3) topology. The (10, 3) decagon rings perpendicular to the *a* axis are formed by metal centers with the same chirality (see Fig. 4) forming layers along the *bc* plane. In these layers, Cr and Mn ions are not in the same plane. Two neighbouring (10, 3) decagon rings belonging to different layers are linked through two oxalate ligands and present opposite chirality (see Fig. 4). Projection of the oxalate network on the *ac* plane is almost identical to that of the chiral 3D oxalate network in the *ab*, *bc* or *ac* planes (see Fig. S7 in the ESI†). However, projection on the *bc* (Fig. 3) or *ab* (Fig. 4) planes are different as a result of the different chirality of the neighbouring (10, 3) decagon rings. Thus, in the *bc* projection an eclipsed disposition of the neighbouring oxalate rings is observed as a result of the heterochiral oxalate junctions among them (see Fig. 3).

The $[Co^{II}(L)_2]^{2+}$ complexes and solvent molecules are enclosed in the channels described by this 3D oxalate network. There is half crystallographically independent $[Co^{II}(L)_2]^{2+}$ complex. Co(II) presents

a distorted N_6 octahedral coordination to the two tridentate L ligands as that of **1**. The Co-N bond lengths of the inner pyridine and triazine rings are 2.089(6) and 2.152(5) Å, respectively, while that of the external pyridine ring is 2.168(6) Å. These distances are very similar to those of **1** and typical of Co(II) in the high-spin state. The trans N(pyridyl)-Co-N(Pyridyl) angle between the two ligands (165.2(3)°) deviates from the ideal octahedron. This deviation is more important for the trans N(triazine)-Co-N(pyridyl) intraligand angle (150.5(2)°) as in **1**.

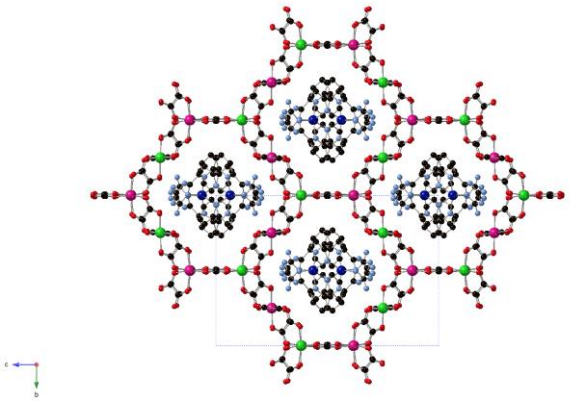

Fig. 3 Projection on the *bc* plane of the structure of **3;** Co (dark blue), C (black), N (blue), O (red), Mn (pink) and Cr (green); hydrogen atoms have been omitted for clarity.

$[Co^{II}(L)_2]^{2+}$ complexes present two short contacts with the two neighbouring ones. These interactions involve a CH group from the external pyridine ring and a N atom from the triazine ring (see Fig. S8 in the ESI†). This gives rise to chains of $[Co^{II}(L)_2]^{2+}$ complexes running along the *a* axis in the channels formed by the bimetallic oxalate-based network. Therefore, the insertion of the complex in the 3D oxalate-based network restricts the intermolecular interactions among the complexes to one dimension. Indeed, these chains of $[Co^{II}(L)_2]^{2+}$ complexes present many short contacts with the surrounding oxalate-based network. Thus, there are hydrogen bonds between the NH_2 groups from the triazine rings and oxygen atoms

from the oxalate network. As in the oxalate-based compounds obtained with $[Fe^{II}(L)_2]^{2+}$,[20] **3** contains disordered solvent molecules in the structure. This is a consequence of the 2+ charge of these Co(II) and Fe(II) complexes used as templating cations of the oxalate-based network. Thus, when In(III) or Fe(III) complexes with the 1+ charge are inserted in similar $Mn^{II}Cr^{III}$ 3D achiral oxalate networks, there is a double number of inserted complexes.[13 b] Due to this, in **3**, as in similar compounds,[13a,i,j] there is more empty space available for solvent molecules.

Due to disorder, solvent molecules could not be modelled. This disorder has been treated with PLATON/SQUEEZE (see experimental section).[24] Indeed, crystals of **3** lose solvent very quickly after filtering leading to a featureless PXRD pattern (data not shown). In contrast to this, PXRD pattern measured in contact with the mother liquor shows a good agreement with the simulated one from the structure at 120 K (see Fig. S9 in the ESI†).

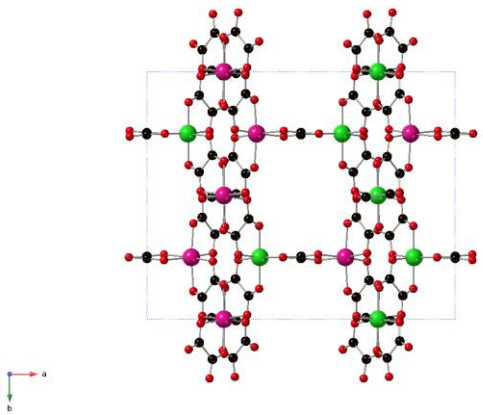

Fig. 4 Two (10, 3) decagon rings perpendicular to the *a* axis in the structure of **3;** C (black), O (red), Mn (pink) and Cr (green).

Table 2. Crystallographic data for **1**, **2** and **3**[‡]

Compound	**1**	**2**	**3**
Empirical formula	$C_{124}H_{134}Cl_8Co_4N_{58}O_{37}$	$C_{38}H_{44}Cl_4Co_2N_2O_{18}$	$C_{39}H_{25}CoCr_2Mn_2N_{15}O_{33}$
Formula weight	3548.20	1328.59	1504.55
Crystal colour	Orange	Orange	Violet
Crystal size	0.16*0.13*0.12	0.11*0.09*0.07	0.14*0.03*0.03
Temperature (K)	120(2)	120(2)	120(2)
Wavelength (Å)	0.71073	0.71073	0.71073
Crystal system, *Z*	Monoclinic, 2	Triclinic, 1	Orthorhombic, 4
Space group	$P2_1/c$	*P*-1	*P*nna
a (Å)	14.8849(2)	10.0029(4)	19.4566(8)
b (Å)	33.6403(5)	11.8949(4)	15.5539(6)
c (Å)	15.7252(2)	12.5420(4)	22.9545(9)
α (°)	90	65.515(3)	90
b (°)	98.895(2)	78.397(3)	90
γ (°)	90	82.037(3)	90
V (Å^3)	7779.42(19)	1327.79(9)	6946.5(5)
ρ_{calc} (Mg/m^3)	1.515	1.662	1.439
$\mu(Mo_{K\alpha})$ (mm^{-1})	0.651	0.917	0.981
θ range (°)	3.299-27.515	3.346-27.486	3.264-27.913
Reflns collected	64541	12287	149747
Independent reflns (R_{int})	17831(0.055)	6074 (0.0232)	8086 (0.3327)
L. S. parameters	1036	379	368
$R1(F)$,[a] $I > 2\sigma(I)$	0.0728	0.0437	0.0846
$wR2(F^2)$,[b] all data	0.2208	0.1093	0.2988
$S(F^2)$,[c] all data	1.032	1.030	1.017

[a]$R1(F) = \Sigma||F_O|-|F_C||/\Sigma|F_O|$; [b]$wR2(F^2) = [\Sigma w(F_O^2-F_C^2)^2/\Sigma wF_O^4]^{1/2}$; [c]$S(F^2) = [\Sigma w(F_O^2-F_C^2)^2/\Sigma n + r - p)]^{1/2}$

Magnetic properties. The thermal dependence of the product of the molar magnetic susceptibility times the temperature (χT) of **1** and **2** is shown in Fig. 5. In both cases χT shows values of 2.7 emu·K·mol^{-1} at 300 K, which are higher than the spin-only value for a high-spin Co(II) (d^7) due to considerable orbital momentum contribution to the magnetic moment. Upon cooling, χT of **1** and **2** decreases continuously with a more abrupt decrease below 50 K due to the strong zero-field splitting (ZFS) to reach values of 1.6 for **1** and 1.7 emu·K·mol^{-1} for **2** at 2 K. The isothermal field (*H*) dependence of

the magnetization (*M*) was measured up to 5 T at temperatures of 2 and 5 K, respectively (Fig 5 inset). The magnetization at 5 T (2.1 and 2.3 B M for **1** and **2**, respectively) is significantly lower than the expected saturation for a system with (S = 3/2 and g > 2). Simultaneous fit of both the susceptibility and magnetization data was performed with MAGPACK program.[25] The best fit values are g = 2.37, D = 48 cm^{-1} and ($R = 2.7\times10^{-4}$) values for **1** and g = 2.47, D = 55 cm^{-1} ($R = 7.8\times10^{-5}$) values for **2**. For E/D different of zero, other solutions with less quality can be found (increase in residual value less than an order of magnitude). These solutions give rise to E/D less than 10^{-3} and a small decrease in D values and increase in g value. This correlation between parameters is due to the mixing in the composition of the Kramers doublets functions (pure for E = 0 but mixture [–3/2, 1/2] and [–1/2, 3/2] for E ≠ 0). More precise spectroscopic measurements should be necessary to avoid this correlation and determine more precisely the parameters.[26] Fittings forcing a negative D value gave solutions with larger residuals (two orders of magnitude greater). These parameters are similar to those found in related compounds.[21,22,26,27]

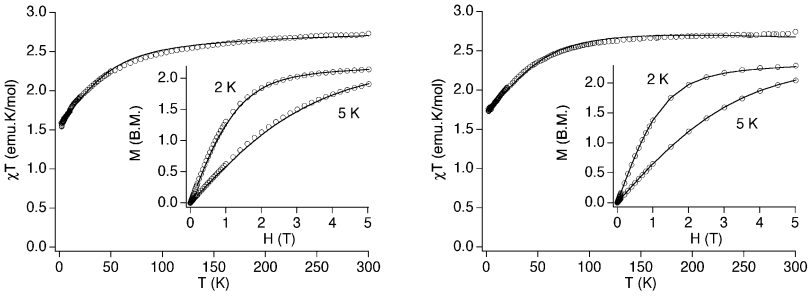

Fig. 5 Temperature dependence of the product of the molar magnetic susceptibility with temperature (χT) at 0.1 T for compounds **1** (left) and **2** (right). Inset: Magnetization vs magnetic field for both compounds measured at T = 2 and 5 K. The blue solid lines are the best-fitting curves.

The relaxation properties of **1** and **2** were studied by susceptibility measurements performed with an alternating magnetic field (AC susceptibility). In the absence of a magnetic field, no signal in the out

of phase molar susceptibility (χ″) is observed. This behavior is not uncommon in mononuclear SMMs and has been attributed to tunnelling, dipolar interactions and/or hyperfine interactions.[26] When magnetic dc fields of 0.1 T for **1** and **2** are applied, strong frequency-dependent peaks in both the in phase molar susceptibility (χ′) and χ″ appear with clear maxima of χ″ below 4 K for **1** and 7.5 K for **2** (Fig. 6). This is a clear indication that the two compounds present a field-induced slow relaxation of magnetization. The variable-frequency AC data at different temperatures of **1** and applied fields of 0.1 T show a single relaxation event with a maximum at 6000 Hz at 3.5 K (see Fig. S12 in the ESI†). There is likely no quantum tunneling occurring, as the relaxation frequency moves to lower values as temperature is decreased with a maximum near 3000 Hz at 2.5 K. In the case of **2** with an applied field of 0.1 T, maxima at 8200 Hz at 8 K and 115 Hz at 2.5 K are observed. The Cole–Cole plots (χ″ vs. χ′) of **1** and **2** at higher temperatures confirm the presence of a single relaxation process (Fig. 7). Thus, at fixed temperatures between 2.5 and 4.5 K for **1** and 2.5 and 8.0 K for **2**, semi-circular plots were obtained and fitted using a generalized Debye model, yielding α parameter in the range of 0.02-0.03 at 2.5-4.5 K for **1** and in the range of 0.14 at the lowest temperature and 0.02 for 8 K for **2**. This indicates that the range of distribution of relaxation times increases when temperature decreases. Additional relaxation mechanisms become inoperative and therefore there is a deviation from the Debye model.

The relaxation times (τ) of **1** were determined from the maximum of χ″ at a given frequency ($\tau = 1/2\pi\nu$) fitting to the Arrhenius expression for a thermally activated process (Orbach, $\tau = \tau_0 \exp(U_{eff}/k_BT)$) leading to $\tau_0 = 1.8\times10^{-6}$ s and $U_{eff} = 5.8$ cm^{-1} at 0.1 T. The U_{eff} values are smaller than experimental energy gap between both Kramers doublets. This may be indicative of the existence of other relaxation mechanisms. In fact, the slow relaxation of magnetization for this type of Kramers ions shows a combination of a direct mechanism

assisted by a very effective hyperfine coupling (I = 7/2), spin–lattice relaxation and Raman processes. [21d] This temperature dependence of relaxation can be fitted with an expression containing two terms: a field-dependent mechanism and Raman terms ($\tau^{-1} = \tau_{FDM}^{-1} + CT^n$). The best fit for **1** is with C = 1207 $s^{-1} \cdot K^{-2.9}$, n = 2.92 and τ_{FDM}^{-1} = 3589 s^{-1} (see Fig. 9) at 0.1 T; n parameters are far from the expected value for Raman term (n = 9), but similar values have been obtained recently for other Co(II) complexes with large positive D values (see Fig. S13 in the ESI†).[21c,22e,f,28,29,30] This reduction in the value of n can be due to different mixture in the eigenvector of the Kramers and the consideration of other phonons.[31]

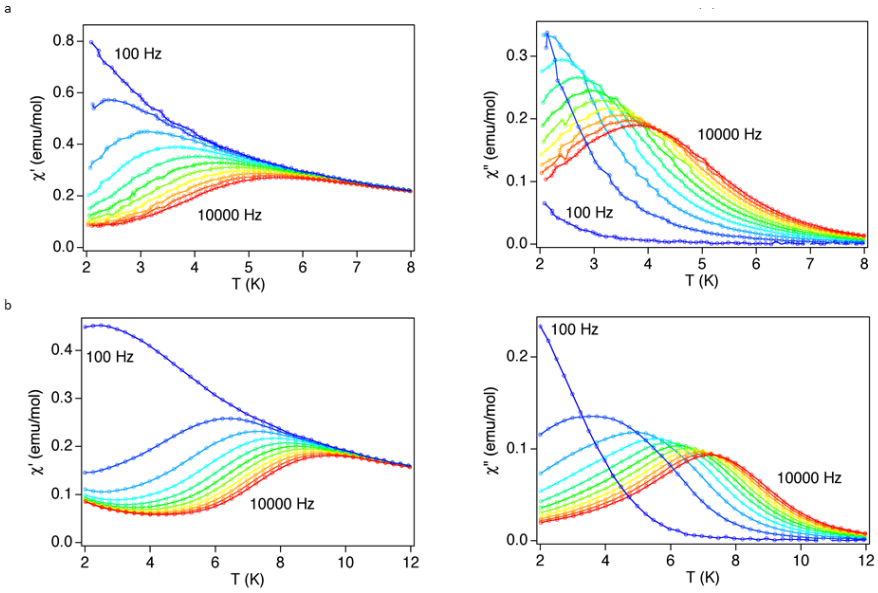

Fig. 6 Temperature dependence of χ' and χ'' of **1** (a) and **2** (b) in an applied dc field of 0.1 T at frequencies in the range 100 to 10000 Hz.

In the case of **2**, the higher value of U_{eff} obtained from Arrhenius expression (τ_0 = 2.7×10^{-7} s and U_{eff} = 20.5 cm^{-1} at 0.1 T) allows to add to the Orbach process other three relaxation processes (field-dependent mechanism and Raman terms). The best fit obtained indicates that only two processes have an important contribution,

the Orbach and the field-dependent processes. The best fit is τ_0 = 1.1×10^{-7} s, U_{eff} = 25.8 cm^{-1} and τ_{FDM}^{-1} = 6060 s^{-1} with a Raman contribution very weak due to a significantly small C parameter, C = 0.21 $s^{-1}\cdot K^{-4.7}$ (see Fig. S13 in the ESI†). The values for the pre-exponential factor and activation energy are consistent with those of the other Co(II) complexes showing this behavior.[32,33,34]

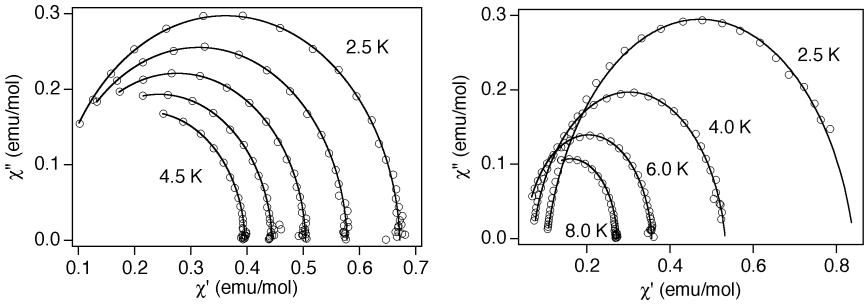

Fig. 7 Cole–Cole plots of **1** (left) and **2** (right) measured at the same temperatures than Fig. 6 under an applied dc field of 0.1 T. Solid lines represent the best fit.

The magnetic properties of **3** were measured in contact with the mother liquor in view of the loss of crystallinity observed in PXRD measurements after extracting the crystals from the mother liquor. The thermal dependence of χT shows a value of 15.3 $cm^3\cdot K\cdot mol^{-1}$ at 300 K (see Fig. 8). This value is approximately equal to the sum of the contributions coming from the two magnetic components: the bimetallic oxalate-based network and the isolated paramagnetic Co(II) ions (expected spin-only value of χT=12.5 $cm^3\cdot K\cdot mol^{-1}$ for two Mn(II) and two Cr(III) plus the χT of **1** at 300 K (2.7 $cm^3\cdot K\cdot mol^{-1}$)). At lower temperatures, χT presents a gradual increase, which is very sharp below 50 K. This indicates the presence of ferromagnetic interactions between neighboring Mn^{II}-Cr^{III} magnetic centers leading to long-range ferromagnetic ordering at low temperature, as observed for other 3D bimetallic oxalate networks. The *M* vs H plot of **3** at 2 K shows a very abrupt increase at low fields, as expected for a ferromagnet, reaching a saturation value of 19.5 BM at 5 T (see Fig.

8). This increase is more gradual at higher fields in agreement with the presence of a paramagnetic Co(II) component. This saturation value is close to the expected contributions for the ferromagnetic oxalate network (16 μ_B for two Mn^{II} and two Cr^{III} ferromagnetically coupled) plus one paramagnetic Co(II) (2.1 B M for **1** at 2 K). This indicates that *M* of **3** is a superposition of the magnetization of each of the two components, with no significant interactions between them. The hysteresis loop at 2 K shows a coercive field of ca. 3 mT (see Fig. S14 in the ESI†), which is typical of a soft ferromagnet and very close to that of other oxalate-based compounds with similar achiral 3D networks and inserted diamagnetic or paramagnetic cations.[13c]

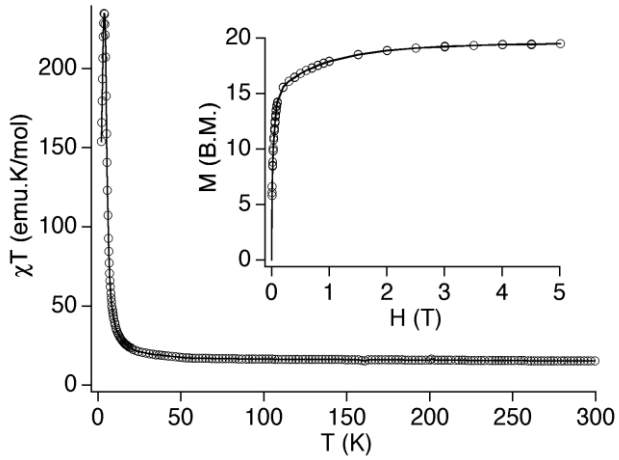

Fig. 8 Temperature dependence of the product of the molar magnetic susceptibility with temperature (χT) at 0.1 T for compound **3**. Inset: Magnetization vs magnetic field for **3** measured at T = 2 K. The continuous line is a guide to the eye.

To confirm the presence of long-range magnetic ordering and to get a more accurate determination of the Curie temperature, AC susceptibility measurements were carried out. A maximum in χ' near 4.6 K and a χ" signal that starts to appear at temperatures just below this temperature are observed (Fig. 9). From this data the Curie

temperature (T_C) of **3** is 4.6 K, a value that is similar to those reported in other $Mn^{II}Cr^{III}$ 3D networks (see Table 1).

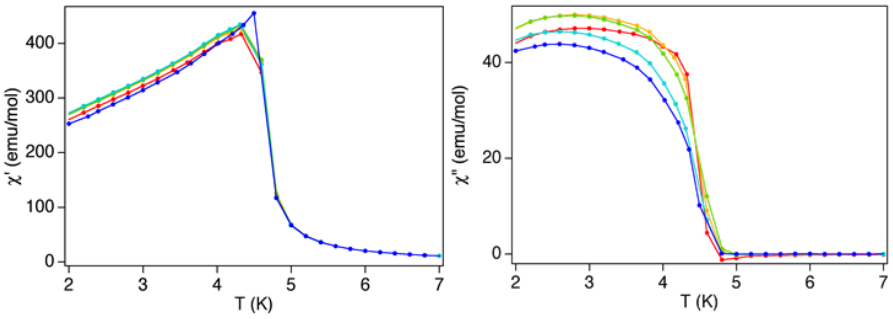

Fig. 9 Temperature dependence of χ' (left) and χ'' (right) of **3** at frequencies in the range 1 (blue) to 997 Hz (red).

These results indicate that the magnetic behavior at low temperatures is dominated by the ferromagnetic bimetallic oxalate network. This is an expected result if one takes into account that the main contribution to χ' and χ'' arises from the strong response of the ferromagnetic fraction. To confirm this, we have studied the magnetic field dependence of χ' and χ'' (see Fig. S15 in the ESI†). Even relatively weak dc magnetic fields H = 100 G suppress the χ' divergence, as expected for a ferromagnetic phase transition. Notice that χ'' tends to vanish in the presence of a magnetic field, showing that magnetic relaxation processes become also considerably faster. In addition to this, magnetic measurements of the published compounds $[In(sal_2\text{-trien})][Mn^{II}Cr^{III}(ox)_3]\cdot solv$ and $[Mn^{III}(salen)(H_2O)]_2[Mn^{II}Cr^{III}(ox)_3]_2\cdot solv$ (solv = solvents) with similar 3D ferromagnetic networks and diamagnetic or SMM cations, respectively, have been used as reference. As shown in Fig. S16 in the ESI†, clear frequency dependence of χ' and χ'' and the presence of additional maxima in χ'' are observed in the compound containing $[Mn^{III}(salen)(H_2O)]_2^{2+}$ SMM and not in that containing diamagnetic $[In(sal_2\text{-trien})]^+$. As the ac magnetic properties of **3** are more similar

to those of [In(sal$_2$-trien)][Mn^{II}Cr^{III}(ox)$_3$]·solv, we conclude that the effect of the inserted [Co^{II}(L)$_2$]$^{2+}$ complexes in the magnetic properties of **3** is fully negligible.

Finally, magnetic properties of filtered crystals of **3** change drastically with respect to those measured in contact with the mother liquor (See Figs. S17 to S19 and related discussion ESI), probably due to structural changes in the bimetallic oxalate network arising from a loss of solvent and the collapse of the structure.

EPR spectroscopy.

X-band EPR spectra of **1** and **3** in contact with the mother liquor were measured to study the magnetic interactions between the two magnetic subnetworks in **3**.

In the case of **1**, the spectrum at 4 K is dominated by an asymmetric band centered at g = 4.3 in addition to a feature at g = 2.3 similar to that of other octahedral Co(II) complexes reported in the literature (See Fig. S20 in the ESI).[35,36] The EPR spectrum at room temperature of **3** shows a single line centered at *g* = 2.00 with a peak-to-peak width Δ*H*pp = 500 G. On lowering the temperature, the intensity of the signal increases. Below the critical temperature (see spectrum at 4 K in Fig. S21 in the ESI), the signal splits into two components centered at g = 1.69 and 2.54. These features coincide with that previously reported for the 2D Mn^{II}Cr^{III} oxalate-based compounds [Fe^{III}Cp*$_2$][Mn^{II}Cr^{III}(ox)$_3$] (Cp* = pentamethylcyclopentadienyl)[7c] and *p*-rad[Mn^{II}Cr^{III}(ox)$_3$]·H$_2$O (*p*-rad = *N*-methylpyridinium cation bearing a nitronyl nitroxide moiety in position 4 of the pyridine ring),[18] which also show a splitting of the signal into two components below the critical temperature. The characteristic intrinsic signal of the inserted Co(II) complex is not observed. Comparing the EPR spectrum of the cobalt monomer **1** with that of compound **3**, both normalized to one mol of each compound, we can see that the monomer signal is not observed when it is intercalated in the oxalate network (see Fig. 10).

This indicates that there must be an interaction between both sublattices as observed in the 2D compound *p*-rad[$Mn^{II}Cr^{III}(ox)_3$]·H_2O[18] and in contrast to [$Fe^{III}Cp^*_2$][$Mn^{II}Cr^{III}(ox)_3$],[7c] which shows the intrinsic signals of the oxalate network and the inserted decamethylferrocenium cation.

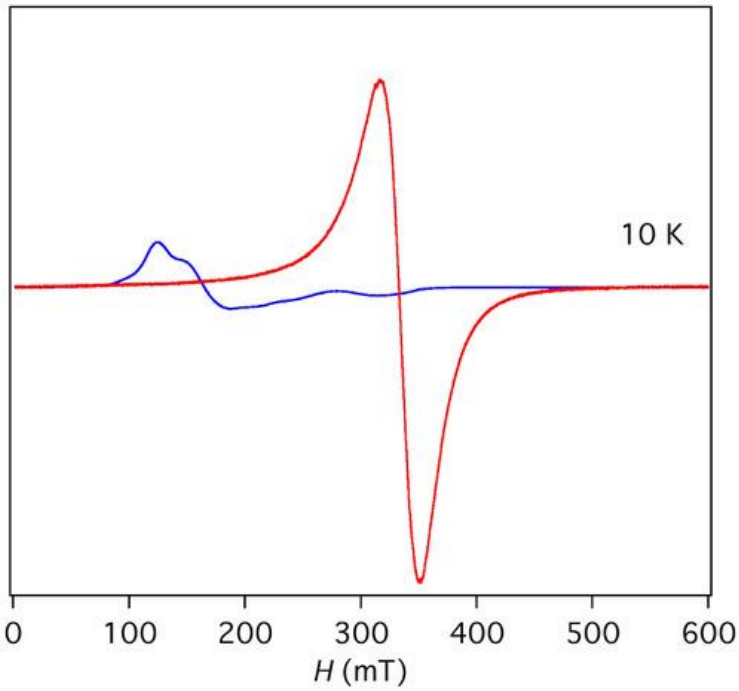

Fig. 10. EPR spectra normalized per mol of **3** (red line) and $[Co^{II}(L)_2]^{2+}$ monomer in **1** (blue line) at 10 K.

Discussion

Magnetic properties of **3** are very similar to those of other ferromagnetic compounds with similar 3D networks being the contribution of the inserted Co(II) complex almost negligible. This could be explained by the absence of strong intermolecular interactions between the two magnetic subnetworks. If we look carefully at the structures of $[Mn^{III}(salen)(H_2O)]_2[Mn^{II}Cr^{III}(ox)_3]_2$·solv

and **3**, the closest intermolecular interactions between inserted cation and the oxalate network are closer to the magnetic center in $[Mn^{III}(salen)(H_2O)]_2[Mn^{II}Cr^{III}(ox)_3]_2\cdot solv$ than in **3**. Thus, they involve a hydrogen bond with a water molecule directly coordinated to the magnetic Mn(III) from the SMM dimer in $[Mn^{III}(salen)(H_2O)]_2[Mn^{II}Cr^{III}(ox)_3]_2\cdot solv$, while in **3** they involve a hydrogen bond with a NH_2 group from L ligand. This suggests a better magnetic isolation of the magnetic cation in the case of **3**. However, these interactions are strong enough to modify the EPR spectra, which is not the sum of the contributions from the oxalate network and the inserted cation as observed in the 2D compound $[Fe^{III}Cp^*_2][Mn^{II}Cr^{III}(ox)_3]$. Therefore, **3** shows an intermediate behavior between those two compounds, in which the magnetic exchange interactions between the moments of the two subnetworks do not modify drastically the magnetic properties of the oxalate network as in $[Mn^{III}(salen)(H_2O)]_2[Mn^{II}Cr^{III}(ox)_3]_2\cdot solv$, but they lead to a unique EPR signal in contrast to $[Fe^{III}Cp^*_2][Mn^{II}Cr^{III}(ox)_3]$.

Conclusions

In this work, we have prepared two Co(II) complexes of the tridentate 6-diaminotriazyl-2,2-bipyridine (L) ligand. Magnetic and structural characterization show that $[Co^{II}(L)_2]^{2+}$ in **1** and $[Co^{II}(L)(CH_3CN)_2(H_2O)]^{2+}$ in **2** exhibit a field-induced slow relaxation of the magnetization due to the magnetic anisotropy of high-spin Co(II), as observed for other octahedral Co(II) complexes with similar tridentate ligands. This result demonstrates that L:Co(II) complexes may behave as SIMs. The main advantage of these complexes is that they open the way to study the interplay between ferromagnetic ordering and SIM behavior in oxalate-based compounds containing $[Co^{II}(L)_2]^{2+}$ templating cations in an analogous way to that reported with the Fe(II) complexes of the same ligand. Interestingly, the structures of the oxalate-based compounds obtained with this

cation, change drastically with respect to those obtained with $[Fe^{II}(L)_2]^{2+}$. Thus, a 3D achiral oxalate-based network is obtained with $[Co^{II}(L)_2]^{2+}$ in compound **3,** in contrast with the compounds obtained for $[Fe^{II}(L)_2]^{2+}$, which present regular 2D or chiral 3D oxalate-based networks. This demonstrates that subtle changes in the geometry of the templating cation can lead to a different structure of the oxalate-based network. Moreover, the crystallisation of the 2D compound **4** in the same synthesis at longer times could suggest a kinetic control.

The magnetic properties of **3** are dominated by the ferromagnetic ordering of the oxalate-based network. This indicates that the magnetic isolation provided by the L ligand prevents strong magnetic interactions between the two subnetworks. However, EPR spectra suggest the presence of magnetic exchange interactions. Magnetic measurements at lower temperatures are needed to verify if this weak magnetic interactions could cause an increase of the coercive field of **3** with respect to similar networks with less anisotropic magnetic inserted cations as observed in $[Mn^{III}(salen)(H_2O)]_2[Mn^{II}Cr^{III}(ox)_3]_2\cdot solv$.

Experimental

Synthesis

L was synthesized as reported in the literature.[19a] $Ag_3[Cr(ox)_3]$ was prepared by metathesis from the corresponding potassium salt.[37]

$[Co^{II}(L)_2](ClO_4)_2\cdot 0.5MeCN\cdot Et_2O\cdot 0.25H_2O$ (1): L (70.0 mg, 0.264 mmol) was suspended in MeCN (40 mL). This was followed by addition of $Co(ClO_4)_2\cdot xH_2O$ (35.0 mg, 0.096 mmol). After stirring for 15 minutes reaction mixture was saturated with a few drops of Et_2O. This was followed by vapour-liquid diffusion of diethyl ether. After three days orange crystals were obtained and filtered (56 mg, 74%). Anal. Calcd for $[Co^{II}(L)_2](ClO_4)_2\cdot 2H_2O$: C, 37.88; H, 3.18; N, 23.79 %. Found: C, 38.25; H, 3.15; N, 23.64 %.

$[Co^{II}(L)(CH_3CN)_2(H_2O)](ClO_4)_2 \cdot MeCN$ (2): L (70.0 mg, 0.264 mmol) was suspended in MeCN (40 mL). This was followed by addition of $Co(ClO_4)_2 \cdot xH_2O$ (96.0 mg, 0.264 mmol). After stirring for 15 minutes the reaction mixture was saturated with a few drops of Et_2O. This was followed by vapour-liquid diffusion of diethyl ether. After three days orange crystals were obtained and filtered (86 mg, 42%). Anal. Calcd for $[Co^{II}(L)(CH_3CN)_2(H_2O)](ClO_4)_2 \cdot MeCN$: C, 34.35; H, 3.34; N, 21.09 %. Found: C, 34.55; H, 3.27; N, 21.18 %.

$[Co^{II}(L)_2][Mn^{II}Cr^{III}(ox)_3]_2 \cdot$(solvate) (3): Crystals of this compound were obtained by slow diffusion of two solutions. The first solution was prepared by adding $MnCl_2 \cdot 4H_2O$ (22 mg, 0.11 mmol) to a suspension of $Ag_3Cr(ox)_3$ (44.6 mg, 0.07 mmol) in 7 mL of methanol. The AgCl precipitate was filtered off. The second solution was obtained by dissolving **1** (16 mg, 0.02 mmol) in 4 mL of nitromethane. After 3 days purple crystals were obtained. If the diffusion was left for longer times (two weeks), crystals of the 2D compound $[Co^{II}(L)_2][Mn^{II}Cr^{III}(ox)_3]_2 \cdot$(solvate) (**4**) appeared mixed with those of **3**. Anal. Calcd for $[Co^{II}(L)_2][Mn^{II}Cr^{III}(ox)_3]_2 \cdot 10H_2O$: C, 30.19; H, 2.80; N, 12.97 %. Found: C, 30.72; H, 3.01; N, 12.57%.

Structural Characterization. Single crystals of all compounds were mounted on glass fibers using a viscous hydrocarbon oil to coat the crystal and then transferred directly to the cold nitrogen stream for data collection. Reflection data of **1**, **2, 3** and **4** were collected at 120 K on a Supernova diffractometer equipped with a graphite-monochromated Enhance (Mo) X-ray Source (λ = 0.7107 Å). The CrysAlisPro, Oxford Diffraction Ltd., program was used for unit cell determinations and data reduction. Empirical absorption correction was performed using spherical harmonics, implemented in the SCALE3 ABSPACK scaling algorithm. The structures of were solved with the ShelXT structure solution program[38] and refined with the SHELXL-2013 program,[39] using Olex2.[40] Non-hydrogen atoms were refined anisotropically, and hydrogen atoms were placed in calculated positions refined using idealized geometries (riding

model) and assigned fixed isotropic displacement parameters. The subroutine SQUEEZE from PLATON has been used to calculate and remove the diffracting component of disordered solvents in **3** and **4**.[23] This results for **3** in a total potential solvent accessible void volume per unit cell of 2790 $Å^3$ (40.2 % of the total unit cell volume). This volume is distributed in one void in 0.091 0.015 0.409, which is occupied by 1190 electrons. This roughly corresponds to 25 $MeNO_2$ and 35 MeOH molecules per unit cell. In **4**, the total potential solvent accessible void volume per unit cell is 3495 $Å^3$ (32.5 % of the total unit cell volume) in a void of 3349 $Å^3$ in -0.121 0.624 0.079 and other smaller voids. The largest void is occupied by 1142 electrons, which roughly correspond to 30 $MeNO_2$ and 10 MeOH molecules per unit cell. CCDC-1486674-75 contain the supplementary crystallographic data for this paper. Data collection and refinement statistics are collected in Tables 2 and S1 in the ESI†. A 1 mm glass capillary was filled with polycrystalline samples of **1, 2** and **3** in the mother liquor and mounted and aligned on an Empyrean PANalytical powder diffractometer, using CuKα radiation (λ = 1.54177 Å). A total of 3 scans were collected at room temperature in the 2θ range 5-40º.

Physical Measurements

Magnetic measurements were performed with Quantum Design MPMS-XL-5 SQUID and PPMS-9 magnetometers on powdered polycrystalline samples measured in contact with the mother liquor in the case of **2** and **3**. EPR measurements of **1** and **3** were recorded in a Bruker ELEXYS E580 spectrometer under X-band irradiation (~ 9.4 GHz). The Co/Mn/Cr and Co/Cl ratios were measured with a Philips ESEM X230 scanning electron microscope equipped with an EDAX DX-4 microsonde. Elemental analyses (C, H, and N) were performed with a CE Instruments EA 1110 CHNS Elemental analyzer.

Notes and References

[1] G. Mínguez Espallargas and E. Coronado, *Chem. Soc. Rev.,* 2018, **47**, 533.

[2] M. Wang, X. Gou, W. Shi and P. Cheng, *Chem. Commun.,* 2019, **55**, 11000.

[3] (a) H. Tamaki, Z. J. Zhong, N. Matsumoto, S. Kida, M. Koikawa, N. Achiwa, Y. Hashimoto and H. Okawa, *J. Am. Chem. Soc.*, 1992, **114**, 6974; (b) H. Tamaki, M. Mitsumi, N. Nakamura, N. Matsumoto, S. Kida, H. Okawa and S. Ijima, *Chem. Lett.*, 1992, 1975; (c) C. Mathonière, J. Nutall, S. G. Carling and P. Day, *Inorg. Chem.*, 1996, **35**, 1201; (d) R. Pellaux, H. W. Schmalle, R. Huber, P. Fisher, T. Hauss, B. Ouladdiaf and S. Decurtins, *Inorg. Chem.*, 1997, **36**, 2301; (e) E. Coronado, J. R. Galán-Mascarós, C. J. Gómez-García, J. M. Martínez-Agudo, E. Martínez-Ferrero, J. C. Waerenborgh and M. Almeida, *J. Solid State Chem.*, 2001, **159**, 391; (f) K. S. Min, A. L. Rhinegold and J. S. Miller, *Inorg. Chem.*, 2005, **44**, 8433; (g) E. Coronado, J. R. Galán-Mascarós and C. Martí-Gastaldo*, J. Mater. Chem.*, 2006, **16**, 2685; (h) M. Sadakiyo, T. Yamada, K. Kato, M. Takata and H. Kitagawa, *Chem. Sci.,* 2016, **7**, 1349.

[4] (a) S. Decurtins, H. W. Schmalle, P. Schneuwly and H. R. Oswald, *Inorg. Chem.,* 1993, **32**, 1888; (b) S. Decurtins, H. W. Schmalle, P. Schneuwly, J. Ensling and P. Gütlich, *J. Am. Chem. Soc.*, 1994, **116**, 9521; (c) S. Decurtins, H. W. Schmalle, R. Pellaux, P. Schneuwly and A. Hauser, *Inorg. Chem.,* 1996, **35**, 1451; (d) M. Hernández-Molina, F. Lloret, C. Ruiz-Pérez and M. Julve, *Inorg. Chem.*, 1998, **37**, 4131; (e) E. Coronado, J. R. Galán-Mascarós, C. J. Gómez-García and J. M. Martínez-Agudo, *Inorg. Chem.*, 2001, **40**, 113; (f) F. Pointillart, C. Train, M. Gruselle, F. Villain, H. W. Schmalle, D. Talbot, P. Gredin, S. Decurtins and M. Verdaguer, *Chem. Mater.*, 2004**, 16**, 832; (g) M. Clemente-León, E. Coronado, C. J. Gómez-García and A. Soriano-Portillo, *Inorg. Chem.*, 2006, **45**, 5653; (h) M. Juric, D: Pajic, D. Zilic, B.

Ravkin, K. Molcanov and J. popovic, *Dalton Trans.*, 2015, **44**, 20626; (i) T. Endo, K. Kubo, M. Yoshitake, S.-i. Noro, N. Hoshino, T. Akutagawa and T. Nakamura, *Cryst. Growth. Des.* 2015, **15**, 1186. (j) M. Mon, T. Grancha, M. Verdaguer, C. Train, D. Armentano and E. Pardo, *Inorg. Chem.,* 2016, **55**, 6845.

[5] M. Clemente-León, E. Coronado, C. Martí-Gastaldo and F. M. Romero, *Chem. Soc. Rev.,* 2011, **40**, 473.

[6] A. E. Thorarinsdottir and T. D. Harris, *Chem. Rev.,* 2020, **120**, 8716.

[7] (a) M. Clemente-León, E. Coronado, J. R. Galán-Mascarós and C. J. Gómez-García, *Chem. Commun.,* 1997, 1727; (b) E. Coronado, J. R. Galán-Mascarós, C. J. Gómez-García and J. M. Martínez-Agudo, *Adv. Mater.,* 1999, **11**, 558; (c) E. Coronado, J. R. Galán-Mascarós, C. J. Gómez-García, J. Ensling and P. Gutlich, *Chem. Eur. J.,* 2000, **6**, 552. (d) M. Clemente-León, E. Coronado and M. López-Jordà, *Dalton Trans.*, 2013, **42**, 5100.

[8] (a) S. Bénard, P. Yu, J. P. Audière, E. Rivière, R. Clèment, J. Ghilhem, L. Tchertanov and K. Nakatami, *J. Am. Chem. Soc.,* 2000, **122**, 9444; (b) S. M. Aldoshin, N. A. Sanina, V. I. Minkin, N. A. Voloshin, V. N. Ikorskii, V. I. Ovcharenko, V. A. Smirnov and N. K. Nagaeva, *J. Mol. Struct.,* 2007, **826**, 6.

[9] (a) E. Coronado, J. R. Galán-Mascarós, C. J. Gómez-García and V. Laukhin, *Nature,* 2000, **408**, 447; (b) A. Alberola, E. Coronado, J. R. Galán-Mascarós, C. Giménez-Saiz and C. J. Gómez-García, *J. Am. Chem. Soc.,* 2003, **125**, 10774; (c) E. Coronado, J. R. Galán-Mascarós, C. J. Gómez-García, E. Martínez-Ferrero and S. Van Smaalen, *Inorg. Chem.,* 2004, **43,** 4808; (d) B. Zhang, Y. Zhang and D. Zhu, *Chem. Commun.,* 2012, **48**, 197.

[10] (a*)* H. Okawa, A. Shigematsu, M. Sadakiyo, T. Miyagawa, K. Yoneda, M. Ohba and H. Kitagawa, *J. Am. Chem. Soc.*, 2009, **131**, 13516; (b) E. Pardo, C. Train, G. Contard, K. Boubekeur, O. Fabelo H. Liu, B. Dkhil, F. Lloret, K. Nakagawa, H. Tokoro, S.-I. Ohkoshi and M. Verdaguer, *J.*

Am. Chem. Soc., 2011, **133**, 15328; (c) M. Sadayiko, H. Okawa, A. Shigematsu, M. Ohba, T. Yamada and H. Kitagawa, *J. Am. Chem. Soc.*, 2012, **134**, 5472; (d) H. Okawa, M. Sadakiyo, T. Yamada, M. Maesato, M. Ohba and H. Kitagawa, *J. Am. Chem. Soc.,* 2013, **135**, 2256; (e) C. Maxim, S. Ferlay, H. Tokoro, S. I. Ohkoshi and C. Train, *Chem. Commun.,* 2014, **50**, 5629; (f) M. Sadayiko, T. Yamada, K. Honda, H. Matsui and H. Kitagawa, *J. Am. Chem. Soc.,* 2014, **136**, 7701; (g) H. Okawa, M. Sadayiko, K. Otsubo, K. Yoneda, T. Yamada, M. Ohba, and H. Kitagawa, *Inorg. Chem.,* 2015, **54**, 8529; (h) M. Mon, J. Vallejo, J. Pasán, O. Fabelo, C. Train, M. Verdaguer, S. I. Ohkoshi, H. Tokoro, K. Nakagawae and E. Pardo, *Dalton Trans.,* 2017, **46**, 15130; (i) H. Okawa, Y. Yoshida, K. Otsubo and H. Kitagawa, *Inorg. Chem.,* 2020, **59**, 623.

[11] (a) T. Endo, T. Akutagawa, S. I. Noro and T. Nakamura, *Dalton Trans*., 2011, **40**, 1491; (b) E. Pardo, C. Train, H. Liu, L.-M. Chamoreau, B. Dkhil, K. Boubekeur, F. Lloret, K. Nakatani, H. Tokoro, S.-I. Ohkoshi and M. Verdaguer, *Angew. Chem. Int. Ed.*, 2012, **51**, 8356.

[12] (a) R. Andrés, M. Gruselle, B. Malézieux, M. Verdaguer and J. Vaissermann, *Inorg. Chem.*, 1999, **38**, 4637; (b) R. Andrés, M. Brissard, M. Gruselle, C. Train, J. Vaissermann, B. Malézieux, J. P. Jamet and M. Verdaguer, *Inorg. Chem.*, 2001, **40**, 4633; (c) M. Clemente-León, E. Coronado, J. C. Dias, A. Soriano-Portillo and R. D. Willett, *Inorg. Chem.*, 2008, **47**, 6458; (d) C. Train, R. Gheorghe, V. Krstic, L. M. Chamoreau, N. S. Ovanesyan, G. L. J. A. Rikken, M. Gruselle and M. Verdaguer, *Nat. Mater.*, 2008, **7**, 729; (e) C. Train, T. Nuida, R. Gheorghe, M. Gruselle and S. Ohkoshi, *J. Am. Chem. Soc.*, 2009, **131**, 16838; (f) M. Gruselle, Y. Li, N. Ovanesyan, V. Markhaev, G. Shilov, F. Mushenok, C. Train and S. Aldoshin, *Chirality*, 2013, **25**, 444; (g) C. Maxim, S. Ferlay and C. Train, *C. R. Chimie*, 2019, **22**, 534.

[13] *(a)* E. Coronado, J. R. Galán-Mascarós, M. C. Giménez-López, M. Almeida and J. C. Waerenborgh, *Polyhedron,* 2007, **26**, 1838; *(b)* M.

Clemente-León, E. Coronado, M. C. Giménez-López, A. Soriano-Portillo, J. C. Waerenborgh, F. S. Delgado and C. Ruiz-Pérez, *Inorg. Chem.*, 2008, **47**, 9111; *(c)* M. Clemente-León, E. Coronado, M. López-Jordà, G. Mínguez Espallargas, A. Soriano-Portillo and J. C. Waerenborgh, *Chem. Eur., J.*, 2010, **16**, 2207; *(d)* M. Clemente-León, E. Coronado and M. López-Jordà, *Dalton Trans.*, 2010, **39**, 4903; *(e)* M. Clemente-León, E. Coronado, M. López-Jordà and J. C. Waerenborgh, *Inorg. Chem.*, 2011, **50**, 9122; *(f)* M. Clemente-León, E. Coronado, M. López-Jordà, C. Desplanches, S. Asthana, H. Wang and J.-F. Létard, *Chem. Sci.,* 2011, **2**, 1121; *(g)* M. Clemente-León, E. Coronado and M. López-Jordà, *Eur. J. Inorg. Chem.,* 2013, 753; *(h)* M. Clemente-León, E. Coronado, M. López-Jordà, J. C. Waerenborgh, C. Desplanches, H. Wang, J.-F. Létard, A. Hauser and A. Tissot, *J. Am. Chem.* Soc., 2013, **135**, 8655; *(i)* A. Ben Djamâa, M. Clemente-León, E. Coronado and M. López-Jordà, *Polyhedron*, 2013, **64**, 142; *(j)* M. López-Jordà, M. Giménez-Marqués, C. Desplanches, G. Mínguez Espallargas, M. Clemente-León and E. Coronado, *Eur. J. Inorg. Chem.* 2016, **2016**, 2187.

[14] S. Benmansour, C. Cerezo-Navarrete, J. Canet-Ferrer, G. Muñoz-Matutano, J. Martínez-Pastor and C. J. Gómez-García, *Dalton Trans.,* 2018, **47**, 11909.

[15] C. Train, M. Gruselle and M. Verdaguer, *Chem. Soc. Rev.*, 2011, **40**, 3279.

[16] M. Clemente-León, E. Coronado, C. J. Gómez-García, M. López-Jordà, A. Camón, A. Repollés and F. Luis, *Chem. Eur. J.*, 2014, **20**, 1669.

[17] B. Zhang, Y. Zhang and D. Zhu, *Dalton Trans.,* 2012, **14**, 8509.

[18] A. Alberola, E. Coronado, C. Giménez-Saiz, C. J. Gómez-García, F. M. Romero and A. Tarazón, *Eur. J. Inorg. Chem.,* 2005, **2005**, 389.

[19] (a) M. C. Young, E. Liew, J. Ashby, K. E. McCoy and R. J. Hooley, *Chem. Commun.*, 2013, **49**, 6331; (b) M. C. Young, E. Liew and R. J. Hooley, *Chem. Commun.,* 2014, **50**, 5043.

[20] C. Sánchez-Sánchez, C. Desplanches, J. M. Clemente-Juan, M. Clemente-León and E. Coronado, *Dalton Trans.,* 2017, **46**, 2680.

[21] (a) J. Vallejo, I. Castro, R. Ruiz-García, J. Cano, M. Julve, F. Lloret, G. De Munno, W. Wernsdorfer and E. Pardo, *J. Am. Chem. Soc.*, 2012, **134**, 15704; (b) E. Colacio, J. Ruiz, E. Ruiz, E. Cremades, J. Krzystek, S. Carretta, J. Cano, T. Guidi, W. Wernsdorfer and E. K. Brechin, *Angew. Chem. Int. Ed.*, 2013, **52***,* 9130; (c) R. Herchel, L. Váhovská, I. Potocnák and Z. Trávnícek, *Inorg. Chem.*, 2014, **53***,* 5896; (d) S. Gómez-Coca, A. Urtizberea, E. Cremades, P. J. Alonso, A. Camón, E. Ruiz and F. Luis, *Nat. Commun.*, 2014, **5**, 4300; (e) S. Roy, I. Oyarzabal, J. Vallejo, J. Cano, E. Colacio, A. Bauza, A. Frontera, A M. Kirillov, M, G. B. Drew and S. Das, *Inorg. Chem.*, 2016, **55**, 8502;(f) A. Switlicka-Olszewska, J. Palion-Gazda, T. Klemens, B. Machura, J. Vallejo, J. Cano, F. Lloret and M. Julve, *Dalton Trans.*, 2016, **45**, 10181;(g) G. Novitchi, S. Jiang, S. Shova, F. Rida, I. Hlavicka, M. Orlita, W. Wernsdorfer, R. Hamze, C. Martins, N. Suaud, N. Guihéry, A. L. Barra and C. Train, *Inorg. Chem.*, 2017, **56**, 14809.

[22] (a) F. Habib, O. R. Luca, V. Vieru, M. Shiddiq, I. Korobkov, S. I. Gorelsky, M. K. Takase, L. F. Chibotaru, S. Hill, R. H. Crabtree and M. Murugesu, *Angew. Chem. Int. Ed.,* **2013**, *52*, 11290; (b) L. Rigamonti, N. Bridonneau, G. Poneti, L. Tesi, L. Sorace, D. Pinkowicz, J. Jover, E. Ruiz, R. Sessoli and A. Cornia, *Chem. Eur. J.*, 2018, **24**, 8857; (c) R. F. Higgins, B. N. Livesay, T. J. Ozumerzifon, J. P. Joyce, A. K. Rappé and M. P. Shores, *Polyhedron*, 2018, **143**, 193; (d) D: Sertphon, K. S. Murray, W. Phonsri, J. Jover, E. Ruiz, S. G. Telfer, A. Alkas, P. Harding and D. J. Harding, *Dalton Trans.,* 2018, **47***,* 859; (e) V. García-López, F. Orts-Mula, M. Palacios-Corella, J. M. Clemente-Juan, M. Clemente-León and E. Coronado. *Polyhedron,* 2018, **150**, 54-60; (f) B. Brachnakova, S. Matejová, J. Moncol, R. Herchel, J. Pavlik, E.

Moreno-Pineda, M. Ruben and I. Salitros, *Dalton Trans.,* 2020, **49**, 1249.

[23] (a) H. A. Goodwin, *Top. Curr. Chem.,* 2004, **234**, 23; (b) S. Hayami, Y. Komatsu, T. Shimizu, H. Kamihata and Y. H. Lee, *Coord. Chem. Rev.,* 2011, **255**, 1981; (c) M. G. Cowan, J. Olguin, S. Narayanaswamy, J. L. Tallon and S. Brooker, *J. Am. Chem. Soc.,* 2012, **134**, 2892; (d) Y. Guo, X. L. Yang, R. J. Wei, L. S. Zheng and J. Tao, *Inorg. Chem.,* 2015, **54**, 7670.

[24]J. Spek, *Appl. Cryst.,* 2003, **36**, 7.

[25] J. J. Borrás-Almenar, J. M. Clemente-Juan, E. Coronado and B. S. Tsukerblar, J. Comput. Chem., 2001, **22(9)**, 985.

[26] E.Y. Misochko, A.V. Akimov, D.V. Korchagin, J. Nehrkorn, M. Ozerov, A.V. Palii, J.M. Clemente-Juan and S.M. Aldoshin, *Inorg. Chem.,* 2019, **58**, 16434.

[27] Y. Z. Zhang, S. Gómez-Coca, A. J. Brown, M. R. Saber, X. Zhang and K. R. Dunbar, *Chem. Sci.,* 2016, **7**, 6519.

[28]E. Colacio, J. Ruiz, E. Ruiz, E. Cremades, J. Krzystek, S. Carretta, J. Cano, T. Guidi, W. Wernsdorfer, and E. K. Brechin, *Angew. Chem. Int. Ed.,* 2013, **52**, 9130.

[29] M. A. Palacios, J. Nehrkorn, E. A. Suturina, E. Ruiz, S. Gómez-Coca, K. Holldack, A. Schnegg, J. Krzystek, J. M. Moreno and E. Colacio, *Chem. Eur. J.,* 2017, **23**, 11649.

[30] F. Kobayashi, R. Ohtani, M. Nakamura, L. F. Lindoy and S. Hayami, *Inorg. Chem.,* 2019, **58**, 7409.

[31] (a) A. Singh and K. Shrivastava, *Phys. Status Solidi B,* 1979, **95,** 273; (b) K. N. Shrivastava, *Phys. Status Solidi B,* 1983, **117**, 437.

[32] Y. Wu, D. Tian, J. Ferrando-Soria, J. Cano, L. Yin, Z. Ouyang, Z. Wang, S. Luo, X. Liu and E. Pardo, *Inorg. Chem. Front.,* 2019, **6**, 848.

[33] J. Vallejo, M. Viciano-Chumillas, F. Lloret, M. Julve, I. Castro, J. Krzystek, M. Ozerov, D. Armentano, G. De Munno and J. Cano, *Inorg. Chem.*, 2019, **58**, 15726.

[34] L. S. Mariano, I. M. L. Rosa, N. R. De Campos, A. C. Doriguetto, D. F. Dias, W. D. do Pim, A. K. S. M. Valdo, F. T. Martins, M. A. Ribeiro, E. E. B. De Paula, E. F. Pedroso, H. O. Stumpf, J. Cano, F. Lloret, M. Julve and M. V. Marinho, *Cryst. Growth Des*., https://dx.doi.org/10.1021/acs.cgd.9b01638.

[35] S. Roy, I. Oyarzabal, J. Vallejo, J. Cano, E. Colacio. A. Bauza, A. Frontera, A. M. Kirillov, M. G. B. Drew and S. Das, *Inorg. Chem.,* 2016, **55**, 8502−8513.

[36] G. K. Gransbury, R. W. Gable, B. Moubaraki, K. S. Murray, L. Sorace, A. Soncini and C. Boskovic, *Chem. Sci.*, 2019, **10**, 8855.

[37] J. C. Baylar, E. M. Jones *,* (Ed. H. S. Booth), in *Inorganic Synthesis*, McGraw-Hill, New York, 1939, Vol 5, p. 35.

[38] G. M. Sheldrick, *Acta Cryst.,* 2015, **A71**, 3.

[39] G. M. Sheldrick, *Acta Cryst.,* 2015, **C71**, 3.

[40] O. V. Dolomanov, L. J. Bourhis, R. J. Gildea, J. A. K. Howard and H. Puschmann, *J. Appl. Cryst.,* 2009, **42**, 339.

Supporting Information: Insertion of single-ion magnets based on mononuclear Co(II) complexes into ferromagnetic oxalate-based networks.

Table of Contents

ESI 1. Structure of 1

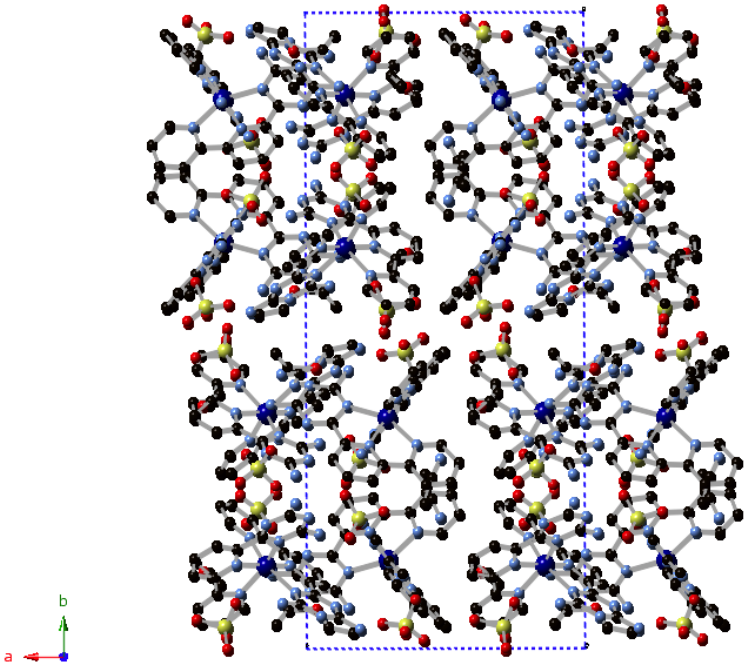

Fig. S1 Projection on the ab plane of the structure of **1**; Co (dark blue), Cl (yellow), C (black), N (blue), O (red); hydrogen atoms have been omitted for clarity.

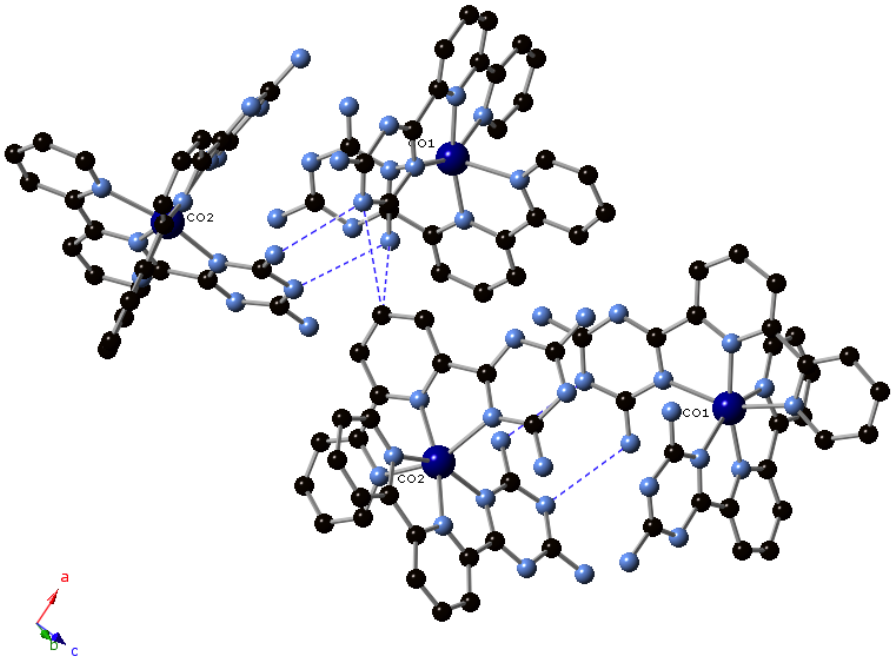

Fig. S2 Two dimers of neighbouring $[Co^{II}(L)_2]^{2+}$ linked through CH···N short contacts in **1**; Co (dark blue), C (black), N (blue), O (red); hydrogen atoms have been omitted for clarity.

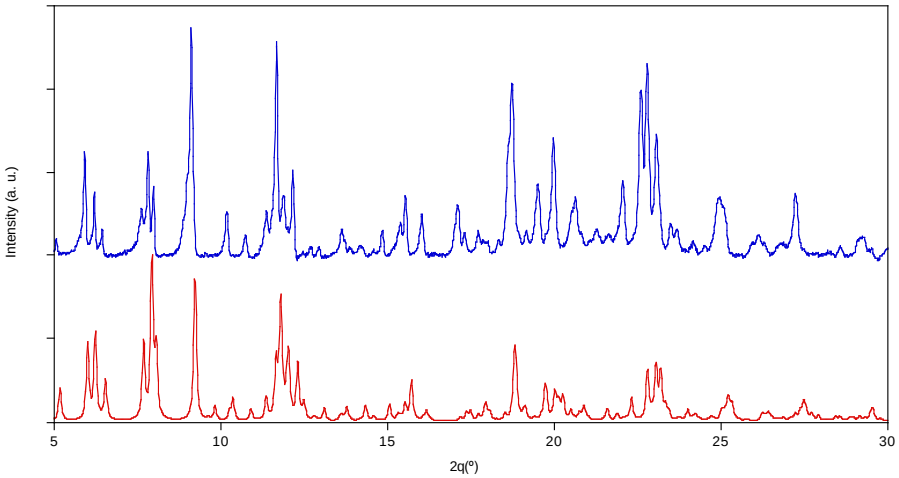

Fig. S3 Powder X-ray diffraction pattern of **1** at room temperature measured in contact with the mother liquor (blue) and simulated one from single crystal X-ray diffraction data at 300 K (red).

ESI 2. Structure of 2

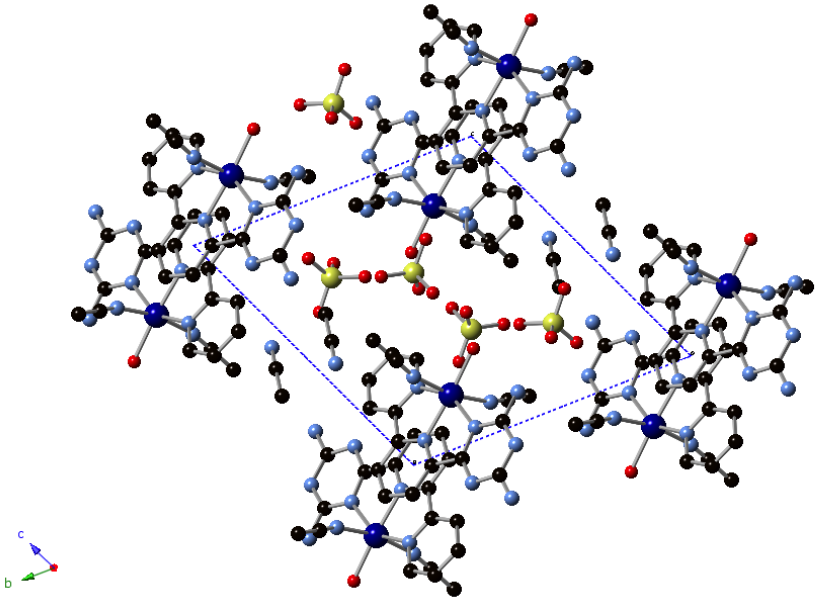

Fig. S4 Projection on the bc plane of the structure of **2**; Co (dark blue), Cl (yellow), C (black), N (blue), O (red); hydrogen atoms have been omitted for clarity.

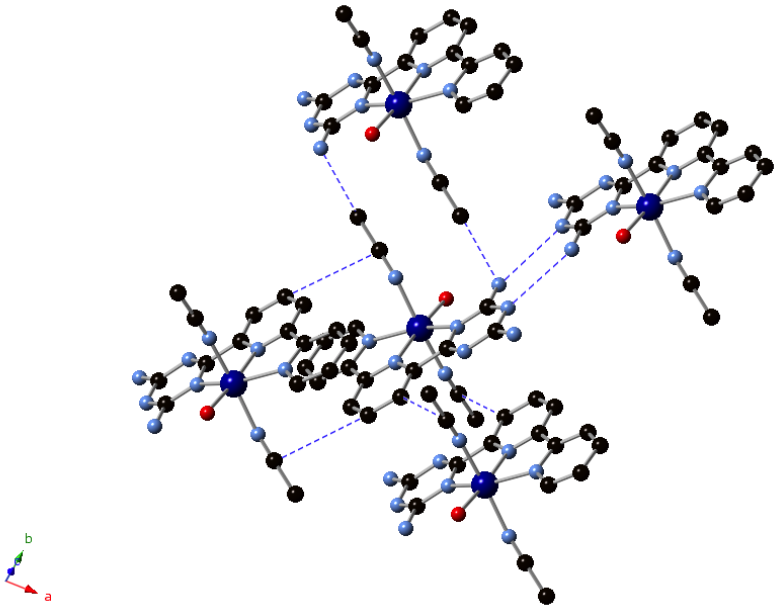

Fig. S5 Short contacts between neighbouring $[Co^{II}(L)(CH_3CN)_2(H_2O)]^{2+}$ complexes in the structure of **2**; Co (dark blue), Cl (yellow), C (black), N (blue), O (red); hydrogen atoms have been omitted for clarity.

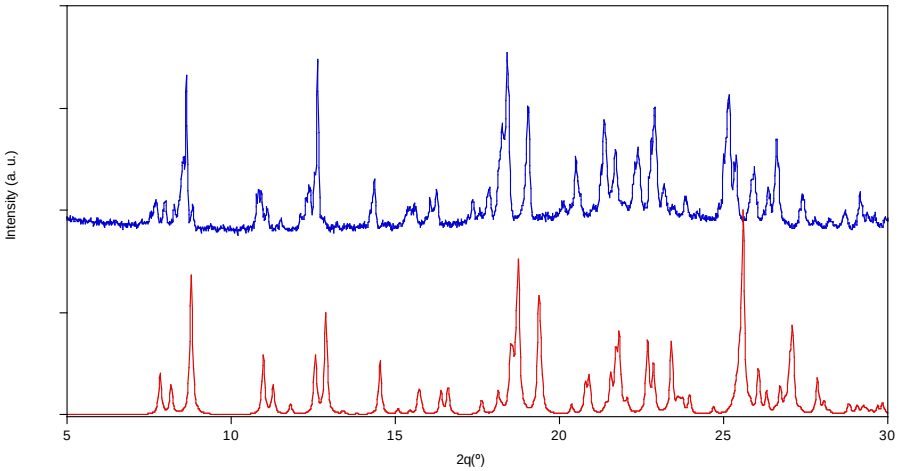

Fig. S6 Powder X-ray diffraction pattern of **2** at room temperature measured in contact with the mother liquor (blue) and simulated one from single crystal X-ray diffraction data at 120 K (red).

ESI 3. Structure of 3

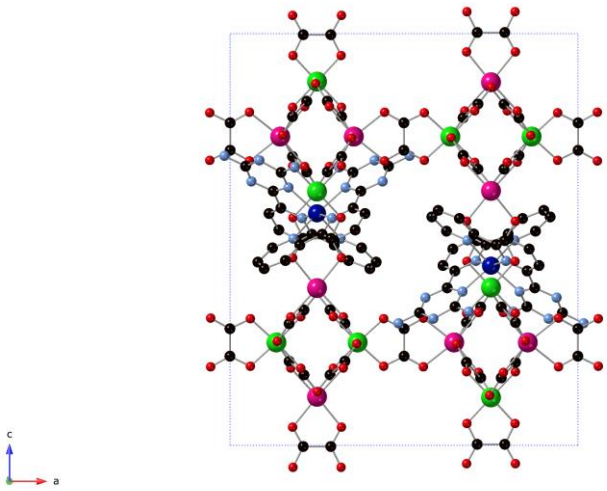

Fig. S7 Projection on the ac plane of the structure of **3**; Co (dark blue), C (black), N (blue), O (red), Mn (pink) and Cr (green); hydrogen atoms have been omitted for clarity.

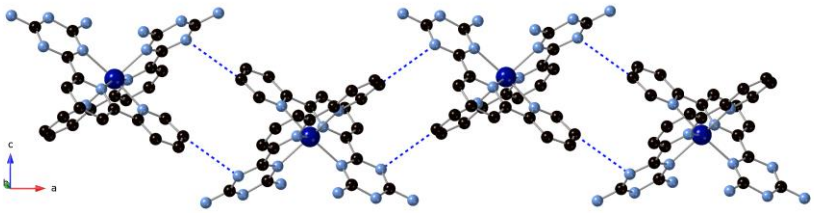

Fig. S8 Chains of $[Co^{II}(L)_2]^{2+}$ complexes running along the a axis linked through CH···N intermolecular interactions (blue dashed lines) in the structure of **3**; Co(dark blue), N (blue), C (black).

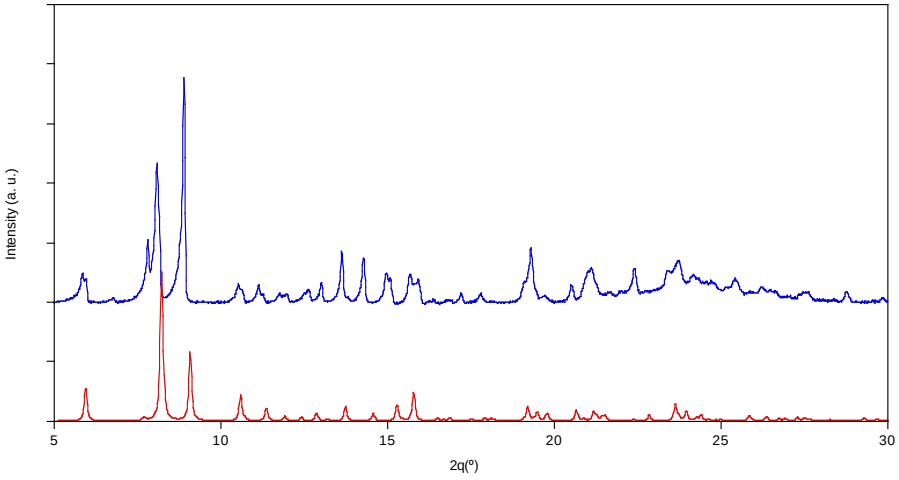

Fig. S9 Powder X-ray diffraction pattern of **3** at room temperature measured in contact with the mother liquor (blue) and simulated one from single crystal X-ray diffraction data at 120 K (red).

ESI 3. Structure of 4

Structure of $[Co^{II}(L)_2][Mn^{II}Cr^{III}(ox)_3]2\cdot$(solvate) (4). **4** crystallizes in the monoclinic space group P21/n. It is formed by anionic layers with a distorted 2D bimetallic oxalate network of formula $[Mn^{II}(H_2O)0.67Cr^{III}(ox)_3]$- in the bc plane alternating with a layer of $[Co^{II}(L)_2]^{2+}$ complexes and disordered solvent molecules (see Fig. S10). The bimetallic oxalate anionic layer presents the well-known honeycomb structure formed by an extended network of Mn(II) and Cr(III) ions linked through oxalate bridges. These oxalate ligands connect the Mn(II) and Cr(III) ions in such a way that each Mn(II) is surrounded by three neighboring Cr(III) and vice-versa. The neighbouring octahedral metal centres of the bimetallic oxalate network present alternated chirality as usual for this type of network. It contains three crystallographically independent Mn(II) ions and Cr(III) ions, which can be distinguished by their typical M-O distances (2.157(8)-2.328(14) Å for Mn and 1.943(9)-2.003(8) Å for Cr). Cr(III) ions exhibit a distorted octahedral coordination as that of one of the three crystallographically independent Mn(II) ions (Mn2). The other two Mn(II) ions (Mn1 and Mn3) are heptacoordinated. Thus, the six O from the three oxalate ligands form a distorted octahedron with Mn–O distances ranging from 2.196(7) to 2.320(9) Å for Mn1 and from 2.198(7) to 2.306(8) Å for Mn3, which is capped with a coordinated water molecule at Mn-O distances of 2.328(14) (Mn1) and 2.196(9) Å (Mn3). The heptahedral coordination of 2/3 of the Mn(II) ions distorts the honeycomb structure in such a way that the Mn(II) ions are out of the plane defined by the Cr(III) ions in contrast to other 2D oxalate structures. This effect is more important for the two heptacoordinated Mn(II) ions (Mn1 and Mn3) that are clearly above and below the plane defined by the Cr(III) ions (Fig. S10). The water solvent molecules coordinated to these two Mn(II) sites are perpendicular to the oxalate layers pointing to opposite neighbouring layers. A similar effect has been observed in other compounds reported in the literature containing honeycomb layers

with solvent molecules coordinated to Mn(II).[1,2] The minimum distance between metal ions belonging to different oxalate layers is 10.62 Å, which is slightly lower to that found in 2D compounds with $[Fe^{II}(L)_2]^{2+}$ (11.24 Å)[3] and $[Fe^{III}(sal_2\text{-trien})]^{+}$ and derivatives (11.609-11.644 Å),[4] due to the distortion of the layers. The space between the oxalate layers is occupied by one and a half crystallographically independent $[Co^{II}(L)_2]^{2+}$ complexes and disordered solvent molecules. The $[Co^{II}(L)_2]^{2+}$ complex with an occupancy 0.5 presents a disorder with two possible configurations. The Co(II) presents a distorted N_6 octahedral coordination to the two tridentate L ligands as that of **1** and **3**.

The Co-N bond lengths of the inner pyridine and triazine rings are 2.050(11)-2.071(10) Å (Co1) and 2.078(18)-2.08(2) Å (Co2) and 2.138(11)-2.191(11) Å (Co1) and 2.145(9)-2.192(18) Å (Co2), respectively, while those of the external pyridine ring are 2.186(10)-2.211(11) Å (Co1) and 2.094(12)-2.162(11) Å (Co2). These distances are very similar to those of **1** and **3** and typical of Co(II) in the high-spin state. There are several hydrogen-bonds between the NH2 from triazine group of L and oxygen atoms from the oxalate network. In contrast to **3**, there are hydrogen-bonds between the two crystallographically independent $[Co^{II}(L)_2]^{2+}$ complexes, which involve one NH2 from triazine and one N atom from the triazine ring of the neighbouring molecule. These interactions lead to isolated chains of hydrogen-bonded $[Co^{II}(L)_2]^{2+}$ complexes running along the c axis (see Fig. S11). As in oxalate-based compounds based on $[Fe^{II}(L)_2]^{2+}$ and in compound **3**, the structure presents voids filled with disordered solvent molecules. Disordered solvent molecules have been treated with PLATON/SQUEEZE (see experimental section).[5]

Table S1. Crystallographic data for **4**[‡]

Compound	**4**
Empirical formula	$C_{42}H_{28}CoCr_2Mn_2N_{16}O_{33}$
Formula weight	1557.61
Crystal colour	Pink
Crystal size	0.26*0.22*0.05
Temperature (K)	120(2)
Wavelength (Å)	0.71073
Crystal system, *Z*	Monoclinic, 4
Space group	$P2_1/n$
a (Å)	27.6225(11)
b (Å)	15.5013(3)
c (Å)	28.2471(12)
β (°)	117.388(5)
V (Å^3)	10739.3(8)
ρ_{calc} (Mg/m^3)	1.253
μ($Mo_{K\alpha}$) (mm^{-1})	0.936
2θ range (°)	6.478 to 60.098
Reflns collected	53497
Independent reflns (R_{int})	273692 (0.1209)
L. S. parameters/ restraints	851/1
$R1(F)$,[a] $I > 2\sigma(I)$	0.1533
$wR2(F^2)$,[b] all data	0.4811
$S(F^2)$,[c] all data	1.105

[a] $R1(F) = \Sigma||F_O|-|F_C||/\Sigma|F_O|$; [b] $wR2(F^2) = [\Sigma w(F_O^2-F_C^2)^2/\Sigma wF_O^4]^{1/2}$; [c] $S(F^2) = [\Sigma w(F_O^2-F_C^2)^2/n + r - p)]^{1/2}$

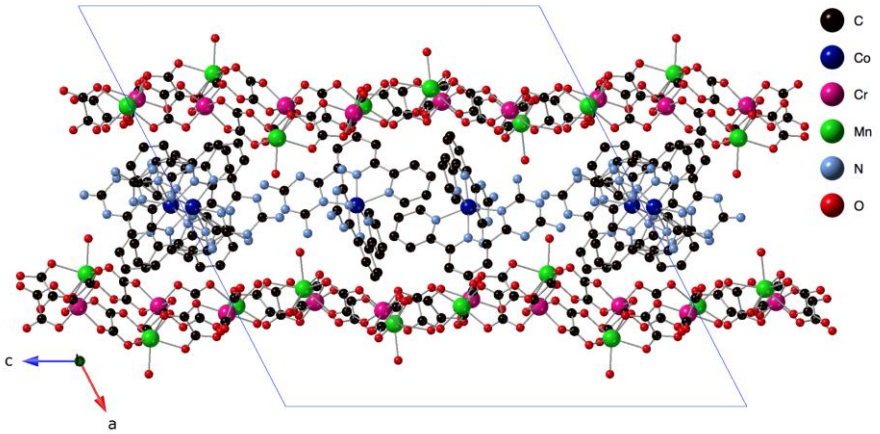

Fig. S10 Projection on the ac plane of the structure of **4**; Co (dark blue), Cl (yellow), C (black), N (blue), O (red); hydrogen atoms have been omitted for clarity.

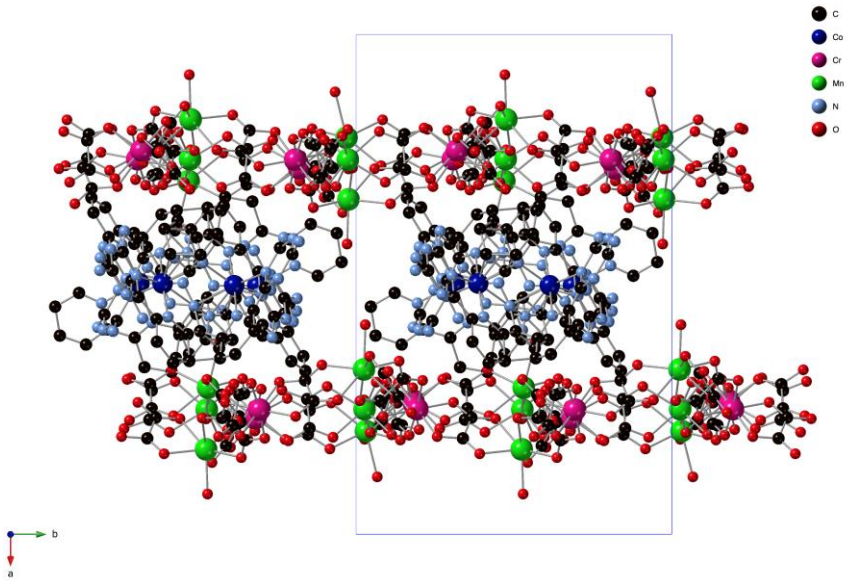

Fig. S11 Projection on the ab plane of the structure of **4**; Co (dark blue), Cl (yellow), C (black), N (blue), O (red); hydrogen atoms have been omitted for clarity.

ESI 5. Magnetic properties of 1 and 2

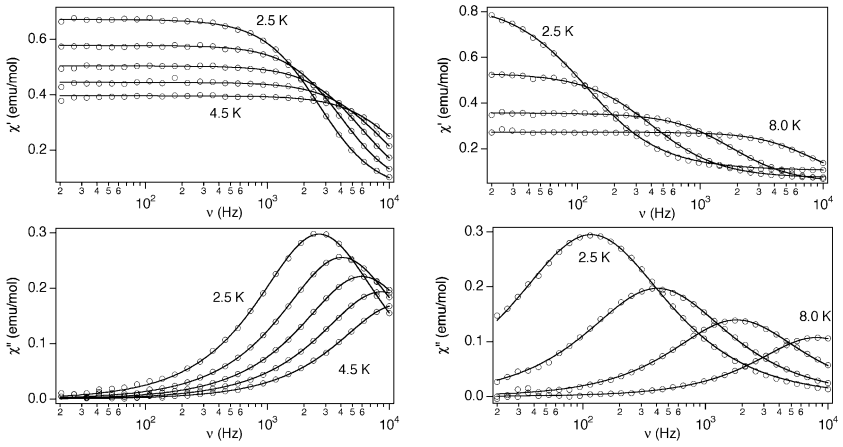

Fig. S12 ac susceptibility in an applied dc field of 0.1 T of **1** (left) and **2** (right) measured as a function of the frequency at the different temperatures (2.5, 3.0, 3.5, 4.0 and 4.5 K for **1**, and 2.5, 4.0, 6.0 and 8.0 K for **2**). Top: Real component. Bottom: Imaginary component. Solid lines represent the best fitting of the experimental data to a Cole-Cole function, yielding R = 0.97-0.98 for 1 and between 0.86-0.98 for 2.

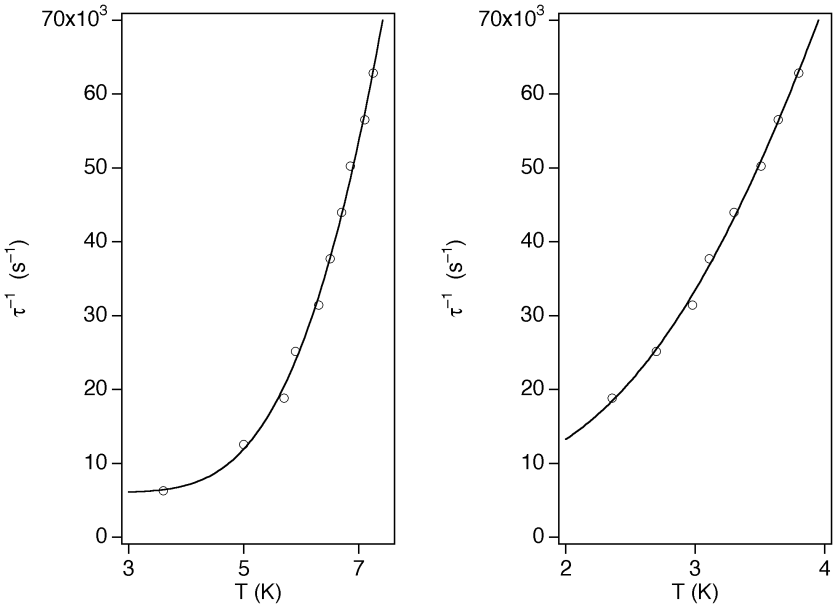

Fig. S13 Thermal dependence of the relaxation time for **1** (left) and **2** (right). Solid lines represent the best fits (see text).

ESI 6. Magnetic properties of 3

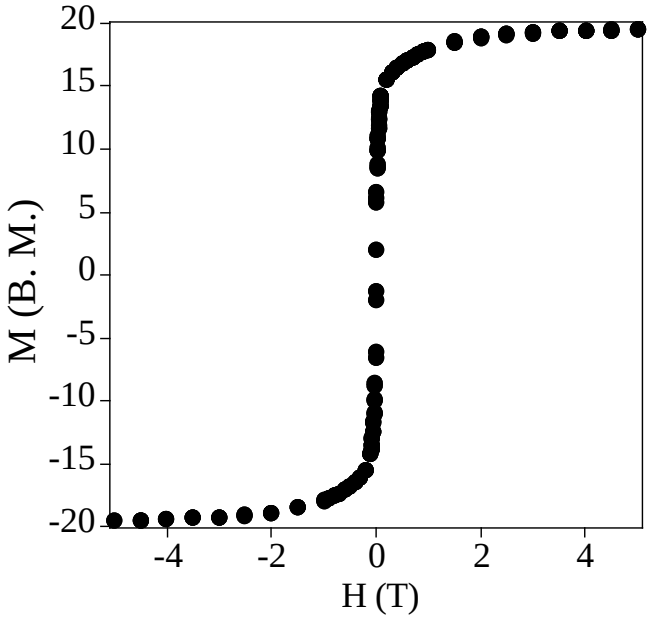

Fig. S14 Magnetization vs magnetic field for **3** measured at T = 2 K.

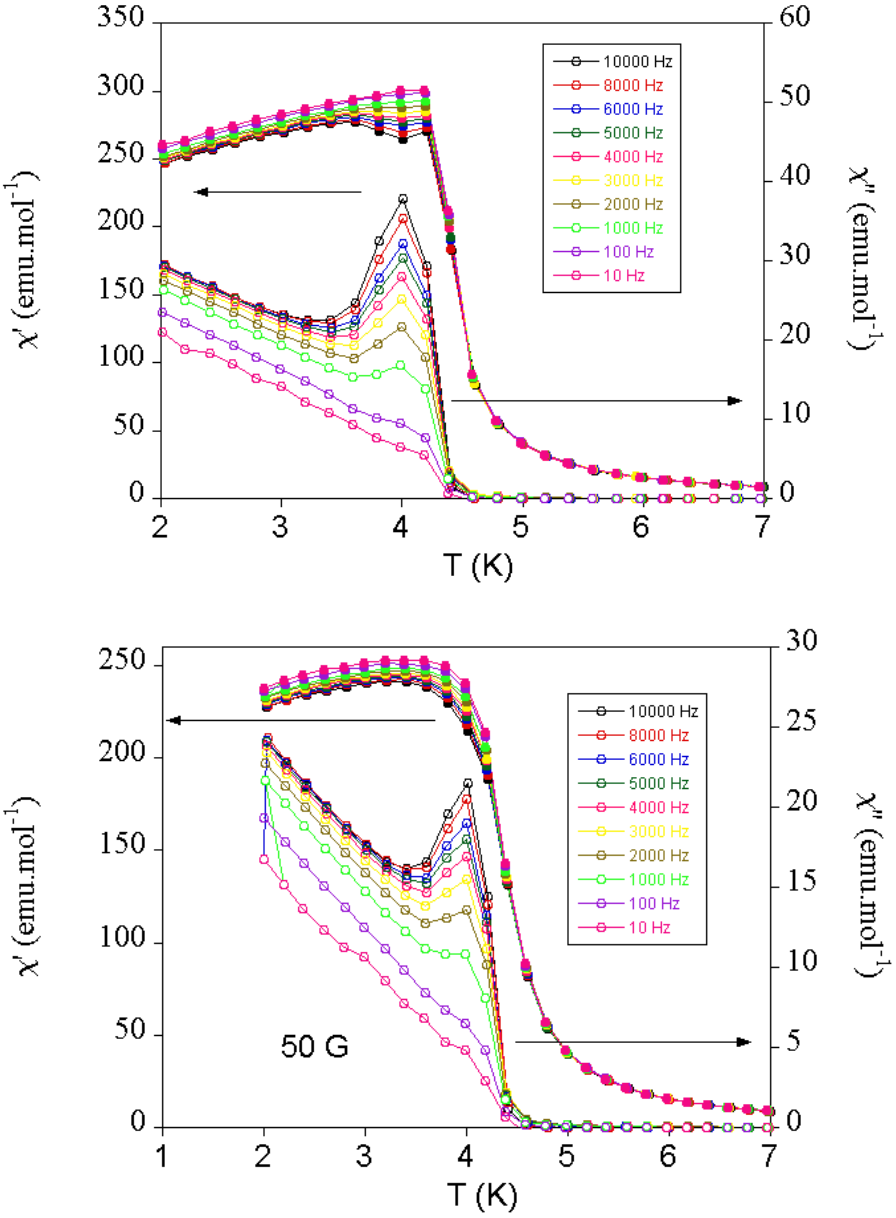

Fig. S15 Temperature dependence of the in-phase AC susceptibility (χ') (filled symbols) and the out-of-phase AC susceptibility (χ") (empty symbols) for **3** measured at several frequencies and under the action of a dc magnetic field of 0 Gauss (top) and 50 Gauss (bottom) .

a)

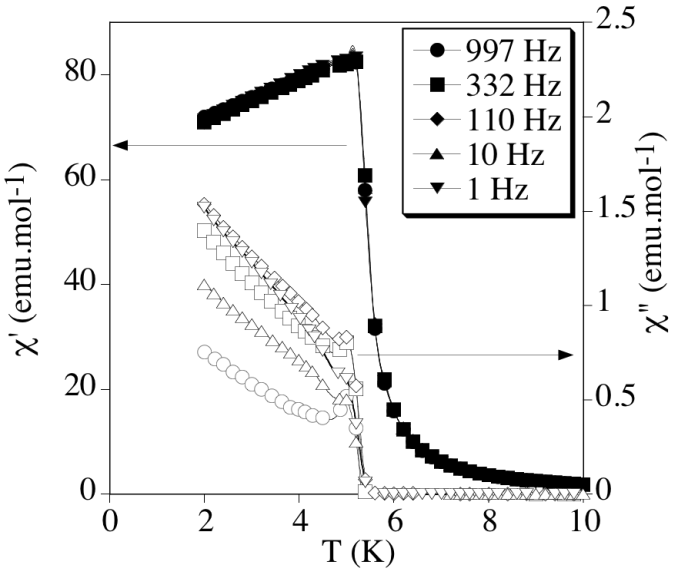
997 Hz
332 Hz
110 Hz
10 Hz
1 Hz
χ' (emu.mol-1)
χ'' (emu.mol-1)
T (K)
0
20
40
60
80
0
0.5
1
1.5
2
2.5
0
2
4
6
8
10

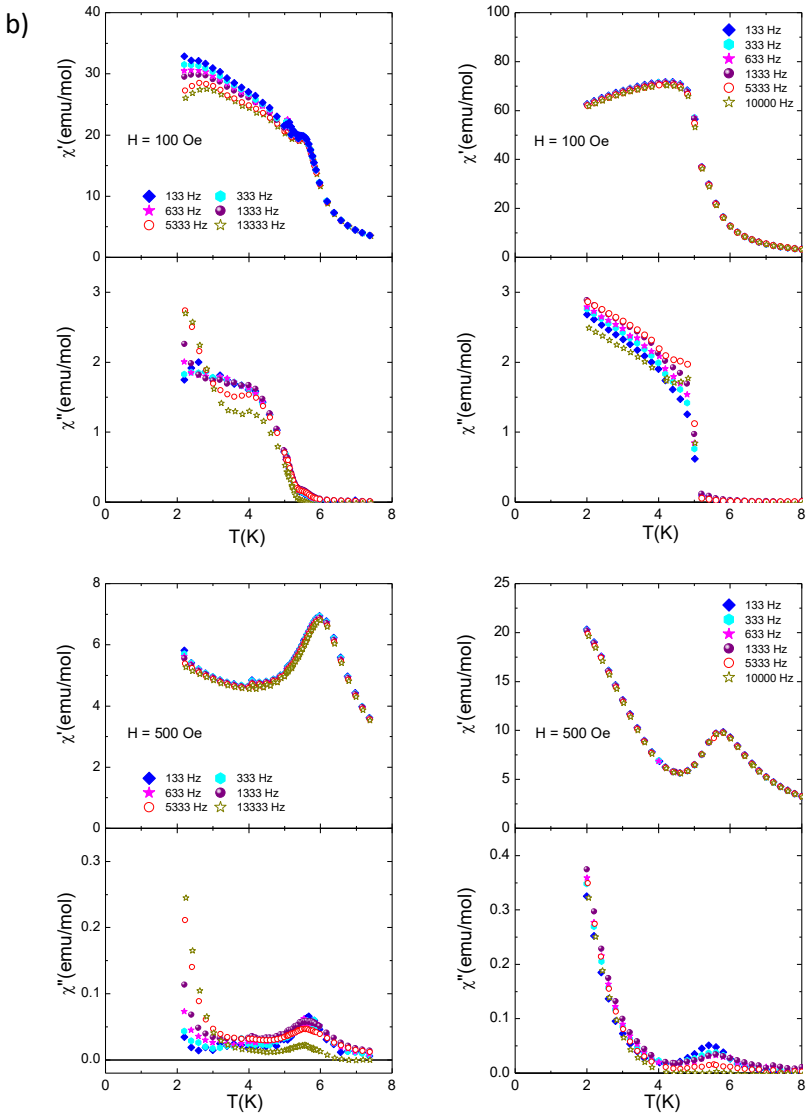

Fig. S16 AC magnetic susceptibility measurements of [In(sal$_2$-trien)][Mn^{II}Cr^{III}(ox)$_3$]·solv at H = 0 Oe extracted from reference 4b (a). AC magnetic susceptibility of [Mn^{III}(salen)(H$_2$O)]$_2$[Mn^{II}Cr^{III}(ox)$_3$]$_2$·solv measured at H = 100 Oe and 500 Oe and for several frequencies (left), compared with that of [In(sal$_2$-trien)][Mn^{II}Cr^{III}(ox)$_3$]·solv (right) extracted from reference 6 (b).

The thermal dependence of χT of filtered crystals of **3** shows a value of 15.3 $cm^3 \cdot K \cdot mol^{-1}$ at 300 K (see Fig. S16) as that of the sample measured in contact with the mother liquor, which is approximately equal to the sum of the expected contribution for the isolated paramagnetic ions of the oxalate-based network plus the χT of **1** at 300 K (2.7 $cm^3 \cdot K \cdot mol^{-1}$). However, at lower temperatures, χT presents a gradual decrease to reach a minimum value of χT = 13.1 $cm^3 \cdot K \cdot mol^{-1}$ at around 55 K instead of the constant increase observed for the sample measured in contact with the mother liquor. At lower temperature there is a sharp increase of χT indicating the onset of a magnetic ordering. The isothermal *M* of filtered crystals of **3** at 2 K shows a more gradual increase at increasing magnetic fields than that of the solvated sample. In addition to this, it reaches a lower *M* value at 5 T of 13.2 μ_B (19.5 μ_B for the solvated sample) (see Fig. S18). This indicates that *M* of **3** is not a superposition of the magnetization of each of the two components in contrast to the solvated sample. This maximum *M* value is consistent with the expected value for an antiferromagnetic coupling between the magnetic moments of the two subnetworks (16 μ_B for two $Mn^{II}Cr^{III}$–2.1 μ_B for Co(II) in **1**) as observed previously in $[Mn^{III}(salen)(H_2O)]_2[Mn^{II}Cr^{III}(ox)_3]_2 \cdot (CH_3OH) \cdot (CH_3CN)_2$.[6] AC susceptibility measurements show a decrease of T_c to a value of 3.2 K in the filtered sample (4.6 K in contact with the mother liquor). Furthermore, it shows a stronger variation with frequency at lower temperatures than that of solvated sample (Fig. S19). All these results could indicate that the magnetic moments of the bimetallic oxalate network and the inserted $[Co^{II}(L)_2]^{2+}$ complexes present some interactions as a consequence of the removal of the solvent molecules of the structure but this has be taken with caution. This drastic change of the magnetic properties after filtering (desolvation) could be also due to changes in distances and angles of the extended

bimetallic oxalate-based network. Indeed, PXRD patterns show a complete lack of crystallinity in the filtered sample, which could be a consequence of a collapse of the extended network after removing the solvent molecules.

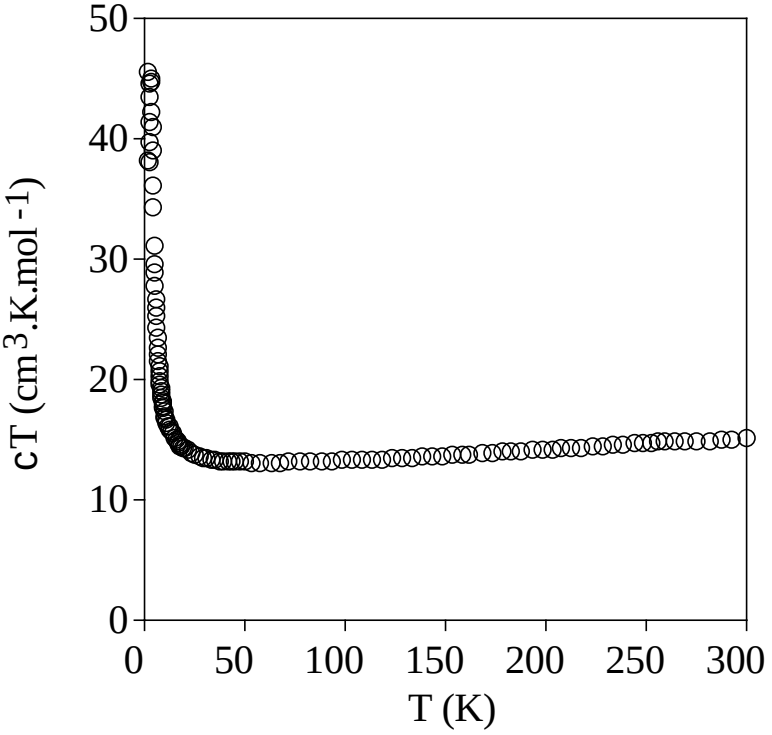

Fig. S17 Temperature dependence of the product of the molar magnetic susceptibility with temperature (χT) at 0.1 T for filtered crystals of **3**.

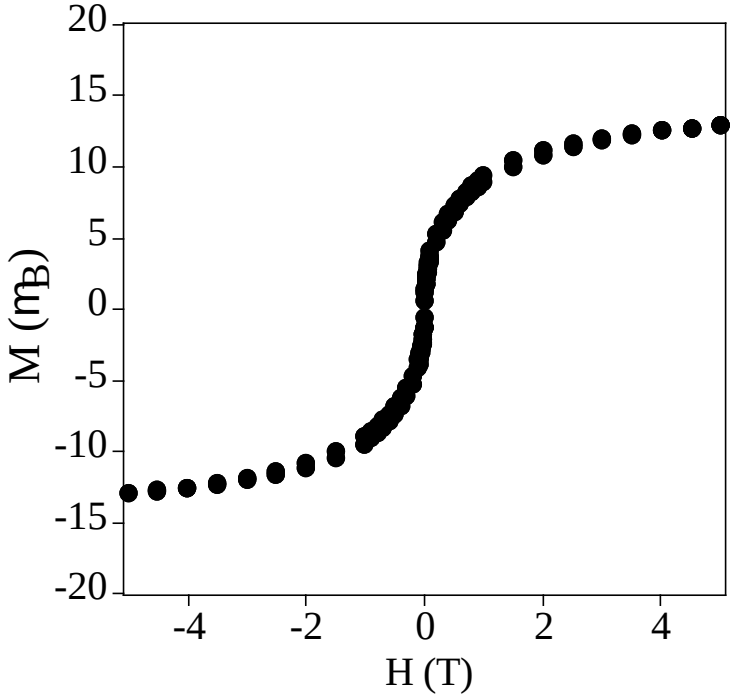

Fig. S18 Field dependence of the magnetization at 2 K for filtered crystals of **3**.

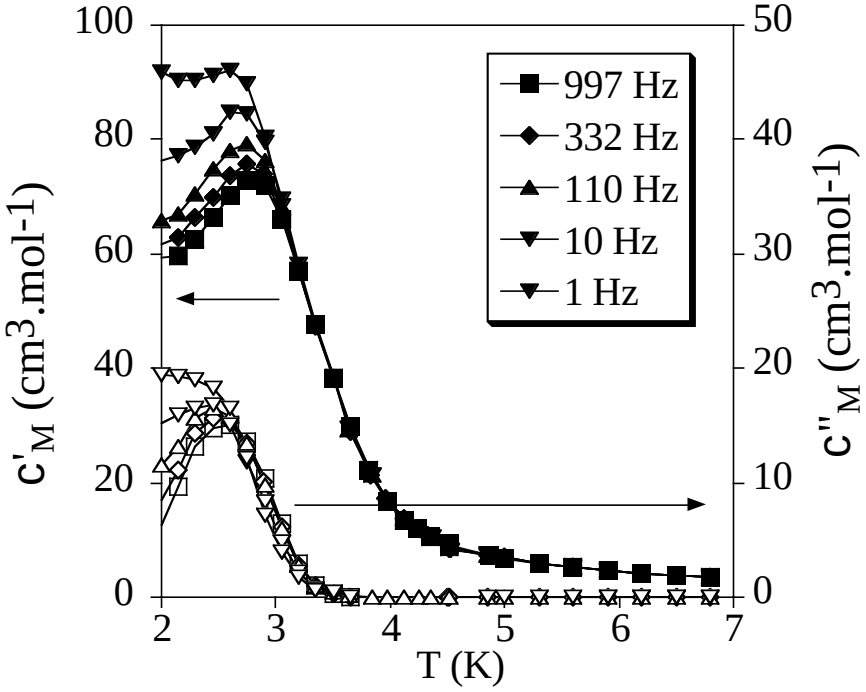

Fig. S19 Temperature dependence of the in-phase AC susceptibility (χ') (filled symbols) and the out-of-phase AC susceptibility (χ") (empty symbols) for filtered crystals of **3**.

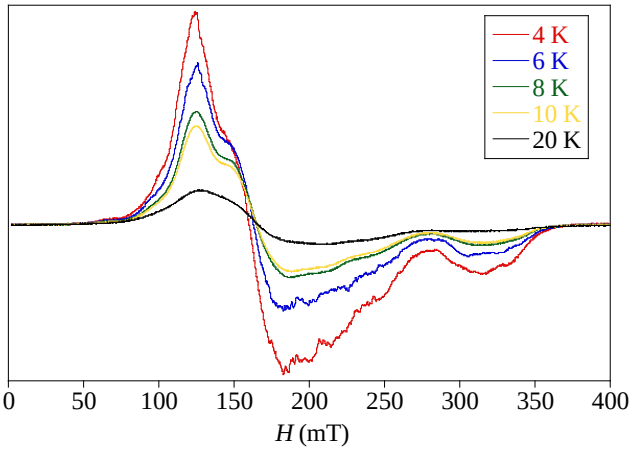

Fig. S20 EPR spectra of **1**.

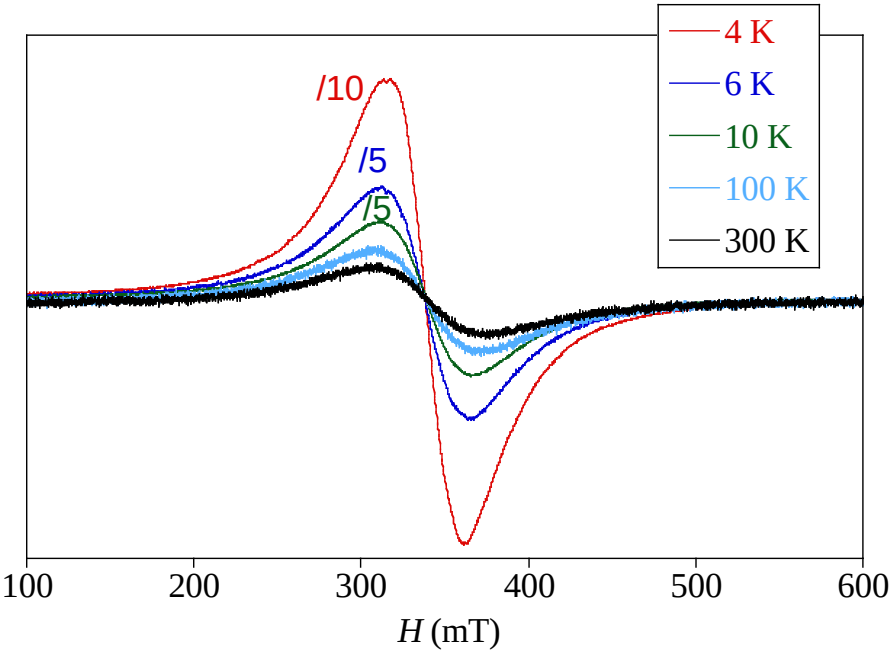

Fig. S21 EPR spectra of **3**.

References

[1] E. Coronado, J.R. Galán-Mascarós, C. Martí-Gastaldo and A. Murcia-Martínez, *Dalton Trans.*, 2006, **2006**, 3294.

[2] M. Clemente-León, E. Coronado, J.C. Dias, A. Soriano-Portillo and R.D. Willett, *Inorg. Chem.*, 2008, **47**, 6458.

[3] C. Sánchez-Sánchez, C. Desplanches, J. M. Clemente-Juan, M. Clemente-León and E. Coronado, *Dalton Trans.,* 2017, **46**, 2680.

[4] *(a)* M. Clemente-León, E. Coronado, M. C. Giménez-López, A. Soriano-Portillo, J. C. Waerenborgh, F. S. Delgado and C. Ruiz-Pérez, *Inorg. Chem.*, 2008, **47**, 9111; *(b)* M. Clemente-León, E. Coronado, M. López-Jordà, G. Mínguez Espallargas, A. Soriano-Portillo and J. C. Waerenborgh, *Chem. Eur., J*., 2010, **16**, 2207; *(c)* M. Clemente-León, E. Coronado and M. López-Jordà, *Dalton Trans.*, 2010, **39**, 4903; *(d)* M. Clemente-León, E. Coronado, M. López-Jordà and J. C. Waerenborgh, *Inorg. Chem.*, 2011, **50**, 9122; *(e)* M. Clemente-León, E. Coronado, M. López-Jordà, C. Desplanches, S. Asthana, H. Wang and J.-F. Létard, *Chem. Sci.,* 2011, **2**, 1121; *(f)* M. Clemente-León, E. Coronado and M. López-Jordà, *Eur. J. Inorg. Chem.,* 2013, 753; *(g)* M. Clemente-León, E. Coronado, M. López-Jordà, J. C. Waerenborgh, C. Desplanches, H. Wang, J.-F. Létard, A. Hauser and A. Tissot, *J. Am. Chem.* Soc., 2013, **135**, 8655.

[5] J. Spek, *Appl. Cryst.,* 2003, **36**, 7.

[6] M. Clemente-León, E. Coronado, C. J. Gómez-García, M. López-Jordà, A. Camón, A. Repollés and F. Luis, *Chem. Eur. J*., 2014, **20**, 1669.

Chapter 4.

Hexakis-Adducts of [60]Fullerene as Molecular Scaffolds of Polynuclear Spin-Crossover Molecules

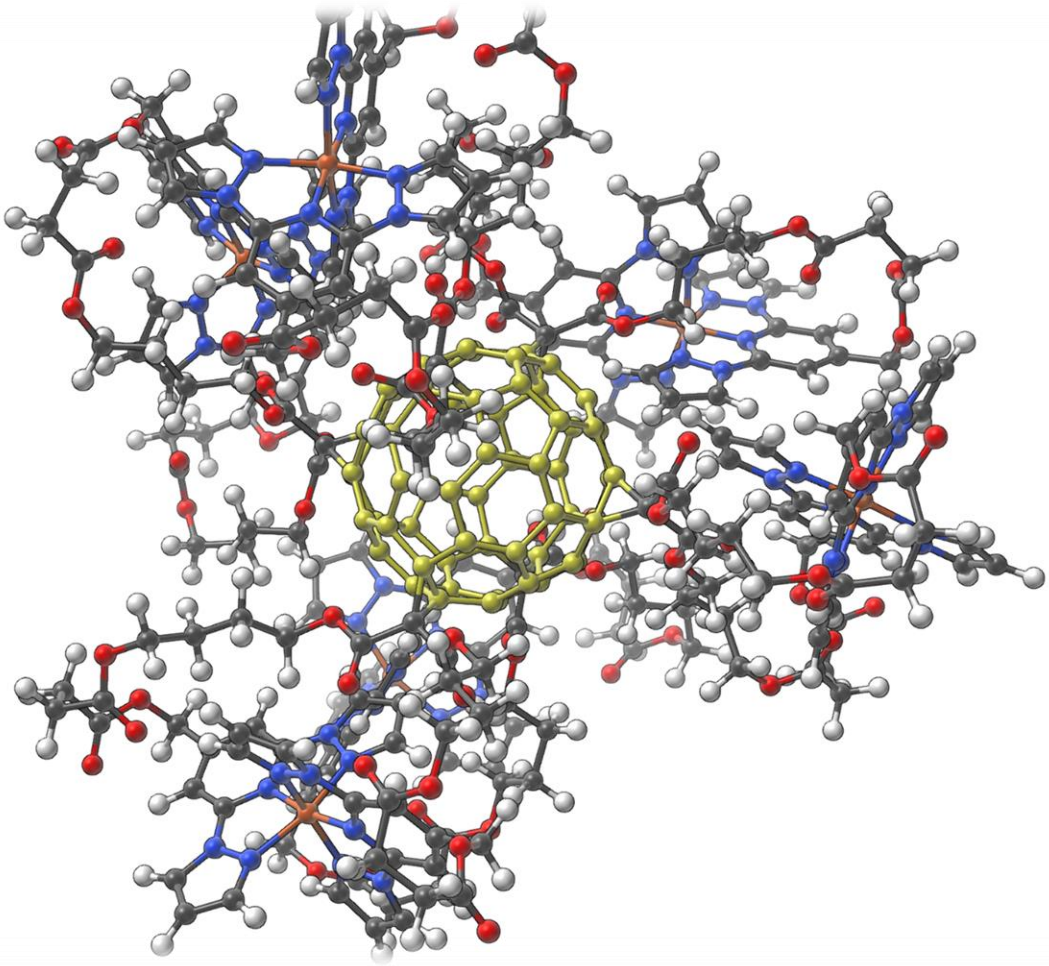

Mario Palacios-Corella, Javier Ramos-Soriano, Manuel Souto, Duarte Ananias, Joaquín Calbo, Enrique Ortí, Beatriz M. Illescas, Miguel Clemente-León, Nazario Martín and Eugenio Coronado, *Chem. Sci.* 2021, **12**, 757-766.

Introduction

Spin crossover (SCO) complexes constitute one of the most spectacular examples of molecular bistability. These complexes can be reversibly switched between two distinct states (high- and low-spin states) by a variety of external stimuli such as light, temperature, pressure, electric field or analytes.[1] Most examples of this kind are provided by Fe(II) complexes, which undergo SCO between the diamagnetic low-spin state (LS, S = 0) and the paramagnetic high-spin state (HS, S = 2).[1] A remarkable family of SCO Fe(II) compounds are bis-chelated complexes of the tridentate 2,6-bis(pyrazol-1-yl)pyridine (bpp) ligand and derivatives. Such complexes often present abrupt thermal spin transitions close to room temperature and SCO induced by irradiation at low temperatures in the solid state [Light-Induced Excited Spin State Trapping (LIESST) effect] at relatively high temperatures and long lifetimes.[2] The incorporation of these molecular species on a substrate, including a surface or a nanoparticle, is an essential step towards real applications of SCO materials,[3] but it still presents severe limitations. Indeed, previous attempts to prepare self-assembled monolayers (SAMs) of $[Fe(bpp)_2]^{2+}$ derivatives on gold[4a] or metal-oxide surfaces[4b] have been unsuccessful owing to the too weak bonding to iron(II) of these ligands grafted on surfaces. A most promising result was the preparation of gold nanoparticle arrays decorated with thiol functionalized $[Fe(bpp)_2]^{2+}$ complexes. Still, the thermal spin transition was very gradual and incomplete.[5]

A loosely unexplored possibility is using fullerenes as a carbon-based platform on which SCO complexes are anchored. Since the discovery of fullerene C_{60}, functional fullerene derivatives have attracted a big deal of attention due to their exceptional electrochemical and photophysical properties and the wide range of applications including molecular electronics and biomedical applications.[6] In this context, transition metal complexes have been incorporated onto

fullerenes for the development of new molecular materials exhibiting additional features and applications[7] but, to our knowledge, [60]fullerene has only been used as bulky end-capping group of mononuclear SCO complexes. These complexes were proposed as the first step towards the preparation of single-molecule junctions in which the bis-fullerene derivative acts as a bridge between two graphene electrodes[8] or as an anchoring group for nanocarbon materials.[9] Very recently, it has also been reported the use of C_{60} as template for the growth of SCO Fe(II) metal-organic cages.[10]

Herein, we propose an alternative approach in which [60]fullerene plays the role of a spherical scaffold surrounded by a shell of $[Fe(bpp)_2]^{2+}$ complexes anchored to it. Thus, we have synthesized hexakis-substituted [60]fullerene adducts[11] with 12 bpp units arranged with icosahedral symmetry around the fullerene surface (Fig. 1). Owing to the flexibility of the malonate-based spacers, up to six Fe(II)-bpp SCO complexes can be coordinated to the 12 bpp groups. The concentration of bpps on the C_{60} core is of interest towards the enhancement of interactions between bpp and Fe(II) leading to polynuclear C_{60}-based SCO complexes of enhanced stability and controlled 3D geometry.

In order to understand the influence of the spacer and substituents on the behavior of these complexes, we have prepared a set of functionalized C_{60} derivatives including three hexakis-substituted [60]fullerene adducts with spacers of different length and different bpp substituents (hexakis-adducts **1**, **2** and **3**) and a model ligand with only two bpp moieties (mono-adduct **4**) (Fig. 1). Spectroscopic characterization in solution has been carried out to demonstrate the formation of the polynuclear Fe(II) complexes based on **1**, **2** and **3**. In addition, DFT calculations have been performed to model the different complexation environments and simulate their electronic properties. Finally, magnetic and

Raman studies in the solid state have been used to characterize the SCO properties of these materials with temperature and light as external stimuli. To the best of our knowledge, this is the first time that highly symmetrical 3D hexakis metallo-[60]fullerenes undergoing SCO are reported, opening new avenues towards the preparation and processing of polynuclear SCO scaffolds, which could incorporate additional electronic functionalities.[11]

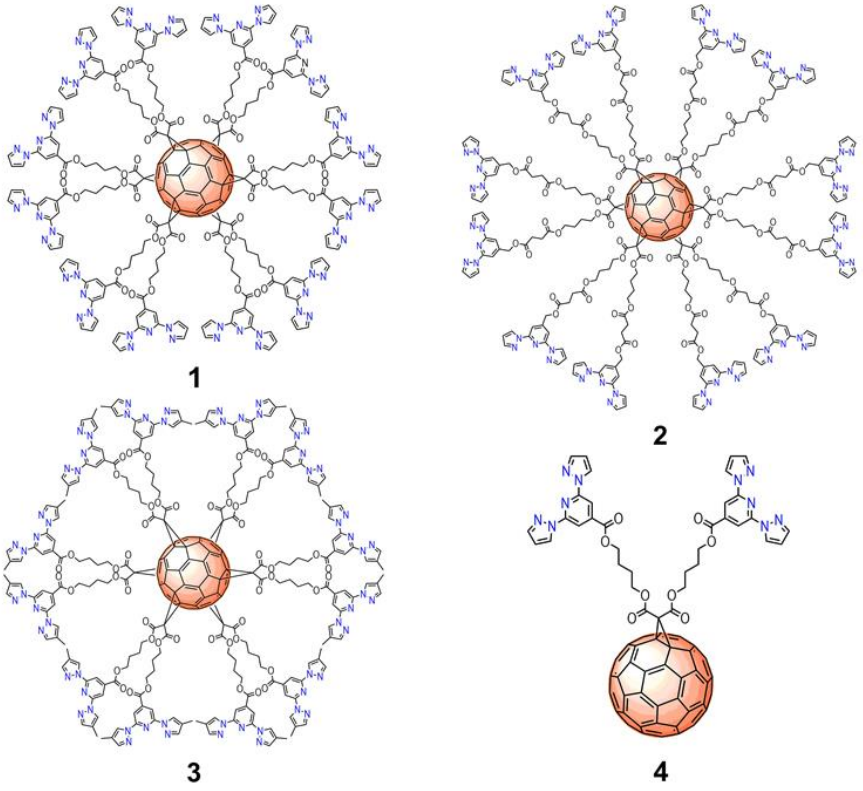

Fig. 1 Molecular structures of C_{60} hexa-adducts **1**, **2**, **3** and mono-adduct **4** functionalized with bpp ligands.

Results and discussion

Formation of the Fe (II) complexes in solution

The C_{60} hexa-adducts **1**, **2**, **3** and the mono-adduct **4** (Fig. 1) were synthesized following the synthetic strategy depicted in Schemes S1-4†. Compounds **1-3** were easily prepared by esterification of hexakisadduct **P1**[11a] with ligands bppCOOH, **L4** and **L5**, respectively, using DCC/DPTS as coupling reagents. After purification using size-exclusion chromatography employing Sephadex, compounds **1-3** were obtained in quantitative yields. Characterization was carried out by standard spectroscopic and analytical techniques (Fig. S1-S3† for **1**, S6-S7† for **2** and S10-S12† for **3**). Owing to the high symmetry of hexakisadducts **1**-**3**, ^{1}H and ^{13}C NMR were very simple.

The assignment of the ^{1}H and ^{13}C NMR spectra was achieved using COSY, HSQC and DEPT NMR spectra. As expected, in the ^{13}C NMR only two signals were observed for the sp^2 carbons of the C_{60} cage (δ ~141 and 146 ppm), thus providing evidence of the highly T_h symmetry of these compounds. The absence of the methylene signal bound to the hydroxy group at ~62.5 ppm (present in compound **P1**) revealed that the esterification reactions were successfully accomplished.

The synthesis of monoadduct **4** was carried out following a synthetic strategy in three steps, as depicted in Scheme S4†. First, P2 was prepared by Bingel-Hirsch cyclopropanation of malonate L6[11a] to [60]fullerene in the presence of DBU and CBr_4 in toluene (see Scheme S4†). Deprotection of the hydroxyl groups by hydrogenation, followed by esterification with bppCOOH using DCC/DPTS afforded **4** in good yield after column chromatography. Compound **4** and its corresponding intermediates were fully characterized by NMR, FTIR spectroscopy and mass spectrometry (Fig. S13-S21†). Thus, the ^{13}C-NMR spectrum reveals the presence of the 15 signals corresponding to the sp^2 carbons of the C_{60} unit, which typically appear for

methanofullerenes between 139 and 146 ppm. Furthermore, MS data obtained using MALDI-TOF spectrometry confirmed the presence of the molecular ion peak.

The Fe(II) complexes were obtained by mixing CH_2Cl_2 solutions of ligands **1**, **2**, **3** or **4** with CH_3CN solutions of $Fe(BF_4)_2{\cdot}nH_2O$ or $Fe(ClO_4)_2{\cdot}nH_2O$ (up to 12 equivalents). Rapid color changes from orange to red (**1**, **3** and **4**) and from orange to yellow (**2**) were observed. The formation of stable solutions after addition of Fe^{2+} in polar solvents such as CH_3CN, in which ligands **1**, **2** and **3** are not soluble, is indicative of the presence of discrete, highly charged, polynuclear polar species. The mono-adduct **4** exhibits a different behavior since a fast precipitation of the metal complex is observed upon addition of Fe^{2+}. This could be related to the lower charge of the complex since only one iron ion can be coordinated by **4**, in contrast to the six iron ions that can be incorporated by the hexa-adducts, or to the formation of polynuclear or polymeric species. Diluted solutions (~5×10^{-6} M) of the metal complexes of **1, 2, 3** and **4** were obtained in an excess of CH_2Cl_2 with a small amount of CH_3CN used to dissolve the Fe^{2+} salts. Such diluted solutions were used for UV-vis and fluorescence spectroscopy studies in order to monitor the formation of the resulting complexes.

Spectroscopic titrations were performed in 2.5×10^{-6} to 7.5×10^{-6} M solutions of ligands **1** and **2** in CH_2Cl_2 (Fig. 2). The ligands exhibited sharp and intense bpp-centered π–π* and charge-transfer (CT) absorption bands in the UV region at 245, 270 and 335 nm for **1** and at 245, 270 and 306 nm for **2**, in agreement with theoretical calculations (see below). The lowest-energy band of **1** is red-shifted, compared to **2** and unsubstituted bpp (λ_{max} = 304 nm), owing to the conjugation of the carboxylic ester group. Addition of aliquots of the Fe^{2+} salt in CH_3CN leads to an intensity decrease of the band at 245 nm and to the appearance of different isosbestic points (Fig. 2). Furthermore, a low-intensity broad band with maximum absorbance at 460 and 430 nm appears after addition of Fe^{2+} for **1** and **2**,

respectively, as a result of the formation of the coordination complex. These lowest-energy absorptions are assigned to metal-to-ligand charge transfer (MLCT) bands in agreement with previous results reported for Fe(II)-bpp complexes[12,13] and theoretical calculations (see below). Saturation of the MLCT bands was reached upon adding 6 equivalents of Fe^{2+} to solutions of **1** and **2** (Fig. 2). Titration of model bpp ligands of **1** and **2** functionalized with an ethyl ester (bppCOOEt) or a hydroxymethyl group (bppCH_2OH), respectively, showed similar trends for the π-π* UV bands (Fig. S22†), thus confirming that the changes in the absorption spectra are induced by the coordination to Fe^{2+}. Furthermore, the MLCT bands of the model complexes appear at similar wavelengths to those observed for **1** and **2** and those reported for complexes formed by bpp ligands functionalized with a pyrene group through ester or methyl ether groups.[14]

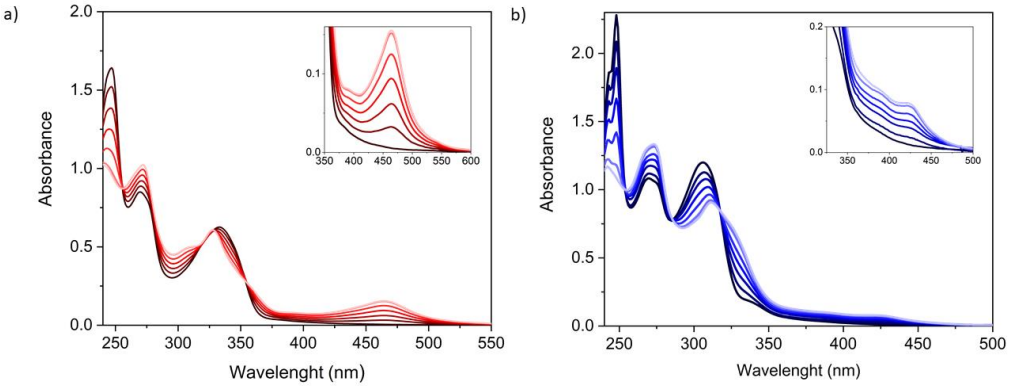

Fig. 2 UV-vis spectra of a) **1** and b) **2** solutions (5×10^{-6} M, in black) and after addition of up to six equivalents of $Fe(ClO_4)_2$. Color scale with increasing transparency represents increasing amount of $Fe(ClO_4)_2$ in steps of 1 equivalent.

It is worth to note that the wavelength of the MLCT bands is related to the different spin state (HS or LS) of the complex. Indeed, UV-vis spectra of pure LS bpp compounds present MLCT bands centered around λ_{max} = 420 nm (ε_{max} = 4–6 × 10^3 $M^{-1}{\cdot}cm^{-1}$), whereas MLCT bands attributed to HS complexes appear not well-resolved at lower wavelengths.[15] This behavior is consistent with a LS state for **1** and a mixture of LS and HS states in the case of **2** after addition of 6 equivalents of Fe^{2+}. The LS MLCT bands for **1** and bppCOOEt complexes are shifted to higher wavelengths with respect to those of **2** or bppCH$_2$OH complexes, as expected for carboxylic ester derivatives due to enhanced conjugation. The increase of the HS fraction in complex **2** with respect to those of complex **1** is also consistent with that observed in solution for Fe(II)-bpp complexes with similar substituents. Indeed, Evans method indicates that the Fe(II) complex of the hydroxymethyl derivative of bpp is around 90% HS,[16] whereas that of the carboxylic ester derivative is around 50% HS in CD_3CN.[17] Finally, molar extinction coefficient values (ε_{max}) of the MLCT bands for complexes **1** and **2** support a concentration of Fe(II) complexes in the range of that obtained with more simple model compounds assuming that all bpp ligands belonging to **1** and **2** are coordinated (Fig. S23†). The ε_{max} value measured for complex **1** at 460 nm divided by six (due to the six coordinated iron atoms) is ~5800 $M^{-1}{\cdot}cm^{-1}$, which is consistent with that registered for other pure LS Fe(II)-bpp complexes in solution (5600 $M^{-1}{\cdot}cm^{-1}$).[18] Otherwise, the ε_{max} values recorded for complex **2** at 385 and 420 nm (around 15000 M^{-1} cm^{-1} in both cases) in comparison with ε_{max} values reported in the literature for pure LS and HS complexes is indicative of a ~75% HS.[17] The presence of polynuclear species of **1** and **2** coordinated to Fe^{2+} is also confirmed by mass spectroscopy of the precipitates obtained in acetonitrile solutions with an excess of Fe^{2+} (see 5.1 section in the ESI†). Theoretical calculations (see below) indicate that the intramolecular complexation of Fe(II) is favored in in both **1** and **2** with respect to an intermolecular complex formation.

These calculations and the similar spectroscopic titrations of **1** and **2** together with the absence of precipitates and the solubility in MeCN, mentioned above, support the presence of discrete polynuclear species rather than oligomeric or polymeric ones formed by coordination to Fe(II) by bpp ligands from different molecules.

To get more insight into the optical properties of the Fe(II) complexes formed by **1** and **2** in solution, fluorescence measurements were carried out by using the same solutions and by excitation at the isosbestic points (320 nm for **1** and 285 nm for **2**). Luminescence of hexa-adducts **1** and **2** in CH_2Cl_2 showed broad emission bands (Fig. 3) with maxima at 380 nm (**1**) and 345 nm (**2**), which are similar to those shown by the bpp ligand (335 nm in DMF),[19] bppCOOEt (370 nm in CH_2Cl_2) and bppCH_2OH (340 nm in CH_2Cl_2) (Fig. S24†). These bands correspond to ligand fluorescence as confirmed by a small Stokes shift and a short excited-state lifetime (see Fig. S25†).[20] Ligand luminescence is completely quenched after addition of 6 equivalents of Fe^{2+}, confirming the 6:1 metal:ligand ratio for **1** and **2** (Fig. 3). This complete quenching is maintained after correcting inner-filter effects taking into account that a small part of the emitted light from the ligand is re-absorbed by the complex, especially in the case of **2** (Fig. S26†).[21] Interestingly, this process was found to be reversible and the emission of **1** was recovered after adding 1,10-phenantroline (phen), which is a well-known bidentate ligand, leading to $[Fe(phen)_3]^{2+}$ (Fig. S27†). A similar behavior was observed in UV-vis and fluorescence spectra with titrations, regardless of using $Fe(ClO_4)_2$ or $Fe(BF_4)_2$ (Fig. S23†). This indicates that the different ion-pair formation with these two anions has an almost negligible effect on the formation and the spin state of the resulting Fe(II) complexes. The fluorescence of the model systems bppCOOEt and bppCH_2OH shows an almost complete quenching of the emission after addition of 1 equivalent of Fe^{2+} (see Fig. S24†). These results confirm that complete coordination of bpp ligands **1** and **2** to Fe^{2+} quenches the emission from bpp, in contrast to what

has been observed for indazolylpyridine ligands.[15] In this context, partial fluorescence quenching of similar derivatives based on the tridentate ligand 2,6-bis(pyrazol-3-yl)pyridine when coordinated to different metals (Co^{2+}, Cu^{2+}, Cd^{2+}, Pb^{2+} and Zn^{2+}) in solution has been reported.[22]

It is worth to note that maximum quenching of the emission bands for **1** and **2** is reached upon addition of the expected six equivalents of Fe^{2+} (Fig. 3). However, in the case of model systems bppCOOEt and bppCH_2OH, at comparable ligand concentrations, a slight excess of Fe^{2+} (0.75 equivalents) is required instead of the expected 0.5 equivalents (Fig. S24†). This observation suggests that confinement of six Fe(II) complexes around the C_{60} hexa-adducts **1** and **2** enhances the affinity of bpp towards Fe^{2+} and decreases the reversibility with respect to that of less confined bppCOOEt or bppCH_2OH ligands.

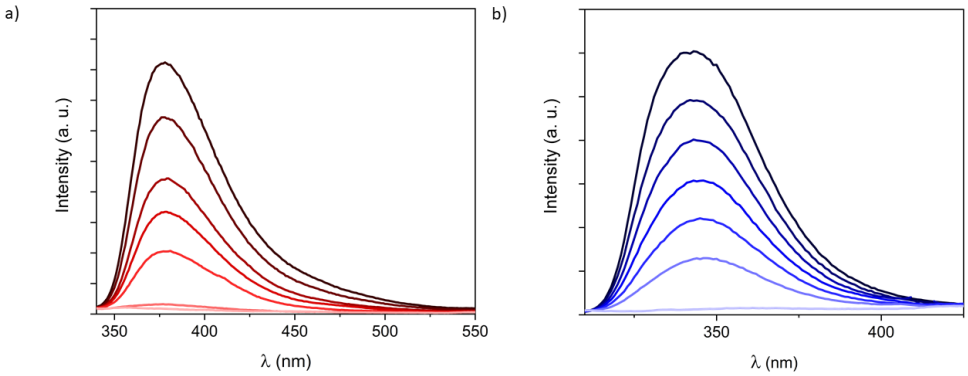

Fig. 3 Fluorescence spectra of a) **1** and b) **2** solutions (5×10^{-6} M, in black) and after addition of up to six equivalents of $Fe(ClO_4)_2$. Color scale with increasing transparency represents increasing amount of $Fe(ClO_4)_2$ in steps of 1 equivalent. Excitation wavelength is 320 nm for **1** and 285 nm for **2**.

The methylated derivative **3** shows an optical behavior upon addition of Fe^{2+}, both in the UV-Vis and emission spectra, very similar to **1**, confirming that the methyl substituent attached to the pyrazolyl rings also favors the LS state (see Fig. S28†).[16,17] The absorption and emission spectra of the monoadduct **4**, which presents only one

malonate branch and two bpp ligands, show a more complex behavior (Fig. S29 and S30†). Due to the smaller number of bpp ligands, the absorption bands in the UV-vis spectrum at 260 (shoulder), 330 and 426 nm (shoulder), characteristic of [60]fullerene mono-adducts,[8,9] are more clearly distinguished than in **1**. After addition of Fe^{2+}, a MLCT band centered at 460 nm is observed, suggesting a LS state, similar to that observed for **1**. Maximum absorbance of the MLCT band is reached after addition of around 1.5 and 0.75 Fe^{2+} equivalents for 1.5×10^{-5} and 4.5×10^{-5} M solutions, respectively (Fig. S29 and S30†), instead of the expected 1 Fe^{2+} equivalent. The emission spectrum of the ligand presents a shoulder at lower wavelengths and is not completely quenched after addition of an excess of Fe^{2+} for the more diluted solution. This suggests a different behavior to that of the hexakis-adducts **1**, **2** and **3**, which could be due to the formation of mixtures of intramolecular and intermolecular complexes. Indeed, theoretical calculations suggest that intramolecular Fe(II) complexes with two bpp ligands from the same malonate branch —the only ones which could be formed in **4**— would present a very distorted geometry (see below).

In an attempt to detect the spin crossover behavior in solution, variable-temperature UV-vis spectra in the range 298 to 283 K of a 7.5×10^{-6} M solution of **2** with six equivalents of Fe^{2+} were recorded. We choose this compound since is the one with the highest fraction of HS Fe(II) at room temperature. A slight increase in the relative intensity of the band with maximum at 420 nm with respect to the shoulder at 385 nm is observed when the temperature is decreased from 298 to 283 K (Fig. S32†). This is consistent with an increase of the LS fraction at decreasing temperature, which is a clear evidence of a spin transition in solution. Still, lower temperatures should be required to complete this preliminary study. Note that ^1H NMR measurements (Evans method) could not be used to evaluate the HS/LS fractions in solution due to the low concentrations available in CH_2Cl_2 of these species. DOSY and Evans NMR experiments require

higher concentrations, typically 1 mM (i.e., a hundred times higher than the available concentration).

Density functional theory (DFT) studies

Theoretical calculations have been performed in a multi-level approach to shed light into the complexation and electronic properties of the Fe(II)-based complexes. First, several Fe(II) environments were modelled using a mono- or a di-malonate derivative bearing short bppCOOR arms as in ligands **1** and **4,** or long bppCH_2OR arms as in **2**. The situations modelled include complex formation between the two bpp arms of a malonate branch (A), between bpp arms of two malonate branches (B) and between bpp arms of vicinal C_{60} molecules (C) (Fig. 4a and S33†). Note that configuration B cannot occur in the mono-branched adduct **4**. Complexes of hexa-adducts **1** and **2** were also calculated, and their structures are displayed in Fig. 4b. All the structures were fully optimized at the cost-effective GFN2-xTB level of theory including representative BF_4^- counterions for electroneutrality. Binding energies for complex formation were calculated at the same theory level (see the ESI for full computational details†) and are summarized in Table 1. Theoretical calculations indicate that the alkyl chain in bppCOOR ligands is too short to efficiently coordinate to Fe^{2+} within a unique malonate branch (A), as evidenced by a faulty octahedral coordination (Fig. S33 and S34a†) and a predicted binding energy (ΔE_{bind}) as small as –7.53 kcal mol^{-1} (Table 1). However, iron complexation by bppCOOR ligands of two branches (B) is relatively more effective (ΔE_{bind} = –15.39 kcal·mol^{-1}), approaching the stability of the lowest-energy configuration C (intermolecular complexation), which is predicted with a ΔE_{bind} = –19.59 kcal·mol^{-1}. The significantly lower stability predicted for the complexation involving the two arms of the same malonate branch supports the incomplete Fe(II) complexation experimentally recorded for mono-adduct **4**.

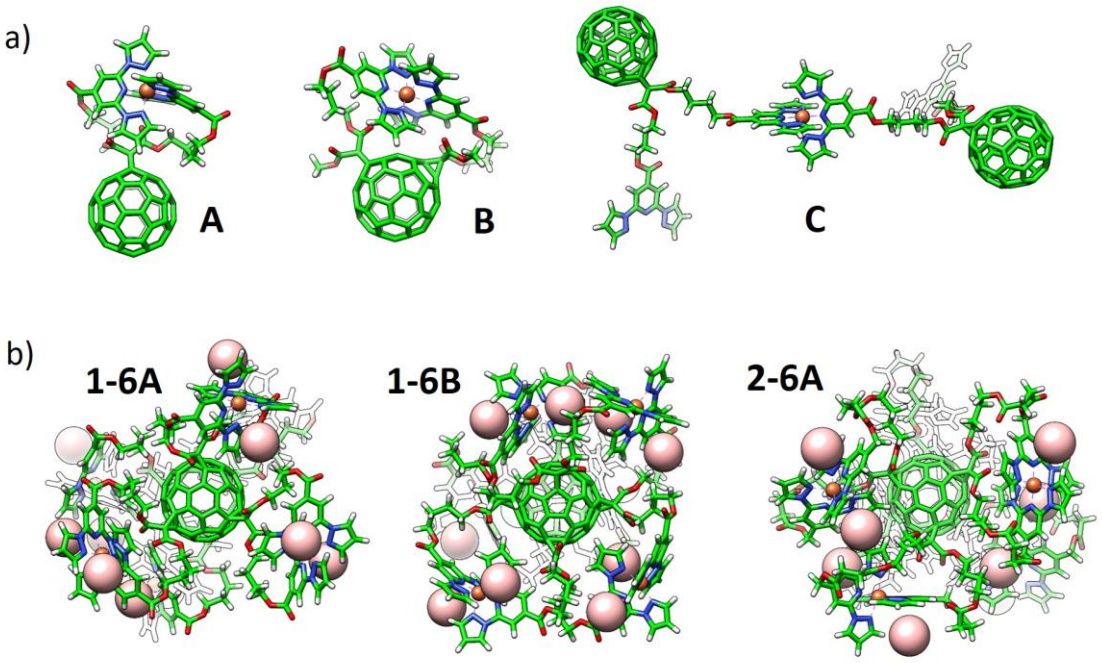

Fig. 4 Minimum-energy geometry calculated for a) representative configurations A, B and C of Fe(II)-complexes with bppCOOR ligands, and b) hexakis Fe(II)-complexes of hexa-adducts **1** (**1**-6A and **1**-6B) and **2** (**2**-6A). BF_4^- counterions are omitted in a) for clarity (see Fig. S33†), and are represented with light pink spheres in b).

On the other hand, the longer chains of the bppCH_2OR arms present in **2** provide enough ligand flexibility for an efficient octahedral complexation (Fig. S33 and S34b†), showing very similar ΔE_{bind} values for configurations A and B (*ca.* –40 kcal·mol^{-1}; see Table 1). In this case, complexation between different molecules (C, –23.48 kcal·mol^{-1}) is significantly unfavoured compared to intramolecular complexation due to the absence of intra-ligand noncovalent interactions (Fig. S33†).

Fe(II) complexes of hexa-adducts **1** and **2** bearing short-chain bppCOOR and long-chain bppCH_2OR ligands, respectively, were also modelled, and their minimum-energy optimized geometries are shown in Fig. 4b. For **1**, intra-branch (**1**-6A) and inter-branch (**1**-6B)

complexations were considered. Theoretical calculations indicate that configuration A is unlikely to be formed for hexakis metallofullerene complexes of **1** because a low total binding energy of only –14.61 kcal·mol^{-1} (–2.44 kcal mol^{-1} per complex formation) is predicted. In contrast, complexation between bpp ligands on different malonate branches (B) is more stable, with a ΔE_{bind} per complex of –11.35 kcal·mol^{-1} (slightly lower than that calculated for the monoadduct, –15.39 kcal·mol^{-1}). The long malonate chains of bppCH$_2$OR in **2** allow a significantly more efficient complexation within the six branches, and the hexakis complex is predicted with a very large binding energy of –178.91 kcal·mol^{-1} (–29.81 kcal·mol^{-1} per complex). Note that in all optimized structures, the BF_4^- counterions remain close to the iron complex to compensate its +2 charge (Fig. 4b and S33†).

Table 1 Binding energies (in kcal·mol^{-1}) calculated for different bppCOOR and bppCH$_2$OR structures including Fe(II)-complexation within a malonate branch (A), between different branches (B), between different molecules (C), and for hexa-adducts **1** (6A and 6B) and **2** (6B).

Structure	Ligand bppCOOR	Ligand bppCH$_2$OR
A	–7.53	–42.95
B	–15.39	–38.63
C	–19.59	–23.48
6A	–14.61	–178.91
6B	–68.08	-

Electronic structure calculations were performed on model Fe(II) complexes bearing bpp (**C0**), bppCOOEt (**C1**) and bppCH$_2$OCOCH$_3$ (**C2**) ligands (see Fig. S35†). The geometry and stability of LS vs HS

configurations is assessed by using the density functional theory (DFT) framework at the B3LYP/def2-SVP/LANL2DZ(Fe) level. The minimum-energy structures computed for low and high-spin states of complexes **C0**-**2** are displayed in Fig. S36†, and show coordination distances of around 0.2 Å longer in the case of the HS configuration, as expected. Theoretical calculations predict a very small energy difference between the two spin states (< 0.07 eV) for all the complexes, being the LS configuration slightly more stable than the HS upon inclusion of solvent effects (Table S1†). Calculations indicate that the HS state is closer in energy to the LS state for the bppCH$_2$OR-based complex **C2** than for **C1** bearing the bppCOOEt ligand by *ca.* 0.02 eV. This nicely supports the experimental observation of a higher percentage of HS in the Fe(II) complex of **2** compared to **1**.

Theoretical absorption spectra were calculated for the simplified complexes **C1** and **C2** and their respective bppCOOEt (**L1**) and bppCH$_2$OCOCH$_3$ (**L2**) ligands to fully assign the experimental UV-Vis bands recorded for the hexa-adducts **1** and **2**, and the absorption changes upon Fe(II) complexation. The lowest-lying electronic excited states of **L1**/**L2** and **C1**/**C2** (Fig. S35†) were computed at the B3LYP*/def2-SVP/LANL2DZ(Fe) level, and the simulated absorption spectra are displayed in Fig. 5a and S37†, respectively (see the ESI for computational details†). The three bands experimentally recorded for **1** at 335, 270 and 245 nm (Fig. 2a) are closely reproduced by the calculations of ligand **L1** with maximum absorption wavelengths at 331, 264 and 248 nm (Fig. 5a), which are described by transitions to the S_1, S_7 and S_{12} singlet excited states, respectively. The lowest-lying state S_1 is predicted with a significant charge-transfer (CT) character, since it implies an electron density transfer from the electron-rich bpp moiety to the electron-withdrawing ester group, whereas S_7 and S_{12} are bpp-centered π–π* states (Fig. S38†). Upon Fe(II) complexation, several low-lying excitations arise above 350 nm for both LS and HS species (Fig. S37a†). Assuming that Fe(II) is in the LS configuration, as experimentally suggested, the titration simulation

of **L1** to form **C1** predicts the appearance of a low-energy intense transition at 400 nm (Fig. 5b), originating from a MLCT excitation (Fig. S37a and S39†), which can be assigned to the growing band experimentally observed at 460 nm (Fig. 2a). In good agreement with the experimental spectra, the three bands corresponding to the ligand are also calculated for **C1**, with the same nature but small wavelength shifts and oscillator strength differences (Fig. 5b).

Moving to ligand **L2**, theoretical calculations predict intense $S_0 \rightarrow S_1$, S_2 and S_8 excitations at 282, 264 and 245 nm with oscillator strengths (*f*) of 0.217, 0.256 and 0.261, respectively (Fig. 5a). These electronic transitions nicely correlate with the experimental bands of derivative **2** recorded at 306, 270 and 245 nm (Fig. 2b). In this case, S_1 presents a π–π* character with negligible CT character due to the low electron activity of the attached $-CH_2OR$ group (Fig. S41†). This explains the significant blue-shift of the lowest-lying absorption band predicted and recorded for **2** compared to **1** (Fig. 2). Similar to that described for **L1**, several low-lying excitations are calculated upon Fe(II) complexation (Fig. S37†). Considering a LS:HS ratio of 25:75, the titration simulation of **L2** to form **C2** predict a long and weak absorption between 330 and 430 nm (Fig. 5c), which correlates with the experimental tail recorded above 330 nm for the Fe(II) complex of **2** (Fig. 2b), and is ascribed to mixed metal/ligand (M/L) and MLCT excitations of both LS and HS states (Fig. S37b, S42 and S43†). High-energy absorptions of **L2** are predicted similarly in **C2** (Fig. 5c), with wavelength and intensity differences that match the experimental evolution of the UV-Vis spectrum of **2** upon complexation (Fig. 2b).

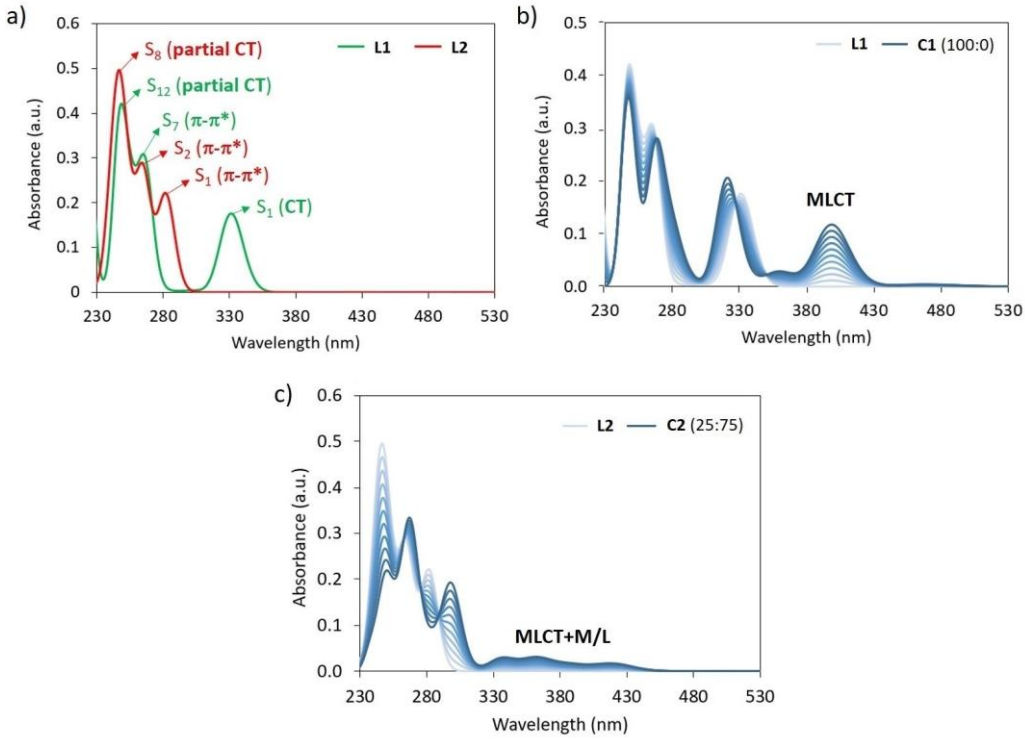

Fig. 5 a) Theoretical absorption spectra calculated for **L1** and **L2** at the B3LYP*/def2-SVP/LANL2DZ(Fe) level including solvent effects. b) and c) Theoretical titration simulations of the absorption spectrum of **L1** and **L2** upon Fe(II) complexation considering a ratio of 100:0 LS:HS for **C1**, and of 25:75 LS:HS for **C2**.

The origin of the emission quenching upon complexation has also been analyzed by means of quantum chemical calculations. The relative energy position of the ground state and the lowest-lying singlet (S_1) and triplet (T_1) excited states was calculated at the time-dependent TD-(U)B3LYP*/def2-SVP/LANL2DZ(Fe) level for isolated ligands **L0**–**2** and for complexes **C0**–**2** (see the ESI for details†). Theoretical calculations predict a large energy gap between the lowest-lying singlet/triplet excited states and the ground state for ligands **L0**–**L2**, with values between 2.5 and 4.4 eV in all cases (Table S2†). Interestingly, excited-state geometry relaxation allows prediction of the emission fluorescence energy, which is calculated

at 374 (3.32) and 333 nm (3.72 eV) for **L1** and **L2**, respectively, in good accord with the experimental values of 380 and 345 nm for **1** and **2**. Upon Fe(II)-complexation, several singlet and triplet transitions are predicted in the low-energy range. In the LS state, the singlet S_1 state is vertically calculated at ~2.1 eV above the ground state for the three complexes **C0**–**2**, whereas the triplet T_1 is computed at ~1.0 eV (Table S2†). Excited-state relaxation from the Frank-Condon geometry leads to an energy difference of ~1.5 eV between S_0 and S_1 at the S_1 minimum-energy geometry, whereas T_1 is computed more stable than S_0 at the T_1 potential well in all complexes (Table S2†). In the HS configuration, the lowest-lying quintuplet excited state Q_1 is at 0.21 eV in the Frank-Condon region, and goes below Q_0 upon excited-state geometry relaxation (Q_0-Q_1 energy crossing). Theoretical calculations therefore predict that complexes **C0**–**2** present low-lying excited states (triplet for LS and quintuplet for HS) that enhance non-radiative relaxation paths and quench photoluminescence processes.

Studies in the solid state

The Fe(II) complexes of **1** and **2**, hereafter named **5** and **6**, respectively, were isolated in the solid state by fast precipitation after addition of diethyl ether to the CH_3CN/CH_2Cl_2 (~7.5/1 ratio) solutions containing **1** or **2** (6.4×10^{-4} M) and 12 equivalents of Fe^{2+} to achieve a complete coordination. Amorphous materials were obtained in both cases, which were characterized by elemental analysis, infrared (IR) and X-ray photoelectron spectroscopy (XPS) and thermogravimetric analysis (TGA) (see Fig. S44 to S47 and section 5.1 in the ESI†). These techniques support the presence of six iron per fullerene unit in the solid state samples. Attempts to obtain crystalline materials by slowing precipitation were unsuccessful. Similar results were obtained using 6 equivalents of Fe^{2+}.

The electrospray ionization mass spectrometry (ESI-MS) of **5** (obtained from the $Fe(ClO_4)_2$ salt) and **6** (obtained from the $Fe(BF_4)_2$

salt) were performed by dissolving these solids in a mixture of dimethylformamide and methanol or CH_3CN. The spectra showed the presence of several species with one molecule of **1** or **2** and a variable number of Fe^{2+} ions (from one to six) plus counteranions (see section 5.1 †). Although this technique does not give an exact view of the composition of the precipitate since it requires re-dissolution and measurement conditions in which the compound could decompose, the presence of fragments with m/z values corresponding to **1** and **2** plus six Fe^{2+} suggests that the hexanuclear species are present in the solid samples.

Magnetic measurements of **5** and **6** were performed on these solid samples isolated by centrifugation after successive washings with diethyl ether and protected with a small amount of clean diethyl ether or embedded in a grease to keep them solvated, since the magnetic properties of this type of compounds are very sensitive to the presence of solvent molecules.[2] Both protection methods gave similar results. In the solvated sample of **5** the LS state is favored, in agreement with the solution data (see above). Thus, magnetic molar susceptibility times temperature ($\chi_M T$) values are close to zero in the temperature range 5–230 K. At higher temperatures, a gradual increase to reach a value of 8.7 emu·K·mol^{-1} at 300 K is observed, which corresponds to a SCO from LS to HS of around 40% of Fe(II) (Fig. 6a) (see section 5.2 in the ESI for calculation details†). The solvated sample of **6** shows an almost constant $\chi_M T$ value close to 9.5 emu K mol^{-1} from 50 to 190 K (~45% of HS fraction) with a gradual increase to reach 22.0 emu·K·mol^{-1} (~100% HS fraction) above 285 K (Fig. 6b). This observation is also in agreement with the results in solution, which indicate that for complexes of **2** the fraction of HS Fe(II) at room temperature is higher than for complexes of **1**. Notice

that these gradual thermal spin transitions are typical of SCO complexes showing long intermolecular distances and weak intermolecular interactions. Interestingly, the polynuclear nature of our complexes force the metal centers to be in close proximity, thus leading to SCO transitions that are much sharper and more complete (~40 % of Fe(II) centers in **5** upon heating the sample from 230 to 290 K and ~55 % of Fe(II) centers in **6** upon heating the sample from 200 to 280 K) than that observed in the mononuclear Fe(II) complex having fullerenes as end-capping groups This last compound shows a very gradual and incomplete spin transition, which extends over a wide temperature range (from 100 to 400 K) in the temperature ranges in which the spin switching occurs in **5** and **6** that corresponds to a spin-crossover of a ~15 %.[9]

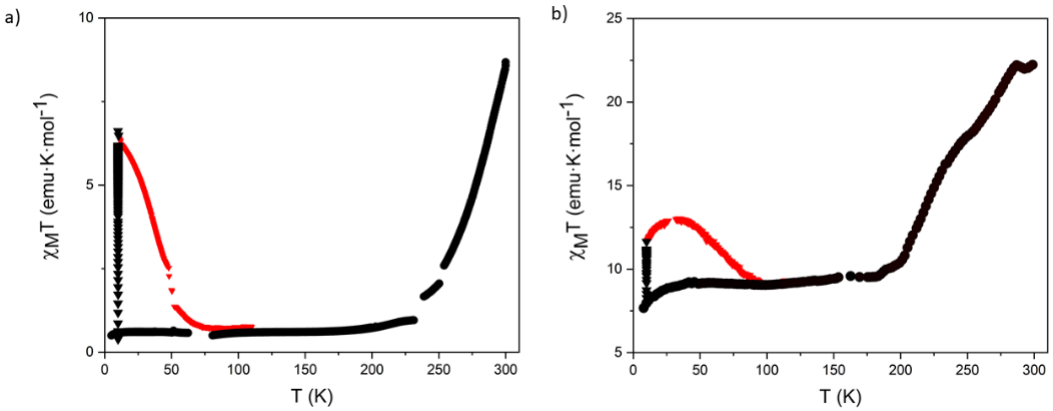

Fig. 6 Temperature dependence of $\chi_M T$ of **5** (a) and **6** (b) measured with a protective layer of clean diethyl ether or a grease to avoid the loss of solvent before (black circles), during (black triangles) and after (red triangles) irradiation with red light at 10 K.

Magnetic measurements after irradiation with red light at 10 K were carried out on solvated samples embedded in a grease. Irradiation with a 633 nm laser at 10 K leads to a drastic increase of the magnetic signal reaching saturation after ca. 1 h. Therefore, both samples exhibit LIESST effect. After switching off the irradiation, the

temperature was increased at a scan rate of 0.3 K·min^{-1} (see Fig. 6). The maximum χ_MT value after irradiation in **5** (6.5 emu·K·mol^{-1}) corresponds approximately to a photo-induced LS to HS transition of two of the six LS Fe(II) centers (Fig. 6).

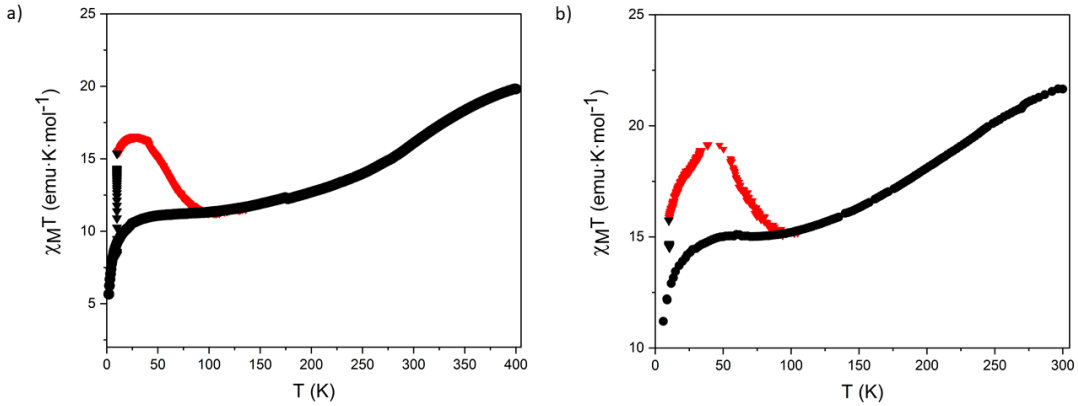

Fig. 7 Temperature dependence of χ_MT of filtered samples of **5** (a) and **6** (b) before (black circles), during (black triangles) and after (red triangles) irradiation with red light at 10 K**.**

Finally, these magnetic and photomagnetic effects were observed to be less pronounced in the same samples of **5** and **6** measured without protecting them with the washing solvent (diethyl ether) or grease to avoid the loss of solvent molecules. These desolvated samples showed higher HS fractions at low temperatures than the solvated ones (see section 5.6 in the ESI and Fig. 7). These differences are frequent in the solvates of $[Fe(bpp)_2]^{2+}$ complexes and their derivatives. In fact, very often, partial or complete desolvation of SCO compounds causes the loss of the spin transition. The use of a solvent or grease covering layer is then a typical procedure to protect the sample,[24] avoiding this undesired process. Indeed, elemental analyses of **5** and **6** in contact with air are consistent with the presence of water molecules (see section 5.6 in the ESI†). This indicates that the volatile solvent molecules that could be found in the structure of **5** and **6** (dichloromethane, acetonitrile

or diethyl ether) are lost and replaced by water molecules from air upon filtering.

Raman μ-spectroscopy also confirmed the incomplete thermal SCO in desolvated samples of **5** and **6** (Fig. S48†). Focusing on the pyridine vibration located in the range of 1000–1100 cm^{-1}, we observed that at 298 K the most intense peak for the two samples appears at ~1015 cm^{-1} accompanied by a low intense peak at ~1040 cm^{-1} for **5**. At 88 K, the relative intensity of this peak increases for **5**, and a new peak at the same position (~1040 cm^{-1}) appears in the spectrum of **6**. Interestingly, the initial spectrum of **6** is recovered after heating again at 298 K confirming the reversibility of the SCO process. The changes in intensity of the peaks at 1040 cm^{-1} (LS) and 1012 cm^{-1} (HS) are in agreement with those observed for $[Fe^{II}(bpp)_2]^{2+}$ complexes in the literature.[23] This suggests that the coordination environment of Fe(II) is very similar in **5** and **6** and close to that encountered for Fe(II) bpp complexes. In addition, the changes in intensity are consistent with the magnetic properties that indicate that the HS fraction decreases from 80 to 50 % in **5** and from 100 to 70 % in **6** in the same range of temperatures (see section 5.6 in the ESI and Fig. S49†)**.** On the other hand, Raman spectrum of **1** was also recorded for comparative purposes (Fig. S49†)**.** The Raman spectra were also theoretically simulated and confirm the assignment of the Raman-active vibrational modes that allow differentiation between HS vs LS configurations (see section 5.7 in the ESI and Fig. S50†).

Conclusions

In this work, we have designed and synthesized different hexakis-substituted [60]fullerene adducts of the well-known bpp ligand. Spectroscopic characterization in solution and theoretical calculations have demonstrated that they are able to form polynuclear spin-crossover Fe(II) complexes. The variety of behaviors exhibited by the different fullerene adducts indicates that the spin state of Fe(II) in these species can be tuned by a proper choice of the

bpp substituents. Indeed, some of these polynuclear complexes show SCO properties induced by temperature and light as external stimuli, with spin transitions that, although gradual, are much sharper than those reported in mononuclear complexes based on fullerene. These results demonstrate that [60]fullerene hexa-adducts are excellent and versatile platforms to develop new spin-switching materials.

In these magnetic molecules, [60]fullerene has been used as a molecular carbon substrate on which 12 peripheral tridentate ligands have been covalently connected through the use of flexible spacers adopting a well-defined 3D spatial arrangement and allowing to organize up to six $[Fe(bpp)_2]^{2+}$ SCO complexes on this substrate. This hybrid nanostructure can provide an ideal molecular platform to investigate hybrid nanostructures formed by SCO complexes anchored on flat 2D substrates such as gold or HOPG. In fact, the preparation of SAMs based on monolayers of these SCO $[Fe(bpp)_2]^{2+}$ complexes has so far been elusive. The various attempts have failed owing to the lability of these Fe(II) complexes,[4] a problem that could be overcome using the ligands developed in the present work as they can be designed so as to exhibit much higher binding energies than those reported in the parent $Fe(bpp)_2]^{2+}$complex.

Finally, in this work we have demonstrated the incorporation of multiple bpp ligands to a central fullerene scaffold. This feature opens the possibility to process these systems from solution, something that was not possible to achieve when [60]fullerene is functionalized with one bpp ligand.[8,9] The resulting polynuclear SCO molecules, conveniently protected to avoid a loss of solvent, may be of interest in molecular spintronics since a modulation of their spin properties by electrical or light stimuli may be possible, as it has recently been demonstrated for single SCO molecules[5] and nanoparticles.[25]

Conflicts of interest

There are no conflicts to declare.

Acknowledgements

Financial support from the EU (ERC Advanced Grant MOL-2D 788222, FET-OPEN COSMICS 766726 and COST action MOLSPIN CA15128), the Spanish MCIU (MAT-2017-89993-R, PGC2018-099568-B-I00 and Unidad de Excelencia María de Maeztu CEX2019-000919-M), the Spanish MINECO (CTQ2017-84327-P, CTQ2017-83531-R), the Generalitat Valenciana (PROMETEO program and iDiFEDER/2018/061) and the Ministry of Education and Science of Russian Federation (Agreement No.14.W03.31.0001) is gratefully acknowledged. We thank J. M. Martínez-Agudo and G. Agustí for magnetic measurements and Prof. M.A. Halcrow for helpful discussions.

Notes and references

[1] See for general reviews: *(a)* Eds. P. Gütlich and H.A. Goodwin, Spin Crossover in Transition Metal Compounds, *Topics in Current Chemistry*, Springer Verlag, Berlin-Heidelberg-New York, 2004, vols. *233-235*; *(b)* Ed. M. A. Halcrow, Spin-Crossover Materials: Properties and Applications, John Wiley & Sons, Chichester, UK, 2013.

[2] *(a)* M. A. Halcrow, *Coord. Chem. Rev.*, 2005, **249**, 2880-2908; *(b)* M. A. Halcrow, *Coord. Chem. Rev.*, 2009, **253,** 2493-2514; *(c)* J. Olguín and S. Brooker, *Coord. Chem. Rev.*, 2011, **255**, 203-240; *(d)* M. A. Halcrow, *New J. Chem.*, 2014, **38,** 1868-1882; *(e)* L. J. Kershaw Cook, R. Mohammed, G. Sherborne, T. D. Roberts, S. Alvarez and M. A. Halcrow, *Coord. Chem. Rev.*, 2015, **289-290**, 2-12.

[3] (a) R. Torres-Cavanillas, R. Sanchis-Gual, J. Dugay, M. Coronado-Puchau, M. Giménez-Marqués and E. Coronado,

Adv. Mater., 2019, 31, 190039; (b) A. Enriquez-Cabrera, A. Rapakousiou, M. Piedrahita Bello, G. Molnár, L. Salmon and A. Bousseksou, Coord. Chem. Rev., 2020, 419, 213396; (c) E. Coronado, Nat. Rev. Mater. 2020, 5, 87.],

[4] (a) L. Pukenas, F. Benn, E. Lovell, A. Santoro, L. J. Kershaw Cook, M. A. Halcrow and S. D. Evans, *J. Mater. Chem. C,* 2015, **3**, 7890-7896; (b) V. García-López, M. Palacios-Corella, V. Gironés-Pérez, C. Bartual-Murgui, J. A. Real, E. Pellegrin, J. Herrero-Martín, G. Aromí, M. Clemente-León and E. Coronado, *Inorg. Chem.*, 2019, **58**, 12199−12208.

[5] (a) T. G. Gopakumar, F. Matino, H. Naggert, A. Bannwarth, F. Tuczek, R. Berndt, Angew. Chem. Int. Ed. 2012, 51,6262-6266; (b) E. J. Devid, P. N. Martinho, M. V. Kamalakar, I. Salitros, Ú. Prendergast, J. F. Dayen, V. Meded, T.Lemma, R. González-Prieto, F. Evers, T. E. Keyes, M. Ruben, B. Doudin and S. Jan van der Molen, ACS Nano, 2015, 9, 4496-4507K; (c) Bairagi, O. Iasco, A. Bellec, A. Kartsev, D. Li, J. Lagoute, C. Chacon, Y. Girard, S. Rousset, F. Miserque, Y. J. Dappe, A. Smogunov, C. Barreteau, M. L. Boillot, T. Mallah and V. Repain, Nat Commun 2016, 7, 12212.

[6] *(a)* H. W. Kroto, J. R. Heath, S. C. O'Brien, R. F. Curl and R. E. Smalley, *Nature,* 1985, **318**, 162–163; *(b)* F. Giacalone and N. Martín, *Chem. Rev.,* 2006, **106**, 5136–5190; *(c)* N. Martín, *Chem. Commun.,* 2006, **2006**, 2093–2104); *(d)* B. M. Illescas, J. Rojo, R. Delgado and N. Martín, *J. Am. Chem. Soc.,* 2017, **139**, 6018−6025.

[7] W. Yan, C. Réthoré, S. Menning, G. Brenner-Weiß, T. Muller, P. Pierrat and S. Bräse, *Chem. Eur. J.,* 2016, **22**, 11522–11526.

[8] E. Nuin, W. Bauer and A. Hirsch, *Eur. J. Org. Chem.,* 2017, **2017**, 790-798.

[9] K. Senthil Kumar, I. Salitros, N. Suryadevara, E. Moreno-Pineda and M. Ruben, *Eur. J. Inorg. Chem.,* 2018, **2018**, 5091-5097.

[10] W. K. Hang, H. X. Zhang, Y. Wang, W. Liu, X. Yan, T. Li and Z. G. Gu, *Chem. Commun.,* 2018, **54**, 12646-12649.

[11] *(a)* **J.** Ramos-Soriano, J. J. Reina, A. Pérez-Sánchez, B. Illescas, J. Rojo and N. Martín, *Chem. Commun.,* 2016, **52**, 10544-10546; *(b)* A. Muñoz, D. Sigwalt, B. M. Illescas, J. Luczkowiak, L. Rodríguez-Pérez, I. Nierengarten, M. Holler, J. S. Remy, K. Buffet, S. P. Vincent, J. Rojo, R. Delgado, J. F. Nierengarten and N. Martín, *Nat. Chem.,* 2016, **8**, 50-57; *(c)* J.-F. Nierengarten, *Chem. Commun.,* 2017, **53**, 11855-11868; *(d)* J. Ramos-Soriano, J. J. Reina, B. M. Illescas, J. Rojo, N. Martín, *J. Org. Chem.*, 2018, **83**, 1727−1736; *(e)* J. Ramos-Soriano, J. J. Reina, B. M. Illescas, N. de la Cruz, L. Rodríguez-Pérez, F. Lasala, J. Rojo, R. Delgado and N. Martín**,** *J. Am. Chem. Soc.,* 2019, **141**, 15403-15412.

[12] J. M. Holland, J. A. McAllister, C. A. Kilner, M. Thornton-Pett, A. J. Bridgeman and M. A. Halcrow, *J. Chem. Soc. Dalton Trans.*, 2002, **2002**, 548-554.

[13] Y. Hasegawa, K. Takahashi, S. Kume and H. Nishihara, *Chem. Commun.,* 2011, **47**, 6846-6848.

[14] K. Senthil Kumar, I. Salitros, E. Moreno-Pineda and M. Ruben, *Dalton Trans.,* 2017, **46**, 9765-9768.

[15] A. Santoro, L. J. Kershaw Cook, R. Kulmaczewski, S. A. Barrett, O. Cespedes and M. A. Halcrow, *Inorg. Chem.,* 2015, **54**, 682-693.

[16] M. A. Halcrow, I. Capel Berdiell, C. M. Pask and R. Kulmaczewski, *Inorg. Chem.,* 2019, **58**, 9811-9821.

[17] L. J. Kershaw Cook, R. Kulmaczewski, R. Mohammed, S. Dudley, S. A. Barrett, M. A. Little, R. J. Deeth and M. A. Halcrow, *Angew. Chem. Int. Ed.,* 2016, **13**, 4327-4331.

[18] J. M Holland, S. A. Barrett, C. A. Kilner and M. A. Halcrow, *Inorg. Chem. Commun.,* 2002, **5**, 328-332.

[19] Y. Jiao, J. Zhu, Y. Guo, W. He and Z. Guo, *J. Mater. Chem. C,* **2017**, *5*, 5214-5222.

[20] J. M. Stanley, X. Zhu, X. Yang and B. J. Holliday, *Inorg. Chem.,* 2010, **49**, 2035-2037.

[21] A. Credi and L. Prodi, *Spectrochim. Acta Part A,* 1998, **54**, 159-170.

[22] *(a)* Y. Pi, H. Liu and D. J. Wang, *Adv. Mater. Res.,* 2014, **906**, 96-100; *(b)* H. Liu, F. X. Li, Y. Pi, D. J. Wang, Y. J. Hu and J. Zheng*, Spectrochimica Acta Part A: Molecular and Biomolecular Spectroscopy,* 2015, **145**, 588-593.

[23] M. Cavallini, I. Bergenti, S. Milita, J. C. Kengne, D. Gentili, G. Ruani, I. Salitros, V. Meded and M. Ruben, *Langmuir,* 2011, **27**, 4076-4081.

[24] G. Chastanet, C. Desplanches, C. Baldé, P. Rosa, M. Marchivie and P. Guionneau, *Chem. Sq.*, 2018, **2**, 2.

[25] J.Dugay, M. Giménez-Marqués, T. Kozlova, H. W. Zandbergen, E. Coronado and H. S. van der Zant, *Adv. Mater.,* 2015*,* **27***,* 1288-1293*.*

Supporting Information: Hexakis-Adducts of [60]Fullerene as Molecular Scaffolds of Polynuclear Spin-Crossover Molecules

Table of contents

1. General methods for synthesis and characterization

Reagents and solvents were purchased as reagent grade and used without further purification. Compounds **P1**,[1] bppCOOH,[2] bppCOOEt (**L1**),[2] bppCH_2OH (**L3**)[3] and **L6**[1] were prepared according to previously reported procedures. Purification was carried out by column chromatography using silica gel 60 (230–400 mesh, 0.040–0.063 mm) purchased from E. Merck or by Sephadex LH20 (GE Healthcare, Barcelona, Spain) gel filtration. Thin layer chromatography (TLC) was performed on aluminium sheets coated with silica gel 60 F_{254} purchased from E. Merck, visualization by UV light. IR spectra (cm^{-1}) were measured on an ATI Mattson Genesis Series FTIR instrument. NMR spectra were recorded on a Bruker AC 300 or AC 500 with solvent peaks as reference. ^1H and ^{13}C NMR spectra were obtained for solutions in $CDCl_3$, CD_3OD and DMSO-d_6. All the assignments were confirmed by one- and two-dimensional NMR experiments (COSY, HSQC and DEPT). Mass spectra were registered on a Bruker BIFLEXTM matrix-assisted laser desorption time-of-flight (MALDI-TOF) mass spectrometer using 2-[(*E*)-3-(4-*tert*-butylphenyl)-2methylprop-2-enylidene]malononitrile (DCTB) as matrix. Electrospray ionization (ESI) mass spectra were recorded with an Esquire 6000 ESI-Ion Trap from Bruker Daltonics using CH2Cl2/MeOH as solvent system. UV-vis absorption spectra were recorded on a Varian Cary 100 Bio spectrometer and emission spectra were recorded on a PTI spectrofluorometer. Luminescence decays were measured using a Compact fluorescence lifetime spectrometer C11367, Quantaurus-Tau. The photolumiscence (PL) lifetime measurement software U11487 was used to register the data. The PL decays were fitted to a biexponential function.

2. Synthesis and characterization of 1, 2, 3 and 4

Synthesis of compound 1.

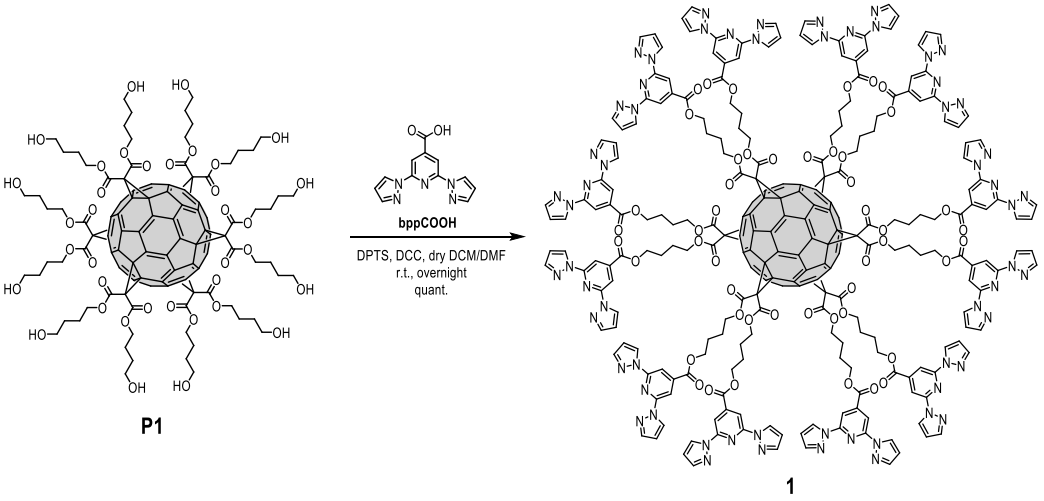

Scheme S1. Schematic representation of the synthesis of **1**

To a solution of **P1** (140 mg, 65.10 μmol), ligand bppCOOH (299 mg, 1.17 mmol) and DPTS (115 mg, 0.39 mmol) in a dry mixture of CH_2Cl_2/DMF (6 mL, 3:1) under Ar atmosphere, and DCC (244 mg, 1.17 mmol) in dry CH_2Cl_2 (1.5 mL) were added. The reaction mixture was stirred at 40 °C overnight. Once the reaction was complete, the dicyclohexylurea was filtered off in a fritted glass filter and washed with CH_2Cl_2. The crude product was purified by size-exclusion chromatography (Sephadex LH-20, MeOH/CH_2Cl_2 1:1), to give **1** (331 mg, quant.) as an orange-red amorphous solid. IR (neat): 3115, 2960, 1731, 1463, 1397, 1239, 1042 cm^{-1}; ^1H NMR (500 MHz, $CDCl_3$) δ/ppm: 8.40 (m, 24H, H-Ar_{pyzl}), 8.19 (m, 24H, H-Ar_{py}), 7.70 (m, 24H, H-Ar_{pyzl}), 6.41 (m, 24H, H-Ar_{pyzl}), 4.37 (m, 48H, OCH_2CH_2CH_2CH_2O), 1.89 (m, 48H, OCH_2CH_2CH_2CH_2O); ^{13}C NMR (125.8 MHz, $CDCl_3$) δ/ppm: 163.7 (CO), 163.6 (CO), 150.5 (C_{ipso}Ar-N), 145.9 ($C_{sp2,fullerene}$), 143.0 (C_{ipso}Ar-CO), 142.7 (CH-Ar_{pyzl}), 141.2 ($C_{sp2,fullerene}$), 127.0 (CH-

Ar_{pyzl}), 108.8 (CH-Ar_{py}), 108.3 (CH-Ar_{pyzl}), 69.2 ($C_{sp3,fullerene}$), 66.4, 65.4 (O*C*H_2CH_2CH_2*C*H_2O), 45.4 ($C_{q,bridge}$), 25.2, 25.1 (OCH_2*C*H_2*C*H_2CH_2CH_2O); MALDI-TOF (DCTB): *m/z* calcd for $C_{270}H_{192}N_{60}O_{48}$: 5044.9; found: 5044.1 $[M]^+$, 5067.2 $[M+Na]^+$, 5083.2 $[M+K]^+$.

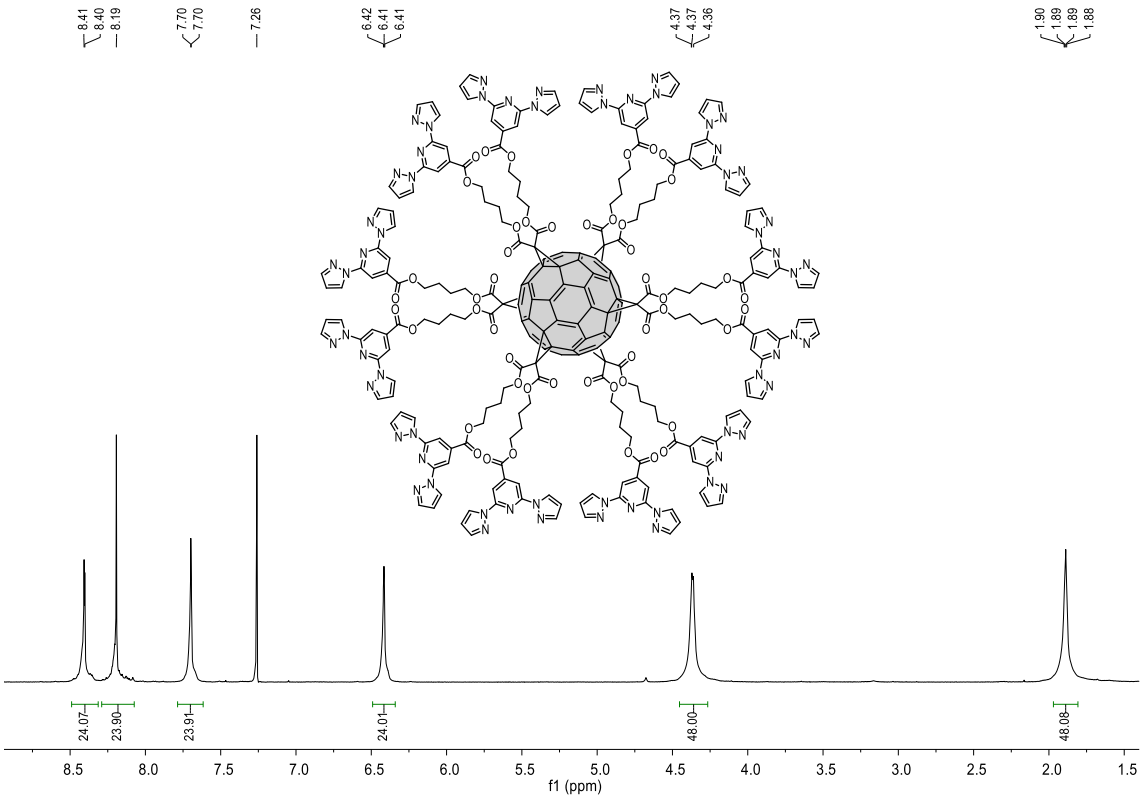

Figure S1. ^{1}H NMR spectrum (500 MHz, $CDCl_3$) of compound **1**

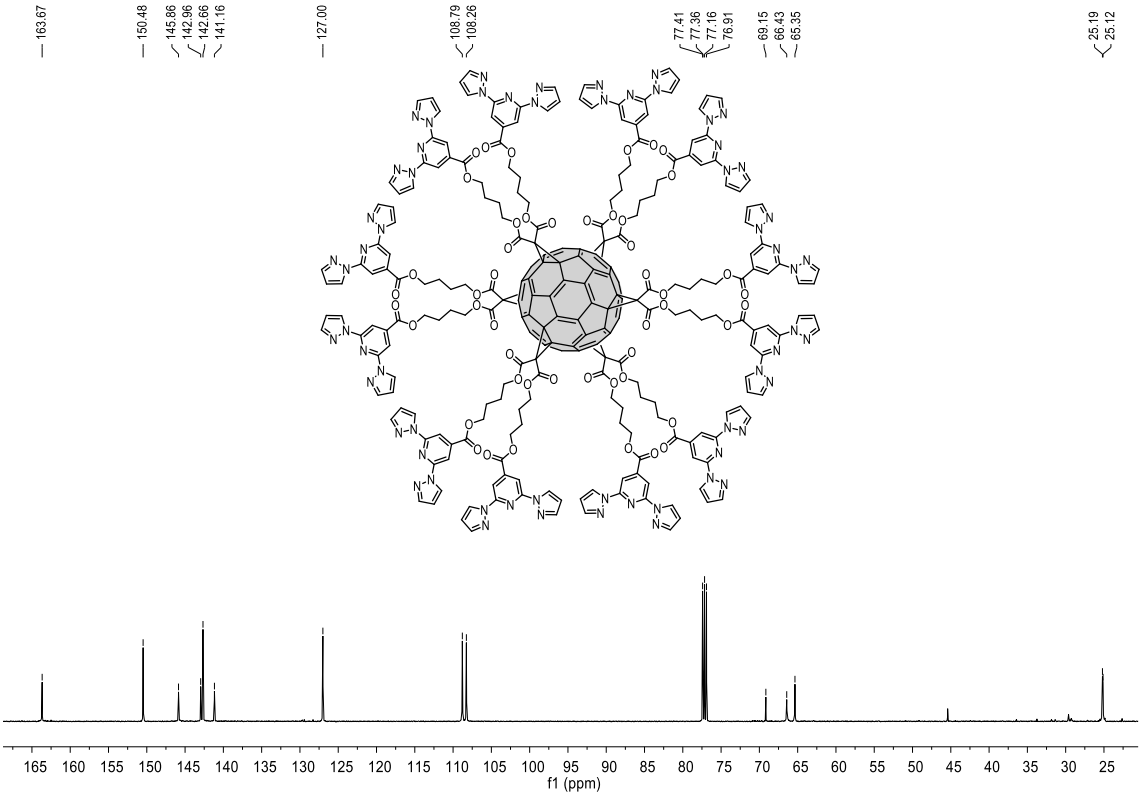

Figure S2. ^{13}C NMR spectrum (125.8 MHz, $CDCl_3$) of compound **1**

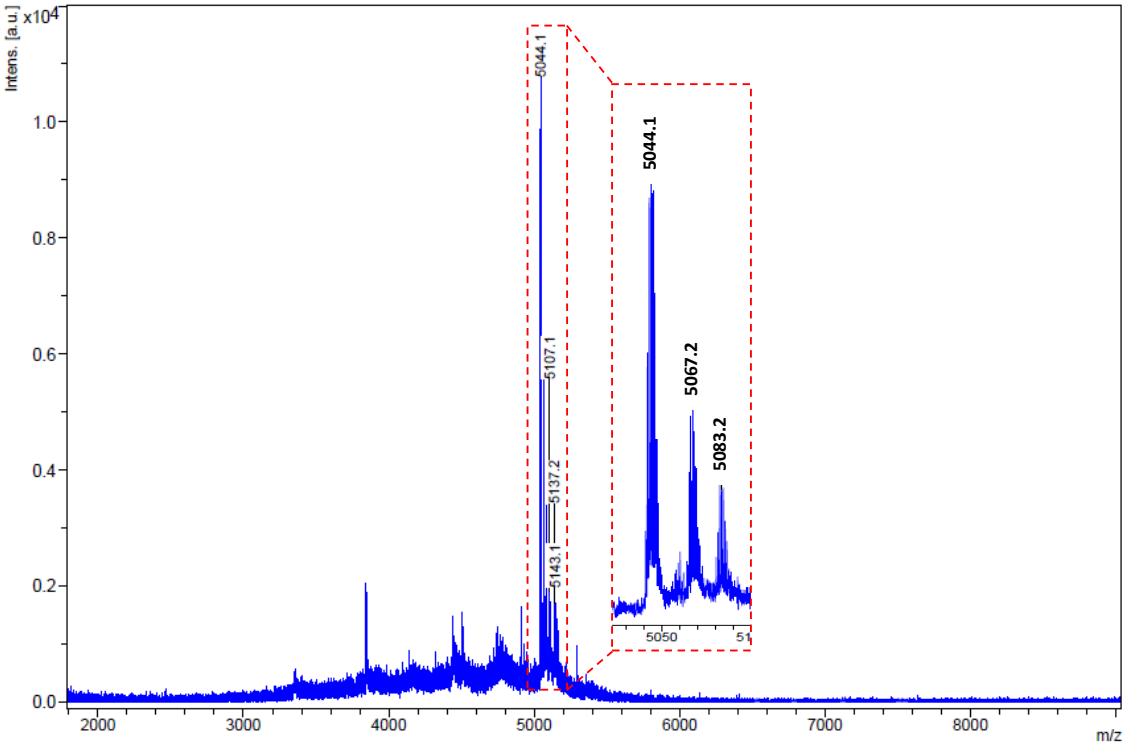

Figure S3. MALDI-TOF spectrum of compound **1**

Synthesis of compound 2.

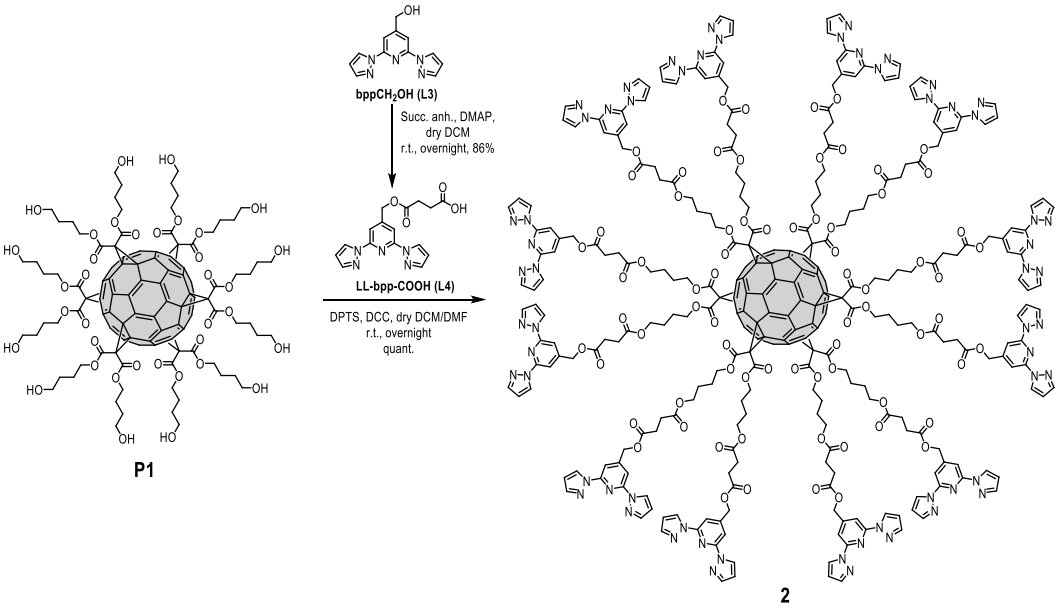

Scheme S2. Schematic representation of the synthesis of **2**

Compound L4

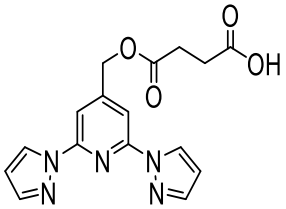

To a solution of bppCH_2OH (**L3)** (300 mg, 1.24 mmol) and succinic anhydride (149 mg, 1.49 mmol) in dry CH_2Cl_2 (8 mL), DMAP (152 mg, 1.24 mmol) was added. The mixture was stirred at room temperature overnight. The solvent was removed under vacuum and Et_2O (10 mL) was added. The resulting solution was washed with 5% Na_2CO_3 (20 mL). The aqueous layer was brought to pH 4 by adding 1 M HCl (20 mL). The resulting aqueous solution was extracted three times with Et_2O. The organic layers were washed with brine, dried over $MgSO_4$, filtered and reduced under vacuum, to give compound **L4** (360 mg, 86%) as a white amorphous solid. ^{1}H NMR (300 MHz, DMSO-d_6) δ/ppm: 12.27 (s, 1H, COOH), 8.95 (d, J = 2.6 Hz, 2H, H-Ar_{pyzl}), 7.88 (m, 2H, H-Ar_{pyzl}), 7.80 (s, 2H, H-Ar_{py}), 6.64 (dd, J = 2.6, 1.6 Hz, 2H, H-Ar_{pyzl}), 5.32 (s, 2H, $CH_{2,Bn}$), 2.67 (m, 2H, $CH_{2,succ.}$), 2.55 (dd, J = 6.9, 2.3 Hz, 2H, $CH_{2,succ.}$); ^{13}C NMR (75 MHz, DMSO-d_6) δ/ppm: 173.3 (CO), 172.0 (CO), 152.2 (C_{ipso}Ar-$CH_{2,Bn}$), 149.8 (C_{ipso}Ar-N), 142.8 (CH-Ar_{pyzl}), 128.2 (CH-Ar_{pyzl}), 108.5 (CH-Ar_{pyzl}), 106.8 (CH-Ar_{py}), 63.9 ($CH_{2,Bn}$), 28.6 ($CH_{2,succ.}$); ESI-HRMS: m/z calcd for $C_{18}H_{17}N_3O_4Na$ [M+Na]+: 364.3168; found: 364.3172.

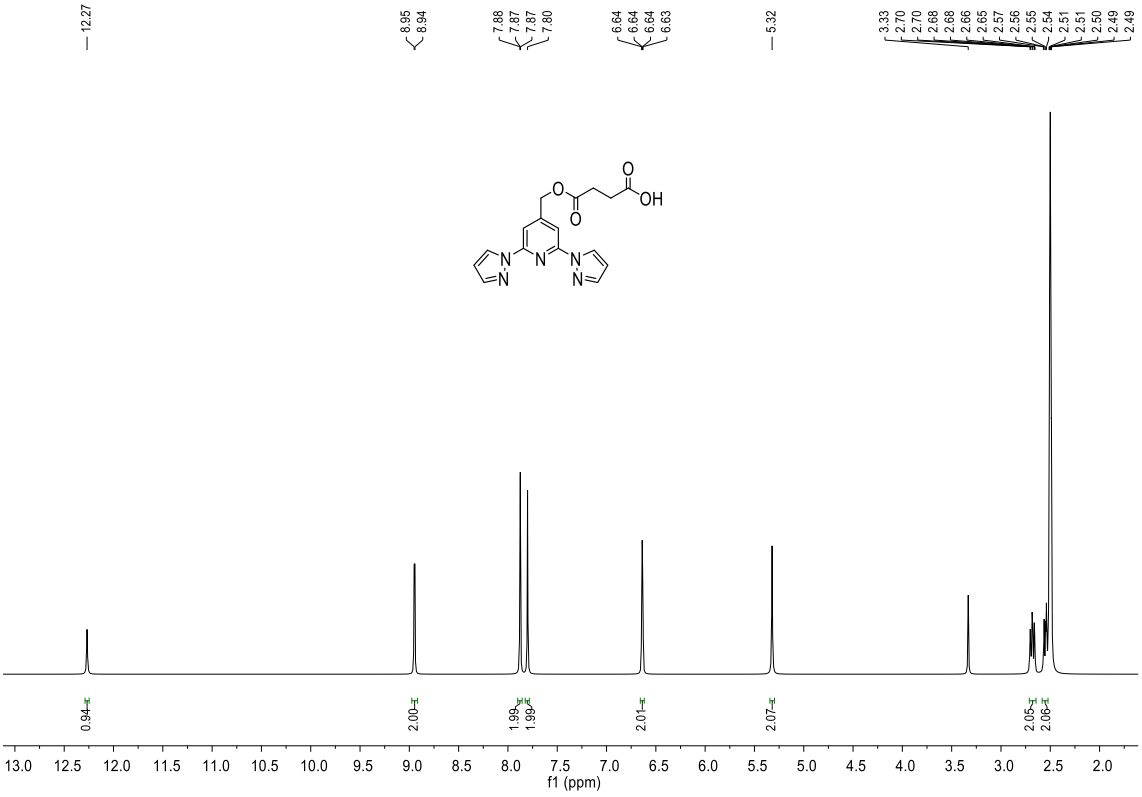

Figure S4. ^{1}H-NMR spectrum (300 MHz, DMSO-d_6) of compound **L4**

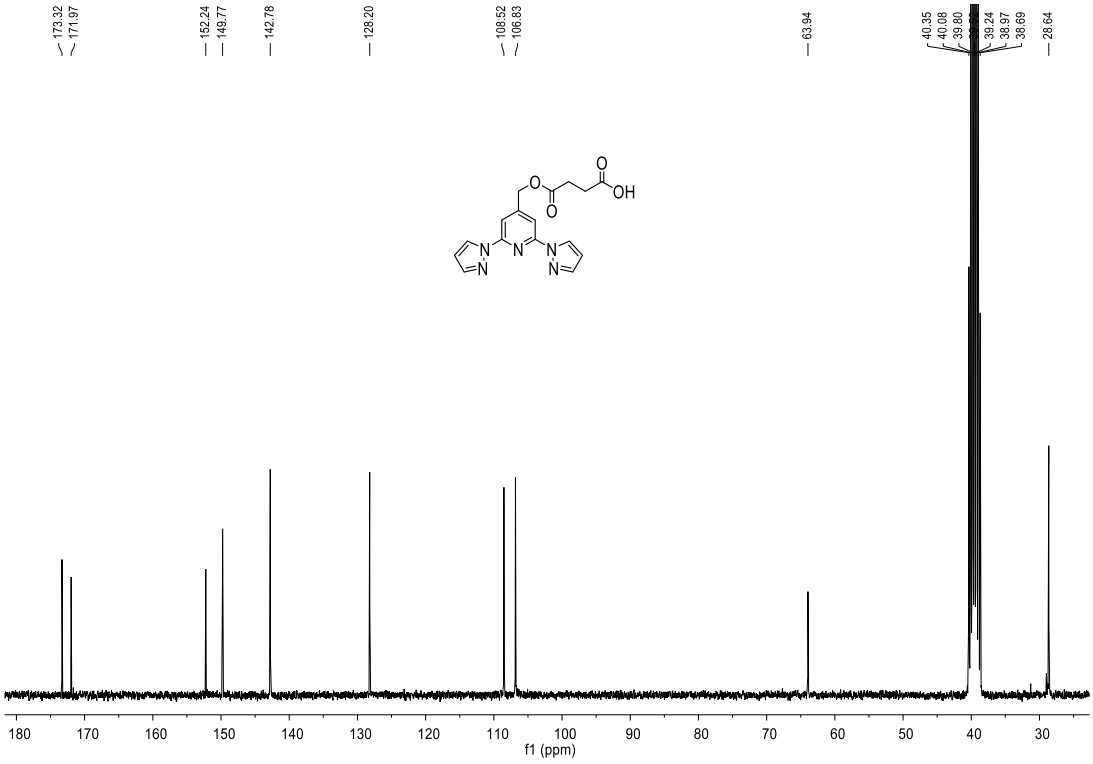

Figure S5. ^{13}C NMR spectrum (75 MHz, DMSO-d_6) of compound **L4**

Compound 2.

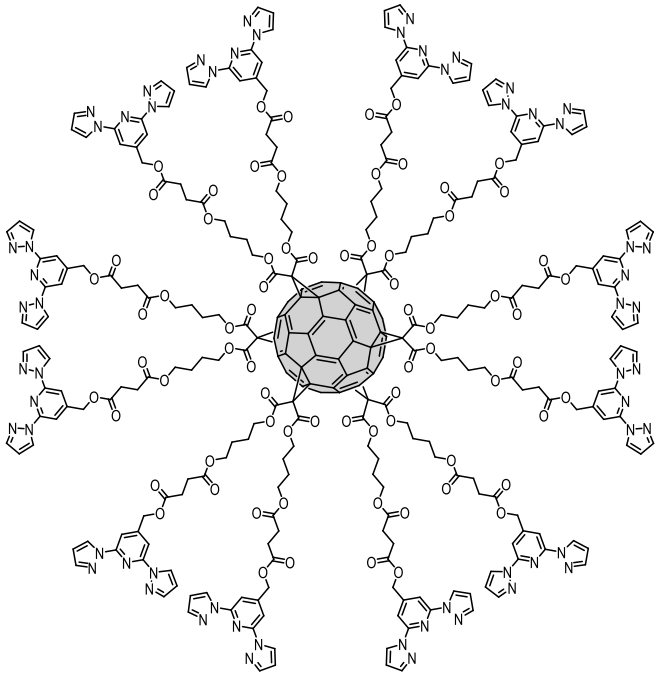

To a solution of **P1** (61 mg, 27.85 µmol), ligand **L3** (170 mg, 0.50 mmol) and DPTS (49 mg, 0.17 mmol) in a dry mixture of CH_2Cl_2/DMF (3 mL, 2:1) under Ar atmosphere, DCC (105 mg, 0.50 mmol) in dry CH_2Cl_2 (1 mL) was added. The reaction mixture was stirred at 40 °C overnight. Once the reaction was complete, the dicyclohexylurea was filtered off in a fritted glass filter and washed with CH_2Cl_2. The crude product was purified by size-exclusion chromatography (Sephadex LH-20, MeOH/CH_2Cl_2 1:1), to give **2** (170 mg, quant.) as an orange-red amorphous solid. IR (neat): 3132, 2959, 2926, 1733, 1463, 1394, 1206, 1154, 1040 cm^{-1}; ^1H NMR (500 MHz, $CDCl_3$) δ/ppm: 8.50 (m, 24H, H-Ar_{pyzl}), 7.81–7.66 (m, 48H, H-Ar_{py}, H-Ar_{pyzl}), 6.45 (m, 24H, H-Ar_{pyzl}), 5.20 (s, 24H, $CH_{2,Bn}$), 4.27 (m, 24H, OC$H_2$$CH_2$), 4.10 (m, 24H, OC$H_2$$CH_2$), 2.75 (m, 24H, $CH_{2,succ.}$), 2.66 (m, 24H,

$CH_{2,succ.}$), 1.78–1.65 (m, 48H, $OCH_2CH_2CH_2CH_2O$); ^{13}C NMR (125.8 MHz, $CDCl_3$) δ/ppm: 172.0 (CO), 171.7 (CO), 163.6 (CO), 151.0 (C_{ipso}Ar-$CH_{2,Bn}$), 150.1 (C_{ipso}Ar-N), 145.7 ($C_{sp2,fullerene}$), 142.3 (CH-Ar_{pyzl}), 141.0 ($C_{sp2,fullerene}$), 127.0 (CH-Ar_{pyzl}), 108.0 (CH-Ar_{py}), 107.1 (CH-Ar_{pyzl}), 69.0 ($C_{sp3,fullerene}$), 66.4 (OCH_2CH_2), 64.3 ($CH_{2,Bn}$), 63.9 (OCH_2CH_2), 45.3 ($C_{q,bridge}$), 28.8 ($CH_{2,succ.}$), 25.0 ($OCH_2CH_2CH_2CH_2O$); MALDI-TOF (DCTB): *m/z* calcd for $C_{318}H_{264}N_{60}O_{72}$: 6073.9; found: A high level of occurring fragmentation avoided the observation of the expected molecular ion peak.

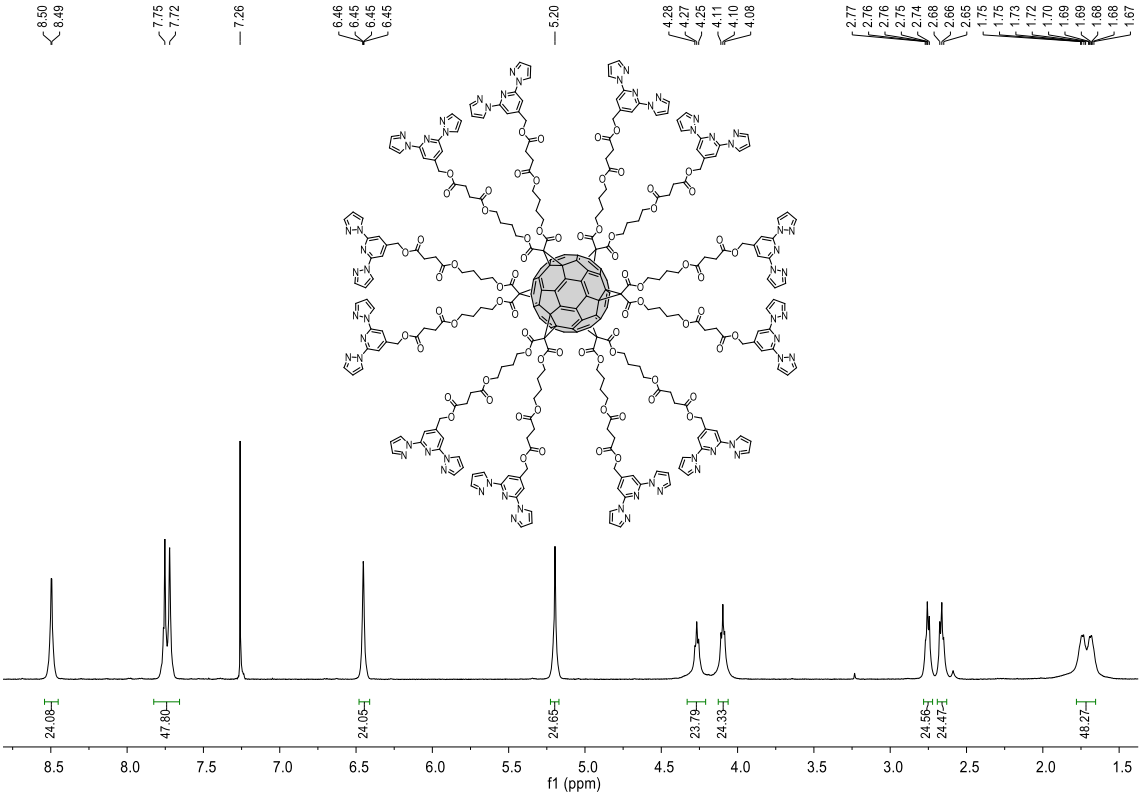

Figure S6. ^1H NMR spectrum (500 MHz, $CDCl_3$) of compound **2**

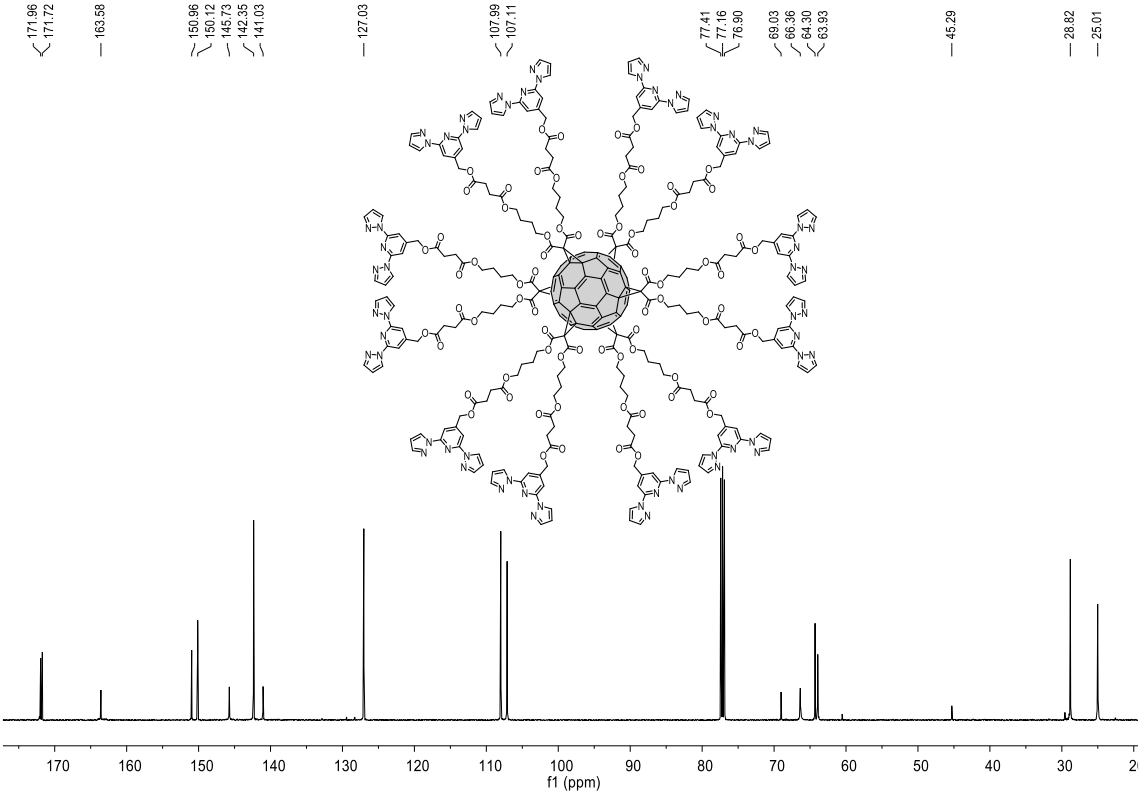

Figure S7. ^{13}C NMR spectrum (125.8 MHz, $CDCl_3$) of compound **2**

Synthesis of compound 3.

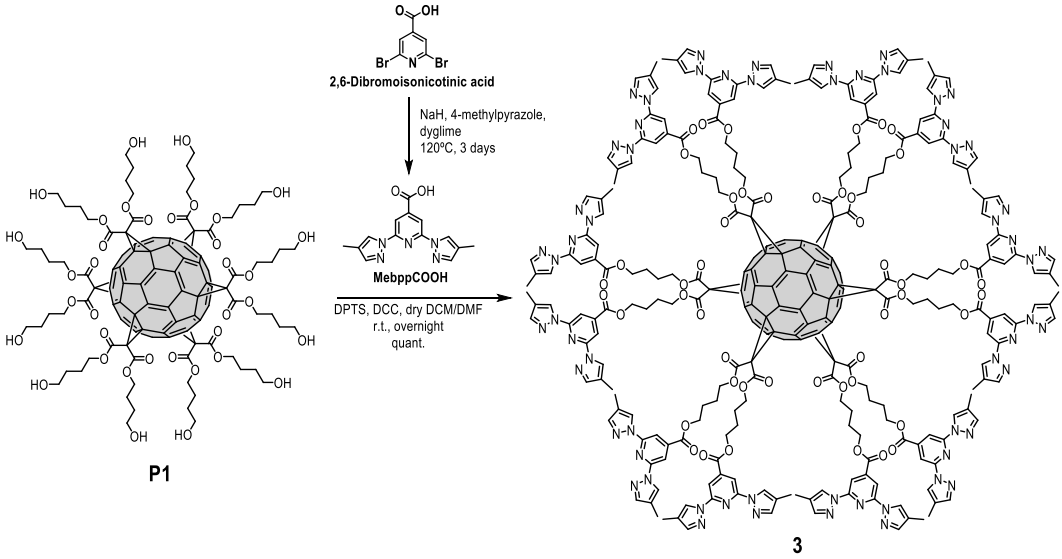

Scheme S3. Schematic representation of the synthesis of **3**

MeppCOOH (L5)

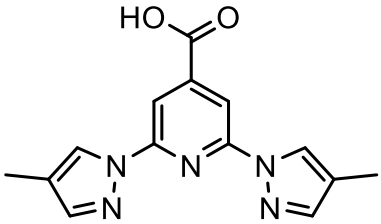

In an Ar atmosphere, NaH (274 mg, 11.4 mmol) was suspended in dry dyglime (8 mL), then 4-methylpyrazole (615 µL, 7.4 mmol) was added dropwise to form a white suspension that turned into a yellowish solution upon heating to 80 ºC for 90 minutes. 2,6-Dibromoisonicotinic acid (540 mg, 1.92 mmol) was then added and the suspension was heated to 120 ºC for 3 days. The solvent was evaporated leaving a very small volume left and water (50 mL) was added. This suspension was acidified with HCl (1 M) to pH 2.75. A white product was formed, which was filtered, washed and dried to the air to give compound **L5** (500 mg, 93%). ^{1}H NMR (300 MHz, DMSO-d_6) δ/ppm: 8.74 (d, J = 2.6 Hz, 2H, H-Ar$_{pyzl}$), 8.07 (m, 2H, H-Ar$_{pyzl}$), 7.73 (s, 2H, H-Ar$_{py}$), 2.15 (s, 6H, CH$_{2,succ.}$). ^{13}C NMR (500 MHz, DMSO-d_6) δ/ppm:165 (CO), 150.8 (C_{ipso}Ar-CO), 144.6 (C_{ipso}Ar-N),144,4 (CH-Ar$_{pyrzl}$),126.8 (CH-Ar$_{pyzl}$), 119.26 (C-Ar$_{pyzl}$), 107.6 (CH-Ar$_{py}$), 9.22 (CH$_3$). ESI-HRMS: m/z calcd for $C_{14}H_{13}N_5O_2Na$ [M+Na]+: 306.0889; found: 306.0955

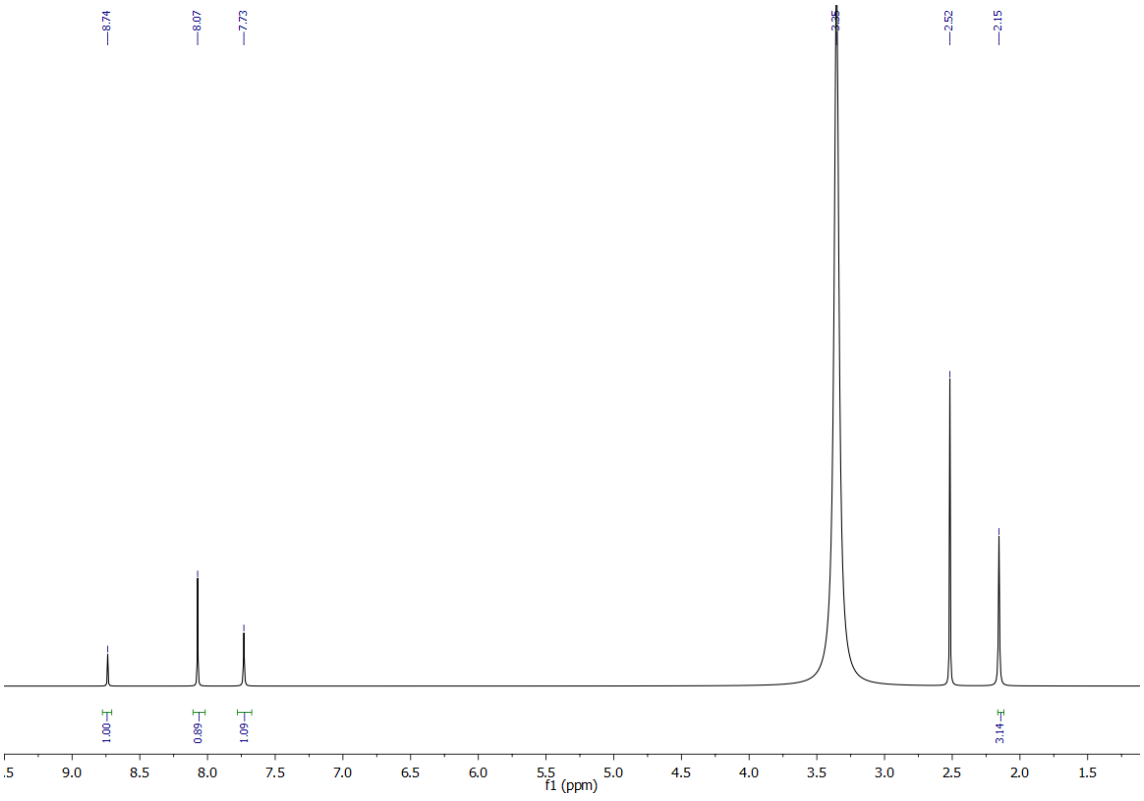

Figure S8. ^{1}H NMR spectrum (500 MHz, DMSO-d_6) of **L5**

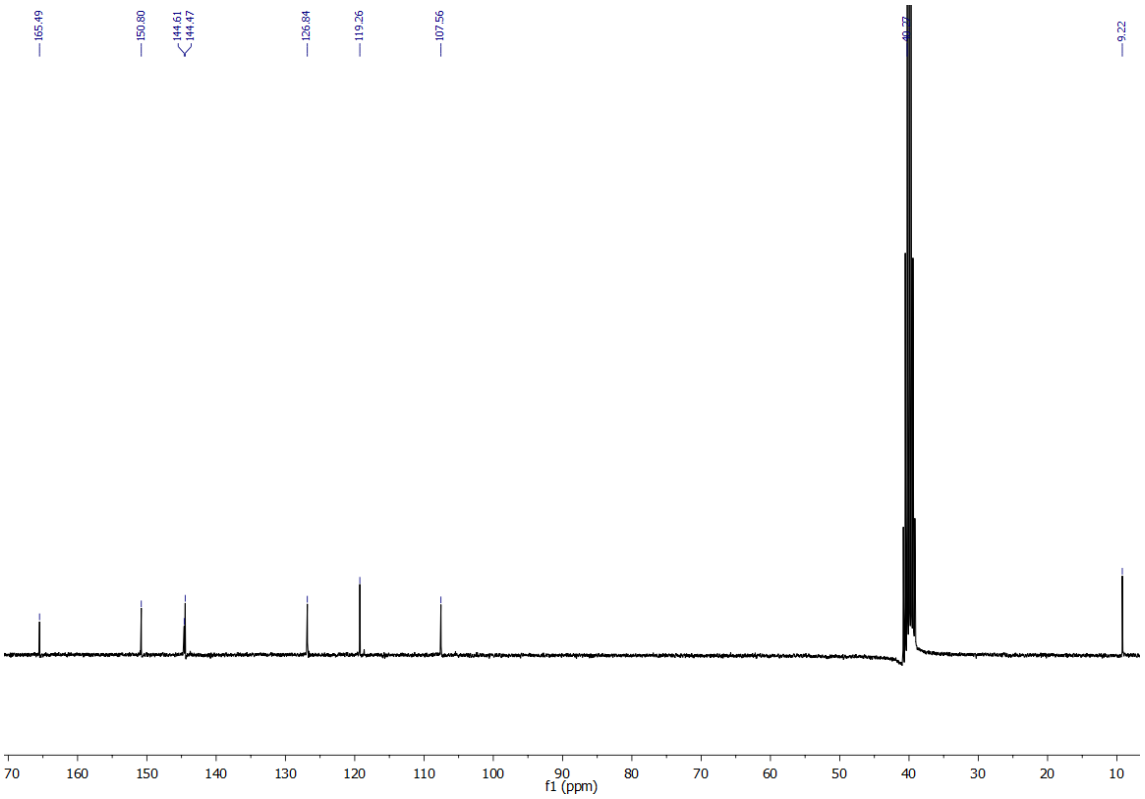

Figure S9. ^{13}C NMR spectrum (500 MHz, DMSO-d_6) of **L5**

Compound 3.

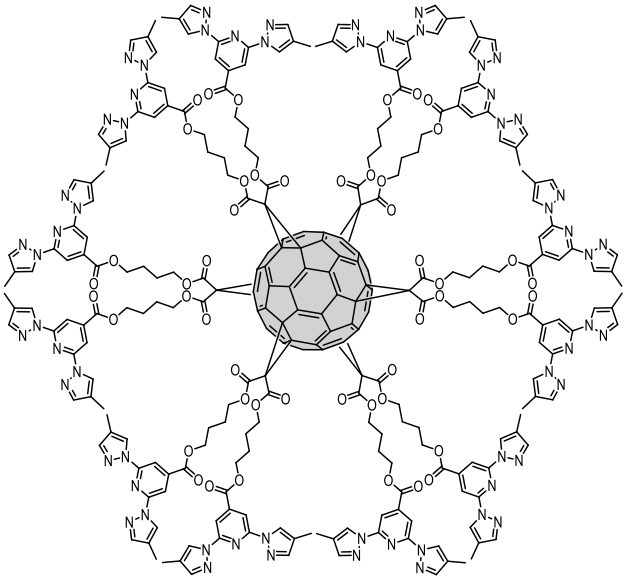

To a solution of **P1** (118 mg, 53.72 µmol), **L5** (274 mg, 0.97 mmol) and DPTS (95 mg, 0.32 mmol) in a dry mixture of CH_2Cl_2/DMF (6 mL, 3:1) under Ar atmosphere, DCC (202 mg, 0.97 mmol) in dry CH_2Cl_2 (1.5 mL) was added. The reaction mixture was stirred at 40 ºC overnight. Once the reaction was complete, the dicyclohexylurea was filtered off in a fritted glass filter and washed with CH_2Cl_2. The crude product was purified by size-exclusion chromatography (Sephadex LH-20, MeOH/CH_2Cl_2 1:1), to give **3** (289 mg, quant.) as an orange-red amorphous solid. IR (neat): 2959, 2925, 1730, 1452, 1214 cm^{-1}; ^{1}H NMR (500 MHz, $CDCl_3$) δ/ppm: 8.13 (m, 24H, H-Ar_{pyzl}), 8.06 (m, 24H, H-Ar_{py}), 7.49 (m, 24H, H-Ar_{pyzl}), 4.37, 4.33 (2m, 48H, O$CH_2CH_2CH_2CH_2$O), 2.10 (s, 72H, CH_3), 1.88 (m, 48H, $OCH_2CH_2CH_2CH_2O$); ^{13}CN MR (125.8 MHz, $CDCl_3$) δ/ppm: 163.9 (CO), 163.8 (CO), 150.5 (C_{ipso}Ar-N), 145.9 ($C_{sp2,fullerene}$), 143.6 (CH-Ar_{pyzl}), 142.6 (C_{ipso}Ar-CO), 141.2 ($C_{sp2,fullerene}$), 125.3 (CH-Ar_{pyzl}), 118.8 (C-Ar_{pyzl}), 107.9 (CH-Ar_{py}), 69.2 ($C_{sp3,fullerene}$), 66.5, 65.3

($OCH_2CH_2CH_2CH_2O$), 45.4 ($C_{q,bridge}$), 25.2, 25.1 ($OCH_2CH_2CH_2CH_2O$), 9.0 (CH_3); MALDI-TOF: *m/z* calcd for $C_{294}H_{240}N_{60}O_{48}$: 5380.5; found: 5380.7 $[M]^+$, 5220.8 $[M\text{-}2(methylpyrazol)+2H]^+$.

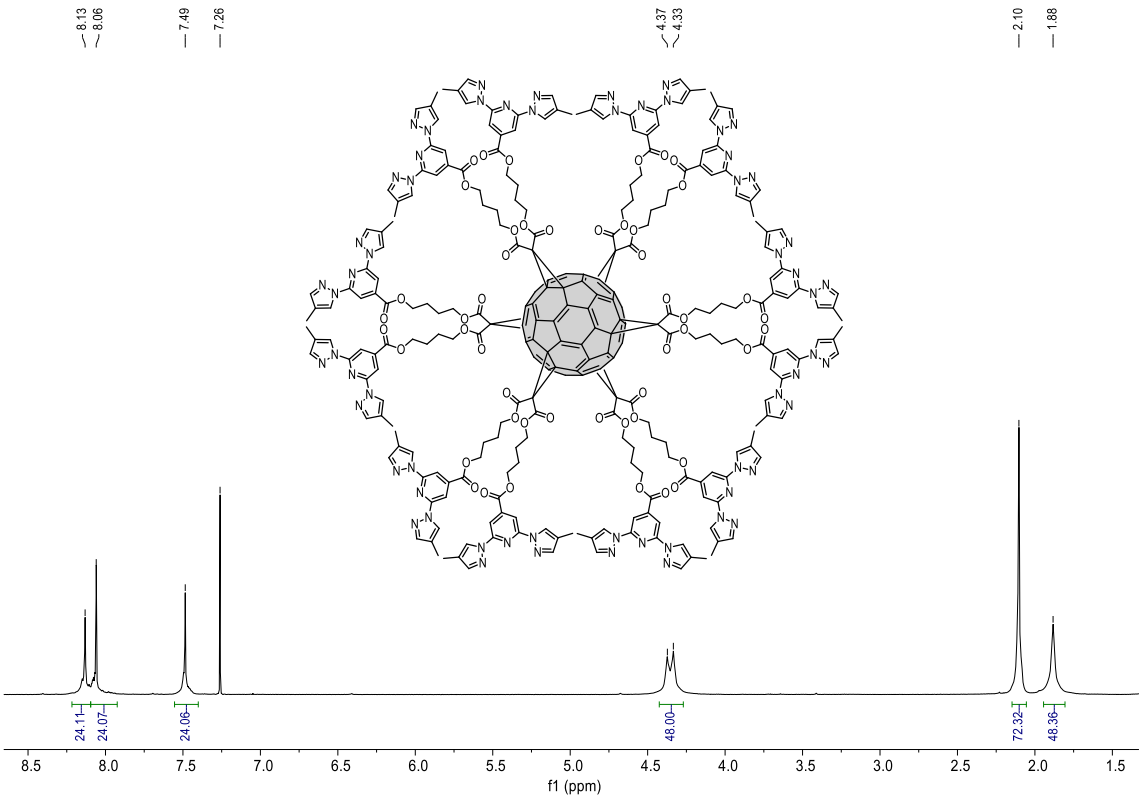

Figure S10. ^1H NMR spectrum (500 MHz, $CDCl_3$) of compound **3**

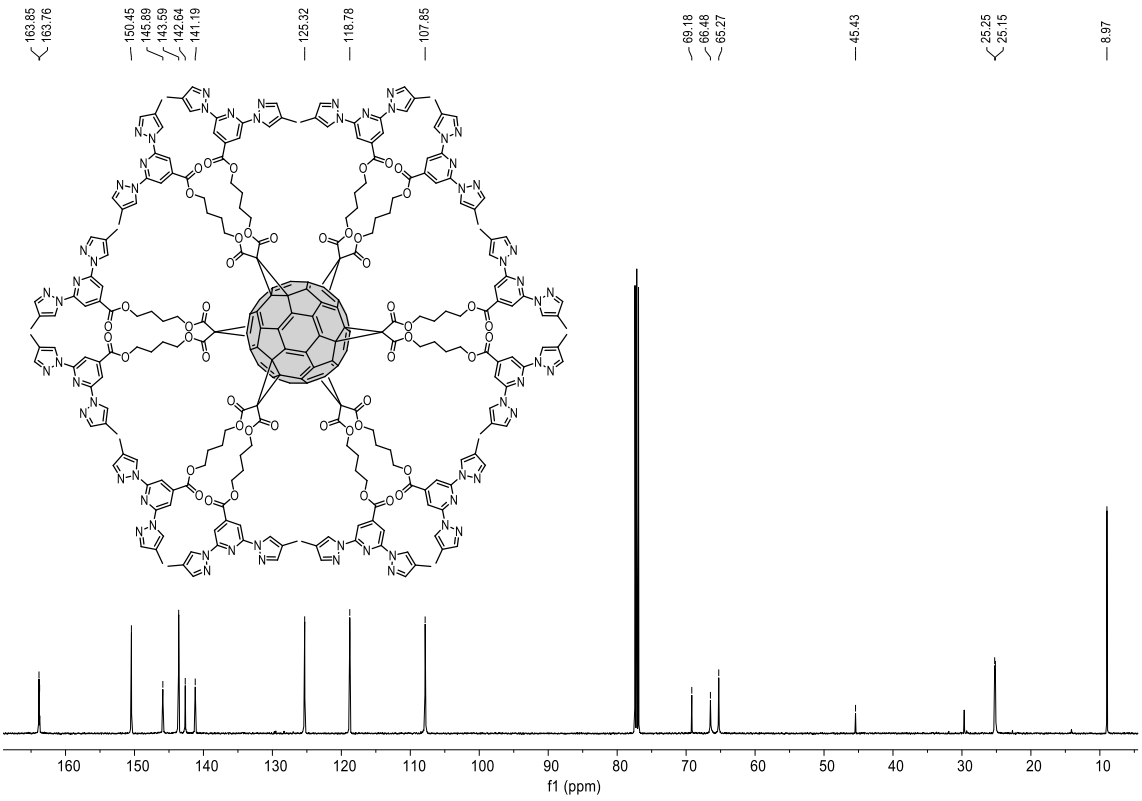

Figure S11. ^{13}C NMR spectrum (125.8 MHz, $CDCl_3$) of compound **3**

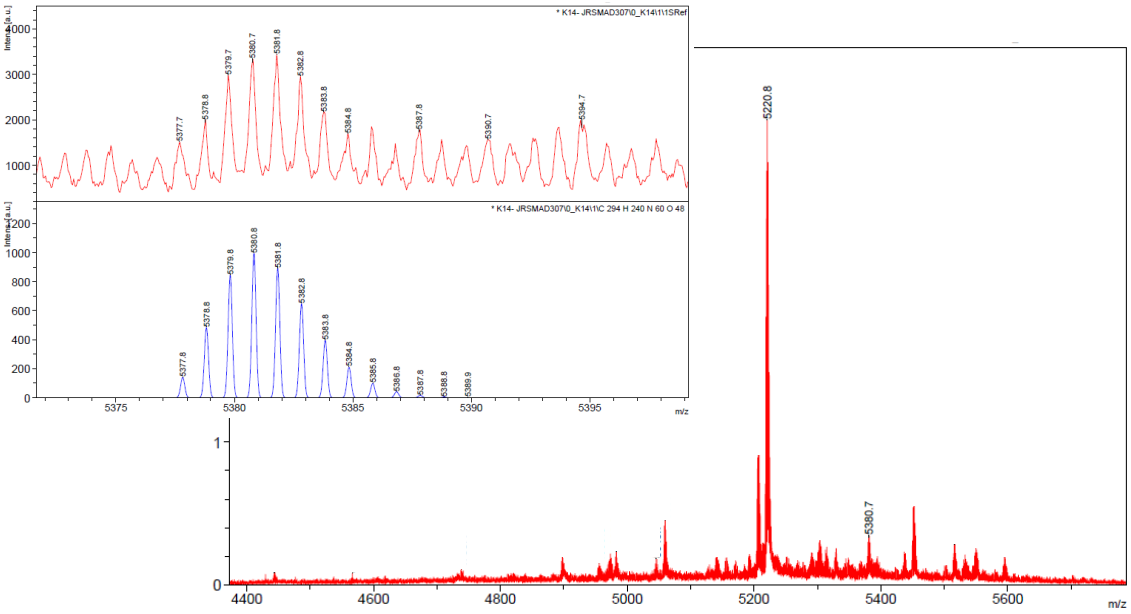

Figure S12. MALDI-TOF spectrum of compound **3**

Synthesis of compound 4.

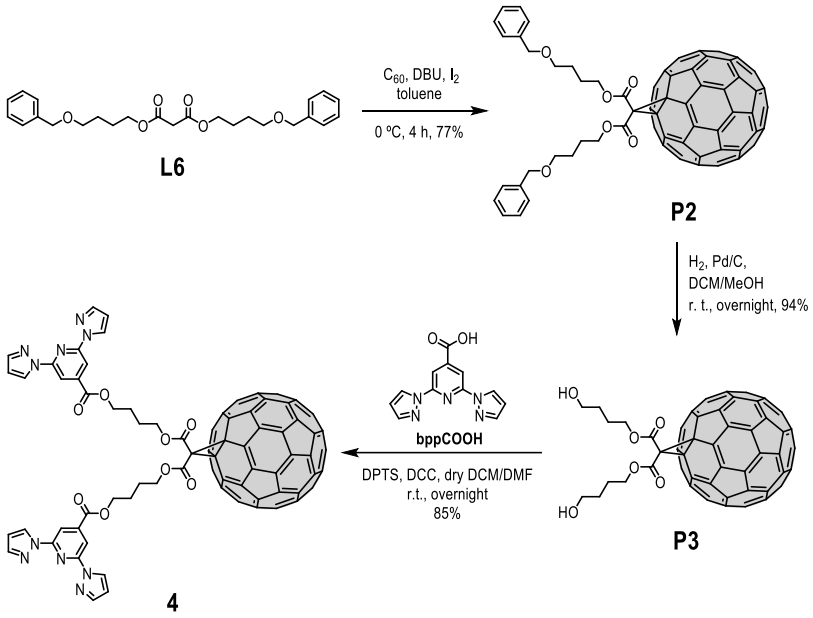

Scheme S4. Schematic representation of the synthesis of **4**

Compound P2.

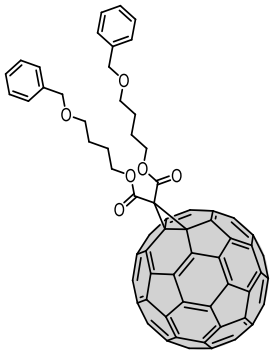

DBU (633 µL, 4.23 mmol) (DBU = 1,8-diazabicyclo[5.4.0]undec-7-ene) was added to a solution of fullerene C_{60} (2.44 g, 3.39 mmol), malonate **L6** (725 mg, 1.69 mmol) and I_2 (1.5 g, 5.93 mmol) in dry toluene (300 mL) at 0 °C under Ar atmosphere. The resulting solution was stirred at 0 °C for 4 h. After this time, the organic layer was washed with saturated $Na_2S_2O_3$ (40 mL), dried over anhydrous $MgSO_4$, filtered and concentrated. The resulting crude was purified by silica gel chromatography column (hexane/CH_2Cl_2, 1:3), furnishing monoadduct **P2** (1.5 g, 77%) as a brown amorphous solid. IR (neat): 2954, 2924, 2857, 1745, 1235, 737 cm^{-1}; ^1H NMR (500 MHz, $CDCl_3$) δ/ppm: 7.34 (m, 8H, H-Ar), 7.28 (m, 2H, H-Ar), 4.54–4.49 (m, 8H, CH_{2Bn}, OCH_2CH_2), 3.53 (t, 4H, J = 6.2 Hz, CH_2CH_2OBn), 1.95 (m, 4H, OCH_2CH_2), 1.79 (m, 4H, CH_2CH_2OBn); ^{13}C NMR (125.8 MHz, $CDCl_3$) δ/ppm: 163.5 (CO), 145.3, 145.2, 145.2, 145.1, 144.8, 144.7, 144.6, 144.56, 143.8, 143.1, 143.0, 142.9, 142.2, 141.9, 140.9, 139.0 ($C_{sp2,fullerene}$), 138.4 (C_{ipso}-Ar), 128.4, 127.6, 127.5 (C-Ar), 72.9 (CH_{2Bn}), 71.6 ($C_{sp3,fullerene}$), 69.5 (CH_2CH_2OBn), 67.2 (OCH_2CH_2), 52.2 ($C_{q,bridge}$), 26.2 (CH_2CH_2OBn), 25.6 (OCH_2CH_2); HRMS (MALDI-TOF): *m/z* calcd for $C_{85}H_{30}O_6$ $[M]^+$: 1146.2042; found: 1146.2077.

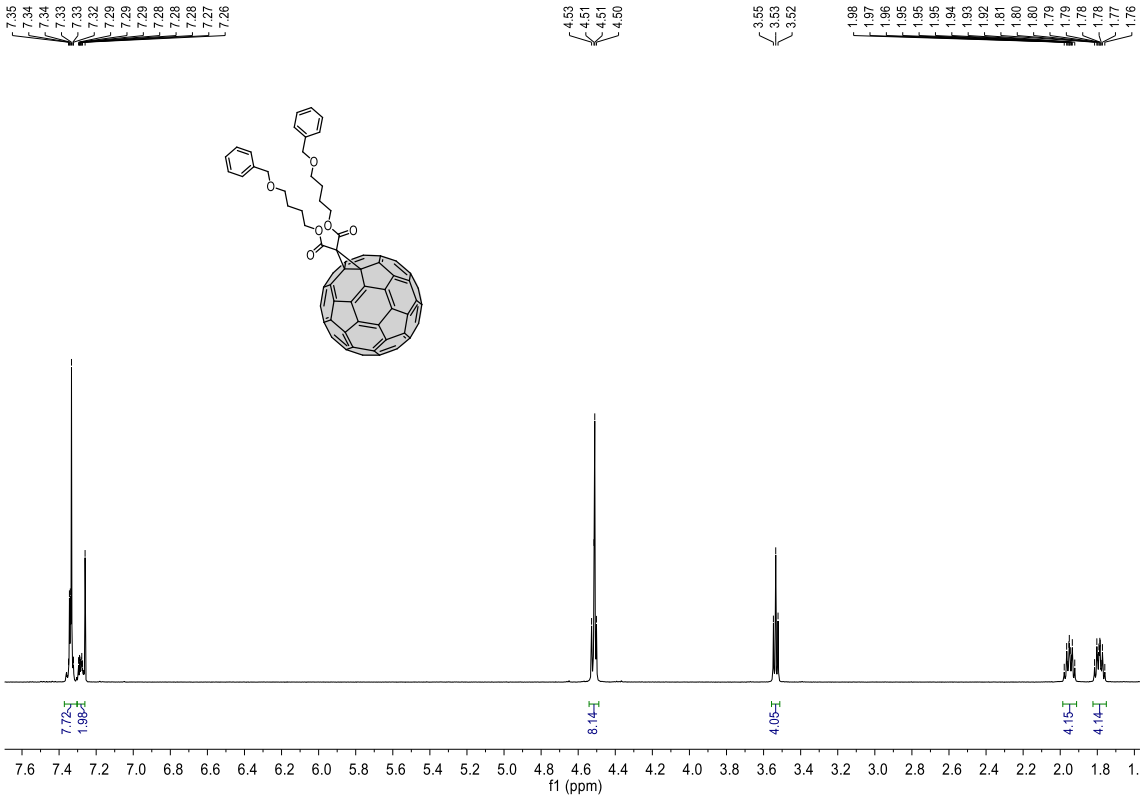

Figure S13. ^{1}H NMR spectrum (500 MHz, $CDCl_3$) of compound **P2**

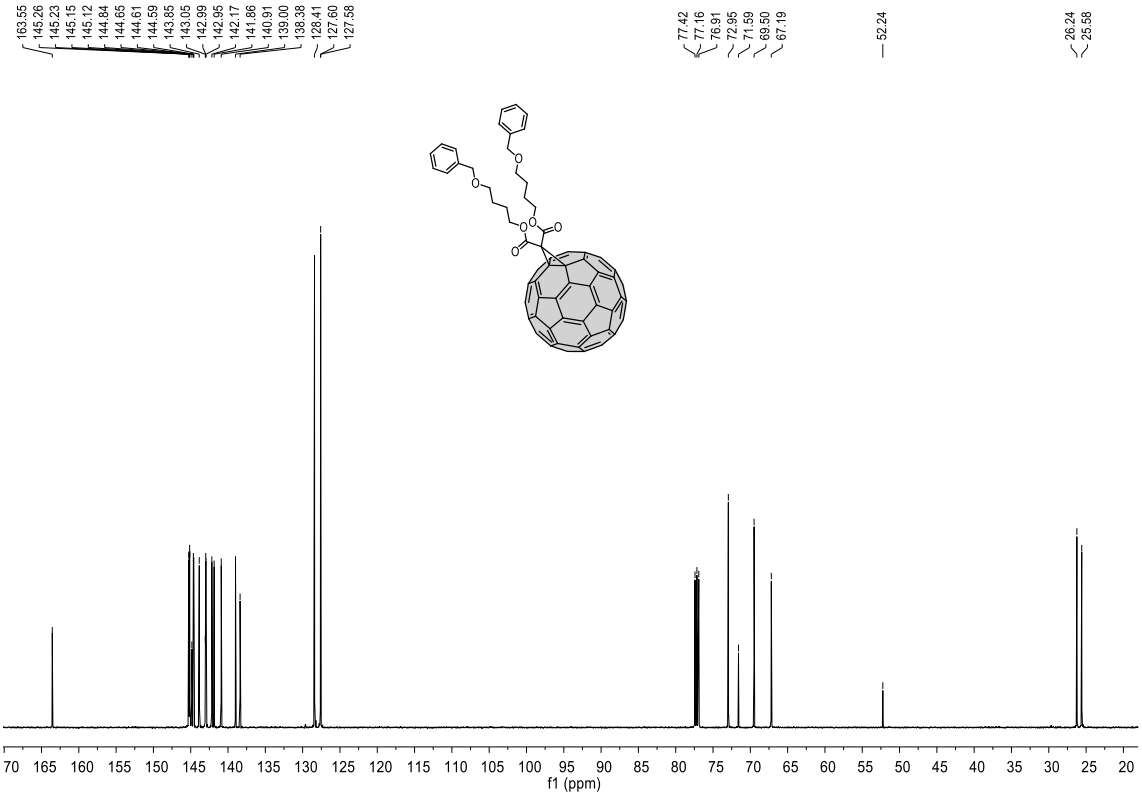

Figure S14. ^{13}C NMR spectrum (125.8 MHz, $CDCl_3$) of compound **P2**

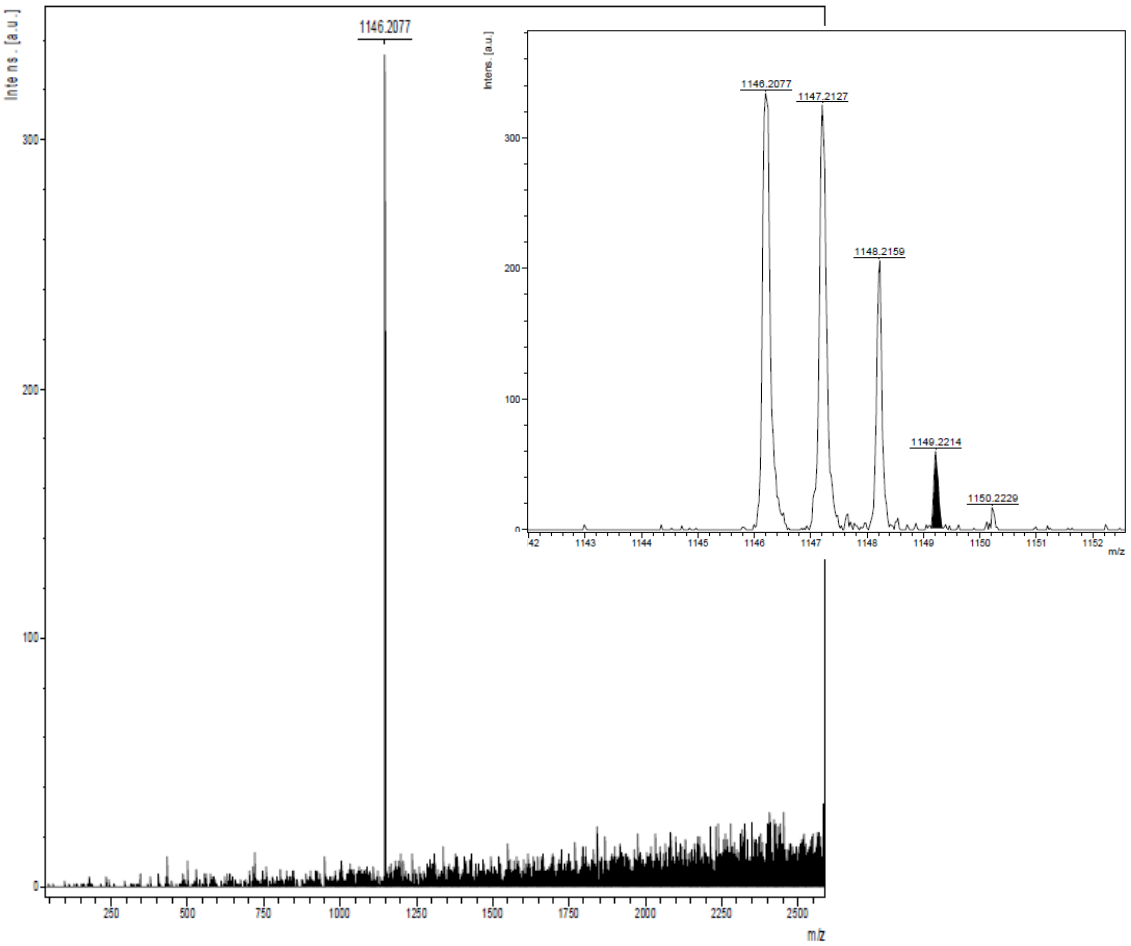

Figure S15. MALDI-TOF spectrum of compound **P2**

Compound P3.

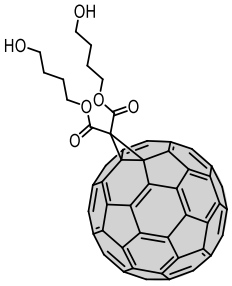

A solution of **P2** (1.3 g, 1.13 mmol) in a mixture of CH_2Cl_2/MeOH (72 mL, 3:1) was hydrogenated under atmospheric pressure at room temperature overnight using Pd-C (10%) as catalyst. Then, the solution was filtered through celite, and the catalyst was washed with CH_2Cl_2/MeOH. The filtered solution was concentrated, furnishing pure **P3** (1.03 g, 94%) as a brown amorphous solid. IR (neat): 3308, 2922, 1741, 1234, 753 cm^{-1}; ^1H NMR (500 MHz, $CDCl_3$ + CD_3OD) δ/ppm: 4.43 (t, 4H, J = 6.6 Hz, OCH_2CH_2), 3.58 (t, 4H, J = 6.5 Hz, CH_2CH_2OH), 1.84 (m, 4H, OCH_2CH_2), 1.64 (m, 4H, CH_2CH_2OH); ^{13}C NMR (125.8 MHz, $CDCl_3$) δ/ppm: 163.8 (CO), 145.4, 145.4, 145.3, 145.3, 145.1, 144.9, 144.8, 144.0, 143.3, 143.2, 143.1, 142.4, 142.0, 141.1, 139.2 ($C_{sp2,fullerene}$), 71.7 ($C_{sp3,fullerene}$), 67.4 (OCH_2CH_2), 62.4 (CH_2CH_2OH), 52.3 ($C_{q,bridge}$), 29.2 (CH_2CH_2OH), 25.3 (OCH_2CH_2); HRMS (MALDI-TOF): *m/z* calcd for $C_{71}H_{18}O_6$ $[M]^+$: 966.1103; found: 966.1078.

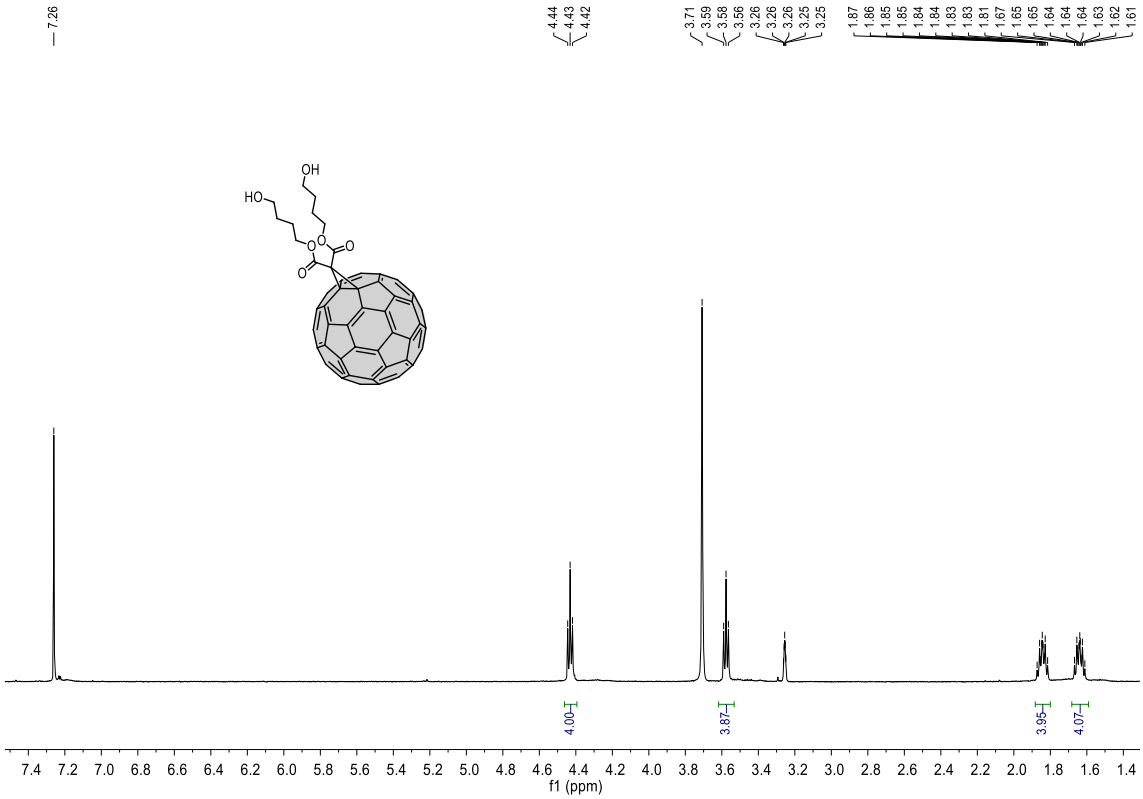

Figure S16. ^{1}H NMR spectrum (500 MHz, $CDCl_3$) of compound **P3**

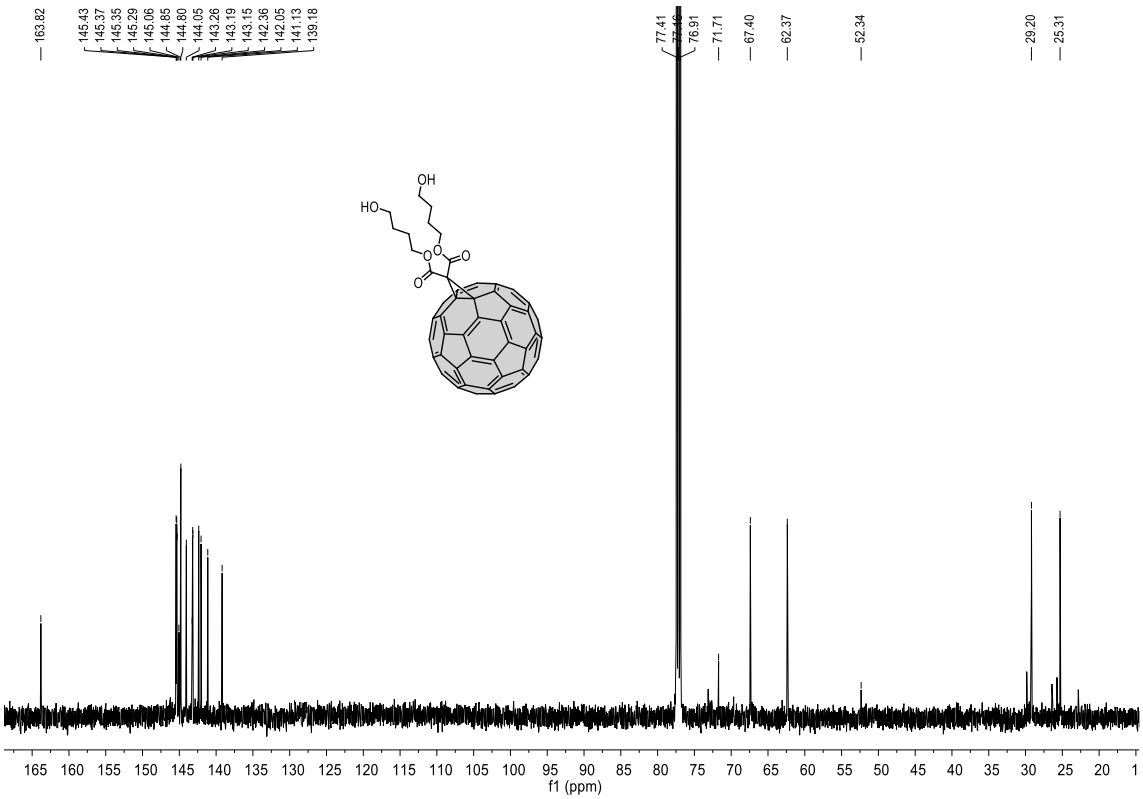

Figure S17. ^{13}C NMR spectrum (125.8 MHz, $CDCl_3$) of compound **P3**

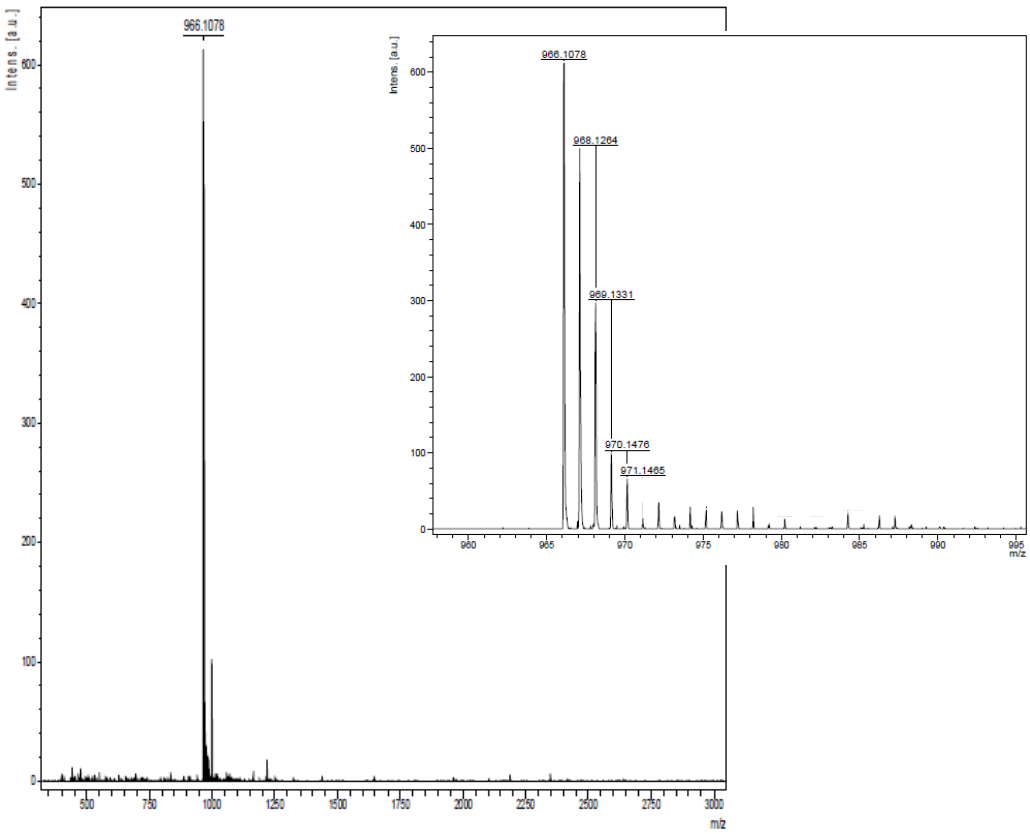

Figure S18. MALDI-TOF spectrum of compound **P3**

Compound 4.

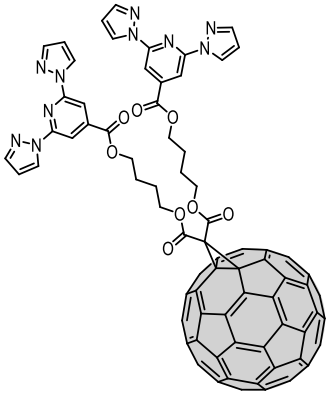

4

To a solution of **P3** (900 mg, 0.93 mmol), ligand **L1** (713 mg, 2.79 mmol) and DPTS (274 mg, 0.93 mmol) in a dry mixture of CH_2Cl_2/DMF (48 mL, 3:1) under Ar atmosphere, DCC (582 mg, 2.79 mmol) in dry CH_2Cl_2 (12 mL) was added. The reaction mixture was stirred at 40 °C overnight. Once the reaction was complete, the dicyclohexylurea was filtered off in a fritted glass filter and washed with CH_2Cl_2. The crude product was purified by silica gel chromatography column (toluene/acetone, 20:1), to give **4** (1.14 g, 85%) as a brown amorphous solid. IR (neat): 2959, 2926, 2855, 1732, 1462, 1237, 763 cm^{-1}; ^1H NMR (500 MHz, $CDCl_3$) δ/ppm: 8.52 (dd, 4H, J = 2.7, 0.7 Hz, H-Ar_{pyzl}), 8.33 (s, 4H, H-Ar_{py}), 7.77 (d, 4H, J = 2.2 Hz, H-Ar_{pyzl}), 6.50 (dd, 4H, J = 2.6, 1.6 Hz, H-Ar_{pyzl}), 4.61 (m, 4H, OCH_2CH_2), 4.48 (m, 4H, OCH_2CH_2), 2.03 (m, 8H, $OCH_2CH_2CH_2CH_2O$); ^{13}C NMR (125.8 MHz, $CDCl_3$) δ/ppm: 163.9 (CO), 163.6 (CO), 150.8 (C_{ipso}Ar-N), 145.2, 145.2, 145.2, 145.1, 144.9, 144.7, 144.6, 144.6, 143.8 ($C_{sp2,fullerene}$), 143.2 (C_{ipso}Ar-CO), 143.0, 143.0, 142.9 ($C_{sp2,fullerene}$), 142.9 (CH-Ar_{pyzl}), 142.2, 141.8, 140.9, 139.0 ($C_{sp2,fullerene}$), 127.3 (CH-Ar_{pyzl}), 109.1(CH-Ar_{py}) , 108.5 (CH-Ar_{pyzl}), 71.5 ($C_{sp3,fullerene}$), 66.8, 65.4 ($OCH_2CH_2CH_2CH_2O$), 52.1 ($C_{q,bridge}$), 25.5, 25.4 ($OCH_2CH_2CH_2CH_2O$); HRMS (MALDI-TOF): *m/z* calcd for $C_{96}H_{33}N_9O_8$ $[M]^+$: 1440.3750; found: 1440.2426.

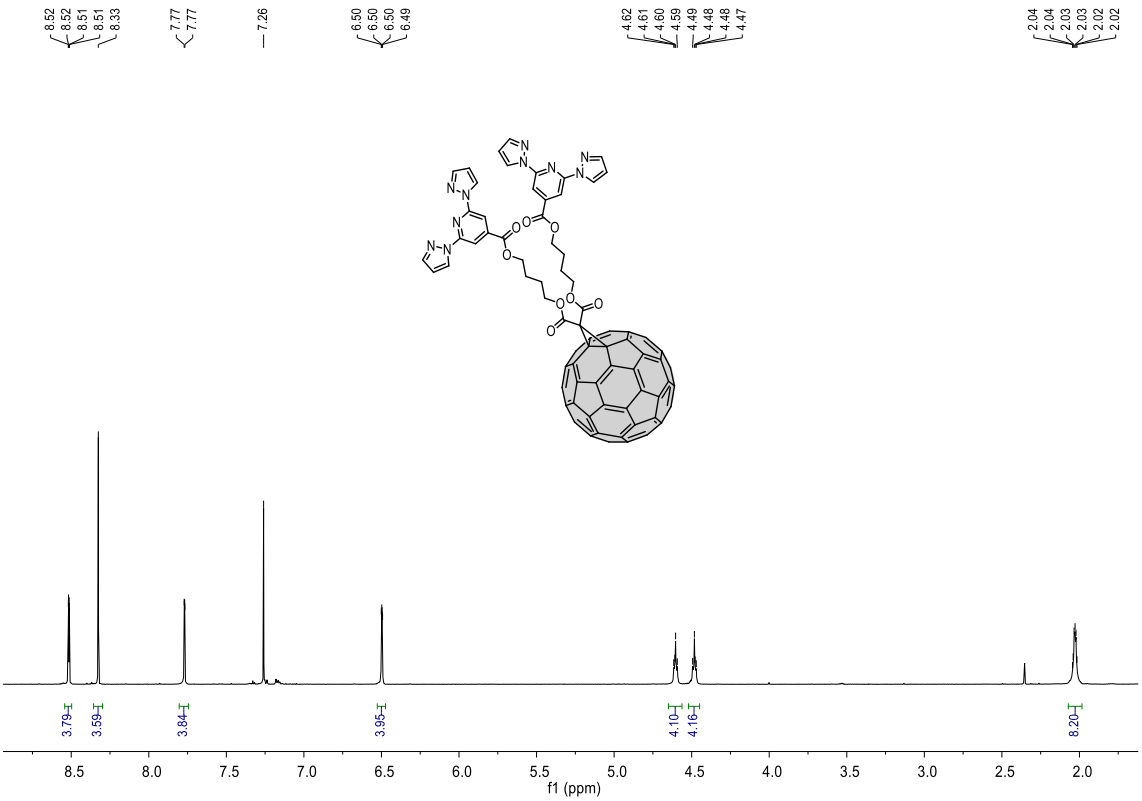

Figure S19. ^{1}H NMR spectrum (500 MHz, $CDCl_3$) of compound **4**

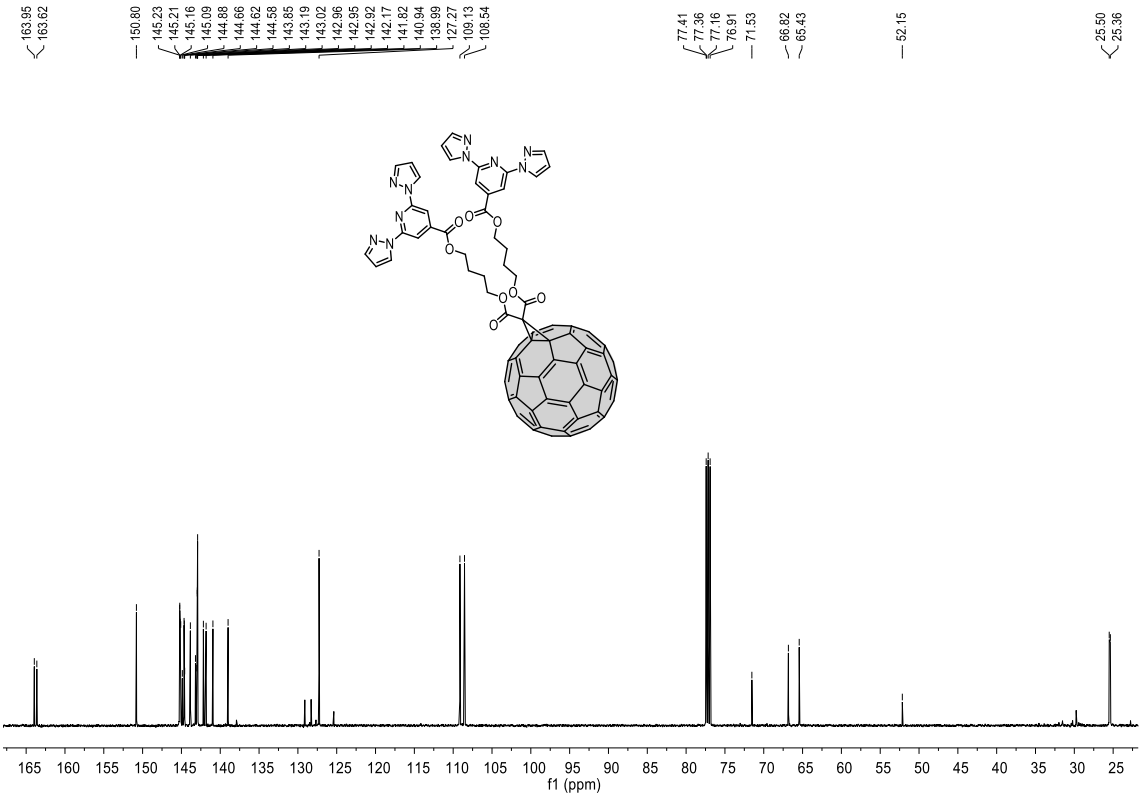

Figure S20. ^{13}C NMR spectrum (125.8 MHz, $CDCl_3$) of compound **4**

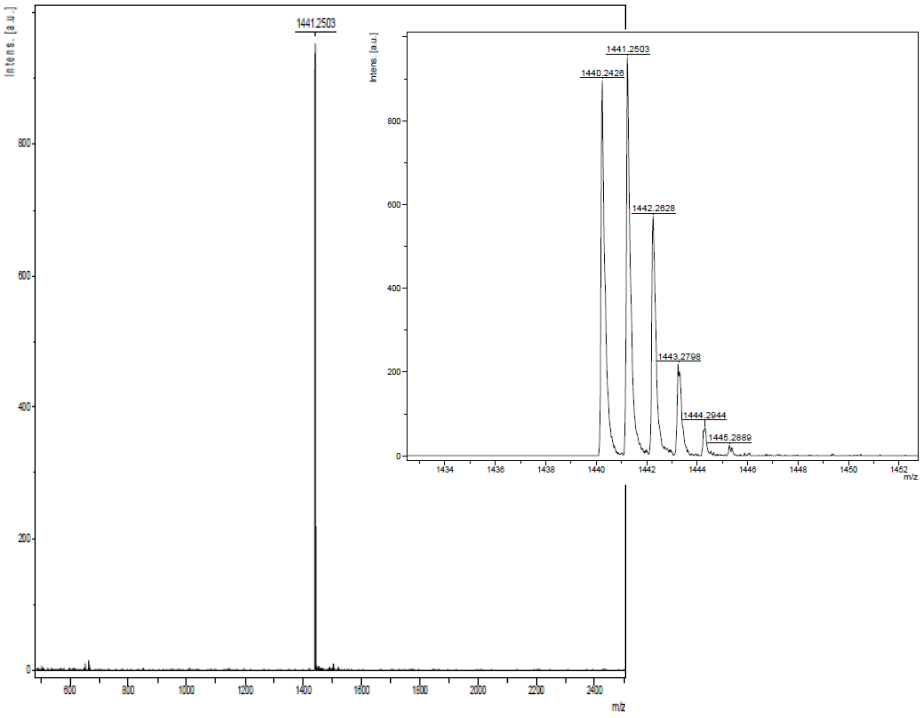

Figure S21. MALDI-TOF spectrum of compound **4**

3. Studies in solution

3.1 UV-vis spectra of **1**, **2** and model ligands with Fe^{2+}.

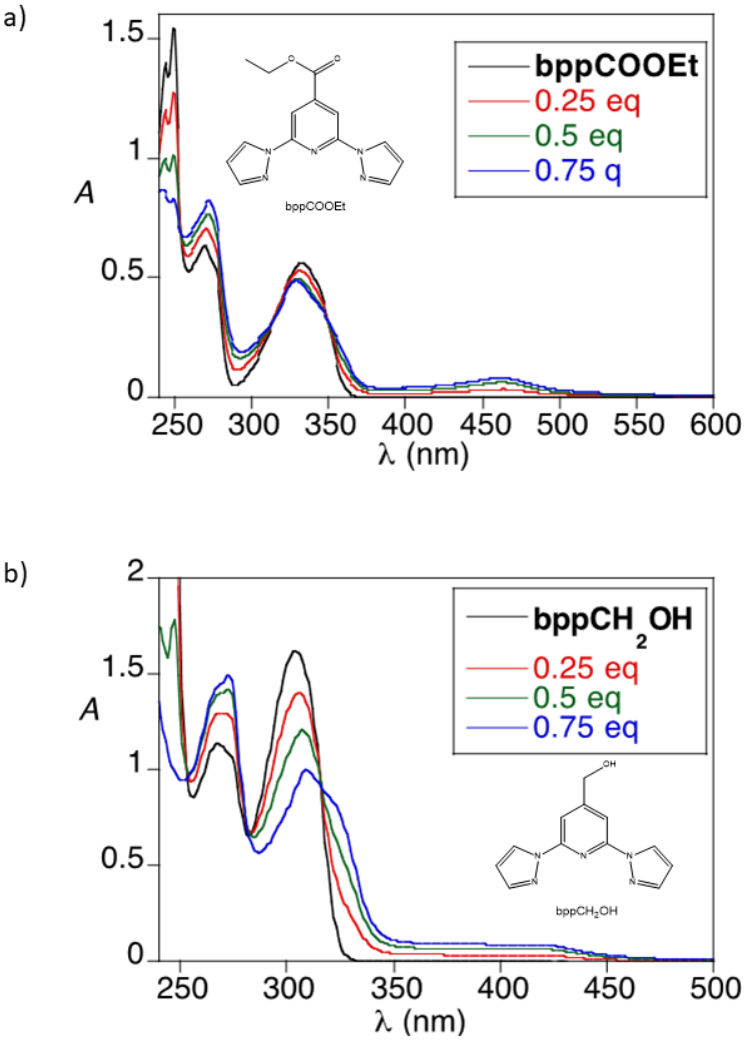

Figure S22. UV-vis spectra of a titration of a 5 × 10^{-5} M solution of model ligands a) bppCOOEt and b) bppCH$_2$OH in CH_2Cl_2 with $Fe(BF_4)_2$.

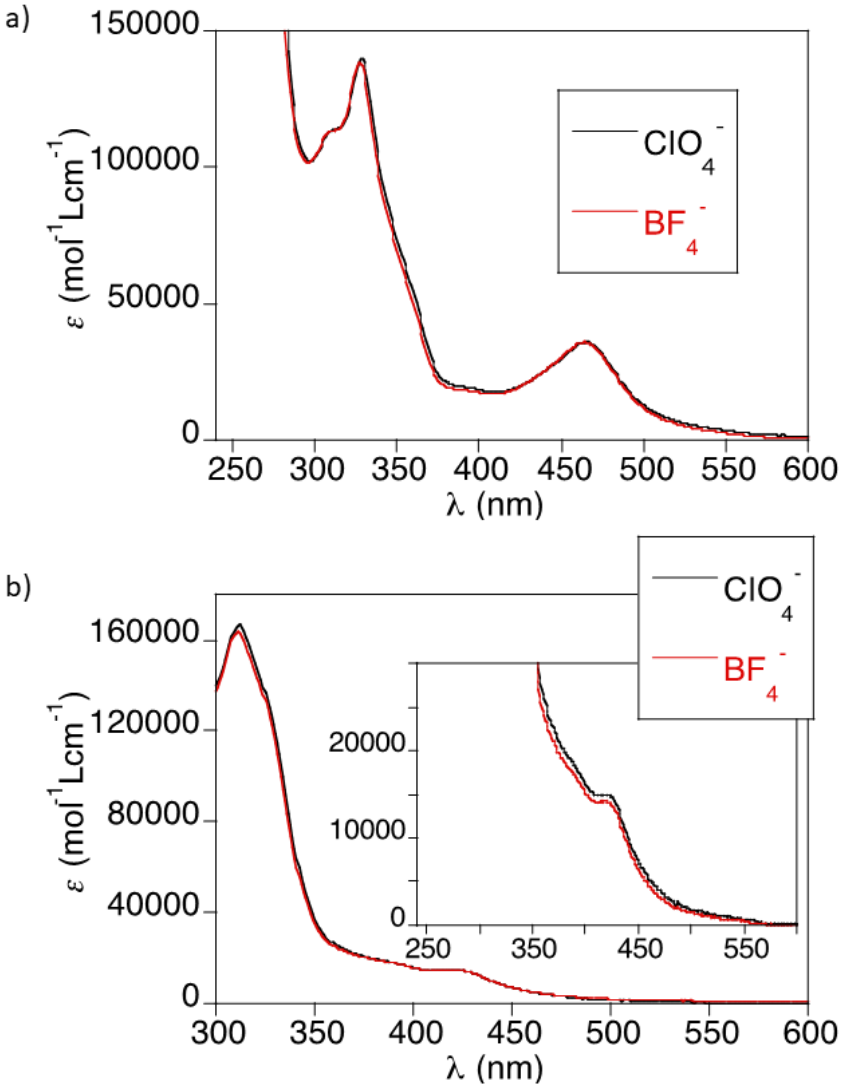

Figure S23. UV-vis spectra of 7.5 × 10^{-6} M solutions of a) **1** and b) **2** in CH_2Cl_2 with six equivalents of $Fe(BF_4)_2$ (red line) or $Fe(ClO_4)_2$ (black line).

3.2 Fluorescence titrations of **1**, **2** and model ligands with Fe^{2+}.

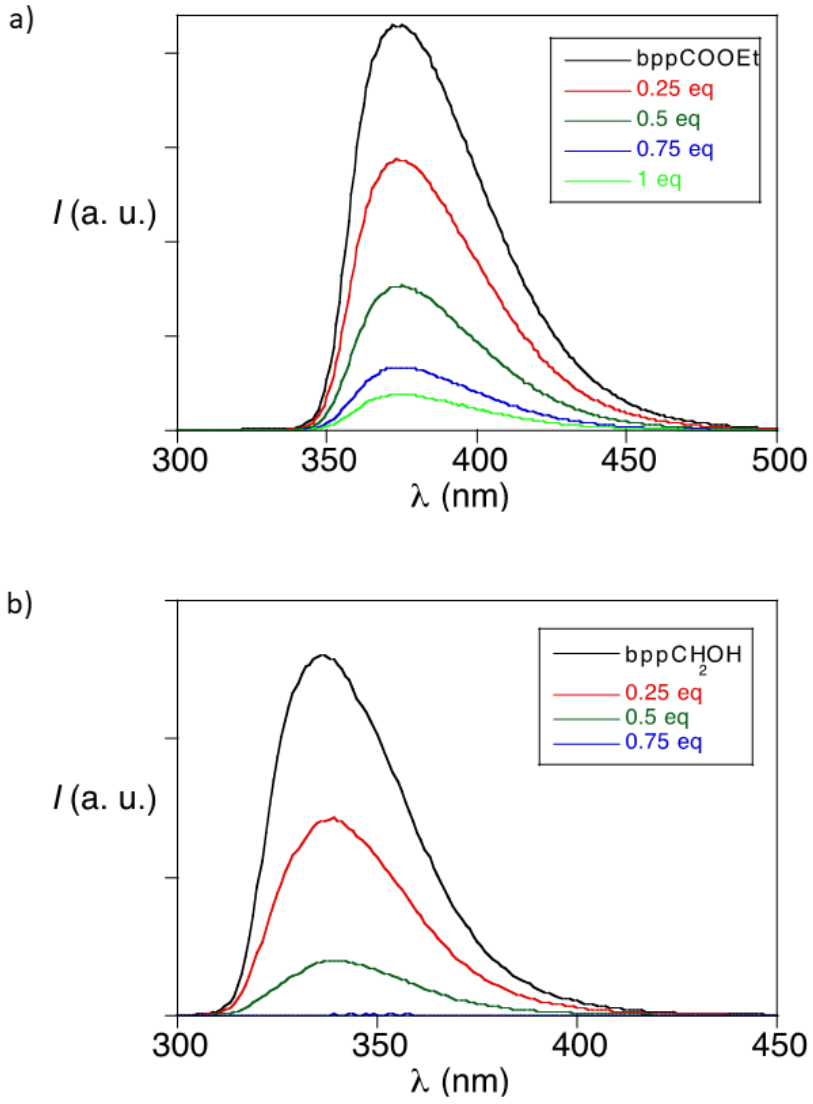

Figure S24. Fluorescence spectra of a titration of 5 $\times 10^{-5}$ M solution of a) bppCOOEt and b) $bppCH_2OH$ in CH_2Cl_2 with $Fe(BF_4)_2$.

Hexa-adduct **1** and **bppCOOEt** exhibit a very short excited-state lifetime indicating that they correspond to ligand fluorescence. The lifetime of **1** (τ = 0.15 ns) decreases one order of magnitude with respect to bppCOOEt ligand (τ = 2.36 ns). After addition of Fe^{2+} equivalents, longer-lived components appear to have a greater contribution to the luminescence decay of **1** (τ ~ 4 ns (6 %) with 6 eqs) and bppCOOEt (τ ~ 5 ns (15 %) with 2 eqs).

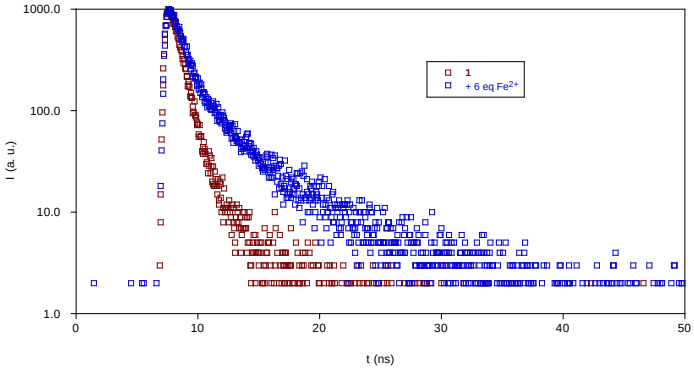

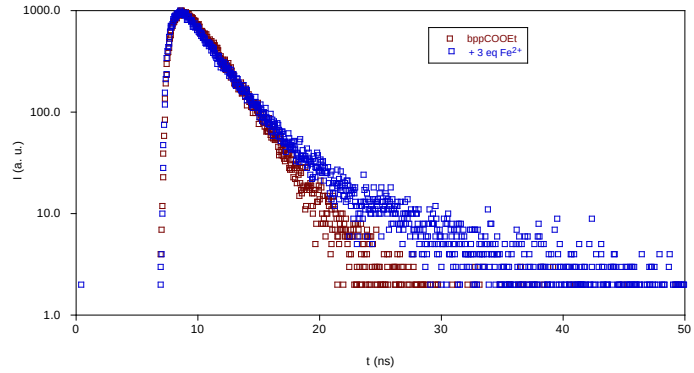

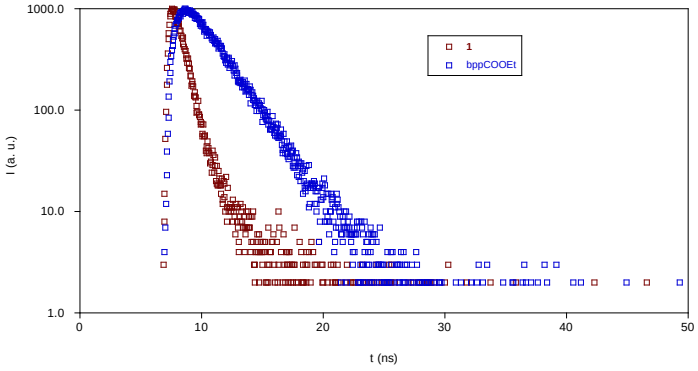

Figure S25. Emission lifetime measurements of **1** and model ligand bppCOOEt.

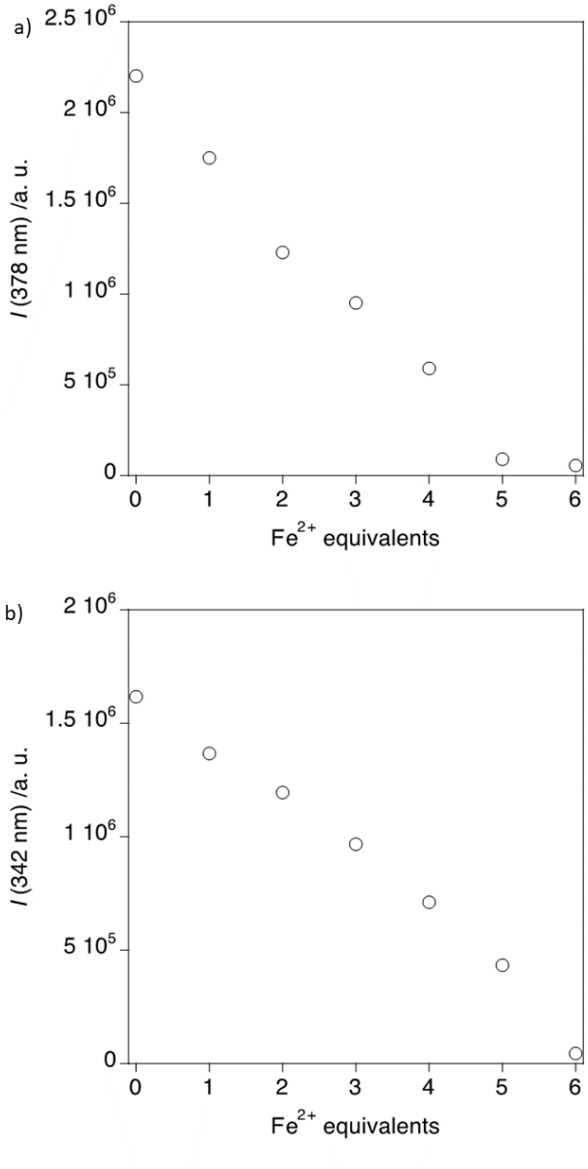

Figure S26. Emission intensity values of 5 × 10^{-6} M solutions after correcting inner filter effects of a) **1** and b) **2** upon addition of $Fe(ClO_4)_2$.

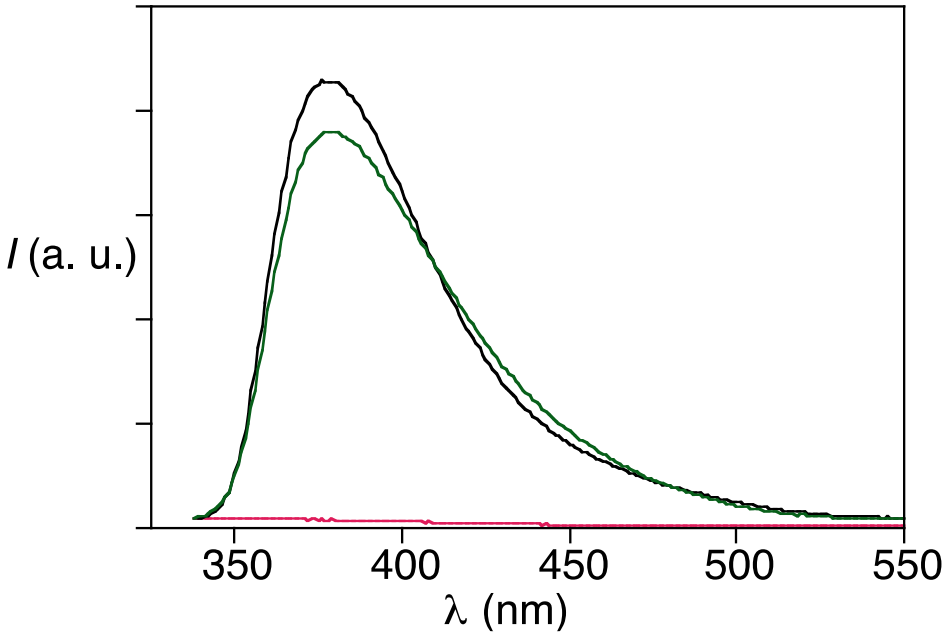

Figure S27. Fluorescence spectra of a 5×10^{-6} M solution of **1** (black line) after addition of 6 equivalents of $Fe(ClO_4)_2$ (red line) and 16 equivalents of 1,10-phenantroline (phen) (green line).

3.3 Absorption and fluorescence titration of methylated derivative **3** with $Fe(ClO_4)_2$

UV-vis and fluorimetric titrations of the methylated derivative **3** presented a similar behavior to that of **1** with a MLCT band in the UV-vis spectrum at 469 nm and an emission of the ligand centered at 390 nm, which was completely quenched after addition of 6 equivalents of Fe^{2+}. This is consistent with a LS state of the metal complexes of this ligand. The same trend was observed for the unsubstituted bpp ligand.[4]

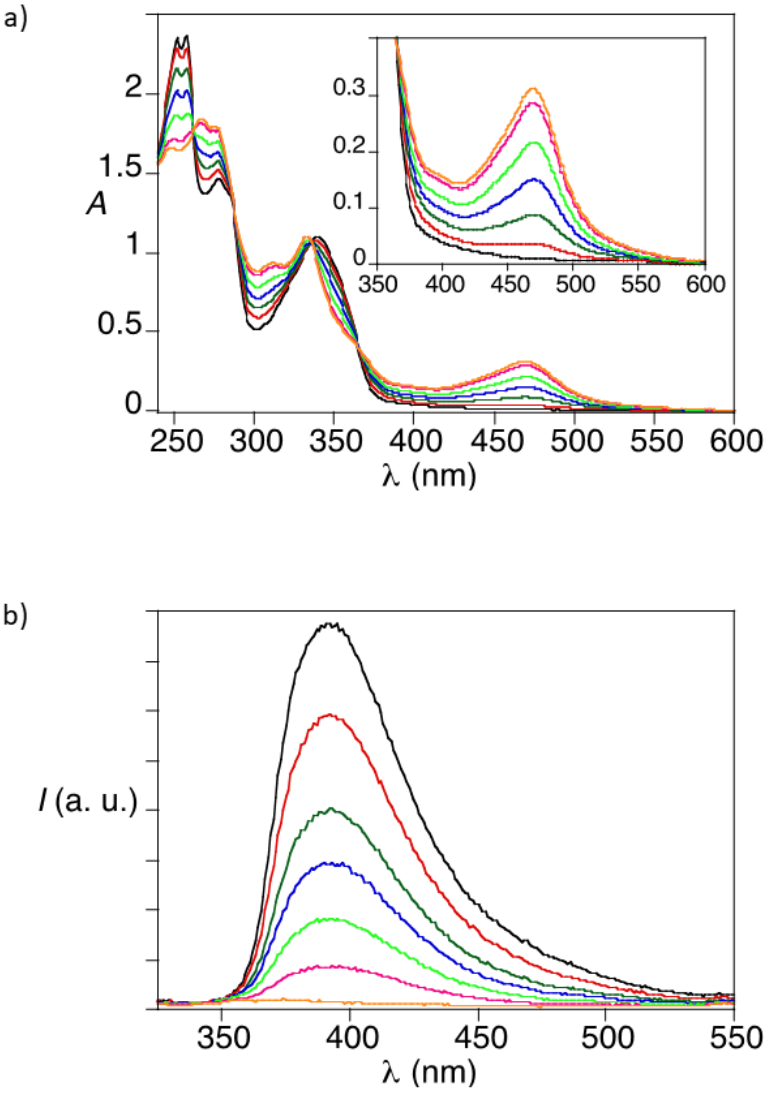

Figure S28. a) UV-vis and b) fluorescence spectra of a titration of a 7.5×10^{-6} M solution of **3** in CH_2Cl_2 with $Fe(BF_4)_2$. Black (0 eq.), red (1 eq.), dark green (2 eq.), blue (3 eq.), clear green (4 eq.), pink (5 eq.) and orange (6 eq.). Excitation wavelength was 320 nm.

3.4 UV-vis absorption and fluorescence titrations of **4.**

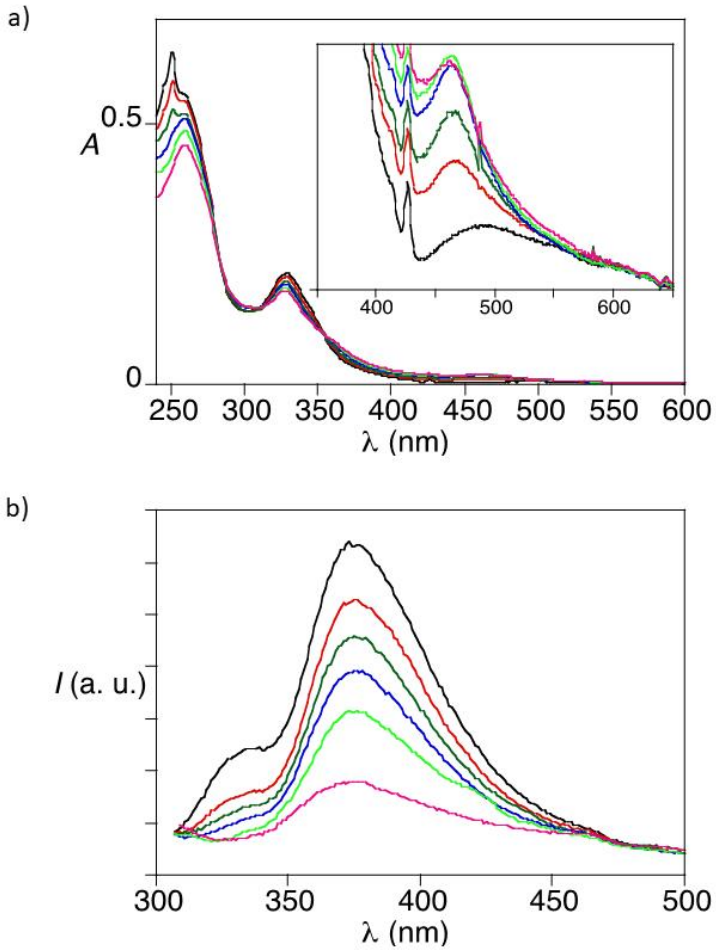

Figure S29. a) UV-vis and b) fluorescence spectra of a 1.5×10^{-5} M solution of **4** after addition of up to 1.5 equivalents of $Fe(ClO_4)_2$. Black (0 eq.), red (0.25 eq.), dark green (0.5 eq.), blue (0.75 eq.), clear green (1 eq.) and pink (1.5 eq.). Excitation wavelength was 285 nm.

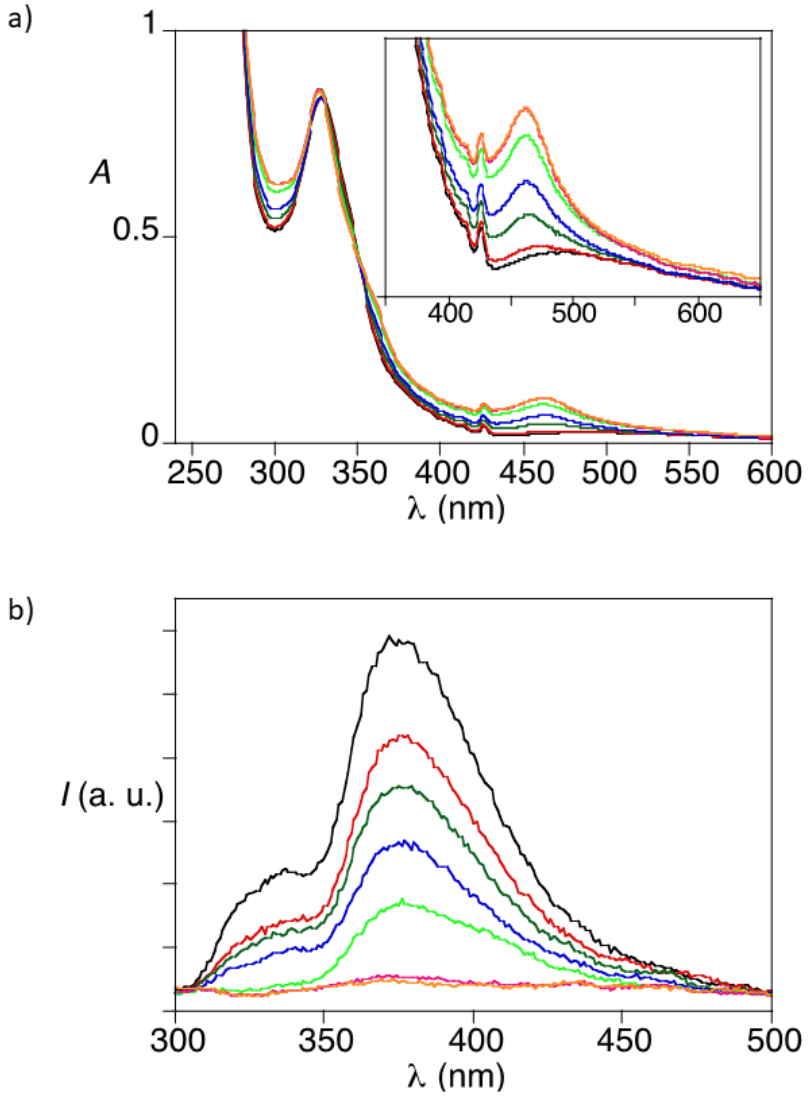

Figure S30. a) UV-vis and b) fluorescence spectra of a 4.5×10^{-5} M solution of **4** after addition of up to 0.75 equivalents of $Fe(ClO_4)_2$ Black (0 eq.), red (0.125 eq.), dark green (0.25 eq.), blue (0.375 eq.), clear green (0.5 eq.), pink (0.675 eq.) and orange (0.75 eq.). Excitation wavelength was 285 nm.

3.5 Excitation and absorption spectra of **1**, **2** and **4**

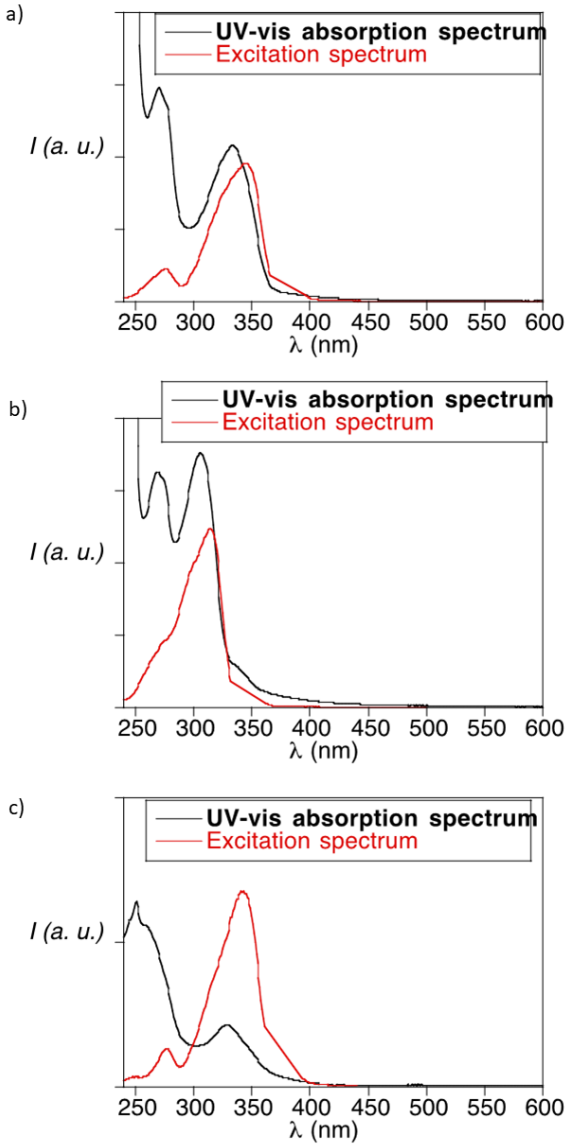

Figure S31. Excitation and absorption spectra of 7.5×10^{-6} M solutions of a) **1**, b) **2** and c) **4** in CH_2Cl_2.

3.6 Temperature dependence of UV-vis absorption spectra of **2**

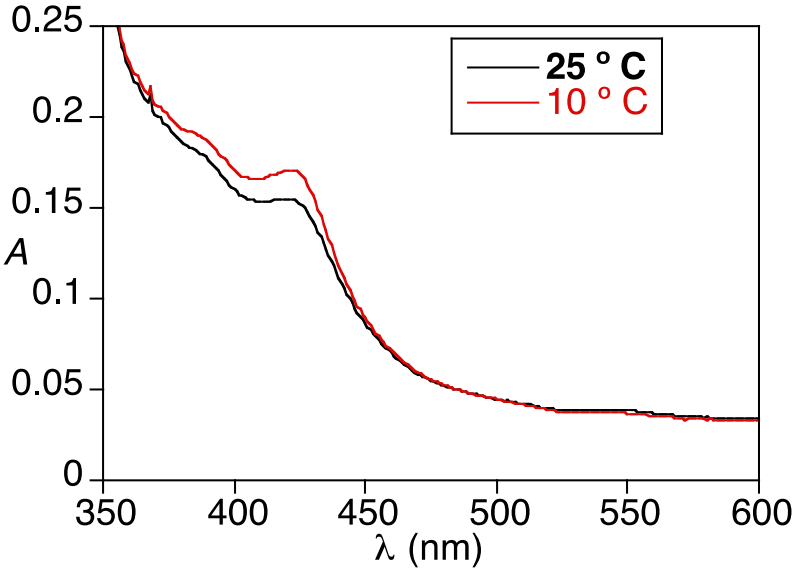

Figure S32. UV-vis spectra of a 7.5 × 10^{-6} M solution of **2** with 6 equivalents of Fe^{2+} in CH_2Cl_2 at 298 (black line) and 283 K (red line).

4. Theoretical calculations

Several complexation environments were modelled using a mono- or a di-malonate derivative bearing short bppCOOR arms as in ligands **1** and **4** or long bppCH_2OR arms as in **2**. The situations modelled include complex formation between the two bpp arms of a malonate branch (A), between bpp arms of two malonate branches (B) and between bpp arms of vicinal C_{60} molecules (C) (Figure S33). Two BF_4^- counterions per complex formation were included for electroneutrality. Minimum-energy geometries and binding energies for the complexation process were calculated under the cost-effective GFN2-xTB approach using the Grimme's xTB program.[5] The GFN2-xTB method is based on a Hamiltonian similar to the well-known DFTB3,[6] uses a minimal valence basis set centered on atoms (STO-mG), and includes the latest density-dependent D4 dispersion correction. Binding energies (Table 1 in the main text) were calculated as the energy difference between products and reactants of the complexation process according to Scheme S5.

$$\Delta E_{\text{bind}} = \left(E_{\text{complex}} + E_{6-\text{water}}\right) - \left(E_{\text{ligand}} + E_{\text{Fe(II)}-\text{water}-\text{BF}_4^-}\right)$$

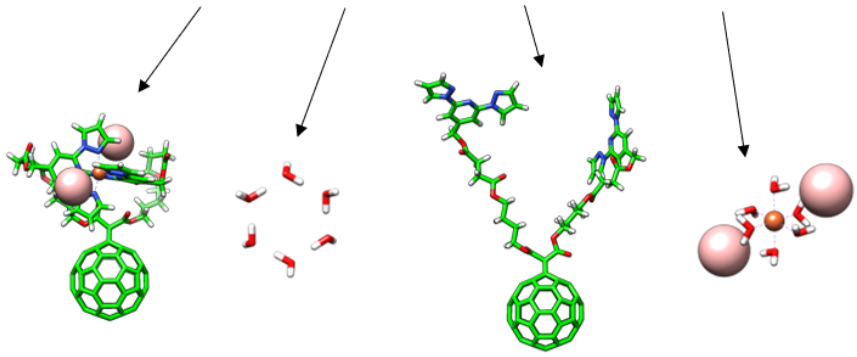

Scheme S5. Calculation of the binding energy of the Fe(II) complex using six water molecules to solvate the Fe^{2+} ion and two BF_4^- counteranions to maintain the electroneutrality. Note that for intermolecular complexation C (Figure S33), the E_{ligand} term is multiplied by two, whereas in complexes of

hexa-adducts **1** and **2** $E_{6-\mathrm{water}}$ and $E_{\mathrm{Fe(II)-water-BF_4^-}}$ are multiplied by six (Figure 4b).

Electronic structure calculations were performed under the density functional theory (DFT) framework by using the Gaussian-16.A02 suite of programs.[7] Simplified complexes **C0-2** (Figure S35) and their corresponding ligands **L0-2** were modelled and their minimum-energy geometries were obtained at the B3LYP/def2-SVP/LANL2DZ(Fe) level of theory.[8] Closed-shell low-spin (LS, 2S+1=1) and open-shell high-spin (HS, 2S+1=5) configurations were considered for the Fe(II) complexes by employing the restricted (R) and unrestricted (U) versions of the B3LYP functional, respectively, and a total charge of +2. Solvent effects were included by means of the self-consistent reaction field (SCRF) approach, with the polarizable continuum model (PCM) and dichloromethane as solvent. Table S1 collects the relative energy of HS complexes **C0-2** with respect to the LS state in both vacuum and solvent.

Theoretical absorption spectra were obtained by calculating the 120 lowest-lying electronic excited states at the time-dependent DFT (TD-DFT) (U)B3LYP*/def2-SVP/LANL2DZ(Fe) level of theory including solvent effects (PCM, dichloromethane). Note that the B3LYP* functional is a reparameterization of B3LYP with a reduced admixture of the Hartree−Fock (HF) exchange (15%), optimal to alleviate the deficiencies of DFT in calculating the energy difference between the ground state and the lowest-lying excited states of iron pseudo-octahedral complexes.[9] For Fe(II) complexes in the LS state, singlet $\rightarrow$ singlet ($S_0 \rightarrow S_n$) electronic transitions were calculated at the geometry optimized for the LS electronic ground state S_0 (Figure S36). In the HS state, quintuplet $\rightarrow$ quintuplet ($Q_0 \rightarrow Q_n$) electronic transitions were calculated using the UB3LYP geometry optimized for the lowest-energy quintuplet Q_0 (Figure S36). The theoretical simulation of the absorption spectra (Figure 5a in the main text and

Figure S37) was obtained by convoluting the electronic transitions with Gaussian functions of full-width-at-half-maximum of 0.1 eV. The nature of the most relevant electronic excitations was assessed by calculating the corresponding natural transition orbitals (NTOs) (Figures S38-S43).[10] The absorption spectrum in a simulated titration experiment was obtained by weighting the initial (ligand **L1** or **L2**) and final (complex **C1** and **C2**) spectra from 1 to 0 and from 0 to 1, respectively, in steps of 0.1 (Figure 5b and 5c in the main text). To calculate the spectra, the experimentally estimated ratio of 100:0 and 25:75 for LS:HS was used in **C1** and **C2**, respectively.

The relative position of the ground state and the lowest-lying singlet/triplet excited states was calculated for ligands **L0**–**1** and complexes **C0**–**2** systems in their LS state at the TD-B3LYP*/def2-SVP/LANL2DZ(Fe) level in DCM (Table S2). The geometry of the lowest-energy singlet (S_1) and triplet (T_1) excited states was fully optimized by using the time-dependent approach along with the OPT keyword of Gaussian16-A03 at the TD-B3LYP/def2-SVP/LANL2DZ(Fe) level.

Theoretical simulations of the Raman spectra (Figure S50) were obtained by performing frequency calculations at the BHandHLYP/def2-SVP/LANL2DZ(Fe) level of theory.[11] Raman-active vibrational modes were represented by means of the Chemcraft software.[12]

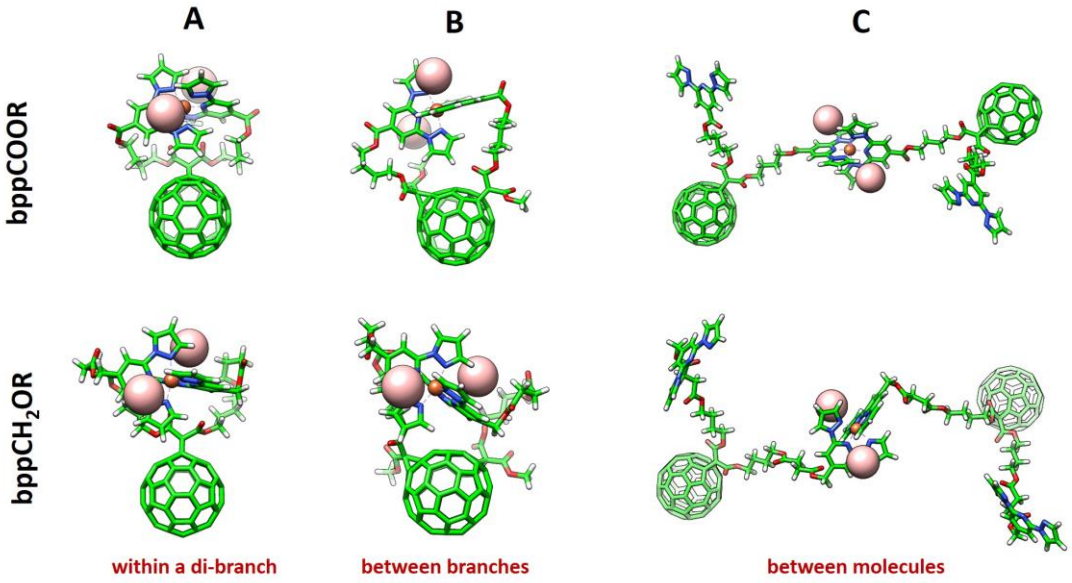

Figure S33. Minimum-energy structures calculated at the GFN2-xTB level of theory for configurations A, B and C of Fe(II) complexes bearing short bppCOOR ligands as in **1** and **4** (top) and long bppCH$_2$OR ligands as in **2** (bottom).

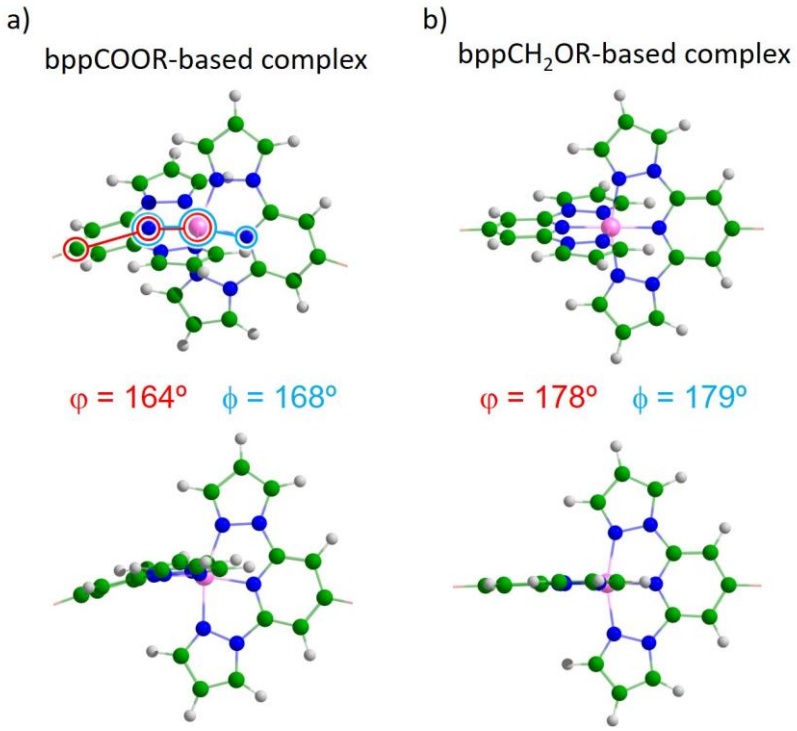

Figure S34. Tilted (top) and lateral (bottom) views of the minimum-energy coordination environment calculated at the GFN2-xTB level for configuration A of the mono-malonate complexes formed by the bppCOOR ligand (a) and the bppCH$_2$OR ligand (b).

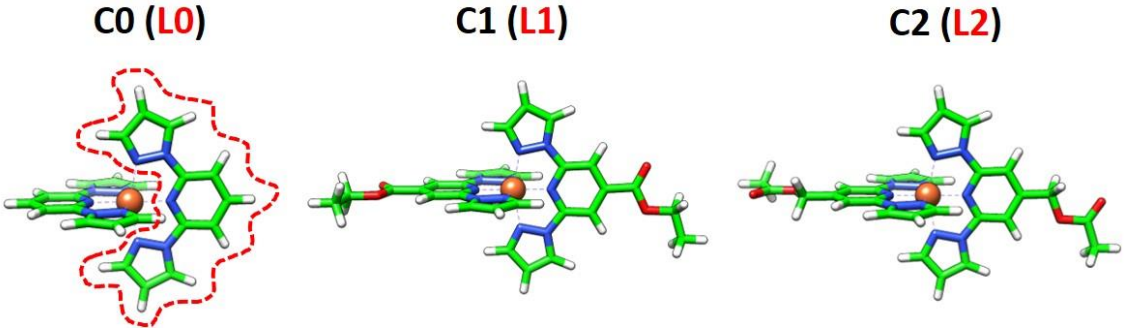

Figure S35. Representation of the model Fe(II) complexes **C0-2** and their respective bpp (**L0**), bppCOOEt (**L1**) and bppCH$_2$OCOCH$_3$ (**L2**) ligands.

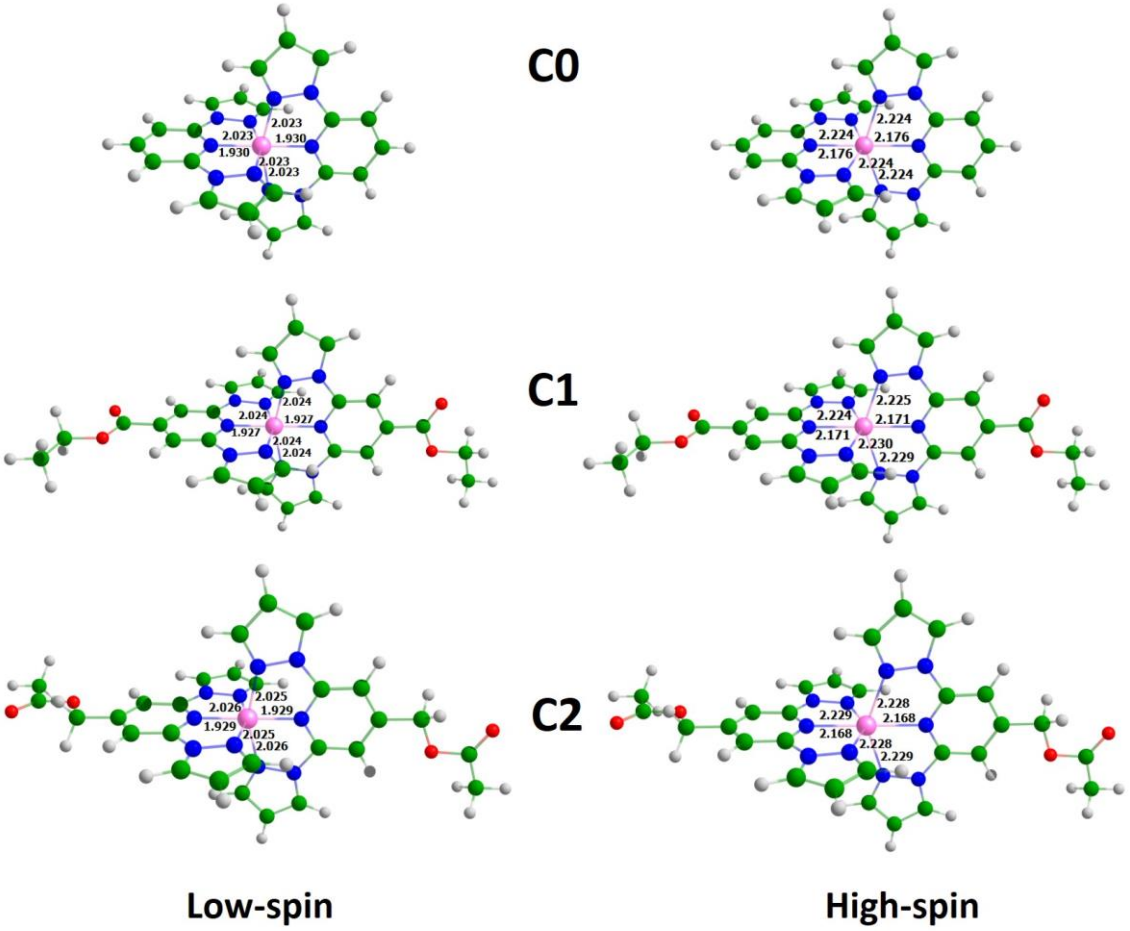

Figure S36. B3LYP/def2-SVP/LANL2DZ(Fe) minimum-energy structures calculated for Fe(II) complexes **C0-2** in their low-spin and high-spin configurations. Coordination bond distances (in Å) are indicated.

Table S1. Energy of the high-spin state relative to the low-spin state (in eV) calculated for complexes **C0-2** at the B3LYP/def2-SVP/LANL2DZ(Fe) level of theory in vacuum and including solvent effects (dichloromethane).

	Vacuum	Solvent (DCM)
C0	–0.0388	0.0595
C1	–0.0311	0.0673
C2	–0.0500	0.0440

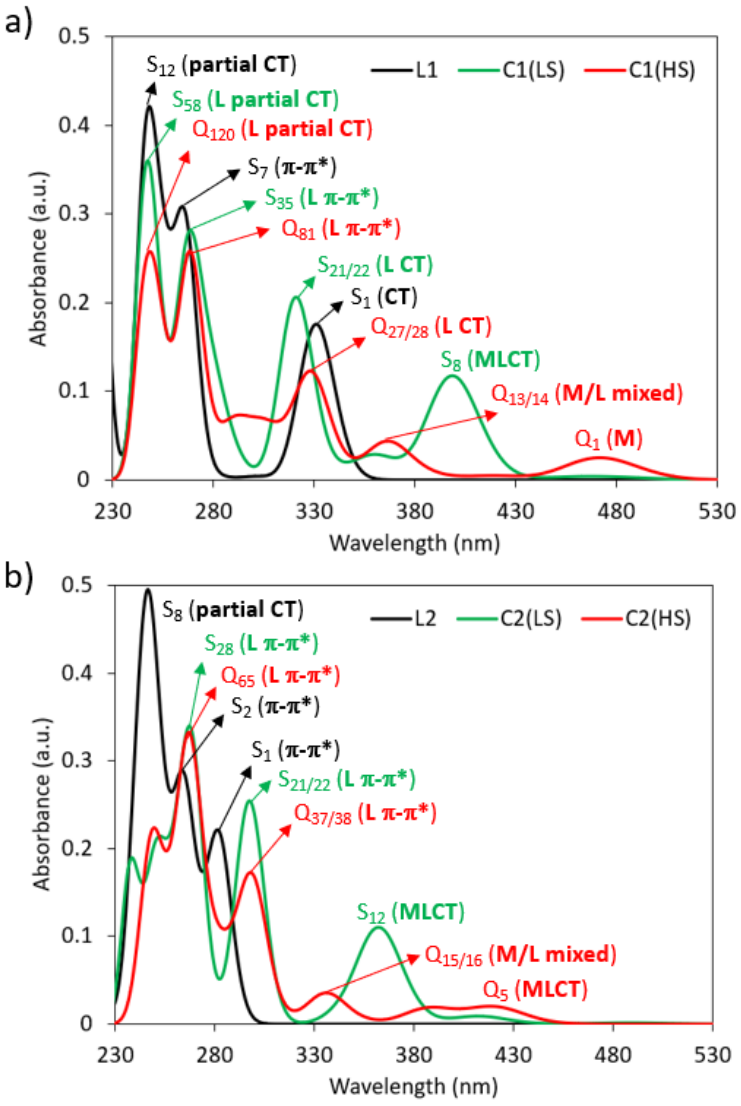

Figure S37. Theoretical absorption spectra calculated for a) **L1/C1** and b) **L2/C2**, at the (U)B3LYP*/def2-SVP/LANL2DZ(Fe) level including solvent effects. The spectra of complexes **C1** and **C2** are computed for both low-spin (LS) and high-spin (HS) states.

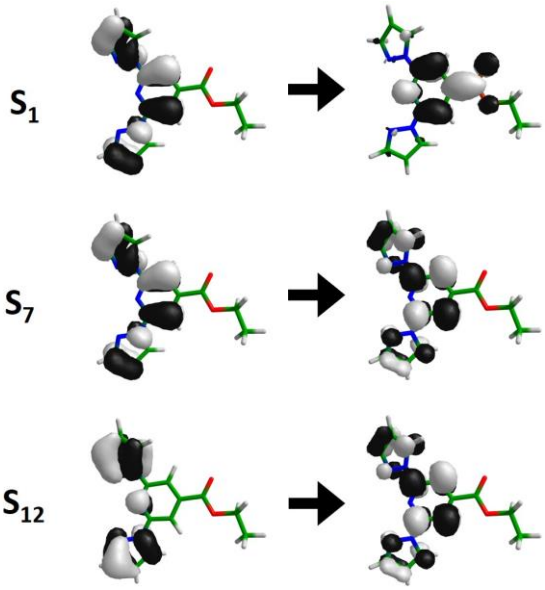

Figure S38. Natural transition orbitals (NTOs) that describe the nature of the most-intense $S_0 \rightarrow S_n$ electronic excitations calculated at the TD-DFT B3LYP*/def2-SVP level in DCM for ligand **L1** (Figure S37a, black line).

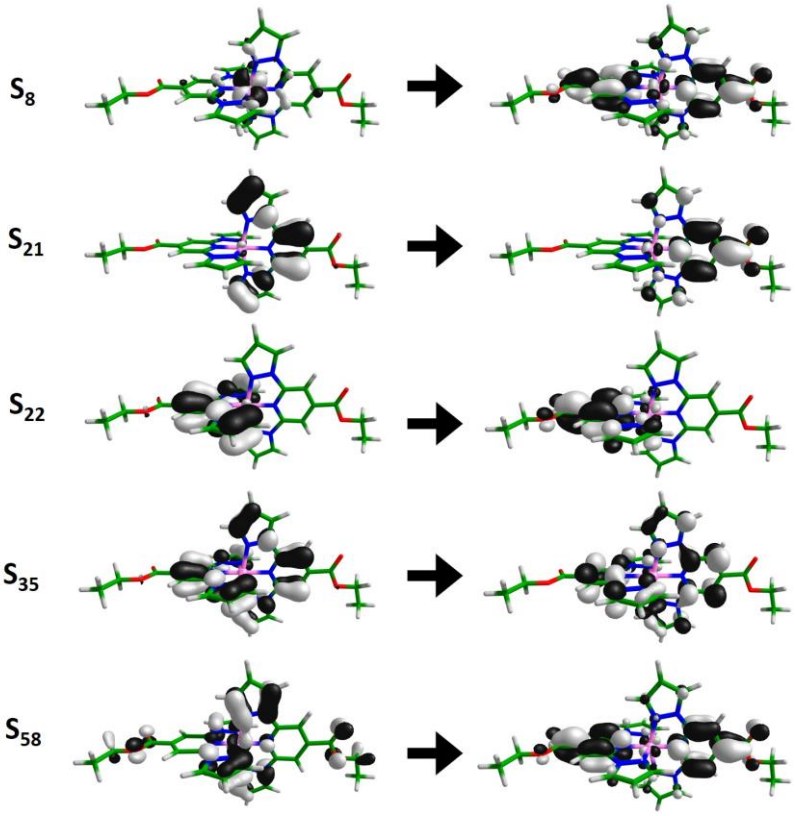

Figure S39. Natural transition orbitals (NTOs) that describe the nature of the most-intense $S_0 \rightarrow S_n$ electronic excitations calculated at the TD-DFT B3LYP*/def2-SVP/LANL2DZ(Fe) level in DCM for complex **C1**(LS) (Figure S37a, green line).

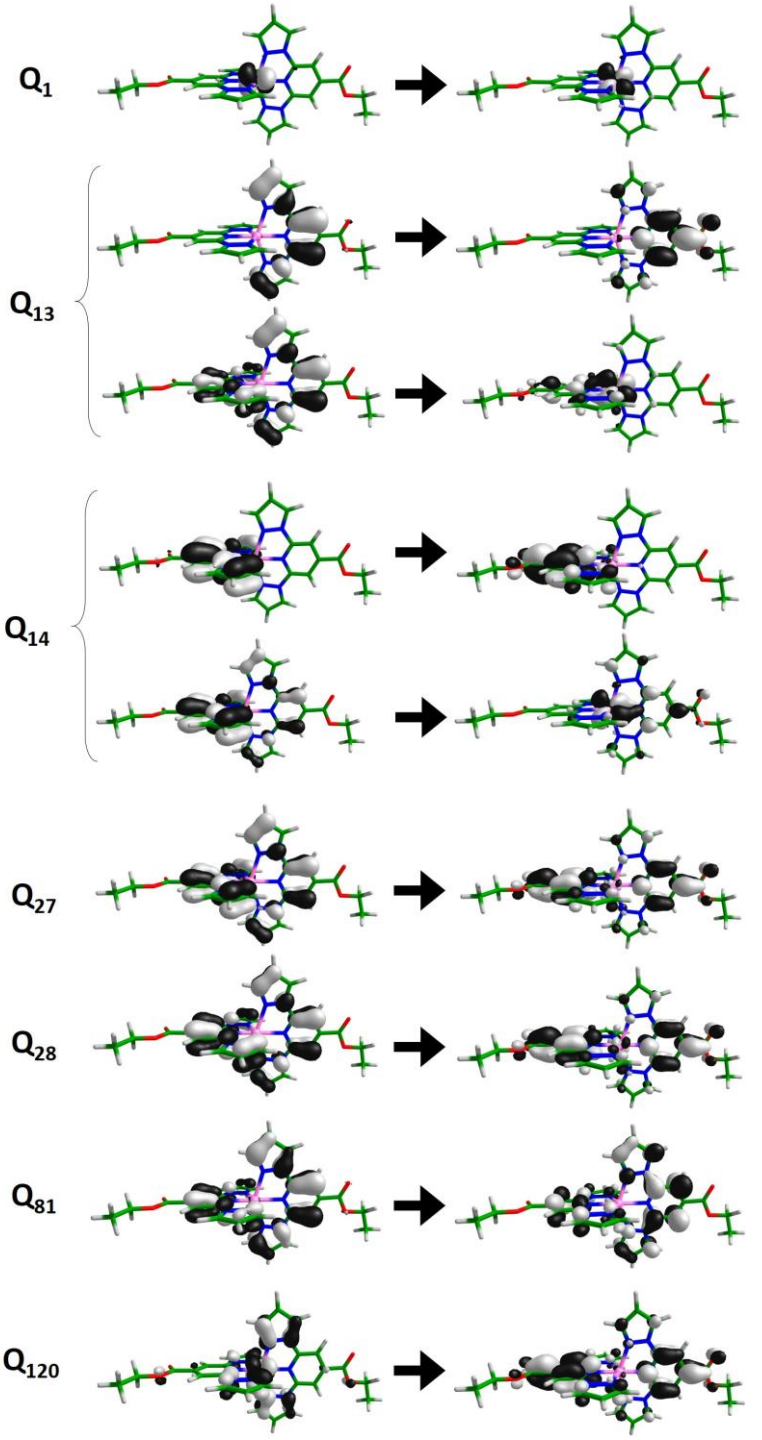
Q_1
Q_{13}
Q_{14}
Q_{27}
Q_{28}
Q_{81}
Q_{120}

Figure S40. Natural transition orbitals (NTOs) that describe the nature of the most-intense $Q_0 \rightarrow Q_n$ electronic excitations calculated at the TD-DFT UB3LYP*/def2-SVP/LANL2DZ(Fe) level in DCM for complex **C1**(HS) (Figure S37a, red line).

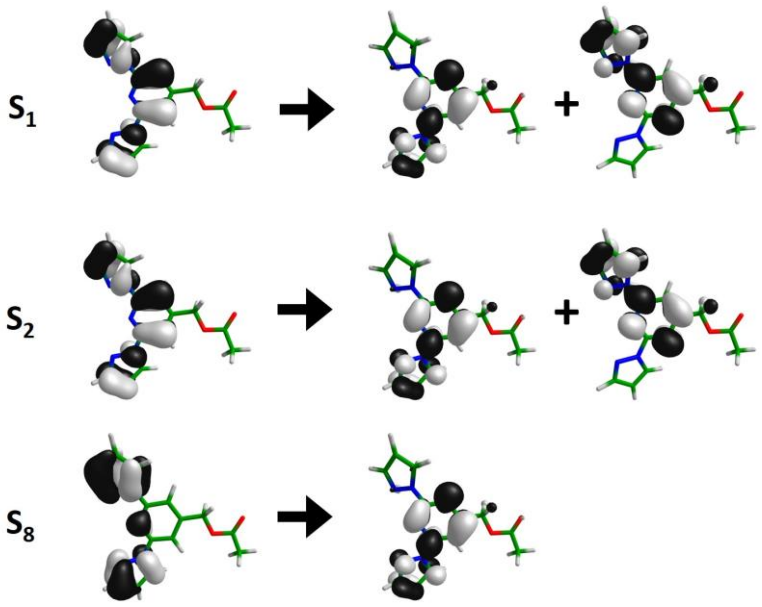

Figure S41. Natural transition orbitals (NTOs) that describe the nature of the most-intense $S_0 \rightarrow S_n$ electronic excitations calculated at the TD-DFT B3LYP*/def2-SVP level in DCM for ligand **L2** (Figure S37b, black line).

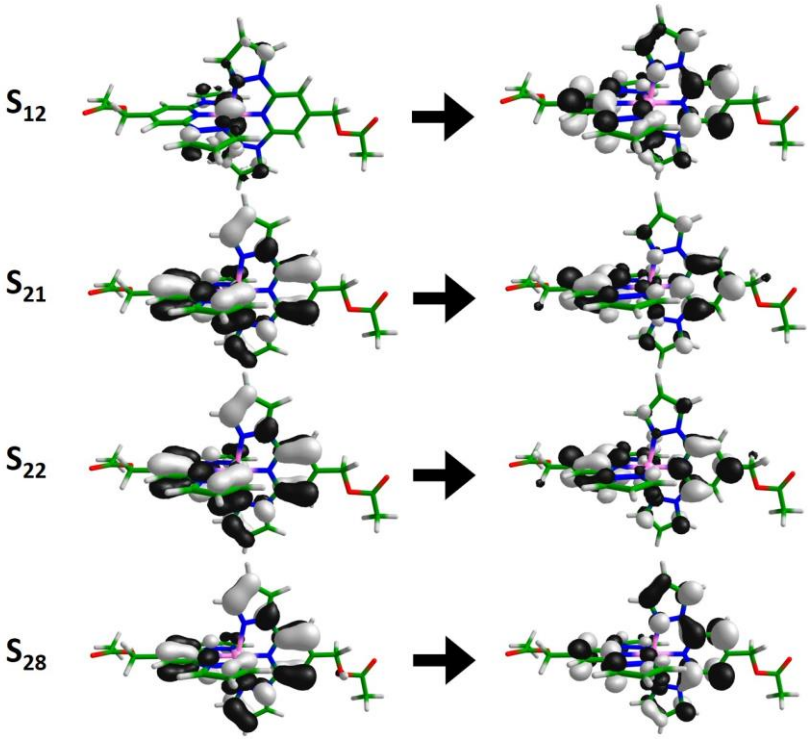

Figure S42. Natural transition orbitals (NTOs) that describe the nature of the most-intense $S_0 \rightarrow S_n$ electronic excitations calculated at the TD-DFT B3LYP*/def2-SVP/LANL2DZ(Fe) level in DCM for complex **C2**(LS) (Figure S37b, green line).

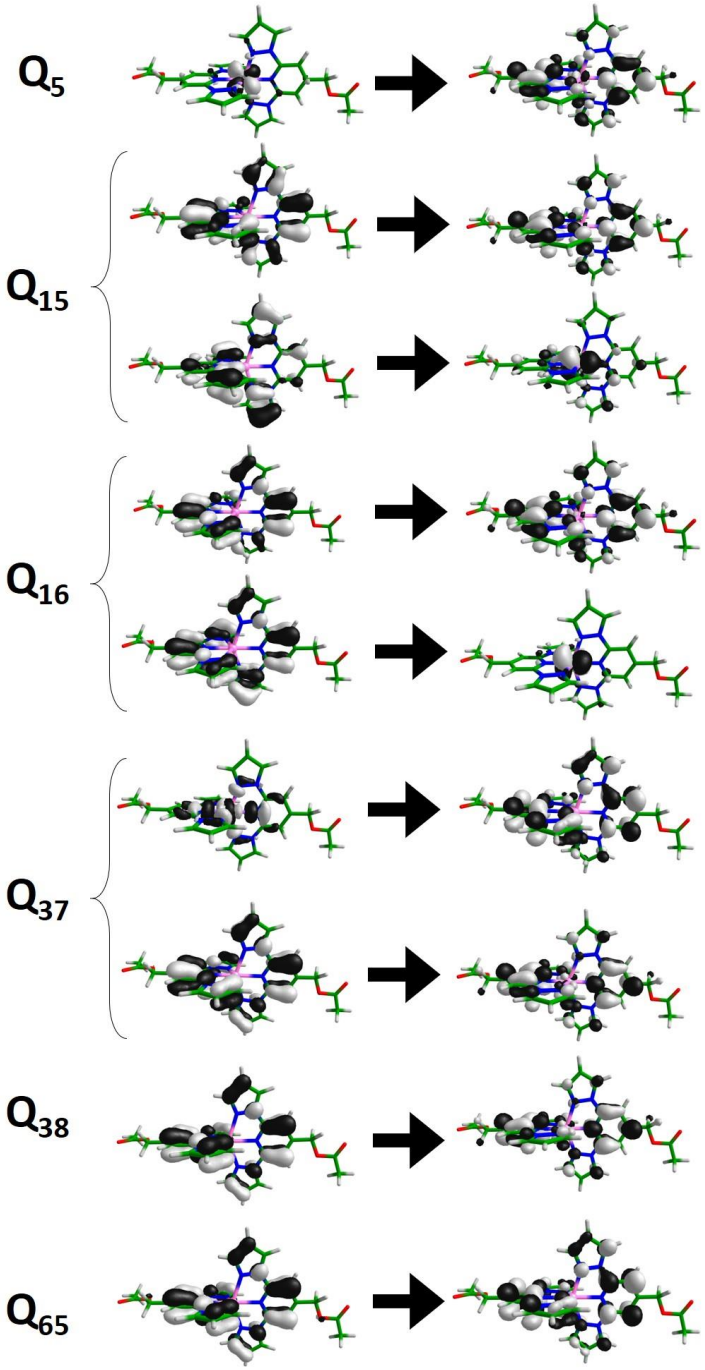
Q_5
Q_{15}
Q_{16}
Q_{37}
Q_{38}
Q_{65}

Figure S43. Natural transition orbitals (NTOs) that describe the nature of the most-intense $Q_0 \rightarrow Q_n$ electronic excitations calculated at the TD-DFT UB3LYP*/def2-SVP/LANL2DZ(Fe) level in DCM for complex **C2**(HS) (Figure S37b, red line).

Table S2. Energy difference (in eV) between the first singlet (S_1) and triplet excited state (T_1) and the ground state (S_0) at the various potential energy wells of ligands **L0**–**1** and complexes **C0**–**2** systems in their LS state at the B3LYP*/def2-SVP/LANL2DZ(Fe) level in DCM.

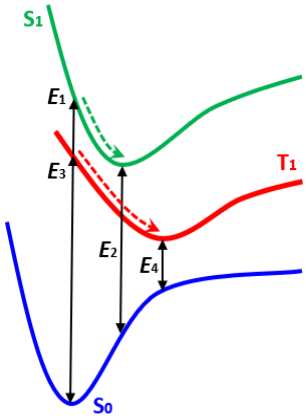

	***E*₁** (S_1-S_0)	***E*₂** (S_1-S_0)	***E*₃** (T_1-S_0)	***E*₄** (T_1-S_0)
L0	4.4159	4.1086	3.4364	3.1371
L1	3.7436	3.3151	3.1313	2.4699
L2	4.3982	3.7217	3.4210	2.5900
C0-LS	2.0976	1.5018	1.0079	–0.7151
C1-LS	2.0937	1.4984	1.0028	–0.7161
C2-LS	2.0837	1.4884	0.9865	–0.7290

5. Studies in the solid state

5.1 Precipitation procedure for **5** and **6** and general characterization

Synthesis of **5**: In a glovebox, **1** (25mg, 0.005 mmol) was dissolved in 0.8 mL of dry dichloromethane. After this, $Fe(BF_4)_2$ was added in a MeCN solution (6.25 mL, 9.6 mM). After the addition of the iron salt, an instantaneous change of color from orange to red takes place. The solution was left stirring for 10 minutes and diethyl ether (40 mL) was added giving rise to a jelly red precipitate. The precipitate was washed several times with diethyl ether and dried in air to yield a homogeneous dark red powder (m_{prod} = 21.3 mg, yield 57%). Elemental analysis calcd for $[(Fe(BF_4)_2)]_6C_{270}H_{192}N_{60}O_{48}(H_2O)_{60}$: C 43.19, N 11.20, H 4.19; found: C 43.23, N 10.74, H 3.91.

Synthesis of **6**: In a glovebox, **2** (25 mg, 0.0041 mmol) was dissolved in 0.8 mL of dry dichloromethane. After this, $Fe(BF_4)_2$ was added in a MeCN solution (5.2 mL, 9.6 mM). After the addition of the iron salt, an instantaneous change of color from orange to yellow takes place. The solution was left stirring for 10 minutes and diethyl ether (40 mL) was added giving rise to a yellow precipitate. The precipitate was washed several times with diethyl ether and dried to the air to yield a homogeneous yellow powder (m_{prod} = 16.8mg, yield 52%). Elemental analysis calcd for $[Fe(BF_4)_2]_6C_{318}H_{264}N_{60}O_{72}(H_2O)_{20}$: C 48.87, N 10.75, H 3.92; found: C 49.02, N 10.15, H 3.81.

Elemental analysis was consistent with the presence of 60 or 20 water molecules (see above). The thermogravimetric analysis (TGA) of **5** (Figure S44) shows a weight loss of solvent molecules at 110 °C (13 %), which is consistent with the loss of 60 water molecules (expected weight loss of 14 %). Complex **6** shows a different behavior, a gradual weight loss starts at 30 °C until a sharp decrease occurs at 230 °C. The weight loss until this point (4.9%) agrees with the expected loss of 20 water molecules (4.6%). The IR spectrum of **5** presents the characteristic bands of BF_4^- counteranions and those

assigned to aromatic C=N and C=C bonds from the bpp units between 1500 and 1700 cm^{-1} (Figure S45). XPS spectra of **5** and **6** confirmed the presence of all the expected atoms (Fe, C, N, O, B and F) (Figures S46 and S47) and provide calculated ratios of 1:7.5:1.9:8 for Fe:N:B:F in **5** and 1:10.3:1.41:8.2 in **6**. These results confirmed that the charge of Fe^{2+} was compensated by the BF_4^- counterions. Although the quantification of the Fe:N ratio is not accurate with this technique, the values obtained for both systems are consistent with the presence of two bpp units per iron atom (the expected Fe:N ratio is 1:10).

The electrospray ionization mass spectrometry (ESI-MS) spectra of the precipitate of **1** and 12 equivalents of $Fe(ClO_4)_2$ dissolved in a mixture of dimethylformamide and methanol showed the presence of several species with up to six Fe^{2+} coordinated to **1** plus ClO_4^- counteranions (being M the fullerene ($C_{270}H_{192}N_{60}O_{48}$). The isolated species were: 2550Da $[M+Fe]^{2+}$, 2677Da [M+2Fe+2(ClO4)]2+, 2805Da[M+3Fe+4(ClO_4)]2+, 1751Da [M+2Fe+(ClO_4)]3+, 1836Da [M+3Fe+3(ClO_4)]3+, 1921Da [M+4Fe+5(ClO_4)]3+, 2006Da [M+5Fe+7(ClO_4)]3+ and 2091Da [M+6Fe+9(ClO4)]3+). The spectra of the precipitate of **2** and 12 equivalents of $Fe(BF_4)_2$ dissolved in acetonitrile showed a similar behavior. Several species with up to six Fe^{2+} coordinated to **2** plus counter anions were detected.

5.2 Physical characterization

Elemental analyses (C, H and N) were performed with a CE Instruments EA 1110 CHNS Elemental analyzer. TGA was performed in Mettler Toledo TGA/SDTA 851e Thermogravimetric and Differential Thermal Analyzer. IR measurements were performed in a Fourier Transformation-Infrared Spectrometer NICOLET 5700. XPS (K-ALPHA, Thermo Scientific) was used to analyze the surfaces of the samples. All spectra were collected using Al Kα radiation (1486.6 eV),

monochromatized by a twin crystal monochromator. Magnetic measurements of **5** and **6** were performed with a Quantum Design MPMS-XL-5 SQUID magnetometer with an applied magnetic field of 0.1 T. Solvated samples of **5** and **6** were deposited in the bottom of a glass tube and covered with the mother liquor. This tube was used as the sample holder. These samples were corrected from the diamagnetism of the compound and sample holder using Pascal constants and the magnetic properties of a sample holder containing only the mother liquor. Photomagnetic measurements were performed irradiating with a 30993 cylindrical Helium-Neon Laser system from Research Electro-Optics (red light, λ= 633 nm, optical power 12 mW cm^{-2}) coupled via an optical fiber to the cavity of the SQUID magnetometer. It was verified that irradiation resulted in no significant change in magnetic response due to heating of the sample. The photomagnetic samples consisted of a thin layer of compound whose weight was corrected by comparison of a thermal spin crossover curve with that of a more accurately weighted sample of the same compound. Solvated samples were protected with an oil immediately after being extracted from the mother liquor. To estimate the HS Fe(II) fraction of these complexes we have assumed a contribution in $\chi_M T$ per HS Fe(II) of 3.5 emu K mol^{-1}, which is an average value taking into account that typical $\chi_M T$ values for this type of complexes range from 3.2 to 3.8 emu K mol-1 depending on the orbital contribution.

5.3 Thermogravimetric analysis (TGA)

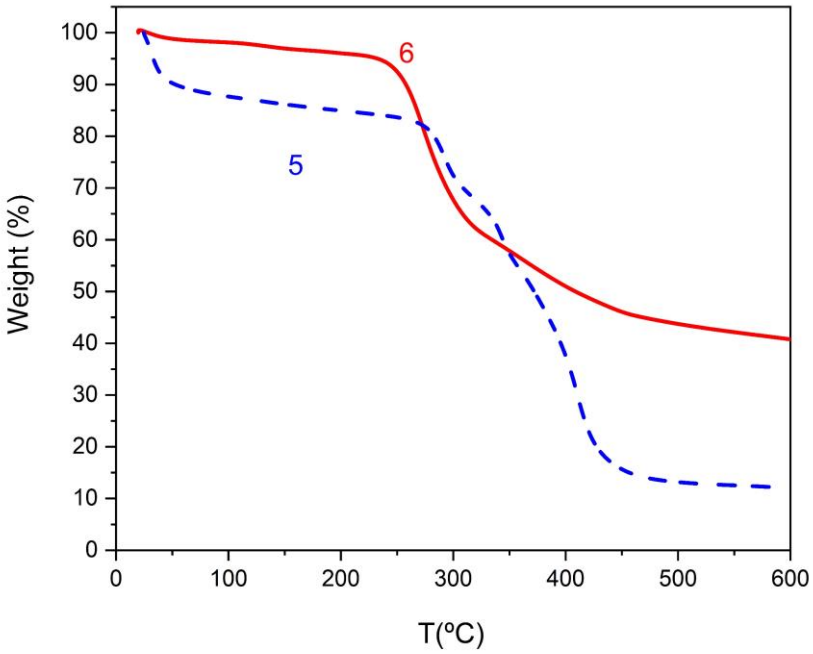

Figure S44. TGA analysis of **5** (dashed line) and **6** (solid line).

5.4 Infrared spectroscopy

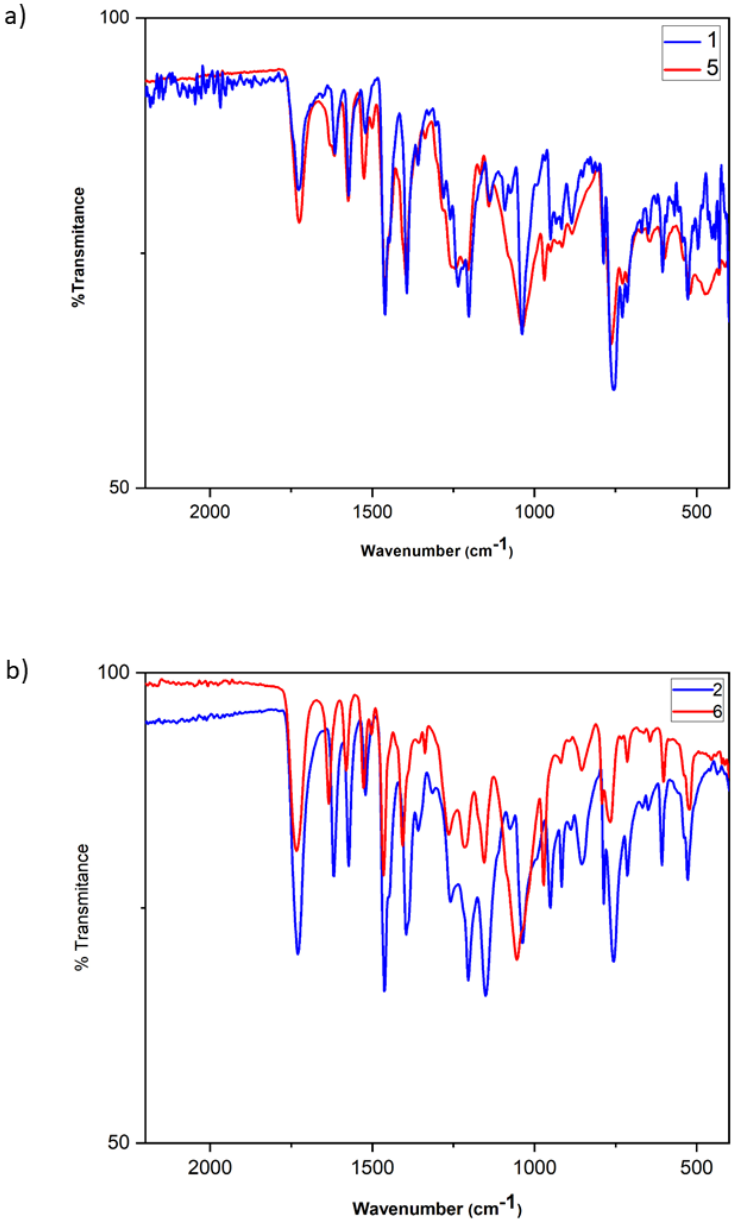

Figure S45. Infrared spectra of **1** and **5** (a) and **2** and **6** (b).

5.5 X-ray photoemission spectroscopy (XPS)

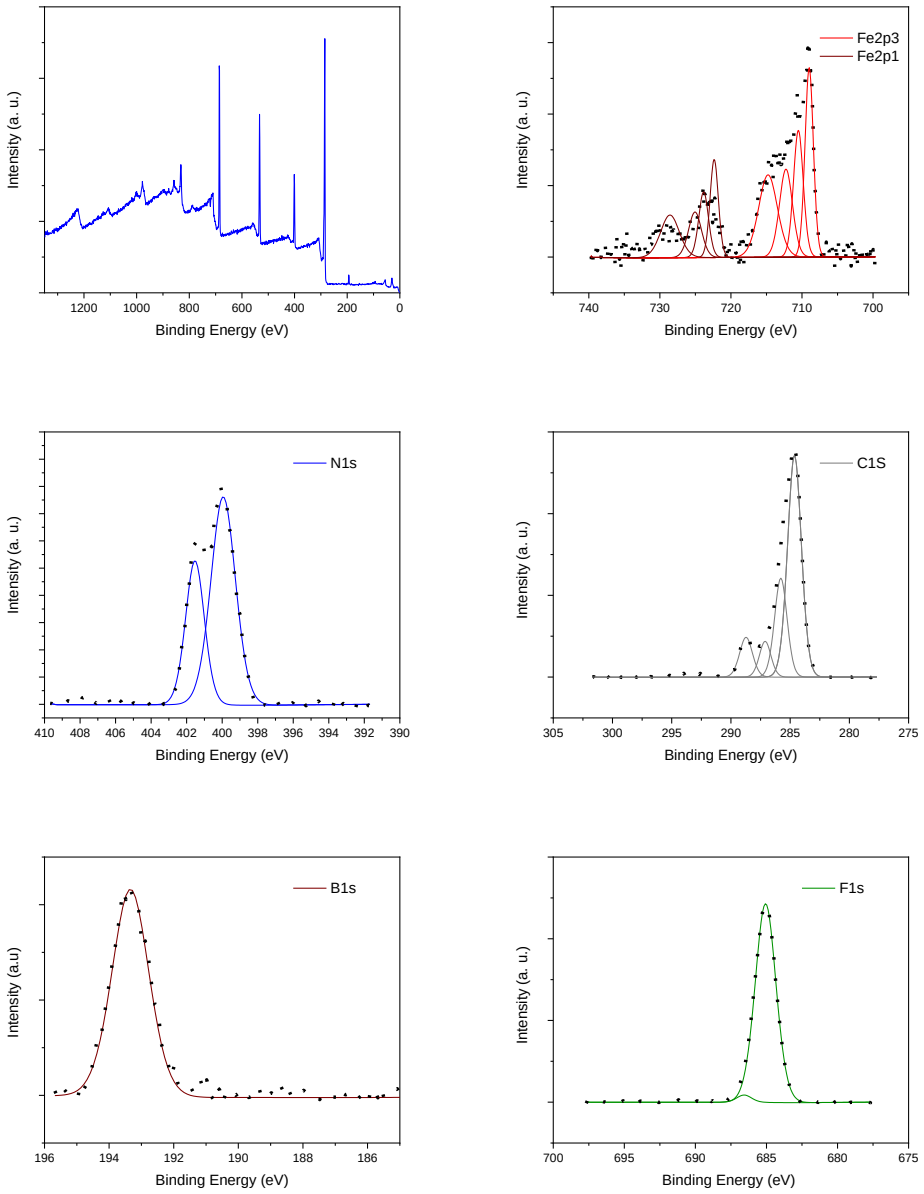

Figure S46. XPS spectra of complex **5.** Black dots represent the experimental spectrum**.**

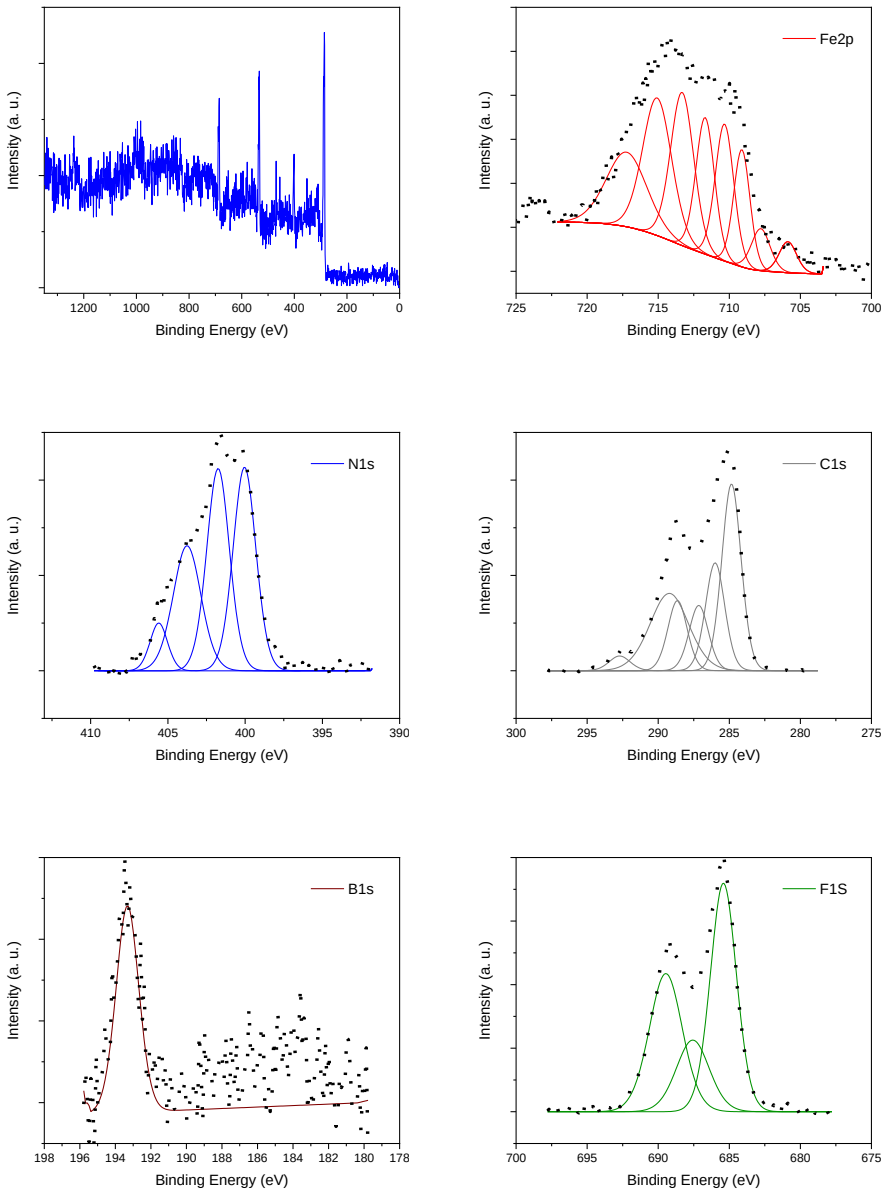

Figure S47. XPS spectra of complex **6**, black dots represent the experimental spectrum.

5.6 Magnetic properties of the filtered samples

Figure 7 shows the temperature dependence of $\chi_M T$ measured for desolvated samples of **5** and **6** measured in absence of a diethyl ether protecting layer or grease. Both samples exhibit a gradual and incomplete spin-crossover with temperature. For **5**, previously heated at 400 K, the gradual decrease of $\chi_M T$ from 20.0 emu K mol^{-1} at 400 K to 11.2 emu K mol^{-1} at 50 K is consistent with a decrease of the HS fraction from around 90 to 50%. Higher $\chi_M T$ values in all the range of temperatures are obtained for a filtered sample of **6**, in line with the higher HS fraction observed in solution for **2** coordinated to Fe^{2+} and for both samples measured in contact with a diethyl ether protecting layer. Thus, $\chi_M T$ of **6** decreases from 21.7 emu K mol^{-1} (~100 % HS fraction) at 300 K to 15.1 emu K mol^{-1} at 50 K (~70 % HS fraction). The more pronounced decrease of $\chi_M T$ observed at lower temperatures for the two compounds is likely due to the zero-field splitting of Fe(II).

Magnetic measurements after irradiation with red light at 10 K were carried out, observing a partial LIESST effect in both samples. Irradiation with a 633 nm laser at 10 K leads to a drastic increase of the magnetic signal reaching saturation after ca. 1 h. An increase of $\chi_M T$ to reach a maximum value of 16.6 emu K mol^{-1} (~80 % HS fraction) for **5** and 19.2 emu K mol^{-1} (~90 % HS fraction) for **6** at around 40 K, reflecting a zero-field splitting of HS Fe(II), was observed. This suggests partial LS to HS photoconversion (see Figure 7).

5.7 Raman

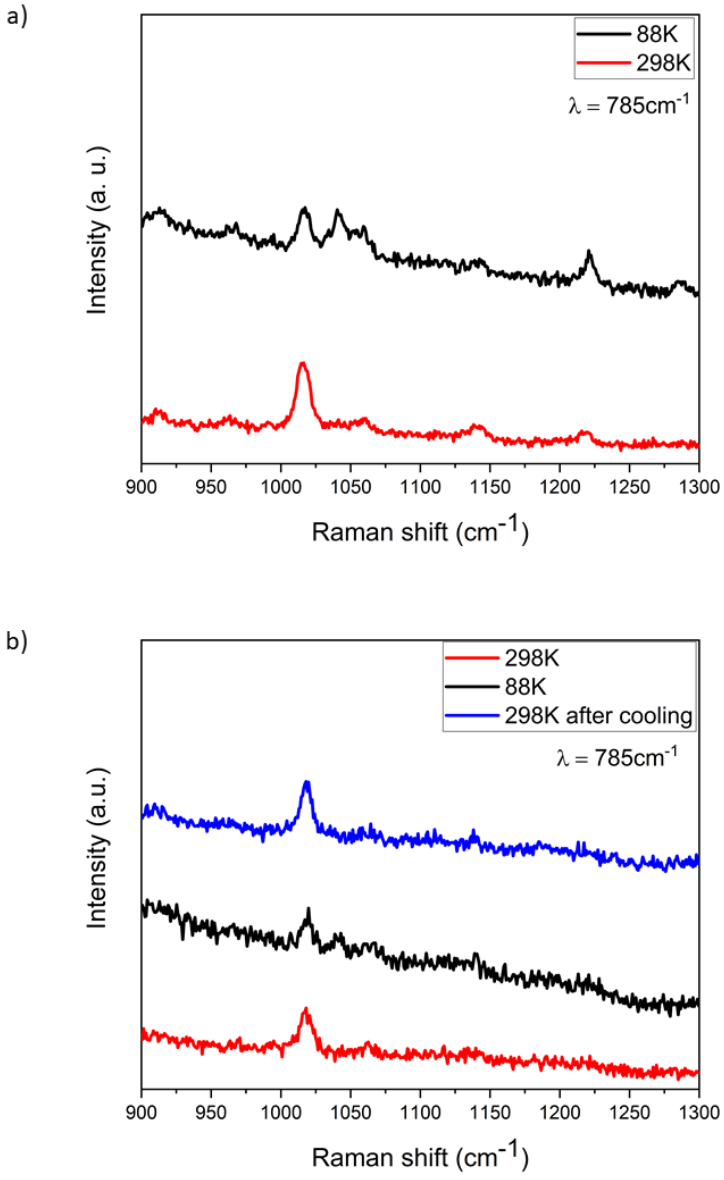

Figure S48. Raman spectra of filtered samples of **5** (a) and **6** (b) complexes at different temperatures.

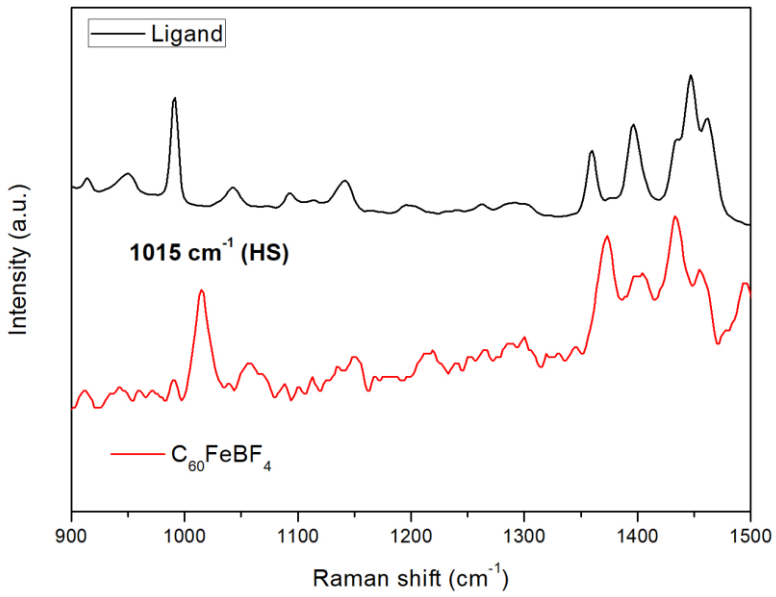

Figure S49. Raman spectra of hexa-adduct **1** (black) and complex **5** (red).

By using complex **C0** as a simple model of the Fe(II)-complex with pristine bpp ligands, the Raman spectra for HS and LS states were calculated at the BHandHLYP/def2-SVP/LANL2DZ(Fe) level of theory (Figure S50). Theoretical calculations indicate that a Raman-active vibration in the 1000–1050 cm^{-1} region is predicted for both LS and HS configurations, which originates from a bbp ring breathing motion coupled with a stretching of the axial N–Fe–N coordination bonds (Figure S50b). Due to the different Fe–N bond distances in low and high-spin configurations, this Raman-active vibration is predicted to appear at smaller wavenumbers for the HS state (1010 cm^{-1}) than for the LS state (1041 cm^{-1}) (Figure S50a), which nicely supports the experimental analysis.

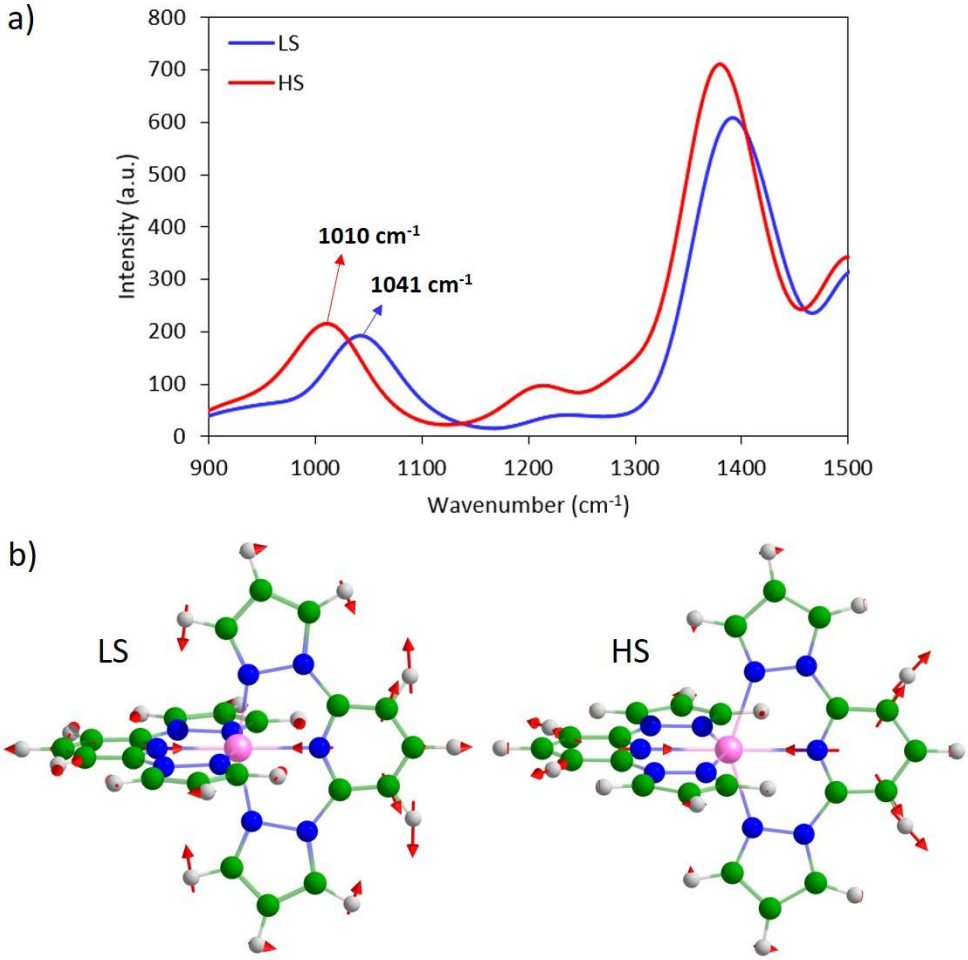

Figure S50. a) Theoretical Raman spectrum calculated for **C0**(LS) and **C0**(HS) at the BHandHLYP/def2-SVP/LANL2DZ(Fe) level. b) Representation of the Raman-active vibrational mode in the 1000-1050 cm^{-1} region for the LS and HS states.

7. References

1. J. Ramos-Soriano, J. J. Reina, A. Pérez-Sánchez, B. M. Illescas, J. Rojo and N. Martín, *Chem. Commun*., 2016, **52**, 10544-10546.

2. T. Vermonden, D. Branowska, A. T. M. Marcelis and E. J. R. Sudhölter, *Tetrahedron,* 2003, **59**, 5039-5045.

3. J. Elhaïk, C. M. Pask, C. A. Kilner and M. A. Halcrow, *Tetrahedron,* 2007, **63**, 291-298.

4. L. J. Kershaw Cook, R. Kulmaczewski, R. Mohammed, S. Dudley, S. A. Barrett, M. A. Little, R. J. Deeth and M. A. Halcrow, *Angew. Chem. Int. Ed.,* 2016, **13**, 4327-4331.

5. C. Bannwarth, S. Ehlert and S. Grimme, *J. Chem. Theory Comput.,* 2019*,* **15**, 1652–1671.

6. *(a)* Y. Yang, H. Yu, D. York, Q. Cui and M. Elstner, *J. Phys. Chem. A.,* 2007, **111**, 10861–10873; *(b)* M. Gaus, A. Goez and M. Elstner, *J. Chem. Theory Comput.,* 2013, **9,** 338–354.

7. Gaussian 16, Revision A.03, M. J. Frisch, G. W. Trucks, H. B. Schlegel, G. E. Scuseria, M. A. Robb, J. R. Cheeseman, G. Scalmani, V. Barone, G. A. Petersson, H. Nakatsuji, X. Li, M. Caricato, A. V. Marenich, J. Bloino, B. G. Janesko, R. Gomperts, B. Mennucci, H. P. Hratchian, J. V. Ortiz, A. F. Izmaylov, J. L. Sonnenberg, D. Williams-Young, F. Ding, F. Lipparini, F. Egidi, J. Goings, B. Peng, A. Petrone, T. Henderson, D. Ranasinghe, V. G. Zakrzewski, J. Gao, N. Rega, G. Zheng, W. Liang, M. Hada, M. Ehara, K. Toyota, R. Fukuda, J. Hasegawa, M. Ishida, T. Nakajima, Y. Honda, O. Kitao, H. Nakai, T. Vreven, K. Throssell, J. A. Montgomery, Jr., J. E. Peralta, F. Ogliaro, M. J. Bearpark, J. J. Heyd, E. N. Brothers, K. N. Kudin, V. N. Staroverov, T. A. Keith, R. Kobayashi, J. Normand, K. Raghavachari, A. P. Rendell, J. C. Burant, S. S. Iyengar, J. Tomasi, M. Cossi, J. M. Millam, M. Klene, C. Adamo, R. Cammi, J. W. Ochterski, R. L. Martin, K. Morokuma, O.

Farkas, J. B. Foresman, and D. J. Fox, Gaussian, Inc., Wallingford CT, 2016.

8. *(a)* A. D. Becke, *J. Chem. Phys.,* 1993, **98**, 5648–52; *(b)* F. Weigend and R. Ahlrichs, *Phys. Chem. Chem. Phys.,* 2005, **7**, 3297-305; *(c)* T. H. Dunning Jr., P. J. Hay, in *Modern Theoretical Chemistry*, Ed. H. F. Schaefer III, Vol. 3 (Plenum, New York, 1977) 1-28.

9. *(a)* M. Reiher, O. Salomon and B. A. Hess, *Theor. Chem. Acc.,* 2001,**107**, 48−55; *(b)* O. Salomon, M. Reiher and B. A. Hess, *J. Chem. Phys.,* 2002, **117**, 4729−4737; *(c)* D.N. Bowman and E. Jakubikova, *Inorg. Chem.,* 2012, **51**, 6011-6019.

10. R. L. Martin, *J. Chem. Phys.*, 2003, **118**, 4775-4777.

11. A. D. Becke, *J. Chem. Phys.,* 1993, **98**, 1372-77.

12. Chemcraft - graphical software for visualization of quantum chemistry computations. https://www.chemcraftprog.com.

Chapter 5.

Redox and Guest Tunable Spin-crossover Properties in a Polymeric Polyoxometalate

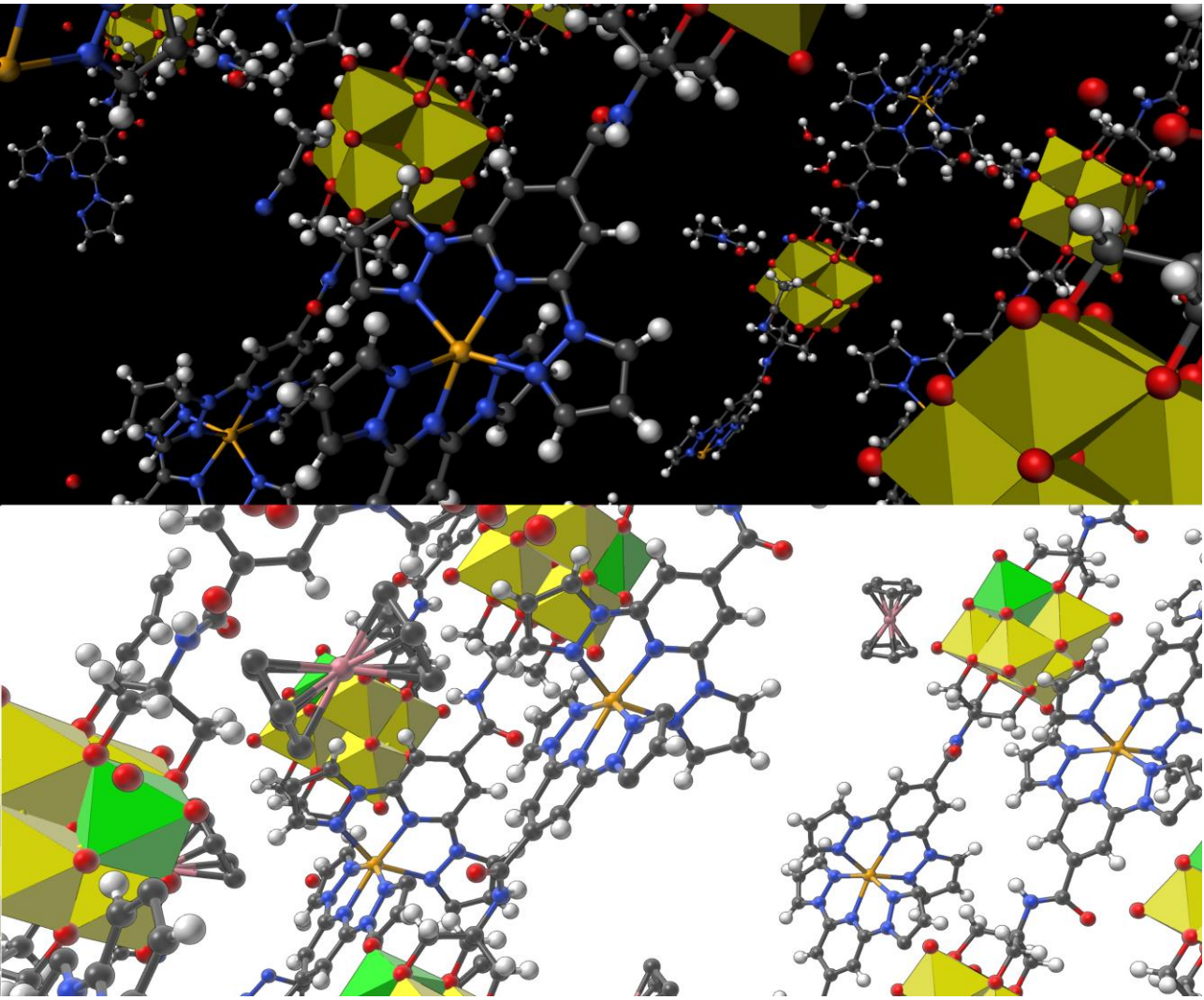

Mario Palacios-Corella, Víctor García-López, Francisco Grueso, Guillermo Mínguez Espallargas, Miguel Clemente-León and Eugenio Coronado, *To be submitted.*

Introduction

Spin crossover (SCO) complexes undergo an entropy-driven spin state change, which can be triggered by a variety of external stimuli (temperature, pressure, analytes or electric fields).[1] The majority of SCO research has been dedicated to the study of octahedral Fe(II) complexes ($3d^6$), which switch between the diamagnetic LS state (S = 0) and the paramagnetic HS state (S = 2). Since this phenomenon induces reversible changes of a number of physical properties, SCO materials are attracting considerable interest due to their potential applications as chemical switches, sensors or memories.[2]

Bis-chelated Fe(II) complexes based on tridentate ligands of the type 2,6-bis(pyrazol-1-yl)pyridine (1-bpp)[3] are an archetypical family of SCO complexes, because they usually present abrupt thermal spin transitions and Light-Induced Excited Spin State Trapping (LIESST) effect[4] at relatively high temperatures.[5] In addition, the spin state of these systems is known to be very sensitive to intermolecular interactions with solvent molecules and counteranions[6,7,8] through the molecular network. Consequently, they could act as chemo-responsive materials. Most of the previous results with this ligand and derivatives are based on salts of mononuclear complexes, which very often lose crystallinity or dissolve in contact with organic solvents. Therefore, the organization of this type of complexes into coordination polymers (CPs) could be a suitable strategy to optimize the SCO properties of these systems by increasing the stability and adding new functionalities such as porosity, magnetism or redox activity. Previous attempts to reach this goal were based on ditopic "back-to-back" neutral 1-bpp ligands.[9,10] However, the resultant materials were often poorly crystalline, with incomplete and very gradual SCO transitions.[11]

In this work, we have tempted an alternative strategy to reach this goal. Instead of using a neutral organic spacer between the two 1-bpp units of the ditopic ligand, we have prepared a charged ligand

containing a polyometalate (POM) moiety. This has afforded a 2-charged ditopic ligand, which could lead to a neutral 1D polymer by reaction with Fe(II) in contrast to the charged 1D polymers so far obtained with 1-bpp. In addition, the POM unit could provide to this hybrid CP the robustness and redox tunability typically observed in POM compounds. In fact, POMs constitute a family of molecular-metal oxides of groups 5 or 6 transition metals in their highest oxidation states. These compounds exhibit exceptional electronic and structural properties,[12] leading to a variety of applications in areas like catalysis,[13] energy conversion, medicine and molecular magnetism,[14] among others. A current strategy to incorporate additional functionalities on POMs involves the covalent linkage of organic moieties. In this sense, the use of tris-alkoxo-amide tripods as anchoring ligands has afforded rationally designed and predictable POM-based hybrid structures,[15,16] which can be used as precursors of robust POM frameworks linked through metal ions,[17] yielding multifunctional compounds with unique properties.[18,19,20]

To our knowledge, there are very few reports of POMs showing SCO behavior.[21] In a previous work, we explored this topic through the incorporation of 1-bpp into a Mn^{III} Anderson POM.[22] We first prepared the 1-bpp bifunctionalized Anderson POM and subsequently, by reaction with Fe^{2+}, the amorphous polymeric compound $(C_{16}H_{36}N)[Fe(MnMo_6O_{24}(C_{16}H_{15}N_6O)_2)]\cdot(H_2O)_4$. This compound showed a LIESST effect with a small but significant photoconversion (~8 %) combined with a field-induced slow relaxation of magnetization due to the presence of isolated Mn(III) anisotropic magnetic ions.

Herein we have extended the same strategy with a different POM unit, the Lindqvist hexavanadate. We have chosen this POM because it can be reversibly reduced. Therefore, it could lead to multifunctional compounds combining the switching properties of the SCO unit with the rich redox chemistry of the POMs. In addition to this, the 2- charge of the functionalized hexavanadate POM

matches with the 2+ charge of the Iron centre. This has enabled us to obtain a crystalline neutral polymer with a 1:1 Fe:POM stoichiometry, which contrasts with the amorphous charged polymer obtained by reacting the 3- charged Anderson POM with Fe^{2+} mentioned above.

Results and discussion

Synthesis and structure

We report first the preparation of the discrete hexavanadate POM bifunctionalized with 1-bpp linkers (**1**). State-of-the-art techniques confirmed the formation of the molecular building block (See Fig. 1 and Figs S1 to S6, Scheme S1 and associated text in the ESI†). The crystallographically independent functionalized POM presents the common Lindqvist hexavanadate structure in which the six V(V) atoms from six octahedral edge-sharing VO_6 form an octahedron. The two 1-bpp ligands linked through a tris-alkoxo-amide tripod, occupy opposite faces of that octahedron in **1** (see ESI†), something that has been observed in other polymeric structures based on functionalized hexavanadate anions and metal ions. [23,24]

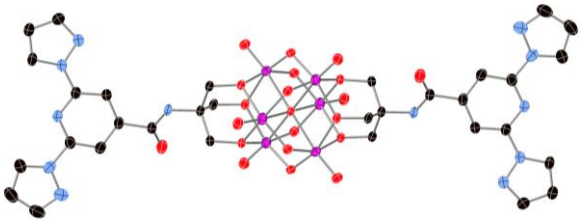

Fig. 1 View of the structure of the functionalized-POM in compound **1**. (V (pink), C (black), N (blue), O (red)). Hydrogen atoms have been omitted for clarity.

In a second step **1** was reacted with one equivalent of Fe^{2+} or Zn^{2+} by slow diffusion in dimethylformamide (DMF)/MeCN mixtures to afford crystalline materials $Fe[V_6O_{19}(C_{16}H_{15}N_6O)_2]\cdot solv$ (**2**) and $Zn[V_6O_{19}(C_{16}H_{15}N_6O)_2]\cdot solv$ (**3**) (solv = solvent). The composition of **2** and **3** was studied by energy dispersive X-ray spectroscopy (EDX) measurements, which are consistent with the expected 1:6 Fe:V and Zn:V ratios, elemental analysis, ^1H NMR and thermogravimetric analysis (TGA) (see experimental section in the ESI† and below). It is important to notice that these solids are not stable in absence of solvent (see below) and therefore need to be characterized and stored in the mother liquor (DMF/MeCN mixture in samples **2·DMF** and **3·DMF**) or in MeCN (samples **2·MeCN** and **3·MeCN**). Powder X-ray diffraction (PXRD) measurements of **2·MeCN** and **3·MeCN** in contact with the solvent confirmed the isostructurallity of the Fe and Zn derivatives (see experimental section, Table **S2** and **Fig. S7** in the ESI†).

The structure of **3** was solved by single crystal X-ray diffraction at 120 K in an as synthesized crystal of **3·DMF** at 120 K. It confirms the formation of a polymeric structure where the 1-bpp bifunctionalized POMs are connected to each other through the metallic center (**Fig. 2**). It crystallizes in the monoclinic space group $P2_1/c$ showing a single molecule of $[V_6O_{19}(C_{16}H_{15}N_6O)_2]^{2-}$ POM, one Zn atom, one MeCN, two DMF with occupancies of 0.75 and disordered H_2O solvent molecules in the asymmetric unit. The Zn atom is six-coordinated to two tridentate 1-bpp ligands from two $[V_6O_{19}(C_{16}H_{15}N_6O)_2]^{2-}$ units, which at the same time are coordinated to two Zn(II) ions through their two terminal 1-bpp ligands. Thus, the Zn(II) ions and the 1-bpp-terminated POMs form one-dimensional (1D) neutral coordination chains of formula $\{Zn[V_6O_{19}(C_{16}H_{15}N_6O)_2]\}_n$ running along the [*10-1*] direction (see Fig. 2).

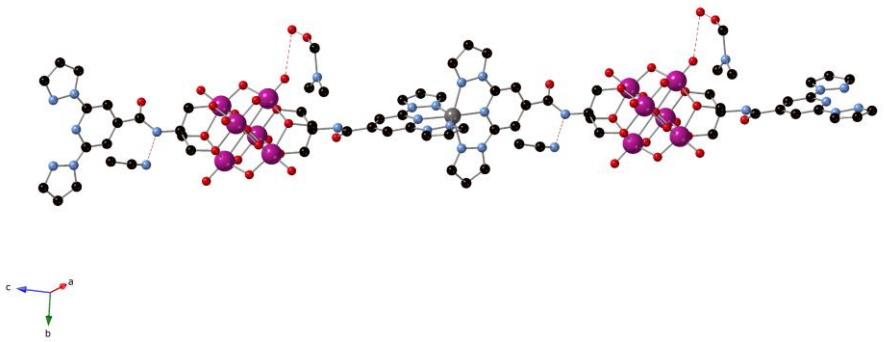

Fig. 2 View of the structure of the chains of compound **3** with hydrogen-bonded solvent molecules (V (pink), C (black), N (blue), O (red), Zn (gray)). Dashed lines represent hydrogen bonds. Hydrogen atoms have been omitted for clarity.

These 1D coordination chains are connected to each other by weak intermolecular interactions leading to double layers in the *ac* plane and channels filled with solvent molecules parallel to the chain direction (see Fig. 3). Chains from different double layers are symmetry related by an inversion center placed at [0, 0, 0]. The interchain interactions involve bridging and terminal oxo groups from the hexavanadate POM with CH groups and C atoms from pyridyl or pyrazolyl groups of 1-bpp from neighboring chains, which also present short interactions with the CO groups and methoxy groups of the amide-tripod linker and DMF solvent molecules. Moreover, one of the two NH groups from the amide groups of $[V_6O_{19}(C_{16}H_{15}N_6O)_2]^{2-}$ form hydrogen bonds with a MeCN molecule (see Fig. 2). Among these interactions, the closest contacts between the coordinated ligands of Zn involve CO groups with CH groups or C atoms from pyrazolyl groups. Each Zn(II) complex interacts through this type of interactions with four complexes from neighboring chains belonging to the same double layer (Fig. S8 in the ESI†). This leads to shortest interchain distance between Zn ions of 10.47 Å, which is much shorter than the shortest intrachain Zn-Zn distance of 25.2 Å. These two distances are longer than those found in salts of

Fe(II) complexes of 1-bpp with similar triol substituents (8.702 Å in $[Fe(1\text{-bpp-triolH}_3)_2](ClO_4)_2 \cdot MeCN$ ($triolH_3$ = $C(O)NHC(CH_2OH)_3$)). [25] Therefore, the insertion into the POM network of these complexes provides a better isolation for the $[Fe(bpp)_2]$ complexes than that reported for simple salts of these complexes with similar substituents. However, since DMF and MeCN solvent molecules occupy the channels and present numerous short contacts with 1-bpp ligands, important structural changes are expected if they are removed or replaced by other solvents.

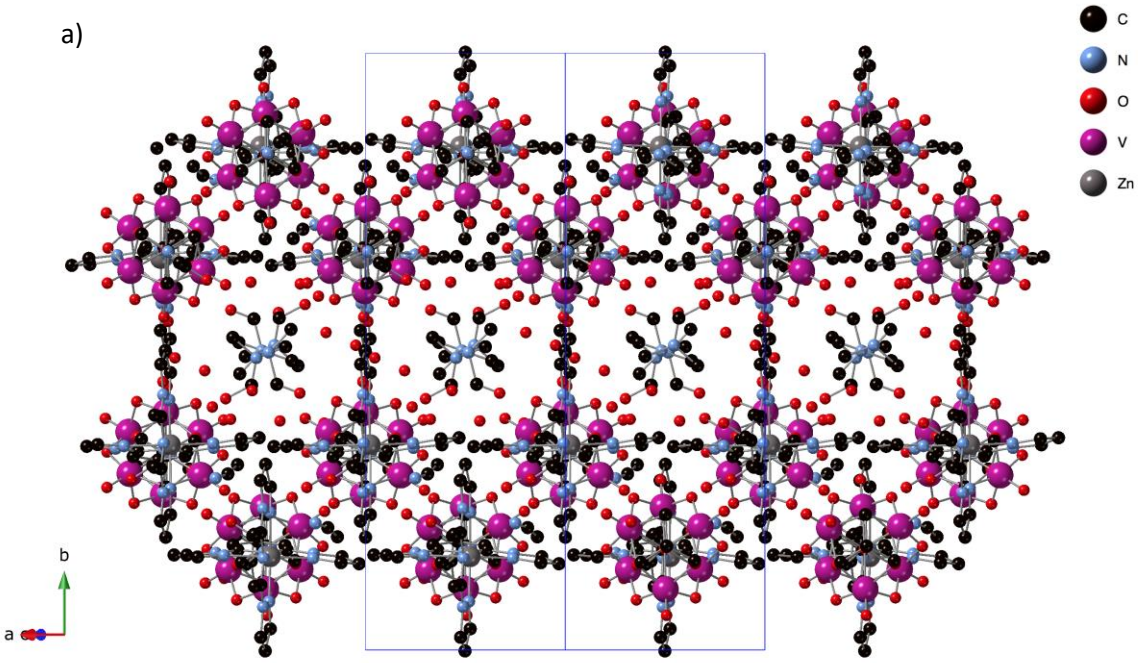

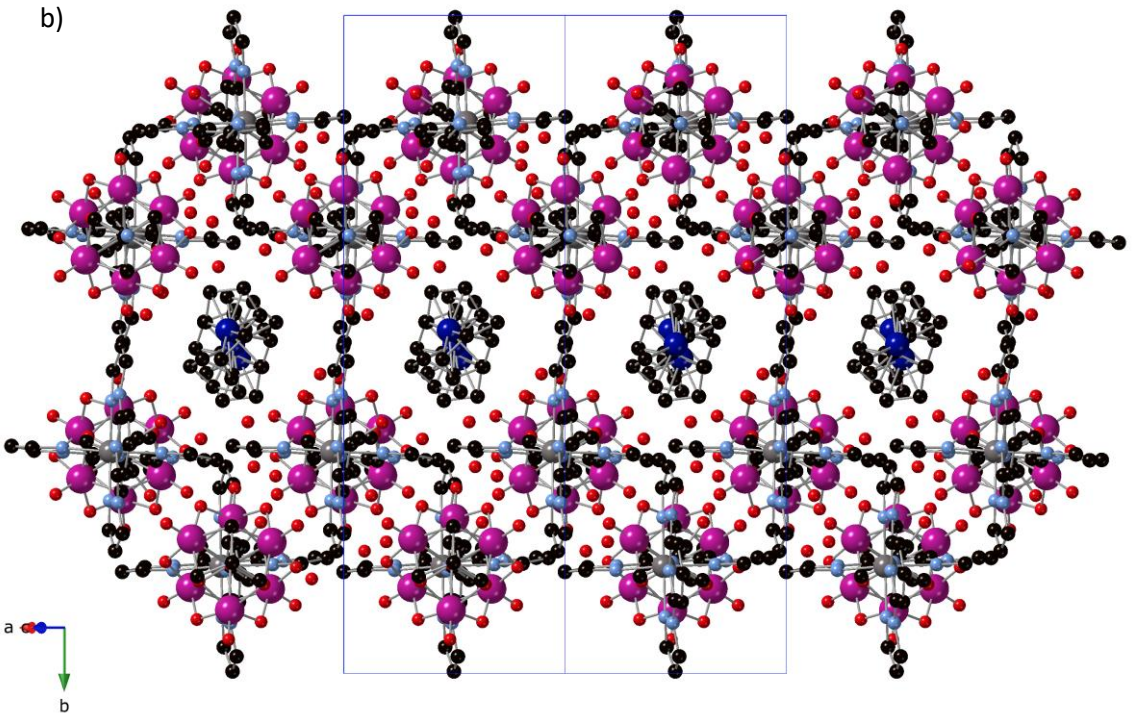

Fig. 3 Projection of structure of **3·DMF** (a) and **Red 3** (b) in the [10-1] plane (V (pink), C (black), N (blue), O (red), Zn (gray), Co(dark blue). Hydrogen atoms have been omitted for clarity.

Exchange of solvents.

Exchange of solvents was tested to study the robustness and flexibility of the CP and how structural changes induced by the exchanged solvents influence the spin state of Fe(II). We first studied the stability of **2** and **3** in absence of solvent. PXRD pattern of a filtered sample of **2·MeCN** reveals drastic changes with respect to that measured in contact with the mother liquor. Thus, it presents fewer and broader peaks than those of the solvated sample (see Fig. S9 in the ESI† and associated text). This indicates a loss of crystallinity and a different packing of the $M[V_6O_{19}(C_{16}H_{15}N_6O)_2]$ chains upon desolvation as a result of the decrease of the space between chains (see Fig. S10 in the ESI† and associated text). Interestingly, it is possible to recover partially the initial pattern by soaking these dry crystals again in acetonitrile (see Fig. S9 in the

ESI†) but with poorer crystallinity. This is an indication of a certain degree of reversibility in the desolvation/resolvation process.

Reversible solvent exchange of the initial DMF/MeCN solvent mixture by different clean MeCN, MeOH, EtOH, nitromethane ($MeNO_2$), benzonitrile (PhCN) or acetone (Me_2CO) solvents could be achieved preserving the crystallinity if the crystals were always kept in contact with the mother liquor or clean solvent. The exchange procedure involves soaking crystals of **2·DMF** or **3·DMF,** covered with a small amount of the mother liquor, in the fresh solvent for 3 days and storing in the same solvent (see ESI†). This gives rise to the already mentioned, **2·MeCN**, and **2·MeOH**, **2·EtOH**, **2·$MeNO_2$**, **2·PhCN**, **2·Me_2CO** and **3·MeCN** exchanged samples. ^{1}H NMR of freshly filtered crystals of these samples dissolved in dimethyl sulfoxide-d_6 was used to detect the presence of solvent molecules in the solvated samples. Whereas ^{1}H NMR of **2·DMF** and **3·DMF** confirms the presence of DMF and MeCN found in the structure of **3·DMF** (see below and Fig. S11 in the ESI), the samples with exchanged solvents present a variety of behaviors. In all of them, the ^{1}H NMR signals from DMF molecules do not appear (**2·MeCN**, **2·EtOH** and **3·MeCN**) or appear with reduced intensities (**2·MeOH**, **2·$MeNO_2$**, **2·PhCN** and **2·Me_2CO**) with respect to that of **2·DMF** or **3·DMF**. On the other hand, the ^{1}H NMR signals from MeCN molecules observed in **2·DMF** completely disappear in **2·MeOH**, **2·EtOH**, **2·$MeNO_2$**, **2·PhCN** and **2·Me_2CO**. The ^{1}H NMR signals of the exchanged solvent are observed in **2·MeCN**, **3·MeCN**, **2·$MeNO_2$**, **2·PhCN** and **2·Me_2CO** but not in the samples exchanged with alcohol solvents (**2·MeOH** and **2·EtOH**). Elemental analyses of the filtered samples, which showed a higher degree of desolvation because they were stored in air for longer times, are consistent with the presence of solvent molecules in the structure of the exchanged samples with less volatile solvents (**2·$MeNO_2$**, **2·PhCN**, **2·DMF** and **3·DMF**) and only water molecules in **2·MeCN**, **2·MeOH**, **2·EtOH**, **2·Me_2CO** and **3·MeCN** (see experimental section in the ESI†). This is consistent with

thermogravimetric (TG) analysis, which shows weight losses below 100 °C and a plateau at higher temperatures for these last five samples. In contrast, **2·PhCN** and **2·DMF** show gradual weight losses up to higher temperatures (ca. 180 °C), which corresponds to the T required for decomposition of 1-bpp ligand[8] (see Fig. S12 in the ESI†). These results indicate that the organic solvent molecules found in the structure of **3·DMF (**DMF and MeCN**)** can be easily replaced by other solvents or water molecules. To test the reversibility of the process, we performed additional solvent exchanges in the sample with the bulkiest solvent (**2·PhCN**), which was subsequently soaked for 3 days in MeCN (sample **2·PhCNtoMeCN**). Finally, **2·PhCNtoMeCN** was successively soaked in PhCN for other 3 days (**2·PhCNtoMeCNtoPhCN**). ^{1}H NMR and elemental analysis of these samples confirm replacement of PhCN by MeCN in **2·PhCNtoMeCN**, which is successively replaced by PhCN in **2·PhCNtoMeCNtoPhCN** (see experimental section and Fig. S13 in the ESI†). PXRD and magnetic data of these two samples are very similar to those of **2·MeCN** and **2·PhCN**, obtained from **2·DMF** (see Fig. S13 in the ESI† and below). This confirms that the exchange of solvents is reversible.

PXRD of all these samples in contact with the mother liquor was performed to understand the structural changes originated by the exchange of solvents (see Fig. S14 in the ESI†). PXRD patterns of all the solvent-exchanged samples suggest a similar structure to that solved by single X-ray diffraction for **3·DMF**. However, close inspection of the powder patterns reveals some differences in the first diffraction peak, corresponding to the (020) planes, which is directly related to the interlayer distance. Specifically, this peak is shifted to lower 2θ values (i.e. larger *d* spacing) for the bulkiest solvent (**2·PhCN**), with a value of 6.2 °, while that containing only water molecules (**2·EtOH**) shows the highest 2θ value of this peak at 6.5°. These data support that the size of the solvents inserted between the layers could tune the distance between the double

layers of chains found in the structure of **3·DMF** in the *ac* plane. A similar trend is observed for the other samples, with lower 2θ values of this peak for the samples with bulkier solvents (**2·DMF** and **2·MeNO$_2$**). On the other hand, these samples show differences in the relative intensity of the peaks due to the different pore filling. PXRD pattern of **2·Me$_2$CO** suggests a mixture of phases corresponding to different solvates as it presents two intense peaks at 2θ values of 6.3 and 6.5°, which could correspond to solvated and desolvated samples, respectively. The PXRD pattern of **2·MeOH** displays broader peaks at similar positions as those of the filtered sample of **2·MeCN** (see above). This could suggest a collapse of the structure in this exchanged sample. Finally, PXRD patterns of **2·PhCNtoMeCN** and **2·PhCNtoMeCNtoPhCN** are very similar to those of **2·MeCN** and **2·PhCN** confirming that it is possible to exchange more than one solvent with the same sample in a reversible way retaining the structural and magnetic properties (see below) of each solvate (see Figs. S13d and S15 in the ESI). Therefore, PXRD data of these exchanged samples suggest that the exchange of solvent molecules does not lead to important structural changes if the crystals are always kept in contact with a small amount of solvent except in the case of MeOH.

Magnetic properties

The temperature dependence of the product $\chi_M T$ (χ_M is the molar paramagnetic susceptibility) of **2·MeCN** measured in contact with the solvent is shown in Fig. 4. From 300 to 200 K, $\chi_M T$ is close to 3.5 $cm^3 \cdot K \cdot mol^{-1}$, which is consistent with most of the Fe(II) in the HS state. At lower temperatures, there is a gradual decrease of $\chi_M T$, which becomes more abrupt below 170 K, to reach a value of 0.9 $cm^3.K.mol^{-1}$ at 100 K. This corresponds to an almost complete spin transition from 200 to 100 K with a ~25 % of residual HS Fe(II) ions below 100 K. The same behavior is observed in the heating and cooling modes with a small thermal hysteresis of 8 K ($T_{1/2}\downarrow$ = 135 K

and $T_{1/2}\uparrow$ = 143 K, $T_{1/2}$ = temperature of 50 % HS to LS conversion) at a scan rate 2 K.min^{-1}. Below 30 K, χ_MT shows an abrupt decrease due to the zero-field splitting of the residual HS Fe(II). To our knowledge, **2** is the first POM compound showing a complete and abrupt SCO. This contrasts the two compounds with similar substituent [Fe(1-bpp-triolH_3)$_2$](ClO_4)$_2$·MeCN[25] and ($C_{16}H_{36}N$)[Fe($MnMo_6O_{24}$($C_{16}H_{15}N_6O$)$_2$)]·(H_2O)$_4$,[22] which remain in the LS state in the same range of temperatures. Therefore, the insertion of the same amide-bpp substituent into a hexavanadate POM framework results in an abrupt spin transition with a significant level of cooperativity, demonstrated by the thermal hysteresis, in spite of the long distances found between the metal centers in the structure of **3·DMF** (see above). This cooperativity could be induced by the intermolecular interactions between [Fe(1-bpp)$_2$]$^{2+}$ complexes of neighboring chains. Thus, the absence of the bulky DMF molecules found in the structure of **3·DMF** reflected by ^{1}H NMR data of **2·MeCN** (see Fig. S11 in the ESI) supports this hypothesis as this would lead to shorter interchain distances. To our knowledge, there is only one example of a polymeric compound containing 1-bpp displaying a similar cooperative SCO behavior. This is the poorly crystalline compound {[FeL]$_n$(BF_4)$_{2n}$}·solv (L = ditopic back-to-back ligand with two 1-bpp coupled through 1,4-phenylene), which shows an hysteresis loop of 10 K.[9a]

Exchange of solvents enables tuning the abruptness, completeness and $T_{1/2}$ of the SCO. The most complete and cooperative ones are observed in **2·MeNO$_2$**, **2·Me$_2$CO** and **2·EtOH** measured in contact with the solvent (see Fig. 4). They present abrupt decreases of $\chi_M T$ from 3.5 cm^3·K·mol^{-1} at 300 K to 0.9 cm^3·K·mol^{-1} (**2·EtOH**) and 0.5 cm^3·K·mol^{-1} (**2·MeNO$_2$** and **2·Me$_2$CO**) below 100 K. This corresponds to almost complete spin transitions with ~25 % (**2·EtOH)** and ~15 % (**2·MeNO$_2$** and **2·Me$_2$CO**) of residual HS Fe(II) ions. **2·MeNO$_2$** and **2·EtOH** present a small thermal hysteresis of 3 K at a scan rate 2 K·min^{-1}. These results indicate that it is possible to tune the

temperature of the SCO by exchanging the solvent with $T_{1/2}$ values ranging from 140 K in **2·MeCN** to 260 K in **2·EtOH** and intermediate values in **2· Me_2CO** and **2·$MeNO_2$** (210 and 220 K, respectively). On the other hand, **2·PhCN** and the as-synthesized **2·DMF** crystals present gradual and incomplete spin transitions (see Fig. 4b). This could suggest that the intercalation of bulky solvent molecules between the $[Fe^{II}(1\text{-bpp})_2]^{2+}$ centers decreases the cooperativity of the SCO in agreement with the presence of DMF molecules intercalated between the POM chains in the crystal structure of **3·DMF** and of PhCN in **2·PhCN**, shown by elemental analysis, TGA and ^{1}H NMR. This is also observed in the reduced sample **Red 2**, which shows a very similar magnetic behavior in agreement with the presence of bulky cobaltocenium cations between the chains (see below). Finally, temperature dependence of $\chi_M T$ of **2·PhCNtoMeCN** and **2·PhCNtoMeCNtoPhCN** are very similar to those of **2·MeCN** and **2·PhCN**, respectively, (see Fig. S16 in the ESI)) confirming that the structure and spin state of Fe(II) in the same crystal can be tuned in a reversible way by successive soaking in different solvents.

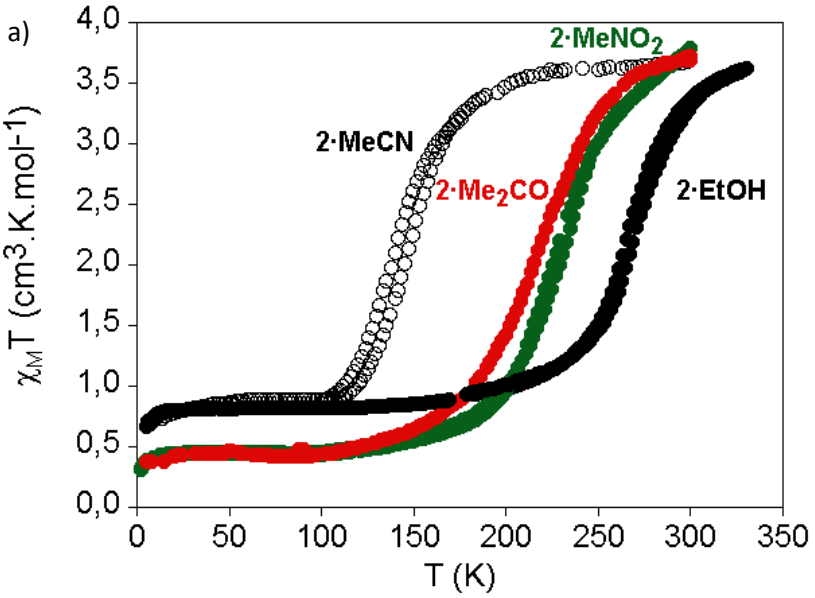

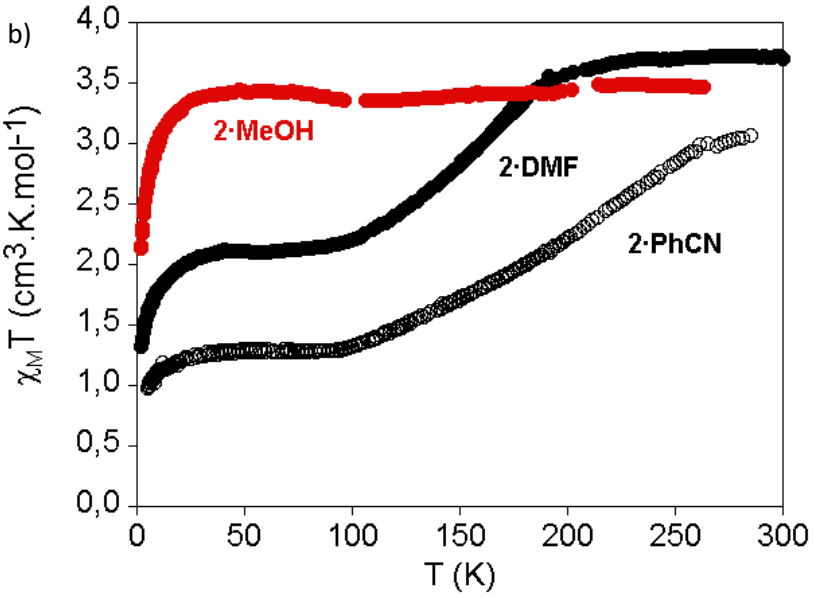

Fig. 4 Thermal variation of $\chi_M T$ of solvent exchanged samples of **2** measured in contact with the solvent. (a) Empty circles: **2·MeCN**; full circles: **2·MeCN**; red full circles: **2·Me$_2$CO**; green full circles**: 2·MeNO$_2$**. (b) Empty circles: **2·PhCN**; full circles: **2·DMF**; red full circles: **2·MeOH**.

A rationalization of these results is difficult to perform without the single crystal structures of all the solvates. Furthermore, the spin state of solvates of the same salt of $[Fe^{II}(1\text{-bpp})_2]^{2+}$ is very sensitive to the intermolecular interactions with solvent molecules or pressure effects due to different solvent filling. Thus, different magnetic behaviors for solvates of the same complex are quite usual.[3,8] A simple magneto-structural trend is the shift in the first and most intense peak of the PXRD pattern of **2·EtOH** to higher 2θ values than those of the other samples. This could indicate larger chemical pressure induced by the decrease in unit cell volume, which could stabilize the LS state, as observed experimentally. In the other samples, a clear trend is not observed as electronic effects could explain the different spin state of Fe(II) together with the steric effect already mentioned. Thus, changes in the ligand field strength

around the Fe(II) center are expected due to intermolecular interactions between guest molecules and the coordinated ligands. Indeed, ^{1}H NMR spectra of freshly filtered crystals of these samples show the presence of the exchanged solvent in all cases except in **2·EtOH** (see above and Fig. S11 in the ESI).

$\chi_M T$ of filtered crystals of **2·MeCN** changes drastically with respect to the same sample measured in contact with the mother liquor. Thus, $\chi_M T$ shows a gradual increase from 2.4 $cm^3 \cdot K \cdot mol^{-1}$ (around 70 % HS fraction) to 2.9 $cm^3 \cdot K \cdot mol^{-1}$ at 300 K (around 80 % HS fraction from 50 to 300 K (see Fig. S17 in the ESI†). Mössbauer spectroscopy measurements in this filtered sample were performed to confirm the oxidation and spin states of Fe(II) in **2** since it was not possible to measure solvated samples due to technical reasons. These measurements show a HS fraction close to 60 % below 200 K, which is consistent with magnetic measurements. In all cases, characteristic spectra of HS or LS Fe(II) were obtained confirming that iron is not oxidized to iron(III) and the presence of a mixture of solvates with different spin states in the filtered samples (see Figs. S18 and S19, table S4 and associated text in the ESI†). A resolvated sample, obtained by soaking the filtered crystals of **2·MeCN** in MeCN, does not recover the spin transition shown by the solvated sample. Thus, $\chi_M T$ values higher than 3.3 $cm^3 \cdot K \cdot mol^{-1}$ are obtained at temperatures above 50 K indicating that the HS state fraction is close to 100 % (see Fig. S17 in the ESI†). The different behavior of this resolvated sample with respect to the **2·MeCN** indicates that the structure of the initial sample is not completely recovered after resolvation as shown by differences in the PXRD pattern (see above). Another factor that could explain this behavior is the cracking of the crystals into smaller crystallites after extracting them from the mother liquor, which could lead to the observed stabilization of the HS state in all the range of temperatures. Similar size effects have been reported in the literature for 1-bpp iron(II) complexes.[26]

Reduction and reoxidation of 2 and 3.

The electrochemical properties of **2** and **3** were studied by cyclic voltammetry (CV) and differential pulse voltammetry (DPV). Nafion 5% and ethanol (1:1) mixtures of the filtered solids of **2·MeCN** and **3·MeCN** were deposited on a glassy carbon disk working electrode and studied at different scan rates in 0.1 M $TBABF_4/CH_3CN$ solutions. CV experiments show a pair of quasi-reversible redox peaks with the mean peak potential of -0.66 V (ΔE_p = 0.13 V) for **2** and -0.86 V (ΔE_p = 0.18 V) for **3** versus Ag/AgCl at a scan rate of 100 mVs^{-1} (see Fig. 5 and S20 in the ESI†). They agree with the quasi-reversible one-electron reduction of hexavanadate observed in solution for Lindqvist-type polyoxovanadates.[27,28] These results are confirmed by DPV analysis (see Fig. S20 in the ESI†).

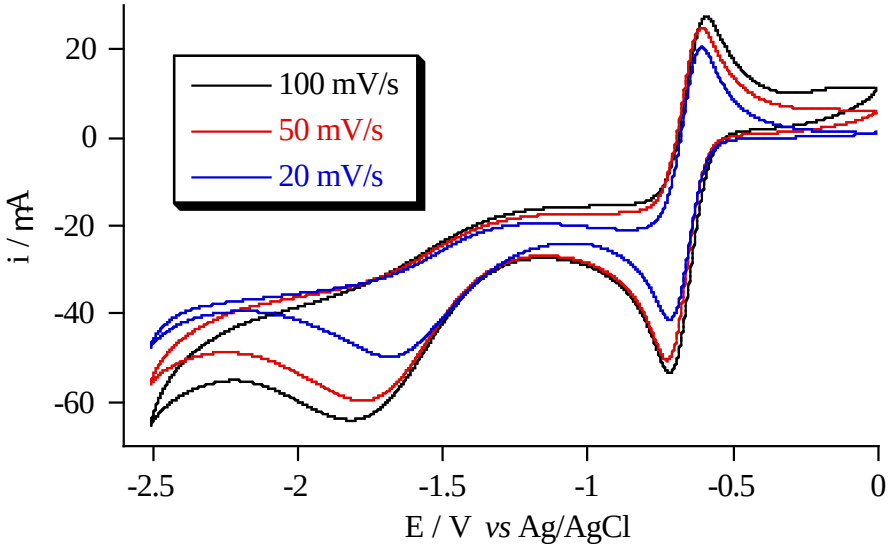

Fig. 5 Cyclic voltammetric behavior of **2.**

In view of the reversible electrochemical reduction of these samples, they were then reduced chemically by suspending crystals of **2·MeCN** and **3·MeCN** in a solution of cobaltocene in MeCN under an inert atmosphere for 5 hours leading to the reduced samples **Red 2**

and **Red 3**. Reoxidized sample of **2** (**Reox 2**) was obtained by suspending crystals of **Red 2** in a MeCN solution of $TBABr_3$ (see experimental section in the ESI†). The reduction and reoxidation of the hexavanadate unit could be easily detected from the distinctive change in color (red in fully oxidized state and dark green in reduced species, see Fig. S20d in the ESI†) and by IR spectroscopy (see section 4 in the ESI† and Fig. S21), showing a red shift of the characteristic ν(V=O) and ν(V–O–V) bands (from 950 and 790 to 930 and 755 cm^{-1}, respectively), in agreement with previous reports.[23,27]

EDAX analysis of **Red 2** and **Red 3** confirmed the expected Fe:V and Zn:V ratios but cobalt appeared in the composition with 1.3:1:6 Co:Fe:V and Co:Zn:V ratios. This suggests the oxidation of cobaltocene to cobaltocenium to compensate the one-electron reduction of the POM and its insertion in the structure. Elemental analyses of these samples are consistent with the formulas $Fe[V_6O_{19}(C_{16}H_{15}N_6O)_2]\cdot[Co(C_5H_5)_2]_{1.3}\cdot 8H_2O$ (**Red 2**) and $Zn[V_6O_{19}(C_{16}H_{15}N_6O)_2]\cdot[Co(C_5H_5)_2]_{1.3}\cdot 11H_2O$ (**Red 3**)**.** Indeed, high-resolution X-ray photoelectron spectroscopy (XPS) of **Red 2** and **Red 3** display two characteristic peaks at 780.7-781.4 (2p3/2) and 795.6-796.3 (2p1/2) eV from cobaltocenium. (Fig. S23 and S25 in the ESI†)[29] The presence of cobaltocenium cations is further confirmed by ^1H NMR of filtered crystals of **Red 2** and **Red 3**, dissolved in dimethyl sulfoxide-d_6 and single crystal X-ray diffraction structure of **Red 3** (see below). ^1H NMR spectra of these samples display a singlet close to 5.9 ppm similar to that reported in literature for cobaltocenium (Fig. S27 in the ESI†).[30] XPS spectra were also used to test the oxidation state of vanadium (see Figs S22 to S25 and associated text in the ESI†). They are consistent with the one-electron reduction of the POM after chemical reduction, which can be inferred from EPR and magnetic data (see below).

Control experiments revealed the necessity of cobaltocene for the reduction process (see ESI and associated text section S4).

Single-crystal X-ray diffraction analysis of **Red 3**, obtained by soaking single crystals of **3·DMF** in the cobaltocene MeCN solution without stirring, was carried out. This measurement revealed the preservation of single crystallinity and enabled the solution of the single crystal structure of **Red 3**. Single-crystal to single-crystal redox transformations in MOFs have been observed but are still a relatively rare phenomenon.[31] Similar to that of **3·DMF**, the structure of **Red 3** was solved in the monoclinic space group $P2_1/c$ with a shortening of ca 0.2 Å in *a* and *b* parameters and an increase of the same order in *c* parameter with respect to those of **3**. The most remarkable structural change is the presence of a chain of disordered cobaltocenium cations parallel to the polyoxovanadate chains occupying the center of the pores in the place of the DMF molecules found in the structure of **3** (Fig. 3) The removal of bulky DMF molecules and the presence of cobaltocenium cations shielding the repulsion between the polyoxovanadate of difference chains could explain the small decrease of unit cell volume in **red 3** with respect to that of **3** (6369.8(15) $Å^3$ in **3** and 6288(2) or 6322.5(16) $Å^3$ in **red 3**).

PXRD patterns of **Red 2** and **Red 3** measured in contact with the mother liquor are shown in Fig. **S7** in the ESI†. They confirm that both compounds are isostructural. The PXRD patterns are similar to those of **2·MeCN** and **3·MeCN** with differences in the relative intensity of the peaks, which could be related to the different pore filling due to the presence of cobaltocenium cations in the reduced samples. An interesting result is that PXRD pattern of dried crystals of **Red 2** is quite similar to that of the same sample measured in contact with the mother liquor in contrast to the initial sample of **2** (see Fig. S28 in the ESI†). This suggests that the inserted cobaltocenium cations stabilize the structure and prevent the collapse of the pores shown by the initial sample.

EDAX of **Reox 2** show 0.5:0.5:1:6 Co:Br:Fe:V ratios indicating that cobaltocenium is still present but in a less extent and that Br^- enters

in the structure after reoxidation. Indeed, elemental analysis is consistent with the formula $Fe[V_6O_{19}(C_{16}H_{15}N_6O)_2]\cdot[Co(C_5H_5)_2]_{0.5}[Br]_{0.5}\cdot 10H_2O$ (see experimental section in the ESI†). XPS and ^1H NMR confirm the presence of cobaltocenium and Br-species (see Figs. S26 and S27 in the ESI† and associated text). PXRD pattern of **Reox 2** resembles that of **Red 2**, as expected for the presence of cobaltocenium cations in the pores (Fig. S29 in the ESI†). In this case, PXRD peaks of a minor phase assigned to the $[Co(C_5H_5)_2]_2[V_6O_{19}(C_{16}H_{15}N_6O)_2]\cdot MeCN$ salt were also detected. This is indicative of partial decomposition of the polymeric chains upon chemical reduction and reoxidation. EDAX analysis suggest that this impurity contains around 4 % of the hexavanadate POM (see Fig. S30 and table S4 in the ESI and associated text).

Magnetic and photomagnetic properties of the reduced and reoxidized samples.

Temperature dependence of $\chi_M T$ of **Red 2** in contact with the mother liquor is shown in Fig. 6. An almost constant value $\chi_M T$ of 3.1 $cm^3\cdot K\cdot mol^{-1}$ was observed from 300 to 240 K. At lower temperatures there is a gradual decrease to reach 1.5 $cm^3\cdot K\cdot mol^{-1}$ at 85 K. The lower HS fraction of this sample compared with that of **2·DMF** is consistent with a higher chemical pressure resulting from the decrease in unit cell observed in **Red 3** with respect to that of **3·DMF** shown by single crystal X-ray diffraction (see above). On the other hand, the spin transition is more gradual than that of **2·MeCN** and leads to higher residual HS fraction at low temperatures with a small contribution from the reduced POM (~0.3 $cm^3\cdot K\cdot mol^{-1}$, see below). This suggests that the intercalation of bulky cobaltocenium molecules between the $[Fe^{II}(bpp)_2]^{2+}$ centers observed in the structure of **Red 2** decreases the cooperativity of the SCO as observed in the samples containing bulky solvent molecules (**2·DMF** and **2·PhCN**). The magnetic properties of **Reox 2**, which has a lower amount of cobaltocenium cations (around 50 % of that of **Red 2**, see

above), confirm this hypothesis since this sample recovers the abrupt SCO shown by **2·MeCN**. Thus, $\chi_M T$ of **Reox 2,** measured in contact with the mother liquor, exhibits a decrease upon cooling from 3.3 $cm^3 \cdot K \cdot mol^{-1}$ at 250 K to 0.4 $cm^3 \cdot K \cdot mol^{-1}$ at 150 K, which becomes sharper in the 240-200 K range (see Fig. 6), with a thermal hysteresis of 11 K ($T_{1/2}\downarrow$ = 224 K and $T_{1/2}\uparrow$ = 213 K at a scan rate of 2 $K.min^{-1}$). This corresponds to an almost complete SCO similar to that observed for the initial **2·MeCN** but shifted to higher temperatures by 80 K. The stabilization of the LS state in **Reox 2** with respect to that of **2·MeCN** could be a consequence of the increased chemical pressure due to the presence of cobaltocenium cations and Br^- species in the channels of the compound but structural data on **Reox 2** are needed to confirm this hypothesis.

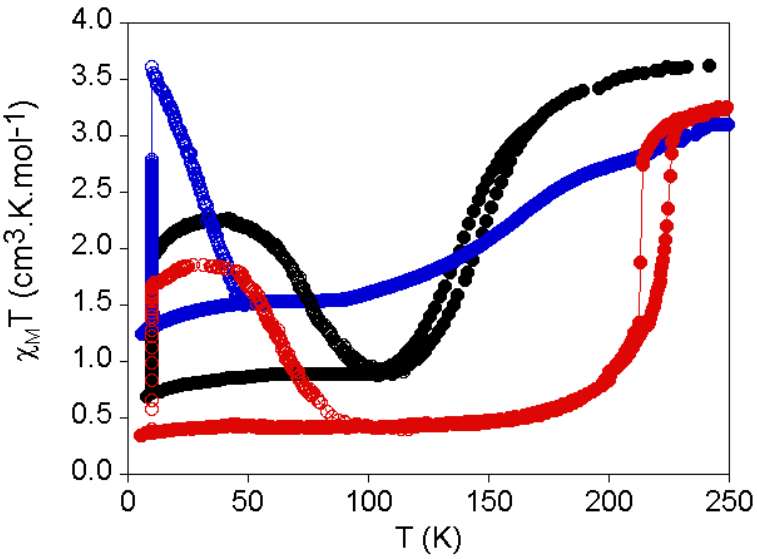

Fig. 6 Thermal variation of $\chi_M T$ of **2·MeCN** (black circles), **Red 2** (blue circles) and **Reox 2** (red circles) measured in contact with the solvent. Full circles: data recorded without irradiation; empty circles: data recorded after irradiation at 10 K.

Magnetic measurements on a reduced sample of **3** (**Red 3**) in contact with the mother liquor were performed to evaluate the contribution of unpaired electrons of the reduced POM chain. $\chi_M T$ of **Red 3** shows an almost constant value of 0.3 $cm^3 \cdot K \cdot mol^{-1}$ from 300 to 2 K. This value is consistent with one electron reduction of the sample and lower than that reported for 2-, 4- and 6-electron reduced functionalized hexavanadates (see Fig. S31 in the ESI†).[27]

The reduction of the POM is evidenced by EPR measurements of **Red 2** and **Red 3** measured in contact with the mother liquor (see Figs. 7 and S32 in the ESI† and associated text). The spectra below 40 K exhibit the eight lines expected for the hyperfine interaction between the electron spin S = 1/2 of V(IV) and the nuclear spins, I = 7/2. These are similar to those observed for the electrochemically-generated trans-$[V^V_5V^{IV}O_{13}[(OCH_2)_3CNO_2]_2]^{3-}$[27] or with cis-$[V^V_5V^{IV}O_{13}[(OCH_2)_3CCH_2OH]_2]^{3-}$.[32] The splitting between the two outermost features of the spectra at 10 K allows calculation of g_{II} (1.96 for **Red 2** and 1.95 for **Red 3**) and A_{II} values (151 G for **Red 2** and 152 G for **Red 3**) under X-band irradiation (~9.5 GHz), which are similar to those found for one-electron reduced hexavanadates.[27,32] Above 40 K, broadening of these characteristic 8-line spectra is observed together with a decrease of the splitting between the two outermost features see Figs. 7 and S32 in the ESI†). This is indicative of electron delocalization between various vanadium centers at increasing temperatures, which is consistent with thermally induced electron transfer between V^{IV} and V^V states. Similar temperature-dependent mobility spectra have been reported in the electrochemically-generated $V^V_5V^{IV}O_{13}[(OCH_2)_3CNO_2]_2]^{3-}$ and heteropolytungstates containing mixed-valence vanadium centers.[27]

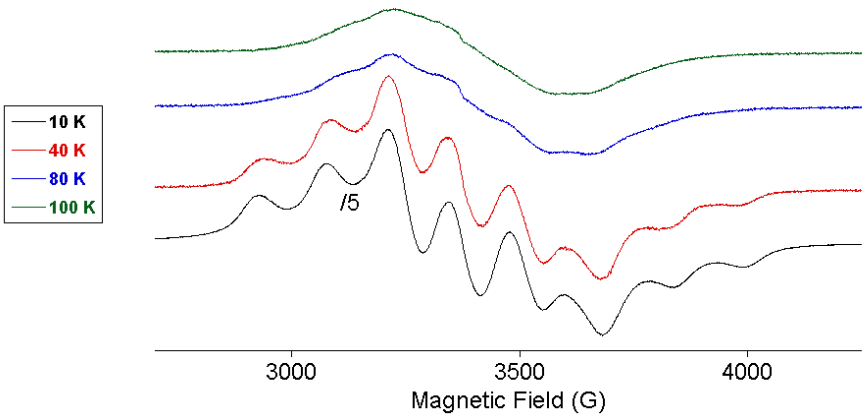

Fig. 7 EPR spectra of **Red 2** in contact with the mother liquor.

Finally, we studied the LIESST effect of **2·MeCN** because it is the sample with the lowest $T_{1/2}$ and mean-field theory predicts an inverse relationship between $T_{1/2}$ and the lifetime of the HS photoinduced metastable state. We completed this study with the photomagnetism of **Red 2** and **Reox 2** to see the combined effect of light and redox stimuli. These samples were protected with a grease to prevent desolvation. After irradiation with a 633 nm laser at 10 K, a drastic increase of the magnetic signal was observed in the three samples. Once saturation was reached, the irradiation was switched off and the samples were heated at a scan rate of 0.3 K·min^{-1} to determine the relaxation process (see Fig. 6). In the 10−30 K temperature range, an increase of χ_MT to reach maximum values of 2.3 cm^3·K·mol^{-1} for **2·MeCN**, 3.5 cm^3·K·mol^{-1} for **Red 2** and 1.9 cm^3·K·mol^{-1} for **Reox 2** was observed, reflecting a zero-field splitting of HS Fe(II). These values suggest LS to HS photoconversion close to 50 % for **2·MeCN,** 100 % for **Red 2** and 40 % for **Reox 2** of the LS centers at this temperature range. The χ_MT values after irradiation are higher than that recorded in the dark at temperatures below 100 K for **2·MeCN** and **Reox 2** and 50 K for **Red 2**. The *T*(LIESST), defined as the minimum of the derivative of $\chi_M T$ after irradiation with

temperature, is 75 K for **2·MeCN**, 40 K for **Red 2** and 65 K for **Reox 2**. Using the empirical linear correlation between $T_{1/2}$ and the T(LIESST) proposed for this family of compounds and described by the formula T(LIESST) = $T_0 - 0.3T_{1/2}$ (T_0 = 150 K) with exceptions,[33] we observe that the T(LIESST) and $T_{1/2}$ values of the three compounds deviate from this linear correlation. This could be a consequence of the structural flexibility of these compounds. Indeed, important deviations from this correlation in other 1-bpp compounds have been related to light-induced crystallographic phase changes, which could be favored in our compounds. Structural measurements after light irradiation are needed to confirm this point.

Conclusions

In this work, we have prepared 1D CPs with alternating hexavanadate POM and SCO $Fe^{II}(1\text{-bpp})_2$ units. The neutral character of this 1D network has proven to be crucial to obtain crystalline compounds in contrast to the previous charged CPs so far obtained with $[Fe^{II}(1\text{-bpp})_2]^{2+}$ complexes. We observed that the remarkable SCO properties which have been obtained typically in salts with small counteranions with strong intermolecular interactions between the complexes (thermal spin transitions with hysteresis and LIESST effect), are preserved in these polymeric neutral compounds. Thus, they are the first POMs to show complete and abrupt spin transitions. In addition to this, the organization of these SCO units in this neutral 1D polymer leads to a flexible and stable structure, which enables reversible exchange of solvents into the channels formed between the POM chains. This allows tuning the abruptness and temperature of the thermal spin transition. Thus, the most abrupt spin transitions are obtained in the exchanged samples containing small solvent molecules (H_2O or MeCN), while the more gradual ones are found in those containing bulky DMF or PhCN solvent molecules. These compounds are less stable than other 2D or 3D polymeric SCO materials with similar tuning solvent capabilities, such as Hofmann clathrates,[34,35,36] requiring a small volume of

solvent to protect the crystals from desolvation. Still, the presence of the redox active POM unit as spacer between the SCO units affords a unique redox tuning capability to our materials, in contrasts with the electrically innocent inorganic or organic spacers used in other polymeric SCO materials. Thus, the chemical reduction and reoxidation of the POM in **2** is accompanied by the entrance or removal of reductant (cobaltocenium) and oxidant species (bromine) acting as counterions. This leads to dramatic changes in their SCO properties. To our knowledge, there are only two very recent reports of SCO 1D and 3D CPs with redox active ligands containing tetrathiafulvalene (TTF), which undergo much less drastic changes on the SCO properties after postsynthetic oxidation with I_2.[37,38] In conclusion, we have prepared a multifunctional material in which SCO switching of the Fe(II) complexes coexists with the redox properties of the POM, which can switch between a diamagnetic state and a paramagnetic state by injection of one electron. These two switching properties can be tuned by a variety of stimuli such as temperature, light, solvent exchange or redox processes.

Notes and references

[1] (a) Eds. P. Gütlich and H.A. Goodwin, Spin Crossover in Transition Metal Compounds, Topics in Current Chemistry, Springer Verlag, Berlin-Heidelberg-New York, 2004, vols. 233-235; (b) Ed. M. A. Halcrow, Spin-Crossover Materials: Properties and Applications, John Wiley & Sons, Chichester, UK, 2013.

[2] (a) K. Senthil Kumar and M. Ruben, Coord. Chem. Rev. 2017, **346**, 176–205; (b) A. Enriquez-Cabrera, A. Rapakousiou, M. Piedrahita Bello, G. Molnár, L. Salmon and A. Bousseksou, Coord. Chem. Rev., 2020, **419**, 213396; (c) E. Coronado, Nat. Rev. Mater. 2020, **5**, 87.

[3] (a) M. A. Halcrow, Coord. Chem. Rev., 2005, **249**, 2880; (b) M. A. Halcrow, Coord. Chem. Rev., 2009, **253**, 2493; (c) J. Olguín and S. Brooker, Coord. Chem. Rev., 2011, 255, 203; (d) M. A. Halcrow, New J. Chem., 2014, **38**,

1868; (e) L. J. Kershaw Cook, R. Mohammed, G. Sherborne, T. D. Roberts, S. Alvarez and M. A. Halcrow, Coord. Chem. Rev., 2015, **2**, 289–290.

[4] (a) S. Decurtins, P. Gütlich, C. P. Köhler, H. Spiering and A. Hauser, Chem. Phys. Lett., 1984, **105** (1), 1–4; (b) A. Hauser, Top Curr. Chem. 2004, **234**, 155-198.

[5] (a) L. J. Kershaw Cook, F. L. Thorp-Greenwood, T. P. Comyn, O. Cespedes, G. Chastanet and M. A. Halcrow, Inorg. Chem., 2015, **54**, 6319; (b) V. García-López, M. Palacios-Corella, S. Cardona-Serra, M. Clemente-León and E. Coronado, Chem. Commun., 2019, **55**, 12227.

[6] L. J. Kershaw Cook, R. Kulmaczewski, O. Cespedes and M. A. Halcrow, Chem. Eur. J., 2016, **22**, 1789.

[7] R. Kulmaczewski, E. Trzop, L. J. Kershaw Cook, E. Collet, G. Chastanet and M. A. Halcrow, Chem. Commun., 2017, **53**, 13268.

[8] V. García-López, M. Palacios-Corella, A. Abhervé, I. Pellicer-Carreño, C. Desplanches, M. Clemente-León and E. Coronado, Dalton Trans., 2018, **47**, 16958.

[9] (a) C. Rajadurai, O. Fuhr, R. Kruk, M. Ghafari, H. Hahn and M. Ruben, Chem. Commun., 2007, 2636; (b) J. Elhaïk, C. M. Pask, C. A. Kilner and M. A. Halcrow, Tetrahedron, 2007, **63**, 291.

[10] M. Attwood and S. S. Turner, Coord. Chem. Rev., 2017, **353**, 247-277.

[11] I. Galadzhun, N. Shahid, I. Capel Berdiell and M. A. Halcrow, CrystEngComm, 2019, **21**, 6330.

[12] (a) M. T. Pope, Comprehensive Coordination Chemistry II, 4, Elsevier Ltd, Oxford, UK, 2004, pp. 635; (b) C. L. Hill, Chem. Rev., 1998, **98**, 1–2 (Special issue: polyoxometalates).

[13] S. S. Wang and G. Y. Yang, Chem. Rev., 2015, **115**, 4893.

[14] J. M. Clemente-Juan, E. Coronado and A. Gaita-Ariño, Chem. Soc. Rev., 2012, **41**, 7464.

[15] M. P. Santoni, G. S. Hanan and B. Hasenknopf, Coord. Chem. Rev., 2014, **281**, 64.

[16] J. Zhang, Y. Huang, G. Li and Y. Wei, Coord. Chem. Rev., 2019, **378**, 395.

[17] L. Vilà-Nadal and L. Cronin, Nat. Rev. Mater., 2017, **2**, 17054.

[18] A. Proust, B. Matt, R. Villanneau, G. Guillemot, P. Gouzerh, and G. Izzet, Chem. Soc. Rev., 2012, **41**, 7605.

[19] K. P. Sullivan, W. A. Neiwert, H. Zeng, A. K. Mehta, Q. Yin, D. A. Hillesheim, S. Vivek, P. Yin, D. L. Collins-Wildman, E. R. Weeks, T. Liu and C. L. Hill, Chem. Commun., 2017, **53**, 11480.

[20] A. V. Anyushin, A. Kondinski and T. N. Parac-Vogt, Chem. Soc. Rev., 2020, **49**, 382.

[21] S. Kuramochi, T. Shiga, J. M. Cameron, G. N. Newton and H. Oshio, Inorganics, 2017, **5**, 48.

[22] A. Abhervé, M. Palacios-Corella, J. M. Clemente-Juan, R. Marx, P. Neugebauer, J. van Slageren, M. Clemente-León and E. Coronado, J. Mater. Chem. C, 2015, **3**, 7936.

[23] J. W. Han, K. I. Hardcastle and C. L. Hill, Eur. J. Inorg. Chem., 2006, **2006**, 2598.

[24] J. W. Han and C. L. Hill, J. Am. Chem. Soc., 2007, **129**, 15094.

[25] N. Bridonneau, L. Rigamonti, G. Poneti, D. Pinkowicz, A. Forni and A. Cornia, Dalton Trans., 2017, **46**, 4075.

[26] K. Senthil Kumar, B. Heinrich, S. Vela, E. Moreno-Pineda, C. Bailly and M. Ruben, Dalton Trans., 2019, **48**, 3825.

[27] Q. Chen, D. P. Gosborn, C. P. Scholes, X. L. Tan, and J. Zubieta, J. Am. Chem. Soc. 1992, **114**, 4667-4681.

[28] C. Allain, S. Favette, L. M. Chamoreau, J. Vaissermann, L. Ruhlmann, and B. Hasenknopf, Eur. J. Inorg. Chem. 2008, **2008**, 3433–3441.

[29] (a) O. Henrion and W. Jaegermann, Surf. Sci., 1997, **387**, L1073, (b) L. Zhang, N. Vilà, A. Walcarius and M. Etienne, ChemElectroChem, 2018, **5**, 2208.

[30] (a) N. El Murr, J. Organomet. Chem., 1976, 112, 189; (b) I. E. Philip and A. E. Kaifer, J. Am. Chem. Soc., 2002, **124**, 12678.

[31] J. A. DeGayner, I. R. Jeon, L. Sun, M. Dinca and T. D. Harris, J. Am. Chem. Soc., 2017, **139**, 4175.

[32] A. Müller, J. Meyer, H. Bögge, A. Stammler and A. Botar, Z. Anorg. Allg. Chem., 1995, **621**, 1818-1831.

[33] (a) S. Marcén, L. Lecren, L. Capes, H. A. Goodwin and J. F. Létard, Chem. Phys. Lett., 2002, **358**, 87; (b) V. A. Money, J. Sánchez-Costa, S. Marcén, G. Chastanet, J. Elhaïk, M. A. Halcrow, J. A. K. Howard and J. F. Létard, Chem. Phys. Lett., 2004, **391**, 273, (c) J. F. Létard, P. Guionneau, O. Nguyen, J. Costa, S. Marcén, G. Chastanet, M. Marchivie and L. Goux-Capes, Chem. Eur. J., 2005, **11**, 4582.

[34] G. J. Halder, C. J. Kepert, B. Moubaraki, K. S. Murray and J. D. Cashion, Science, 2002, **298**, 1762.

[35]Z. P. Ni, J. L. Liu, N. Hoque, W. Liu, J. Y. Li, Y. C. Chen and M. L. Tong, Coord. Chem. Rev., 2017, **335**, 28.

[36] R. Turo-Cortés, C. Bartual-Murgui, J. Castells-Gil, M. C. Muñoz, C. Martí-Gastaldo and J. A. Real, Chem. Sci., 2020, **11**, 11124.

[37] H. Y. Wang, J. Y. Ge, C. Hua, C. Q. Jiao, Y. Wu, C. F. Leong, D. M. D'Alessandro, T. Liu, and J. L. Zuo, Angew. Chem. Int. Ed., 2017, **56**, 5465.

[38]L. Zappe, S. Schönfeld, G. Hörner, K. A. Zenere, C. F. Leong, C. J. Kepert, D. M. D'Alessandro, B. Weber and S. M. Neville, Chem. Commun., 2020, **56**, 10469.

Supporting Information: Redox and Guest Tunable Spin-crossover Properties in a Polymeric Polyoxometalate

Table of contents

1. Experimental Section

$(C_{16}H_{36}N)_3[H_3V_{10}O_{28}]$[1] and TRIS-bpp (See Scheme S1)[2] were synthesized according to the literature. All other materials and solvents were commercially available and used without further purification. Syntheses of **2**, **red 2** and **red 3** were performed in a glove box.

Synthesis of $(C_{16}H_{36}N)_2[V_6O_{19}(C_{16}H_{15}N_6O)_2]\cdot(C_4H_9NO)_2$ (1).

$(C_{16}H_{36}N)_3[H_3V_{10}O_{28}]$ (1 g, 0.6 mmol) and TRIS-bpp (0.54 g, 1.5 mmol) were dissolved in 12 mL of dry dimethylacetamide (DMAc) and heated to 80°C under an Ar atmosphere. After 48 hours a brownish solution was obtained and filtered. Red cubic shaped crystals (600 mg, 54 %) were obtained after 5 days of slow evaporation of the solvent. ^{1}H NMR (CD_3CN, 300 MHz): 8.741 (d, J = 2.7 Hz, 4H, H_{Im1}), 8.11 (br, 4H, H_{Pyr}), 7.831 (d, J = 1.5 Hz, 4H, H_{Im2}), 6.59 (dd, J = 2.7, 0.9 Hz, 4H, H_{Im3}), 5.49 (s, 12H, H_{CH2}), 3.13 (m, 16H, H_{C1}), 1.62 (q, J = 7.8 Hz, 16H, H_{C2}), 1.36 (sx, J = 7.5 Hz, 16H, H_{C3}), 0.99 (t, J = 7.5 Hz, 24H, H_{C4}) (presence of 2 equiv. of DMAc confirmed by peaks at 1.74, 2.85 and 2.99 ppm). IR (KBr pellet, cm^{-1}): 2959 (ν C-H, s), 2935 (ν C-H, s), 2874 (ν C-H, s), 1673 (m), 1627 (s), 1569 (m), 1549(m), 1524 (m), 1484 (sh), 1460 (s), 1396 (ν C-H, s), 1362 (w), 1320 (w), 1284 (w), 1258 (w), 1207 (w), 1097 (ν C-O, s), 1057 (ν C-O, vs), 986 (w), 953 (ν V=O, vs), 882 (w), 812 (ν V-O-V, s), 800 (ν V-O-V, s), 767 (w), 719 (ν V-O-V, vs), 681 (w), 610 (w), 584 (m), 513 (w), 467 (w), 420 (m). Anal. Calcd (found) for $(C_{16}H_{36}N)_2[V_6O_{19}(C_{16}H_{15}N_6O)_2]\cdot(C_4H_9NO)_2$: C, 45.91 (46.11); H, 6.42 (6.61); N, 11.90 (11.99) %.

Synthesis of $Fe[V_6O_{19}(C_{16}H_{15}N_6O)_2\cdot$solv (2·DMF and 2·MeCN).

A solution of **1** in dry dimethylformamide (DMF) (6 mL, 5 mM) was added to the bottom of a 16 mL diffusion tube. On top of this solution a solution of $Fe(ClO_4)_2$ in dry MeCN was added slowly (6 mL, 5 mM). After 2 weeks a crystalline material was found in the walls of the diffusion tube. It was collected and washed with acetonitrile several times. Samples were stored under fresh dry MeCN. IR (cm^{-1}):

3092(w), 1675 (m), 1628 (m), 1573(w), 1525 (m), 1498 (sh), 1458 (s), 1403 (νC-H, s),1318 (w), 1268 (w), 1207 (w), 1100 (νC-O, s), 1046 (ν C-O, vs), 946 (νV=O, vs), 865 (w), 789 (m), 707 (νV-O-V, s), 577 (m), 511 (w), 456 (w), 420 (m). Anal. Calcd (found) for $Fe[V_6O_{19}(C_{16}H_{15}N_6O)_2]\cdot DMF\cdot MeCN\cdot 5H_2O$ (**2·DMF**): C, 29.94 (29.85); N, 13.21 (13.31); H, 3.40 (3.34) (Filtered sample of the as-synthesized crystals). Anal. Calcd (found) for $Fe[V_6O_{19}(C_{16}H_{15}N_6O)_2\cdot 7H_2O$ (**2·MeCN**): C, 27.33 (27.34); N, 11.95 (11.95); H, 3.15 (3.00) (Filtered sample, stored in MeCN). Anal. Calcd (found) for $Fe[V_6O_{19}(C_{16}H_{15}N_6O)_2\cdot 5H_2O$: C, 28.05 (28.18); N, 12.27 (12.15); H, 3.15 (2.94) (Sample heated to 400 K).

Synthesis of $Zn[V_6O_{19}(C_{16}H_{15}N_6O)_2$·solv (3·DMF and 3·MeCN).

Two different methods were employed in the synthesis of the zinc derivative. Method I was used to obtain single crystals and method II to obtain bulk material.

Method I. A solution of **1** in DMF (6 mL, 5 mM) was added to the bottom of a 16 mL diffusion tube in air. A mixture of 2 mL of MeCN and 2 mL of DMF was added on top of this solution as an interface between the two reactant solutions. A solution of $Zn(ClO_4)_2$ in MeCN (6 mL, 5 mM) was added slowly on top of this solution. After several weeks, very few single crystals of **3** were found in the walls of the diffusion tube, which were used to determine the single crystal structure without washing with MeCN (**3·DMF sample)**. Anal. Calcd (found) for $Zn[V_6O_{19}(C_{16}H_{15}N_6O)_2]\cdot DMF\cdot MeCN\cdot 6.5H_2O$ (**3·DMF**): C, 29.22 (29.21); N, 12.89 (12.90); H, 3.51 (3.43).

Method II. A solution of **1** in a mixture MeCN:DMF 10:1 (6 mL, 5 mM) was added to the bottom of a 16 mL diffusion tube in a glove box. 2 mL of MeCN with one drop of DMF was added on top of this solution as an interface. Finally, a solution of $Zn(ClO_4)_2$ in MeCN (6 mL, 5 mM) was added slowly. After 3 days a crystalline powder material was found in the walls of the diffusion tube, it was collected and washed with acetonitrile several times (**3·MeCN** sample). IR (cm^-

[1]): 3099(w), 1685 (m), 1630 (w), 1577(w), 1528 (m), 1500 (sh), 1457 (s), 1403 (ν C-H, s),1336 (w), 1268 (m), 1211 (w), 1096 (ν C-O, s), 1046 (ν C-O, vs), 946 (ν V=O, vs), 863 (w), 791 (m), 707 (ν V-O-V, s), 577 (m), 509 (w), 456 (w), 420 (m). Anal. Calcd (found) for $Zn[V_6O_{19}(C_{16}H_{15}N_6O)_2]\cdot 6H_2O$ (**3·MeCN**): C, 27.50 (27.46); N, 12.02 (12.09); H, 3.03 (2.93).

Synthesis of $Fe[V_6O_{19}(C_{16}H_{15}N_6O)_2]\cdot[Co(C_5H_5)_2]_{1.2}\cdot 8H_2O$ (Red 2) and $Zn[V_6O_{19}(C_{16}H_{15}N_6O)_2]\cdot[Co(C_5H_5)_2]_{1.2}\cdot 11H_2O$ (Red 3).

In a glovebox, bis(cyclopentadienyl)cobalt(II) (50 mg) was dissolved in 10 mL of MeCN. To this solution, **2·MeCN** or **3·MeCN** (20 mg) were added. The suspension was slowly stirred for 5 hours. A rapid change in color during the first minutes was observed from orange to dark green. After this reaction time, supernatant was removed without leaving the crystals uncovered and the sample was washed with dry MeCN three times. IR (cm^{-1}): 3090 (w), 1652 (m), 1630 (w), 1567(w), 1524 (m), 1499 (sh), 1459 (s), 1404 (ν C-H, s),1330 (w), 1267 (m), 1101 (ν C-O, s), 1045 (ν C-O, vs), 935 (ν V=O, vs), 863 (w), 796 (sh), 753 (ν V-O-V, s), 714 (s), 681 (s), 580 (s), 494 (w), 456 (w), 409 (m) (**Red 2**); 3080 (w), 1651 (m), 1630 (w), 1567(w), 1526 (m), 1500 (sh), 1456 (s), 1400 (ν C-H, s),1333 (w), 1267 (m), 1103 (ν C-O, s), 1044 (ν C-O, vs), 974 (m), 930 (ν V=O, vs), 863 (w), 796 (sh), 754 (ν V-O-V, s), 678 (s), 582 (s), 494 (w), 456 (w), 405 (m) (**Red 3**). Anal. Calcd (found) for $Fe[V_6O_{19}(C_{16}H_{15}N_6O)_2]\cdot[Co(C_5H_5)_2]_{1.3}\cdot 8H_2O$ (**Red 2**): C, 32.36 (32.27); N, 10.06 (9.86); H, 3.56 (3.50). Anal. Calcd (found) for $Zn[V_6O_{19}(C_{16}H_{15}N_6O)_2]\cdot[Co(C_5H_5)_2]_{1.3}\cdot 11H_2O$ (**Red 3**): C, 31.18 (31.07); N, 9.90 (10.21); H, 3.50 (3.25).

Synthesis of $Fe[V_6O_{19}(C_{16}H_{15}N_6O)_2][Co(C_5H_5)_2]_{0.5}[Br]_{0.5}\cdot 10H_2O$ (Reox 2).

Red 2 (20 mg) was suspended in MeCN. 30 mg of $TBABr_3$ were then added to the suspension and slow stirring for 18 hours was employed to avoid the breaking of the small crystallites, which

yielded an orange material. After this time, supernatant was removed without leaving the crystals uncovered and the sample was washed with dry MeCN several times. IR (cm^{-1}): 3096 (w), 1685 (w), 1628 (w), 1567(w), 1524 (m), 1499 (sh), 1459 (s), 1403 (ν C-H, s),1322 (w), 1267 (m), 1208 (w), 1098 (ν C-O, m), 1047 (ν C-O, vs), 951 (ν V=O, vs), 863 (w), 792 (m), 710 (ν V-O-V, s), 577(m), 509 (w), 457 (w). Anal. Calcd (found) for $Fe[V_6O_{19}(C_{16}H_{15}N_6O)_2]\cdot[Co(C_5H_5)_2]_{0.5}[Br_5]_{0.5}\cdot 10H_2O$ (**Reox 2**): C, 28.40 (28.42); N, 10.46 (10.62); H, 3.45 (3.49).

Syntheses of samples with exchange of solvents: 2·MeOH, 2·EtOH, 2·$MeNO_2$, 2·PhCN, 2·Me_2CO, 2·PhCNtoMeCN and 2·PhCNtoMeCNtoPhCN.

Most of the mother liquor (DMF/MeCN mixture) was removed leaving a small volume covering the crystals of **2·DMF** to avoid complete desolvation and loss of crystallinity. The exchanged solvent (MeOH, EtOH, $MeNO_2$, PhCN or Me_2CO) was added covering the crystals for 3 days. During this time, several additions of clean solvent were performed without leaving the crystals uncovered. Finally, the exchanged material was stored in the same solvent. **2·PhCNtoMeCN** was prepared in the same way starting from crystals of **2·PhCN**, which were soaked for 3 days in MeCN. **2·PhCNtoMeCNtoPhCN** was prepared in the same way soaking crystals of **2·PhCNtoMeCN** for three days in PhCN. Anal. Calcd (found) for $Fe[V_6O_{19}(C_{16}H_{15}N_6O)_2]\cdot 5.5H_2O$ (**2·MeOH**): C, 27.84 (27.84); N, 12.18 (12.34); H, 2.99 (3.01)). Anal. Calcd (found) for $Fe[V_6O_{19}(C_{16}H_{15}N_6O)_2]\cdot 3H_2O$ (**2·EtOH**): C, 28.42 (28.60); N, 12.43 (12.09); H, 2.83 (3.12). Anal. Calcd (found) for $Fe[V_6O_{19}(C_{16}H_{15}N_6O)_2]\cdot 0.8MeNO_2\cdot 4H_2O$ (**2·$MeNO_2$**): C, 28.12 (27.99); N, 12.80 (12.89); H, 2.91 (2.91). Anal. Calcd (found) for $Fe[V_6O_{19}(C_{16}H_{15}N_6O)_2]\cdot 6H_2O$ (**2·Me_2CO**): C, 27.69 (27.63); N, 12.11 (12.01); H, 3.05 (3.12). Anal. Calcd (found) for $Fe[V_6O_{19}(C_{16}H_{15}N_6O)_2]\cdot 3PhCN\cdot 2H_2O$ (**2·PhCN**): C, 39.16 (39.03); N, 12.95 (13.19); H, 3.04 (3.24). Anal. Calcd (found) for

$Fe[V_6O_{19}(C_{16}H_{15}N_6O)_2]\cdot 6H_2O$ (**2·PhCNtoMeCN**): C, 27.69 (27.58); N, 12.11(12.10); H, 3.05 (2.98). Anal. Calcd (found) for $Fe[V_6O_{19}(C_{16}H_{15}N_6O)_2]\cdot 3PhCN\cdot 2H_2O$ (**2·PhCNtoMeCNtoPhCN**): C, 39.16 (39.23); N, 12.95 (13.12); H, 3.04 (3.15).

Physical measurements

IR spectra (cm^{-1}) were measured on an ATI Mattson Genesis Series FTIR instrument and a Nicolet Avatar 320 FTIR spectrometer. C, H and N elemental analyses were done using a CE Instruments EA 1110 CHNS Elemental analyser. The V:Fe, V:Zn, Co:Fe:V, Co:Zn:V and Co:Fe:V:Br ratios were measured using a Philips ESEM X230 scanning electron microscope equipped with an EDAX DX-4 microprobe. ^1H NMR spectra were acquired using a Bruker AVANCE DRX 300 spectrometer. A Q-TOF Premier mass spectrometer with an orthogonal Z-spray electrospray source (Waters, Manchester, UK) was used for electrospray ionization mass spectrometry (ESI-MS). The temperature of the source block was set to 100 1C and the desolvation temperature to 120 1C. A capillary voltage of 3.3 kV was used in the negative scan mode, and the cone voltage was set to 5 V to control the extent of fragmentation of the identified species. TOF mass spectra were acquired in the W-mode operating at a resolution of ca. 15 000 (fwhm). Mass calibration was performed using a solution of sodium iodide in isopropanol/ water (50 : 50) from m/z 50 to 3000. Acetonitrile sample solutions were infused via syringe pump directly connected to the ESI source at a flow rate of 10 mL min^{-1}. The observed isotopic pattern of each compound perfectly matched the theoretical isotope pattern calculated from their elemental composition using the MassLynx 4.1 program. TGA was performed in Mettler Toledo TGA/SDTA 851e Thermogravimetric and Differential Thermal Analyzer. XPS (K-ALPHA, Thermo Scientific) was used to analyze the surfaces of the samples. All spectra were collected using Al Kα radiation (1486.6 eV), monochromatized by a twin crystal monochromator.

Single crystals of **1, 3·DMF** and **Red 3** were mounted on glass fibres using a viscous hydrocarbon oil to coat the crystal and then were transferred directly to the cold nitrogen stream for data collection. All reflection data were collected at 120 K using a Supernova equipped with a graphite-monochromated Enhance (Mo) X-ray Source (l = 0.7107 Å). The CrysAlisPro program, Oxford Diffraction Ltd., was used for unit cell determinations and data reduction. Empirical absorption correction was performed using spherical harmonics, implemented in the SCALE3 ABSPACK scaling algorithm. Crystal structures were solved and refined against all F2 values by using the SHELXTL and Olex2 suite of programs.[3] All non-hydrogen atoms were refined anisotropically except as noted and hydrogen atoms were placed in calculated positions and refined isotropically with a riding model. The structure of **2** showed a weak diffraction due to the presence of disordered solvent molecules in the structure. Due to this, it was not possible to refine anisotropically C and N atoms. Initial refinements revealed the presence of a substantial volume of unresolvable solvent (DMF) molecules in **2**. The subroutine SQUEEZE from PLATON was used to remove the diffracting component of disordered solvents resulting in a void of ca. 741.5 $Å^3$ and 142 electrons per cell omitted. This corresponds to ca. 3 DMF molecules per unit cell. Crystallographic data are summarized in Table S1.

Polycrystalline samples were filled into 0.7 and 1 mm borosilicate capillaries prior to being mounted and aligned on an Empyrean PANalytical powder diffractometer, using Cu Kα radiation (λ = 1.54056 Å). For each compound, three repeated measurements were collected at room temperature (2θ = 2–40°) and merged in a single diffractogram. Pawley refinements[3] were performed using the TOPAS computer program[4] and revealed an excellent fit to a one-phase model for compounds **2** (R_{wp} = 0.0201; GOF = 7.447, Figure S7a), **3** (R_{wp} = 0.0151; GOF = 2.2432, Figure S7b), **Red 2** (R_{wp} = 0.0113; GOF = 1.480, Figure S7c) and **Red 3** (R_{wp} = 0.0124; GOF = 1.620,

Figure S7d).The unit cell parameters for each compound are shown in Table S2. In the Zn derivatives, the unit cell obtained from the Pawley refinement is consistent with those obtained by single crystal diffraction (see Table S1).

The electrochemical experiments were performed using an Autolab electrochemical workstation (Autolab-128N potentiostat/galvanostat) connected to a personal computer that uses Nova 2.1 electrochemical software. The powdered materials (2 mg) were mixed in 2 ml of Nafion 5% and ethanol (1:1) and deposited on a 3 mm diameter glassy carbon disc working electrode (which was polished sequentially with 0.3, 0.1 and 0.05 μm alumina powders and washed with deionised water before each experiment). A typical three-electrode experimental cell equipped with a platinum wire as the counter electrode, and a silver wire as the pseudoreference electrode was used for the electrochemical characterization of the working electrodes. All measurements were carried out with magnetic agitation and nitrogen bubbling. The electrochemical properties were studied measuring the CV at different scan rates in 0.1 M $TBABF_4/CH_3CN$ solution. Ferrocene was added as an internal standard upon completion of each experiment. All potentials are reported in V versus Ag/AgCl

Magnetic measurements were performed with a Quantum Design MPMS-XL-5 SQUID magnetometer with an applied magnetic field of 0.1 T. Solvated samples were deposited in the bottom of a glass tube and covered with the mother liquor. This tube was used as the sample holder. Photomagnetic measurements were performed irradiating with a 30993 cylindrical Helium-Neon Laser system from Research Electro-Optics (red light, λ = 633 nm, optical power 12 mW cm^{-2}) coupled via an optical fiber to the cavity of the SQUID magnetometer. It was verified that irradiation resulted in no significant change in magnetic response due to heating of the sample. The photomagnetic samples consisted of a thin layer of compound whose weight was corrected by comparison of a thermal

spin crossover curve with that of a more accurately weighted sample of the same compound. Solvated samples were protected with a grease immediately after being extracted from the mother liquor. EPR measurements were recorded in a Bruker ELEXYS E580 spectrometer under X-band irradiation (~9.4 GHz) in samples protected with the mother liquor and prepared and sealed in the glove box. Mössbauer spectra of the **2·MeCN** filtered sample were collected between 295 and 4 K in transmission mode using a conventional constant-acceleration spectrometer and a 25 mCi ^{57}Co source in a Rh matrix. The velocity scale was calibrated using α-Fe foil. Isomer shifts, IS, are given relative to this standard at room temperature. The absorbers were obtained by gently packing the sample into a perspex holder. Absorber thickness was calculated on the basis of the corresponding electronic mass-absorption coefficients for the 14.4 keV radiation, according to Long *et al*. (1983).[5] Low-temperature measurements were performed in a bath cryostat with the sample immersed in He exchange gas. The spectra were fitted to Lorentzian lines using a non-linear least-squares method.[6]

2. Synthesis and characterization of 1

1-bpp-functionalized Lindqvist POM (**1**) was synthesized following adapted literature procedures (see Scheme 1).[2, 7] The starting material for the preparation of the functionalized POM was a tris-(hydroxymethyl)-functionalized 1-bpp (TRIS-bpp), which was obtained from 1-bpp-4´-carboxyethylester.[2] The functionalization of the POM was performed by reaction of TRIS-bpp and the polyoxovanadate precursor, $TBA_3H_3[V_{10}O_{28}]$ (TBA = tetrabutylammonium), in dry dimethylacetamide (DMAc). Single crystals were obtained by slow evaporation of the DMAc solution of the compound. ^1H NMR spectra confirm the purity of **1** and the grafting of 1-bpp to the POM in **1** (see **Fig. S1**). As observed previously in terpyridine-functionalized Lindqvist POM,[7] the electronic influence of the cluster (diamagnetic V^V) induces changes in the chemical shifts of the methylene protons of the ligand but not in those of the aromatic ones. Further characterization of **1** has been performed by elemental analysis, IR spectroscopy (**Fig. S2**), and electrospray ionization mass spectrometry (ESI-MS) (**Figs. S3 and S4**). Thus, the IR bands at 953 cm^{-1} (ν V=O), 812, 800 and 719 cm^{-1} (ν V-O-V), correspond to the Lindqvist structure,[8] while the bands at 1673 cm^{-1} (νC=O), 1097, and 1057 cm^{-1} (νC–O) confirm the grafting of TRIS-bpp onto the POM (**Fig. S2**). On the other hand, ESI-MS is consistent with the bifunctionalization of the POM. **Fig. S3** shows the ESI-MS (negative mode) analysis of a solution of **1** in acetonitrile. The two most intense peaks appear at m/z values of 611.9, and 1224.9, which correspond respectively to the $[V_6O_{19}(C_{16}H_{15}N_6O)_2]^{2-}$ ($[\mathbf{1}]^{\mathbf{2-}}$) and $H[V_6O_{19}(C_{16}H_{15}N_6O)_2]^-$ ($H^+ + [\mathbf{1}]^{\mathbf{2-}}$) species. As these peaks arise from species in which the POM remains intact, we can conclude that the structure of the polyanion is preserved in solution. The charge of the species present in the spectrum has been characterized by single ion recording (SIR) at the highest resolution of the spectrometer with monoisotopic peaks separated by 1/z. **Fig. S4**, shows the isotopic distributions of the most intense peaks. The simulated profile does

not fit exactly with the experimental one. This could be due to the presence of reduced vanadium centers (V(IV) formed as a consequence of the high voltages utilized in the mass spectrometry ion-transfer process. Indeed, the presence of molybdenum and tungsten in reduced oxidation states in ESI-MS experiments of polyoxomolybdates and polyoxotungstates has been reported.[9] Furthermore, a similar effect seems to be observed in the ESI-MS spectrum of the same hexavanadate functionalized with terpyridine.[7]

Structure of $(C_{16}H_{36}N)_2[V_6O_{19}(C_{16}H_{15}N_6O)_2]\cdot(C_4H_9NO)_2$ (1)

1 crystallizes in the monoclinic space group $P2_1/c$. The asymmetric unit is composed by half crystallographically independent anion, one TBA^+ cation and one DMAc solvent molecule. The crystallographically independent anion contains an inversion centre placed in the central O atom, O7. It presents the common Lindqvist hexavanadate structure, in which the six V atoms from six octahedral edge-sharing VO_6 form an octahedron. The two trisalkoxo ligands occupy opposite faces of that octahedron (**Fig. S5**). The presence of the trisalkoxy ligands deforms the regular hexavanadate core as observed in similar compounds. Thus, **1** possesses six doubly bridging oxo groups and six doubly bridging alkoxy groups with averageV-O distances of 1.827 (2) and 2.017(2) Å, respectively.[8] The crystallographically independent POM is surrounded by TBA^+ cations and solvent molecules (**Fig. S6**). Hydrogen bonds are observed between the two NH groups of the POMs and carbonyl group from DMAc molecules. Furthermore, the POM presents π-π stacking interactions with the DMAC molecule and numerous short contacts between the oxo group and the CH groups from TBA^+ cations. In contrast to the terpyridine-hexavanadate derivative, clear π-π stacking interactions are not observed between 1-bpp units of neighbouring functionalized-POM. Thus, the pyrazole units from neighbouring functionalized POM present shortest contacts of 3.327 Å and are almost perpendicular (angle between the pyrazole rings close to 80.4°).

The phase purity of the bulk material was evaluated by PXRD. The

experimental PXRD pattern at room temperature matches well with that of the calculated one from the single crystal data at 120 K confirming the purity of the compound (**Fig. S7**).

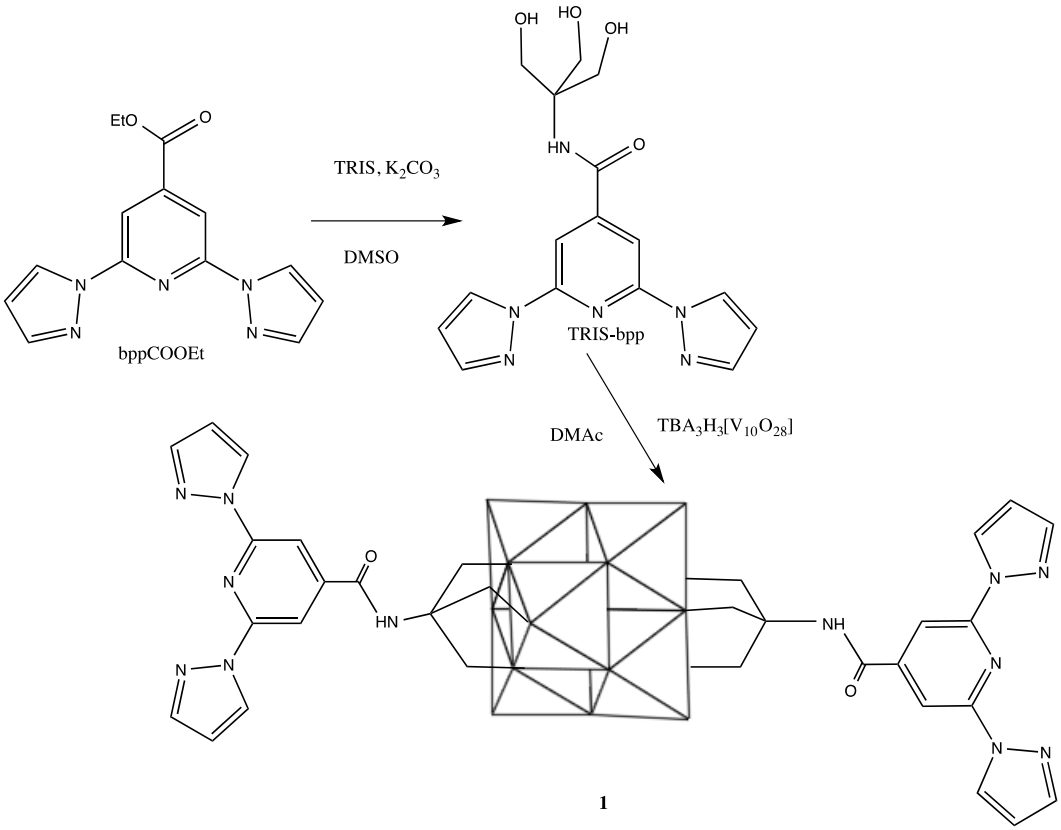

Scheme S1. Synthesis of TRIS-bpp and **1**.

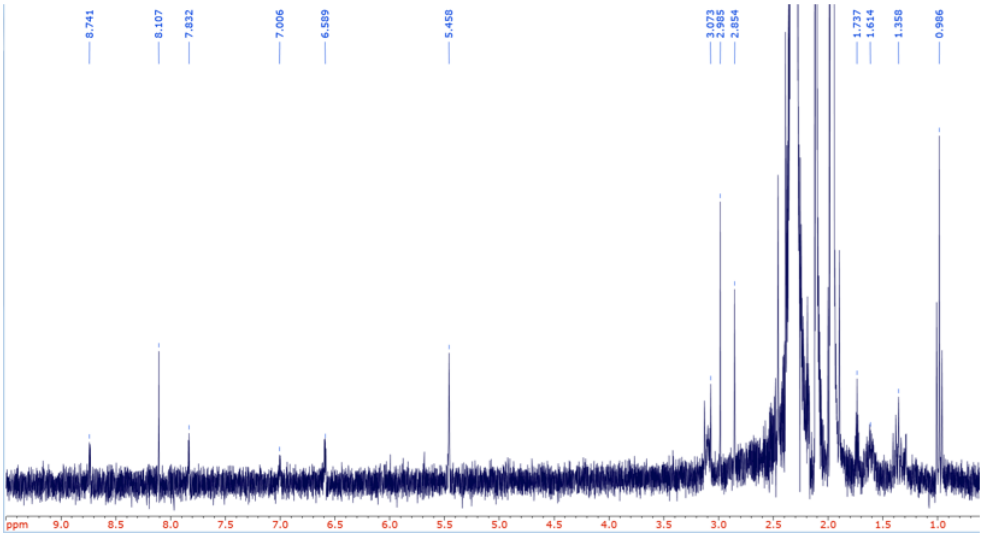

Fig. S1 ^{1}H NMR spectra of **1**.

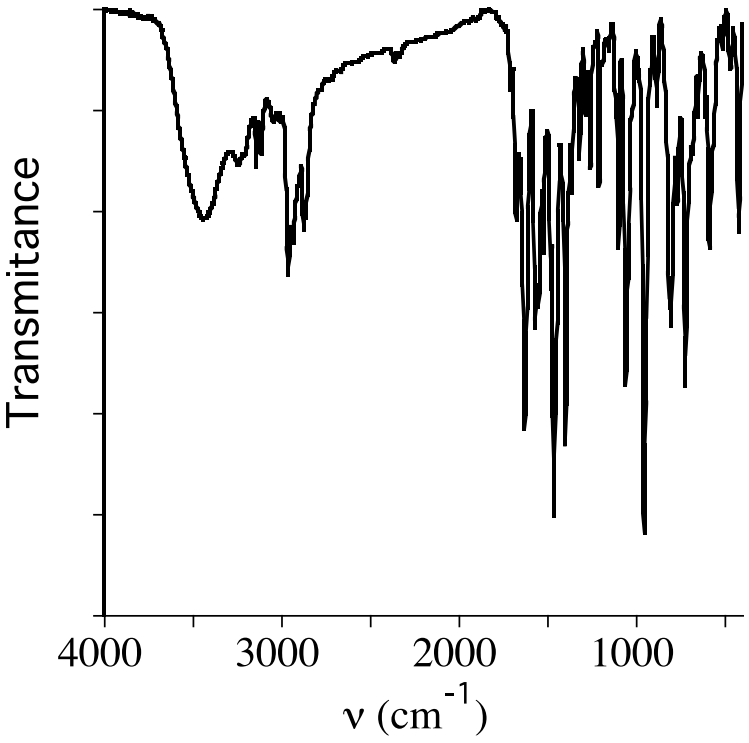

Fig. S2 IR spectrum of **1**.

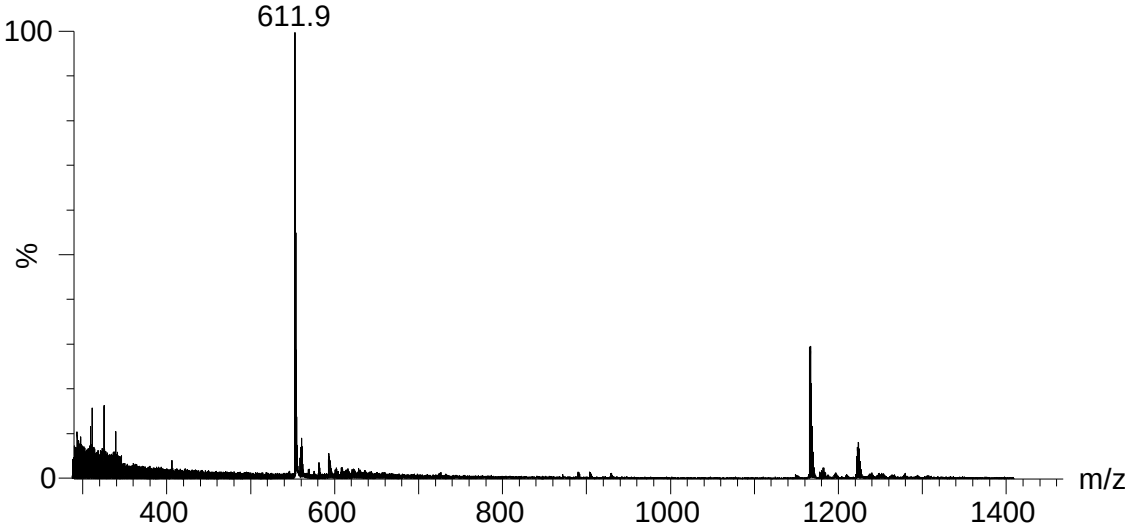

Fig. S3 ESI mass spectrum of acetonitrile solutions of compound **1** recorded at Uc = 5 V.

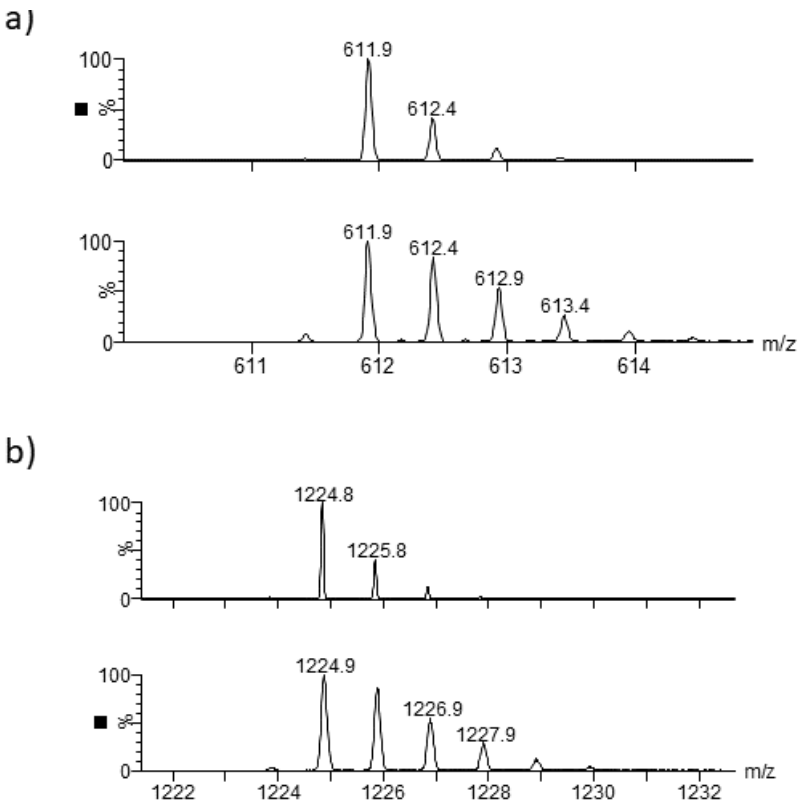

Fig. S4 Simulated (a) and experimental (b) isotopic distribution for the identified species, $[\mathbf{1}]^{2-}$ (top) and $[\mathbf{1} + H]^{-}$ (bottom).

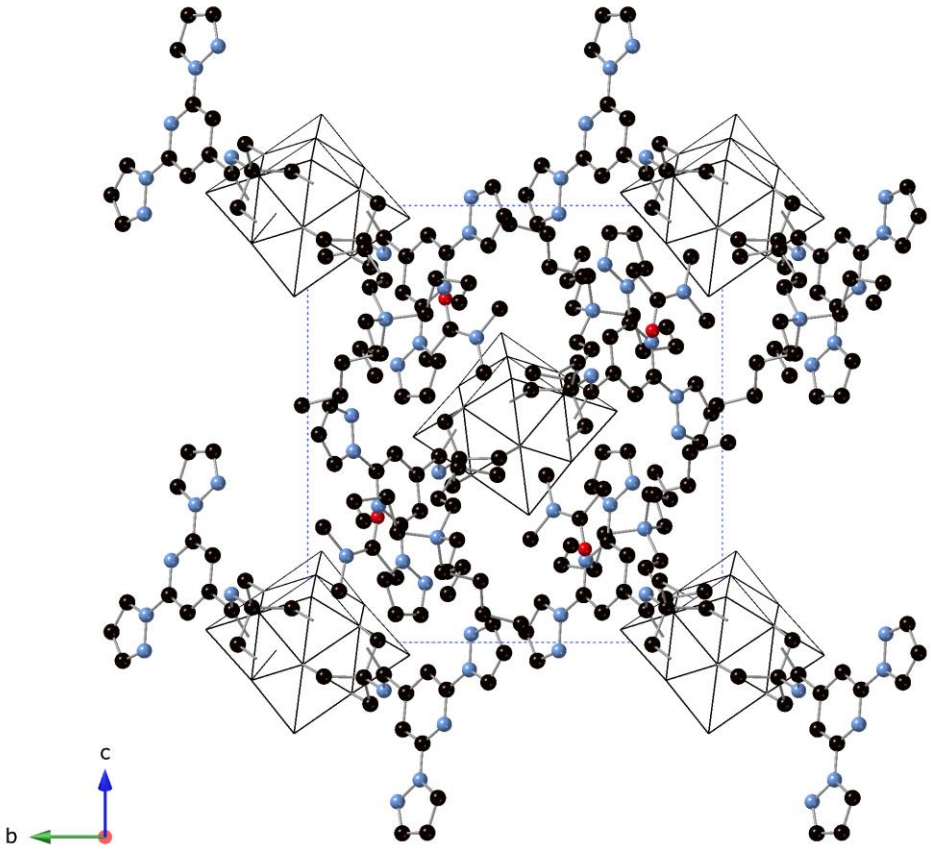

Fig. S5 Projection of the structure of **1** in the *bc* plane (V (white), C (black), N (blue), O (red)). Hydrogen atoms have been omitted for clarity.

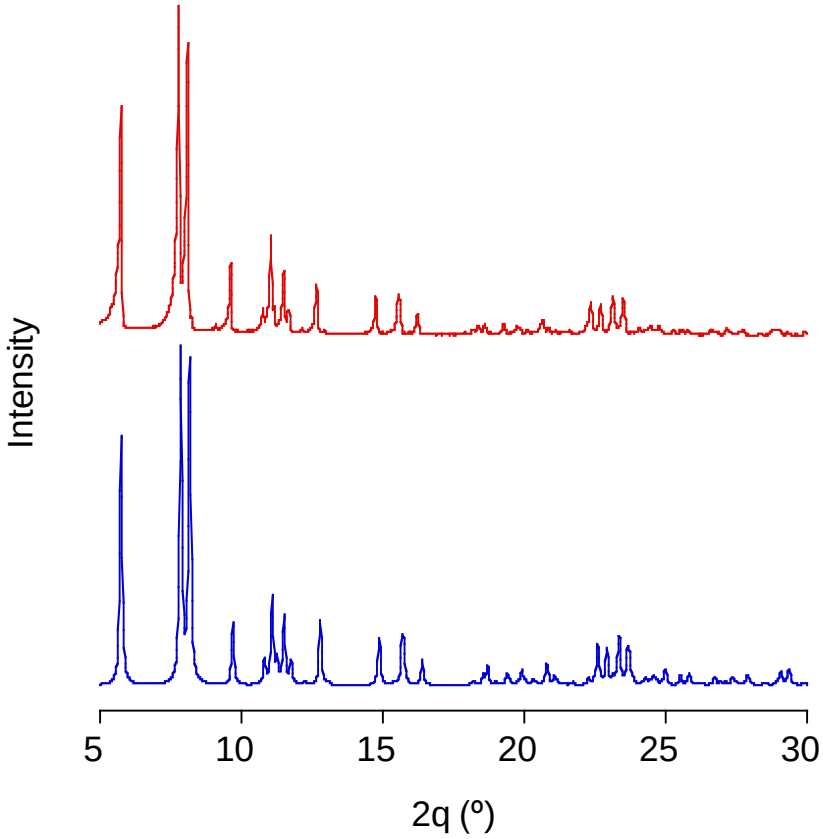

Fig. S6 Experimental (top) and simulated (bottom) X-ray powder diffraction patterns of **1**.

3. Structural data for 2·MeCN, 3·MeCN, Red 2 and Red 3

a)

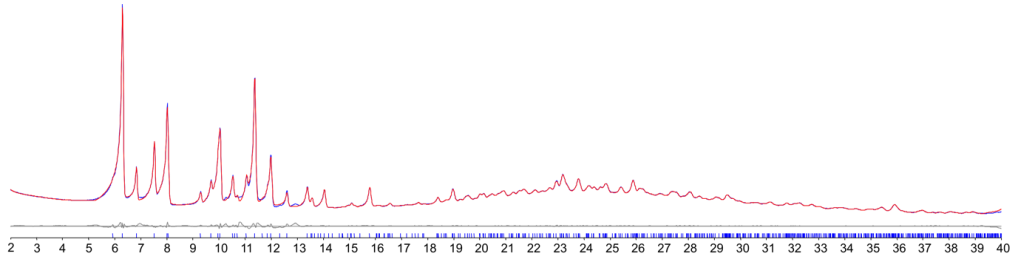

b)

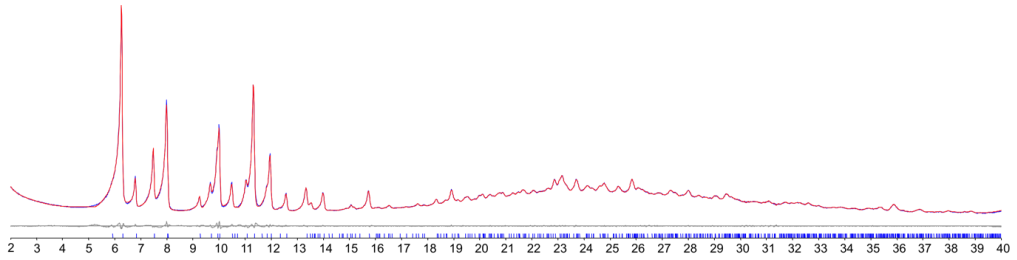

c)

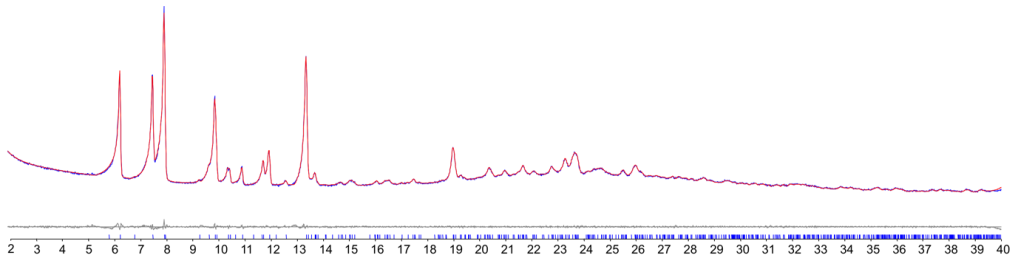

d)

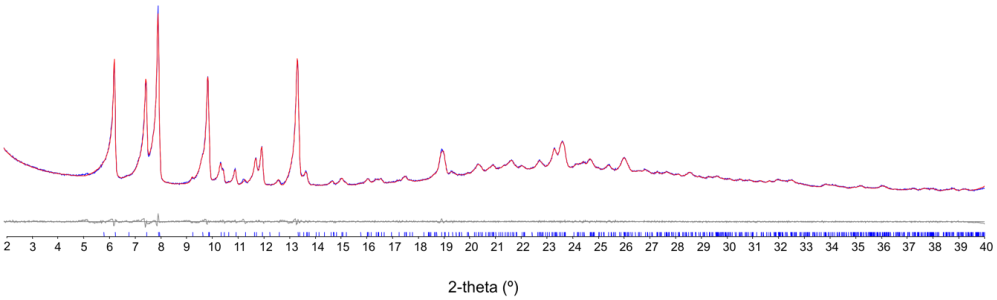

Figure S7. Observed (blue) and calculated (red) profiles and difference plot [(I_{obs}– I_{calcd})] (grey) of the Pawley refinements of compounds **2·MeCN** (a), **3·MeCN** (b), **Red 2** (c) and **Red 3** (d). (2θ range 2–40 º;λ = 1.54056 Å).

Table S1. Crystallographic data for **1**, **3** and **Red 3**.

Compound	**1**	**3**	**Red3**
Empirical formula	$C_{72}H_{120}N_{16}O_{23}V_6$	$C_{39}H_{45}N_{15}O_{23}V_6Zn$	$C_{55}H_{63}N_{20}O_{37}V_9Zn_{1.5}Co_{0.5}$
Formula weight	1883.47	1460.87	2179.22
Crystal colour	Red	Orange	Dark brown
Crystal size	0.2x0.15x0.017	0.06x0.05x0.03	0.05x0.05x0.02
Temperature (K)	120(2)	120(2)	120(2)
Wavelength (Å)	0.71073	0.71073	0.71073
Crystal system	Monoclinic	Monoclinic	Monoclinic
Space group	$P2_1/c$	$P2_1/c$	$P2_1/c$
a (Å)	17.1948(3)	13.2016(16)	13.0362 (19)
b (Å)	15.4967(2)	27.457(4)	27.263(3)
c (Å)	18.2880(4)	18.236(2)	18.471(8)
β (°)	116.7	105.5	105.6
V (Å^3)	4352.96(17)	6369(15)	6288.9(17)
ρ_{calc} (Mg/m^3)	1.437	1.521	1.588
$\mu(Mo_{K\alpha})$ (mm^{-1})	0.697	1.21	1.370
2θ range (°)	6.62 to 55.038	6.474 to 41.628	6.49 to 27.458
Reflns	114963	51146	19518

collected			
Independent reflns (R_{int})	9981(0.084)	6645 (0.517)	1940 (0.25)
L. S. parameters, *p*/ restraints, *r*	529/0	377/0	322/0
$R1(F)$,[a] $I > 2\sigma(I)$	0.049	0.1233	0.1138
$wR2(F^2)$,[b] all data	0.1242	0.3308	0.2793
$S(F^2)$,[c] all data	1.048	0.992	1.080

Table S2. Unit cell parameters obtained from Pawley refinements for compounds **Fe**, **Fe-red**, **Zn** and **Zn-red**.

	a (Å)	b (Å)	c (Å)	α (º)	β (º)	γ (º)
2·MeCN	13.3974(9)	28.090(19)	18.2329(11)	90	104.910(4)	90
Red 2	13.2843(9)	27.9038(19)	18.3913(12)	90	105.135(5)	90
3·MeCN	13.3992(6)	28.085(13)	18.2259(7)	90	104.712(2)	90
Red 3	13.3114(12)	27.872(3)	18.3681(18)	90	104.804(6)	90
Data from single crystal:						
3·DMF	13.2014(14)	27.454(4)	18.232(2)	90	105.500(12)	90
Red 3	13.0362(19)	27.263(3)	18.471(3)	90	105.594(16)	90

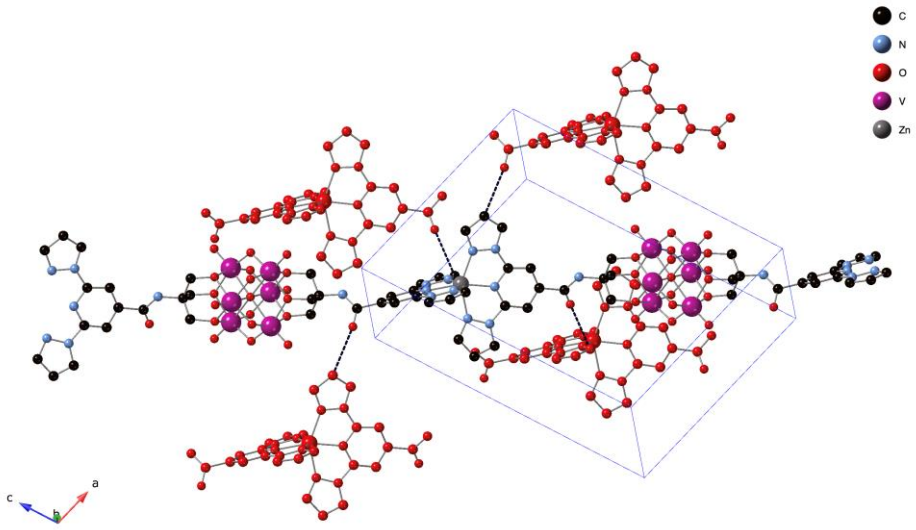

Figure S8. Short interchain contacts (blue dashed line) between $[Zn(1\text{-}bpp)_2]^{2+}$ complexes in **3·DMF**. $[Zn(1\text{-}bpp)_2]^{2+}$ complexes from neighboring chains are colored in red.

4. General characterization for solvent exchanged samples

PXRD pattern of a filtered sample of **2·MeCN** presents fewer and broader peaks than that of the solvated sample (see Fig. S9). These changes indicate a loss of crystallinity and a different packing of the $M[V_6O_{19}(C_{16}H_{15}N_6O)_2]$ chains upon desolvation. The shift of the most intense peak at lower theta values (2ϑ = 6.3° in contact with the mother liquor to 2ϑ = 6.9° in the filtered sample), suggests that the space between chains is being reduced. Indeed, simulated PXRD from the single crystal structure of **3** reducing *b* parameter, which is related the distance between the double layers, by 2 Å (from 27.4573 to 25.4573 Å) leads to similar features in the simulated PXRD pattern (see Fig. S10).

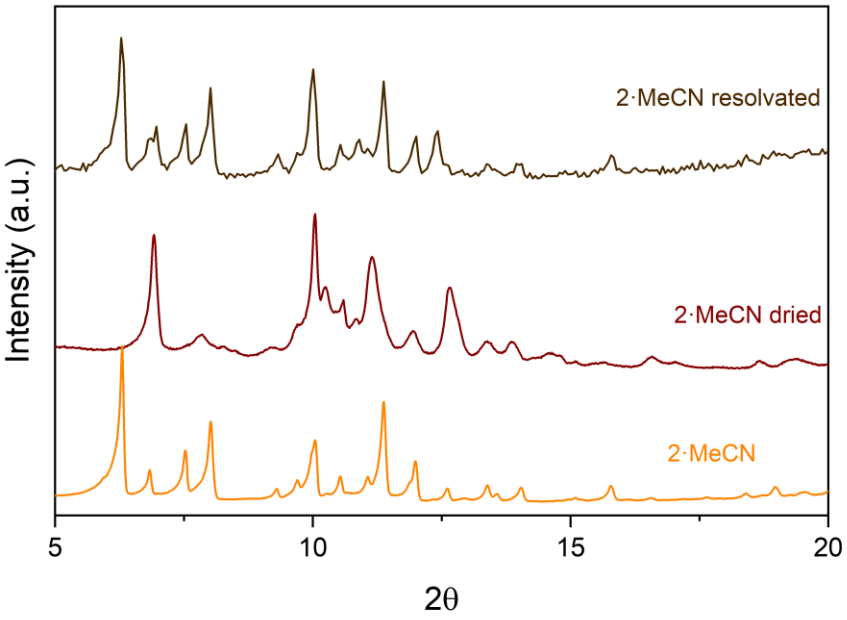

Fig. S9 PXRD patterns of **2·MeCN** in contact with the mother liquor (orange line), filtered sample of **2·MeCN** (brown line) and resolvated **2·MeCN** in contact with the mother liquor (green line).

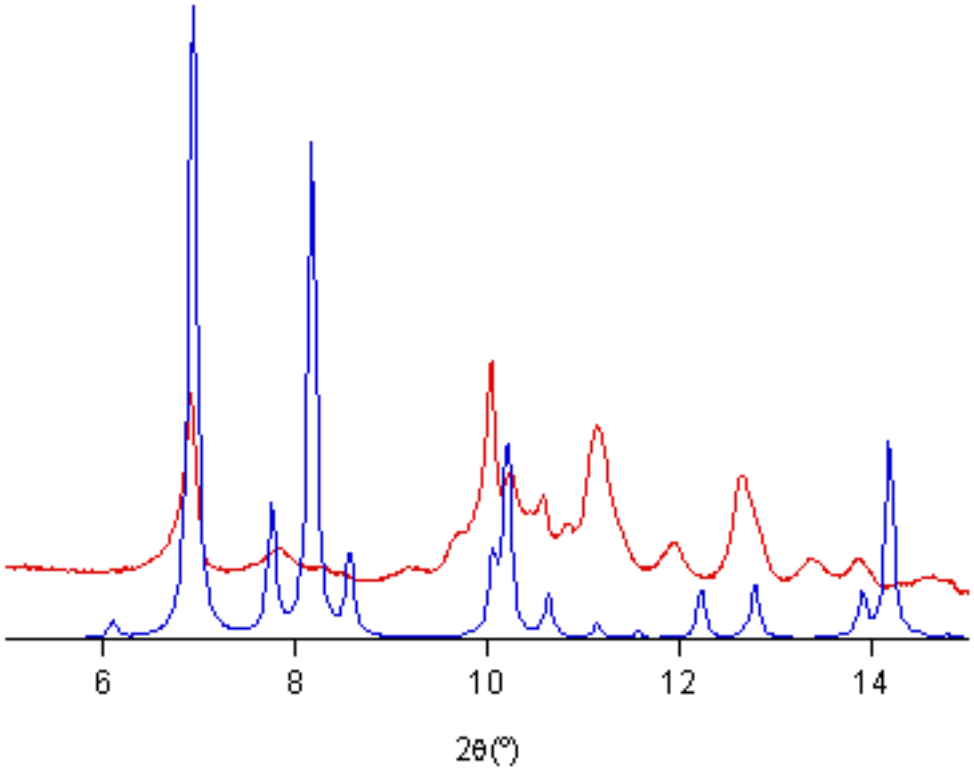

Fig. S10 Simulated PXRD pattern from the single crystal structure of **3·DMF** reducing by 2 Å *b* parameter (red line) and experimental PXRD pattern of a filtered sample of **2·MeCN** (red line).

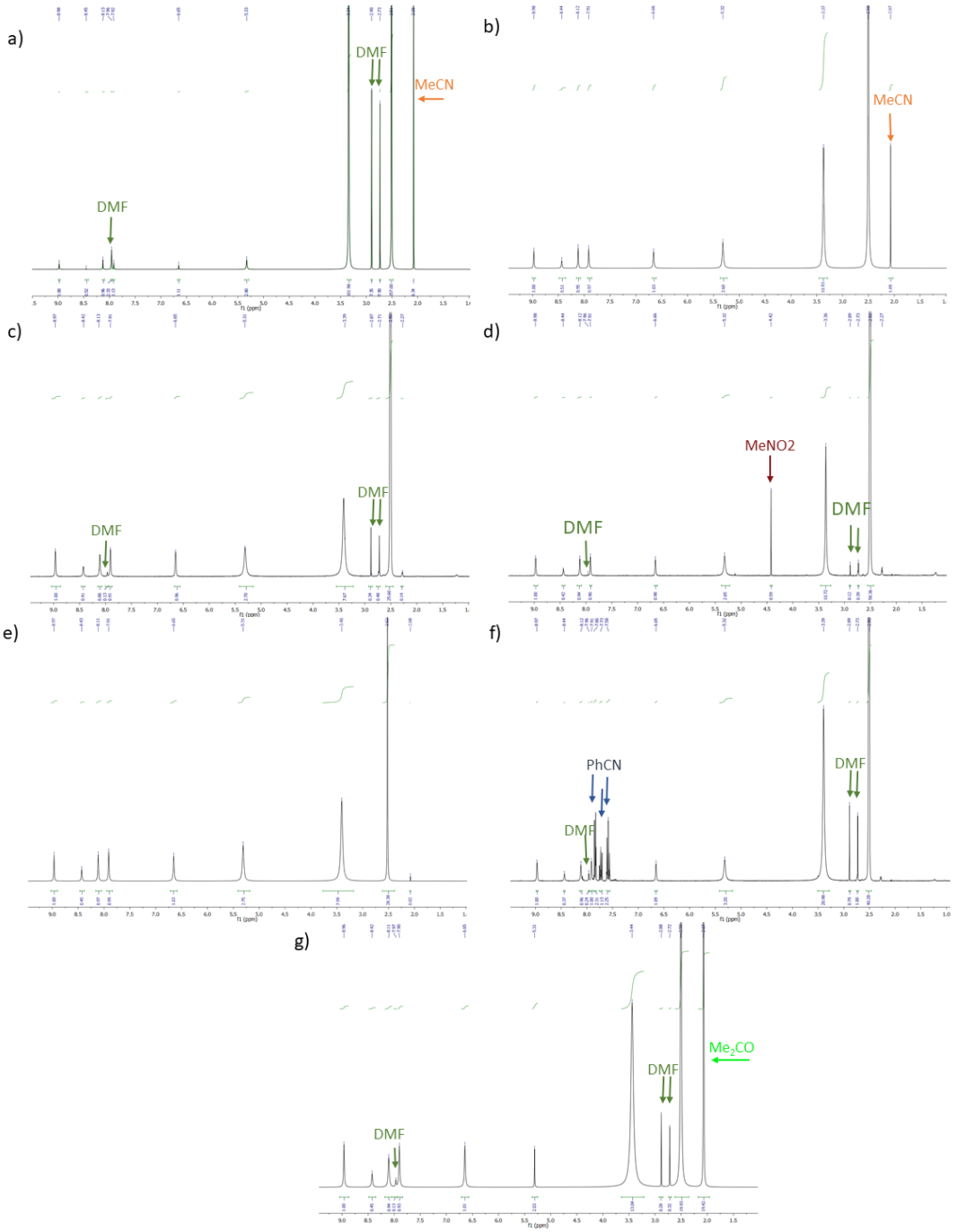

Fig. S11 ^{1}H NMR spectra of freshly filtered crystals of **2·DMF (a), 2·MeCN (b), 2MeOH (c), 2MeNO$_2$ (d), 2·EtOH (e), 2·PhCN (f), 2·Me$_2$CO (g).**

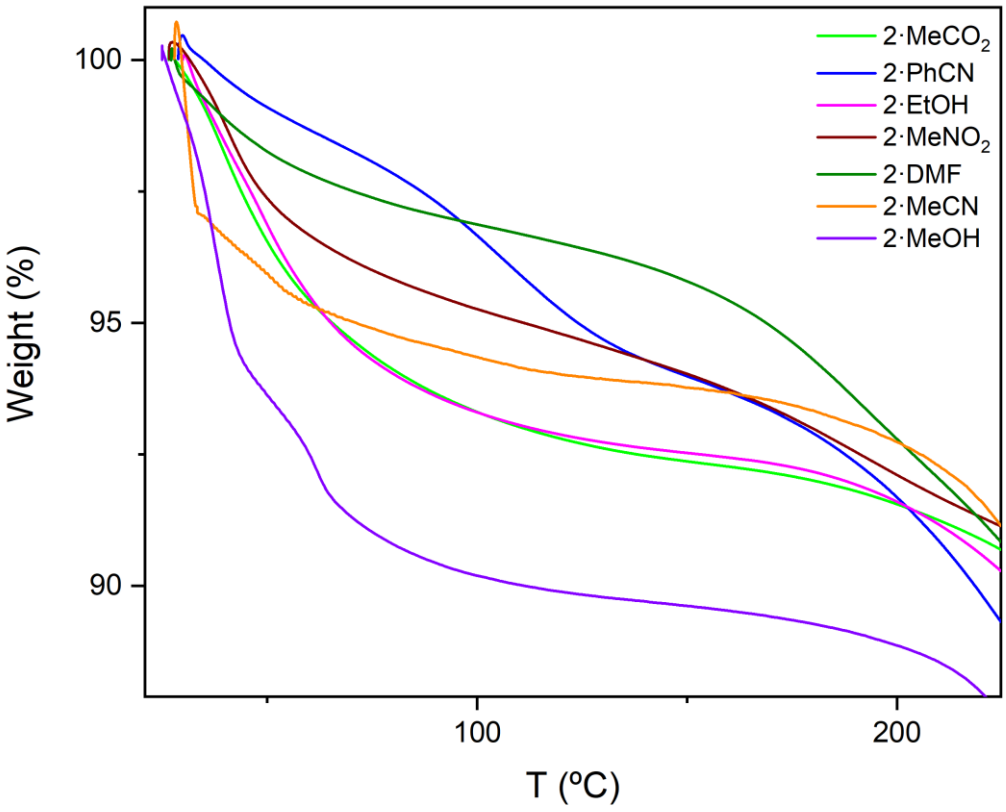

Fig. S12 Thermogravimetric analysis of **2·DMF, 2·MeCN, 2MeOH, 2MeNO$_2$, 2·EtOH, 2·PhCN** and **2·Me$_2$CO**.

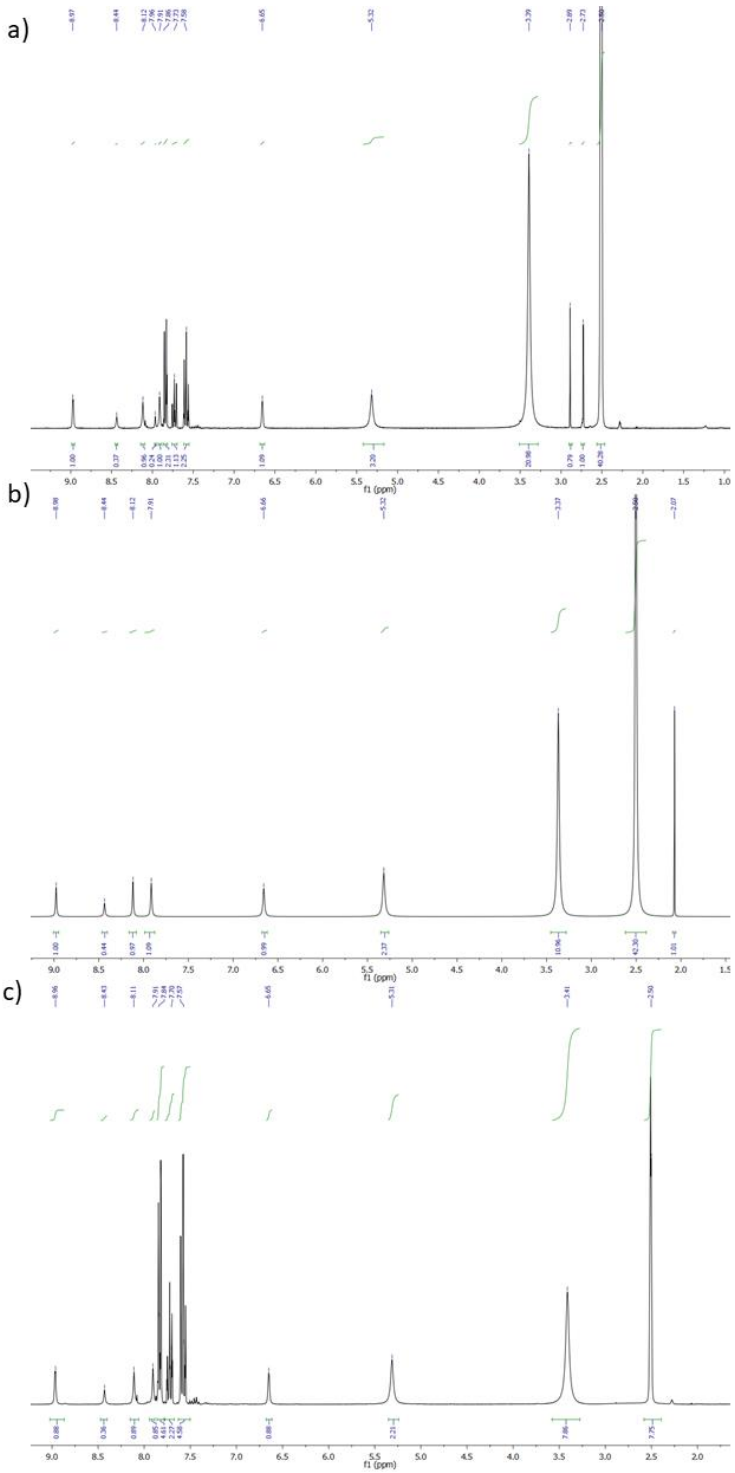
a)
b)
c)
f1 (ppm)

d)

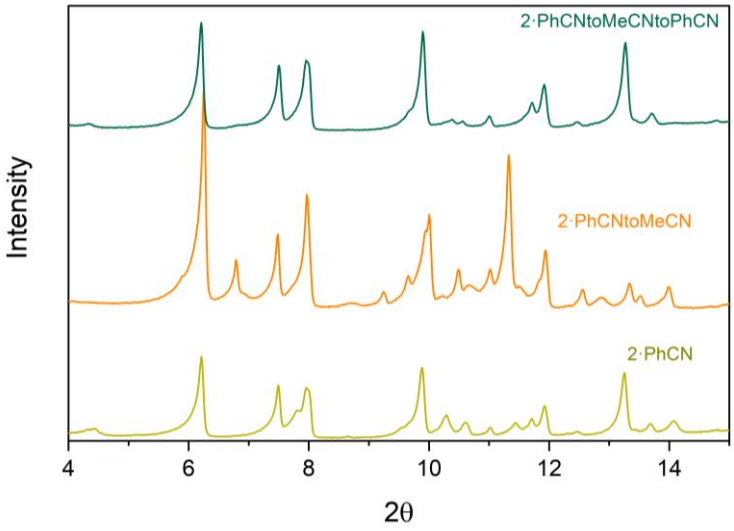

e)

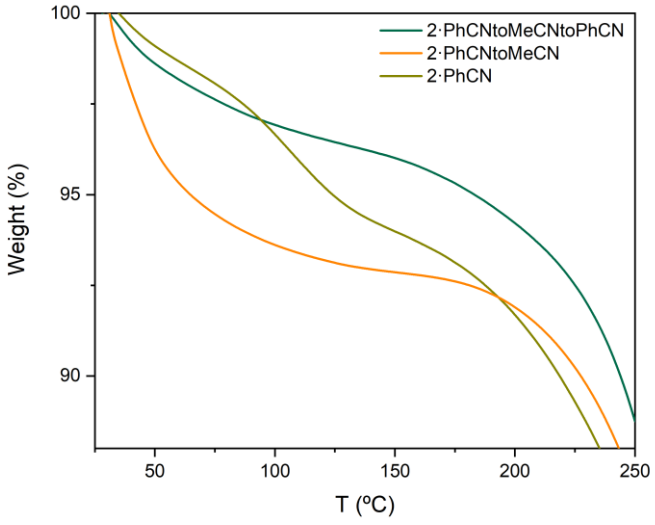

Fig. S13. ^{1}H NMR of freshly filtered crystals of **2·PhCN** (a), **2·PhCNtoMeCN** (b) and **2·PhCNtoMeCNtoPhCN** (c). PXRD of the same samples measured in contact with the mother liquor (d), Thermogravimetric analysis of the same samples (e).

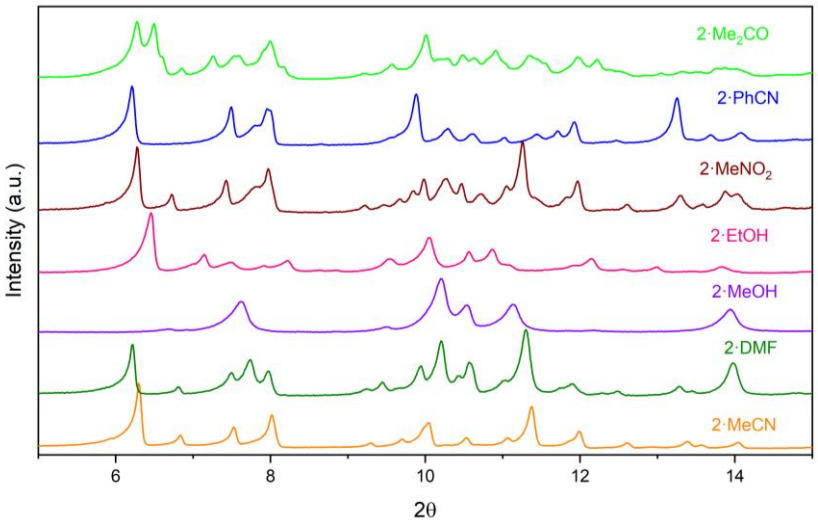

Fig. S14 PXRD patterns of **2·DMF, 2·MeCN, 2·MeOH, 2·MeNO2, 2·EtOH, 2·PhCN, 2·Me_2CO.**

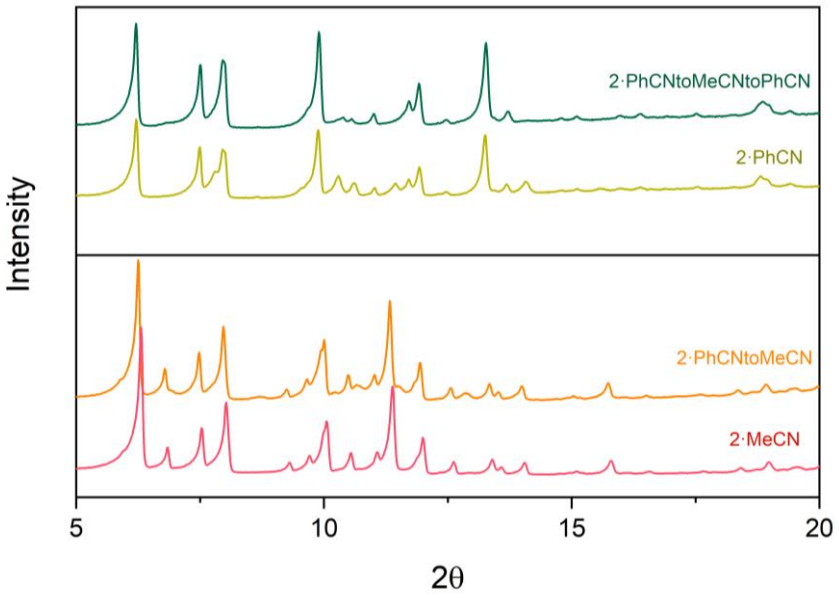

Fig. S15 PXRD patterns comparing structural similarities between **2·MeCN** and **2·PhCNtoMeCN** (bottom) and between **2·PhCN, 2·PhCNtoMeCNtoPhCN** (top).

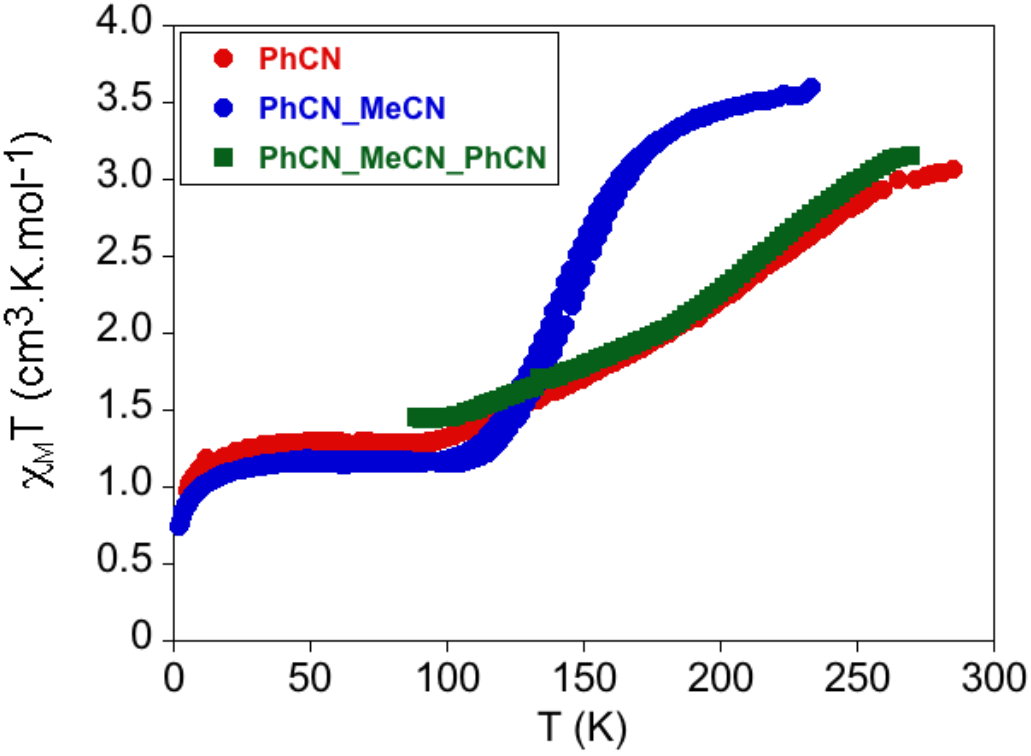

Fig. S16. Thermal variation of $\chi_M T$ of **2·PhCN**, **2·PhCNtoMeCN** and **2·PhCNtoMeCNtoPhCN**.

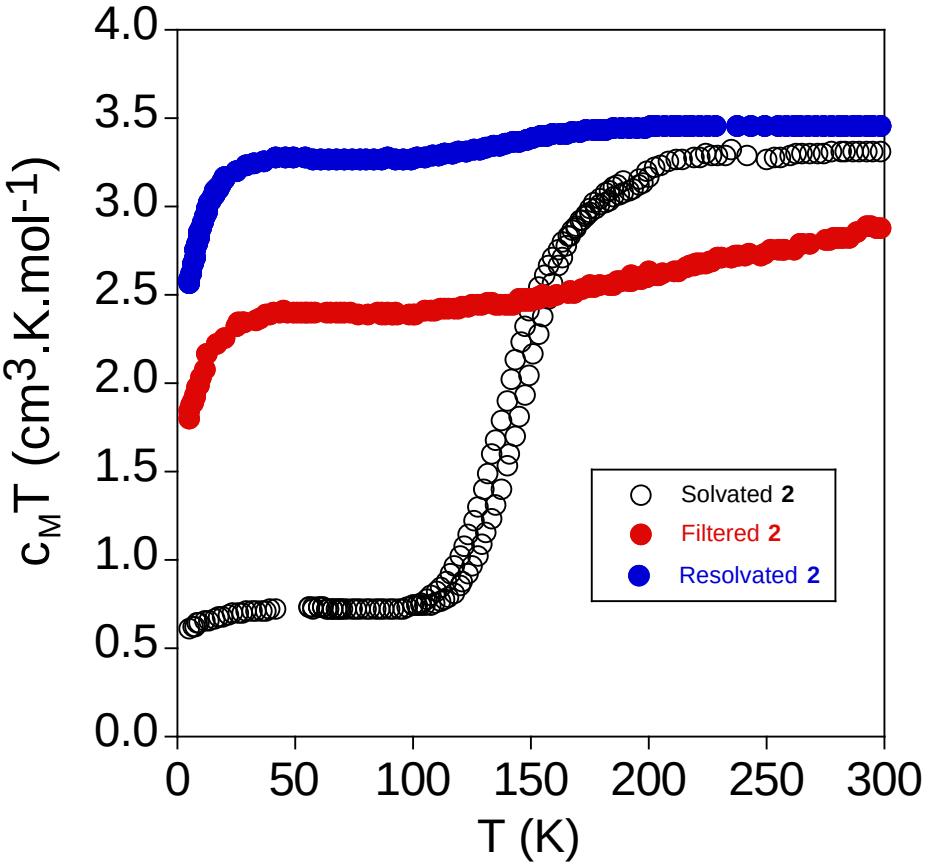

Fig. S17 Thermal variation of $\chi_M T$ of **2·MeCN**. Empty circles: Crystals in contact with the mother liquor; full red circles: Dried crystals after filtering; full blue circles: Dried crystals reimmersed in MeCN.

The Mössbauer spectra (Fig. S18) taken at 200 K and below are fitted with three quadrupole doublets (Table S3). The doublet with lower isomer shift relative to metallic αFe at 298 K, IS, and lower quadrupole splitting, QS, (Table S3) is consistent with LS, Fe^{II} (S=0).,[10,11] The doublets with higher IS and QS are typical of HS, Fe^{II} (S=2). The presence of two doublets for HS Fe^{II} may be related to the presence of two phases with different solvation degree. The relative areas of the LS and HS doublets do not change significantly in the range 4 - 200 K the fraction of LS Fe^{II} being approximately 37%.

If a spectrum of this same sample is taken in vacuum at room temperature, the spectrum accumulation starting after keeping the sample in vacuum at 295 K for one day, the fraction of LS Fe^{II} decreases down to approximately 17% (Fig. S19, Table S3). Most probably the sample is desolvated, which stabilizes the HS state. Furthermore, low temperature spectra of this sample indicate that no spin-crossover occurs in the 4 - 295 K temperature range.

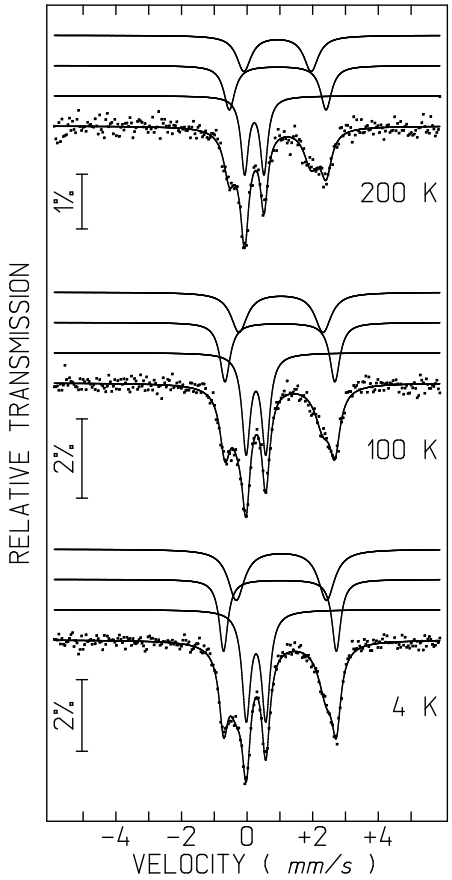

Fig. S18 Mössbauer spectra taken at different temperatures of freshly filtered crystals of **2**.

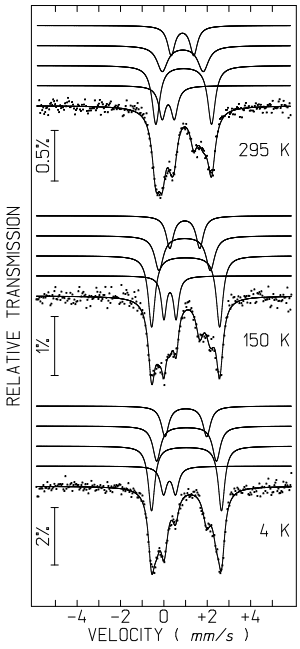

Fig. S19 Mössbauer spectra taken at different temperatures of **2** after being in vacuum for one day at 295 K.

Table S3. Estimated parameters from the Mössbauer spectra of **2** taken at different temperatures T.

	T	IS	QS, ε	Fe^{II} spin	I
Fresh filtered crystals of **2**	200 K	0.33 1.05 1.04	0.59 2.95 2.05	LS HS HS	36% 31% 33%
	100 K	0.38 1.11 1.15	0.60 3.35 2.56	LS HS HS	38% 30% 32%
	75 K	0.39 1.11 1.15	0.60 3.40 2.66	LS HS HS	37% 30% 33%
	4 K	0.39 1.11 1.16	0.59 3.44 2.75	LS HS HS	38% 27% 35%
desolvated sample under vacuum at 295 K	295 K	0.31 1.03 0.98 0.97	0.56 2.57 1.89 1.04	LS HS HS HS	18% 39% 24% 19%
	150 K	0.40 1.12 1.08 1.08	0.55 3.17 2.33 1.38	LS HS HS HS	17% 39% 25% 19%
	4 K	0.31 1.15 1.16 1.13	0.55 3.22 2.75 1.92	LS HS HS HS	15% 38% 25% 21%

IS (mm/s) isomer shift relative to metallic α-Fe at 295 K; QS (mm/s) quadrupole splitting; Γ (mm/s) full width at half maximum; I relative area. Below 250 K estimated errors $\leq$ 0.02 mm/s for IS, QS, Γ and <4% for I.

5. General characterization of Red 2, Red 3, Reox 2 and Reox 3

(a)

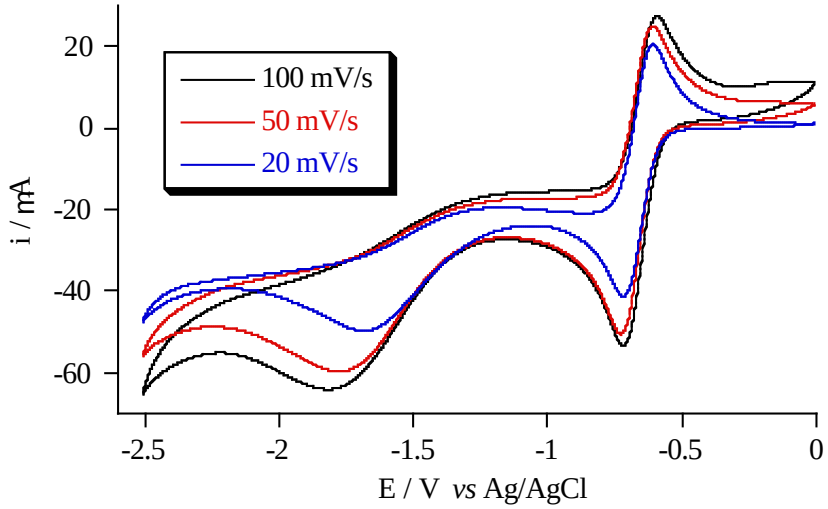

(b)

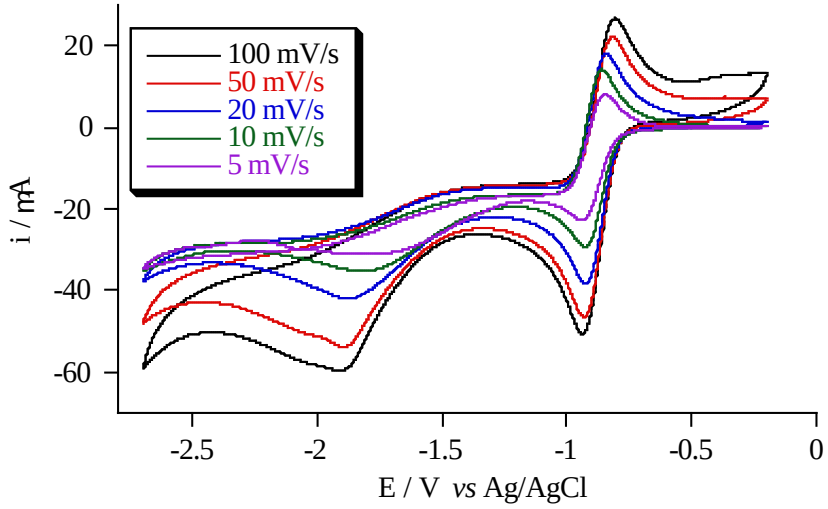

(c)

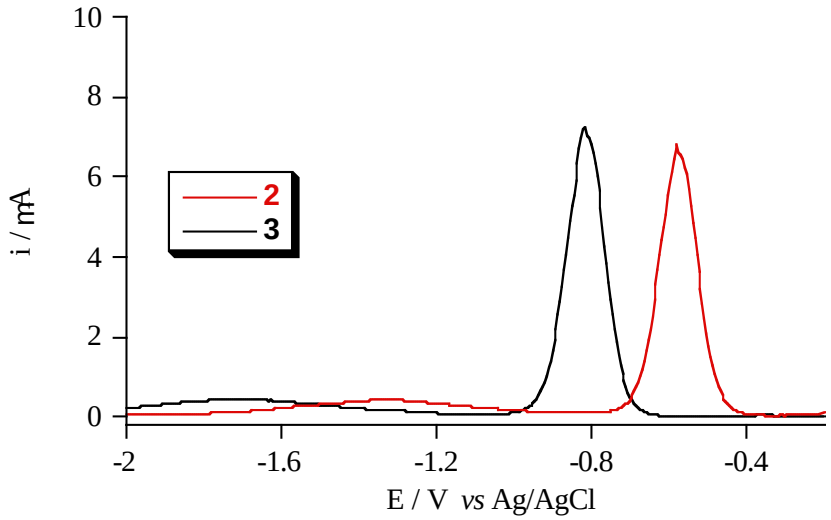

(d)

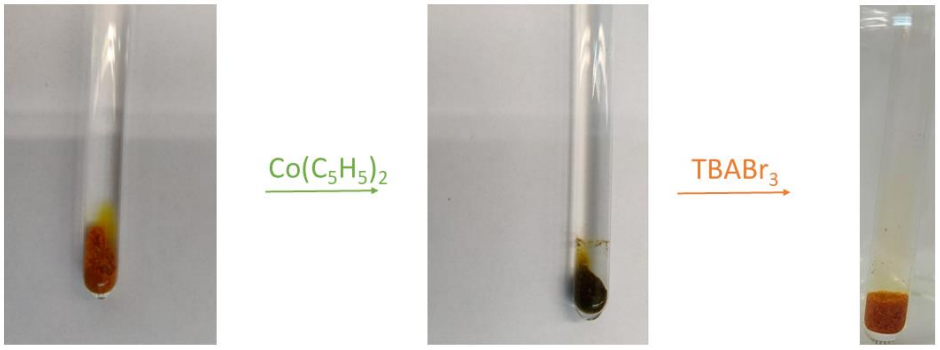

Fig. S20 Cyclic voltammetric behavior of **2** (a) and **3** (b) and differential pulse voltammograms of **2** (red line) and **3** (black line) (c). Crystals of **2** (left) and **red 2** (right) (d) Pictures of crystals of **2·MeCN**, **Red 2** and **Reox 2.**

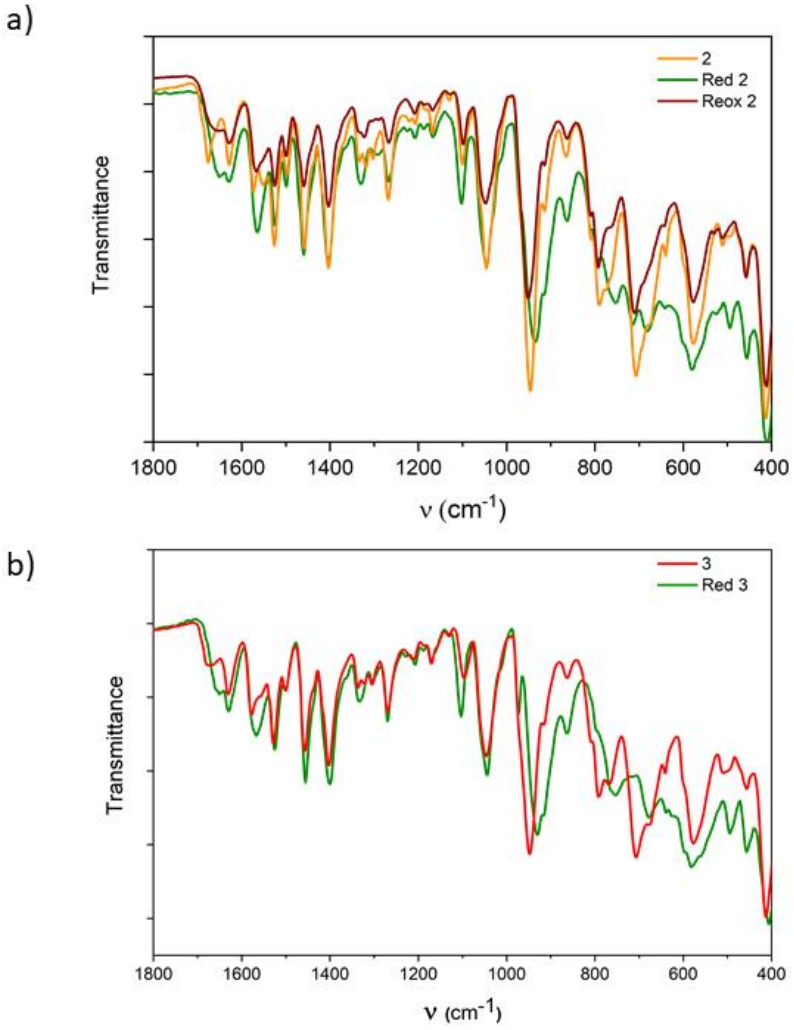

Fig. S21 (a) IR spectra of **2·MeCN, Red 2** and **Reox 2**; (b) IR spectra of **3·MeCN**, **Red 3 and** Reox 3.

IR spectra of **2·MeCN** and **3·MeCN** show the characteristic stretching vibrations of the fully oxidized hexavanadate cage at ca. 950 (νV=O) and 790 cm^{-1} (νV–O–V). These bands are shifted to a lower energy for **Red 2** and **Red 3** samples (ca. 930 cm^{-1} (νV=O) and 755 cm^{-1} (νV–O–V), see Fig. **S21**). These changes are reversible as these bands are again shifted to higher energies upon reoxidation in **Reox 2** sample (950 cm^{-1} (νV=O) and

790 cm^{-1} (νV–O–V), see Fig. S21). A similar trend has been reported in the stretching νV=O band of fully alkylated hexavanadate derivatives. This has been attributed to the smaller positive charge on the vanadium atoms in the reduced species, which diminishes the polarity of the bonds to the respective terminal oxygen atoms thus shifting to lower frequencies upon reduction of the cluster.[12] On the other hand, similar values of the νV–O–V band upon reduction have been reported for coordination polymers formed by bis(pyridyl)-capped hexavanadate linked to divalent first-row transition-metal ions. [13]

Control experiments were performed soaking crystals of **3·MeCN** in ferrocene or decamethylferrocenium tetrafluoroborate MeCN solutions. EDAX analysis of these samples indicated the absence of iron from ferrocene or decamethylferrocenium. This confirms that reduction of hexavanadate by cobaltocene is a necessary condition for the entrance of cobaltocenium countercations in the structure of **3**, since ferrocene, which is a weaker reducing agent,[14] or decamethylferrocenium, which is a cationic oxidant with a similar structure to that of colbaltocenium, do not enter in the structure in similar synthetic conditions.

High resolution XPS spectra of **2·MeCN** and **3·MeCN** present two characteristic peaks centered at 516.2 (2p3/2) and 523.5 eV (2p1/2) for **2·MeCN** and at 517.1 (2p3/2) and 524.6 eV (2p1/2) for **3·MeCN**, which are characteristic of V(V) (see Figs. S22 and S24).[15] XPS spectra of **Red 2** and **Red 3** show an increase of peak width indicative of a mixture of V(IV) and V(V), which could be fitted to a minor contribution at 515.3 (2p3/2) for **Red 2** and at 516.2 (2p3/2) for **Red 3**, assigned to V(IV), and to a major contribution at 516.5 (2p3/2) for Red 2 and at 517.3 (2p3/2) for **Red 3**, assigned to V(V) (see Figs. S23 and S25). High resolution XPS spectra of the reoxidized sample could be fitted at electron binding energies of at 517.3 (2p3/2), assigned to V(V). Finally, XPS Br 3d spectra was used to determine the Br species present in **Reox 2**. This sample displays broad peaks indicating a mixture of polybromide species (component centered at ~69.5 eV)[15c].

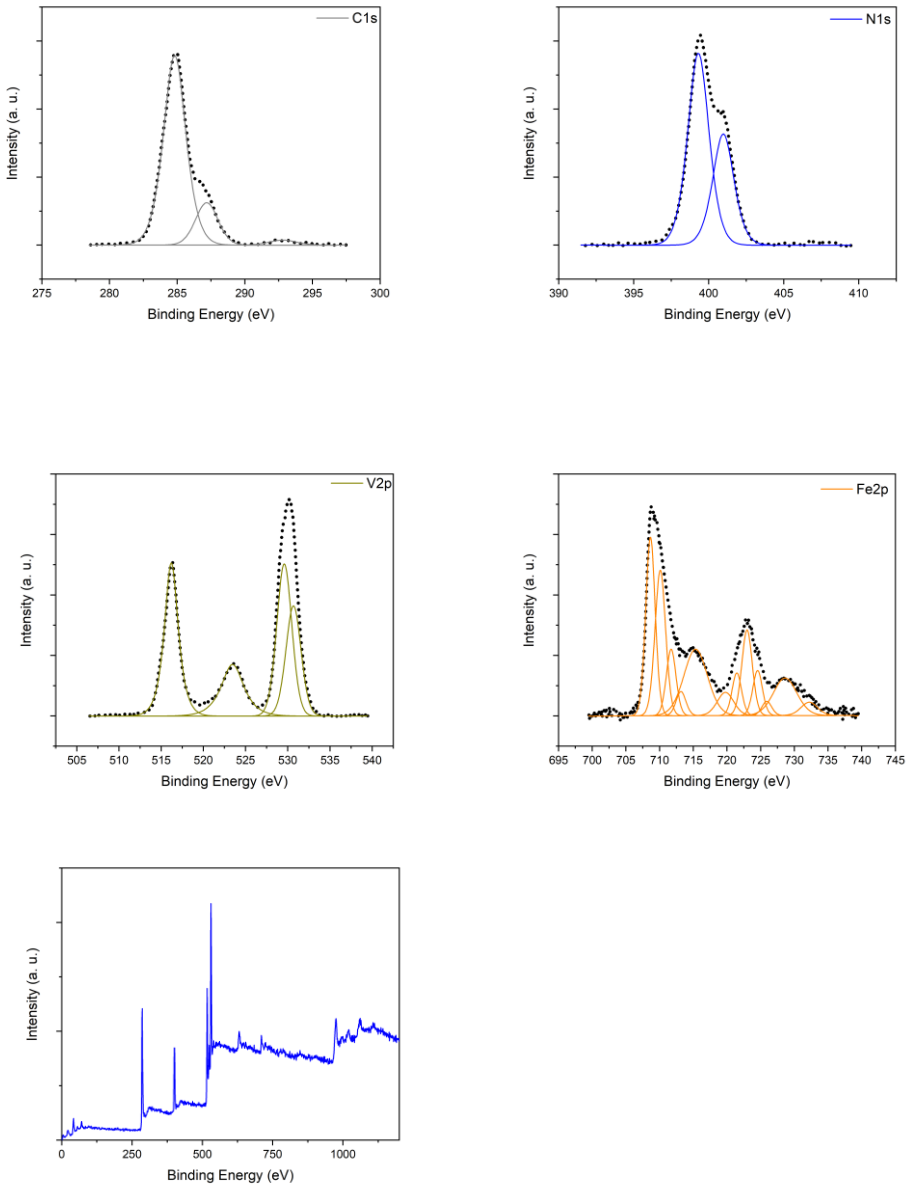

Fig. S22 XPS of **2·MeCN**

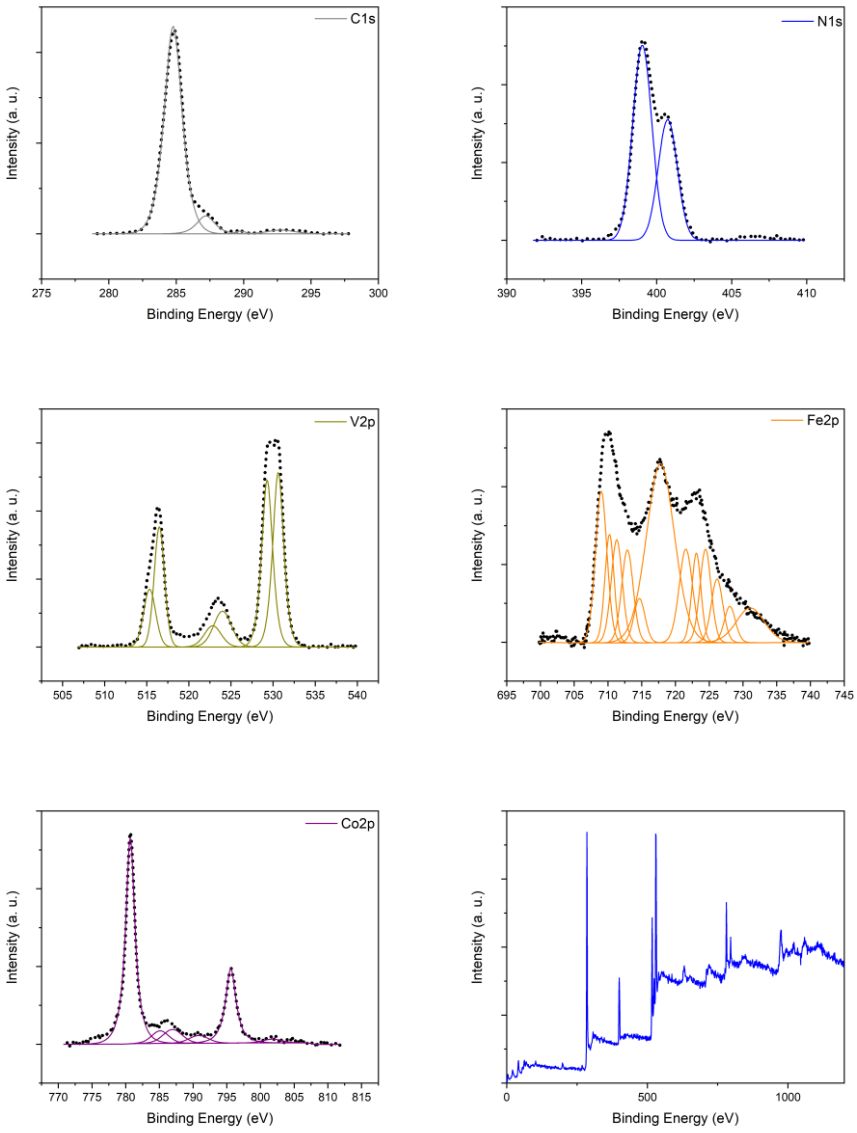

Fig. S23 XPS of **Red 2**

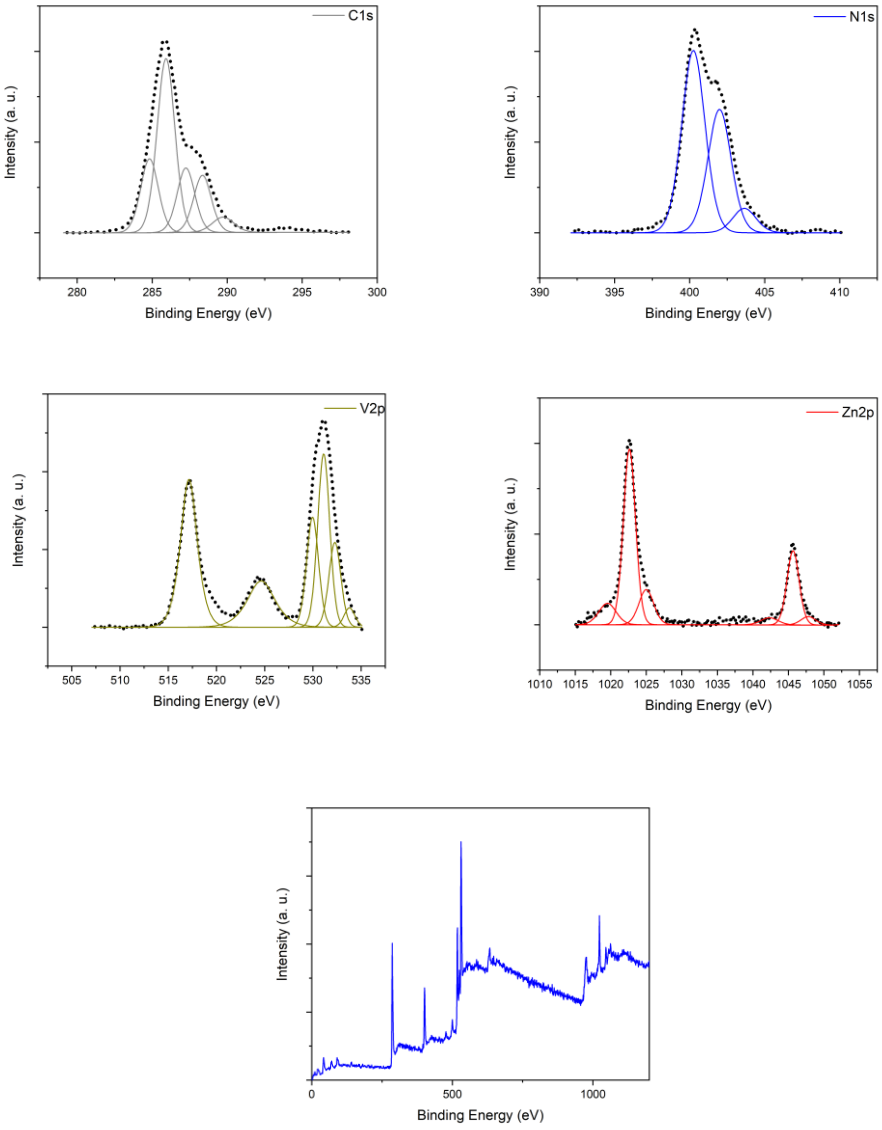

Fig. S24 XPS of **3·MeCN**

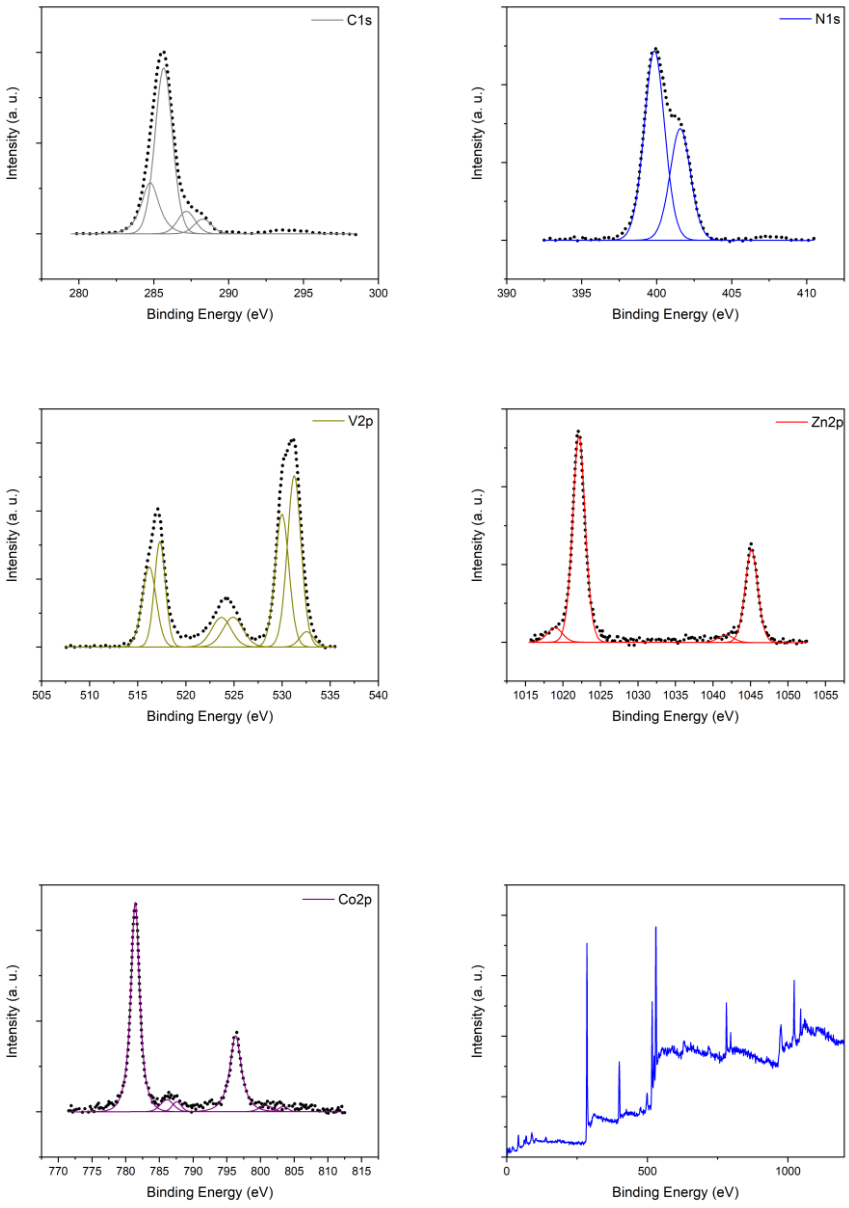

Fig. S25 XPS of **Red 3**

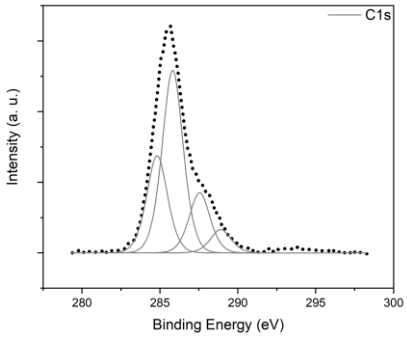
C1s
Intensity (a. u.)
280
285
290
295
300
Binding Energy (eV)

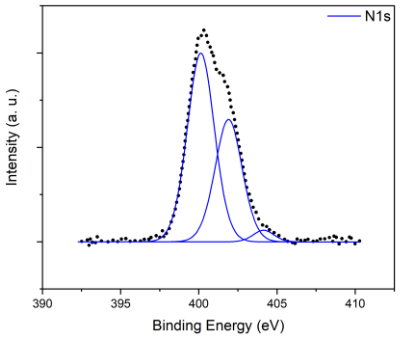
N1s
Intensity (a. u.)
390
395
400
405
410
Binding Energy (eV)

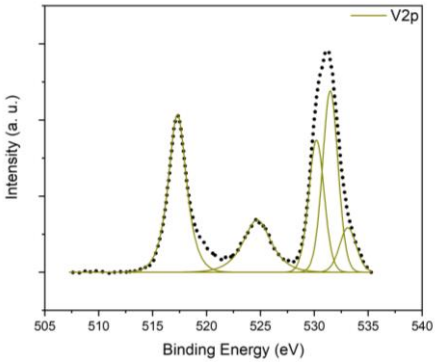
V2p
Intensity (a. u.)
505
510
515
520
525
530
535
540
Binding Energy (eV)

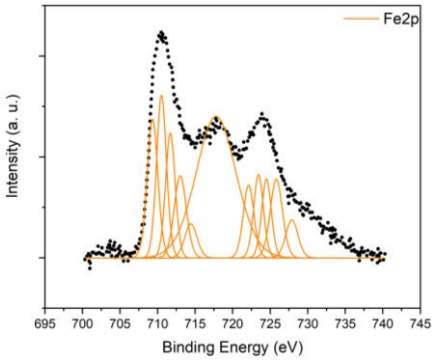
Fe2p
Intensity (a. u.)
695
700
705
710
715
720
725
730
735
740
745
Binding Energy (eV)

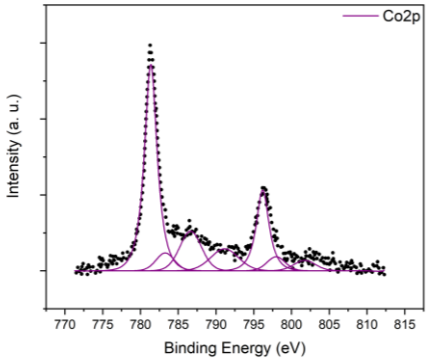
Co2p
Intensity (a. u.)
770
775
780
785
790
795
800
805
810
815
Binding Energy (eV)

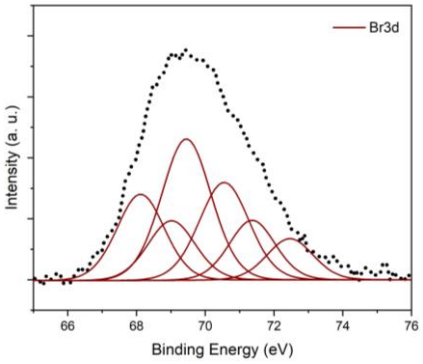
Br3d
Intensity (a. u.)
66
68
70
72
74
76
Binding Energy (eV)

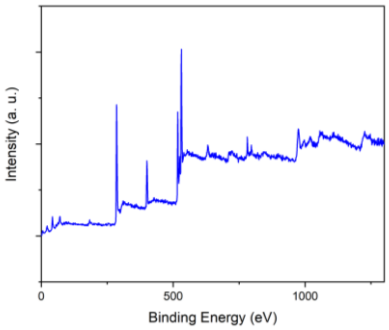

Fig. S26 XPS of **Reox 2**

a)

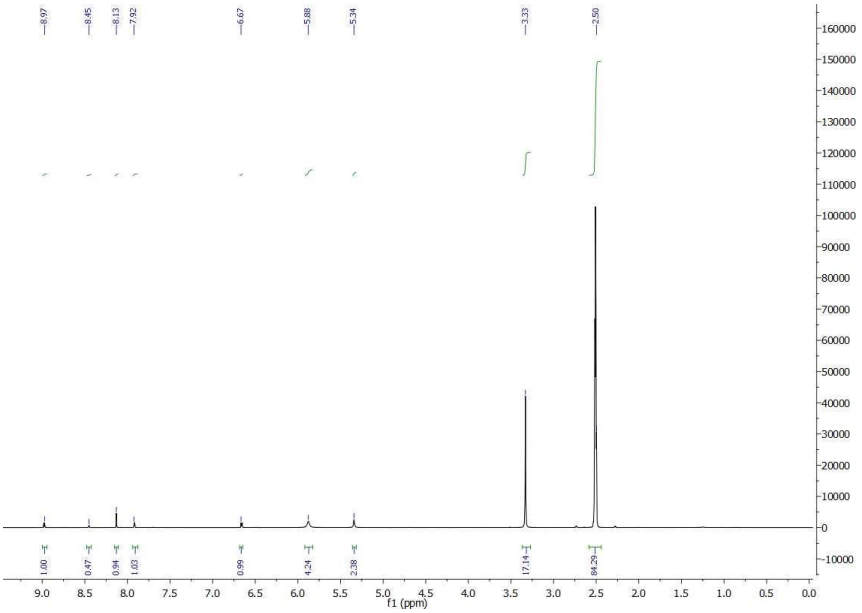
8.97
8.45
8.13
7.92
6.67
5.88
5.34
3.33
2.50
1.00
0.47
0.94
1.03
0.99
4.24
2.38
17.14
84.29
f1 (ppm)

b)

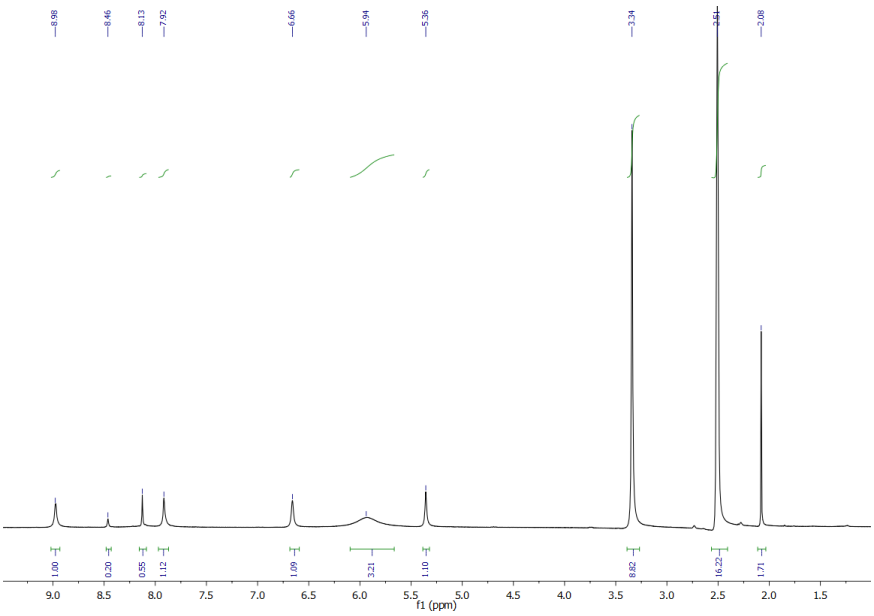
8.98
8.46
8.13
7.92
6.66
5.94
5.36
3.34
2.61
2.08
1.00
0.20
0.55
1.12
1.09
3.21
1.10
8.82
16.22
1.71
f1 (ppm)

c)

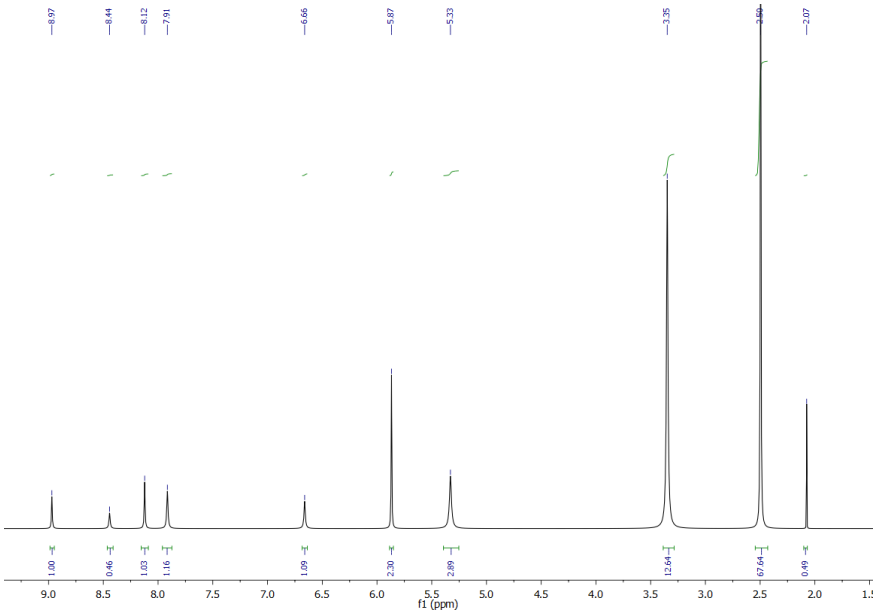

Fig. S27 ^{1}H NMR spectra of crystals of **Red 2** (a) **Red 3** (b) and **Reox 2** (c) in dimethyl disulfoxide-d_6

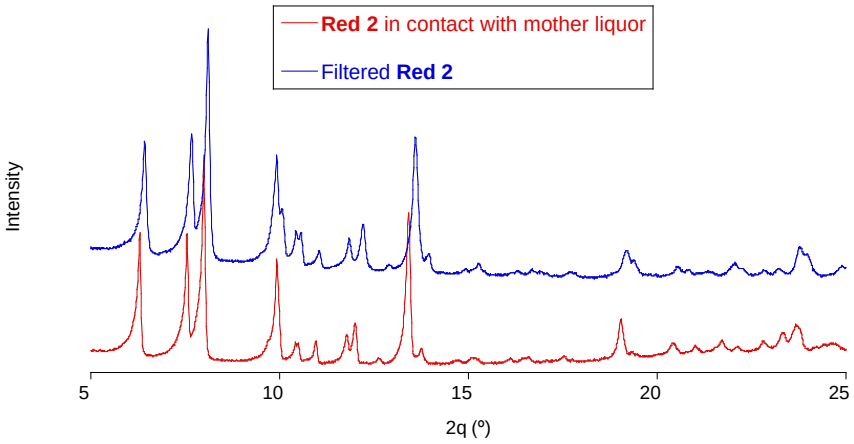

Fig. S28 PXRD patterns of **Red 2** measured in contact with the mother liquor (red line) and a dried sample of filtered crystals of **Red 2** (blue line).

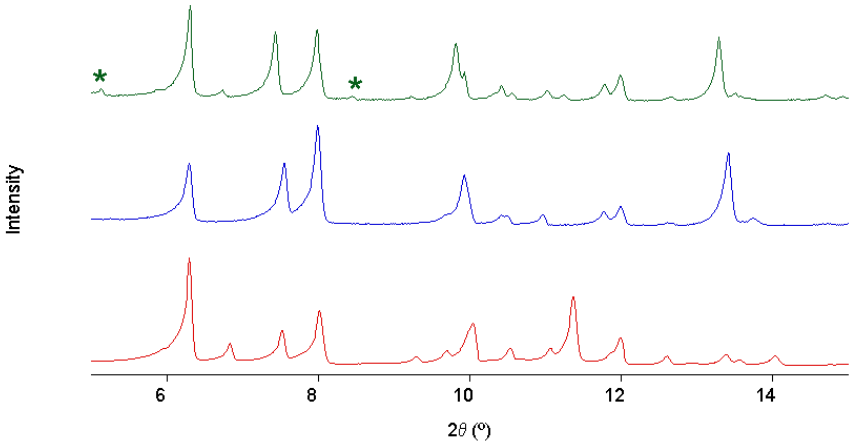

Fig. S29 PXRD patterns of **2·MeCN** (red line), **Red 2** (blue line) and **Reox 2** (green line) measured in contact with the mother liquor.

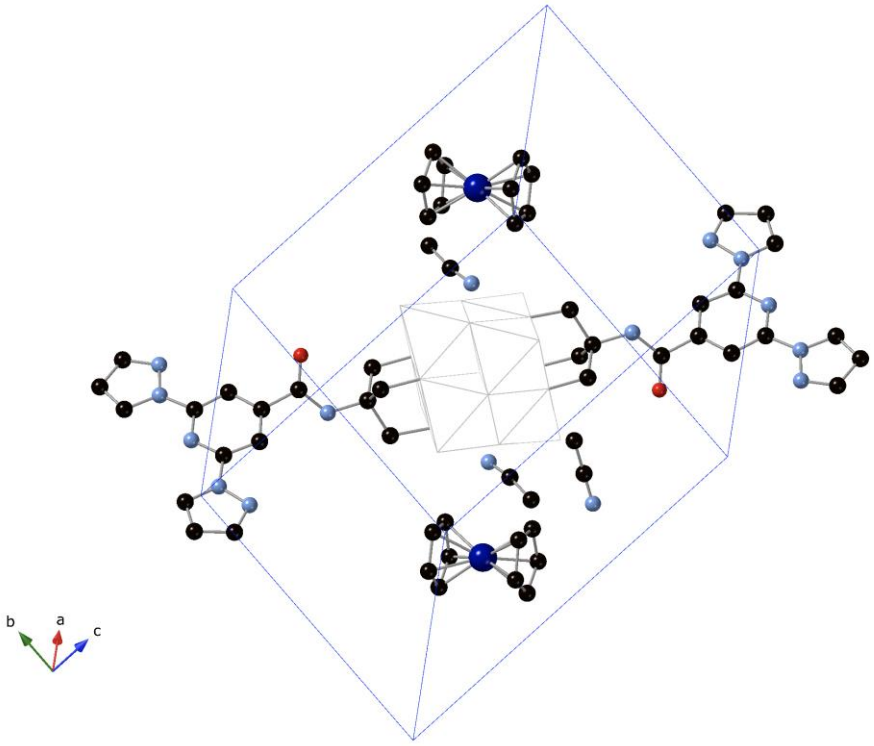

Fig. S30 Structure of $[Co(C_5H_5)_2]_2[V_6O_{19}(C_{16}H_{15}N_6O)_2]\cdot MeCN$ (Co (dark blue), V (white), C (black), N (blue), O (red)). Hydrogen atoms have been omitted for clarity.

Red crystals of $[Co(C_5H_5)_2]_2[V_6O_{19}(C_{16}H_{15}N_6O)_2]\cdot MeCN$ were obtained as a minority product from crystals of **Red 3** placed in a solution of $TBABr_3$ in MeCN for several days

Table S4. Crystal data and structure refinement for $[Co(C_5H_5)_2]_2[V_6O_{19}(C_{16}H_{15}N_6O)_2]\cdot MeCN$.

Empirical formula	$C_{30}H_{32}CoN_8O_{10.5}V_3$
Formula weight	884.38
Temperature/K	120.00(10)
Crystal system	triclinic
Space group	P-1
a/Å	9.8603(3)
b/Å	12.1228(4)
c/Å	17.2505(4)
α/°	79.422(2)
β/°	80.163(2)
γ/°	76.369(3)
Volume/Å^3	1952.25(10)
Z	2
ρ_{calc}g/cm^3	1.504
μ/mm^{-1}	1.175
F(000)	896.0
Crystal size/mm^3	0.38 × 0.31 × 0.11
Radiation	MoKα (λ = 0.71073)
2Θ range for data collection/°	5.958 to 59.792
Index ranges	-13 ≤ h ≤ 13, -16 ≤ k ≤ 16, -22 ≤ l ≤ 24
Reflections collected	37801
Independent reflections	10216 [R_{int} = 0.0538, R_{sigma} = 0.0601]
Data/restraints/parameters	10216/3/476
Goodness-of-fit on F^2	1.058
Final R indexes [I>=2σ (I)]	R_1 = 0.0729, wR_2 = 0.2192
Final R indexes [all data]	R_1 = 0.1093, wR_2 = 0.2514
Largest diff. peak/hole / e Å^{-3}	1.95/-0.57

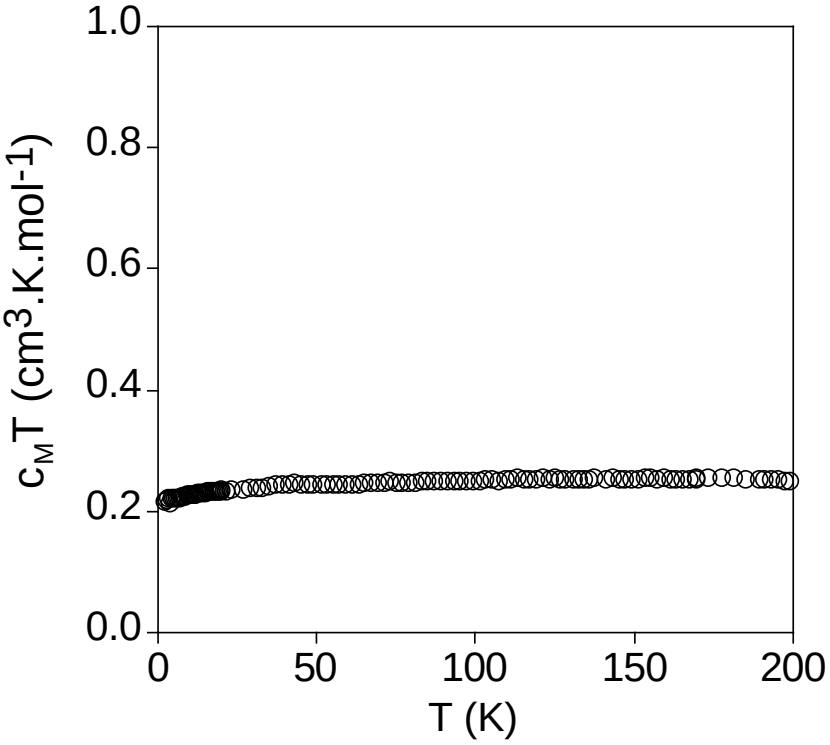

Fig. S31 Thermal variation of $\chi_M T$ of **3** measured in contact with the mother liquor.

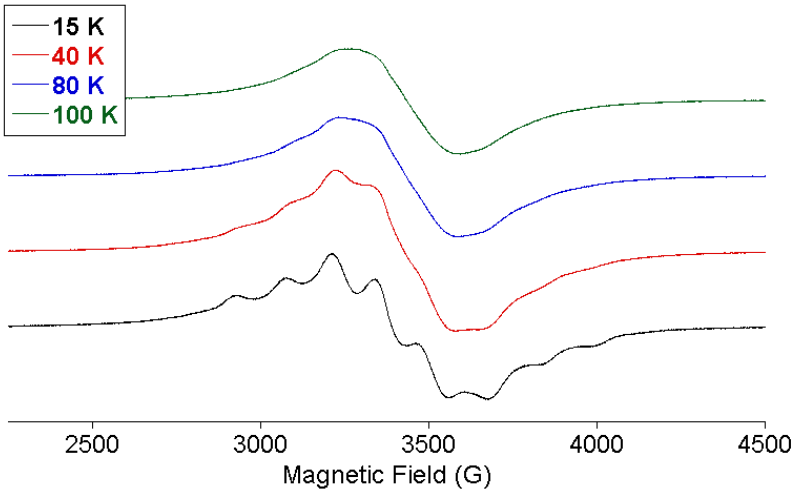

Fig. S32 EPR spectra of **Red 3** measured in contact with the mother liquor.

EPR spectra are completely different to those of cobaltocene in diluted diamagnetic matrices[16] confirming the absence of residual Cobaltocene and the oxidation state III of the inserted cobaltocenium cations. This is confirmed by measurements of the filtered samples in contact with air, in which cobaltocene is not stable, which are similar to those of **2** and **3** samples measured in contact with the mother liquor.

6. References

[1] V. W. Day, W. G. Klemperer and D. J. Maltbie, *J. Am. Chem. Soc.,* 1987, **109**, 2991-3002.

[2] A. Abhervé, M. Palacios-Corella, J. M. Clemente-Juan, R. Marx, P. Neugebauer, J. van Slageren, M. Clemente-León and E. Coronado, *J.Mater.Chem.C*, 2015 , **3**, 7936-7945.

[3](a)G. M. Sheldrick, *Acta Cryst.,* 2015, **A71**, 3;(b)G. M. Sheldrick, *Acta Cryst.,* 2015, **C71**, 3;(c)O. V. Dolomanov, L. J. Bourhis, R. J. Gildea, J. A. K. Howard and H. Puschmann, *J. Appl. Cryst.,* 2009, **42**, 339;(d) G. S. Pawley, *J. Appl. Crystallogr*., 1981, **14**, 357-361; (d) J. Spek, *Appl. Cryst.,* 2003, **36**, 7

[4] A. A. Coelho, TOPAS–Academic, Version 4.1, 2007, see http://www.topas-academic.net.

[5] G. J. Long, T. E. Cranshaw, G. Longworth, *Mossb. Effect. Ref. Data J.*, 1983, **6**, 42.

[6] J.C. Waerenborgh, P. Salamakha, O. Sologub, A.P. Gonçalves, C. Cardoso, S. Sério, M. Godinho, M. Almeida, *Chem. Mater.* 2000, **12**, 1743-1749

[7] M. P. Santoni, A. K. Pal, G. S. Hanan, A. Proust, B. Hasenknopf, *Inorg. Chem.* 2011, **50**, 6737-6745.

[8] Q. Chen, D. P. Goshorn, C. P. Scholes, X.-L. Tan, J. Zubieta, *J. Am. Chem. Soc.* 1992, **114**, 4667-4681.

[9] E. F. Wilson, H. N. Miras, M. H. Rosnes, L. Cronin, *Angew. Chem. Int. Ed.* 2011, **50**, 3720-3724.

[10] Gütlich, P.; Garcia, Y.; Goodwin, H. A. *Chem. Soc. Rev.* 2000, **29**, 419-427.

[11] Greenwood,N.N., Gibb,T.C. "Mössbauer Spectroscopy" Chapman and Hall, Ltd. Publishers, London (1971).

[12] C. Daniel and H. Hartl, J. Am. Chem. Soc., 2005, **127**, 13978.

[13] J. W. Han, K. I. Hardcastle and C. L. Hill, Eur. J. Inorg. Chem., 2006, **2006**, 2598.

[14] N. G. Connelly and W. E. Geiger, Chem. Rev., 1996, **96**, 877.

[15] (a) J. K. Li, X. Q. Huang, S. Yang, H. W. Ma, Y. N. Chi and C. W. Hu, *Inorg. Chem.,* 2015, **54**, 1454; (b) X. Hu, Z. Xiao, B. Huang, X. Hu, M. Cheng, X. Lin, P. Wu and Y. Wei, *Dalton Trans.*, 2017, **46**, 8505;(c) L.G. Bulusheva, E.V. Lobiak, Y.V. Fedoseeva, J.-Y. Mevellec, A.A. Makarova, E. Flahaut and A.V. Okotrub, *Synth. Met.,* 2020, **259**, 116233.

[16] J. L. Robbins, N. Edelstein, B. Spencer and J. C. Smart, *J. Am. Chem. Soc.* 1982, **104**, 1882.

Chapter 6.

Conclusions and Perspectives.

This thesis has been focused on molecular magnetic multifunctional materials. It represents an effort to improve the understanding over multifunctional molecular magnetic materials through the use of a variety of functional building blocks (including bimetallic magnetic networks based on oxalate and anilate ligands, spin crossover complexes and POMs) and their characterization with state-of-the art techniques. Two main approaches to succeed in this quest were employed: the first of them involved the combination of two ionic networks to give rise to two-network neutral materials; and in the second approach, covalent bonds were used to prepare one-network materials formed by two molecular building blocks.

Regarding the first approach, in chapter 2 we reported the synthesis of four novel 2-D extended networks as a result of the combination of salts of anilate-metal complexes and templating ammonium cations of formula $(C_vN_yH_z)_3Cr(C_6O_4X_2)_3$ (X =Cl, Br) ($C_vN_yH_z$ = $Me_2NH_2^+$, $Et_2NH_2^+$, Et_3NH^+ and $[(Et)(i\text{-}Pr)_2NH]^+$) with Mn^{2+}. The resulting neutral networks showed a hexagonal honeycomb like structure, of general formula $(C_vN_yH_z)MnCr(C_6O_4X_2)_3$ with the cations inserted in the hexagonal channel. The size of the cations proved to be a differentiating factor in the differently assembled 2D networks. Smaller cations, such as methyl, diethyl or triethylammonium were found inserted within the channels in the hexagonal layers; while in the case of the bigger sized diisopropilethylammonium, the cations could be also found between the layers. Such differences in the placement of the cations led to interesting solvate dependent metamagnetic properties of the latter, while the rest of the 2D materials order ferrimagnetically below 9 K, values very similar to those reported already for this kind of networks. These materials also showed moderate proton conduction values comparable to those of bimetallic oxalate-based compounds containing acidic cations without reaching the best values of these systems. They were the first anilate-based materials reported in literature to show coexistence of proton conductivity and magnetic ordering. Possible

strategies to improve these two properties and enhance the synergy among them are increasing the magnetic interactions and the enhancement of the interlayer and intralayer transport trough the proton carriers. These goals could be achieved reducing the ligand of the compounds, using other acidic cations that have given the best results with oxalate-based networks (ammonium cations containing carboxylic acidic substituents) or with the homometallic anilate-based compounds reported in the literature containing partially reduced anilate ligands, since they show relatively high magnetic ordering temperatures (~100 K) and an eclipsed disposition of the layers and double number of proton carriers. However, they present stability problems in contact with air. Additional advantages of the heterometallic compounds prepared in this work are related to the neutral character of the anilate-based layers due to the presence of the countercations into the hexagonal channels of the 2D network of the structure. This opens interesting perspectives for the exfoliation of single magnetic layers of these compounds which could be incorporated in nanodevices for sensing.

Chapter 3 can be understood as a continuation of the methodology followed in Chapter 2, but in this case with the aim to combine a single-molecule magnet with a ferromagnetic network. In chapter 3 we synthesized two novel different cobalt complexes that behave as single molecule magnets. These molecules crystallized as 1:1 and 1:2 Co:L ((L = 6-(3,5-Diamino-2,4,6-triazinyl)2,2'-bipyridine)) cationic complexes when stoichiometric amounts of the ligand were added to the metal salt. Combination of the 1:2 complex with an oxalate network gave rise to a 3-D achiral coordination polymer of formula $[Co^{II}(L)_2][Mn^{II}Cr^{III}(ox)_3]_2\cdot$(solvate), where the cations are inserted in the 3-D channels. This hybrid material showed the typical ferromagnetic ordering coming from the bimetallic network, combined with the paramagnetism coming from the Co(II) moiety. X-band EPR measurements suggested that a small interaction between the two magnetic sublattices exists due to the insertion of the

magnetic cation in the channels. Magnetic measurements at lower temperatures are needed to verify if these weak magnetic interactions could cause an increase of the coercive field with respect to similar networks with less anisotropic magnetic inserted cations. These results showed that the intermolecular interactions between the inserted cation and the ferromagnetic network could play a crucial role in the magnetic exchange between the two magnetic subnetworks. They could be helpful in the design of new hybrid compounds in which these interactions are enhanced leading to improved magnetic properties. Possible strategies to reach this goal could be the combination of anilate-based networks, as they show higher magnetic ordering temperatures and magnetic properties more sensitive to the interlayer separation and inserted cation, and smaller Co(II) complexes, which could be placed into the pores as the compounds of chapter 2.

A different approach consisting on the covalent addition of a tridentate ligand to fullerene scaffolds allowed us to design and prepare hexakis-substituted [60]fullerene adducts of bpp in chapter 4. These macromolecules where successively combined with Fe(II), which afforded SCO molecules with up to 6 SCO complexes per fullerene. These were the first polynuclear SCO complexes based on [60]fullerene. Spectroscopic UV-VIS and fluorescence techniques were employed as a tool to determine the formation of the Fe(II) complexes. The variety of behaviors exhibited by the different fullerene adducts indicated that the spin state of Fe(II) of these species in solution could be tuned by a proper choice of the 1-bpp substituents. Indeed, some of them showed SCO properties in the bulk induced by temperature and light as external stimuli, with spin transitions that, although gradual, were sharper than those reported in mononuclear complexes based on [60]fullerene. This comprehensive study demonstrated that [60]fullerene hexa-adducts are excellent and versatile platforms to develop new SCO materials and provide an interesting alternative to study and prepare SAMs of

this tridentate ligand, a possibility that has remained unsuccessful due to the lability of these Fe (II) complexes. This may be of interest in molecular spintronics since a modulation of their spin properties by electrical or light stimuli once deposited may be possible.

Chapter 5 continues with the covalent approach by preparing a novel functional polyoxometalate, which incorporates 1-bpp to a well-known Lindqvist hexavanadate cluster. The bifunctionalized derivative $[V_6O_{19}(C_{16}H_{15}N_6O)_2]^{2-}$, was reacted afterwards with Fe(II) and Zn(II). Crystallization of the latter, with formula $Zn[V_6O_{19}(C_{16}H_{15}N_6O)_2]_2 \cdot solv$, allowed us to determine the structure, which is formed by 1-D polymeric chains where the polyoxometalates are linked to each other through the divalent metallic centre. Magnetic measurements on the isostructural Fe(II) derivative revealed a complete and abrupt spin transition with temperature for the first time in a POM. The organization of these SCO units in this neutral 1-D polymer afforded a flexible and stable structure, which enabled reversible exchange of solvents. This allowed tuning the abruptness and temperature of the thermal spin transition. On the other hand, the presence of the redox active POM units as spacer between the SCO units afforded a unique redox tuning capability to these materials, in contrasts with the electrically innocent inorganic or organic spacers used in other polymeric SCO materials. Thus, the chemical reduction and reoxidation of the POM was accompanied by the entrance or removal of reductant and oxidant species acting as counterions. This led to dramatic changes in their SCO properties, which were more drastic than those observed recently in other polymeric SCO compounds with redox-active organic linkers. Hence, we have prepared a rare type of versatile switching multifunctional material in which SCO properties of the Fe(II) complexes coexist with the redox properties of the POM and can be tuned by a variety of stimuli such as light, solvent exchange or redox. An interesting possibility that remained unexplored was to look for a synergy between the mixed-valence state of the reduced

POM and the switching capabilities of SCO center. This will be studied by conductivity measurements although this type of compounds usually display low conductivities. In this sense, an interesting perspective is to induce a closer electronic communication between the polyoxometalate center and the SCO complex than that provided by the tris-alkoxo-amide linking unit. A possible strategy could be to prepare functionalized POMs in which metallic ions from the POM moiety and the SCO ion share the same ligand. This could be achieved by the replacement of terminal oxo ligands by imido ligands.

In conclusion, the bottom-up approach employed during this thesis has demonstrated to be a very versatile way to obtain multifunctional materials.

Contributions to Scientific Journals

1. M. Palacios-Corella, J. Ramos-Soriano, M. Souto, Duarte Ananias, J. Calbo, E. Ortí, B. M. Illescas, M. Clemente-León, N. Martín and E. Coronado. ***Hexakis-Adducts of [60]Fullerene as Molecular Scaffolds of Polynuclear Spin-Crossover Molecules***, 2021, **12**, 757-766.

2. A. Terzopoulou, X. Wang, X.-Zhong Chen, M. Palacios-Corella, C. Pujante, J. Herrero-Martín, X.-Hua Qin, J. Sort, A. J deMello, B. J. Nelson, J. Puigmartí-Luis, S. Pané. ***Biodegradable Metal–Organic Framework-Based Microrobots (MOFBOTs)***. *Adv. Healthcare Mat.*, 2020, **55**, 2001031.

3. V. García-López, M. Palacios-Corella, S. Cardona-Serra, M. Clemente-Leon and Eugenio Coronado. ***Spin-crossover iron (II) complex showing thermal hysteresis around room temperature with symmetry breaking and an unusually high T (LIESST) of 120 K***. *Chem. comm*., 2019, **55**, 12227-12230.

4. V. García-López, M. Palacios-Corella, V. Gironés-Pérez, C. Bartual-Murgui, J. Antonio Real, E. Pellegrin, J. Herrero-Martín, G. Aromí*M. Clemente-León, Eugenio Coronado. ***Heteroleptic Iron(II) Spin-Crossover Complexes Based on a 2,6-Bis(pyrazol-1-yl)pyridine-type Ligand Functionalized with a Carboxylic Acid.*** *Inorg. Chem. 2019, **58,** 18,* 12199–12208.

5. J. de Bruijckere, P. Gehring, M. Palacios-Corella, M. Clemente-León, E. Coronado, J. Paaske, P. Hedegård, and H. S. J. van der Zant. ***Ground-state spin blockade in a single-molecule junction***. *Phys. Rev. Lett*., 2019, **122**, 197701.

6. V. García-López, M. Palacios-Corella, M. Clemente-León, E. Coronado. ***Fe (II) spin crossover complexes of a derivative of 2, 6-bis (pyrazol-1-yl) pyridine (1-bpp) functionalized with a carboxylic acid in the 3-pyridyl position***. *Polyhedron*, 2019, **170**, 95-100.

7. V. García-López, M. Palacios-Corella, A. Abhervé, I. Pellicer-Carreño, C. Desplanches, M.Clemente-Leon, E. Coronado. ***Spin-crossover compounds based on iron (II) complexes of 2,6-bis(pyrazol-1-yl)pyridine (bpp) functionalized with carboxylic acid and ethyl carboxylic acid***. *Dalton Trans*., 2018, **47**, 16958-16968.

8. V. García-López, M. Palacios-Corella, M. Clemente-León, E. Coronado. ***Iron (II) complex of 2-(1H-pyrazol-1-yl) pyridine-4-carboxylic acid (ppCOOH) suitable for surface deposition***. *J. Coord. Chem,* 2018. ***71,*** 763-775.

9. V. García-López, F.J. Orts-Mula, M. Palacios-Corella, J.M. Clemente-Juan, M. Clemente-León, E. Coronado, ***Field-induced slow relaxation of magnetization in a mononuclear Co (II) complex of 2,6-bis (pyrazol-1-yl) pyridine functionalized with a carboxylic acid*****.** *Polyhedron*, 2018, **150**, 54-60.

10. M. Palacios-Corella, A. Fernández-Espejo, M. Bazaga-García, E. R. Losilla, A. Cabeza, M. Clemente-León, E. Coronado. ***Influence of Proton Conducting Cations on the Structure and Properties of 2D Anilate-Based Magnets***. *Inorg. Chem*., 2017, **56**, 22.

11. A. Abhervé, M. Palacios-Corella, J. M. Clemente-Juan, R. Marx, P. Neugebauer, J. van Slageren, M. Clemente-León, E. Coronado. ***Bimetallic Mn^{III}–Fe^{II} hybrid complexes formed by a functionalized Mn^{III} Anderson polyoxometalate coordinated to Fe^{II}: observation of a field-induced slow relaxation of magnetization in the Mn^{III} centres and a photoinduced spin-crossover in the Fe^{II} centres***. *J. Mater. Chem. C*, 2015, **3**, 7936-7945.